Physical and numerical modeling of the dynamics of high-energy electrons trapped in the outer radiation belt of the Earth's magnetosphere

Vivien Loridan

université PARIS-SACLAY

DE LA RECHERCHE À L'INDUSTRIE
cea

école normale supérieure paris–saclay

NNT : 2018SACLN043

Thèse de doctorat

Physical and numerical modeling of the dynamics of high-energy electrons trapped in the outer radiation belt of the Earth's magnetosphere

Thèse de doctorat de l'Université Paris-Saclay
préparée au Commissariat à l'Énergie Atomique et aux Énergies Alternatives

École doctorale n°574 École Doctorale de Mathématiques Hadamard (EDMH)
Spécialité de doctorat: Mathématiques aux interfaces

Thèse présentée et soutenue à Cachan, le 17 Octobre 2018, par

VIVIEN LORIDAN

Composition du Jury :

Jean-Michel GHIDAGLIA École Normale Supérieure (ENS) Paris-Saclay	Président
Viviane PIERRARD Institut d'Aéronomie Spatiale de Belgique (BIRA-IASB)	Rapporteur
Benoit LAVRAUD Institut de Recherche en Astrophysique et Planétologie (IRAP)	Rapporteur
Yuri SHPRITS GeoForschungsZentrum (GFZ) Potsdam	Examinateur
Gregory CUNNINGHAM Los Alamos National Laboratory (LANL)	Examinateur
Daniel BOUCHE Commissariat à l'Énergie Atomique (CEA)	Examinateur
Florian DE VUYST École Normale Supérieure (ENS) Paris-Saclay	Directeur de thèse
Jean-François RIPOLL Commissariat à l'Énergie Atomique (CEA)	Directeur de thèse

à Mamita, à Nonno
à Zoé

Remerciements

Si vous cherchez votre nom, il se trouve (probablement) dans le paragraphe qui suit ! Les remerciements constituant généralement la partie la plus en vue du manuscrit de thèse pour la plupart d'entre vous, j'ai à coeur de mentionner tous ceux qui m'ont accompagné, de près ou de loin, dans cette aventure scientifique que représente la thèse de doctorat. Cette dernière s'est essentiellement déroulée au sein du Commissariat à l'Énergie Atomique (CEA), mais a également été jalonnée par de nombreux passages à l'École Normale Supérieure (ENS) de Cachan ainsi que par un séjour à Los Alamos, aux États-Unis.

Tout d'abord, je remercie chaleureusement Jean-François Ripoll, directeur de thèse au CEA. Merci Jean-François pour m'avoir fait confiance et pour m'avoir ouvert les portes de la recherche scientifique en m'offrant l'opportunité de réaliser cette thèse. Ton dévouement et le temps passé avec moi m'ont beaucoup apporté, que ce soit en termes scientifique ou personnel. Ton enthousiasme, ton dynamisme et ton soutien remarquable en toutes circonstances ont également été très apréciables tout au long de la thèse. Ma gratitude vient aussi à Florian de Vuyst, directeur de thèse à l'ENS Cachan. Merci Florian pour ta bienveillance et tes conseils avisés, notamment sur les aspects analytiques de cette thèse. Je souhaite par ailleurs saluer Gregory Cunningham, avec qui j'ai eu la chance de travailler durant près de trois mois au Los Alamos National Laboratory (LANL) durant l'été 2016, dont la gentillesse et le discernement scientifique m'ont permis de faire avancer remarquablement mes travaux de thèse. Un grand merci aux rapporteurs, Vivianne Pierrard et Benoit Lavraud, pour avoir sacrifié une partie de leurs vacances à lire et évaluer ce long manuscrit. Vos questions et remarques pertinentes m'ont amené à clarifier certains points et m'ont ainsi conduit à améliorer substanciellement la qualité du présent document. J'ai été honoré de la présence à ma soutenance de thèse de Jean-Michel Ghidaglia, Yuri Shprits et Daniel Bouche en tant, respectivement, que Président du jury et examinateurs. Je vous adresse toute ma reconnaissance pour avoir pris part à mon jury.

Le CEA, par ses moyens techniques et scientifiques de haut niveau, s'est avéré être le cadre idéal pour réaliser ma thèse. Tout d'abord, je remercie l'équipe qui m'a acueilli au département de physique : Catherine et Jean-Pierre, Florian, et Sylvain. Durant ma thèse, j'ai eu la chance de cotoyer des personnes qui m'ont marqué, non seulement par leur talent et leur savoir, mais aussi par leur sympathie manifeste et la bonne ambiance qu'ils faisaient régner quotidiennement. J'ai avant tout une pensée amicale pour les actuels courageux thésards et futurs docteurs : Bertrand, Alisée, Jérémy (un grand merci pour ton aide sur latex), Antoine, Pierre-Louis, Arnaud V. et Manuel. Je salue au passage mes glorieux ainés : Simon, Julien, Pedro, Mathieu, Sébastien et Charles, ainsi que les postdocs et ex-postdocs : Gaetan, Xavier V., Witold et Guillaume qui ont placé la barre très haut ! Parmi les chercheurs accomplis, j'adresse un clin d'oeil tout particulier à Xavier D., qui a eu la lourde tâche de partager son bureau avec moi. Je remercie également Laurent,

Didier, Arnaud D., Benoit, Serge (pour ta bonhommie) et Jean-Etienne pour l'animation que vous avez apporté durant les pauses café (ô combien sacrées) du midi. Je souhaite une bonne continuation à tous les anciens stagiaires qui sont passés très vite : Lise, Arthur, Lucas, Pauline, Victor et Luke. La vie du couloir n'aurait pas non plus été la même sans Sylvie, toujours présente et prête à aider, et dont je salue ici la gentillesse.

Je suis en outre très reconnaissant envers les membres du Centre de Mathématiques et Leurs Applications (CMLA) de l'ENS Cachan, notamment Véronique pour sa prévenance, ainsi que le personnel du secrétariat, Alina et Virginie, pour leur gentillesse. Je salue également Sandra pour sa bonne humeur, Agnès D. pour son suivi et Atman pour son aide sur le fonctionnement du mur d'images le jour J. Mes pensées vont également aux thésards, post-docs ou aux embauchés du CEA rencontrés à Cachan, en particulier Christina, Alexandre, Lei, John, Lucas B., Matthieu, Marie, Thibault, Michael, Maxime et Suzanne.

C'est toujours avec émotion que je me remémore ces trois mois passés au Nouveau-Mexique en 2016, dans le cadre de la *Los Alamos Space Weather Summer School*. J'en profite pour remercier Misa Cowee pour son organisation. Merci Shantanab pour cette colocation à Los Alamos. Je n'oublie pas ta cuisine de feu qui me reste en travers de la gorge, et j'espère te revoir bientôt ! Je remercie également Lilla (j'ai encore les courbatures de notre sortie en vélo sur les chemins rocailleux du Nouveau-Mexique) et Rosie. Je garde un souvenir mémorable de notre journée marathon à Roswell et White Sand. Au sein du groupe, je salue également Anthony, Yuguang, Kateryna et Oleksandr. J'adresse également une salutation amicale à Nathanael, dont la présence (et la voiture) nous a grandement facilité la vie.

Enfin, je suis reconnaissant envers ma famille pour son soutien, en particulier mes parents, Olivier, Let et Ben ainsi que leur petite Zoé. Merci également à Amel pour l'aide apportée lors du pot de thèse. J'embrasse enfin Agnès, avec qui je partage ma vie depuis toutes ces années : merci pour tes encouragements continuels et pour avoir pris le temps de cuisiner de nombreux gâteaux pour le pot de thèse !

Amitiés, et bon vent à tous !

Présentation de la thèse en français

Principaux enjeux relatifs aux ceintures de Van Allen

Les lancements du satellite russe Spoutnik en 1957 et de son confrère américain Explorer 1 une année plus tard ont marqué le début de la conquête spatiale. La première avancée scientifique majeure associée à ces deux missions a été la découverte de deux ceintures de radiation[1] entourant la Terre, constituées de particules de haute énergie piégées par le champ magnétique terrestre. Ces deux ceintures de radiation sont communément appelées ceintures de Van Allen, en hommage au scientifique américain James Van Allen qui a conçu le détecteur ayant révélé leur existence (*Van Allen and Frank*, 1959).

Les particules fortement énergétiques des ceintures de Van Allen constituent un environnement très hostile pour les satellites actuellement en orbite autour de la Terre. De nombreux défauts techniques sont effectivement régulièrement signalés lorsque les satellites traversent les zones les plus sensibles des ceintures de radiation (*Baker et al.*, 1994; *Lam et al.*, 2012). De tels incidents peuvent avoir des conséquences néfastes sur le fonctionnement des services inhérents aux systèmes de surveillance et de télécommunication qui façonnent le monde connecté du XXI$^{\text{ème}}$ siècle. Assurer la protection et le bon fonctionnement de ces satellites nécessite une meilleure prédiction de la dynamique des électrons évoluant au sein de la magnétosphère. Dans une optique similaire à la prévision météorologique, la vocation ultime des sciences spatiales est d'anticiper et de prévenir les potentiels désastres que pourraient occasionner les orages magnétiques de forte intensité. Au regard de la complexité et de la variété des processus physiques engagés, ce noble objectif relève pour le moment davantage d'un idéal à atteindre que d'une finalité imminente.

La problématique générale à laquelle cette thèse s'attache à apporter des éléments de réponse se traduit de la manière suivante : sommes-nous en mesure de mieux comprendre la dynamique de la ceinture de radiation externe, et sommes-nous capables de la modéliser de façon prédictive, avec une précision suffisante et quantifiée ? Cet objectif constitue le fil rouge de ce travail de thèse.

Dans cette perspective, et afin de contribuer à faire avancer notre compréhension globale de la physique de la magnétosphère, cette thèse de doctorat a pour but de modéliser la dynamique des électrons de haute énergie piégés dans les ceintures de radiation. Une attention particulière est portée à la ceinture externe qui s'étend jusqu'à l'orbite géostationnaire. L'étude est d'abord menée sous le biais d'une résolution analytique (voir le chapitre 3) pour s'acheminer vers des simulations numériques de différentes natures (chapitres 4 à 7), chacune se focalisant sur un effet physique particulier des ceintures de Van Allen.

Contextualisation

Comme évoqué plus haut, les ceintures de radiation constituent la région de l'espace où les particules chargées se retrouvent piégées par le champ magnétique de la Terre (*Van Allen*, 1959). Les ions et les électrons présents dans les ceintures sont apportés soit par le vent solaire, soit par l'ionosphère. Les électrons, dont les énergies vont de 100 keV jusqu'à atteindre plusieurs MeV, se réorganisent en particulier en une ceinture interne et une ceinture externe.

[1] *Ceintures de radiation* (singulier) ou *ceintures de radiations* (pluriel) ? Historiquement, la dénomination française officielle employait le pluriel (car plusieurs radiations), mais l'utilisation du singulier est désormais courante, autant pour les documents scientifiques de référence que pour les articles de vulgarisation. Au risque de froisser les plus anciens d'entre nous, c'est cette dernière convention qui est choisie pour la thèse.

La ceinture interne jouxte la partie supérieure de la haute atmosphère et peut s'étendre jusqu'à 2 rayons terrestres, comptés à partir du centre de la Terre. Les électrons peuvent y rester piégés durant plusieurs mois, voire des années, conférant à la ceinture interne une stabilité qui ne peut être éprouvée que lors de violents orages géomagnétiques.

La ceinture externe se situe typiquement entre 4 et 6 rayons terrestres. Contrairement à sa consoeur, elle est fortement soumise aux aléas du vent solaire, ce qui en fait une région particulièrement dynamique (temps d'évolution de l'ordre du jour, voire de l'heure).

Ces deux ceintures sont séparées par une région dépeuplée en électrons, qui, comme nous le verrons, est caractéristique de l'action de certaines ondes électromagnétiques de la magnétosphère.

Cadre théorique

La physique des ceintures de radiation est traitée dans cette thèse via une approche cinétique, régulièrement appliquée à la description des plasmas non-collisionnels (*Baumjohann and Treumann*, 1996). Nous associons à cette description usuelle les hypothèses supplémentaires propres à la théorie quasi-linéaire (*Fälthammar*, 1965; *Kennel and Engelmann*, 1966; *Lerche*, 1968). Cette dernière traite les ondes électromagnétiques, qui fleurissent dans la magnétosphère (*Millan and Thorne*, 2007; *Thorne*, 2010), comme des perturbations large bande dont l'amplitude est faible par rapport au champ magnétique terrestre ambiant.

Cette propriété nous permet de réduire le nombre de dimensions relatives au problème physique (*Schulz and Lanzerotti*, 1974). La densité d'électrons, typiquement décrite dans l'espace des phases en fonction des trois coordonnées canoniques des moments et de trois coordonnées spatiales (six dimensions), peut ainsi se réduire en une fonction de distribution moyennée sur les phases du mouvement, ne dépendant plus que de trois variables que l'on identifie à trois invariants adiabatiques (*Schulz and Lanzerotti*, 1974). Ces trois invariants adiabatiques, introduits par la théorie hamiltonienne (e.g., *Cary and Brizard*, 2009; *Ukhorskiy and Sitnov*, 2013), sont chacun associés à l'un des mouvements de l'électron piégé dans le champ magnétique non-uniforme de la Terre.

Le premier invariant relève du mouvement rapide de giration de l'électron autour d'une ligne de champ magnétique (fréquence de l'ordre du kHz), le deuxième invariant tient compte du mouvement de rebond de l'électron de long d'une ligne de champ (fréquence de l'ordre du Hz), tandis que le troisième invariant est issu du mouvement de dérive longitudinale de l'électron transversalement aux lignes de champ (fréquence de l'ordre du mHz) (*Northrop and Teller*, 1960; *Northrop*, 1963a) et est lié à la position de la particule.

Si le champ magnétique ambiant est statique, et en l'absence de toute interaction onde-particules, les invariants sont des quantités conservées et les électrons piégés restent soumis indéfiniment et invariablement aux trois mouvements décrits ci-dessus. Cependant, les ondes électromagnétiques qui prolifèrent au sein de la magnétosphère, même de faible amplitude, sont en mesure d'affecter la topologie du champ magnétique ambiant. De telles perturbations peuvent potentiellement briser la propriété de conservation d'un ou plusieurs invariants selon le processus impliqué. Un invariant adiabatique est effectivement altéré si la fréquence de la perturbation électromagnétique est du même ordre de grandeur que la fréquence du mouvement associé à l'invariant en question.

Lorsque les trois invariants sont violés, la dynamique des particules est décrite via une équation 3-D de Fokker-Planck (*Schulz and Lanzerotti*, 1974). Celle-ci s'écrit sous la forme d'une équation de diffusion dont les variables sont les trois invariants adiabatiques.

Elle régit l'évolution de la fonction de distribution des électrons citée plus haut, moyennée sur les phases du mouvement, dans l'espace des invariants adiabatiques. L'équation de Fokker-Planck fait également intervenir des coefficients de diffusion dont on présuppose la connaissance a priori. Ce sont ces derniers qui tiennent compte des effets associés aux ondes électromagnétiques de faible amplitude imposés par la théorie quasi-linéaire (*Fälthammar*, 1965; *Kennel and Engelmann*, 1966; *Lerche*, 1968; *Lyons et al.*, 1971, 1972; *Lyons*, 1974a,b).

Cette approche cinétique simplifiée, qui consiste à décrire la fonction de distribution des électrons par le biais d'une équation de diffusion, s'avère être un bon compromis entre pertinence et simplicité. Son utilisation est parfaitement justifiée par son efficacité à reproduire le comportement des ceintures de radiation depuis les années 1970 (*Lyons and Thorne*, 1973; *Schulz and Lanzerotti*, 1974).

Au cours de cette thèse, nous nous sommes essentiellement concentrés sur deux processus de diffusion distincts. Le premier est le transport diffusif radial des électrons, induit par l'interaction résonante des électrons avec des ondes ultra basses fréquences (UBF). Cette diffusion altère le troisième invariant, en quelque sorte la position de la particule, tout en gardant constants les deux premiers invariants. Ce transport radial a notamment pour conséquence d'accélérer les électrons à mesure qu'ils diffusent en direction de la Terre (accélération bétatron). Dans une moindre mesure, nous nous sommes également intéressés à la diffusion des électrons en angle d'attaque, induite par l'interaction résonante des électrons avec des ondes très basses fréquences (TBF) par exemple. Via ce processus, les électrons sont amenés à parcourir des latitudes de plus en plus élevées le long d'une ligne de champ magnétique donnée, jusqu'à atteindre des latitudes telles qu'ils finissent par précipiter dans l'atmosphère. Sur un intervalle de temps suffisamment grand relatif à ce processus de diffusion, ces pertes peuvent être modélisées par un temps de vie en lieu et place d'un coefficient de diffusion. La combinaison de ces deux processus permet de travailler sur une équation dite de Fokker-Planck réduite (*Walt*, 1970; *Lyons and Thorne*, 1973). Ce formalisme est adopté dans une grande partie de la thèse dans les chapitres 3, 4 (en partie), 5 et 6. Les résultats associés à ce modèle simplifié seront également comparés et vérifiés par rapport à des simulations 3-D qui modélisent le transport, les pertes et l'accélération des électrons au sein des ceintures de radiation.

Afin de pouvoir comparer nos résultats théoriques avec les observations, les diverses fonctions de distribution calculées au cours de cette thèse seront systématiquement converties en flux d'électrons, qui sont les quantités effectivement mesurées par les satellites. Cette correspondance entre flux et fonction de distribution nécessite également de convertir les coordonnées des trois invariants adiabatiques en un espace physique davantage approprié pour le traitement des données. Cet espace physique se construit sur l'énergie cinétique de l'électron, son angle d'attaque équatorial (angle entre le vecteur vitesse de la particule et la direction du champ magnétique) ainsi que sa distance radiale.

Enfin, nous présentons diverses métriques statistiques (*Morley*, 2016; *Morley et al.*, 2018) nous permettant d'évaluer la performance de nos modèles numériques au cours des chapitres 5 et 6.

Organisation de la thèse

Ce travail de thèse s'articule autour de 7 chapitres. Les chapitres 1 et 2 ont pour vocation de présenter un état de l'art de l'étude des ceintures de radiation, respectivement d'une manière globale et qualitative pour le chapitre 1, et de façon plus quantitative et davantage tournée vers les concepts théoriques pour le chapitre 2. Ce dernier pourra

notamment permettre au lecteur de s'approprier les outils mathématiques et physiques utilisés pour la suite de ce travail. Les deux premiers chapitres résument donc les principaux concepts qui sont le plus souvent invoqués dans les sciences spatiales et qui peuvent se trouver facilement dans la foisonnante littérature de la magnétosphère. Le but du chapitre 3 est de présenter une approche originale permettant de calculer la solution analytique de l'équation de Fokker-Planck réduite, pour la première fois avec un terme de perte non uniforme. L'expression mathématique obtenue s'avère très utiles pour révéler certaines propriétés physiques des ceintures de radiation. Le chapitre 4 généralise les résultats obtenus en présentant les solutions associées au code de résolution numérique de l'équation de Fokker-Planck réduite. Nous décrivons notamment le code mis à disposition en début de thèse et les schémas numériques mis en place par *Bussutil* (2014). Ce code a ensuite été développé durant la thèse sur ses aspects dynamiques (incluant des conditions d'entrée, des temps de vie et des champs magnétiques plus réalistes) et structurels (prise en compte d'un espace complet en termes d'invariants adiabatiques, paralélisation sur les supercalculateurs). Le bon fonctionnement du code est vérifié grâce aux solutions analytiques du chapitre 3. Nous nous saisissons également de l'opportunité de pouvoir simuler les flux d'électrons pour différentes énergies et localisations, et ce dans un cadre théorique idéal. Nous démontrons ainsi que la structure globale des ceintures de radiation ainsi que leur temps d'évolution ne dépendent que de quelques facteurs bien choisis. Le chapitre 5 améliore cette analyse en détaillant plusieurs simulations numériques relatives à un évènement particulier de retour au calme après un orage magnétique, mesuré en mars 2013 par les satellites de la NASA (les *Van Allen Probes* A et B) dédiés à l'étude des ceintures de radiation. Nous démontrons plus spécifiquement que les pertes des électrons de la ceinture externe sont principalement induites par des ondes électromagnétiques de type siffleur confinées au sein de la plasmasphère (région constituée d'un plasma froid et dense apporté par l'ionosphère). Afin d'étendre notre capacité à reproduire des évènements géomagnétiques plus actifs et de plus grande ampleur, les chapitres 6 et 7 explorent les influences du champ magnétique terrestre sur la dynamique des électrons des ceintures de radiation. Nous étudions dans un premier temps l'asymétrie significative du champ magnétique au niveau de la ceinture externe, par temps calme puis lors d'un orage géomagnétique, de manière à comprendre comment celle-ci affecte le calcul du flux électronique via les transformations géométriques utilisées pour concilier théorie et observations (chapitre 6). Cette étude repose sur les mesures de la mission de la NASA *Combined Release and Radiation Effects Satellite* (CRRES). Nous explorons également l'importance de l'irrégularité naturelle du champ magnétique au plus proche voisinage de la Terre et de son rôle dans l'émergence de certains processus diffusifs nouveaux et cachés au sein de la ceinture interne.

Afin de mettre en avant la méthodologie et les conclusions inhérentes à chacun des chapitres, nous donnons ci-dessous une description plus détaillée du travail effectué dans cette thèse.

Résolution analytique de l'équation de Fokker-Planck réduite

L'équation de Fokker-Planck réduite, qui modélise le transport et les pertes des électrons, régit, pour une grande partie, la dynamique des ceintures de Van Allen (*Lyons and Thorne*, 1973). Une solution analytique complète de ce problème est primordiale car, à travers son expression mathématique, elle nous amène à une meilleure compréhension de la physique des ceintures de radiation. Les résultats présentés au cours de ce chapitre ont fait l'objet d'une publication scientifique (*Loridan et al.*, 2017).

Nous généralisons en effet plusieurs travaux théoriques effectués durant ces 40 dernières années (e.g., *Haerendel*, 1968; *Walt*, 1970; *Thomsen et al.*, 1977a,b; *Schulz*, 1986; *Jentsch*, 1984; *Schulz and Newman*, 1988; *Hood*, 1983), et dont le but a été de résoudre l'équation de Fokker-Planck réduite munie d'un coefficient de diffusion radiale évoluant avec une puissance de la distance radiale ainsi que d'un terme de perte constant. Nous proposons ici une méthode analytique originale pour pouvoir appliquer ces précédentes études à un terme de perte non-uniforme. Nous considérons dans un premier temps deux conditions limites statiques et une condition initiale arbitraire. Afin de traiter la résolution de ce problème, notre stratégie a été de décomposer le temps de vie non uniforme par une fonction constante par M morceaux. Cela nous permet de traiter le problème séparément sur chaque sous-intervalle, chacun faisant intervenir un temps de vie constant pour lequel une solution analytique existe, comme en témoignent différents travaux menés dans les années 1980 (e.g., *Schulz*, 1986). En s'intéressant à une solution continue, et de dérivée première en espace également continue, nous sommes en mesure de traiter un problème bien posé, bâtit sur 2M-2 conditions aux interfaces, en plus de deux conditions limites. La méthode mathématique de résolution de la solution sur un sous-intervalle donné repose sur une technique de décomposition spectrale bien connue. Cela consiste à scinder la solution en deux termes (ici un terme stationnaire et un terme transitoire). L'idée est de se ramener, pour le terme transitoire, à l'étude d'un problème homogène sur lequel s'applique un procédé usuel de séparation des variables spatiale et temporelle (e.g., *Mei*, 1997).

Le terme stationnaire s'obtient en résolvant l'équation stationnaire munie des deux conditions aux bords, et s'exprime avec des fonctions de Bessel modifiées. Le raccordement de chacune des solutions sur l'intervalle complet s'effectue en utilisant analytiquement et itérativement le système formé des deux conditions limites et des conditions aux interfaces.

Le terme transitoire est quant à lui solution du problème homogène (deux conditions aux bords nulles) muni d'une condition initiale translatée. Il fait intervenir une composante purement spatiale et une composante purement temporelle. La composante spatiale, tout d'abord, est une fonction propre solution d'un problème aux valeurs propres, dit de Sturm-Liouville. Elle s'exprime avec des fonctions de Bessel ou des fonctions de Bessel modifiées, selon un critère lié aux propriétés du temps de vie dans le sous-intervalle considéré. Les valeurs propres associées sont calculées en tenant compte du fait que le déterminant du système (formé par les conditions aux bords nulles et par les conditions aux interfaces) est nécessairement nul. Les solutions de ce déterminant, calculées numériquement (sauf cas particulier), sont précisément les valeurs propres recherchées. Une fois ces valeurs propres obtenues, il est possible de définir entièrement les fonctions propres, puis d'effectuer le raccordement des solutions sur l'intervalle complet. Enfin, la composante temporelle est solution d'un problème de Cauchy tenant compte de la condition initiale du problème (cette dernière étant issue d'une projection orthogonale sur la base des vecteurs propres). Le calcul des solutions analytiques requiert une phase importante de calcul numérique (calcul des valeurs propres et des intégrales liées aux projections orthogonales) qui a été entièrement développée durant la thèse.

A partir de ce résultat, la solution peut facilement être étendue pour prendre en compte des condition limites plus générales dépendant du temps qui peuvent modéliser soit une injection graduelle d'électrons dans la magnétosphère ou bien au contraire une perte progressive d'électrons au-delà de la magnétopause. Ce travail, bien que centré sur des solutions analytiques, a nécessité un développement numérique de grande ampleur, que ce soit dans le calcul des valeurs propres (parallélisation sur plusieurs processeurs)

ou dans les integrations numériques liées aux projections orthogonales de la condition initiale sur la base des fonctions propres. Ce nouveau code, entièrement développé durant la thèse, constitue le *code analytique*.

La validité de la solution analytique complète est vérifiée par comparaison avec des solutions calculées par une méthode purement numérique (relatives au *code numérique*), développée (en partie) conjointement au cours de la thèse. L'excellente correspondance entre les solutions analytiques et numériques calculées pour des temps de vie fortement non-uniformes témoigne de la possibilité d'appliquer la méthode analytique sur des temps de vie réalistes.

Par ailleurs, nous avons pu estimer analytiquement un critère donnant le nombre de modes propres à calculer afin d'obtenir une solution analytique convergente, et ce via deux formulations. La première montre que le nombre de modes est inversement proportionnel au temps. De fait, la méthode analytique est optimisée pour résoudre la solution sur les temps longs, ce qui s'avère être un bon complément aux méthodes numériques classiques. L'efficacité de ces dernières à calculer rapidement les fonctions de distribution est en effet mise à mal lorsque les temps de diffusion s'allongent. La seconde formulation du critère de convergence suggère que le nombre de modes augmente avec la puissance du coefficient de diffusion radiale. Ainsi la méthode analytique présentée est d'autant plus efficace sur les processus diffusifs de faible puissance, comme le transport diffusif radial des électrons autour des planètes Jupiter et Saturne, par exemple.

Finalement, le temps d'équilibre, défini comme étant le temps requis pour atteindre une solution quasi-stationnaire, est estimé via une expression analytique (relativement simple pour certains cas particuliers) ou numériquement dans le cas général. La notion de temps d'équilibre est discutée plus précisément au cours du chapitre 4 par le biais de simulations numériques.

Caractérisation de la dynamique des ceintures de radiation

Comme évoqué plus haut, les satellites ne peuvent mesurer, au mieux, que des flux d'électrons pour diverses localisations, énergies et angles d'attaque, et non directement des fonctions de distribution en terme d'invariants adiabatiques. Le chapitre 4 a précisément pour but de compléter l'étude analytique des fonctions de distribution du chapitre 3 par une analyse numérique des flux d'électrons dans un cadre encore formel mais plus réaliste. L'objectif est d'aborder la notion d'état d'équilibre des ceintures de radiation en mettant en évidence les conditions pour lesquelles cet état d'équilibre est physiquement réalisable, tout en se concentrant sur la dynamique sous-jacente à cet état d'équilibre. Ces travaux ont également été publiés (*Ripoll et al.*, 2016a).

Le *code numérique* de résolution de l'équation de Fokker-Planck réduite fourni en début de thèse reposait sur une méthode de différences finies. Il s'agit plus spécifiquement d'un schéma explicite de Crank-Nicholson (ordre 1 en temps, ordre 2 en espace) qui permet l'obtention des fonctions de distribution dans l'espace des invariants adiabatiques (*Bussutil*, 2014). Ces dernières étaient ensuite converties en flux d'électrons décrits dans un espace physique construit sur les quantités observables que sont l'énergie cinétique, l'angle d'attaque et la distance radiale. La conversion dans l'espace physique était implémentée via une méthode numérique d'inversion de type Newton-Raphson, avec l'aide d'approximations analytiques valables dans le cas d'un champ dipolaire uniquement.

Au cours de ce travail de thèse, nous avons pu développer tout l'aspect dynamique du code de résolution de l'équation de Fokker-Planck réduite. Les conditions limites retranscrivent désormais la variabilité des flux observés par les satellites. Le code est également

en capacité d'intégrer des temps de vie réalistes (nuages de points) spécifiques à la période géomagnétique étudiée (voir chapitre 5 ainsi que les travaux publiés dans (*Ripoll et al.*, 2017, 2018, in print)). Enfin les transformations effectuées entre les invariants et les variables physiques peuvent tenir compte d'une plus grande variété de champs magnétiques modélisant, par exemple, les aspérités du champ magnétique au voisinnage de la Terre ou l'action du vent solaire sur la topologie de la ceinture externe (voir chapitres 6 et 7, ainsi que les travaux menés dans (*Cunningham et al.*, 2018; *Loridan et al.*, 2018, in preparation)). Une part non négligeable de la thèse a également consisté à généraliser le calcul des fonctions de distribution pour un large spectre d'invariants adiabatiques. Ces calculs sont conduits simultanément grâce à une parallélisation numérique qui permet de répartir la fonction de distribution sur des domaines d'invariants restreints et disjoints sur de multiples processeurs des supercalculateurs du CEA. Cet aspect nous a permis de reproduire la structure des flux d'électron sur une gamme étendue en énergie et angles d'attaques (chapitres 4, 5 et 6 ainsi que les travaux publiés dans (*Ripoll et al.*, 2016a,b, 2017, 2018, in print)).

Dans le cadre du chapitre 4, le code prend en compte des temps de vie d'électrons réalistes calculés pour les processus physiques de collisions coulombiennes et d'interactions avec des ondes de mode siffleur se propageant respectivement au sein et au-delà de la plasmasphère (pertes des électrons par précipitation dans l'atmosphère). Différents modèles de coefficients de diffusion radiale sont également considérés (transport radial induit par les interactions avec des ondes ultra basses fréquences).

Nous nous focalisons ici uniquement sur les flux d'électrons dont l'angle d'attaque est de 90 degrés, c'est-à-dire aux populations d'électrons confinées au niveau de l'équateur géomagnétique. Les simulations numériques nous permettent de cartographier les flux d'électrons en termes d'énergie et de distance radiale. Dans ce contexte, nous démontrons notamment que sur les temps longs (à partir d'une vingtaine de jours jusqu'à une année), les flux d'électrons ont tendance à se réorganiser en une structure remarquable qui prend la forme d'un S. Cet arrangement tout particulier a très récemment été observé pendant des périodes géomagnétiques calmes par les satellites de la mission NASA des *Van Allen Probes* (*Reeves et al.*, 2016). Nous mettons ainsi en évidence l'action des ondes électromagnétiques de type siffleur agissant au sein de la plasmasphère, capables de façonner la région dépeuplée en électrons enlacée par la ceinture externe et la ceinture interne (*Ripoll et al.*, 2016a).

En fin de compte, nous prouvons que la structure des ceintures de radiation ainsi que leur temps d'évolution ne dépendent que de quelques facteurs physiques bien choisis. La forme quasi-stationnaire des flux d'électrons est en effet essentiellement gouvernée par le rapport entre les temps caractéristiques de diffusion radiale sur la diffusion en angle d'attaque (ce dernier n'étant rien d'autre que le temps de vie de l'électron). Le temps d'équilibre est quant à lui intimement lié au temps caractéristique moyen d'évolution, défini par la moyenne harmonique de tous les processus physiques engagés (diffusion radiale et en angle d'attaque). Nous montrons par la suite que le temps d'équilibre est aussi gouverné par l'état initial des ceintures de radiation, ce qui se recoupe avec l'étude analytique menée au chapitre 3 et les travaux présentés dans l'article (*Ripoll et al.*, 2016a).

Une attention toute particulière est portée sur la notion de convergence à l'état d'équilibre (ou stationnaire). Celle-ci nécessite plusieurs centaines de jours au sein de la ceinture interne et ne peut être atteinte que pour une petite sélection d'énergies et de distances radiales. Ce résultat conteste la vision usuelle de deux ceintures de radiation à l'équilibre telle qu'elle nous a été inspirée par les travaux historiques et théoriques de *Lyons and Thorne* (1973).

Modélisation du dépeuplement de la ceinture externe après un orage magnétique

Nous nous attachons par la suite à perfectionner l'identification de la structure dynamique des ceintures de radiation initiée académiquement au cours des chapitres 3 et 4. Dans cette perspective, nous reproduisons un évènement tout particulier correspondant à la période de retour au calme (12 jours) succédant à l'orage magnétique du 1er mars 2013. Cette période a été recensée par l'instrument MagEIS du satellite *Van Allen Probe* A. Nous utilisons les mesures de haute résolution des flux d'électrons pour bâtir les conditions initiale et limites dans le modèle de l'équation de Fokker-Planck réduite.

Les pertes substantielles d'électrons observées durant cet évènement sont vraisemblablement causées par de la diffusion en angle d'attaque induite par les ondes plasmasphériques de mode siffleur. Dans cette optique, nous considérons le coefficient de diffusion en angle d'attaque ainsi que son temps de vie associé, construits sur les propriétés de ces ondes électromagnétiques et ayant été spécifiquement calculés pour la période étudiée de mars 2013 au cours du travail mené dans (*Ripoll et al.*, 2017) (le calcul du coefficient de diffusion lui-même s'inscrivant en dehors du cadre de cette thèse).

Afin de valider le modèle à notre disposition des ondes plasmasphériques, nous effectuons diverses analyses numériques relatives à la résolution de l'équation de Fokker-Planck réduite. Pour ce faire, différents coefficients de diffusion radiale sont utilisés, ainsi que divers modèles associés au temps de vie de l'électron. Parmi ces derniers, nous considérons le temps de vie bâti sur les données empiriques de mars 2013 précédemment évoqué (*Ripoll et al.*, 2017) et d'autres temps de vie existants dans la littérature construits sur une approche statistique (*Lyons et al.*, 1972; *Orlova et al.*, 2014, 2016).

Au cours de cette première étude paramétrique, nous nous préoccupons uniquement des données de type L2 (non résolues en angle d'attaque) issues du satellite *Van Allen Probe* A. Les simulations consistent à calculer des flux unidirectionnels d'électrons confinés à l'équateur magnétique (angle d'attaque équatorial de 90 degrés). Pour des raisons de simplicité, dans un premier temps, nous faisons l'hypothèse que les flux unidirectionnels sont distribués uniformément en angle d'attaque, de telle sorte que que les flux omnidirectionnels observés par les satellites soient directement liés (à une constante près) aux flux unidirectionnels simulés. Nous montrons ainsi, via l'utilisation de métriques statistiques spécifiquement adaptées (*Morley et al.*, 2018), que l'utilisation du temps de vie dédié à l'évènement étudié amène à l'une des meilleures reproductions des données.

Nous améliorons la pertinence de nos simulations en tenant compte du fait que la distribution en angle d'attaque possède un caractère non uniforme. Nous tenons compte des données de type L3 (résolues en angle d'attaque) pour reproduire les flux unidirectionnels et omnidirectionnels d'électrons. Les résultats obtenus nous permettent d'expliquer la structure complète en forme de S dans le plan en énergies et distances radiales, ainsi que la formation et l'élargissement progressif de la région dépeuplée, entre les deux ceintures de radiation, par l'action des ondes plasmasphériques. Nous confirmons également numériquement l'absence d'électrons de haute énergie dans la ceinture interne (*Fennell et al.*, 2015).

L'étape primordiale de ce chapitre est d'aller au-delà de notre capacité à résoudre l'équation de Fokker-Planck réduite et d'utiliser pour la première fois au CEA/DAM une formulation 3-D de l'équation de Fokker-Planck adaptée à la magnétosphère. L'une des raisons de cette direction prise est de pouvoir estimer la pertinence et précision du modèle 1-D pour l'évènement en question.

Dans ces perspectives, la première étude consiste à utiliser un code Fokker-Planck 3-

D préexistant pour effectuer les simulations en tenant compte du coefficient de diffusion en angle d'attaque spécifique à l'évènement en question. C'est le code VERB-3D qui a été développé durant ces dix dernières années (*Subbotin and Shprits*, 2009; *Shprits et al.*, 2009; *Subbotin et al.*, 2010; *Kim et al.*, 2011) qui a été choisi. Ce dernier apporte davantage de précisions sur les pertes d'électrons (diffusion en angle d'attaque) et tient compte de l'accélération locale des électrons (diffusion en énergie). Afin d'estimer l'influence de la distribution initiale en angle d'attaque, nous construisons soit des flux unidirectionnels à partir des données omnidirectionnelles de type L2 combinées à une distribution conceptuelle en angle d'attaque (*Shi et al.*, 2016), soit dans un deuxième temps en tirant directement profit des données de type L3 devenues disponibles en 2017. Dans les deux cas, les flux omnidirectionnels sont reconstruits une fois les simulations achevées, puis comparés avec les données L2 ou L3 via différentes métriques. Nous constatons quelques améliorations avec l'utilisation des données L3 pour la reproduction des données, ce qui démontre qu'il est nécessaire d'utiliser des modèles relatifs à l'évènement étudié et bâtis sur des données empiriques pour pouvoir mieux corroborer les observations. Les erreurs obtenues sur les flux omnidirectionnels par le code 1-D et 3-D sont respectivement de 100% et de 85% (moins d'un facteur 2 entre les données et les simulations). Ce travail valide donc les deux approches.

Les résultats correspondants on été publiés sous le biais de (*Ripoll et al.*, 2016b) ainsi que dans la dernière section de (*Ripoll et al.*, 2017) pour ce qui concerne les résultats des simulations. Une future publication (*Ripoll et al.*, 2018, in print) devrait également voir le jour à propos de la structure des ceintures tridimensionnelle en espace, energies et angles d'attaques.

Quantification de l'impact du champ magnétique terrestre sur la dynamique de la ceinture externe

Dans l'optique de pouvoir simuler des évènements géomagnétiques plus actifs, nous nous focalisons sur l'influence du champ magnétique dans le calcul des flux d'électrons au sein de la ceinture de radiation externe. Au premier ordre, le champ magnétique terrestre est représenté par un modèle dipolaire, de sorte que les lignes de champ sont alors parfaitement symétriques par rapport à l'axe du dipôle. Cependant, au cours de périodes géomagnétiques de forte intensité, le champ magnétique est considérablement affecté par le vent solaire, qui comprime les lignes de champ côté jour et les étire davantage côté nuit. De fait, la symétrie du champ magnétique est mise à mal dans un environnement réaliste.

Le chapitre 6 est exclusivement axé sur l'impact de la géométrie du champ magnétique via la transformation indispensable liant l'espace physique (adapté aux observations) à l'espace des invariants adiabatiques (approprié aux études numériques et théoriques). Durant le processus de simulation, nous faisons la distinction entre les étapes de traitement des données (conversion des flux observés en une fonction de distribution et reconstruction des flux à partir de la fonction de distribution simulée) et l'étape de calcul (à savoir la résolution numérique de l'équation de Fokker-Planck). Si la plupart des récents travaux dédiés aux ceintures de radiation tiennent compte d'un champ magnétique non dipolaire durant les étapes de traitement des données, il est rare d'utiliser un champ magnétique réaliste durant l'étape de calcul elle-même, pour laquelle il est plus aisé d'utiliser un champ magnétique dipolaire. Dans cette étude, nous saisissons l'opportunité de quantifier l'influence d'un champ magnétique réaliste (en opposition au champ dipolaire) pour le traitement des données mais également durant l'étape de calcul.

L'approche adoptée, qui consiste à prendre en considération un champ magnétique variable dans le but de calculer des flux d'électrons, repose essentiellement sur une librairie numérique préexistante, LANLGeoMag, ainsi que sur les travaux de *Cunningham* (2016). Nous vérifions avec succès la validité du développement numérique effectué grâce à la reproduction d'un évènement de faible intensité géomagnétique, mesuré par le satellite CRRES durant l'année 1990. Pour la période en question, qui s'étend du 24 septembre au 2 octobre 1990 (9 jours), nous obtenons, comme prévu, des résultats similaires entre l'utilisation du champ magnétique réaliste T89 (*Tsyganenko*, 1989) et du champ magnétique dipolaire.

Une fois cette étape de validation effectuée, nous mettons le nouveau modèle numérique à l'épreuve en tentant de reproduire les flux d'électrons observés par CRRES durant une seconde période, qui s'étend cette fois-ci du 9 au 15 octobre 1990 (7 jours). Cet évènement, bien connu dans la littérature (*Brautigam and Albert*, 2000; *Albert et al.*, 2009), se caractérise par une forte activité géomagnétique et met en exergue une perte abrupte d'électrons, éjectés au-delà de la magnétopause, suivi par un repeuplement significatif en terme de flux d'électrons. Une des interrogations importantes relatives à cet évènement est de savoir si le repeuplement des électrons est dû à un phénomène d'accélération locale (interaction avec des ondes très basses fréquences de type choeur) ou plutôt à une accélération de type bétatron induite par de la diffusion radiale (interaction avec des ondes ultra basses fréquences). A partir de deux simulations incluant respectivement un champ magnétique dipolaire et le champ magnétique plus réaliste T89 (*Tsyganenko*, 1989), nous montrons que la topologie du champ magnétique a un impact plus important sur les étapes de traitement des données par rapport à l'étape de calcul. De manière plus spécifique, nous démontrons que l'utilisation d'un champ dipolaire mène à des inexactitudes sur la reconstruction de la fonction de distribution des électrons. Ces erreurs, qui apparaissent durant l'étape initiale de traitement des données (conversion des flux mesurés en fonction de distribution), ont également été soulignées par plusieurs études antérieures qui s'étaient également appuyées sur des données satellite (*Selesnick and Blake*, 2000; *Green and Kivelson*, 2004). Nous expliquons ici pourquoi les distributions en électrons obtenues avec un champ dipolaire sont contaminées par des pics isolés et artificiels, qui peuvent être interprétés à tort comme étant des effets inhérents à des accélérations locales induites par les ondes électromagnétiques. En utilisant un champ magnétique plus réaliste, la plupart de ces pics non physiques sont amenés à disparaitre, de telle sorte que l'essentiel de la distribution en électrons est caractérisée par de la diffusion radiale, reproductible in fine par nos simulations de l'équation de Fokker-Planck réduite (1-D).

Comme précédemment, les erreurs par rapport au modèle sont quantifiées au moyen de métriques statistiques appliquées notamment aux flux omnidirectionnels. Si l'erreur commise s'élève à 200% (facteur 3) dans le cas d'un champ dipolaire, elle se réduit à 100% (facteur 2) dans le cas du champ magnétique asymétrique et réaliste.

Il reste toutefois certains effets propres à de l'accélération locale dans le problème étudié (*Albert et al.*, 2009), lesquelles ne peuvent être reproduites par notre modèle d'équation de Fokker-Planck réduite (qui ne tient pas compte de la diffusion en énergie). Ces résultats feront l'objet d'une prochaine publication (*Loridan et al.*, 2018, in preparation).

Mise en évidence de la diffusion radiale néoclassique

Au niveau de la ceinture interne, le champ magnétique généré par la Terre est également disparate, notamment au niveau de l'Atlantique sud où l'intensité du champ chute

brutalement. Nous explorons ainsi l'émergence de processus diffusifs cachés induits par l'irrégularité naturelle du champ magnétique terrestre. Parmi les nouveaux artefacts qui se dessinent, un coefficient de diffusion radiale supplémentaire peut se manifester à partir de la combinaison de deux effets physiques distincts.

Le premier effet, inhérent aux asymétries du champ magnétique terrestre, relève du changement du contour de dérive des électrons. Les particules issues d'une même position sont en effet amenées à peupler différents contours de dérive selon leurs angles d'attaque. Le second phénomène est relatif à de la diffusion d'électrons en angle d'attaque. La conjonction de ces deux effets conduit à un nouveau processus de diffusion radiale qui se produit à énergie constante. Elle est dite anormale (*Roederer et al.*, 1973; *O'Brien*, 2014, 2015; *Zheng et al.*, 2016) lorsque la diffusion en angle d'attaque provient des interactions des électrons avec les ondes électromagnétiques de la magnétosphère (typiquement dans la ceinture externe), et appelée néoclassique (*Cunningham et al.*, 2018) lorsque la diffusion en angle d'attaque est issue des collisions des électrons avec les molécules situées dans l'atmosphère terrestre (ceinture interne).

En se concentrant ici sur le plus proche voisinage de la Terre, la diffusion en angle d'attaque est largement dominée par les précipitations des électrons dans la haute atmosphère via des collisions coulombiennes élastiques (*Walt and MacDonald*, 1964; *Selesnick*, 2012). Nous quantifions notamment le coefficient de diffusion radiale néoclassique correspondant en couplant les deux processus de changement de contour de dérive (*Cunningham*, 2016) et de collisions coulombiennes (*Selesnick*, 2012). Nous montrons que le coefficient de diffusion radiale résultant des calculs numériques est une fonction décroissante de la distance radiale, et se distingue par là-même fortement des coefficients plus classiques de diffusion radiale calculés à partir des interactions avec les ondes ultra basses fréquences. La valeur de ces cofficients de diffusion radiale, usuellement employés, augmente avec la distance radiale. Nous montrons que cet aspect caractéristique, en accord avec deux études empiriques menées durant la fin des années 1960 (*Newkirk and Walt*, 1968; *Farley*, 1969), est finalement une signature de la diffusion néoclassique. Les résultats quantitatifs obtenus confirment également l'importance de la diffusion néoclassique et son influence sur la dynamique de la ceinture de radiation interne.

Les résultats propres à ce chapitre (*Loridan et al.*, 2016) ont été confortés par la suite par une analyse plus détaillée qui a donnée lieu à une publication (*Cunningham et al.*, 2018).

Nomenclature

General physical parameters

Symbol	Description
c	Speed of light
γ	Relativistic factor
m_0	Particle's rest mass
$m = \gamma m_0$	Particle's mass
q	Particle's charge
ε_0	Vacuum permittivity
μ_0	Vacuum permeability

Electromagnetic quantities

Symbol	Description
$\boldsymbol{B}$	Magnetic field vector
$\boldsymbol{\mathcal{E}}$	Electric field vector
ρ	Charge density
$\boldsymbol{\mathcal{J}}$	Current density vector
$\boldsymbol{\mathcal{A}}$	Magnetic vector potential
V	Electric scalar potential
B	Magnetic field intensity
B_E	Equatorial magnetic field intensity on the Earth's surface
B_0	Equatorial magnetic field intensity
B_m	Magnetic field intensity at the mirror point
B_L	Magnetic field intensity at the loss point ($\sim$ 100 km)
ψ_i, ψ_e	Internal and external scalar magnetic potentials

Particle's motion and adiabatic invariants

Symbol	Description
ρ_c	Larmor radius
ω_g, f_g, τ_g	Gyro-pulsation, frequency, and period
ω_b, f_b, τ_b	Bounce-pulsation, frequency, and period
ω_d, f_d, τ_d	Drift-pulsation, frequency, and period
(J_1, J_2, J_3)	First, second, and third (canonical) adiabatic invariants
μ, $\mathscr{M}$	First (noncanonical) invariant and magnetic moment
J, I, K	Second (noncanonical) invariants
Φ, L^*	Third (noncanonical) invariants

Physical space

Symbol	Description
E	Particle's kinetic energy
$\boldsymbol{p}$, $\boldsymbol{v}$	Particle's momentum and velocity vectors
α	Particle's local pitch angle
α_0	Particle's equatorial pitch angle
x_0, y_0	cosine and sine of the particle's equatorial pitch angle

Electron distribution and fluxes

Symbol	Description
F	Phase Space Density (PSD)
f	Phase-averaged electron distribution function
j	Differential unidirectional electron flux
J_O	Differential omnidirectional electron flux
J_{IO}	Integral omnidirectional electron flux

Diffusive processes

Symbol	Description
D_{LL}	Radial diffusion coefficient
D_{pp}	Energy diffusion coefficient
$D_{\alpha_0\alpha_0}$	Pitch angle diffusion coefficient
$D_{\alpha_0 p}$	Mixed diffusion coefficient
τ	Electron lifetime
G	Jacobian determinant

Contents

Introduction

Year 2018 celebrates the 60 years anniversary of the launch of the first US space mission: Explorer 1. Along with the Sputnik satellite (launched by the USSR one year earlier in 1957), both probes sparked a new era of space discovery and the beginning of the space odyssey. The first breakthrough associated to these early missions has been the discovery of high energy particles organized in two distinct regions surrounding the Earth. These two regions constitute the radiation belts, also called the Van Allen radiation belts as a tribute to the American scientist James Van Allen who designed the instrument that revealed their existence (*Van Allen and Frank*, 1959).

Due to the high energy electrons trapped by the Earth's magnetic field within the radiation belts, the latter zones are a very hostile environment for the orbiting satellites. Many events have indeed shown that spacecraft are prone to breakdowns when passing through the radiation belts. Such recurrent technical failures can heavily impact the connected world and jeopardize the global economy. The need of ensuring satellites' protection requires to predict accurately the dynamics of electrons evolving into the magnetosphere. Similarly to weather forecasting, the ultimate (and not yet reached) goal of the so-called space weather science is to anticipate and prevent potential disasters that might be induced by strong geomagnetic storms (e.g., *Baker et al.*, 1994, 2016).

From this general perspective, the present PhD thesis aims at modeling the dynamics of high energy electrons trapped in the radiation belts as a contribution to our physical understanding of the magnetosphere. A particular focus is made on the outer belt, which encompasses the geostationary orbit. The main questions on which this PhD thesis has to shed light can be formulated as follow: are we able to better understand the dynamics of the outer radiation belt, and can we model it in a predictive way within a sufficient and measurable reliability? The study is first carried out through an analytical method (Chapter 3) and further developed with numerical simulations (Chapter 4 to 7).

Contextualization of the study

The theory of the radiation belts relies on three adiabatic invariants, each one corresponding to a specific motion of the electron trapped into the Earth nonuniform magnetic field. The first adiabatic invariant results from the rapid gyromotion of the electron around the magnetic field line, the second invariant takes account of the electron bounce motion along a field line while the third invariant is linked to the electron longitudinal drift motion across the field lines (*Northrop and Teller*, 1960; *Northrop*, 1963a). These three invariants constitute an adequate coordinate system onto which the electron phase-averaged distribution function is defined (*Schulz and Lanzerotti*, 1974). If the ambient magnetic field is static and in absence of wave-particle interactions, the invariants are conserved and the trapped electrons remain subjected to those three motions. However, electromagnetic waves arise in the magnetosphere and even small-amplitude perturbations can affect the background magnetic field. These perturbations can potentially break one or several adiabatic invariants from various processes.

If all three invariants are violated, a 3-D Fokker-Planck equation is established. It writes under a general diffusion equation expressed in terms of the three aforementioned adiabatic invariants and governs the evolution of the phase-averaged electron distribution function in the adiabatic space. The Fokker-Planck equation assumes the prior knowledge of various diffusion coefficients that take account of the effect of small amplitude waves.

During the PhD, we mainly focus on two distinct diffusive processes. The first one is the diffusive radial transport of electrons. It is induced by drift-resonant interactions

of electrons with ultra low frequency (ULF) waves. This radial transport enables to accelerate the electrons as they diffuse Earthward. To a lesser extent, we also study pitch angle diffusion of electrons, which is due to gyro-resonant interactions with very low frequency (VLF) waves. Through this process, the electrons are more field-aligned, until reaching latitudes at which they end up precipitating into the Earth's atmosphere. On a sufficiently long time period, the electron loss can be approximated by a loss term that involves only an electron lifetime rather than diffusion coefficients. The combination of the two diffusion processes enable to deal with a so-called reduced Fokker-Planck equation. This equation, which is the backbone of the PhD, will be used to describe the dynamics of the radiation belts. The results will also be compared and verified with 3-D simulations modeling the transport, loss, and acceleration of electrons in the radiation belts.

Organization of the PhD thesis

The present PhD thesis is organized on the basis of 7 chapters. Chapters 1 and 2 are dedicated to present the state of the art of the study of the radiation belts, respectively in a very general manner and qualitatively (Chapter 1) and more physically and quantitatively (Chapter 2). These first two chapters summarize some of the main known concepts invoked in space science that can be found in the existing literature. The purpose of Chapter 3 is to present an original approach to perform the analytical solution (via a so-called *analytical code*) of the reduced Fokker-Planck equation. This code has been entirely developed during the PhD thesis. The obtained mathematical expressions prove to be useful at unveiling various physical properties of the radiation belts. Chapter 4 generalizes the previous results by presenting the reduced Fokker-Planck code, referred as the *numerical code*, which has first been developed by *Bussutil* (2014) (numerical scheme and stationary distribution functions) and further extended during the PhD. It has been fully verified by the aforementioned analytical solutions. We take the opportunity of simulating electron fluxes for various energies and locations in an ideal framework and we demonstrate that the global structure of the radiation belts as well as their dynamical timescale only depend on a few well chosen parameters. Chapter 5 improves the analysis by detailing the simulation of the March 2013 storm recovery observed by the two NASA satellites of the Van Allen Probes mission. We specifically prove that the electron depletion of the outer belt is induced by whistler mode hiss waves that develop within the plasmasphere. In the perspective of reproducing more geomagnetically active events, Chapters 6 and 7 explore the influences of the Earth's magnetic field on the dynamics of the electron radiation belts. We first study the significant magnetic field asymmetry in the outer belt to understand how it can affect the geometrical transformations used to reconcile theory and observations (Chapter 6). We finally investigate the natural irregularity of the magnetic field in the inner belt and its role in the emergence of hidden diffusive processes (Chapter 7).

In order to emphasize the methodology and the conclusions inherent to each chapter, a more detailed description of the thesis is given below.

Chapter 1

We first very briefly and generally introduce the radiation belts and we relate their historical discovery in the 1950's. We then contextualize the present study into the

global topology of the magnetosphere, before emphasizing the current motivations and challenges associated to space science. We spotlight the space missions relevant to this thesis dedicated to space weather forecasting.

Chapter 2

Here we specifically describe the physical and mathematical concepts involved in the study of the radiation belts, which can be found in the rich existing literature. An effort has been deliberately made to synthesize the main theoretical aspects related to the physics of trapped particles. It serves as a solid baseline for Chapters 3, 4, 5, 6 and 7, as well as a good starting point to any people showing interest to the colorful picture of magnetospheric physics. One fundamental purpose of Chapter 2 is also to relate the historical standard formalisms to the new outstanding concrete discoveries that have been made possible thanks to the development of numerical clusters and the recent space missions.

The dynamics related to one single electron trapped into a nonuniform magnetic field is presented, emphasizing the motion of gyration as well as the bounce and drift motions. From this framework, the three adiabatic invariants, which come from Hamiltonian theory (e.g., *Cary and Brizard*, 2009; *Ukhorskiy and Sitnov*, 2013), are introduced.

We then describe the approach adopted in the present work among the methods usually considered in plasmas physics. We use a so-called simplified kinetic approach, which is the combination of the common kinetic description of collisionless plasmas (*Baumjohann and Treumann*, 1996) with the additional assumptions related to quasilinear theory (*Fälthammar*, 1965; *Kennel and Engelmann*, 1966; *Lerche*, 1968). The latter treats the electromagnetic waves as perturbations whose amplitudes are small compared with the ambient Earth's magnetic field. This property enables to reduce the number of dimensions of the physical problem (*Schulz and Lanzerotti*, 1974). The typical phase space density used in kinetic theory, which initially depends on the six phase space coordinates, is here reduced into a phase-averaged distribution function that rather evolves with respect to the three adiabatic invariants (only) (*Schulz and Lanzerotti*, 1974). This simplified kinetic theory is a good compromise between simplicity and accuracy. Its use is fully justified by its efficiency at reproducing the behavior of the radiation belts since the 1970's (*Lyons and Thorne*, 1973). The complete Fokker-Planck equation that governs the evolution of the electron phase-averaged distribution function in the adiabatic space is derived (*Chandrasekhar*, 1943, 1960; *Roederer*, 1970; *Schulz and Lanzerotti*, 1974). Focusing on radial and pitch angle diffusion, the latter equation is transformed into a reduced Fokker-Planck equation (*Walt*, 1970).

We subsequently relate the theoretical electron phase-averaged distribution function to the empirical electron fluxes measured by satellites. This correspondence also requires to convert the three adiabatic invariant coordinates into a physical space that is more appropriate to data processing. The physical space is built on the electron kinetic energy, the equatorial pitch angle, and the radial distance.

Finally, we present some useful statistical error metrics that are dedicated to the field of space weather (*Morley*, 2016; *Morley et al.*, 2018). They are used to quantify the accuracy of our numerical models compared with satellite observations (see Chapters 5 and 6).

Chapter 3

This chapter is devoted to present a newly derived analytical solution of the reduced Fokker-Planck equation. A complete analytical solution of this problem is essential, since, through its mathematical expression, its leads us to a better understanding of the physics of the radiation belts. The presented results have been published in (*Loridan et al.*, 2017).

We generalize some previous theoretical works that have been done during the past forty years (e.g., *Haerendel*, 1968; *Walt*, 1970; *Thomsen et al.*, 1977a,b; *Schulz*, 1986; *Jentsch*, 1984; *Schulz and Newman*, 1988; *Hood*, 1983), whose purpose was to solve the reduced Fokker-Planck equation by considering a diffusion coefficient proportional to a power law in radial distance and a constant loss term. We propose here an original analytical method applied to a nonuniform loss term. We start by considering two static boundary conditions combined with an arbitrary initial condition. Our strategy is to decompose the nonuniform lifetime into a piecewise-constant function on M subintervals. It enables us to deal separately with each subinterval, each involving a constant lifetime for which an analytical solution exists, as shown by many pioneering works made during the 1980's (e.g., *Schulz*, 1986). Assuming the continuity of both the distribution function and its first spatial derivatives, we are able to deal with a well-posed problem made of $2M-2$ interface conditions in addition to the two boundary conditions. The mathematical method used to find the so-called specific solution related to one given subinterval relies on a well-known eigenfunction approach. That consists of splitting the specific solution into two terms: one steady term and one transient term (e.g., *Mei*, 1997).

The specific steady term is obtained by solving the steady equation along with its two boundary conditions. The connection of each specific steady solution on the complete interval is carried out by using analytically and iteratively the system built on the two boundary conditions and the interface conditions. As for the specific transient term, it is the solution of an homogeneous problem (two vanishing boundary conditions) combined with a translated initial condition. It involves a purely spatial component and a purely temporal component. The spatial component is an eigenfunction that is solution of a Sturm-Liouville problem (eigenvalue problem). The associated eigenvalues, which are computed numerically, are the zeros of a determinant characterizing the global problem. Once these eigenvalues are obtained, it is possible to entirely define the eigenfunctions and then to perform the connection of the solutions on the complete interval. Finally, the temporal component is the solution of a so-called Cauchy problem that takes account of the initial condition. Based on this result, the solution can be easily extended to take account of time-dependent boundary conditions that either model gradual injections of electrons into the magnetosphere or gradual dropouts.

The validity of the complete analytical solution is verified as we further show an excellent agreement between both the analytical solutions and the solutions obtained directly from numerical simulations. The verification is carried out for different loss terms of various shapes. It also demonstrates that the proposed analytical method can well be applied to realistic lifetimes.

Furthermore, we analytically emphasize two convergence criteria that give the number of eigenvalues that we have to include in order to obtain a converged analytical solution. The first formulation shows that the number of eigenmodes required to get an accurate snapshot of the analytical solution at time t_0 is proportional to $1/\sqrt{t_0}$. Hence the analytical method is optimized to solve the solution for long times, which can be a good complement to the classical numerical methods that are computationally more expensive to simulate longer times. The second formulation suggests that the number

of eigenmodes increases with the diffusion power. Therefore the presented analytical method is more efficient as the diffusion power decreases, which is well adapted to the diffusive transport of electrons around other planets like Jupiter or Saturn, for example, better than for Earth.

Finally, the equilibrium time, defined as the time to nearly reach the steady solution, is estimated by a closed-form expression and discussed as we have estimated this quantity from numerical simulations (cf. Chapter 4).

Chapter 4

Since satellites are measuring electron fluxes rather than the electron phase-averaged distribution functions, the purpose of Chapter 4 is to complement the study of Chapter 3 by numerically analyzing the flux dynamics in a more realistic background. The results have been published in (*Ripoll et al.*, 2016a). We first highlight the transformations in use to convert the theoretical adiabatic space into the observed physical space made of energy, equatorial pitch angle, and L-shell. We also briefly describe the numerical model partly implemented during the PhD that is used to solve the reduced Fokker-Planck equation and that serves to quantify the electron fluxes within a simplified framework of the radiation belts. The latter code includes realistic electron lifetimes derived from Coulomb collisions and interactions with whistler mode hiss and chorus waves respectively inside and outside the plasmasphere, as well as different empirical models of the radial diffusion coefficient. Moreover, at the level of development, we start focusing only on a 90 degrees unidirectional flux.

Long-time simulations (up to one year) reveal a very specific structure for the electron fluxes plotted in the plane built on L-shell and energy. The latter feature, which displays the same interesting S shape of the inner edge of the outer belt as recently observed by the Van Allen Probes (*Reeves et al.*, 2016), is shown to be a signature of the action of wave-particle interactions. We demonstrate that whistler mode hiss waves are able to sculpt the slot region between the radiation belts during geomagnetically quiet times (*Ripoll et al.*, 2016a).

Finally, we put forward that the structure of the radiation belts as well as their dynamical timescales only depend on a few well chosen physical quantities. The long-time shape of the electron fluxes is indeed essentially governed by the ratio of the characteristic times of radial diffusion over pitch angle diffusion (the latter being the electron lifetime). As for the equilibrium time, it is closely related to the mean characteristic time defined as the harmonic average of all physical processes involved (both radial and pitch angle diffusions). The equilibrium time is further shown to be also governed by the initial state of the belts, which confirms the study conducted in Chapter 3 (*Ripoll et al.*, 2016a).

We emphasize that convergence to equilibrium, i.e. steady state, requires hundreds of days in the inner belt and is practically reachable only for small selected energies and radial distances. This result challenges the usual view of the two radiation belts at equilibrium inspired by the early theoretical works of *Lyons and Thorne* (1973).

Chapter 5

Chapter 5 aims at improving the identification of the dynamical structure of the radiation belts initiated in Chapter 4. The results have been published in (*Ripoll et al.*, 2016b) and in the last sections of *Ripoll et al.* (2017) dedicated to simulation results. In this perspective, we reproduce a specific quiet event that occurred during the storm recovery 12 day-period that followed the 1st of March 2013 storm, which has been observed

by the MagEIS instrument on board Van Allen Probe A. The high resolution electron flux data are used as realistic initial and time-dependent boundary conditions in the reduced Fokker-Planck model. Since the electron depletion occurring during this event is likely to be caused by pitch angle diffusion inferred from whistler mode hiss waves, we consider a hiss-related pitch angle diffusion coefficient and the corresponding hiss lifetime that have been previously calculated in a former work (*Ripoll et al.*, 2017) (that is not part of this PhD) specifically for the studied period of March 2013.

For the purpose of validating the hiss model at disposal, we perform several numerical simulations of the reduced Fokker-Planck equation for different radial diffusion coefficients and by using either the aforementioned data-driven hiss lifetime or other different statistical electron lifetime models (*Ripoll et al.*, 2017). Only the L2 data (not resolved in pitch angle) taken from Van Allen Probe A is considered in this first parametric study. The latter consists at simulating 90 degrees unidirectional fluxes. For simplicity, we assume that the unidirectional fluxes are uniformly distributed in pitch angle, such that the omnidirectional flux observed by the satellite can be directly related (modulo a constant factor) to the simulated unidirectional flux. The use of dedicated error metrics from *Morley et al.* (2018) (the median absolute error, the median absolute percentage error, the median symmetric accuracy and the median log accuracy ratio) shows that one of the best data reproduction is obtained with the use of the event-specific lifetime.

We then perform more accurate simulations by taking account of the fact that the pitch angle distribution is more likely to be nonuniform. We use the L3 (pitch angle resolved) MagEIS data to simulate unidirectional and omnidirectional fluxes. Our results enable us to explain the full S shape structure in energy and L-shell of the belts as well as the slot formation by hiss scattering during storm recovery. We also numerically confirm the existence of an inner belt devoid of high energy electrons (*Fennell et al.*, 2015).

The last step, and one of the main achievement of this work, has been to go beyond the reduced Fokker-Planck capability we had and to use a full 3-D Fokker-Planck formulation. One reason was to assess the accuracy of the reduced Fokker-Planck model. Another was to be able to address in the future more complex configurations of the magnetosphere, such as storms. Within these perspectives, the first study has been to use an existing 3-D Fokker-Planck code to verify the aforementioned event-specific and data-driven pitch angle diffusion coefficient inferred from hiss waves activity. The latter code is the VERB-3D model that has been implemented at UCLA during the last ten years (e.g., *Subbotin and Shprits*, 2009; *Shprits et al.*, 2009; *Subbotin et al.*, 2010; *Kim et al.*, 2011) and is now mainly developed at the GFZ Potsdam in Germany. The VERB-3D code is able to take account of radial diffusion as well as local diffusion in energy and pitch angle. To assess the influence of the initial pitch angle distribution, we either built unidirectional fluxes from the L2 MagEIS data by assuming a conceptual pitch angle distribution (*Shi et al.*, 2016), or by taking advantage of the L3 (pitch angle resolved) MagEIS data newly released in 2017. In both cases, the omnidirectional fluxes are reconstructed after the simulations and are compared with either the L2 or L3 data. We notice some improvements with the use of L3 data in reproducing the observations, which demonstrate the need for using data-driven and event-specific models to better corroborate the satellite observations. This work is part of an article that is currently submitted for publication on the 3-D (L, energy, pitch angle) structure of the radiation belts (*Ripoll et al.*, 2018, in print).

Chapter 6

For the purpose of simulating more active geomagnetic events, Chapter 6 focuses on the influence of the magnetic field model in the computation of electron fluxes in

the outer radiation belt. During intense geomagnetic activity, the magnetic field in the outer belt is known to be strongly affected by the solar wind, which compresses the field lines on the dayside and stretches them out in the night side, breaking drastically the symmetry of the magnetic field topology.

We exclusively discuss the impact of the magnetic field geometry on the transformation between the physical space adapted for observations and the adiabatic space that is more appropriate to theoretical investigations and imposed by the numerical framework. To contextualize the whole study, we first report the typical adopted approach that is used to include a varying (non-dipole) magnetic field model within numerical simulations of electron fluxes. In the simulation process, we distinguish between the step of data processing and the step of computation (i.e. the numerical resolution of the Fokker-Planck equation). If the most recent works devoted to radiation belts modeling commonly involve a non dipole magnetic field for the pre-processing and post-processing steps, it is still unusual to invoke a realistic field in the computational step itself, for which a symmetric dipole field is often preferred by simplicity. In this chapter, we take the opportunity to quantify the influence of a realistic field (compared with the formal dipole field) in both the processing and computational steps.

We first detail the numerical implementation of a realistic field model within the reduced Fokker-Planck code. The validity of the last development is successfully verified upon the reproduction of a quiet geomagnetic event, which has been reported by the Combined Release and Radiation Effects Satellite (CRRES) during the year 1990. For the quiet decay period event at stake, which is chosen to lie between September 24 and October 2, 1990, we obtain, as expected, similar results with the use of a realistic field than with a dipole field.

Once this validation step has been proceeded, we test the model further and attempt to reproduce the electron fluxes observed by CRRES during another period, from October 9 to October 15, 1990. This is the famous storm of October 1990, which is characterized by a strong geomagnetic activity and exhibits a sharp electron depletion followed by a significant enhancement of electron fluxes. One of the important issue inherent to this event is to know whether the electron enhancement arises from whistler (VLF) wave-particle interactions (here local acceleration) or rather from radial diffusion (betatron acceleration induced by interactions with ULF waves). By running simulations with the respective use of a dipole field and a realistic field, we prove that the magnetic field topology has a greater impact during the data-processing steps compared with the computational step. More specifically, we demonstrate that the use of a dipole field leads to inaccuracies on the reconstruction of phase space density during the pre-processing step, which corroborates some previous studies that relied on satellite observations (*Selesnick and Blake*, 2000; *Green and Kivelson*, 2004). We explain why the latter dipole-reconstructed PSD is indeed contaminated by artificial isolated peaks that can be wrongly interpreted as an effect of in-situ acceleration induced by whistler mode chorus waves. By using a more realistic magnetic field, these non physical peaks are expected to vanish, so that most of the PSD features are rather shaped by radial diffusion, which is more easily replicable by our simulations.

Nevertheless some local acceleration phenomena remain for this problem (*Albert et al.*, 2009), which the reduced Fokker-Planck formulation is unable to incorporate (since energy diffusion cannot be included in this model). This causes significant error that is quantified thanks to dedicated error metrics applied to unidirectional fluxes as well as omnidirectional and integral electron fluxes.

Chapter 7

Sticking to the influence of the magnetic field topology, Chapter 7 explores the emergence of hidden diffusive processes due to the natural irregularity of the Earth's magnetic field. Among these new looming diffusive artefacts, an extra radial diffusion coefficient can be inferred from two different physical effects that combine together. The first effect is inherent to the asymmetries of the Earth magnetic field and makes particles of different equatorial pitch angles populate different drift shells. This is the so-called drift-shell splitting effect. The second phenomenon is related to pitch angle diffusion of electrons. The combination of both leads to what has been referred as anomalous radial diffusion when it occurs in the outer radiation belt (*Roederer et al.*, 1973; *O'Brien*, 2014, 2015; *Zheng et al.*, 2016). Focusing here on a similar effect but in the closest vicinity of the Earth, pitch angle diffusion is induced by electron scattering in the upper atmosphere via the process of Coulomb collisions (*Walt and MacDonald*, 1964; *Selesnick*, 2012) rather by than interactions with VLF waves at higher L-shells. There, scattering of electrons (pitch angle diffusion), from a decrease of their pitch angle, causes the electrons to drift along different drift shells (drift shell splitting), which makes them diffuse radially. Such extra radial diffusion occurring at constant energy is referred as neoclassical radial diffusion (*Cunningham et al.*, 2018).

In this chapter we thus investigate neoclassical radial diffusion and attempt to quantify the related neoclassical radial diffusion coefficient by coupling both processes of drift shell splitting (*Cunningham*, 2016) and Coulomb collisions (*Selesnick*, 2012). We show that the radial diffusion coefficient arising from the numerical calculations strongly differs from the classical diffusion coefficients inferred from interactions with ULF waves, as it exhibits a significant decrease with increasing L-shells. This characteristic feature, which is in agreement with two empirical studies made in the late 1960's (*Newkirk and Walt*, 1968; *Farley*, 1969), is shown to be a signature of neoclassical diffusion. The obtained quantitative result also supports the importance of neoclassical diffusion and its influence on the dynamics of the inner belt. The results of this chapter (*Loridan et al.*, 2016) were confirmed afterwards by a deeper analysis that has been published in (*Cunningham et al.*, 2018).

Conclusions and perspectives

As a final chapter, we summarize the main achievements of the PhD thesis and discuss the obtained results by confronting them to the present context and knowledge of radiation belt physics. The development of more efficient numerical simulations as well as the spread of more reliable satellite observations make the upcoming days a new golden era for space science and weather forecasting.

Chapter 1

The radiation belts within the magnetosphere

Before focusing on the physical aspects inherent to the dynamics of the radiation belts, let us briefly have an overview of the global morphology of the Earth's magnetosphere and its interactions with the Solar activity. We first contextualize the study by giving a short description of the radiation belts and their historical discovery in the 1950's. We then present the solar wind and its impact on the Earth's geomagnetic environment. We conclude this chapter by emphasizing the importance of the study of the outer space environment by presenting the different tools in use worldwide for space weather and by describing the recent space missions that have been sent in orbit to better understand the physics of the radiation belts.

1.1 Introducing the radiation belts

1.1.1 Properties of the radiation belts

The radiation belts constitute the region of the outer space around Earth where most of the charged particles (coming originally either from the solar wind or the Earth's ionosphere) are trapped into the Earth's magnetic field (*Van Allen*, 1959). There are two electron radiation belts (one inner belt and one outer belt) and one proton belt. The electron belts consist mostly of high energy electrons (energy above 100 keV). The inner electron radiation belt, which is located close to the Earth, is very stable and is only perturbed during very large geomagnetic storms. The electrons can remain there during several months, even years. The electron outer radiation belt, located approximatively from 4 to 6 Earth radii, is on the contrary very dynamic and changes over timescales of hours and days. Both radiation belts are separated by a so-called slot region devoid of electrons. The trapped proton population only creates one unique proton radiation belt (up to 10 MeV) overlapping the inner electron belt. Like the inner electron radiation belt, the proton belt is extremely stable.

1.1.2 Discovery of the radiation belts: a brief history

If the end of the 1950's has been characterized by a climax of tension between the USA and the USSR, it has been a very prolific period for the field of space physics. The successful launch of the Sputnik satellite (first spacecraft ever put into orbit) by the USSR, on October 4, 1957, has been a cornerstone in space exploration. The US dedication to take the lead of the conquest of space has then been rewarded by the successful launch of the Explorer 1 rocket, on January 31, 1958 (historical picture shown in Figure 1.1). The Explorer 1 satellite had the specificity of carrying several science instruments, and among them a cosmic ray detector designed by James Van Allen. It happened that the cosmic ray detector indicated a much lower cosmic ray count than expected. Van Allen attributed this discrepancy to a saturation of the instrument by strong radiations. He made the assumption that the radiations were induced by high energy charged particles that have been trapped in the Earth's magnetic field (*Van Allen and Frank*, 1959). Two months later, the Explorer 3 mission brought him the confirmation of his theoretical prospects: two electron radiation belts and one proton belt coexist around the Earth in a region that spread from the Earth to the geostationary orbit (around six Earth radii) and further away. The radiation belts are known today as the Van Allen belts.

Figure 1.1 – The Explorer 1 team: William Pickering (left), James Van Allen (middle) and Wernher von Braun (right) hold up a model of the Explorer 1 rocket after the success of the mission. Source: https://www.nasa.gov/mission_pages/rbsp/science/rbsp-history.html.

1.2 Overview of the geospace environment

Before getting into the main body of the PhD thesis, let us give a global picture of the geospace environment and the role played by the radiation belts. The present purpose of this section is to describe briefly step by step the different regions that compose the geospace environment, starting from the Sun and getting closer to the Earth.

1.2.1 The Sun

The Sun, as every other active stars, perpetually ejects particles in all directions. This continuous stream of charged particles is called the solar wind. It propagates into interplanetary space at speed comprised between 200 and 900 km/s, such that it takes about 100 hours (4 days) to travel the Sun-Earth distance (1.5×10^8 km). The solar wind is primarily composed of electrons and protons H^+, with some evidences of He^{++}. The Sun has its own magnetic field, whose intensity is 10^5 nT at the Sun's surface (*Meyer-Vernet*, 2007).

The solar wind also drives the Sun's magnetic field in all directions. The streamed magnetic field is commonly called the Interplanetary Magnetic Field (IMF). The radial outflow of the solar wind coupled with the rotation of the Sun (rotation rate of 27 days) makes the IMF lines follow a Parker spiral (*Parker*, 1991). In the vicinity of Earth, the solar wind density is around 6 particles/cm^3, the temperature is 7 eV for ions and 15 eV for electrons. The IMF intensity is about 6 nT over there. Several types of solar wind plasma have yet been identified, such as the coronal-hole origin plasma, the streamer-belt-origin plasma, and ejecta. Streamer belt plasmas have recently been divided into two groups: streamer belt plasma and sector reversal regions (*Xu and Borovsky*, 2015). They are illustrated in Figure 1.2.

The coronal hole plasma originates from regions of open magnetic field lines (the coronal holes). It is a fast (600 km/s) and homogeneous plasma that follows the Parker

spiral (26% of the total observed solar wind plasma at Earth). The streamer belt plasma (41% of the time at Earth) is a slow (400 km/s) and inhomogeneous plasma that also follows the Parker spiral. The latest is discriminated from the reversal region plasma (20% of the time at Earth), which is a very slow plasma (<350 km/s). The last and third type of solar wind plasma is ejecta associated to coronal mass ejections (CME). Contrary to its aforementioned counterparts, ejecta (13% of the time at Earth) are blast-off that do not follow the Parker spiral (*Xu and Borovsky*, 2015).

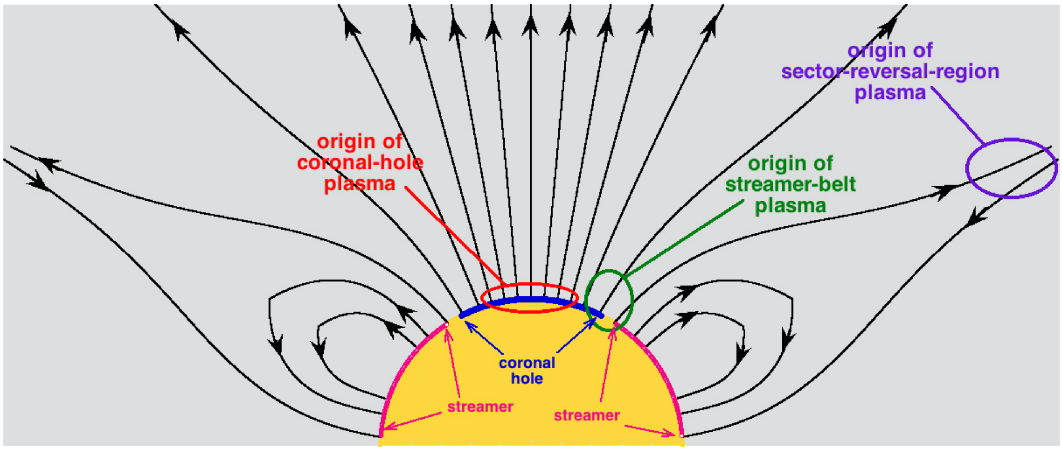

Figure 1.2 – Origins of the different solar wind plasmas: the coronal hole plasma, the streamer belt plasma, and the sector reversal regions plasmas. The third and last type, ejecta, are not shown. Source: (*Xu and Borovsky*, 2015).

1.2.2 The solar wind and the magnetosphere

The Earth also has its own magnetic field, which is naturally oriented to the north: the magnetic field lines flow out of the south pole and dive into the north pole. The entire region (outside the Earth) where the dynamics of charged particles is primarily controlled by the Earth's magnetic field is called the magnetosphere. Due to the action of the solar wind, the magnetosphere is naturally compressed on the day side of the Earth and stretched out on the night side into a long tail, called the magnetotail (cf. the magnetic field topology emphasized in Chapter 6). The length of the tail varies with the conditions of the solar wind, but can typically reach more than 150 Earth radii.

The Earth's magnetic field is a magnetic obstacle for the upcoming solar wind and a shock structure called bow shock is generated on the dayside of the Earth. The bow shock slows down supersonic solar wind to subsonic speeds, and diverts the solar wind flow around the magnetosphere. The bow shock is located at 14 Earth radii from the Earth's surface, and its thickness is about 100 to 1000 km. At 8-11 Earth radii from Earth starts the magnetosphere. Its boundary, which separates the solar wind from the Earth's magnetic field, is called the magnetopause. Its thickness is from several hundred to a thousand kilometers. The region between the bow shock and the magnetopause, called the magnetosheath, is a turbulent region of space filled with downstream solar wind plasma. The magnetosheath plasma is hotter (1 keV), denser, and slower flowing than the unshocked solar wind plasma. Its width (around 3-4 Earth radii) mostly depends on solar activity. The described interactions between solar wind and the magnetosphere are illustrated in Figure 1.3.

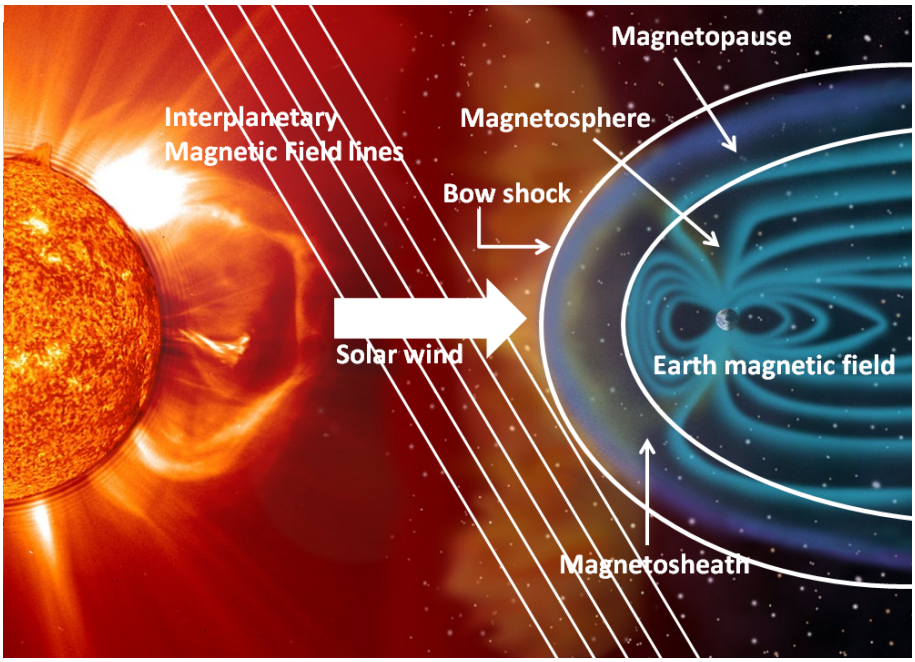

Figure 1.3 – Interactions between the solar wind and the magnetosphere. Adapted from https://www.nasa.gov/topics/aeronautics/features/airline-radiation.html.

Recurrently, magnetic reconnection between the field lines of the IMF and the Earth's magnetic field occurs and enables the solar wind plasma to penetrate into the Earth's magnetosphere (e.g., *Richardson*, 2013). When the IMF is oriented to the north, reconnection between the IMF and the Earth's magnetic field that also points northward does not occur in the equatorial region of the magnetopause (even if it can still happen in the magnetotail lobes, which are described below). In this case, the solar wind is most likely to flow around the magnetopause. When the IMF is however oriented southward, the IMF can more easily connect to the Earth's northward magnetic field and a magnetic reconnection takes place at the magnetopause. This process is known as the dayside merging. The reconnected field lines are then dragged from the dayside to the nightside, bringing the solar wind plasma into the magnetotail (*Lavraud et al.*, 2011). Consequently, field lines of opposite direction (northward and southward) stretch out along the magnetotail and get closer to each other. Reconnection inevitably happens again between two opposite field lines, this time in the middle of the magnetotail. This second reconnection process gives birth to new closed field lines, which return back to Earth. A large amount of energy and particles is abruptly released at both sides of the reconnection points, the earthward injection being called a substorm. Reconnection into the tail also disconnects the solar wind from the magnetosphere and allows the magnetic flux to convect particles from the nightside to the dayside. The process of magnetic reconnection is illustrated in Figure 1.4 (*Baumjohann et al.*, 2010).

Distinction is often made between the inner magnetosphere whose population comes from the ionosphere (H^+, O^+, He^+, plus solar wind particles during storms and substorms) and the outer magnetosphere fed by the solar wind (H^+, He^{++}).

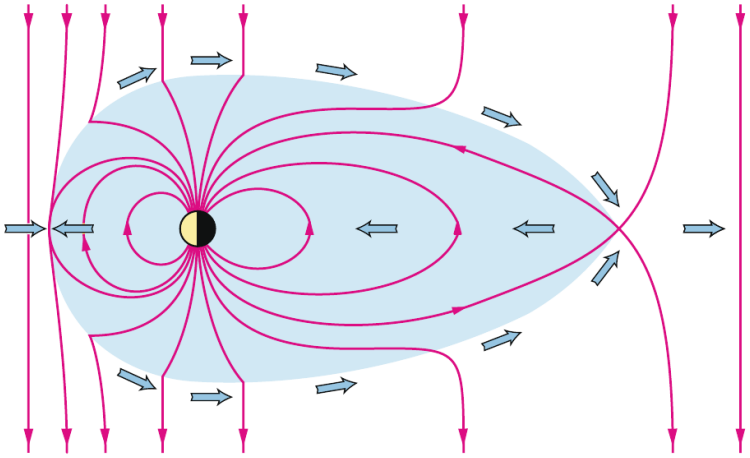

Figure 1.4 – Magnetic reconnection between the field lines of the IMF and the magnetosphere. Source: (*Baumjohann et al.*, 2010).

1.2.3 The outer magnetosphere

One of the largest regions that compose the outer magnetosphere is the plasma sheet. This is a region of closed field lines in the equatorial magnetotail, consisting of hot (several keV) and low-density (1 cm^{-3}) plasma. The plasma sheet is 6 Earth radii thick in the north-south direction. In the middle of the plasma sheet is a neutral sheet that bifurcates the plasma into a northern portion and a southern portion. Across the neutral sheet the direction of the magnetic field in the plasma sheet reverses: the magnetic field points sunward (earthward) north of the neutral sheet and points anti-sunward (tailward) south of the neutral sheet.

In the magnetotail, the regions located above and below the flat plasma sheet are made of open field lines and are devoid of hot plasma. These regions are respectively the northern and southern lobes. The plasma sheet boundary layers (PSBL) separate the plasma sheet from the lobes.

The magnetospheric boundary layers are regions close to the Earth's magnetopause in which the magnetosheath plasma has a strong influence. Among the boundary layers, the low latitude boundary Layers (LLBL) are transferring a large fraction of plasma from the magnetosheath into the magnetosphere. The northern and southern cusps (or clefts) of the magnetosphere separate regions of sunward magnetic field lines from regions of tailward magnetic field lines (*Lavraud et al.*, 2005). The northern and southern cusps of the magnetosphere are magnetically connected to the surface of the Earth respectively near the geographic north pole and south pole. Magnetosheath plasma can penetrate through the magnetopause into the cusps to reach the upper atmosphere. The high latitude boundary layer, or plasma mantle, covers much of the high latitude region poleward of the cusp region. All of these specific features are represented in Figure 1.5 (left).

1.2.4 The inner magnetosphere

The inner magnetosphere encompasses different regions that are known to be the plasmasphere, the warm plasma and the radiation belts (*Ebihara and Miyoshi*, 2011). Figure 1.5 (right) depicts the different regions of the inner magnetosphere.

1.2.4.a The plasmasphere

The plasmasphere is a dense (50-2000 particles/cm^3) and cold (1 eV) plasma typically located between 1 and 5 Earth radii. The plasmasphere originates from ionosphere upwelling, so that its population is mainly composed of electrons, H^+, O^+ and He^+ (*Sandel and Denton*, 2007; *Ebihara and Miyoshi*, 2011). The outer boundary of the plasmasphere is known as the plasmapause and indicates the location of a sharp drop of particle density by about one order of magnitude (*Carpenter*, 1963). The size of the plasmasphere depends on the geomagnetic activity. The plasmapause can be located at 7 Earth radii during geomagnetically quiet times, but can also be brought to radial distances less than 2 Earth radii during the most active events (*Baker et al.*, 2004). The plasmasphere tends to corotate with the Earth.

1.2.4.b The warm plasma

The warm plasma consists of an ion population of intermediate energies (from a few eV to a few keV) (*Chappell et al.*, 2008) that originates from both the ionosphere and plasma sheet.

1.2.4.c The radiation belts

Last but not least, the radiation belts, which have already been presented in section 1.1.1, encompass the trapping region of high energy particles (above 100 keV) and belong to the inner magnetosphere (*Hess*, 1968). They overlap the plasma sheet (fed by solar wind particles) and the plasmasphere (fed by the ionosphere).

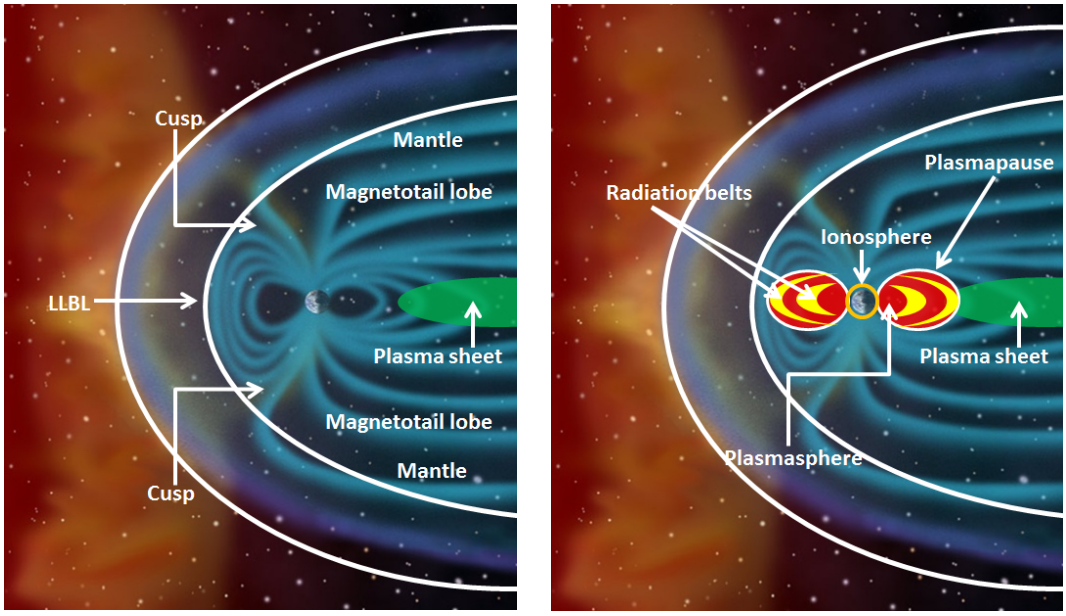

Figure 1.5 – Properties of the outer (left) and inner (right) magnetosphere. Adapted from https://www.nasa.gov/topics/aeronautics/features/airline-radiation.html.

1.2.5 The ionosphere

Let us conclude this picturesque description by briefly mentioning the ionosphere. This region is located from 60 to 1000 km above ground, and is primarily made of ionized gas (0.1 to a few eV). The ionosphere is mostly created by UV and X-ray photons from the Sun which partially ionizes the neutral atmosphere. During geomagnetic storms, the O^+ population is likely to escape the ionosphere and reaches the magnetosphere.

1.2.6 Currents flowing in the magnetosphere

Ions and electrons do not necessarily move in the same direction in the magnetosphere, and different electric currents are then created. These currents depend on the solar wind and other geomagnetic parameters, and can severely impact the Earth background magnetic field.

On the dayside, the compression of the magnetopause under the influence of the coming solar wind stream is associated with a current flow across the magnetopause surface, which is called the magnetopause current or the Chapman-Ferraro current. On the opposite side, a so-called tail current sheet (neutral sheet) flows in the equatorial plane of the magnetotail in the east to west direction. The latter current separates the northern and southern magnetotail lobes. In the heart of the magnetosphere flows the ring current around Earth. It is located approximately between 3 and 5 Earth radii and consist mostly of ions (1-100 keV) that have been trapped in the magnetic field and drift in the westward direction (*Baumjohann et al.*, 2010; *Ebihara and Miyoshi*, 2011). Finally, let us mention that the field-aligned currents that flow along the magnetic field lines entering the atmosphere at high latitudes, and connect the magnetospheric plasma with the ionosphere. They are primarily composed of electrons. All of these aforementioned currents are illustrated in Figure 1.6.

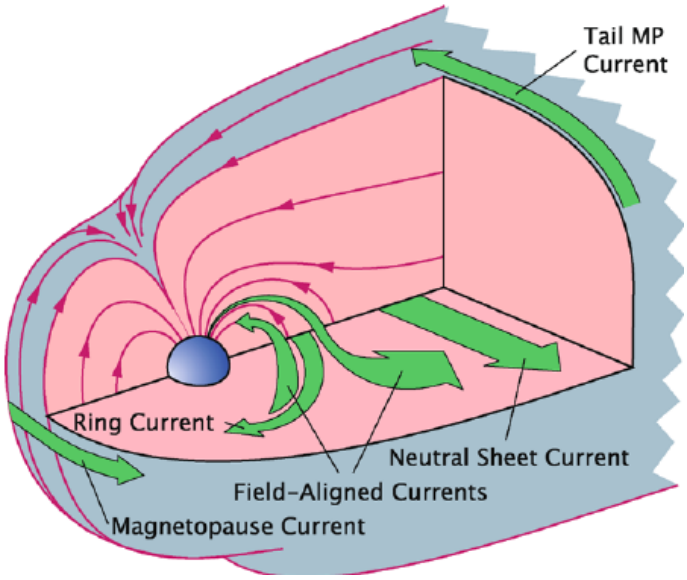

Figure 1.6 – Schematic illustration of the different currents flowing in the magnetosphere. Source: (*Baumjohann et al.*, 2010).

1.3 Electromagnetic waves in the magnetosphere

The magnetosphere is subjected to the influence of many electromagnetic waves from different origins. The electromagnetic waves perturb the static background magnetic field and, as we will see in the next chapters, make the electrons diffuse according to different physical processes. The amplitude of the electromagnetic waves that proliferate in the magnetosphere is about a few nT, which is very weak compared with the ambient Earth's magnetic field intensity, which is about 10^4 nT at $r \sim 1.5\ R_E$ and 10^2 nT at $r \sim 6\ R_E$ (corresponding respectively to 10^{-1} G and 10^{-3} G). In this section, we briefly describe the different electromagnetic waves that are at stake in the magnetosphere (see Figure 1.7).

The following description relies on the reviews made in (*Millan and Thorne*, 2007; *Thorne*, 2010) as well as some recent results brought by the Van Allen Probes mission.

1.3.1 Ultra Low Frequency waves

The Ultra Low Frequency (ULF) waves have frequencies lying between 1 mHz and 1 Hz. Solar wind impulses can excite the dayside magnetosphere and thus generate ULF waves at the magnetopause boundary. The ULF waves' amplitude is a few nT for the magnetic component and a few mV/m for the electric component (*Thorne*, 2010; *Takahashi et al.*, 2014). Among the ULF waves, one can distinguish the Alfven waves from the magnetosonic waves. The Alfven waves are transverse plasma waves, which propagate along the magnetic field direction, whereas the magnetosonic waves propagate transversally to the magnetic field direction. The latter are merely located near the magnetic equator and are also known as the equatorial noise. As we will see, the ULF waves are involved on the Earthward or outward radial transport of electron.

1.3.2 ElectroMagnetic Ion Cyclotron waves

The ElectroMagnetic Ion Cyclotron (EMIC) waves are discrete electromagnetic emissions, which occur in distinct frequency bands separated by multiples of the ion gyrofrequencies. Their frequency range is from 0.1 to 5 Hz, such that the EMIC waves are technically still ULF waves. Their amplitude is around 1-10 nT in the magnetic component, and about 1 mV/m in the electric component (*Kersten et al.*, 2014; *Saikin et al.*, 2016). EMIC waves are transverse plasma waves, propagating in the direction parallel to the direction of the ambient magnetic field. The EMIC source region is typically confined with ~ 10 degrees of the geomagnetic equatorial plane (cf. Figure 1.7). EMIC waves occurrence increases with radial distance and solar wind dynamic pressure, and are specifically enhanced during magnetic storms (*Engebretson et al.*, 2015, 2018). The EMIC waves are known to be a cause for the depletion of ultrarelativistic electrons (energies above 2 MeV).

1.3.3 Very Low Frequency waves

The Very Low Frequency (VLF) waves have frequencies between 50 Hz and 2.5 kHz. They are known to be an efficient mechanism for scattering the electrons into the atmosphere (losses) but also for local acceleration of electrons. Two modes of VLF are commonly considered in radiation belt physics: whistler mode hiss waves and whistler mode chorus waves.

1.3.3.a Whistler mode chorus waves

Chorus emissions are discrete coherent whistler mode waves, which occur in two distinct frequency bands (respectively the upper and lower band). The lower band is comprised between 0.05 and 0.5 the electron gyrofrequency f_g while the upper band goes from 0.5 to 0.8 f_g (*Santolík et al.*, 2004; *Li et al.*, 2016a). Chorus waves are enhanced over a broad low density spatial region outside the plasmapause (cf. Figure 1.7). Their amplitude is about a few pT in the magnetic component, and typically between 1 and 10 mV/m in the electric component. Some peak amplitudes of about 20 mV/m have however been observed (*Santolík et al.*, 2004). Whistler mode chorus waves are known to be excited in the vicinity of the geomagnetic equator. Chorus waves play a dual role in both the loss (atmospheric precipitation) and local acceleration of radiation belt electrons. They are sought to be the intrinsic source of plasmaspheric hiss (*Bortnik et al.*, 2008a).

1.3.3.b Whistler mode hiss waves

Hiss is an incoherent whistler-mode emission mostly confined within the dense plasmasphere and within dayside plasmaspheric plumes (cf. Figure 1.7). Hiss waves are thought to originate from a subset of chorus emission. Their frequency range lies between 50 Hz and 2 kHz with a mean frequency around 600 Hz. Recent studies based on the Van Allen Probes data have shown that the whistler mode hiss waves occurrence peak can be located as low as between 100 and 300 Hz, with smaller values at larger L-shells (*Li et al.*, 2015). Their amplitude is typically between 1 and 100 pT for the magnetic component (*Meredith et al.*, 2004). Plasmaspheric hiss is likely to propagate along with the magnetic field lines near the geomagnetic equator and more obliquely at higher latitudes. Hiss wave amplitude has been recently found to be increasing with increasing density in the plasmasphere above $L = 2.5$ (*Malaspina et al.*, 2018). As emphasized in Chapter 5, whistler mode hiss waves are responsible for the formation of the quiet time electron slot between the inner and the outer radiation belts (*Ripoll et al.*, 2016b, 2017).

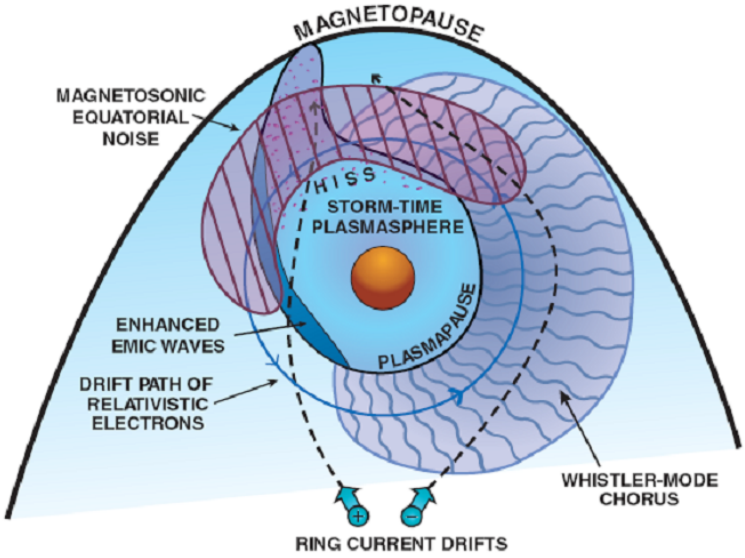

Figure 1.7 – Illustration of the different electromagnetic waves that populate the magnetosphere. Source: (*Thorne*, 2010).

1.4 Space weather and radiation belts

1.4.1 Space weather

The name of "space weather" is now commonly used to identify the field of science dedicated to the understanding of Sun-Earth interactions. The purpose hidden behind this expression is to be able to forecast the magnetic storms as meteorologists can forecast weather storms. However, the variety of the physical phenomena at stakes and the still limited and sparse data that are available today makes this objective rather an ideal goal, such that space weather forecasting is still an open issue.

1.4.2 Some harmful effects of space weather

On September 1, 1859, Richard Carrington observed some unusually large sunspots in the Sun's northern solar hemisphere. A few hours later, aurora borealis appeared and expanded across the northern Earth hemisphere to reach low latitude regions. Expectational outbursts of light were observed in the sky of unexpected places like Hawaii or Rome. The aurora were also combined with a general failure in telegraph systems all over Europe and North America. This geomagnetic storm is referred as the Carrington event, and is famous for being the largest geomagnetic storms ever recorded by ground-based magnetometers (*Lanzerotti*, 2007). This anecdote shows how vulnerable the electric transmission systems are when faced to severe geomagnetic conditions.

During a geomagnetic storm, the large variations of the electric currents flowing in the magnetosphere and ionosphere can induce anomalous currents on the Earth surface: the so-called geomagnetically induced currents (GIC). These punctual GIC are likely to flow through the conductive buried cables and consequently damage the associated transmission systems like the wire-line telegraph communications during the Carrington event. For example, on March 1989, a geomagnetic storm caused a general collapse of major transformers of the region of Quebec, Canada, resulting in a power outage during one day (*Bolduc*, 2002). Geomagnetic storms, by disturbing the ionosphere physical characteristics, also affect wireless communications that rely on the radio wave-reflecting property of the atmosphere's upper layers. Last but not least, satellites disruptions in the region of the radiation belts due to space radiation effects are legion in the recent history. One typical example of such disturbances took place in January 1994, when two Canadian satellites (the Anik satellites) experienced interruptions after being subjected during several days to a severe dose of high energy electrons (*Baker et al.*, 1994; *Lam et al.*, 2012). Since a 3 MeV electron can penetrate aluminium up to 6 mm in depth, the radiation belts are a very hostile environment for most of the orbiting satellites.

1.4.3 Quantification of space weather

Several indices exist to quantify the different properties associated to the various space weather conditions (K_p, Dst, AE, AL...). In this PhD thesis, we consider the common K_p index, which is used to quantify geomagnetic disturbances. The name K_p originates from German "planetarische Kennziffer", which simply means planetary index. Introduced by Julius Bartels in 1949, it indicates the global intensity of geomagnetic disturbances over a 3-hour-range. Sporadic magnetic changes are constantly monitored by 13 ground-based geomagnetic observatories that specifically record the three magnetic field components. The 13 stations are located between 44 degrees and 60 degrees northern or southern geomagnetic latitudes across the globe (Canada, USA, Sweden, Denmark, Scotland, England, Germany, Australia, New-Zealand). The global K_p index

is obtained as the mean value of the observed disturbance levels in the two horizontal field components, resulting in an average integer lying between 0 and 9. A K_p index above 5 typically indicates a magnetic disturbance related to a geomagnetic storm (*Love and Remick*, 2007). The K_p index, which is officially adopted by the International Association for Geomagnetism and Aeronomy (IAGA), is today derived at the German Research Centre for Geosciences (GFZ) in Potsdam (Germany). In the present thesis, we particularly assess the geomagnetic environment with the use of the K_p index (see Chapter 6).

1.4.4 The radiation belts space missions

1.4.4.a The CRRES mission

The Combined Release and Radiation Effects Satellite (CRRES) is a joint program of the National Aeronautics and Space Administration (NASA) and the US Department of Defense. It was launched on July 25, 1990, on an elliptical orbit of a 18.1 degrees inclination. The purpose was to investigate fields, plasmas, and energetic particles inside the Earth's magnetosphere in the framework of a nominal three-year mission. The mission ended however on October 12, 1991, due to onboard battery failure.

Data of this mission have been used extensively since 1991 and until very recently as this mission has been the first one to provide measurements of the wave environment surrounding the Earth (e.g., *Meredith et al.*, 2004, 2006a, 2009; *Orlova et al.*, 2014; *Orlova and Shprits*, 2014). Some of the CRRES electron flux data and wave models will be used in Chapter 6.

1.4.4.b The Van Allen Probes

The Van Allen Probes mission is conducted by the NASA. The two Van Allen Probes, also referred as the Radiation Belt Storm Probes (RBSP), were launched on August 30, 2012. This is the first mission to use two spacecraft in tandem (respectively the RBSP A and B), with one spacecraft following the other along the same orbit. The orbits are highly elliptical and lie nearly in the Earth's equatorial plane (apogee of 5.8 R_E, orbital period of about 9 hours, spin period of 11 seconds), enabling both satellites to cross diverse areas within the belts. The end of the mission is scheduled on June 2019. Since their launch, the two Van Allen Probes have measured over more than 65 storms.

The combination of two identical spacecraft is necessary to discriminate global events (i.e. events that occur simultaneously at different positions) from localized events or from those that move through different regions of the belts over time.

Different instruments are embedded in the Van Allen Probes, among which the Radiation Belt Storm Probes Ion Composition Experiment (RBSPICE), the Relativistic Proton Spectrometer (RPS), the Electric Field and Waves Suite (EFW), the Electric and Magnetic Field Instrument Suite and Integrated Science (EMFISIS) and the Energetic Particle, Composition, and Thermal Plasma Suite (ECT), which is made of three separate components: the Helium Oxygen Proton Electron (HOPE), the Magnetic Electron Ion Spectrometer (MagEIS) and the Relativistic Electron Proton Telescope (REPT). Each instrument is precisely described in (*Mauk et al.*, 2013).

In this PhD thesis, we will use electron flux measurements from the MagEIS instrument (*Blake et al.*, 2013) on board Van Allen Probe A (see Chapter 5).

Chapter 2

The physics of the radiation belts

The purpose of Chapter 2 is to synthesize the various theoretical concepts that are at stake in the physics of radiation belts, upon which rely the next Chapters 3, 4, 5, 6 and 7. Our primary goal is to pave a simple but quite exhaustive gradual pathway to understand, step by step, the formulations and approximations that have been considered throughout the years since the beginning of the 1950's.

Of course this chapter does not intend to replace the fundamental textbooks as the one of *Schulz and Lanzerotti* (1974) or *Roederer* (1970), which have fed several generations of researchers and whose results are still being currently debated within fruitful scientific meetings. At the apogee of theoretical studies of trapped particles motion (1950-1975), satellites' data were sparse and always debated (e.g., *McCormac*, 1969), such that no unique well-accepted explaination always existed to describe a given physical phenomenon. Consequently, at this time, an outstanding conceptual result could be left orphaned of any concrete application. By gathering today these pioneering concepts, it is however still possible to make some of them more accessible, especially within the scope of today's flourishing development of space instrumentation and computer capabilities. The present overview can also serve as a seedbed for the potential following PhD students who will choose to embrace the physics of the radiation belts.

We start the chapter by justifying the retained theoretical approach for the study of the radiation belts among the common conceptual existing methods in plasmas physics (*Baumjohann et al.*, 2010). After this contextualization, we present the three types of motions of a charged particle subjected to a nonuniform magnetic field: a gyromotion of the particle around the magnetic field line, a bounce motion along the field line, and a drift motion across the field lines (*Northrop*, 1963b,a; *Roederer*, 1970). These three motions have different frequencies that are well separated by orders of magnitude (*Roederer and Zhang*, 2014). This hierarchy of motions constitutes the cornerstone of the adiabatic space (*Northrop and Teller*, 1960; *Northrop*, 1963a; *Schulz and Lanzerotti*, 1974) built on three adiabatic invariants. The adiabatic space is primordial as it is theroretically well adapted to describe the distribution of electrons trapped in the radiation belts (*Lyons and Thorne*, 1973), which is the heart of the present PhD thesis. As emphasized by their denominations, the adiabatic invariants remain constant in time if the geospace environment is not perturbed by electromagnetic waves. If small perturbations occur, we investigate the necessary conditions that enable the violation of one or several adiabatic invariants (*Fälthammar*, 1965; *Fälthammar*, 1968; *Roederer*, 1970; *Schulz and Lanzerotti*, 1974), and we derive a so-called Fokker-Planck equation that governs the evolution of the distribution of electrons in the radiation belts under such a disturbed environment (*Chandrasekhar*, 1943, 1960; *Kennel and Engelmann*, 1966; *Lerche*, 1968; *Haerendel*, 1968; *Lyons et al.*, 1972; *Schulz and Lanzerotti*, 1974). We mainly focus on two diffusive processes that drive the dynamics of electrons: radial diffusion and pitch angle diffusion (*Walt*, 1970; *Lyons and Thorne*, 1973). We close this chapter by linking the theoretical phase space density to the particle fluxes, which is a quantity commonly measured by the orbiting satellites (*Roederer*, 1970; *Schulz and Lanzerotti*, 1974; *Walt*, 1994; *Roederer and Zhang*, 2014).

2.1 Contextualization of the present study

2.1.1 Different approaches to study space plasma physics

The full dynamics of a plasma is described by the equation of motion applied to each particle of the plasma, coupled with the four Maxwell equations written in Appendix

A.3.a. It rapidly appears that such a complete description is very difficult to concretely implement. Solving the entire system for each particle would require an unrealistic large amount of computational resources, and it would exhibit an overdetailed description that would completely disregard all the average behaviors inherent to the whole system (such as density or temperature) and hide the physical concepts of the particles' dynamics. Hence different approaches have been implemented over the past few decades to overcome the aforementioned technical difficulties (*Baumjohann and Treumann*, 1996).

2.1.1.a Single particle motion

The simplest approach is the description of the various motions of a single particle. It pictures the dynamics of one charged particle under the influence of background electric and magnetic fields. By doing so, this method neglects all collective behaviors inherent to a plasma and is not appropriate to fully describe the radiation belts. However it can serve as an interesting starting point to identify the different motions of a charged particle under the influence of a static (time-independent) but nonuniform (space-dependent) magnetic field.

2.1.1.b Kinetic approach

The second approach is the kinetic theory that adopts a statistical perspective. This is so far the most developed theory in plasma physics. Instead of solving the equation of motion for each particle, it looks at the particles' distribution in phase space. In such statistical approach, the related distribution function is usually governed by a nonlinear six-dimensional Vlasov equation, coupled with the Maxwell equations. In this description, the distribution function and the electromagnetic fields can have arbitrarily large and fast fluctuations. The so-called Particle-In-Cell (PIC) codes are dedicated to solve the Vlasov equation, and can generate self-consistent wave-particle interactions over small spatio-temporal scales. The publicly available LANL Vector Particle-In-Cell (VPIC) Project is one example of such model (*Bowers et al.*, 2008a,b, 2009). However the PIC codes show their limitations in performing the calculation of the distribution function over large spatio-temporal scales, as it requires expansive computational resources. Many other models specifically dedicated to the magnetosphere also follow a kinetic description without solving the full Vlasov equation like the PIC codes. They rather focus on a Fokker-Planck equation (similarly to the ones detailed in section 2.6). For example, the LANL Ring Current-Atmosphere Interactions Model (RAM) computes the low-energy ion distribution functions for ring current plasma, which provide the anisotropic pressure to the Self-Consistent Magnetic Field (SCB) model. Balance between the forces related to both pressure and magnetic field then enables the SCB model to calculate self-consistently the magnetic field topology for the ring-current (RAM) plasma (*Jordanova et al.*, 2006; *Zaharia et al.*, 2006; *Jordanova et al.*, 2010; *Welling et al.*, 2011).

2.1.1.c Magnetohydrodynamic approach

As the extreme counterpart of the single particle description, the magnetohydrodynamic approach consists of neglecting all single particle aspects and focus on the whole collective behavior of a plasma. The plasma is treated as a conducting fluid and is described through its macroscopic variables. Such dynamics can be depicted with the use of the devoted MagnetoHydroDynamic (MHD) codes. They do not solve the Vlasov equation itself but rather several integrated forms of the Vlasov equation giving birth

to moments (of different orders) of the distribution function. MHD simulations have the ability to give a description of the dynamics over large spatio-temporal scales, for example the interaction of the solar wind with the bow shock and the impact on the entire magnetosphere over many days. The American Block-Adaptive-Tree-Solarwind-Roe-Upwind-Scheme (BATS-R-US code) (*Powell et al.*, 1999; *Zeeuw et al.*, 2000; *Gombosi et al.*, 2002) and the Open Geospace General Circulation Model (Open GGCM) models are both MHD codes dedicated to the physics of magnetosphere. They can also generate hydrodynamic low frequency waves (mHz), but fail to treat higher frequency waves (kHz).

2.1.2 An adapted kinetic approach for the radiation belts

The approach adopted in the present PhD thesis is a statistical approach as depicted by the kinetic theory, but with additional underlying simplifications and assumptions related to the properties of the radiation belts. As mentioned before, the Vlasov equation that is put forward by the kinetic theory is a nonlinear six-dimensional equation that describes the particle distribution over the entire phase space (all positions and velocities). To that extent, its numerical resolution is still a challenging task to achieve. In the context of this thesis, a new coordinate system equivalent to the traditional phase space is built. It consists of three new variables called adiabatic invariants associated to the three phases of the periodic motions of the particle. This new coordinate system appears to be well adapted to the dynamics of the particles trapped into the radiation belts. Assuming efficient "phase mixing", we can ignore the aforementioned phases of motions, such that the nonlinear six-dimensional Vlasov equation can be reduced into a linear three-dimensional Fokker-Planck equation that takes the form of a diffusion equation. In return, the Fokker-Planck equation requires the prerequisite calculation of some diffusion coefficients that represent the effect of small-amplitude waves on the distribution function. All the effects induced by the electromagnetic waves are included in these diffusion coefficients, which are calculated in the framework of quasilinear theory (e.g., *Fälthammar*, 1965; *Kennel and Engelmann*, 1966; *Lerche*, 1968; *Lyons et al.*, 1971, 1972; *Lyons*, 1974a,b). This means that the waves must be specified prior to the Fokker-Planck simulations, they are not calculated by the code itself like in MHD or PIC simulations. The Fokker-Planck codes have proven to be useful for modeling the trapped energetic electrons response to small-amplitude waves (from mHz to kHz frequency range), and are widely used in the radiation belt scientific community. The most famous models are the American LANL Dynamic Radiation Belt Environment Assimilation Model (DREAM) 3-D code (e.g., *Tu et al.*, 2013; *Cunningham*, 2016; *Cunningham et al.*, 2018), the Versatile Electron Radiation Belt (VERB-3D) code (e.g., *Subbotin and Shprits*, 2009; *Shprits et al.*, 2009; *Subbotin et al.*, 2010; *Kim et al.*, 2011), the British BAS Radiation Belt Model (BAS-RBM) (e.g., *Glauert et al.*, 2014) or the French Salammbô code (e.g., *Beutier et al.*, 1995). Also let us mention the pioneering work from *Lyons and Thorne* (1973) who have been the first to theoretically exhibit the two-belt structure the radiation belts with a reduced-Fokker-Planck code (cf. Chapter 4).

2.2 Single particle motion

In the purpose of building an efficient theoretical framework devoted to the study of the radiation belts, we first describe the motion of a charged particle subjected to an electromagnetic field. This section serves as an opportunity to identify the useful

physical properties inherent to the motion of a charged particle trapped into a background magnetic field.

2.2.1 Gyromotion

Before entering the details of the whole dynamics of the radiation belts, let us spend some time to properly introduce this chapter by the very basic physics of magnetic trapping. As a starting point, following (*Jackson*, 1975, Chapter 12, section 3), we consider here a simple illustrative example in which a charged particle of mass m and charge q (positive for protons, negative for electron) is subjected to a uniform (no dependence in space) and static (no dependence in time) magnetic field $\boldsymbol{B}$. This example aims at emphasizing the inherent properties of a charged particle motion and to define some important quantities that we will use later in the thesis.

Let us consider a fixed frame of reference associated with a Cartesian set of coordinates (x, y, z) and the normalized vectors of the Cartesian base $(\hat{\boldsymbol{x}}, \hat{\boldsymbol{y}}, \hat{\boldsymbol{z}})$. Let us take a background magnetic field of intensity B_0 that points in the $\hat{\boldsymbol{z}}$ direction, and consider that the initial particle starts at the coordinate point $(0, 0, 0)$ with the initial velocity $\boldsymbol{v_0} = v_{0,x}\,\hat{\boldsymbol{x}} + v_{0,z}\,\hat{\boldsymbol{z}}$. Since the charged particle is subjected to the Lorentz force $\boldsymbol{F} = q\,\boldsymbol{v} \times \boldsymbol{B}$, for which $\boldsymbol{v}$ is the particle's instantaneous velocity, Newton's second law (also known in this case as the Lorentz equation) simply gives

$$m\,\frac{\mathrm{d}\boldsymbol{v}}{\mathrm{d}t} = q\,\boldsymbol{v} \times \boldsymbol{B}.$$

By projecting the above equation on the Cartesian coordinate system, we obtain

$$\begin{cases} m\,\dfrac{\mathrm{d}^2x}{\mathrm{d}t^2} &= \quad qB_0\,\dfrac{\mathrm{d}y}{\mathrm{d}t}, \\ m\,\dfrac{\mathrm{d}^2y}{\mathrm{d}t^2} &= -qB_0\,\dfrac{\mathrm{d}x}{\mathrm{d}t}, \\ m\,\dfrac{\mathrm{d}^2z}{\mathrm{d}t^2} &= \quad 0. \end{cases}$$

We solve the above system by taking account of the initial position of the particle and its initial velocity to eventually obtain the parametric equations of the particle trajectory

$$\begin{cases} x(t) &= \dfrac{v_{0,x}}{\omega_g}\sin(\omega_g t), \\ y(t) &= \dfrac{q}{|q|}\dfrac{v_{0,x}}{\omega_g}\left[\cos(\omega_g t) - 1\right], \\ z(t) &= v_{0,z}\,t, \end{cases}$$

for which

$$\omega_g = \frac{|q|B_0}{m} \tag{2.1}$$

is called the cyclotron pulsation, or the pulsation of gyration (*Jackson*, 1975). Let us mention that this expression is also valid is the relativistic case, for which $m = \gamma m_0$, with γ being the relativistic factor defined in Appendix A.1. Expressing the pulsation of

gyration is capital in radiation belts physics, since, as we will see, ω_g lays a first stone at setting up an adapted coordinate system for expressing the distribution of electrons trapped in the Earth's magnetic field. One can also derive the associated cyclotron period $\tau_g = 2\pi/\omega_g$. The cyclotron (or gyration) period will be used to define one of the two adiabatic assumptions that describe the theoretical framework of particle motion in a more complex general nonuniform magnetic field (see below). From above, we notice that

$$y(t) + \frac{q}{|q|}\frac{v_{0,x}}{\omega_g} = \frac{q}{|q|}\frac{v_{0,x}}{\omega_g}\cos(\omega_g t),$$

and so the projection of the three above parametric equations onto the horizontal plane generated by $(\hat{\boldsymbol{x}}, \hat{\boldsymbol{y}})$ gives

$$x(t)^2 + \left(y(t) + \frac{q}{|q|}\frac{v_{0,x}}{\omega_g}\right)^2 = \left(\frac{v_{0,x}}{\omega_g}\right)^2.$$

It represents a circle whose center has coordinates $\left(0, -\frac{q}{|q|}\frac{v_{0,x}}{\omega_g}\right)$ and whose radius ρ_c is

$$\rho_c = \frac{v_{0,x}}{\omega_g} = \frac{m\, v_{0,x}}{qB_0} \tag{2.2}$$

with $m = \gamma m_0$ in the relativistic case. Radius ρ_c is called the Larmor radius. Its estimation will be necessary to properly describe the one of the adiabatic assumption , as shown below, as well as defining the first adiabatic invariant. The strongest the magnetic field intensity is, the highest is the cyclotron pulsation and the lowest is the Larmor radius. The later is larger for protons than for electrons. Reversely, the electron gyrofrequency is higher for electrons. The geometric center of the cyclotron orbit is called the guiding center of the particle. Figure 2.1 illustrates the motion of a trapped proton (left) and electron (right) in a uniform and static magnetic field $\boldsymbol{B}$ pointing in the z direction. In the frame moving with the guiding center, the motion is purely circular.

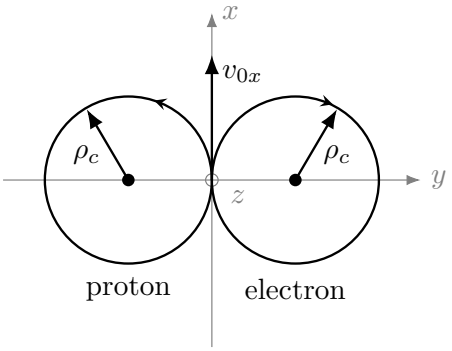

Figure 2.1 – Gyromotion of proton and electron starting at O with initial velocity $\boldsymbol{v_0} = v_{0x}\,\hat{\boldsymbol{x}}$. The scales related to the Larmor radius for the proton and electron have not been respected for clarity.

It is well known that there is no magnetic power $\mathcal{P}$ induced by the magnetic force, because $\mathcal{P} = \boldsymbol{F}\cdot\boldsymbol{v} = (q\,\boldsymbol{v}\times\boldsymbol{B})\cdot\boldsymbol{v} = 0$. In other words, the magnetic force does not work, and hence the kinetic energy E of the particle is conserved during the whole trajectory

according to the relation $\mathrm{d}E/\mathrm{d}t = \mathcal{P} = 0$. The kinetic energy is given (in a non relativistic case) by

$$E = \frac{1}{2}mv^2 = \frac{1}{2}m\left(v_x^2 + v_y^2 + v_z^2\right) = \frac{1}{2}m\left(v_{0,x}^2 + v_{0,z}^2\right).$$

We can also define the local pitch angle α of the charged particle as the angle between the magnetic field direction and the direction of the particle velocity. In mathematical terms, the pitch angle obeys the relation $\tan(\alpha) = v_\perp / v_\parallel$ for which $v_\perp$ is the intensity of the velocity component perpendicular to the magnetic field direction, and $v_\parallel$ is the intensity of the velocity component parallel to the magnetic field direction. The pitch angle is a key geometrical quantity since, as emphasized below, it enables to discriminate trapped electron populations from electrons that are lost in the atmosphere. In our case we have

$$\begin{cases} \cos(\alpha) = \dfrac{v_\parallel}{v} = \dfrac{v_z}{v} = \dfrac{v_{0,z}}{\sqrt{v_{0,x}^2 + v_{0,z}^2}}, \\ \sin(\alpha) = \dfrac{v_\perp}{v} = \dfrac{\sqrt{v_x^2 + v_y^2}}{v} = \dfrac{v_{0,x}}{\sqrt{v_{0,x}^2 + v_{0,z}^2}}. \end{cases}$$

Any change of one velocity component (increase or decrease) will reversely affect the other component in order to conserve the kinetic energy.

As a last usefulness of this example, we emphasize that the particle gyromotion is equivalent to a circular loop of an electric current $\mathcal{I}$ given by

$$\mathcal{I} = \frac{|q|}{\tau_g} = \frac{q^2 B_0}{2\pi m}$$

with $m = \gamma m_0$ as before. The electric current is the same for the particles that have a positive or a negative charge. The magnetic moment $\mathscr{M}$ of the particle is defined by the product of the electric current $\mathcal{I}$ with the surface S enclosed by the current loop (i.e. the cyclotron trajectory), such that

$$\mathscr{M} = \mathcal{I}S = \mathcal{I}\pi\rho_c^2 = \frac{mv_\perp^2}{2B_0} = \frac{p_\perp^2}{2mB_0} = \frac{p_\perp^2}{2\gamma m_0 B_0}, \tag{2.3}$$

in which $p_\perp$ is the intensity of the momentum component perpendicular to the magnetic field, recalling that the total momentum $\boldsymbol{p}$ is given by $\boldsymbol{p} = m\,\boldsymbol{v} = \gamma m_0\,\boldsymbol{v}$. Since B is constant and $p_\perp = mv_{0,x}$ during the whole motion, the magnetic moment $\mathscr{M}$ is a conserved quantity like the kinetic energy. Let us mention that the conservation of the magnetic moment in the non-relativistic case is a fundamental property that is prevalent in radiation belt physics and that will be assumed in the remaining of the thesis.

To sum up, the whole particle trajectory is a vertical helix around the magnetic field line (*Jackson*, 1975). In this situation, we can easily split the trajectory into a cyclotron trajectory around the field line and a rectilinear trajectory along the field line. The total particle velocity $\boldsymbol{v}$ can be recast as follows:

$$\boldsymbol{v} = \boldsymbol{v}^* + \boldsymbol{V}$$

for which

$$\boldsymbol{v}^* = v_{0,x}\cos(\omega_0 t)\,\hat{\boldsymbol{x}} - v_{0,x}\sin(\omega_0 t)\,\hat{\boldsymbol{y}}$$

is the pure cyclotron velocity and

$$\boldsymbol{V} = v_{0,z}\,\hat{\boldsymbol{z}}$$

is the velocity of the guiding center of the particle. This idea of splitting the velocity into its gyromotion and its guiding center motion is at the basis of the guiding center approximation that we describe below.

2.2.2 Guiding center approximation

2.2.2.a Adiabatic conditions

In a very general case, the full motion of a charged particle can be described by the second law of Newton, providing that a given inertial frame of reference has initially been specified. In magnetospheric physics, and as mentioned above, one often look for a moving frame in which the motion of the charged particle would be nearly circular around the magnetic field line (see Figure 2.2). Such assumption, which is called the guiding center approximation, holds as long as the two following adiabatic conditions are satisfied (*Roederer and Zhang*, 2014). The magnetic field should vary only a little along the cyclotron trajectory of the particle, i.e.

$$\rho_c \ll \frac{B}{\nabla B} \tag{2.4}$$

and the magnetic field should change only a little during a cyclotron period such that

$$\tau_g \ll \frac{B}{\mathrm{d}B/\mathrm{d}t}. \tag{2.5}$$

The two guiding-center approximations (2.4) and (2.5) are essential and will be assumed (for electrons) in all the remaining of the present thesis. Violation of these two assumptions can occur in the motion of particle heavier than electrons, such as ions, and its related consequences will be briefly discussed in the Conclusions.

In the previous illustrative example, both relations were verified because the magnetic field was considered uniform ($\nabla B = 0$) and static ($\mathrm{d}B/\mathrm{d}t = 0$). We focus now on the general situation of a non uniform magnetic field with the restrictions emphasized the adiabatic conditions (2.4) and (2.5). In such a situation, we are allowed to split the velocity $\boldsymbol{v}$ of the charged particle in the original frame of reference into the velocity $\boldsymbol{V}$ of the guiding center system according to the fixed original frame of reference, and $\boldsymbol{v}^*$, the velocity of the particle in the guiding center system (which is the cyclotron velocity). We have thus $\boldsymbol{v} = \boldsymbol{v}^* + \boldsymbol{V}$.

Let us conduct the study in a local coordinate system that follows the guiding center motion along a field line (*Roederer and Zhang*, 2014). The origin of the local Cartesian frame is the guiding center point C (see Figure 2.3). Let us define a z-axis parallel to $\boldsymbol{B}$ at the guiding center point, and the (x, z) plane as the osculating plane of the field line through C. Axis x is normal to that plane. The unit vector $\boldsymbol{e}$ is parallel to $\boldsymbol{B}$, $\boldsymbol{n}$ lies in the osculating plane and is normal to the field line, and the binormal $\boldsymbol{b}$ is perpendicular to both. We emphasize the fact that the moving unit vectors $\boldsymbol{b}$, $\boldsymbol{n}$ and $\boldsymbol{e}$ have nonzero spatial derivatives.

Let us first have a comprehensive approach of condition (2.4). In the local natural coordinate system defined above, $\nabla_\perp B = -B/R_c$, for which R_c is the radius of curvature of the magnetic field (see (*Roederer and Zhang*, 2014)). Hence, equation (2.4) can also be written as

$$\rho_c \ll \frac{B}{\nabla_\perp B} = R_c,$$

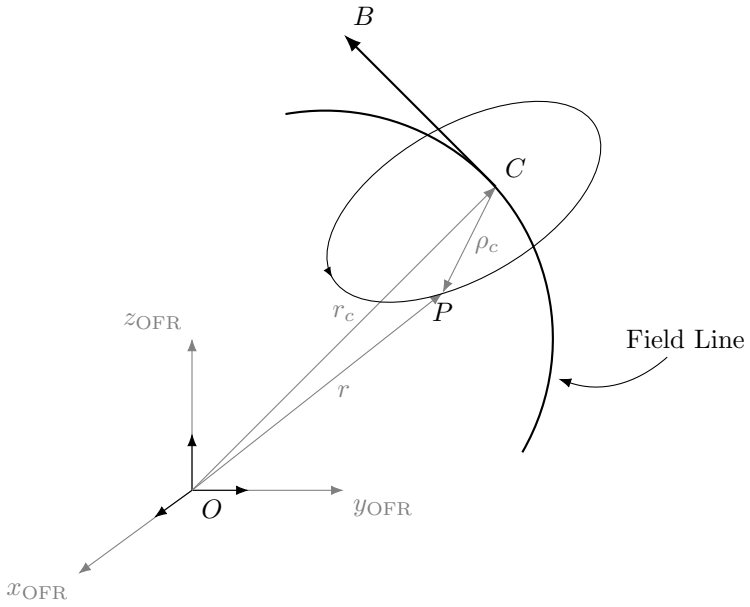

Figure 2.2 – Original frame of reference and guiding center system. Adapted from *Roederer and Zhang* (2014).

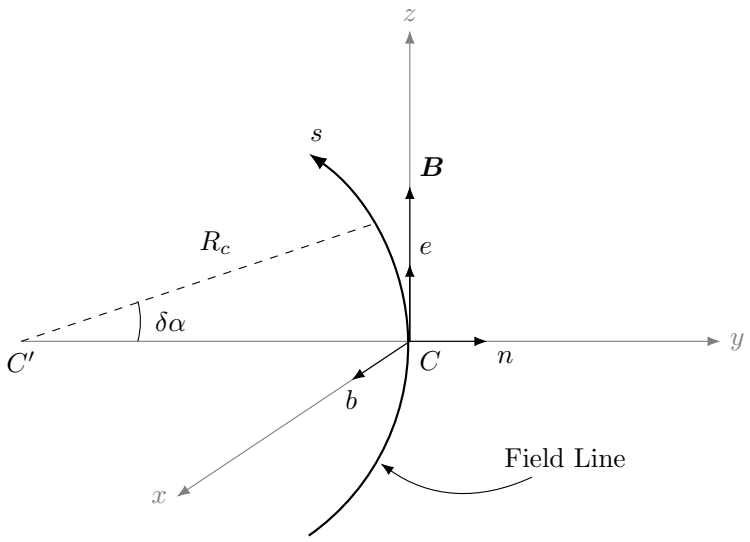

Figure 2.3 – Guiding center system. Adapted from *Roederer and Zhang* (2014).

which emphasizes the necessity of having a Larmor radius well below the radius of curvature of the magnetic field. In the second condition (2.5), the time derivative is a total time derivative that takes account of both the local time derivative of B and the spatial variation of B as seen by the particle in the moving guiding center system. If we make the assumption of a constant (in time) magnetic field intensity, the local time derivative vanishes and we have $\mathrm{d}B/\mathrm{d}t = v_\parallel \nabla_\parallel B$ (convective derivative). We note $l_\parallel = v_\parallel \tau_g$ the parallel distance travelled by the particle during one gyration. Taking account once again of the geometrical properties of the local natural frame, we have $\nabla_\parallel B = \partial B/\partial s$, and

then (2.5) becomes

$$l_{\parallel} \ll \frac{B}{\nabla_{\parallel} B} = \frac{B}{\partial B / \partial s}.$$

Speaking in terms of perpendicular and parallel velocity components, we end up with the following relation between the three aforementioned velocities (note that $\boldsymbol{v}_{\parallel}^{*} = \boldsymbol{0}$ in the guiding center system)

$$\begin{cases} \boldsymbol{v}^{*} &= \boldsymbol{v}_{\perp}^{*} \\ \boldsymbol{V} &= \boldsymbol{V}_{\parallel} + \boldsymbol{V}_{\perp} \end{cases}$$

The particle velocity can also be decomposed into a perpendicular motion across the magnetic field line and into a parallel motion along the magnetic field line, such that

$$\begin{cases} \boldsymbol{v}_{\perp} &= \boldsymbol{v}_{\perp}^{*} + \boldsymbol{V}_{\perp} \\ \boldsymbol{v}_{\parallel} &= \boldsymbol{V}_{\parallel}. \end{cases}$$

The perpendicular motion of the particle is decomposed into the motion of the particle in the guiding center system, i.e. the gyromotion around the magnetic field line that we have previously highlighted, represented by $\boldsymbol{v}_{\perp}^{*}$, and into a drift motion of the guiding center system across the field lines, emphasized by $\boldsymbol{V}_{\perp}$. For some reasons that we emphasize later, we refer to the parallel motion of the particle along the field lines as the bounce motion, whose velocity is $\boldsymbol{V}_{\parallel}$.

2.2.2.b Lorentz equation

In the fixed original frame of reference, the equation of motion that governs the dynamics of a charged particle subjected to the force induced by an electric field, the force induced by a magnetic field, and a force $\boldsymbol{F}$ induced by any other unspecified effects, writes

$$m \frac{\mathrm{d}\boldsymbol{v}}{\mathrm{d}t} = q\,\boldsymbol{\mathcal{E}} + q\,\boldsymbol{v} \times \boldsymbol{B} + \boldsymbol{F},$$

for which $\boldsymbol{\mathcal{E}}$ is the electric field, $\boldsymbol{B}$ is the magnetic field and q is the particle's charge.

Considering now the motion of the charged particle in the moving guiding center system, the equation of motion becomes

$$m \frac{\mathrm{d}\boldsymbol{v}^{*}}{\mathrm{d}t} = q\,\boldsymbol{\mathcal{E}}^{*} + q\,\boldsymbol{v}^{*} \times \boldsymbol{B}^{*} + \boldsymbol{F} + \boldsymbol{F_i}$$

where $\boldsymbol{B}^{*}$ and $\boldsymbol{\mathcal{E}}^{*}$ are respectively the magnetic and electric field in the moving guiding center system, and $\boldsymbol{F_i}$ is the inertial force induced by the motion of the guiding center system in the fixed original frame of reference. The electric and magnetic fields in a the moving frame change according to the Lorentz transformation

$$\begin{cases} \boldsymbol{B}^{*} &= \boldsymbol{B}, \\ \boldsymbol{\mathcal{E}}^{*} &= \boldsymbol{\mathcal{E}} + \boldsymbol{V} \times \boldsymbol{B}. \end{cases} \tag{2.6}$$

Moreover, since there is no motion of rotation of the guiding center system from the original frame of reference, the inertial force $\boldsymbol{F_i}$ reduces to $\boldsymbol{F_i} = -m\,\mathrm{d}\boldsymbol{V}/\mathrm{d}t$ and thus

$$m \frac{\mathrm{d}\boldsymbol{v}^{*}}{\mathrm{d}t} = q\,\boldsymbol{\mathcal{E}} + q\,\boldsymbol{V} \times \boldsymbol{B} + q\,\boldsymbol{v}^{*} \times \boldsymbol{B} + \boldsymbol{F} - m \frac{\mathrm{d}\boldsymbol{V}}{\mathrm{d}t}.$$

2.2.2.c Averaging over the gyrophase

The properties of the gyromotion ($\boldsymbol{v}^*$) being known from the previous section, the purpose here is to determine the characteristics of the motion of the particle's guiding center (velocity $\boldsymbol{V}$). Let us average the above equation over one cyclotron period. Over one cyclotron period, the particle in the guiding center system makes a full circle around the field line so that $\langle \boldsymbol{v}^*_\perp \rangle = \boldsymbol{0}$. Since $\boldsymbol{v}^*_\parallel = \boldsymbol{0}$, $\langle \boldsymbol{v}^* \rangle = \boldsymbol{0}$, the (gyro-averaged) equation of the guiding center motion is obtained (*Roederer and Zhang*, 2014)

$$q\,\langle \boldsymbol{\mathcal{E}} \rangle + q\,\langle \boldsymbol{V} \times \boldsymbol{B} \rangle + q\,\langle \boldsymbol{v}^* \times \boldsymbol{B} \rangle + \langle \boldsymbol{F} \rangle - m \left\langle \frac{\mathrm{d}\boldsymbol{V}}{\mathrm{d}t} \right\rangle = \boldsymbol{0}. \tag{2.7}$$

The next step is to calculate each terms of the above equation so as to identify the properties of the particle bounce and drift motions.

2.2.3 Bounce and drift motions

2.2.3.a Drift velocity

The adiabatic condition (2.4) enables us to expand the gyro-averaged Lorentz equation (2.7) about the guiding center up to the first order in space. As detailed in Appendix B.1, which is based on the derivations of *Roederer and Zhang* (2014), equation (2.7) becomes

$$q\,\boldsymbol{\mathcal{E}} + q\,\boldsymbol{V} \times \boldsymbol{B} - \mathscr{M}\,\boldsymbol{\nabla} B + \boldsymbol{F} - m\,\frac{\mathrm{d}\boldsymbol{V}}{\mathrm{d}t} = \boldsymbol{0}, \tag{2.8}$$

We notice the influence of a force $\mathscr{M}\,\boldsymbol{\nabla} B$ that is decomposed into a mirror force $\mathscr{M}\,\boldsymbol{\nabla}_\parallel B$ arising from the magnetic field curvature, and into a force $\mathscr{M}\,\boldsymbol{\nabla}_\perp B$ induced by the gradient of the magnetic field intensity.

The acceleration component of the inertial force $\mathrm{d}\boldsymbol{V}/\mathrm{d}t$ is a total time derivative of the guiding center velocity $\boldsymbol{V}$ that can be further expanded to lead to the following equation (recalling that the unit vector $\boldsymbol{b}$, $\boldsymbol{n}$, and $\boldsymbol{e}$ have nonzero spatial derivatives),

$$\frac{\mathrm{d}\boldsymbol{V}}{\mathrm{d}t} = \frac{\mathrm{d}v_\parallel}{\mathrm{d}t}\boldsymbol{e} + v_\parallel^2\,\frac{\partial \boldsymbol{e}}{\partial s} + v_\parallel\,(\boldsymbol{V}_\perp \cdot \boldsymbol{\nabla})\,\boldsymbol{e} + v_\parallel\,\frac{\partial \boldsymbol{e}}{\partial t} + \frac{\mathrm{d}\boldsymbol{V}_\perp}{\mathrm{d}t},$$

which is the same formulation as in (*Roederer and Zhang*, 2014, equation (2.13)). In the above expression, the drift velocity can be expressed as the contribution of drift velocities of different orders of approximation, as emphasized in Appendix B.2. At first order, the drift motion is only carried by the electric field and the external force, such that the first order drift velocity $\boldsymbol{V}_{1\perp}$ is

$$\boldsymbol{V}_{1\perp} = \frac{\boldsymbol{\mathcal{E}} \times \boldsymbol{B}}{B^2} + \frac{\boldsymbol{F} \times \boldsymbol{B}}{qB^2}.$$

Second-order contributions to the transverse drift velocity are mainly due to the non uniformity (in space) of the magnetic field and are expressible as

$$\boldsymbol{V}_{2\perp} = \frac{m v_\perp^{*2}}{2qB^3}\,\boldsymbol{B} \times \boldsymbol{\nabla}_\perp B + \frac{m v_\parallel^2}{qB^2}\,\boldsymbol{B} \times \frac{\partial \boldsymbol{e}}{\partial s}.$$

Particularly, the first term results from the gradient of the magnetic field intensity (often call gradient-drift velocity) and the second term comes from the curvature of the magnetic field (often called curvature-drift velocity). The expression of the gradient-drift velocity

depends on the charge q of the particle into consideration and will be used to quantify the period of gyro-motion in the following section as well as applying the drift-average of local quantities such as the particle's pitch angle (see Chapter 6). Finally, some higher order terms add up to the aforementioned drift velocities. They can be written as

$$\boldsymbol{V}_{3\perp} = \frac{m}{qB^2}\boldsymbol{B}\times v_{\parallel}\frac{\partial \boldsymbol{e}}{\partial t} + \frac{m}{qB^2}\boldsymbol{B}\times v_{\parallel}\left(\boldsymbol{U}\cdot\boldsymbol{\nabla}\right)\boldsymbol{e} + \frac{m}{qB^2}\boldsymbol{B}\times\frac{\mathrm{d}\boldsymbol{U}}{\mathrm{d}t},$$

for which the velocity $\boldsymbol{U}$ denotes the "$\mathcal{E}$ cross B" drift and is defined by ($\boldsymbol{U} = \boldsymbol{\mathcal{E}}\times\boldsymbol{B})/B^2$. The first term arises from the time dependence of the direction of the magnetic field, the second terms takes account of the spatial variation of the direction of the magnetic field, and the last term is called the polarization drift.

Hence the total drift velocity perpendicular to the magnetic field line is

$$\boldsymbol{V}_{\perp} = \boldsymbol{V}_{1\perp} + \boldsymbol{V}_{2\perp} + \boldsymbol{V}_{3\perp}. \tag{2.9}$$

The expression of the drift velocity will be used in many aspects of the present PhD thesis. For example, as shown by *Schulz and Lanzerotti* (1974) and stated in the following section, it enables to quantify the importance of the electric field on the particle's motion compared with the magnetic field. It also emphasizes the complexity of dealing with both a nonuniform magnetic field and electric field.

2.2.3.b Bounce motion

After some more tedious calculations as shown in Appendix B.3, we obtain from (2.7) the equation of the parallel motion (*Roederer and Zhang*, 2014, equation (2.22))

$$m\frac{\mathrm{d}v_{\parallel}}{\mathrm{d}t} = q\mathcal{E}_{\parallel} + F_{\parallel} - \mathscr{M}\frac{\partial B}{\partial s} + mv_{\parallel}\boldsymbol{V}_{\perp}\cdot\frac{\partial \boldsymbol{e}}{\partial s} + m\boldsymbol{V}_{\perp}\cdot\frac{\partial \boldsymbol{e}}{\partial t} + m\boldsymbol{V}_{\perp}\cdot\left(\boldsymbol{V}_{\perp}\cdot\boldsymbol{\nabla}\right)\boldsymbol{e}. \tag{2.10}$$

The first two terms on the right hand side of the above equation are zero-order terms, the third term (that represents the mirror force) is a first-order term, and all the other remaining terms are of higher order. As we will discuss later for the case of a geomagnetic filed (merely a dipole field), equation (2.10) involves the mirror force $-\mathscr{M}\partial B/\partial s$ and is thus likely to describe the bounce motion of the particle along a given field line.

The next section, which specifies the magnetic and electric environment of the radiation belts, will enable us to further simplify (2.10) and to characterize the electrons' bounce motion along a magnetic field line.

2.3 The Earth's magnetic and electric fields

Once the equations of motion have been derived for a very general case, let us describe the common formulations in use to model both the Earth's magnetic and electric fields before investigating the motion of the trapped electrons within the radiation belts.

2.3.1 The Earth's magnetic field

2.3.1.a The different origins of the Earth's magnetic field

The origins of the Earth's magnetic field are multiple, and investigating the different natural processes at stakes is still an open question and the topic of current research

works. As far as we know, the major part of the magnetic field is produced by a hydrodynamic dynamo in the Earth's liquid outer core (located at 2900-5100 km depth) and constitutes over 99% of the total magnetic field. This is the main or core field (*Walt*, 1994). A second part of the field comes from the magnetized rocks present in the Earth's lithosphere (below 50 km depth): this is the litospheric or crustal field (*Walt*, 1994). A third part of the Earth's magnetic field takes its origin from the electric currents in the near-Earth space (over 100 km altitude): this is the external field (*Walt*, 1994). The external contribution is on average less than 1‰ of the main field. However, during geomagnetic storms, the external contribution can reach up to several percentage of the main field during a few hours.

The Earth's magnetic field is also subjected to different temporal variations (*Courtillot and Le Mouel*, 1988). Changes in the strength and direction of the electric currents in the Earth's liquid outer core give birth of secular variations that have a timescale of several years. On the other hand, rapid transient variations also happen. They are caused by the electric currents in the near-Earth space that are driven by solar activity. They induce changes in the Earth's magnetic field at a more rapid timescale of hours or seconds.

2.3.1.b Modeling the Earth's magnetic field induced by internal effects

A formulation of the Earth's magnetic field (and by extension the magnetic field of the Sun and other planets) relies on the Maxwell equations (see Appendix A.3.a). We summarize the approach adopted in (*Walt*, 1994) to obtain the expressions of the internal magnetic field and the dipole field, the latter being used in Chapters 4, 5, and partially in Chapter 6. Considering first a steady state for Maxwell's equations, and, second, that there is no current passing through the magnetosphere in the region of interest, the curl of the magnetic field vanishes in Maxwell-Ampere equation. Hence the internal magnetic field $\boldsymbol{B}$ can be represented as the gradient of a scalar quantity ψ_i. The divergence of the magnetic field being zero, the aforementioned scalar potential ψ_i has to be the solution of a Laplace's equation $\nabla^2\psi_i = 0$. Laplace's equation in spherical geographic coordinates (r, θ, φ), with r being the radial distance, θ the magnetic colatitude and φ the magnetic longitude, is given by

$$\frac{1}{r^2}\frac{\partial}{\partial r}\left(r^2\frac{\partial\psi}{\partial r}\right) + \frac{1}{r^2\sin(\theta)}\frac{\partial}{\partial\theta}\left(\sin(\theta)\frac{\partial\psi}{\partial\theta}\right) + \frac{1}{r^2\sin^2(\theta)}\frac{\partial^2\psi}{\partial\varphi^2} = 0. \tag{2.11}$$

We finally obtain for the internal (core) magnetic field (*Walt*, 1994)

$$\psi_i(r,\theta,\varphi) = R_E\sum_{n=1}^{\infty}\left(\frac{R_E}{r}\right)^{n+1}\sum_{m=0}^{n}\left[g_n^m\cos(m\varphi) + h_n^m\sin(m\varphi)\right]\widetilde{P}_n^m(\cos(\theta)), \tag{2.12}$$

for which R_E is the Earth radius (about 6370 km) and $\widetilde{P}_n^m$ are the normal Legendre functions (Schmidt semi-normalization). This strategy of resolution is called the multipole expansion. The coefficients g_n^m and h_n^m are spherical harmonic coefficients that are adjusted to fit experimental values of the magnetic field sampled on a worldwide basis. Let us mention that the above expression (2.12) is obtained by considering a vanishing internal potential for $r \to \infty$ (*Walt*, 1994).

2.3.1.c The dipole magnetic field

The first and dominant term of the scalar potential expression (2.12) is given for $n = 1$ and $m = 0$, and represents the dipole field. The scalar potential expression for a

dipole field is (*Walt*, 1994)

$$\psi_i(r,\theta,\varphi) = R_E \left(\frac{R_E}{r}\right)^2 g_1^0 \cos(\theta).$$

In a dipole field, $g_1^0 = -B_E$, with $B_E = 0.311$ G being the strength of the equatorial magnetic field at the Earth's surface. Hence, from relation $\boldsymbol{B} = -\boldsymbol{\nabla}\psi_i$ we end up with the dipole magnetic field expressed in spherical coordinates (e.g., *Schulz and Lanzerotti*, 1974; *Walt*, 1994)

$$\begin{cases} B_r = -\dfrac{\partial\psi}{\partial r} = -2B_E \left(\dfrac{R_E}{r}\right)^3 \cos(\theta) \\ \\ B_\theta = -\dfrac{1}{r}\dfrac{\partial\psi}{\partial\theta} = -B_E \left(\dfrac{R_E}{r}\right)^3 \sin(\theta) \\ \\ B_\varphi = -\dfrac{1}{r\sin(\theta)}\dfrac{\partial\psi}{\partial\varphi} = 0. \end{cases} \tag{2.13}$$

We notice that there is no longitudinal dependence (φ variable) of the dipole magnetic field, so that the dipole field is symmetric in longitude. Describing the properties of a simple dipole field enables us, by comparison, to emphasize the inherent complexity of the concrete magnetospheric magnetic field, as discussed in Chapters 6 and 7 for example.

Since the guiding center of electrons trapped in the magnetic field follows the curve of the so-called field line, as discussed for example in (*Roederer and Zhang*, 2014, section 2.2), deriving the field line equation in the dipole field is essential to compute the electron dynamics. The equation of a field line is obtained by solving $\mathbf{d}\boldsymbol{s} \times \boldsymbol{B} = \mathbf{0}$, for which the $\mathbf{d}\boldsymbol{s}$ vector is the element of the field line commonly expressed in spherical coordinates (r,θ,φ). It leads, for a dipole field, to

$$\mathrm{d}\varphi = 0$$

and

$$\frac{\mathrm{d}\ln(r)}{\mathrm{d}\theta} = \frac{B_r}{B_\theta} = 2\cot(\theta).$$

The first expression is simply equivalent to $\varphi = \varphi_0$ (the field line equation does not depend on the azimuth), while the integration of the second expression between the equatorial radial distance r_0 and local radius r corresponding to colatitude θ leads to

$$r(\theta) = L\,R_E \sin^2(\theta), \tag{2.14}$$

for which $L = r_0/R_E$ is the (normalized) equatorial radial distance of the field line from the center of the Earth, expressed in Earth radii. The L parameter, emphasized by the dipole field line equation, is of prime importance since it characterizes, as we will discuss below, the radial diffusive transport of electrons in the radiation belts.

The total intensity, B, of the dipole magnetic field is a also a key quantity to track the trapped electron populations within the radiation belts according to their kinetic energy and pitch angles, as emphasized by the transformation (4.1) of Chapter 4 for example. It writes $B = \left(B_r^2 + B_\theta^2 + B_\varphi^2\right)^{1/2}$ so that for any position in space (r,θ,φ), the magnetic dipole field intensity is

$$B(r,\theta) = B_E \left(\frac{R_e}{r}\right)^3 \left[1 + 3\cos^2(\theta)\right]^{1/2}.$$

On a magnetic field line, $r(\theta) = L\,R_e \sin^2(\theta)$ such that the dipole magnetic field intensity becomes

$$B(L,\theta) = \frac{B_E}{L^3}\frac{\left[1+3\cos^2(\theta)\right]^{1/2}}{\sin^6(\theta)}. \tag{2.15}$$

The equatorial magnetic field intensity B_0 is also simply defined as $B_0(L) = B_E/L^3$.

2.3.1.d The IGRF model

More accurate geomagnetic models takes account of more than one term in the summation (2.12). The International Geomagnetic Reference Field (IGRF) (e.g., *Thébault et al.*, 2015) is a standard mathematical description of the large-scale structure of the Earth's main magnetic field based on the scalar potential given by equation (2.12). The different parameters are fitted from surveys, observatories, and satellites across the globe. The IGRF model has been produced and updated under the direction of the International Association of Geomagnetism and Aeronomy (IAGA) since 1965. The potential ψ_i is extended to the most important terms in the summation, leading to a geomagnetic model that breaks its symmetry in longitude. An interesting feature of the core field is the so-called South Atlantic Anomaly (SAA), as shown in Figure 2.4 that represents the total magnetic field intensity. This is a large area of very low field intensity (less than 20 000 nT) over South America, the southern Atlantic, and southern Africa. This is problematic for satellites orbiting Earth, and the majority of technical breakdowns occurs when they pass through this region. The properties of the IGRF model and its related SAA are discussed and quantified in Chapter 7.

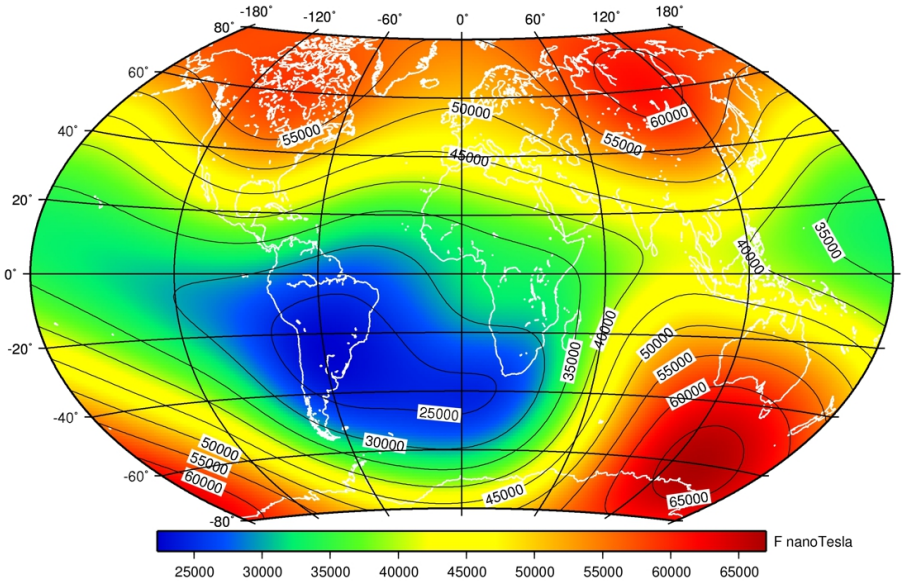

Figure 2.4 – Total magnetic field intensity as modeled by the IGRF model. The massive drop in intensity of the Atlantic coast of Brazil is called the South Atlantic Anomaly (SAA). Source: http://www.geomag.bgs.ac.uk/research/modelling/IGRF.html.

2.3.1.e Modeling the Earth's magnetic field induced by external effects

The previously presented multipole expansion method can also be used to develop some aspects of the magnetic field induced by external currents. Because the previous formulation relies on the assumption that there is no current flowing in the system (the curl of the magnetic field vanishes), the magnetic field produced by the ring current, the tail current sheet, and the field-aligned currents (*Baumjohann et al.*, 2010) are out of the scope of the multipole expansion and cannot be derived under such formalism (*Walt*, 1994). Only the magnetic field produced by the external magnetopause currents (Chapman-Ferraro), which are confined to the surface of the magnetosphere, can be represented by Laplace's equation (2.11). In that case, the corresponding external magnetic field is given by (*Walt*, 1994)

$$\psi_e(r,\theta,\varphi) = R_E \sum_{n=1}^{\infty} \left(\frac{R_E}{r}\right)^{-n} \sum_{m=0}^{n} \left[q_n^m \cos(m\varphi) + s_n^m \sin(m\varphi)\right] \widetilde{P}_n^m(\cos(\theta)). \tag{2.16}$$

The coefficients q_n^m and s_n^m are also spherical harmonic coefficients parametrized to fit experimental values of the magnetic field. Expression (2.16) is deduced by considering a vanishing external potential at $r = 0$.

2.3.1.f The external magnetic field models

Many magnetic field models induced by external currents have also been developed to include the effects of the diversity of the currents flowing into the magnetosphere. Most of them rely on the geomagnetic activity as well as the characteristics of the solar wind. The most famous among them are the Tsyganenko magnetic field series (e.g., *Tsyganenko*, 1989; *Tsyganenko and Stern*, 1996; *Tsyganenko et al.*, 2003; *Tsyganenko and Sitnov*, 2005, 2007). They take advantage of both measured field values and theoretical magnetospheric models to develop parametrized field models. They take account of the external magnetic field contributions induced by the magnetopause (Chapman-Ferraro) currents, the ring current, the magnetotail current and the field-aligned currents.

Chapter 6 particularly emphasizes the impacts of the (*Tsyganenko*, 1989) model (also referred as the T89 field model) on the radiation belt dynamics.

2.3.2 The Earth's electric field

Let us now have a look on typical models for the Earth's electric field and relate its impact on the particle motion compared with the influence of the magnetic field. The most simple models consider two distinct contributions of the electric field, coming from different origins (e.g., *Schulz and Lanzerotti*, 1974; *Roederer and Zhang*, 2014). We can first build an (internal) electric field induced by the rotation of the magnetic field lines with the Earth. We designate this electric field as the corotation electric field $\boldsymbol{\mathcal{E}}_{\text{coro}}$. Furthermore we can build an (external) electric field driven from the solar wind flow, referred as the convection electric field $\boldsymbol{\mathcal{E}}_{\text{conv}}$. For the present purpose, the ambient magnetic field is here considered as a dipole field.

2.3.2.a Corotation induced electric field

In the inner belt, the magnetic field lines, located at radial distance r from the Earth's center, are corotating with the Earth (*Mozer*, 1973). The corotating velocity $\boldsymbol{V_0}$ is such

that $\boldsymbol{V_0} = (\boldsymbol{\Omega_0} \times \boldsymbol{r})$, for which $\Omega_0 = 7.27 \times 10^{-5}$ rad/s is the angular rotational speed of the Earth.

In the rotating frame of reference, the electric field is $\boldsymbol{\mathcal{E}}^*_{\text{coro}} = \boldsymbol{\mathcal{E}}_{\text{coro}} + \boldsymbol{V_0} \times \boldsymbol{B}$ according to Lorentz transformation (2.6), for which $\boldsymbol{\mathcal{E}}_{\text{coro}}$ is the electric field in the inertial reference frame. The current density $\boldsymbol{\mathcal{J}}^*$ in the rotating frame is governed by Ohm's law (21), i.e.

$$\boldsymbol{\mathcal{J}}^* = \sigma \boldsymbol{\mathcal{E}}^*_{\text{coro}} = \sigma \left(\boldsymbol{\mathcal{E}}_{\text{coro}} + \boldsymbol{V_0} \times \boldsymbol{B} \right),$$

with σ the conductivity of the ionosphere (*Baumjohann and Treumann*, 1996).

We derive an expression of the corotation induced electric field $\boldsymbol{\mathcal{E}}_{\text{coro}}$ according to the approach led by (*Baumjohann and Treumann*, 1996, Chapter 5). Maxwell-Ampere equation (15) states that $\boldsymbol{\nabla} \times \boldsymbol{B} = \mu_0 \boldsymbol{\mathcal{J}}^* = \mu_0 \sigma \left(\boldsymbol{\mathcal{E}}_{\text{coro}} + \boldsymbol{V_0} \times \boldsymbol{B} \right)$. Taking the curl of the previous equation and accounting for the fact that $\boldsymbol{\nabla} \cdot \boldsymbol{B} = 0$ (Maxwell-Flux equation (14)) gives

$$\boldsymbol{\nabla} \times (\boldsymbol{\nabla} \times \boldsymbol{B}) = -\nabla^2 \boldsymbol{B} = \mu_0 \sigma \boldsymbol{\nabla} \times \left(\boldsymbol{\mathcal{E}}_{\text{coro}} + \boldsymbol{V_0} \times \boldsymbol{B} \right).$$

Since Maxwell-Faraday equation states that $\boldsymbol{\nabla} \times \boldsymbol{\mathcal{E}}_{\text{coro}} = -\partial \boldsymbol{B} / \partial t$, it gives

$$\frac{\partial \boldsymbol{B}}{\partial t} = \boldsymbol{\nabla} \times (\boldsymbol{V_0} \times \boldsymbol{B}) + \frac{1}{\mu_0 \sigma} \nabla^2 \boldsymbol{B}.$$

If we consider an infinite ionosphere conductivity $\sigma \to \infty$, the magnetic diffusive term $1/(\mu_0 \sigma) \nabla^2 \boldsymbol{B}$ becomes negligible. It implies that any field changes occur as if the field lines move rigidly with the ionospheric plasma. This inferred simultaneous motion of particles and magnetic field is commonly called the frozen field line approximation (e.g., *Fälthammar*, 1965; *Fälthammar*, 1968; *Baumjohann and Treumann*, 1996). Hence

$$\frac{\partial \boldsymbol{B}}{\partial t} = \boldsymbol{\nabla} \times \left(\boldsymbol{V_0} \times \boldsymbol{B} \right),$$

and taking account of Maxwell-Faraday equation, we obtain

$$\frac{\partial \boldsymbol{B}}{\partial t} = \boldsymbol{\nabla} \times (\boldsymbol{V_0} \times \boldsymbol{B}) = -\boldsymbol{\nabla} \times \boldsymbol{\mathcal{E}}_{\text{coro}},$$

i.e.

$$\boldsymbol{\mathcal{E}}_{\text{coro}} = -\boldsymbol{V_0} \times \boldsymbol{B} = -(\boldsymbol{\Omega_0} \times \boldsymbol{r}) \times \boldsymbol{B}. \tag{2.17}$$

Let us mention that the derivation of (2.17) can be also obtained with the use of the magnetic vector potential $\boldsymbol{\mathcal{A}}$ (*Roederer and Zhang*, 2014). Back to the Lorentz transform, the above relation simply tells us that the frozen field line approximation implies $\boldsymbol{\mathcal{E}}^*_{\text{coro}} = \boldsymbol{0}$, indicated that in the rotating reference frame, the ionospheric plasma is at rest. Equation (2.17) has also been obtained by *Mozer* (1973) starting directly from the assumption of $\boldsymbol{\mathcal{E}}^*_{\text{coro}} = \boldsymbol{0}$.

Despite being an induced field, the electric field $\boldsymbol{\mathcal{E}}_{\text{coro}}$ can also be written as the gradient of a scalar potential $V_{\mathcal{E}\text{coro}}$ such that $\boldsymbol{\mathcal{E}}_{\text{coro}} = \boldsymbol{\nabla} V_{\mathcal{E}\text{coro}}$ with (for a magnetic dipole field) (*Schulz and Lanzerotti*, 1974; *Roederer and Zhang*, 2014)

$$V_{\mathcal{E}\text{coro}} = -B_E \frac{\Omega_0 R_E^2}{L} = -B_E \frac{\Omega_0 R_E^3}{r} \sin^2(\theta).$$

2.3.2.b Convection electric field

Even if, formally, the electric field driven by solar wind flows cannot be directly derived from a scalar potential, a model of a scalar potential $V_{\mathcal{E}\text{conv}}$ can be built, from which the convection electric field can be extracted. The scalar potential has commonly the following expression (*Schulz and Lanzerotti*, 1974; *Roederer and Zhang*, 2014)

$$V_{\mathcal{E}\text{conv}} = \mathcal{E}_c L R_E \sin(\varphi) = \mathcal{E}_c r \sin^{-2}(\theta) \sin(\varphi).$$

Under typical quiet conditions, the $\mathcal{E}_c$ parameter is such that $\mathcal{E}_c \sim 4\mu\text{V/cm}$ (*Schulz and Lanzerotti*, 1974).

2.3.2.c Quantifying the influence of the electric field

To quantify the effects of the electric field compared with the influence of the magnetic field on a trapped particle population, let us recall that, at first order, a drifting particle moves across the magnetic field lines under the combined effects of the electric field and the curvature of the magnetic field. For equatorially mirroring particles ($B = B_0$), the corresponding drift velocity given by (2.9) reduces (up to the second order) in this specific case to the combination of the "E cross B" drift and the gradient drift such that

$$\boldsymbol{V}_D = -\boldsymbol{\nabla}_\perp \left(\frac{\mathscr{M}}{q} B_0 + V_{\mathcal{E}\text{coro}} + V_{\mathcal{E}\text{conv}} \right) \times \frac{\boldsymbol{B}_0}{B_0^2}. \tag{2.18}$$

This formula clearly states that such a particle drifts by following the curves of constant potential W (*Roederer and Zhang*, 2014)

$$W = \frac{\mathscr{M}}{q} B_0 + V_{\mathcal{E}\text{coro}} + V_{\mathcal{E}\text{conv}}.$$

The associated total energy qW also remains constant along a drift path, and so, in a dipole magnetic field at the geomagnetic equator

$$qW = \mathscr{M} \frac{B_E}{L^3} - qB_E \frac{\Omega_0 R_E^2}{L} + q\mathcal{E}_c \, L R_E \sin(\varphi).$$

The first term at the right hand side represents the internal energy that is related to the particle's gyromotion and the two last terms are the potential energy induced by the combined electric fields. Denoting the particle's (non-relativistic) kinetic energy by $E = mv_\perp^2/2 = \mathscr{M} \, B_E/L^3$ (for equatorial particles of 90 degree pitch angle), the effects of the magnetic field dominate if

$$E \gg q\mathcal{E}_c \, L R_E \sim 4L \text{ keV}$$

and if (*Schulz and Lanzerotti*, 1974)

$$E \gg qB_E \frac{\Omega_0 R_E^2}{L} \sim \frac{100}{L} \text{ keV}.$$

Hence the background electric field can be neglected for electrons having an energy larger than a few keV, i.e. for most of the electrons trapped in the radiation belts (*Schulz and Lanzerotti*, 1974). Note that in this case, the drift velocity reduces to

$$\boldsymbol{V}_D = -\frac{\mathscr{M}}{qB_0^2} \left(\boldsymbol{\nabla}_\perp B_0 \times \boldsymbol{B}_0 \right), \tag{2.19}$$

which means that the equatorial particles drift over contours of constant B_0, which correspond to the contours of minimum field intensity.

2.4 Particle trapping

Having the possibility to discard the electric field for high energy particles, let us go back to the previous formulation of particle motion and apply it more specifically to the radiation belts environment. This section recalls the most important results related to bounce motion obtained in (*Roederer*, 1970; *Roederer and Zhang*, 2014).

2.4.1 Pitch angle and magnetic field intensity

2.4.1.a Conservation of magnetic moment

As we will see, the $\mu = \gamma \mathscr{M}$ quantity, which relates to the magnetic moment $\mathscr{M}$ in the non-relativistic case, is a conserved quantity (*Northrop*, 1963b), so that its value at the magnetic equator s_0 is the same as its value at any point s of the magnetic field line, i.e. $\mu(s_0) = \mu(s)$, which writes

$$\frac{m v_{0\perp}^2}{2B_0} = \frac{m v_{s\perp}^2}{2B_s},$$

in which $v_{0\perp}$ and B_0 are respectively the particle's velocity and the magnetic field intensity at the equatorial point, and $v_{s\perp}$ and B_s are respectively the particle's velocity and the magnetic field intensity at the point s of the field line. Hence, the local perpendicular velocity of a particle on a given point on the field line can be deduced from the equatorial velocity through the relation $v_{s\perp}^2 = v_{0\perp}^2 B_s/B_0$. Since $v_{0\perp} = v_0 \sin(\alpha_0)$, for which α_0 is the equatorial pitch angle of the particle, we have the following expression for the perpendicular velocity component

$$v_{s\perp}^2 = v_0^2 \frac{\sin^2(\alpha_0)}{B_0} B_s. \tag{2.20}$$

2.4.1.b Conservation of energy

The total energy is also a conserved quantity along the field line, which means that $E_0 + W_0 = E_s + W_s$, for which E_0 and W_0 are respectively the kinetic and potential energy at the magnetic equator, and E_s and W_s are respectively the kinetic and potential energy at the point s of the field line. Hence (still working on a non-relativistic case)

$$\frac{1}{2} m \left(v_{0\parallel}^2 + v_{0\perp}^2 \right) + W_0 = \frac{1}{2} m \left(v_{s\parallel}^2 + v_{s\perp}^2 \right) + W_s,$$

so that $v_{s\parallel}^2 = v_0^2 - v_{s\perp}^2 - 2\,(W_s - W_0)/m$. By using (2.20) we deduce the parallel velocity component writes

$$v_{s\parallel}^2 = v_0^2 \left[1 - \frac{\sin^2(\alpha_0)}{B_0} B_s \right] - \frac{2}{m} (W_s - W_0). \tag{2.21}$$

Now, from the definition of the pitch angle at point s of the magnetic field line, $\sin^2(\alpha_s) = v_{s\perp}^2/v_s^2$, and by using equations (2.20) and (2.21) that respectively express the perpendicular and parallel velocity components, recalling that the kinetic energy is $E_0 = 1/2\, m v_0^2$, we end up with (*Roederer and Zhang*, 2014)

$$\sin^2(\alpha_s) = \frac{\sin^2(\alpha_0)}{B_0} B_s \left[1 - \frac{W_s - W_0}{E_0} \right]^{-1}. \tag{2.22}$$

This means that the particle's local pitch angle is deduced from the equatorial pitch angle, knowing the local and equatorial magnetic field intensity and potential energy.

2.4.1.c Equipotential field lines

If we consider now the specific case for which the potential energy is constant along a field line (we speak in this case of equipotential field lines), then (2.22) becomes

$$\sin^2(\alpha_s) = \frac{\sin^2(\alpha_0)}{B_0} B_s. \tag{2.23}$$

An electron that moves along the field line towards higher latitudes encounters regions of stronger magnetic field intensity. By doing so, its parallel velocity component decreases at the expanse of the perpendicular velocity component, until the particle reaches a so-called mirror point s_m at which the parallel velocity component vanishes, characterized by a local pitch angle of 90 degrees. At this location, all the electron's kinetic energy is included its the perpendicular velocity component, i.e. $v_{m\perp} = v_m$ and $v_{m\parallel} = 0$. Writing B_m the magnetic field intensity at the mirror point, relation (2.23) can be further extended as

$$\frac{B_s}{\sin^2(\alpha_s)} = \frac{B_0}{\sin^2(\alpha_0)} = B_m, \tag{2.24}$$

and thus

$$\sin(\alpha_0) = \left(\frac{B_0}{B_m}\right)^{1/2} \quad \text{and} \quad \cos(\alpha_0) = \left(1 - \frac{B_0}{B_m}\right)^{1/2}.$$

The above relations state that the value of the particle's equatorial pitch angle determines the magnetic field intensity at the mirror point and thus the mirror point location on the field line.

2.4.1.d Equatorial pitch angle and mirror point

For a dipole field, with the help of equation (2.15), the equatorial pitch angle and the mirror point colatitude θ_m are linked by the following relationship (e.g., *Roederer and Zhang*, 2014)

$$\sin^2(\alpha_0) = \frac{\sin^6(\theta_m)}{[1 + 3\cos^2(\theta_m)]^{1/2}},$$

which enables us to determine the equatorial pitch angle of a particle if we know the mirror point latitude (Figure 2.5, left), or, reversely, to predict the mirror point position from the knowledge of its equatorial pitch angle (Figure 2.5, right). Note that for the latter case, a numerical computation is needed to extract the colatitude θ_m (or the corresponding latitude $\lambda_m = \pi/2 - \theta_m$) in the above equation.

2.4.2 Bounce motion and trapping

Going back to the equation of parallel motion (2.10), neglecting all the terms of order higher than 2, and considering that there is no electric field (neglected for high-energy particles) nor any other external forces, we can simply write

$$m\frac{\mathrm{d}v_\parallel}{\mathrm{d}t} = -\mathscr{M}\frac{\partial B}{\partial s}.$$

The mirror force $f_\parallel = -\mathscr{M}\partial B/\partial s$ acts like a spring force that pulls the particle back toward the magnetic equator once the particle has reached the mirror point (*Roederer and Zhang*, 2014). To emphasize this point, let us consider a particle with a high pitch angle,

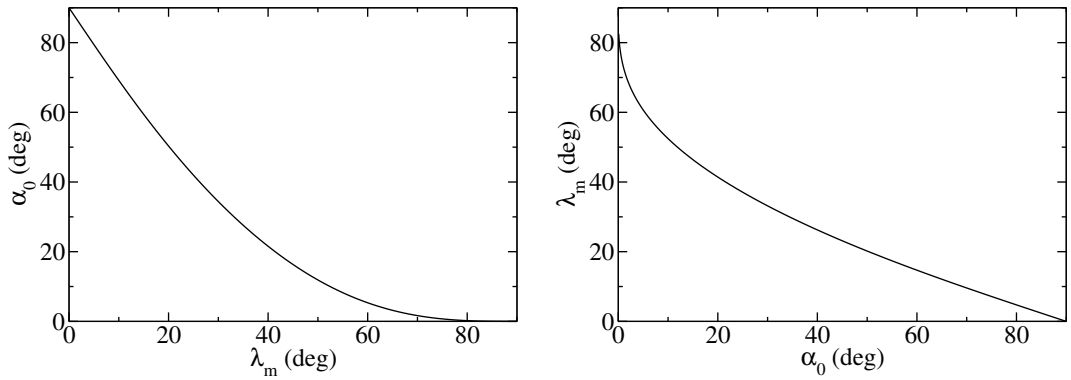

Figure 2.5 – Evolution of the equatorial pitch angle α_0 vs the mirror point latitude λ_m (left) and evolution of the mirror point latitude λ_m vs the equatorial pitch angle α_0 (right).

i.e. a particle whose velocity is nearly perpendicular to the magnetic field direction. In this case, the mirror point s_m would be very close to the equatorial point s_0, and so at any point s of the field line that lies between $s_0 = 0$ and s_m, we can expand the magnetic field intensity so that

$$B(s) = B_0 + s \left(\frac{\partial B}{\partial s}\right)_{s_0=0} + \frac{s^2}{2}\left(\frac{\partial^2 B}{\partial s^2}\right)_{s_0=0}.$$

Since the equatorial point corresponds, by definition, to the minimum intensity of the magnetic field on a given field line, we have $(\partial B/\partial s)_{s_0=0} = 0$ and so

$$B(s) = B_0 + \frac{s^2}{2}\left(\frac{\partial^2 B}{\partial s^2}\right)_{s_0=0}.$$

Differentiating the above expression of $B(s)$ with respect to s, we have

$$\frac{\partial B}{\partial s}(s) = s\left(\frac{\partial^2 B}{\partial s^2}\right)_{s_0=0} = s\,a, \text{ with } a = \left(\frac{\partial^2 B}{\partial s^2}\right)_{s_0=0}.$$

Note that a is positive number because the magnetic field intensity is a convex function in the neighborhood of the equatorial point. Hence

$$m\frac{\mathrm{d}v_\parallel}{\mathrm{d}t} = -\mathscr{M}\, a\, s,$$

i.e. with $v_\parallel = \mathrm{d}s/\mathrm{d}t$

$$\frac{\mathrm{d}^2 s}{\mathrm{d}t^2} + \omega_b^2\, s = 0,$$

for which the bounce pulsation ω_b is given by (*Roederer and Zhang*, 2014)

$$\omega_b = \sqrt{\frac{\mathscr{M}\, a}{m}}. \tag{2.25}$$

Similarly to the gyro-pulsation ω_g, the bounce pulsation will serve at building the theoretical framework on which relies the electron distribution function. Taking initial

conditions such that $s(t=0)=0$ and $v_{\parallel}(s=0)=v_{0\parallel}$, the solution of the harmonic oscillator expressed by the above equation is then simply $s(t)=v_{0\parallel}/\omega_b \sin(\omega_b t)$. This shows that the particle is just moving back and forth along the field line (around the magnetic equator) between the two mirror points as if it was subjected to a spring force (here, the mirror force).

2.4.3 Drift velocity

For a particle population with an equatorial pitch angle below 90 degrees, the bounce-averaged drift velocity (2.18) can be generalized as

$$\boldsymbol{V}_D = -\frac{\mathscr{M}}{qB_0^2}\left(\boldsymbol{\nabla}_{\perp} B_m \times \boldsymbol{B}_0\right),$$

which means that the particles drift on equatorial contours that are such that the magnetic field intensity at the mirror point is conserved.

2.4.4 Gyration, bounce, and drift properties

It is primordial to quickly evaluate the frequencies associated to the gyration, bounce and drift motion of a particle trapped in a magnetic field because it gives the timescale of the particle dynamics. The construction of an appropriate coordinate system (adiabatic invariants) to study the distribution of electrons also relies on the scale of the gyration, bounce and drift frequency. In the following, we only consider a magnetic dipole field configuration.

2.4.4.a Gyro-frequency

The equatorial gyration frequency is given in a general formulation by (2.1), and writes in a dipole field

$$\omega_g = \frac{qB_E}{mL^3} = \frac{qB_E}{\gamma m_0 L^3}. \tag{2.26}$$

For an equatorial electron of 1 MeV energy and located at $L=4\ R_E$, we find, by using equation (8) for the γ relativistic factor, that $f_g = 5$ kHz, i.e. $\tau_g = 0.2$ ms.

The guiding center assumption (2.5) is here fully justified, since a gyro-period of a few ms is much less than the secular evolution timescale of the ambient magnetic field, which is about several years. To prove the validity of the first guiding center approximation (2.4), we can compute the Larmor radius ρ_c in a dipole field as

$$\rho_c = \frac{\gamma m_0 v L^3}{qB_E}$$

by using equation (2.2). We find that $\rho_c \sim 10$ km for a 1 MeV electron that is located at $L=4\ R_E$ from the Earth's center. On the other hand, the radius of curvature $R_c = B/\nabla_{\perp} B$ in a dipole field is simply $R_c = LR_E/3 \sim 8500$ km for $L=4$ (see expression (2.15) for the dipole magnetic field intensity at the equator), which is much larger than the Larmor radius.

In the perspective of the process of averaging over a complete gyration, we recall that,

$$\tau_g = \oint_l \frac{1}{v_g}\mathrm{d}l = \int_{\varphi=0}^{\varphi=2\pi} \frac{1}{\omega_g}\mathrm{d}\varphi = \frac{2\pi}{\omega_g} = \frac{2\pi m}{qB},$$

for which the fourth term of the above expression is obtained in the framework of the guiding center approximations. For any quantity F that depends on the gyro-phase φ_g, we define the averaged $\langle F \rangle_\varphi$ function over the gyromotion as

$$\langle F \rangle_\varphi = \frac{\int_{\varphi=0}^{\varphi=2\pi} \frac{1}{\omega_g} F(\varphi)\,\mathrm{d}\varphi}{\int_{\varphi=0}^{\varphi=2\pi} \frac{1}{\omega_g}\,\mathrm{d}\varphi} = \frac{1}{\tau_g}\int_{\varphi=0}^{\varphi=2\pi} \frac{1}{\omega_g} F(\varphi)\,\mathrm{d}\varphi = \frac{1}{\tau_g \omega_g}\int_{\varphi=0}^{\varphi=2\pi} F(\varphi)\,\mathrm{d}\varphi = \frac{1}{2\pi}\int_{\varphi=0}^{\varphi=2\pi} F(\varphi)\,\mathrm{d}\varphi, \tag{2.27}$$

with, again, the use of the guiding center approximations in the fourth term.

2.4.4.b Bounce frequency

The bounce frequency is derived from (2.25)

$$\omega_b = \sqrt{\frac{\mathscr{M} a}{m}}$$

for which the parameter a represents the value of the second derivative in space of the magnetic field intensity at the equator. In a dipole field, we calculate (*Roederer and Zhang*, 2014).

$$a = \left(\frac{\partial^2 B}{\partial s^2}\right)_{s=0} = \frac{9 B_E}{L^5 R_E^2}$$

and $\mathscr{M} = m v^2 L^3/(2B_E)$ so that

$$\omega_b = \frac{3v}{\sqrt{2} L R_E}. \tag{2.28}$$

For an equatorial electron of 1 MeV energy and located at $L = 4\ R_E$, $f_b = 4$ Hz, i.e. $\tau_b = 0.25$ s (here we used (9) to relate the electron's velocity with its kinetic energy).

In Chapter 7, we will need to bounce-average a pitch angle diffusion coefficient (accounting for atmospheric Coulomb collisions) in a non-dipole magnetic field. For this purpose, let us recall that

$$\tau_b = 2\int_{s=s_1}^{s=s_2} \frac{1}{v_\parallel}\,\mathrm{d}s = \frac{2}{v}\int_{s=s_1}^{s=s_2} \frac{1}{\cos(\alpha)}\,\mathrm{d}s = \frac{2}{v}\int_{s=s_1}^{s=s_2} \frac{1}{\sqrt{1 - \frac{B(s)}{B_m}}}\,\mathrm{d}s = \frac{2}{v} S_b$$

for which S_b is the bounce path length. For any quantity F that depends on the bounce phase θ (i.e. the magnetic colatitude), we define the averaged $\langle F \rangle_\theta$ function over the bounce motion as

$$\langle F \rangle_\theta = \frac{\frac{2}{v}\int_{s=s_1}^{s=s_2} \frac{1}{\sqrt{1 - \frac{B(s)}{B_m}}} F(s)\,\mathrm{d}s}{\frac{2}{v}\int_{s=s_1}^{s=s_2} \frac{1}{\sqrt{1 - \frac{B(s)}{B_m}}}\,\mathrm{d}s} = \frac{1}{S_b}\int_{s=s_1}^{s=s_2} \frac{1}{\sqrt{1 - \frac{B(s)}{B_m}}} F(s)\,\mathrm{d}s. \tag{2.29}$$

2.4.4.c Drift frequency

The calculation of the drift frequency in a dipole field is based on the zero-order equation of motion derived by *Fälthammar* (1965, equations (4b) and (5)). We should first emphasize that, as stated earlier, the effects induced by the background electric field on the motion of an electron having an energy above 100 keV can be neglected towards the effects induced by the background magnetic field. Hence the drift velocity of the electron given by equation (2.9) reduces to the single gradient drift velocity

$$\boldsymbol{V}_\perp = \frac{mv_\perp^{*2}}{2qB^3}\boldsymbol{B}\times\boldsymbol{\nabla}_\perp B.$$

For a dipole field, considering the geographic spherical coordinates $(\hat{\boldsymbol{r}},\hat{\boldsymbol{\theta}},\hat{\boldsymbol{\varphi}})$ and focusing at the equator $(\theta=\pi/2)$,

$$\boldsymbol{V}_\perp = -\frac{3mv^2L^2}{2qR_EB_E}\hat{\boldsymbol{\varphi}},$$

i.e.

$$V_\perp = \frac{3mv^2L^2}{2qR_EB_E} = r\omega_d = LR_E\,\omega_d.$$

Hence we obtain

$$\omega_d = \frac{3mv^2L}{2qR_E^2B_E} = \frac{3\gamma m_0v^2L}{2qR_E^2B_E}. \tag{2.30}$$

For an equatorial electron of 1 MeV energy and located at $L=4\ R_E$, $f_d=1$ mHz, i.e. $\tau_d=17$ min. From the calculations derived above, we conclude that $\omega_d \ll \omega_b \ll \omega_g$ (again we used equations (8) and (9) for the calculation).

In the perspective of the process of averaging over a complete drift, we recall that

$$\tau_d = \oint_l \frac{1}{v_\varphi}\mathrm{d}l = \int_{\varphi=0}^{\varphi=2\pi}\frac{1}{v_\varphi}r\sin(\theta)\,\mathrm{d}\varphi = \int_{\varphi=0}^{\varphi=2\pi}\frac{1}{\left(\frac{v_\varphi}{r\sin(\theta)}\right)}\mathrm{d}\varphi = \int_{\varphi=0}^{\varphi=2\pi}\frac{1}{\left(\frac{\mathrm{d}\varphi}{\mathrm{d}t}\right)}\mathrm{d}\varphi = \int_{\varphi=0}^{\varphi=2\pi}\frac{1}{\omega_d}\mathrm{d}\varphi$$

for which the drift frequency $\omega_d = V_d^\varphi/r_0$ is calculated from the bounce-averaged drift velocity V_d^φ projected onto the particles drift shell. Its vectorial expression, calculated in (*Lejosne*, 2013; *Roederer and Zhang*, 2014), is equivalent to (2.18) and can also be given by

$$\boldsymbol{V}_D = \frac{2p}{q\tau_bB_0^2}\left(\boldsymbol{\nabla}_\perp I\times\boldsymbol{B}_0\right). \tag{2.31}$$

This latter equation will be used in Chapter 6 for drift-averaging in a non-dipole magnetic field. For any quantity F that depends on the drift phase φ_d (i.e. the magnetic longitude), we define the averaged $\langle F\rangle_\varphi$ function over the drift motion as

$$\langle F\rangle_\varphi = \frac{\int_{\varphi=0}^{\varphi=2\pi}\frac{1}{\omega_d}F(\varphi)\,\mathrm{d}\varphi}{\int_{\varphi=0}^{\varphi=2\pi}\frac{1}{\omega_d}\mathrm{d}\varphi} = \frac{1}{\tau_d}\int_{\varphi=0}^{\varphi=2\pi}\frac{1}{\omega_d}F(\varphi)\,\mathrm{d}\varphi. \tag{2.32}$$

2.4.4.d Overview of trapping motions

To summarize the dynamics of trapped electrons within the radiation belts, we illustrate in Figure 2.6 the motions of gyration, bounce and drift of an electron trapped in the Earth's magnetic field.

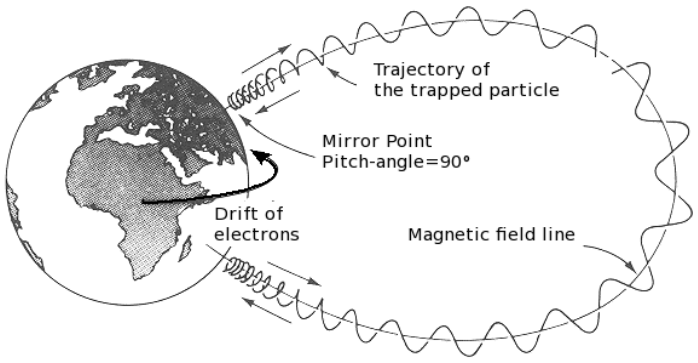

Figure 2.6 – Summary of the three motions of an electron trapped into the Earth's magnetic field. Source: (*Walt*, 1994).

2.4.5 Particle losses

Charged particles can, however, escape the trapping region by precipitating into the atmosphere (atmospheric scattering) or by being expelled out of the magnetopause (magnetopause shadowing). Such losses can occur during the bounce or drift motion.

2.4.5.a Bounce loss cone

During its bounce motion, a particle can precipitate into the Earth's atmosphere if the magnetic mirror point s_m is located at a higher latitude than the point of the field line s_L where the particle reaches the Earth's dense atmosphere (near the surface). Let us call B_L the magnetic field intensity at the loss point s_L. If $B_m < B_L$, the particle is reflected at the mirror point, and so from (2.24), $\sin(\alpha_0) = (B_0/B_m)^{1/2} > (B_0/B_L)^{1/2}$. If $B_m > B_L$, the particle precipitates into the Earth's atmosphere before reaching the mirror point, and then $\sin(\alpha_0) = (B_0/B_m)^{1/2} < (B_0/B_L)^{1/2}$. At the limit of $B_m = B_L$, the equatorial pitch angle corresponding to the loss cone α_{0LC} is defined by

$$\sin(\alpha_{0LC}) = \left(\frac{B_0}{B_L}\right)^{1/2}. \tag{2.33}$$

We commonly state that a particle precipitates into the atmosphere at an altitude h of about 100-120 km above the Earth's surface. In a dipole field, the field line equation (2.14) gives us the limit radial distance of precipitation r_L as $r_L = R_E\,(1 + h/R_E) = LR_E \sin^2(\theta_L)$, i.e.

$$\sin^2(\theta_L) = \frac{1}{L}\left(1 + \frac{h}{R_E}\right). \tag{2.34}$$

This expression will be useful for deriving the expression of the magnetic flux in the dipole framework, which is at the basis of the third adiabatic invariant. From the expression of

the magnetic field intensity in a dipole configuration (2.15), we also obtain, after a first order Taylor expansion in h/R_E,

$$B_L = B_E \left(1 - 3\frac{h}{R_E}\right) \left[4 - \frac{3}{L}\left(1 + \frac{h}{R_E}\right)\right]^{1/2},$$

such that (2.33) becomes

$$\sin(\alpha_{0LC}) = \left(\frac{B_0}{B_L}\right)^{1/2} = \frac{1 + \frac{3}{2}\frac{h}{R_E}}{L^{3/2}\left[4 - \frac{3}{L}\left(1 + \frac{h}{R_E}\right)\right]^{1/4}}. \tag{2.35}$$

Equation (2.35) is useful for the computation of the omnidirectional electron fluxes in a dipole field as it gives the lower bound for integration, as shown in section 2.7.4.b and Chapter 5. If the integration has to be computed in a general non-dipole field, the more general equation (2.33) should be used instead (see Chapter 6).

In this context, Figure 2.7 shows the evolution of the equatorial loss cone with respect to the radial distance. The atmospheric bounce loss cone is considered as a major driver for particle losses in the radiation belts. As emphasized in Chapters 4 and 5, electromagnetic waves of the plasmasphere induce a decrease in the electrons' equatorial pitch angle, bringing them into the bounce loss cone, which results in atmospheric electron scattering.

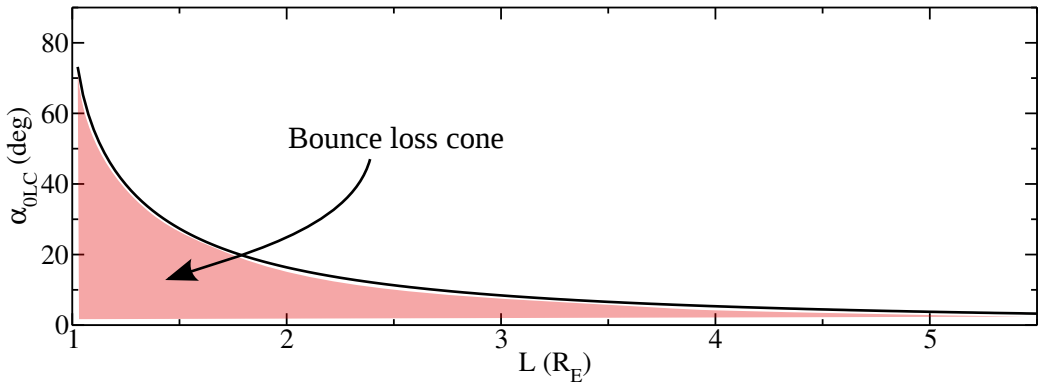

Figure 2.7 – Evolution of the equatorial bounce loss cone vs L. The red area corresponds to the radiation belts region where particles are lost in the bounce loss cone (dipole field).

2.4.5.b Drift loss cone

Due to the effects of the gradient-drift velocity, an equatorial particle drifts on contours of constant minimum magnetic field intensity B_0. By recalling that the gradient drift velocity depends on the sign of the charge q, the protons drift westwards and the electrons drift eastwards. In a dipole field, the B_0 intensity does not depend on the magnetic longitude, and the drift contour is then simply a circle. In any other more realistic field, the symmetry with respect to the magnetic longitude breaks, such that B_0 is a function of the longitude. The drift contour is no more a circle. In this situation, it

can happen that a particle cannot complete an orbit around the Earth on a drift shell. We subsequently say that the particle is in the drift loss cone.

Such losses can occur for a number of reasons. Particles can first be lost in the outer space. Particles starting on the dayside can run into the open magnetic field lines in the tail regions (tail-shadowing), even more if their pitch angle is low. Particles starting on the night side can also cross the magnetopause, especially for high pitch angle particles. This latter effect is called the magnetopause shadowing (*Yu et al.*, 2013).

Drift losses can also happen in the inner belt when particles enter the Earth's atmosphere. At some specific longitudes, a particle's drift shell may drop in the dense atmosphere due to the internal magnetic field asymmetries in the vicinity of Earth. The privileged loss region is the South Atlantic Anomaly (SAA) presented in section 2.3.1.d and put forward in Chapter 7.

Losses induced by the drift loss cone are not widely considered in classical numerical simulations as it is still being investigated. It is however thought to cause dramatic outer belt electron dropouts during geomagnetic storms (magnetopause shadowing) (e.g., *Yu et al.*, 2013).

2.5 The adiabatic invariants

2.5.1 Definition

The periodicity of the three motions of a trapped particle (gyration, bounce and drift) differ from each other from several orders of magnitude, as shown above (section 2.4.4). Since the three motions are well separated in frequencies, the Hamiltonian theory tells us that one can associate to each periodic motion one action variable J_i, for $i = 1, 3$, that is canonically defined as the path integral (*Northrop and Teller*, 1960; *Northrop*, 1963b,a; *Schulz and Lanzerotti*, 1974)

$$J_i = \oint_i \boldsymbol{\pi} \cdot \mathrm{d}\boldsymbol{s_i}$$

for which $\boldsymbol{\pi}$ is the canonical momentum defined as

$$\boldsymbol{\pi} = \boldsymbol{p} + q\boldsymbol{\mathcal{A}},$$

where $\boldsymbol{p}$ is the momentum and $\boldsymbol{\mathcal{A}}$ the vector potential commonly associated to the magnetic field.

2.5.1.a First invariant

The first invariant J_1 relates to the gyromotion of a particle around a field line, and is obtained by integrating $\boldsymbol{\pi}$ over the length of the gyrating path (*Walt*, 1994),

$$J_1 = \oint [\boldsymbol{p} + q\boldsymbol{\mathcal{A}}] \cdot \mathrm{d}\boldsymbol{l} = p_\perp \cdot 2\pi\rho_c + q \oint \boldsymbol{\mathcal{A}} \cdot \mathrm{d}\boldsymbol{l},$$

where ρ_c is the Larmor radius defined in (2.2). As emphasized in (*Walt*, 1994) for example, by using the expression of the Larmor radius in the first term and by applying Stokes theorem (10) in the second term, we obtain

$$J_1 = p_\perp \cdot 2\pi \frac{p_\perp}{qB} + q \oint \boldsymbol{\nabla} \times \boldsymbol{\mathcal{A}} \cdot \mathrm{d}\boldsymbol{S},$$

where $\mathrm{d}\boldsymbol{S}$ is an element of the surface enclosed by the path of gyration. Since by definition of the vector potential $\boldsymbol{B} = \boldsymbol{\nabla} \times \boldsymbol{\mathcal{A}}$, J_1 writes

$$J_1 = p_\perp \cdot 2\pi \frac{p_\perp}{qB} + q \oint \boldsymbol{\nabla} \times \boldsymbol{\mathcal{A}} \cdot \mathrm{d}\boldsymbol{S} = 2\pi \frac{p_\perp^2}{qB} + q \oint \boldsymbol{B} \cdot \mathrm{d}\boldsymbol{S} = 2\pi \frac{p_\perp^2}{qB} + qB\pi\rho_c^2 = 2\pi \frac{p_\perp^2}{qB} - \frac{\pi p_\perp^2}{qB},$$

so that

$$J_1 = \pi \frac{p_\perp^2}{qB}.$$

Recall that we define the magnetic moment $\mathscr{M}$ as

$$\mathscr{M} = I \cdot S = \frac{qv_\perp}{2\pi\rho_c} \cdot \pi\rho_c^2 = \frac{mv_\perp^2}{qB} = \frac{p_\perp^2}{2mB} = \frac{p_\perp^2}{2\gamma m_0 B},$$

for which $\gamma = 1/\sqrt{1-(v/c)^2}$ is the relativistic factor, m_0 the rest mass of the particle and $m = \gamma m_0$. The μ paramter can also be defined as (*Roederer and Zhang*, 2014)

$$\mu = \gamma \mathscr{M} = \frac{p_\perp^2}{2m_0 B}, \tag{2.36}$$

which is the non relativistic limit ($\gamma \to 1$) of the magnetic moment $\mathscr{M}$. The quantity μ relates to the first adiabatic invariant J_1 by the relation (*Walt*, 1994)

$$J_1 = \frac{2\pi m_0}{q}\mu.$$

In what follows, we will refer the parameter μ to the first adiabatic invariant despite the fact that, according to Hamiltonian theory, μ and the first adiabatic invariant J_1 are different quantities.

2.5.1.b Second invariant

The second invariant J_2 is associated with the bounce motion of the particle along a field line, and is obtained by integrating $\boldsymbol{\pi}$ over the length of the bounce path (*Walt*, 1994),

$$J_2 = \oint [\boldsymbol{p} + q\boldsymbol{\mathcal{A}}] \cdot \mathrm{d}\boldsymbol{l}.$$

By using Stokes theorem for the second term (see (*Walt*, 1994)) we obtain

$$J_2 = \oint \boldsymbol{p} \cdot \mathrm{d}\boldsymbol{l} + q \oint (\boldsymbol{\nabla} \times \boldsymbol{\mathcal{A}}) \cdot \mathrm{d}\boldsymbol{S} = \oint \boldsymbol{p} \cdot \mathrm{d}\boldsymbol{l} + q \oint \boldsymbol{B} \cdot \mathrm{d}\boldsymbol{S}.$$

The second term vanishes because the guiding center trajectory does not enclose any magnetic flux (*Walt*, 1994). The second adiabatic invariant can then be written as

$$J_2 = \oint p_\parallel \mathrm{d}s. \tag{2.37}$$

We often use notation $J = J_2$ to relate to the second adiabatic invariant.

2.5.1.c Third invariant

The third invariant J_3 refers to the drift motion of the particle across a field line, and is obtained by integrating $\boldsymbol{\pi}$ over the length of the drift path (*Walt*, 1994).

$$J_3 = \oint [\boldsymbol{p} + q\boldsymbol{\mathcal{A}}] \cdot \mathrm{d}\boldsymbol{l}.$$

Stokes theorem applied to the second term (see (*Walt*, 1994)) leads to

$$J_3 = \oint \boldsymbol{p} \cdot \mathrm{d}\boldsymbol{l} + q \oint (\boldsymbol{\nabla} \times \boldsymbol{\mathcal{A}}) \cdot \mathrm{d}\boldsymbol{S}$$

where $\mathrm{d}\boldsymbol{S}$ is the surface element of the surface encircled by the drift contour. The first term is negligible compared with the second term, so that J_3 becomes, by using the definition of the potential vector

$$J_3 = q \oint \boldsymbol{B} \cdot \mathrm{d}\boldsymbol{S}.$$

We relate the magnetic flux Φ encompassed by the drift shell to the third adiabatic invariant as

$$J_3 = q\,\Phi,$$

with

$$\Phi = \oint \boldsymbol{B} \cdot \mathrm{d}\boldsymbol{S}. \tag{2.38}$$

Again we will speak of the third adiabatic invariant in terms of quantity Φ rather than J_3. Since $\boldsymbol{B} = \boldsymbol{\nabla} \times \boldsymbol{\mathcal{A}}$, with $\boldsymbol{\mathcal{A}}$ the vector potential, the magnetic flux can also be calculated as

$$\Phi = \iint (\boldsymbol{\nabla} \times \boldsymbol{\mathcal{A}}) \cdot \mathrm{d}\boldsymbol{S},$$

and with Stokes's theorem we end up with

$$\Phi = \oint \boldsymbol{\mathcal{A}} \cdot \mathrm{d}\boldsymbol{l}, \tag{2.39}$$

for which the integration is performed over the closed drift path of the particles.

A particular attention is paid to the computation of the magnetic flux given by (2.38), because the magnetic field can exhibit a singularity at the origin. This happens for a dipole field. That is why the magnetic flux should be computed over the portion of the equatorial surface that lies outside the drift shell (surface denoted as Σ_1) and not inside. For non-dipole magnetic field models, the integration of the magnetic flux is also often computed over the polar cap Σ_2 that lies on the Earth's surface. The aforementioned surface is generated by finding the intersection of the magnetic field lines outside the equatorial drift shell with the Earth's surface (of either hemisphere) (*Roederer and Zhang*, 2014).

Let us define the infinitesimal $\delta\Omega$ surface that links a small section $\delta\Sigma_1$ of the equatorial plane to the corresponding Σ_2 unit surface lying on the Earth's polar cap by following the field lines. From Maxwell-Flux equation, $\boldsymbol{\nabla} \cdot \boldsymbol{B} = 0$, we have $(\boldsymbol{\nabla} \cdot \boldsymbol{B})\ \delta\Omega = 0$, and the use of the divergence theorem reduces the latter equality to

$$\boldsymbol{B}_1 \cdot \boldsymbol{\delta\Sigma}_1 + \boldsymbol{B}_2 \cdot \boldsymbol{\delta\Sigma}_2 = 0 \tag{2.40}$$

since no contribution is brought by the lateral surfaces that are normal to the magnetic field direction. Here $\boldsymbol{B}_1$ is the magnetic field applied to the unit surface $\delta\Sigma_1$ and $\boldsymbol{B}_2$ the magnetic field applied to $\delta\Sigma_2$. In spherical coordinates, the unit vector $\boldsymbol{\delta\Sigma}_1$ and $\boldsymbol{\delta\Sigma}_2$ are oriented outward the $\delta\Omega$ surface by convention, such that $\boldsymbol{\delta\Sigma}_1$ is oriented southward ($\boldsymbol{\delta\Sigma}_1 = \hat{\boldsymbol{\theta}} = -\hat{\boldsymbol{z}}$ at the equator) and $\boldsymbol{\delta\Sigma}_2$ is oriented radially inward ($\boldsymbol{\delta\Sigma}_2 = -\hat{\boldsymbol{r}}$). Integrating equation (2.40) leads to

$$\iint_{\Sigma_1} \boldsymbol{B} \cdot \mathrm{d}\boldsymbol{S} = -\iint_{\Sigma_2} \boldsymbol{B} \cdot \mathrm{d}\boldsymbol{S},$$

which confirm that both formalisms are equivalent.

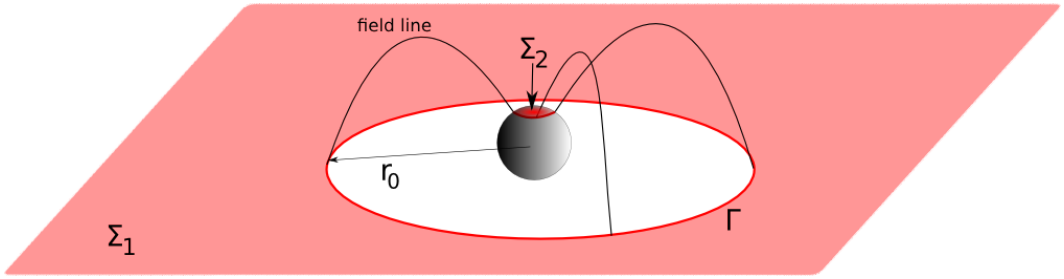

Figure 2.8 – Illustration of the correspondence between the magnetic flux integration over the equatorial surface that lies outside the drift shell Σ_1 and over the polar cap Σ_2. The electron drift path is located by the red curve. Adapted from *Roederer* (1970).

2.5.2 Quantities related to the adiabatic invariants

As we will see, it is useful to express the three adiabatic invariants for a dipole field, especially if one wants to relate the three adiabatic invariants with the kinetic energy, the equatorial pitch angle and the radial distance of a particle (E, α_0, L), as put forward in equation (4.1) (Chapter 4). Furthermore, expressing the invariants in a dipole field enables, as we will see below, to define other more physical quantities that are commonly at stake in the physics of radiation belts, such as the McIlwain L_m-value, the Kaufman K parameter or the Roederer L^*-value. In this PhD thesis, we will extensively consider the two latters.

2.5.2.a First invariant in a dipole field

By definition, the first adiabatic invariant (2.36) is

$$\mu = \frac{p^2 \sin^2(\alpha)}{2m_0 B}.$$

From relation (2.24) we relate the local magnetic field intensity with the equatorial magnetic field intensity so that

$$\frac{\sin^2(\alpha)}{B} = \frac{\sin^2(\alpha_0)}{B_0} = \frac{1}{B_m},$$

and for which the equatorial magnetic intensity B_0 of a dipole field is given by $B_0 = B_E/L^3$. Hence, in a dipole field, the first adiabatic invariant reduces to (*Schulz and*

Lanzerotti, 1974)

$$\mu = \frac{p^2 y^2 L^3}{2 m_0 B_E}.$$

2.5.2.b Second invariant and McIlwain L-value

(i) Second invariant in a dipole field

From (2.37), the second adiabatic invariant is defined by

$$J = \int_{\text{bounce}} p_{\parallel}\, \mathrm{d}s = \int_{\text{bounce}} p \cos(\alpha)\, \mathrm{d}s.$$

Using again relation (2.24) we obtain

$$J = \int_{\text{bounce}} p \left(1 - \frac{B(s)}{B_m}\right)^{1/2} \mathrm{d}s.$$

In a dipole field, one can develop

$$1 - \frac{B(s)}{B_m} = 1 - \sin^2(\alpha_0)\frac{B(s)}{B_0} = 1 - \sin^2(\alpha_0)\frac{\left[1 + 3\cos^2(\theta)\right]^{1/2}}{\sin^6(\theta)}$$

and the differential length of the field line $\mathrm{d}s$ can also be expressed as

$$\mathrm{d}s = L R_E \sin(\theta) \left[1 + 3\cos^2(\theta)\right]^{1/2} \mathrm{d}\theta.$$

Denoting $y_0 = \sin(\alpha_0)$, and since the momentum p is constant along a field line, we end up with (*Schulz and Lanzerotti*, 1974)

$$J = 4 p L R_E \int_{\theta_m}^{\pi/2} \frac{\sin(\theta)\left[1 + 3\cos^2(\theta)\right]^{1/2}}{\left[1 - y_0^2 \sin^{-6}(\theta)\left[1 + 3\cos^2(\theta)\right]^{1/2}\right]^{-1/2}} \mathrm{d}\theta. \tag{2.41}$$

Defining the quantity Y such that

$$Y(y_0) = 2 \int_{\theta_m}^{\pi/2} \frac{\sin(\theta)\left[1 + 3\cos^2(\theta)\right]^{1/2}}{\left[1 - y_0^2 \sin^{-6}(\theta)\left[1 + 3\cos^2(\theta)\right]^{1/2}\right]^{-1/2}} \mathrm{d}\theta$$

we express more simply the second adiabatic invariant as (*Schulz and Lanzerotti*, 1974)

$$J = 2 p L R_E Y(y_0).$$

(ii) Kaufman parameter

The adiabatic invariant J has the drawback of depending on both the energy of the particle (emphasized by the presence of the particle momentum p in the above expression) and on the field line geometry, emphasized by the $Y(y_0)$ term. Hence it can be useful to derive another invariant quantity (related to J) that only depends on the geometry of the magnetic field line and nor on the particle's energy. One can define a new invariant I such that $I{=}J/(2p)$ or more commonly the K quantity (from *Kaufmann* (1965)). The latter uses the invariance of μ and is defined by

$$K = \frac{\sqrt{B_m}}{2p} J = \frac{1}{2\sqrt{2m_0\mu}} J = \sqrt{B_m}\, I.$$

We can also express K as

$$K = \int_{s_m}^{n_m} \sqrt{B_m - B(s)}\, \mathrm{d}s$$

which now only depends on the field line geometry.

(iii) Bounce period

The bounce period is given by

$$\tau_b = 2 \int_{\text{bounce}} \frac{\mathrm{d}s}{v_\parallel} = \frac{2}{v} \int_{\text{bounce}} \frac{\mathrm{d}s}{\cos(\alpha)} = \frac{2}{v} \int_{\text{bounce}} \frac{\mathrm{d}s}{\left(1 - \dfrac{B(s)}{B_m}\right)^{1/2}}.$$

For a dipole field, the bounce period τ_b turns to be

$$\tau_b = \frac{4}{v} LR_E \int_{\theta_m}^{\pi/2} \frac{\sin(\theta)\left[1 + 3\cos^2(\theta)\right]^{1/2}}{\left[1 - y_0^2 \sin^{-6}(\theta)\left[1 + 3\cos^2(\theta)\right]^{1/2}\right]^{1/2}} \mathrm{d}\theta.$$

Let us denote

$$T(y_0) = \int_{\theta_m}^{\pi/2} \frac{\sin(\theta)\left[1 + 3\cos^2(\theta)\right]^{1/2}}{\left[1 - y_0^2 \sin^{-6}(\theta)\left[1 + 3\cos^2(\theta)\right]^{1/2}\right]^{1/2}} \mathrm{d}\theta, \tag{2.42}$$

so that

$$\tau_b = \frac{4}{v} LR_E T(y_0) = \frac{4mLR_E}{p} T(y_0).$$

The quantity $T(y_0)$ is often called the normalized bounce period (for a dipole field) and is widely used, as we will see, in the Fokker-Planck equation governing the electron distribution related to pitch angle and kinetic energy.

The normalized bounce period $T(\alpha_0)$ and the $Y(\alpha_0)$ function have been analytically approximated with excellent accuracy (up to 0.04% for $y_0 > 0.36$) by *Davidson* (1976). Other more basic approximations for the normalized bounce period $T(y_0)$ are given in (*Schulz and Lanzerotti*, 1974) as

$$T(y_0) \approx 1.38 - 0.32 \left(y_0 + y_0^{1/2}\right).$$

In view of the expressions for $Y(y_0)$ and $T(y_0)$, and for further purposes, we keep in mind that

$$Y(y_0) - y_0 Y^{'}(y_0) = 2T(y_0),$$

and knowing that $Y(y_0 = 1) = 0$, the Y function is solution of the above differential equation and can therefore be approximated by (*Schulz and Lanzerotti*, 1974)

$$Y(y_0) \approx 2.76(1 - y_0) + 0.64 \left(y_0 \ln(y_0) + 2y_0 - 2y_0^{1/2} \right).$$

The latter equation is useful to relate the particle's pitch angle and energy to the three adiabatic invariants (see Chapter 4).

(iv) McIlwain L_m-value

In a dipole field, we obtain from (2.15) the expression of the magnetic field intensity B_m at the mirror point with respect to the mirror point colatitude θ_m as

$$B_m = \frac{B_E}{L^3} \frac{\left[1 + 3\cos^2(\theta_m)\right]^{1/2}}{\sin^6(\theta_m)}.$$

Noting

$$h_1(\theta_m) = \frac{\left[1 + 3\cos^2(\theta_m)\right]^{1/2}}{\sin^6(\theta_m)}$$

and $X = B_m L^3 / B_E$ we obtain

$$h_1(\theta_m) = X$$

i.e.

$$\theta_m = h_2(X)$$

for which the $h_2 \equiv h_1^{-1}$ function is the inverse function of h_1, which has to be tabulated numerically. Since $y_0^2 = B_E/(B_m L^3) = X^{-1}$ in a dipole field and because $I = J/(2p)$, and noting

$$h_3(X) = 2 \int_{h_2(X)}^{\pi/2} \frac{\sin(\theta) \left[1 + 3\cos^2(\theta)\right]^{1/2}}{\left[1 - X^{-1} \sin^{-6}(\theta) \left[1 + 3\cos^2(\theta)\right]^{1/2}\right]^{-1/2}} \mathrm{d}\theta,$$

we obtain from (2.41)

$$I = L R_E \, h_3(X).$$

Powering each side of the latter expression by 3, and multiplying by B_m/B_E gives $I^3 B_m / B_E = R_E^3 X h_3^3(X)$. We finally obtain

$$\frac{I^3 B_m}{R_E^3 B_E} = h_4(X)$$

with $h_4(X) = X h_3^3(X)$. The reverse relation gives

$$F\left(\frac{I^3 B_m}{R_E^3 B_E}\right) = X$$

with $F \equiv h_4^{-1}$. By taking the expression for X, the result for L is

$$L = \left(\frac{B_E}{B_m}\right)^{1/3} f\left(\frac{I^3 B_m}{R_E^3 B_E}\right)$$

with $f \equiv F^{1/3}$. For any other non dipole (realistic) magnetic field, one defines the L_m parameter, also called McIlwain's L-value (*McIlwain*, 1961, 1966a; *Roederer*, 1970; *Roederer and Lejosne*, 2018), as

$$L_m = \left(\frac{B_E}{B_m}\right)^{1/3} f\left(\frac{I^3 B_m}{R_E^3 B_E}\right).$$

The L_m parameter represents approximately the distance to the equatorial point of a given field line (*McIlwain*, 1961). This geometric interpretation only holds if the magnetic field does not deviate too much from a dipole field, which is the case in the inner belt or during quiet times (when external magnetic contributions can be neglected). In a static magnetic field, L_m remains constant along a drift shell because it only depends on B_m and I, which do not change as the particle drifts.

2.5.2.c Third invariant and Roederer L^*-value

(i) Third invariant in a dipole field

From (2.38), the third adiabatic invariant relates to

$$\Phi = \oint \boldsymbol{B} \cdot \mathrm{d}\boldsymbol{S}.$$

We first compute the third adiabatic invariant by using the surface Σ_{outside} that lies outside the drift path. Since the dipole field has a singularity at the origin point the evaluation of the magnetic flux inside the drift shell (i.e. from $r = 0$ to $r = r_0$) is not obtainable. Hence

$$\Phi = \iint_{\Sigma_{\text{outside}}} \boldsymbol{B} \cdot \mathrm{d}\boldsymbol{S}.$$

From the discussion led previously in 2.4.5.b, the equatorial electrons drift path is a circle, i.e. $r(\varphi) = r_0$. In spherical coordinates, $\mathrm{d}S = r\sin(\theta)\mathrm{d}r\mathrm{d}\varphi$, and the infinitesimal surface $\mathrm{d}S_0$ of the equatorial plane is then $\mathrm{d}S_0 = r\mathrm{d}r\mathrm{d}\varphi$. The $\mathbf{d}\boldsymbol{S}_0$ unit surface vector is oriented southward at the equator, such that $\mathbf{d}\boldsymbol{S}_0 = \hat{\boldsymbol{\theta}}$, and $\boldsymbol{B}_\theta(r, \pi/2) = -B_E R_E^3/r^3\,\hat{\boldsymbol{\theta}}$ (see the dipole field components defined by equation (2.13)). Integrating the whole dipole magnetic flux passing through the equatorial plane from an infinite radial distance to $r = r_0$ gives

$$\Phi = -\int_{r_0}^{+\infty}\int_0^{2\pi}\left(\frac{B_E R_E^3}{r^3}\right) r\mathrm{d}r\mathrm{d}\varphi = -2\pi B_E R_E^3 \int_{r_0}^{+\infty}\frac{\mathrm{d}r}{r^2} = -\frac{2\pi B_E R_E^3}{r_0}.$$

The equatorial radial distance r_0 and the equatorial radial distance L being related by the relation $r_0 = LR_E$, one obtain, in absolute value

$$\Phi = \frac{2\pi R_E^2 B_E}{L}.$$

(ii) Roederer L^*-value

Similarly to the previous mathematical procedure aiming at defining the McIlwain L_m-value from the second adiabatic invariant, one can directly relate, for a pure dipole field, the radial distance L with the third adiabatic invariant through the relation

$$L = \frac{2\pi R_E^2 B_E}{\Phi}.$$

For any other non dipole (realistic) magnetic field, one define the L^* parameter, also called Roederer's L-value (*Roederer*, 1970), as

$$L^* = \frac{2\pi R_E^2 B_E}{\Phi}.$$

It is clear that the L^* parameter is an invariant quantity. In any non dipole magnetic fields, L^* represents the radial parameter of the shell on which a particle would end up if the real magnetic field were adiabatically transformed into a dipole reference field, with all other forces (electric field) adiabatically turned off (*Roederer and Zhang*, 2014). Contrary to the McIlwain L_m-value whose computation only requires the knowledge of one given field line, the calculation of L^* is computationally more expensive as it requires the tracing of all field lines corresponding to the entire drift-shell (*Roederer*, 1970).

We can also perform the integration on the surface lying on the Earth's polar cap. The corresponding $\mathbf{d}\boldsymbol{S}_r$ unit surface vector is oriented radially inward, such that $\mathbf{d}\boldsymbol{S}_r = -\hat{\boldsymbol{r}}$, and $\boldsymbol{B}_r(R_E, \theta) = -2B_E \cos(\theta)\, \hat{\boldsymbol{r}}$ (see the dipole field components defined by (2.13))). The magnetic flux is integrated through the polar cap, from $\theta = 0$ to $\theta = \theta_c$ for which θ_c is the colatitude of the intersection of the field line located at an equatorial distance r_0 with the Earth's surface. It leads to (*Roederer and Zhang*, 2014)

$$\Phi = 2B_E \int_0^{2\pi} \int_0^{\theta_c(\varphi)} \cos(\theta)\, R_E^2 \sin(\theta)\, \mathrm{d}\theta \mathrm{d}\varphi = B_E R_E^2 \int_0^{2\pi} \sin^2(\theta_c)\, \mathrm{d}\varphi.$$

Since $\theta_c = \arcsin\left(\sqrt{R_E/r_0}\right)$ (see (2.34) with $h = 0$ and $L = r_0/R_E$), we obtain

$$\Phi = \frac{2\pi B_E R_E^3}{r_0},$$

which is consistent with the expression of the magnetic flux obtained after integrating over the equatorial plane.

(iii) General case

Let us mention that a general magnetic field is often constructed on the contribution of an internal magnetic field and an external magnetic field. The internal part has a singularity at $r = 0$, see (2.12), and the external part has a singularity at $r \to \infty$, see (2.16). Then the corresponding magnetic flux has to be properly calculated as

$$\Phi = \Phi_i + \Phi_e = \iint_{\Sigma_{\text{outside}}} \boldsymbol{B_i} \cdot \mathrm{d}\boldsymbol{S} + \iint_{\Sigma_{\text{inside}}} \boldsymbol{B_e} \cdot \mathrm{d}\boldsymbol{S}.$$

In Appendix E we calculate the magnetic flux Φ as well as L^* for a non-dipole field. The obtained property will be used in Chapter 6.

2.5.2.d Differences between the McIlwain L_m-value and the Roederer L^*-value

As mentioned in (*Roederer and Lejosne*, 2018), the L_m parameter does not remain constant if the magnetic field is subjected to time-variations that are slow compared with the drift period and cannot be considered as an adiabatic invariant. To emphasize this specific point, let us consider a 90-degree particle that mirrors at the equatorial point. In this case, the mirror colatitude is $\theta_m = \pi/2$ and therefore $h_1(\theta_m) = 1$. Since $X = h_1(\theta_m) = 1$ and taking account of the expression of X given above, we conclude that $L_m = (B_E/B_0)^{1/3}$ (with here $B_m = B_0$). This last expression shows that L_m changes following an adiabatic change in the magnetic field intensity B_0, contrary to the L^* invariant that remains constant (providing that the variation is longer than the drift period). This also means that L_m can be altered without being linked to radial diffusion, contrary to the L^* parameter. This is why it is inadequate for storm-time (see Chapter 6) and, for the sake of consistency, the McIlwain L_m-value will be discarded in the rest of this PhD thesis.

2.6 The Fokker-Planck equation

As mentioned in the introduction of this chapter, we now have to relate the newly defined coordinate system $(J_1, J_2, J_3, \varphi_1, \varphi_2, \varphi_3)$ built on the three adiabatic invariants and their related phases of motion (respectively the gyrophase, the bounce phase and the drift phase) with the common phase space (v_x, v_y, v_z, x, y, z).

2.6.1 Phase Space Density (PSD) and distribution function

2.6.1.a Liouville's theorem and phase space density

For each canonical doublet of momentum and space position $(\boldsymbol{\pi}, \mathbf{q})$ we associate the corresponding canonical Phase Space Density (PSD) $F(\boldsymbol{\pi}, \mathbf{q}, t)$. The PSD represents the number of particles per unit volume of the six-dimensional space composed of the three spatial dimensions $\mathbf{q}$ and the three conjugate momentum $\boldsymbol{\pi}$. The canonical momentum $\boldsymbol{\pi}$ and canonical position $\mathbf{q}$ are related to the Hamiltonian function $\mathcal{H}$ of the system by (e.g., *Schulz and Lanzerotti*, 1974)

$$\begin{cases} \dfrac{\mathrm{d}\pi_\mathrm{i}}{\mathrm{d}t} &= -\dfrac{\partial \mathcal{H}}{\partial \mathrm{q}_i}, \\ \dfrac{\mathrm{d}\mathrm{q}_\mathrm{i}}{\mathrm{d}t} &= +\dfrac{\partial \mathcal{H}}{\partial \pi_i}. \end{cases}$$

The Hamiltonian function related to the motion of charged particles in the magnetosphere is given by (*Ukhorskiy and Sitnov*, 2013)

$$\mathcal{H} = \sqrt{m_0^2 c^4 + p^2 c^2} + qV_\mathcal{E},$$

which is equivalent to the total energy (made of a relativistic kinetic contribution and an electric potential contribution). The PSD F obeys the Liouville's theorem (e.g., *Haerendel*, 1968; *Schulz and Lanzerotti*, 1974; *Walt*, 1994)

$$\frac{\mathrm{d}F}{\mathrm{d}t} = \frac{\partial F}{\partial t} + \sum_{i=1}^{3} \left[\frac{\mathrm{d}\mathrm{q}_\mathrm{i}}{\mathrm{d}t} \frac{\partial F}{\partial \mathrm{q}_i} + \frac{\mathrm{d}\pi_\mathrm{i}}{\mathrm{d}t} \frac{\partial F}{\partial \pi_i} \right] = 0.$$

It means that the PSD along a dynamical path remains constant. In what follow, we rather use the coordinates made of momentum $\boldsymbol{p}$ and position $\boldsymbol{r}$. As mentioned previously, they are linked to the previous canonical variables as

$$\begin{cases} \boldsymbol{\pi} &= \boldsymbol{p} + q\boldsymbol{\mathcal{A}}, \\ \mathfrak{q} &= \boldsymbol{r}, \end{cases}$$

for which $\boldsymbol{\mathcal{A}}$ is the electromagnetic vector potential. Since the transformation from the canonical variables $(\boldsymbol{\pi}, \mathfrak{q})$ and $(\boldsymbol{p}, \boldsymbol{r})$ has a unit Jacobian, it follows than the phase space density is the same for both coordinate systems, i.e. $F(\boldsymbol{\pi}, \mathfrak{q}, t) \equiv F(\boldsymbol{p}, \mathfrak{q}, t)$, where we have substituted $r = \mathfrak{q}$ into the second term. Using these new variables, the number δN of particles inside the volume $\mathrm{d}p\mathrm{d}q$ at time t is

$$\delta N(t) = F(\boldsymbol{p}, \mathfrak{q}, t)\, \mathrm{d}p^3\, \mathrm{d}\mathfrak{q}^3. \tag{2.43}$$

The PSD F obeys the Vlasov equation (also referred in this context as the collisionless Boltzmann equation) (e.g., *Haerendel*, 1968; *Schulz and Lanzerotti*, 1974; *Walt*, 1994)

$$\frac{\mathrm{d}F}{\mathrm{d}t} = \frac{\partial F}{\partial t} + \sum_{i=1}^{3} \left[\frac{\mathrm{d}\mathfrak{q}_\mathrm{i}}{\mathrm{d}t} \frac{\partial F}{\partial \mathfrak{q}_i} + \frac{\mathrm{d}\mathrm{p}_\mathrm{i}}{\mathrm{d}t} \frac{\partial F}{\partial p_i} \right] = 0. \tag{2.44}$$

which is equivalent to Liouville's theorem in the $(\boldsymbol{p}, \mathfrak{q})$ space.

2.6.1.b Distribution function

Each doublet of momentum and space position corresponds to a unique doublet in invariants and its associated phase variable $(\boldsymbol{X}, \boldsymbol{\varphi}) \equiv (J_1, J_2, J_3; \varphi_1, \varphi_2, \varphi_3)$. The Jacobian determinant $G(\boldsymbol{p}, \mathfrak{q}; \boldsymbol{X}, \boldsymbol{\varphi})$ of the transformation from the canonical variables $(\boldsymbol{p}, \mathfrak{q})$ to the adiabatic invariants and phase variables $(\boldsymbol{X}, \boldsymbol{\varphi})$ is such that (*Kruskal*, 1962)

$$G(\boldsymbol{p}, \mathfrak{q}; \boldsymbol{X}, \boldsymbol{\varphi}) = \left| \frac{\partial(\boldsymbol{p}, \mathfrak{q})}{\partial(\boldsymbol{X}, \boldsymbol{\varphi})} \right| = 1. \tag{2.45}$$

Hence the PSD $F(\boldsymbol{p}, \mathfrak{q}, t)$ corresponds to a unique distribution function in the adiabatic invariant space $F(\boldsymbol{X}, \boldsymbol{\varphi}, t)$. Therefore, the latter distribution function is still governed by the Vlasov equation (2.44) written in the adiabatic invariant space

$$\frac{\mathrm{d}F}{\mathrm{d}t} = \frac{\partial F}{\partial t} + \sum_{i=1}^{3} \left[\frac{\mathrm{dJ_i}}{\mathrm{d}t} \frac{\partial F}{\partial J_i} + \frac{\mathrm{d}\varphi_\mathrm{i}}{\mathrm{d}t} \frac{\partial F}{\partial \varphi_i} \right] = 0. \tag{2.46}$$

We will discuss in the next section the conditions for which $\mathrm{dJ_i}/\mathrm{d}t \neq 0$, i.e. the conditions leading to the violation of the conservation property of the adiabatic invariant J_i.

From relation (2.45), we can deduce the Jacobian that drives the coordinate transformation from the canonical variables $(\boldsymbol{p}, \mathfrak{q})$ to any other non canonical variables $(\boldsymbol{Y}, \mathfrak{q})$:

$$G(\boldsymbol{p}, \mathfrak{q}; \boldsymbol{Y}, \boldsymbol{\varphi}) = \left| \frac{\partial(\boldsymbol{p}, \mathfrak{q})}{\partial(\boldsymbol{Y}, \boldsymbol{\varphi})} \right| = \left| \frac{\partial(\boldsymbol{p}, \mathfrak{q})}{\partial(\boldsymbol{X}, \boldsymbol{\varphi})} \right| \left| \frac{\partial \boldsymbol{X}}{\partial \boldsymbol{Y}} \right| = \left| \frac{\partial \boldsymbol{X}}{\partial \boldsymbol{Y}} \right| = G_{XY}(\boldsymbol{X}; \boldsymbol{Y}). \tag{2.47}$$

In magnetospheric physics, it is common to average the distribution function over the phase variables (efficient phase mixing). This step is fully justified because, in practice, the timescales associated to the three phases are much faster that the evolution timescales

related to the three adiabatic invariants, such that the distribution function gets rapidly uniform over the three phases of motions. Therefore, we work with the normalized phase-averaged distribution function $\bar{F}(\boldsymbol{Y},t)$ given by the general averaging formula (*Haerendel*, 1968)

$$\bar{F}_Y(\boldsymbol{Y},t) = \frac{\displaystyle\int_{\varphi_1}\int_{\varphi_2}\int_{\varphi_3} F\left(\boldsymbol{p}(\boldsymbol{Y},\varphi_i),\mathfrak{q}(\boldsymbol{Y},\varphi_i),t\right)\, G(\boldsymbol{p},\mathfrak{q};\boldsymbol{Y},\boldsymbol{\varphi})\,\mathrm{d}\varphi_1\mathrm{d}\varphi_2\mathrm{d}\varphi_3}{\displaystyle\int_{\varphi_1}\int_{\varphi_2}\int_{\varphi_3} G(\boldsymbol{p},\mathfrak{q};\boldsymbol{Y},\boldsymbol{\varphi})\,\mathrm{d}\varphi_1\mathrm{d}\varphi_2\mathrm{d}\varphi_3}. \tag{2.48}$$

Note that the phase-averaged distribution function $\bar{F}_Y(\boldsymbol{Y},t)$ has the same dimension as the PSD $F(\boldsymbol{p},\mathfrak{q},t)$ independently of the chosen variable $\boldsymbol{Y}$. Indeed, for two different coordinates $\boldsymbol{Y}$ and $\boldsymbol{Z}$, relations (2.47) and (2.48) show that

$$\bar{F}_Y(\boldsymbol{Y},t) \equiv \bar{F}_Z(\boldsymbol{Z},t).$$

In the field of radiation belts, one often use the units MeV/c for one momentum component p and units cm for one position component $\mathfrak{q}$, such that, by using (2.43), both the aforementioned functions are commonly expressed in $(\mathrm{c/Mev/cm})^3$. Let us define the "relative" phase-averaged distribution function $\bar{f}_Y$ as

$$\bar{f}_Y(\boldsymbol{Y},t) = \int_{\varphi_1}\int_{\varphi_2}\int_{\varphi_3} F\left(\boldsymbol{p}(\boldsymbol{Y},\varphi_i),\mathfrak{q}(\boldsymbol{Y},\varphi_i),t\right)\, G(\boldsymbol{p},\mathfrak{q};\boldsymbol{Y},\boldsymbol{\varphi})\,\mathrm{d}\varphi_1\mathrm{d}\varphi_2\mathrm{d}\varphi_3$$

and the phase-averaged Jacobian $\bar{G}_Y$ as

$$\bar{G}_Y = \int_{\varphi_1}\int_{\varphi_2}\int_{\varphi_3} G(\boldsymbol{p},\mathfrak{q};\boldsymbol{Y},\boldsymbol{\varphi})\,\mathrm{d}\varphi_1\mathrm{d}\varphi_2\mathrm{d}\varphi_3$$

such that (2.48) reduces to

$$\bar{F}_Y(\boldsymbol{Y},t) = \frac{1}{\bar{G}_Y}\,\bar{f}_Y(\boldsymbol{Y},t).$$

On the contrary to the normalized phase-averaged distribution function that keeps the same dimension whatever the variables at stakes (canonical or not), the dimension of the relative distribution function $\bar{f}_Y(\boldsymbol{Y},t)$ changes with respect to the chosen variable. So considering two different coordinate systems represented respectively by the $\boldsymbol{Y}$ and $\boldsymbol{Z}$ variables, the infinitesimal number of particles $\delta N(t)$ is given by

$$\delta N(t) = (2\pi)^3\,\bar{f}_Y(\boldsymbol{Y},t)\,\mathrm{d}Y^3 = (2\pi)^3\,\bar{f}_Z(\boldsymbol{Z},t)\,\mathrm{d}Z^3$$

from which we deduce that (*Roederer and Zhang*, 2014)

$$\bar{f}_Z(\boldsymbol{Z},t) = G_{YZ}\,\bar{f}_Y(\boldsymbol{Y},t)$$

where G_{YZ} is the Jacobian of the transformation from $\boldsymbol{Y}$ to $\boldsymbol{Z}$. Note that for $\boldsymbol{X} \equiv (J_1, J_2, J_2)$ we have

$$\bar{F}_Y(\boldsymbol{Y},t) \equiv \bar{F}_X(\boldsymbol{X},t) \equiv (2\pi)^3\,\bar{f}_X(\boldsymbol{X},t).$$

2.6.2 Violation of the adiabatic invariants

The previous discussion enabled us to link any 3-dimensional normalized phase-averaged distribution function $\bar{F}$ to the full 6-dimensional phase space density F. This procedure has two main advantages. First, it greatly simplifies the physics by reducing a function of six spatial dimensions to an averaged function of "only" three dimensions. Secondly, it enables us to express the distribution function with respect to the adiabatic invariants. In the real world, small magnetic and electric disturbances ($\boldsymbol{b}$ and $\boldsymbol{e}$ respectively, the so-called electromagnetic waves) often add up to the background magnetic and electric field (presented in a previous section) and can potentially break the conservation property of one or several adiabatic invariants. The total magnetic field $\boldsymbol{B}$ typically writes

$$\boldsymbol{B}(r,\theta,\varphi,t) = \boldsymbol{B}_0(r,\theta,\varphi) + \boldsymbol{b}(r,\theta,\varphi,t)$$

for which $\boldsymbol{B}_0$ refers to the static background magnetic field and can be one of the field models presented in the previous section. The total electric field $\boldsymbol{\mathcal{E}}$ generally writes

$$\boldsymbol{\mathcal{E}}(r,\theta,\varphi,t) = \boldsymbol{e}(r,\theta,\varphi,t),$$

because the background electric field is often set to zero. Some of these magnetic and electric perturbations ($\boldsymbol{b}$ and $\boldsymbol{e}$ respectively) have been calculated by *Fälthammar* (1968) for example. As done in (*Roederer and Zhang*, 2014), let us consider different short term variations δt of the electromagnetic field perturbations. If

$$\tau_g \ll \tau_b \ll \delta t \leq \tau_d$$

the conservation property of the third adiabatic invariant is violated. If

$$\tau_g \ll \delta t \leq \tau_b \ll \tau_d$$

the second and third adiabatic invariants are violated simultaneously. If

$$\delta t \leq \tau_g \ll \tau_b \ll \tau_d$$

all the three adiabatic invariants are violated. For the latter case, the guiding center approximation is no longer valid. In a nutshell, a given adiabatic invariant can be violated when forces controlling the motion vary on a timescale comparable to or smaller than the associated period of motion. Since a mHz frequency range electromagnetic perturbation is sufficient to affect the third adiabatic invariant, the latter is most likely broken compared with the first two invariants, for which their violation requires the presence of higher frequency perturbations (Hz-kHz).

2.6.3 Deriving the Fokker-Planck equation

The aim of this part is to present the Fokker-Planck equation that governs the evolution of the distribution function $\bar{f}_X(\boldsymbol{X},t)$ in the adiabatic space $(X_1,X_2,X_3) \equiv (J_1,J_2,J_3)$. When the electromagnetic field is driven by small random fluctuations, the three adiabatic invariants (X_1,X_2,X_3) are subjected to small variations. Let Δt be a time interval long enough for a particle to suffer a large number of displacements but still short enough to violate one or several adiabatic invariants. Using the formalism of (*Chandrasekhar*, 1943; *Haerendel*, 1968), we can then define the transition probability $\Psi(\boldsymbol{X},\Delta\boldsymbol{X})$ that a particle is displaced by increment $\Delta\boldsymbol{X} = \boldsymbol{x}$ during the time interval Δt. Hence, taking account of the small stochastic perturbations of the three adiabatic

invariants and using a Taylor expansion, *Chandrasekhar* (1943, 1960) derived a Fokker-Planck equation of the form

$$\frac{\partial \bar{f}_X}{\partial t} = -\sum_{i=1}^{3} \frac{\partial}{\partial X_i}\left(\Pi_i \bar{f}_X\right) + \frac{1}{2}\sum_{i=1}^{3} \frac{\partial}{\partial X_i}\left[\sum_{j=1}^{3} \frac{\partial}{\partial X_j}\left(\Pi_{ij} \bar{f}_X\right)\right],$$

for which

$$\Pi_i = \frac{1}{\Delta t} \iiint\limits_{X-\mathtt{space}} x_i \Psi \, \mathrm{d}x_1 \mathrm{d}x_2 \, \mathrm{d}x_3$$

and

$$\Pi_{ij} = \frac{1}{\Delta t} \iiint\limits_{X-\mathtt{space}} x_i x_j \Psi \, \mathrm{d}x_1 \mathrm{d}x_2 \, \mathrm{d}x_3.$$

It can be shown (e.g., *Fälthammar*, 1966; *Haerendel*, 1968) that

$$\Pi_i = \frac{1}{2}\sum_{j=1}^{3} \frac{\partial \Pi_{ij}}{\partial X_j},$$

and introducing the diffusion coefficient $D_{X_i X_j}$ such that

$$D_{X_i X_j} = \frac{1}{2}\Pi_{ij} = \frac{1}{2\Delta t} \iiint\limits_{X-\mathtt{space}} x_i x_j \Psi \, \mathrm{d}x_1 \mathrm{d}x_2 \, \mathrm{d}x_3, \tag{2.49}$$

the Fokker-Planck equation governing the evolution of the phase-averaged distribution function f_X in the adiabatic invariant space is obtained (*Schulz and Lanzerotti*, 1974)

$$\frac{\partial \bar{f}_X}{\partial t} = \sum_{i=1}^{3} \frac{\partial}{\partial X_i}\left[\sum_{j=1}^{3} D_{X_i X_j} \frac{\partial \bar{f}_X}{\partial X_j}\right]. \tag{2.50}$$

The derivation of Fokker-Planck equation corresponding to the diffusion with respect to the third adiabatic invariant Φ is emphasized in Appendix C.

If one wants to use any coordinate system $\boldsymbol{Y} \equiv (Y_1, Y_2, Y_3)$ different from the invariant space $\boldsymbol{X} \equiv (Y_1, Y_2, Y_3)$, then the Fokker-Planck equation (2.50) that governs the evolution of the relative phase averaged distribution function $\bar{f}_Y$ writes (*Walt*, 1970; *Roederer*, 1970)

$$\frac{\partial \bar{f}_Y}{\partial t} = \sum_{i=1}^{3} \frac{\partial}{\partial Y_i}\left[\sum_{j=1}^{3} G_{XY} \, D_{Y_i Y_j} \frac{\partial}{\partial Y_j}\left(\frac{\bar{f}_Y}{G_{XY}}\right)\right]$$

for which G_{XY} is the Jacobian of the transformation from the adiabatic $\boldsymbol{X}$ variables to the (non necessarily canonical) $\boldsymbol{Y}$ variables, and $D_{Y_i Y_j}$ is the new corresponding diffusion coefficient. Several authors (e.g., *Walt*, 1970; *Roederer*, 1970) use this latter formalism.

However, as stated earlier, the $\bar{f}_Y$ function has the drawback of not being normalized in the sense that its value depends on the choice of coordinates $\boldsymbol{Y}$, and its dimension is not necessarily the same as the PSD governed by Liouville's equation. From this context, we prefer using a second formalism that involves the normalized phase-averaged

distribution function $\bar{F}_Y$ in the Fokker-Planck equation. The latter writes (*Haerendel*, 1968; *Schulz and Lanzerotti*, 1974)

$$\frac{\partial \bar{F}_Y}{\partial t} = \frac{1}{G_{XY}} \sum_{i=1}^{3} \frac{\partial}{\partial Y_i} \left[\sum_{j=1}^{3} G_{XY}\, D_{Y_i Y_j} \frac{\partial \bar{F}_Y}{\partial Y_j} \right]. \tag{2.51}$$

In both formalisms, the Jacobian transform G_{XY} is

$$G_{XY} = \begin{vmatrix} \dfrac{\partial X_1}{\partial Y_1} & \dfrac{\partial X_1}{\partial Y_2} & \dfrac{\partial X_1}{\partial Y_3} \\ \dfrac{\partial X_2}{\partial Y_1} & \dfrac{\partial X_2}{\partial Y_2} & \dfrac{\partial X_2}{\partial Y_3} \\ \dfrac{\partial X_3}{\partial Y_1} & \dfrac{\partial X_3}{\partial Y_2} & \dfrac{\partial X_3}{\partial Y_3} \end{vmatrix} \tag{2.52}$$

and the diffusion coefficient expressed in the new coordinate system relates to the older one through the relation (*Schulz and Lanzerotti*, 1974)

$$D_{Y_i Y_j} = \sum_{k=1}^{3} \frac{\partial Y_i}{\partial X_k} \sum_{l=1}^{3} D_{X_k X_l} \frac{\partial Y_j}{\partial X_l}. \tag{2.53}$$

Note that it is often more straightforward to express the diffusion coefficient directly related to a new set of physical (or observable) variables $\boldsymbol{Y}$ rather than starting from a diffusion coefficient expressed in terms of the pesky adiabatic variables $\boldsymbol{X}$ and performing the transformation into $D_{Y_i Y_j}$. Let us also highlight here that the determinant $G(J_1, J_2, J_3; \mu, J, \Phi)$ of Jacobian that takes account of the transformation from the three canonical adiabatic invariants (J_1, J_2, J_3) to the resized invariants (μ, J, Φ) is a constant equal to $2\pi m_0$, and so the original Fokker-Planck equation (2.50) writes the same for both the aforementioned coordinate systems. Some useful Jacobian determinants are given in Appendix C.2. For readability purpose, we will now denote the phase-averaged distribution function $\bar{F}_X$ or $\bar{F}_Y$ by f.

2.6.4 Radial diffusion

Let us have a more concrete look at the Fokker-Planck equation (2.51) in some specific situations. Under drift-resonant interactions of electrons with Ultra Low Frequency (ULF) waves (mHz), the third adiabatic invariant is violated, while the two first invariants are preserved, leading to a diffusive process in Φ (*Kellogg*, 1959). However, it is more convenient to work with the L^* variable rather than magnetic flux Φ. We recall that in a dipole field, L^* represents the equatorial radial distance of the magnetic field line, such that a diffusion with respect to the third adiabatic invariant corresponds to a radial diffusion. In this case, the Fokker-Planck equation (2.51) writes

$$\frac{\partial f}{\partial t} = \frac{1}{G(\Phi; L)} \frac{\partial}{\partial L} \left[G(\Phi; L)\, D_{LL} \frac{\partial f}{\partial L} \right],$$

for which D_{LL} is called the radial diffusion coefficient. The determinant $G(\Phi; L)$ of the Jacobian transformation from Φ to L^* is calculated with (2.52) and gives

$$G(\Phi; L) = \left| \frac{\partial \Phi}{\partial L^*} \right| = \frac{2\pi R_E^2 B_E}{L^2},$$

so that the radial diffusion equation becomes

$$\frac{\partial f}{\partial t} = L^2 \frac{\partial}{\partial L}\left[\frac{D_{LL}}{L^2}\frac{\partial f}{\partial L}\right].$$

From the expression of the first invariant μ in a dipole field, the momentum of the particle writes

$$p^2 = \frac{2m_0\mu B_E}{\sin^2(\alpha_0)} L^{-3}.$$

Hence, as μ is conserved, an outward radial diffusion (increasing values of L) leads to a loss of energy whereas an inward radial diffusion (decreasing values of L) is inherent to a gain of energy: this is known as the betatron acceleration.

2.6.5 Pitch angle diffusion

Gyro-resonant interactions of electrons with Very Low Frequency (VLF) waves (Hz-kHz) are likely to affect the velocity direction of the particles, so that a population of particles on a given field line is pitch angle scattered, i.e. their equatorial pitch angles are likely to decrease (e.g., *Lyons et al.*, 1971, 1972). The total energy being constant along a field line, the decrease of the equatorial pitch angle makes the parallel momentum component $p_\parallel = p\cos(\alpha_0)$ increase, and so, little by little, the particle is able to reach higher latitudes on the magnetic field line, until being ultimately lost in the upper atmosphere (precipitation). Hence the pitch angle diffusion, by bringing particles to the loss cone, is a loss process. Since this process conserves the particle energy, it is useful to rewrite the Fokker Planck equation with respect to the new variables (E, α_0, L) rather than in terms of the three conventional adiabatic invariants. In this case, the Fokker-Planck equation (2.51) writes

$$\frac{\partial f}{\partial t} = \frac{1}{G(\mu, J, \Phi; E, \alpha_0, L)}\frac{\partial}{\partial \alpha_0}\left[G(\mu, J, \Phi; E, \alpha_0, L)\, D_{\alpha_0\alpha_0}\frac{\partial f}{\partial \alpha_0}\right],$$

for which the expression of the Jacobian in a dipole field is

$$G(\mu, J, \Phi; E, \alpha_0, L) = 4\pi R_E^3 \gamma p \sin(2\alpha_0) L^2 T(\alpha_0),$$

with $T(\alpha_0)$ being the electron bounce normalized period defined earlier in equation (2.42). Coefficient $D_{\alpha_0\alpha_0}$ is called the pitch angle diffusion coefficient. Hence the pitch angle diffusion equation becomes

$$\frac{\partial f}{\partial t} = \frac{1}{T(\alpha_0)\sin(2\alpha_0)}\frac{\partial}{\partial \alpha_0}\left[T(\alpha_0)\sin(2\alpha_0)\, D_{\alpha_0\alpha_0}\frac{\partial f}{\partial \alpha_0}\right]. \tag{2.54}$$

The equation of pitch angle diffusion is at the heart of Chapter 5.

2.6.6 Energy diffusion

VLF waves can also accelerate electrons that are located mostly outside the plasmasphere. In this case, supplementary diffusion terms arise in equation (2.54), which

becomes (e.g., *Lyons*, 1974a,b)

$$\frac{\partial f}{\partial t} = \frac{1}{T(\alpha_0)\sin(2\alpha_0)}\frac{\partial}{\partial \alpha_0}\left[T(\alpha_0)\sin(2\alpha_0)\,D_{\alpha_0\alpha_0}\,\frac{\partial f}{\partial \alpha_0}\right]_{(p,L)} + \frac{1}{p^2}\frac{\partial}{\partial p}\left[p^2\,D_{pp}\,\frac{\partial f}{\partial p}\right]_{(\alpha_0,L)} + \frac{1}{T(\alpha_0)\sin(2\alpha_0)}\left.\frac{\partial}{\partial \alpha_0}\right|_{(p,L)}\left[T(\alpha_0)\sin(2\alpha_0)\,D_{\alpha_0 p}\left.\frac{\partial f}{\partial p}\right|_{(\alpha_0,L)}\right] + \frac{1}{p^2}\left.\frac{\partial}{\partial p}\right|_{(\alpha_0,L)}\left[p^2\,D_{\alpha_0 p}\left.\frac{\partial f}{\partial \alpha_0}\right|_{(p,L)}\right]. \tag{2.55}$$

Coefficients D_{pp} are referred as the energy diffusion coefficient, and $D_{\alpha_0 p}$ are the so-called cross diffusion coefficients. The equation of pitch angle and energy diffusion is also considered in Chapter 5.

2.6.7 The reduced Fokker-Planck equation

So far we have investigated a radial diffusion process that enables particles to diffuse radially across the magnetic field lines, and that goes along an energization of a particle population if they diffuse Earthward. Secondly, a pitch angle diffusion occurs when a particle population interacts with whistler waves (VLF). This process induces a decrease in the particle's pitch angle, allowing it to travel through larger paths along a given field line until being lost in the atmosphere at high latitudes. In practice, the two effects occur simultaneously, so that the radial diffusion equation and the pitch angle diffusion equations can be combined (in the absence of energy diffusion) to give (*Schulz and Lanzerotti*, 1974)

$$\frac{\partial f}{\partial t} = L^2\frac{\partial}{\partial L}\left[\frac{D_{LL}}{L^2}\frac{\partial f}{\partial L}\right]_{(\mu,K)} + \frac{1}{T(\alpha_0)\sin(2\alpha_0)}\frac{\partial}{\partial \alpha_0}\left[T(\alpha_0)\sin(2\alpha_0)\,D_{\alpha_0\alpha_0}\,\frac{\partial f}{\partial \alpha_0}\right]_{(E,L)}. \tag{2.56}$$

2.6.7.a First approximation: one dominant eigenmode

Since the pitch angle scattering effect is faster than radial diffusion, the pitch angle distribution is rather close to its steady state at the timescale of radial diffusion. Hence the solution of the pitch angle diffusion equation alone can be approximated by its first eigenmode (*Walt*, 1970; *Lyons et al.*, 1972). In this perspective, the pitch angle distribution function exhibits a pure exponential decay. The associated decay rate τ is extracted from the first eigenvalue associated with the first eigenmode of the pitch angle diffusion operator, and is often referred as the electron lifetime. This simplification leads to the following so-called reduced Fokker-Planck equation

$$\frac{\partial f}{\partial t} = L^2\frac{\partial}{\partial L}\left[\frac{D_{LL}}{L^2}\frac{\partial f}{\partial L}\right]_{(\mu,K)} - \frac{f}{\tau}. \tag{2.57}$$

Physically, reducing (2.56) to (2.57) implies that the phase-averaged distribution function decays uniformly with respect to pitch angle.

Historically, *Walt* (1970) related the electron lifetime to the lowest eigenvalue of the pitch angle diffusion operator by using an equation involving simultaneous radial and pitch angle diffusion written with respect to the variables (ζ, x_0, L) with $x_0 = \cos(\alpha_0)$ and

$\zeta = \mu/p^2$ (which was slightly different from the common pitch angle diffusion equation presented above). The eigenfunction expansion approach invoked by *Walt* (1970) will be used in Chapter 3 to derive a more general analytical solution of the reduced Fokker-Planck equation (2.57).

A few years later, *Lyons et al.* (1972) presented a general numerical method to extract the lifetime from a general pitch angle diffusion operator. More recently, *Albert and Shprits* (2009) performed lifetime estimations on the basis of analytical solutions of the pitch angle diffusion equation.

Such approximation is also fully justified regarding the shape of electron decays in the radiation belts for some specific events. For example, *O'Brien et al.* (2014) used the Van Allen Probes data to identify a single exponential decay from December 24, 2012 to January 12, 2013, indicating the presence of a pure eigenmode (i.e. the lowest eigenmode) in the pitch angle diffusion operator. The measured decay rates gave him the opportunity to derive event-specific pitch angle diffusion coefficient. In this perspective, this formalism is widely used in the literature (e.g., *Brautigam and Albert*, 2000; *Shprits et al.*, 2006; *Tu et al.*, 2009; *Ozeke et al.*, 2014; *Li et al.*, 2014b; *Ripoll et al.*, 2016a,b) as it represents a good compromise between accuracy and simplicity. This reduced Fokker-Planck equation (2.57) is considered in Chapters 3, 4, 5 and 6.

2.6.7.b Second approximation: independent processes

As discussed in (*Ripoll et al.*, 2016a), if the pitch angle diffusion coefficient $D_{\alpha_0\alpha_0}$ of equations (2.54) or (2.56) accounts for several independent diffusive processes (e.g. electron scattering by whistler mode hiss or chorus waves, Coulomb collisions), it is possible to derive a global lifetime τ that includes all processes together.

The global pitch angle diffusion coefficient can be written as $D_{\alpha_0\alpha_0} = \sum_i \mathbb{1}_i D^i_{\alpha_0\alpha_0}$, for which $D^i_{\alpha_0\alpha_0}$ is the pitch angle diffusion coefficient associated to a single diffusive process. Considering that the different diffusive processes occur on different separated L-domains, the $\mathbb{1}_i$ function is the indicator function related to $[L_i, L_{i+1}]$, i.e. it is set to 1 if $L \in [L_i, L_{i+1}]$ and zero otherwise (see also Chapter 3). Let us further assume that f can be written as $f = \sum_i \mathbb{1}_i f_i$. The pitch-angle diffusion equation (2.54) thus becomes

$$\begin{aligned}\sum_i \mathbb{1}_i \frac{\partial f^i}{\partial t} &= \frac{1}{G}\frac{\partial}{\partial \alpha_0}\left[G \sum_j \mathbb{1}_j D^j_{\alpha_0\alpha_0} \sum_i \mathbb{1}_i \frac{\partial f^i}{\partial \alpha_0}\right] \\ &= \frac{1}{G}\frac{\partial}{\partial \alpha_0}\left[G \sum_i \sum_j \delta_{i,j} \mathbb{1}_i D^j_{\alpha_0\alpha_0} \frac{\partial f^i}{\partial \alpha_0}\right]\end{aligned}$$

with $\delta_{i,j}$ being the Kronecker delta symbol ($\delta_{ij} = 1$ if $i = j$, zero otherwise). The result is

$$\sum_i \mathbb{1}_i \frac{\partial f^i}{\partial t} = \frac{1}{G}\frac{\partial}{\partial \alpha_0}\left[G \sum_i \mathbb{1}_i D^i_{\alpha_0\alpha_0} \frac{\partial f^i}{\partial \alpha_0}\right] \Rightarrow \sum_i \mathbb{1}_i \left[\frac{\partial f^i}{\partial t} - \frac{1}{G}\frac{\partial}{\partial \alpha_0}\left(G\, D^i_{\alpha_0\alpha_0} \frac{\partial f^i}{\partial \alpha_0}\right)\right] = 0.$$

Since all processes are independent from each other, we end up with one pitch angle diffusion equation governing each related distribution function f^i

$$\frac{\partial f^i}{\partial t} = \frac{1}{G}\frac{\partial}{\partial \alpha_0}\left(G\, D^i_{\alpha_0\alpha_0} \frac{\partial f^i}{\partial \alpha_0}\right).$$

Approximating as before (first assumption) each solution f^i by their lowest eigenmode $1/\tau_i$, one finds that

$$\frac{\partial f^i}{\partial t} = -\frac{f^i}{\tau_i}.$$

By recombining the independent pitch angle diffusive processes all together, we finally obtain

$$\sum_i \mathbb{1}_i \frac{\partial f^i}{\partial t} = -\sum_i \mathbb{1}_i \frac{f^i}{\tau_i} = -\sum_i \sum_j \delta_{i,j} \mathbb{1}_i f^i \frac{1}{\tau_j} = -\left(\sum_i \mathbb{1}_i f^i\right)\left(\sum_j \mathbb{1}_j \frac{1}{\tau_j}\right)$$

i.e

$$\frac{\partial f}{\partial t} = -f\left(\sum_j \mathbb{1}_j \frac{1}{\tau_j}\right) = -\frac{f}{\tau}$$

with the global electron lifetime τ being given by the harmonic average of all single lifetimes

$$\tau = \left(\sum_j \mathbb{1}_j \frac{1}{\tau_j}\right)^{-1}. \tag{2.58}$$

2.6.8 Quasilinear theory

The Fokker-Planck equation (2.51) has been introduced in 2.6.3 and Appendix C through a mathematical statistical approach (*Chandrasekhar*, 1943, 1960; *Roederer*, 1970; *Roederer and Zhang*, 2014), considering small stochastic perturbations of the three adiabatic invariants and writing the related diffusion coefficients (2.49) with the use of a transition probability function. Under this view it is rather difficult to see where the influence of the electromagnetic perturbations occur. In practice the diffusion coefficients are computed under the more physical concepts of quasilinear theory, which enables to relate the statistically-derived Fokker-Planck equation with the physical plasma dynamics related to the common Vlasov equation (*Chandrasekhar*, 1960).

Quasilinear theory basically describes the evolution of the phase space density in response to small-amplitude electromagnetic waves. Quasilinear theory implies that the electromagnetic waves that proliferate in the magnetosphere are broadband and small-amplitude waves (compared with the amplitude of the background Earth magnetic field). The aforementioned phase-mixing property is also required. Such theory is commonly adopted for the computation of diffusion coefficients.

2.6.8.a Radial diffusion

A prelude of quasilinear theory has first been put forward by *Fälthammar* (1965). He showed that both small magnetic perturbations (along with their induced electric perturbations) as well as electrostatic perturbations cause radial motion of electrons, breaking the conservation of the third adiabatic invariant. He quantified the resulting change in radial distance up to the first order.

This work served as a basis in the calculation of the radial diffusion coefficient involved in the Fokker-Planck equation. *Fälthammar* (1968) first calculated the radial diffusion coefficient inferred from drift-resonant interactions of electrons with ULF electromagnetic waves, showing a dependence with a power law in L-shell, more specifically in L^{10} for the D_{LL} calculated from electromagnetic perturbations (that includes the effects of electric induction) and in L^6 from the one inferred from electrostatic perturbations. If such

decomposition has also been used by *Brautigam and Albert* (2000), more recent works (e.g., *Ozeke et al.*, 2014) rather split the radial diffusion coefficient into an (azimuthal) electric component and a (compressional) magnetic component. Such radial diffusion coefficients will be considered in Chapters 3, 4, 5 and 6.

2.6.8.b Pitch angle and energy diffusion

Quasilinear theory has also been extended at the same time by *Kennel and Engelmann* (1966) and *Lerche* (1968). Their pioneering work consisted in splitting the distribution function as well as the magnetic and electric fields into a spatially homogeneous component and a small rapidly fluctuating part. The separation assumed a homogeneous and collisionless plasma immersed in a nearly uniform and static magnetic field (in the sense of the adiabatic conditions (2.4) and (2.5)). The derivation of a new quasilinear diffusion equation, which governs the gyro-averaged slow evolution of the distribution function, was carried out by expanding the Vlasov equation (also known as the collisionless Boltzmann equation) for the presumed particle distribution.

Lyons et al. (1971) have further applied the aforementioned quasilinear diffusion equation to pitch angle diffusion due to cyclotron-resonant wave particle interactions (e.g., *Stix*, 1962), which enabled them to obtain a tractable expression for pitch angle diffusion coefficient. *Lyons et al.* (1972) focused on the evolution of the equatorial pitch angle distribution. In this perspective, they averaged the quasilinear diffusion equation over the bounce period, which is shown to be equivalent to the Fokker-Planck equation related to pitch angle diffusion (2.54). This step enabled to link for the first time the general Vlasov equation to the Fokker-Planck equation related to pitch angle diffusion. Other following studies also rely on quasilinear theory to put forward closed form expressions for the pitch angle, energy and mixed diffusion coefficients (*Lyons*, 1974a,b). The data-driven pitch angle diffusion coefficient used in Chapter 5 (see also (*Ripoll et al.*, 2017)) relies on these pioneering aforementioned works.

2.6.8.c Diffusion in the adiabatic space

Whereas *Kennel and Engelmann* (1966) and *Lerche* (1968) applied quasilinear theory to the Vlasov equation (2.44) written in the canonical space $(\boldsymbol{p}, \mathbf{q})$, it is also possible (and less time-consumming) to derive the diffusion equation (2.50) in the adiabatic space on the basis of the Hamiltonian theory (e.g., *Ukhorskiy and Sitnov*, 2013). The initial Vlasov equation at stake is written with respect to the adiabatic invariants and phases of motions (action-angle coordinates) as in equation (2.46). The resulting diffusion coefficients directly account for resonant wave-particle interactions in the adiabatic space.

2.7 Electron fluxes

As we have just seen, the phase-averaged distribution function of electrons (abusively often called PSD) is of great interest for theoretical prospects (see Chapter 3), but suffers from a lack of intuitive and physical meaning, and is not clearly representative of what the orbiting satellites really measure. That is why it is necessary to define a more physical quantity that has a direct link to the observational data: the electron flux (see Chapters 4, 5 and 6).

2.7.1 Definition of the differential directional flux

The differential directional flux for a given location, direction, and energy is the number of particles coming from a given direction which cross a unit area oriented perpendicularly to their direction of incidence per unit time, unit solid angle and unit energy (*Roederer*, 1970; *Walt*, 1994). From this definition, the number δN of particles passing through the surface element $\delta A_\perp$ having an energy comprised between E and $E + \delta E$ within the solid angle $\delta\Omega$ during time δt is

$$\delta N = J\,\delta A_\perp\,\delta\Omega\,\delta E\,\delta t, \tag{2.59}$$

in which J is the differential directional flux. From this definition, the directional, differential flux is commonly expressed in $(\#.\mathrm{cm}^{-2}.\mathrm{s}^{-1}.\mathrm{ster}^{-1}.\mathrm{keV}^{-1})$. The most convenient reference direction is the geomagnetic field vector $\boldsymbol{e}$, and the local flux direction $\boldsymbol{u}$ (direction of velocity) is then controlled by the local pitch angle α of the trapped particles, so that

$$\delta N = (J\boldsymbol{u}) \cdot (\delta A\boldsymbol{e})\,\delta\Omega\,\delta E\,\delta t$$

with $\boldsymbol{u} \cdot \boldsymbol{e} = \cos(\alpha)$, i.e.

$$\delta N = J\,\delta A\cos(\alpha)\,\delta\Omega\,\delta E\,\delta t,$$

from which we can specify the unit area oriented perpendicularly to the magnetic field direction as $\delta A_\perp = \delta A\cos(\alpha)$. The above properties are illustrated in Figure 2.9.

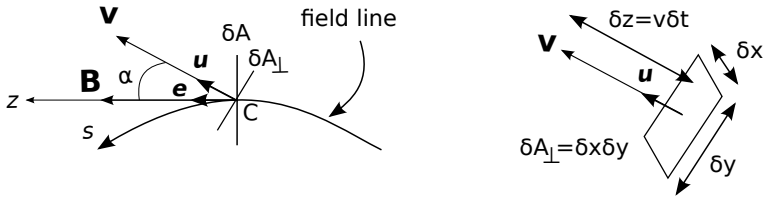

Figure 2.9 – Illustration of the surface of incidence δA and the perpendicular $\delta A_\perp = \delta A\cos(\alpha)$.

2.7.2 Relation between flux and PSD

The differential directional flux that is available from direct satellite instruments is closely related to the theoretical phase-averaged distribution function. The link between the electron flux and the phase-averaged distribution function has been obtained, for example, by *Schulz and Lanzerotti* (1974). Relying on their derivation, we first recall that the number of particles coming from a given direction which cross a unit area oriented perpendicularly to their direction of incidence per unit time, unit solid angle and unit energy (2.43) should be equal to the number of particles confined in the corresponding phase space volume (2.59). We thus end up with

$$\delta N = J\,\delta A_\perp\,\delta\Omega\,\delta E\,\delta t = F\,\delta p^3\,\delta \mathfrak{q}^3.$$

Rewriting the space volume as $\delta \mathfrak{q}^3 = \delta A_\perp\,(p/m)\delta t$, we find that (*Schulz and Lanzerotti*, 1974)

$$J\,\delta E\,\delta\Omega = (p/m)F\,\delta^3 p, \tag{2.60}$$

From the relativistic energy formula (see Appendix A.1) we have

$$\left(E + m_0c^2\right)^2 = p^2c^2 + \left(m_0c^2\right)^2$$

and so by differentiation we obtain

$$2\left(E + m_0c^2\right)\delta E = 2p\,\delta p\,c^2,$$

such that (knowing that $E + m_0c^2 = mc^2$)

$$\delta E = (p/m)\,\delta p. \tag{2.61}$$

Moreover, in spherical coordinates we have

$$\delta^3 p = p^2 \sin(\alpha)\delta\alpha\,\delta\varphi\,\delta p = p^2\,\delta\Omega\,\delta p. \tag{2.62}$$

Inserting (2.61) and (2.62) into (2.60) we obtain $J = p^2F$. We can also average over the phases of motion by using relation (2.48) to end up with the phase-averaged distribution function f and the phase-averaged flux j, verifying (*Schulz and Lanzerotti*, 1974)

$$j = p^2 f.$$

2.7.3 On the use of Liouville's theorem

Liouville's theorem can be recast in a more common expression, leading to a very useful conservation property that applies to electron fluxes as well as PSD. As shown by *Roederer* (1970), we will see below how the latter property can be applied for the calculation of omnidirectional electron fluxes (see Chapters 5 and 6).

The differential directional flux $J(E, \alpha, L, \varphi_g, \lambda, \varphi_d, t)$ is defined by

$$\delta N = J\,\delta A\cos(\alpha)\,\delta\Omega\,\delta E\,\delta t.$$

By expanding the solid angle element $\delta\Omega$ such that $\delta\Omega = \sin(\alpha)\,\delta\alpha\,\delta\varphi_g$, we obtain

$$\delta N = J\,\delta A\cos(\alpha)\sin(\alpha)\mathrm{d}\alpha\mathrm{d}\varphi\,\delta E\,\delta t,$$

i.e. with $x = \cos(\alpha)$,

$$\delta N = J\,\delta A x\mathrm{d}x\mathrm{d}\varphi\,\delta E\,\delta t$$

Considering that the flux is gyrotropic, we can write

$$\delta N = 2\pi\,J\,\delta A x\mathrm{d}x\,\delta E\,\delta t.$$

Now, let us relate the electron differential directional flux at two points P and Q on a given field line, as show on Figure 2.10 by using the different laws of conservation that are at stake in such a situation. The derivation presented below is based on a calculation provided by *Roederer* (1970). First, let us refer by J_P the flux at point P, i.e. $J_P(E_P, \alpha_P, L, t) \equiv J(E_P, \alpha_P, L, \lambda_P, t)$, and by J_Q the flux at point Q of the field line.

The number of particle should be conserved between P and Q, which leads to

$$J_P\,\delta A_P x_P \delta x_P\,\delta E_P = J_Q\,\delta A_Q x_Q \delta x_Q\,\delta E_Q. \tag{2.63}$$

Secondly, the magnetic flux is also conserved, so that

$$B_P\,\delta A_P = B_Q\,\delta A_Q. \tag{2.64}$$

On the given field line, the energy should be conserved, i.e.

$$\delta E_P = \delta E_Q. \tag{2.65}$$

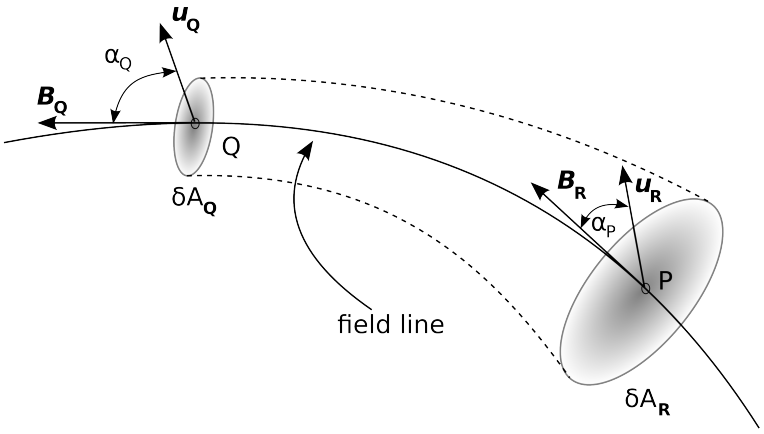

Figure 2.10 – Particles trapped at location P of the field line, having a local pitch angle α_P are drained along the field line to reach point Q. There, their pitch angle is α_Q, higher than α_P if the magnetic field intensity increases from P to Q. Adapted from *Roederer* (1970).

Finally, the first adiabatic invariant $\mu = p^2 \sin^2(\alpha)/(2m_0 B)$ is conserved. We can subsequently write

$$\frac{p_P^2 \left(1 - x_P^2\right)}{B_P} = \frac{p_Q^2 \left(1 - x_Q^2\right)}{B_Q},$$

and by differentiating the above relation with respect to $x = \cos(\alpha)$, we end up with

$$\frac{p_P^2 x_P \delta x_P}{B_P} = \frac{p_Q^2 x_Q \delta x_Q}{B_Q}. \tag{2.66}$$

Now, combining (2.63) with (2.64), (2.65), and (2.66) leads to

$$\frac{J_P}{p_P^2} = \frac{J_Q}{p_Q^2}$$

i.e. $f_P = f_Q$. This is equivalent to Liouville's theorem (*Roederer*, 1970). For equipotential field lines, we simply end up with $J_P = J_Q$, which is a very useful property to compute omnidirectional fuxes as shown below. The conservation of the unidirectional flux along an equipotential field line is illustrated in Figure 2.11.

2.7.4 Integral and omnidirectional fluxes

2.7.4.a Integral flux

We can define the integral (as opposed to differential) directional flux J_I as the number of particles crossing a unit area per unit solid angle and unit time (*Walt*, 1994), i.e.

$$J_I(\alpha, L, \varphi_g, \lambda, \varphi_d, t) = \int_E J(E, \alpha, L, \varphi_g, \lambda, \varphi_d, t)\, \mathrm{d}E$$

with φ_g being the phase related to the gyromotion of the particle around a field line.

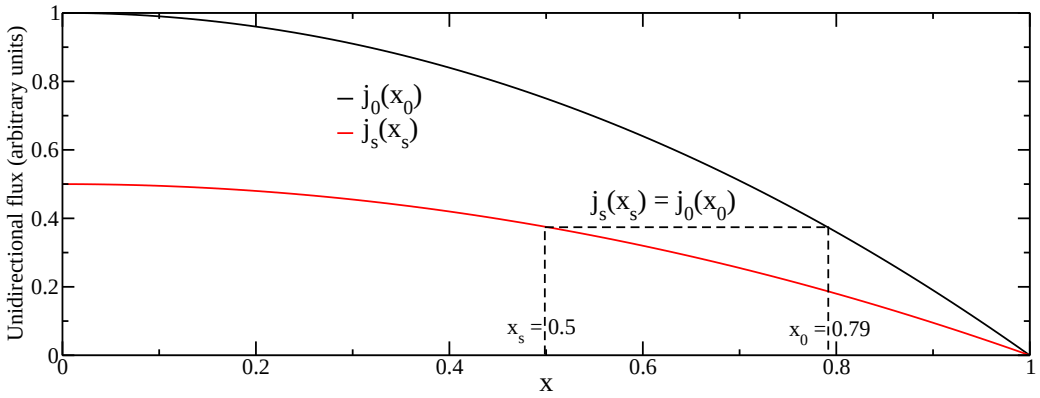

Figure 2.11 – An illustration of the flux conservation along a field line through Liouville's theorem. The local flux $j_s(x_s)$ (red curve) at a given location s on the field line is equal to the equatorial flux $j_0(x_0)$ (black curve) for the corresponding x_0. Adapted from *Roederer and Zhang* (2014).

2.7.4.b Omnidirectional flux

We can also define the omnidirectional (as opposed to directional) differential flux J_O as the number of particles crossing a unit area per unit energy and unit time (*Walt*, 1994), i.e.

$$J_O(E, L, \lambda, \varphi_d, t) = \iint_{\Omega} J(E, \alpha, L, \varphi_g, \lambda, \varphi_d, t)\, \mathrm{d}\Omega.$$

By expanding the solid angle element such that $\delta\Omega = \sin(\alpha)\, \delta\alpha\, \delta\varphi_g$, we obtain

$$\begin{aligned} J_O(E, L, \lambda, \varphi_d, t) &= \int_{\varphi_g=0}^{\varphi_g=2\pi} \int_{\alpha=0}^{\alpha=\pi} J(E, \alpha, L, \varphi_g, \lambda, \varphi_d, t)\, \sin(\alpha)\, \mathrm{d}\alpha\, \mathrm{d}\varphi_g \\ &= 2 \int_{\varphi_g=0}^{\varphi=2\pi} \int_{\alpha=0}^{\alpha=\pi/2} J(E, \alpha, L, \varphi_g, \lambda, \varphi_d, t)\, \sin(\alpha)\, \mathrm{d}\alpha\, \mathrm{d}\varphi_g. \end{aligned}$$

The flux is said to be gyrotropic if it does not depend on the cyclotron phase φ_g (*Roederer and Zhang*, 2014). In such a case the omnidirectional differential flux writes

$$J_O(E, L, \lambda, \varphi_d, t) = 4\pi \int_{\alpha=0}^{\alpha=\pi/2} J(E, \alpha, L, \lambda, \varphi_d, t)\, \sin(\alpha)\, \mathrm{d}\alpha. \tag{2.67}$$

or in terms of $x_0 = \cos(\alpha_0)$,

$$J_O(E, L, \lambda, \varphi_d, t) = 4\pi \int_{x_0=0}^{x_0=x_{0LC}} J(E, x_0, L, \lambda_0, \varphi_d, t)\, \mathrm{d}x_0.$$

When the radiation belt research was at its early stages, only the omnidirectional differential fluxes were measured by satellites whose instruments were not able do distinguish the

different directions of upcoming electrons. This quantity relates to the energy radiation level received by embedded instruments on board orbiting spacecraft.

The above omnidirectional differential flux is calculated at a given point of latitude λ of the field line and requires the knowledge of the unidirectional flux J at λ as a function of local pitch angle α. In simulations however, the phase-averaged distribution function f is calculated in the (μ, K, L) space, which is equivalent to the (E, α_0, L) space. The corresponding phase-averaged flux j is then a function of the equatorial pitch angle α_0 rather than α. Hence it is useful to relate the expression of the omnidirectional flux in terms of the equatorial directional flux rather than local directional flux. Rewriting (2.67) with respect to variable $x_s = \cos(\alpha_s)$ (s being the local curvilinear position of the particle on the field line) leads to

$$J_O(E, L, \lambda_s, \varphi_d, t) = 4\pi \int_{x_s=0}^{x_s=x_{sLC}} J(E, x_s, L, \lambda_s, \varphi_d, t)\, \mathrm{d}x_s.$$

From Liouville's theorem described above, we obtain

$$J(E, x_s, L, \lambda_s, \varphi_d, t) = J(E, x_0, L, \lambda_0, \varphi_d, t).$$

Moreover, the conservation of the first adiabatic invariant implies that $B_0/(1 - x_0^2) = B_s/(1 - x_s^2)$ so that

$$x_0 = \sqrt{1 - \frac{B_0}{B_s}(1 - x_s^2)}.$$

Hence the integrand lower limit $x_s = 0$ gives $x_0 = x_{01} = \sqrt{1 - B_0/B_s}$ and the integrand upper limit $x_s = x_{sLC} = \sqrt{1 - B_s/B_L}$ gives $x_0 = x_{0LC} = \sqrt{1 - B_0/B_L}$, such that the omnidirectional flux is calculated by

$$J_O(E, L, \lambda_s, \varphi_d, t) = 4\pi \int_{x_{01}}^{x_{0LC}} J(E, x_0, L, \lambda_0, \varphi_d, t)\, \frac{\mathrm{d}x_s}{\mathrm{d}x_0} \mathrm{d}x_0.$$

The conservation of the first adiabatic invariant (2.24) also states that

$$x_s = \sqrt{1 - \frac{B_s}{B_0}\left(1 - x_0^2\right)}$$

so that

$$\frac{\mathrm{d}x_s}{\mathrm{d}x_0} = \frac{B_s}{B_0} \frac{x_0}{\sqrt{1 - \frac{B_s}{B_0}\left(1 - x_0^2\right)}}.$$

Finally the omnidirectional differential flux at latitude λ_s of the field line is related to the equatorial unidirectional flux by (*Roederer*, 1970)

$$J_O(E, L, \lambda_s, \varphi_d, t) = 4\pi \frac{B_s}{B_0} \int_{x_{01}}^{x_{0LC}} J(E, x_0, L, \lambda_0, \varphi_d, t) \frac{x_0}{\sqrt{1 - \frac{B_s}{B_0}\left(1 - x_0^2\right)}} \mathrm{d}x_0. \tag{2.68}$$

Equation (2.68) is used in Chapter 5 and 6 to numerically compute omnidirectional electron fluxes for a given time, energy, L-shell and compare them with satellite observations.

A specific dedicated Romberg's method has been considered in Chapter 5 and 6 to take account of the singularity point at the mirror location $s = s_m$, for which $B_s = B_m$ and $\mathrm{d}x_s/\mathrm{d}x_0 \to +\infty$.

Let us also mention that it is *theoretically* possible to calculate the pitch angle distribution of electrons (i.e. the unidirectional fluxes at each equatorial pitch angle) from the knowledge of the omnidirectional flux at all latitudes along a given field line. The derivation of the corresponding unidirectional fluxes can be performed via the resolution of the so-called Abel's integral equation (e.g., *Ray*, 1960; *Farley and Sanders*, 1962; *Vette*, 1966). In practice however, the orbits of satellites lie in a near equatorial plane, such that only the omnidirectional flux within 20 degree-latitude can be observed. This lack of data along the whole field line does not allow to use the aforementioned mathematical approach to find the related pitch angle distribution. To bypass this difficulty, pre-computed empirical models for the pitch angle distribution (*Vampola*, 1997; *Horne et al.*, 2003; *Gannon et al.*, 2007; *Xudong et al.*, 2011; *Zhao et al.*, 2014a,b; *Chen et al.*, 2014; *Ni et al.*, 2015; *Shi et al.*, 2016) are instead traditionally considered. This is particularly done in Chapter 5 to infer the pitch angle electron distribution from omnidirectional fluxes observed by the Van Allen Probes.

2.7.4.c Integral Omnidirectional flux

Finally we define the integral omnidirectional flux as the number of particles crossing a unit area per unit time (*Walt*, 1994), i.e

$$J_{IO}(L, \lambda_s, \varphi_d, t) = \int_E \iint_{\Omega_s} J(E, \alpha_s, L, \varphi_g, \lambda_s, \varphi_d, t)\, \mathrm{d}\Omega_s\, \mathrm{d}E.$$

Using as before the equatorial unidirectional flux in the integrand rather than the local unidirectional flux leads to

$$J_{IO}(L, \lambda_s, \varphi_d, t) = 4\pi \frac{B_s}{B_0} \int_{E=0}^{+\infty} \int_{x_{01}}^{x_{0LC}} J(E, x_0, L, \lambda_0, \varphi_d, t)\, \frac{x_0}{\sqrt{1 - \frac{B_s}{B_0}\left(1 - x_0^2\right)}}\, \mathrm{d}x_0\, \mathrm{d}E.$$

The integral omnidirectional flux is also calculated in Chapter 6. Since the integration is performed over 2 dimensions (E and α_0), the corresponding numerical method can be computationally costly.

2.8 About electron transport, acceleration, and loss

The dynamics of electrons within the radiation belts is a profuse picture based on transport, acceleration, and loss (e.g., *Friedel et al.*, 2002; *Reeves et al.*, 2003; *Millan and Thorne*, 2007; *Shprits et al.*, 2008a,b; *Millan and Baker*, 2012; *Turner et al.*, 2013a) that is based on the formalism we presented. Here we briefly describe the different physical processes leading to the transport, acceleration, and loss of the radiation belt electrons. Applicability within the framework of the diffusion theory presented above is also discussed. Transport and loss processes, and to a lesser extent acceleration, will be extensively addressed in the next chapters.

2.8.1 Radial transport and acceleration

Electron acceleration can result from inward radial diffusion (betatron acceleration) or wave-particle interactions (in-situ acceleration) (e.g., *Millan and Baker*, 2012).

2.8.1.a Radial diffusion and global acceleration

As mentioned previously, drift resonant interactions between the electrons and ULF waves cause radial diffusion. As the electrons diffuse radially inward toward regions of higher magnetic intensity, the conservation of the first adiabatic invariant makes them accelerate through the process of betatron acceleration (e.g., *Shprits et al.*, 2008a).

Other phenomena can deviate from the quasilinear theory, such as drift orbit bifurcation (*Ukhorskiy et al.*, 2011, 2014), whose influence on the enhancement of betatron acceleration has been identified through test particle simulations. Interactions with narrow-band ULF waves can also lead to non-diffusive effects as described in (*Degeling et al.*, 2008).

2.8.1.b Local acceleration

Energy diffusion, which arises from gyro-resonant interactions between the electrons and VLF (mainly whistler mode chorus, outside the plasmasphere) waves, results in local, or in-situ, acceleration (e.g., *Horne et al.*, 2005; *Shprits et al.*, 2008b). The effects of chorus acceleration have been studied via global diffusion simulations (e.g., *Subbotin et al.*, 2010; *Thorne et al.*, 2013; *Li et al.*, 2014a).

Nonlinear interactions, which cannot be represented by a Fokker-Planck equation, may also play a role in the electron acceleration as well as electron losses (e.g., *Albert*, 2002; *Bortnik et al.*, 2008b; *Tao et al.*, 2012; *Albert et al.*, 2013). The validity of the quasilinear theory at the basis of diffusion holds if the wave field amplitude is small and broadband. *Santolík et al.* (2004) have shown that whistler mode chorus waves are narrow-band (discrete) and coherent waves field. Their amplitude is usually larger than the maximum amplitude allowed by the quasilinear theory. Consequently, whistler mode chorus waves might not be fully described by diffusion theory, and advective terms might be necessary to account for their effects on charged particles. Quasilinear diffusion theory is relevant for broadband waves (such as plasmaspheric hiss), but may not be always consistent for coherent and quasi monochromatic waves like chorus. Nonlinear theory may thus be required to obtain a reliable picture of the effects of whistler mode chorus waves.

2.8.2 Losses

Losses can be the result of three contributions arising from different physical processes: adiabatic effects (*Dst effect*) and nonadiabatic processes such as atmospheric losses or magnetopause losses (e.g., *Green et al.*, 2004).

2.8.2.a Adiabatic effects

Historically, the observed flux dropout during the main phase of a geomagnetic storm have been explained via a fully reversible adiabatic effect (*McIlwain*, 1966b; *Kim and Chan*, 1997), which implies the conservation of all the three adiabatic invariants. During storm-time, the buildup of the ring current is accompanied by a drop in the magnetic field intensity, which makes the drift shell expand to fulfill the conservation of the magnetic

flux (third invariant). By doing so, the related electrons loose their energy. Since the electron phase space density f has to be conserved with regards to Liouville's theorem, the resulting flux $j = p^2 f$ decreases. This is the *Dst effect*, as named by (*Li et al.*, 1997), also known as the ring current effect. This effect seems however to be marginal compared with the other so-called nonadiabatic effects that are briefly described below.

2.8.2.b Atmosheric losses

Interactions between charged particles with electromagnetic waves induce the decrease of the electron local pitch angles, which drive them into the bounce loss cone and make them precipitate into the Earth's atmosphere. Such pitch angle scattering process, which can be described in the framework of the Fokker-Planck equation via pitch angle diffusion, is mostly due to the action of whistler mode hiss (inside the plasmasphere) or chorus (outside the plasmasphere) waves (*Thorne et al.*, 2005), as well as the EMIC wave (e.g., *Shprits et al.*, 2008b). Whistler mode hiss waves are known to be responsible for the formation of the slot region between the two radiation belts (e.g., *Lyons and Thorne*, 1973; *Ripoll et al.*, 2017), while whistler mode chorus waves can be spotted under the form of microbursts responsible for the rapid loss of relativistic electrons (*Thorne et al.*, 2005). The EMIC waves have recently been related to the depletion of ultrarelativistic electrons in the outer zone (*Usanova et al.*, 2014; *Shprits et al.*, 2016). As mentioned before, atmospheric losses can also be related to the drift loss cone: electrons can be brought into the ionsosphere because of a drop in their drift shell in the vicinity of Earth (see the previous discussion about the South Atlantic Anomaly).

Other processes may also be considered out of the scope of quasilinear theory. Another mechanism responsible for the rapid electron depletion in the atmosphere is the current sheet scattering (*Sergeev et al.*, 1983). In the magnetotail, the radius of curvature of the stretched field lines can be comparable to the Larmor radius (gyroradius) of the trapped electron, leading possibly to a decrease of the electron's pitch angle and to its ultimate loss into the atmosphere. In this situation, the adiabatic condition (2.4) is violated and the first adiabatic invariant is no more conserved, such that the entire theoretical framework on which the Fokker-Planck theory is built collapses. The nonlinear processes outlined above can also be applied to the depletion of electrons inferred from whistler mode chorus waves.

2.8.2.c Magnetopause losses

Particles can also be lost in the outer space. The combination of magnetopause shadowing with outward radial diffusion can result in drastic electron dropouts during storm-time (*Brautigam and Albert*, 2000; *Kim et al.*, 2008; *Shprits et al.*, 2006; *Miyoshi et al.*, 2003; *Turner et al.*, 2012; *Yu et al.*, 2013). Drift shell bifurcations also drive the electron into their drift loss cone and bring them beyond the dayside magnetopause (*Kim et al.*, 2008; *Saito et al.*, 2010; *Ukhorskiy et al.*, 2011).

2.9 Dedicated error metrics for validation

As mentioned above, reproducing radiation belts electron fluxes (unidirectional or omnidirectional) by numerical simulations enable direct comparison with satellite observations. According to the accuracy of the numerical model, a specific physical process can be confirmed or disproved. In this context, many different statistical metrics have been used through the field of the radiation belt physics. As a preliminary to Chapters 5

and 6, we distinguish here the statistical metrics based on the forecast error, the relative error and the accuracy ratio, following (*Morley*, 2016; *Morley et al.*, 2018). The statistical metrics presented here will specifically be applied to prove the importance of using the data-driven pitch angle diffusion coefficient used in Chapter 5, which is devoted to the March 2013 storm-recovery. The error metrics that we present below will also confirm the impact of the magnetic field topology on the dynamics of radiation belts electrons (see Chapter 6).

2.9.1 Statistical metrics based on the forecast error

The forecast error ε is simply defined as the difference between the predicted fluxes with the observed fluxes, i.e.

$$\varepsilon(E,L,t) = J_O^{\text{simu}}(E,L,t) - J_O^{\text{data}}(E,L,t)$$

for which $J_O^{\text{simu}}(E,L,t)$ is the omnidirectional flux predicted by the simulation at kinetic energy E, radial distance L and time t, and $J_O^{\text{data}}(E,L,t)$ is the observed omnidirectional flux. From the forecast error, we can typically calculate the mean absolute error (MAE) such that $\text{MAE} = \text{Av}(|\varepsilon|)$, for which Av is the common average function, or the root mean squared error (RMSE) defined as $\text{RMSE} = \sqrt{\text{Av}(\varepsilon^2)}$. These two metrics have the same dimension of the electron omnidirectional fluxes. If they are easy to implement, they have the drawback of penalizing the errors made on the largest values of the data. As mentioned in (*Morley*, 2016; *Morley et al.*, 2018), the median function, here denoted as Med, is a more robust metric to estimate the central tendency than the average function. Hence we can improve the aforementioned indices by replacing the average function by the median function, by defining (for example) the median absolute error (MdAE) as

$$\text{MdAE} = \text{Med}(|\varepsilon|). \tag{2.69}$$

The MdAE index is further used to estimate the median forecast error inherent to the model.

2.9.2 Statistical metrics based on the relative error

The previously defined forecast error metrics do not give any information on the percentage error made by the model. For this purpose, we can normalize the forecast error by the local magnitude of the observed flux, leading to a local relative error η that writes

$$\eta(E,L,t) = \left[J_O^{\text{simu}}(E,L,t) - J_O^{\text{data}}(E,L,t)\right] / J_O^{\text{data}}(E,L,t).$$

The local relative error is at the basis of the mean absolute percentage error (MAPE) commonly used in the field of magnetospheric physics. It is defined as $\text{MAPE} = 100 \times \text{Av}(|\eta|)$ (%). Again, the robustness of the MAPE index can be improved by using the median rather than the average, such that we define the median absolute percentage error (MdAPE) index as

$$\text{MdAPE} = 100 \times \text{Med}(|\eta|). \tag{2.70}$$

As emphasized by *Morley* (2016); *Morley et al.* (2018), the MAPE and MdAPE have also the drawback of penalizing over-prediction compared with under-predictions, and thus favor under-forecasting models.

2.9.3 Statistical metrics based on the accuracy ratio

In order to remove this non-homogeneity, we define the accuracy ratio Q (quotient) as

$$Q(E, L, t) = J_O^{\text{simu}}(E, L, t)/J_O^{\text{data}}(E, L, t).$$

We immediately see that Q is positively skewed (going from 0 to ∞). In magnetospheric physics, errors can be large so that one can also rely on the logarithm of the accuracy ratio ($\log(Q)$). In this context, *Morley* (2016) calculated two global error indices devoted to radiation belts modeling applications, among which, principally, electron flux error predictions. The first index relying on the accuracy ratio is the median symmetric accuracy, indicated here as MdSA. It represents the percentage error between observation and prediction, treating model overestimation and underestimation equivalently. It is calculated as

$$\text{MdSA} = 100 \times \left(10^{\text{Med}(|\log_{10}(Q)|)} - 1\right). \tag{2.71}$$

The second index, referred as MdLQ, is the median log accuracy ratio. It is a symmetric bias between observations and predictions, being negative if the model underestimates the data, and positive if the model overestimates the data. Its formulation is also recalled here,

$$\text{MdLQ} = \text{Med}(\log_{10}(Q)). \tag{2.72}$$

If both statistics are meaningful and easy to interpret, they have the drawback of treating the discrepancy between predictions and observations equally for low and large electron fluxes. However, an error of prediction when the flux values are very low should be negligible, compared with an error of the same order of magnitude when the electron fluxes are important. All the metrics in use are summarized in Table 2.1, with their corresponding drawbacks indicated.

2.9.4 Comparison

The advantages and drawbacks of the aforementioned error metrics are summarized in Table 2.1, following (*Morley et al.*, 2018).

Now that the required physical concepts of radiation belts have been defined and the framework of the study clarified, the next chapters are devoted to describe concretely the work done during the PhD by applying extensively the mathematical tools presented above.

Table 2.1 – Error metrics based on the forecast error, relative error and accuracy ratio computed with the use of the average function and the median function. Adapted from *Morley et al.* (2018).

Metric	Definition	Based on	Comments
Root Median Squared Error	$\text{RMdSE} = \sqrt{\text{Med}(\epsilon^2)}$	Forecast error	Penalty on large errors
Median Absolute Error	$\text{MdAE} = \text{Med}(\lvert\epsilon\rvert)$	Forecast error	Penalty on large errors
Median Absolute Percentage Error	$\text{MdAPE} = 100 \times \text{Med}(\lvert\eta\rvert)$	Relative error	Penalty on over-predictions
Median Log Accuracy Ratio	$\text{MdLQ} = \text{Med}\left(\log_{10}(Q)\right)$	Accuracy ratio	Low and large values equally penalized
Median Symmetric Accuracy	$\text{MdSA} = 100 \times \left[10^{\text{Med}(\lvert\log_{10}(Q)\rvert)} - 1\right]$	Accuracy ratio	Low and large values equally penalized

Chapter 3

The analytical solution of the radial diffusion equation

Many works have been done during the past forty years to perform the analytical solution of the radial diffusion equation (2.57) that models the transport and loss of electrons in the magnetosphere, considering a diffusion coefficient proportional to a power law in L-shell and a constant loss term. In this chapter, we propose an original analytical method to address this challenge when the loss term is nonuniform. The strategy is to match any L dependent electron losses with a piecewise-constant function on M subintervals, i.e. dealing with a constant lifetime on each subinterval. Applying an eigenfunction expansion method, the eigenvalue problem becomes a Sturm-Liouville problem with M interfaces. Assuming the continuity of both the distribution function and its first spatial derivatives, we are able to deal with a well-posed problem and to find the full analytical solution. We further show an excellent agreement between both the analytical solutions and the solutions obtained directly from numerical simulations for different loss terms of various shapes and with a diffusion coefficient $D_{LL} \sim L^6$. We also give two expressions for the required number of eigenmodes N to get an accurate snapshot of the analytical solution, highlighting that N is proportional to $1/\sqrt{t_0}$, where t_0 is a time of interest, and that N increases with the diffusion power. Finally, the equilibrium time, defined as the time to nearly reach the steady solution, is estimated by a closed-form expression and discussed. Applications to Earth but also Jupiter and Saturn are discussed.

This chapter is a detailed overview of the analytical work that has already been published as (*Loridan et al.*, 2017). Before going through the heart of the analytical solutions, we contextualize the study (Section 1) and spend some time to explain more the adopted analytical approach in a general view (Section 2). We then develop the analytical calculations that apply to the radiation belts models of Sections 3 to 6, most of them being discussed in (*Loridan et al.*, 2017). We also take the opportunity to newly derive here some specific solutions related to radial diffusion occurring either during gradual time-varying injections of electrons into the magnetosphere or during gradual time-varying dropouts. Section 7 is devoted to the possible future prospects brought by the present analytical solutions.

3.1 Motivations of the study

The motivation of this study lies on a better understanding of how the analytical solution of the radial diffusion equation combined with a general loss term is built. One can also investigate the efficiency of an alternative numerical method based on an analytical formulation to solve the common radial diffusion problem or to verify numerical schemes.

3.1.1 Historical background

Analytical understanding of the radial diffusion process has indisputably progressed during the last decades, and relies mostly on the works that began in the 1960-1970's when the theory describing the radiation belts was still at its early stages and satellite data were limited. The aforementioned studies started with the derivation of the steady solution. Analytical expressions of the steady distribution function of particles trapped in the radiation belts have first been investigated by *Haerendel* (1968), who calculated the stationary proton distribution governed by a radial diffusion equation. Assuming that both the radial diffusion coefficient and the lifetime evolve as a power law with respect to the radial adiabatic invariant L, he gave a stationary solution built on modified Bessel functions. Such hypothesis made on the radial diffusion coefficient is not as strong as it

appears at a first sight, since radial diffusion induced by drift-resonant interactions with ULF waves leads to such power-law dependence in L-shell for the D_{LL} (e.g., *Fälthammar*, 1965; *Fälthammar*, 1968; *Brautigam and Albert*, 2000; *Ozeke et al.*, 2014). This steady solution has been used, for example, by *Thorne* (1972), in order to better explore the shape of the outer radiation belt. The theoretical works from *Haerendel* (1968) have also been applied by *Baker and Goertz* (1976) and *Goertz et al.* (1979) to explain the quiet time distribution of electrons trapped in the vicinity of Jupiter. These initiatives aimed at comparing the theoretical results to satellite observations in order to give an expression for the radial diffusion coefficient. From this perspective, *Thomsen et al.* (1977a,b) calculated a steady distribution function of protons in Jupiter's magnetosphere on a discontinuous domain involving a piecewise-constant lifetime split on 3 interfaces. Their purpose was to compare their analytical results with data taken from instruments on Pioneer 11 in order to derive a radial diffusion coefficient for the diffusion of protons in Jupiter's magnetosphere. Conditions of continuity of the distribution function and its first spatial derivatives at the interface points are used similarly to what will be done in this chapter. *Jentsch* (1984) rather focused on the steady state distribution of protons including the losses of protons induced by charge exchange and an energy degradation term. He also considered an electric radial diffusion coefficient proportional to a fixed power of L. As a final comment on the analytical steady problem, let us mention that *Hood* (1983) also gave an analytical expression for the steady distribution function of protons in Saturn's magnetosphere.

While the previous studies focused on the steady solutions, other works discussed time-varying solutions. *Walt* (1970) dealt with the dynamical electron distribution given by a Fokker-Planck equation that can be simplified to a single radial diffusion equation with a constant loss term. Considering again a power-law dependence on L of the radial diffusion coefficient, he put forward a steady distribution, solution of the stationary problem, combined with a transient distribution, solution of the time-dependent problem. He indicated that the steady solution was expressible in terms of modified Bessel functions, and that the transient solution, which could be obtained from a separation between the time and radial variables, was expressible in terms of Bessel functions (although he did not write the full solution explicitly). *Schulz* (1986) examined the radial transport of magnetospheric ring-current ions and described a general analytical method for obtaining both steady state and dynamical solutions. In his study, the dependence of the radial diffusion coefficient, D_{LL}, upon L could deviate slightly from a strict power law. An eigenfunction expansion approach was used to derive a general expression for the transient solutions. Some examples of closed-form expressions of the distribution function when D_{LL} is proportional to a power law of L were also given in his paper. *Schulz and Newman* (1988) exhibited closed-form expressions for the steady and the transient solutions of the radial diffusion equation with no source term but allowing a time-dependent outer boundary condition. Their transient solutions were also derived from an eigenfunction decomposition method and were expressed with Bessel functions of fractional order. Their work also put forward a criteria evaluating the required number of eigenmodes for any computation in order to reach the convergence of the analytical solution. They found that this number can be quite large. We will see below how our work follows the steps of the fundamental studies of *Schulz* (1986) and *Schulz and Newman* (1988).

3.1.2 Applications

The radial diffusion equation we solve in this chapter is the reduced Fokker-Planck equation presented in (2.57). It includes a nonuniform loss term that approximately

models the scattering effect of pitch-angle diffusion. We restrict the study to a strict power law dependence of the radial diffusion coefficient upon L such that $D_{LL} = D_0 L^n$, with n any positive real or integer ($n \geq 0$). Considering such a power law dependence is a fully consistent hypothesis that falls entirely within the framework of previous studies that predicted a $D_{LL} \sim L^n$, either for a radial diffusion driven by fluctuating electric fields ($n \sim 6$) and magnetic fields ($n \sim 10$) in the Earth's radiation belts (e.g., *Schulz and Lanzerotti*, 1974; *Brautigam and Albert*, 2000; *Ukhorskiy and Sitnov*, 2008; *Ozeke et al.*, 2014; *Liu et al.*, 2016), or for a radial transport induced by ionospheric dynamo fields in the vicinity of Jupiter, for which $n \sim 2 - 3$ (e.g., *Brice and Mcdonough*, 1973; *Coroniti*, 1974; *Birmingham et al.*, 1974; *Thomsen et al.*, 1977a,b; *de Pater and Goertz*, 1990, 1994; *Woodfield et al.*, 2014), or Saturn ($n \sim 4$) (*Hood*, 1983).

The main step forward of the present chapter is to generalize the aforementioned historical studies, and particularly the work carried out by *Schulz and Newman* (1988). The purpose here is to include any L-dependent lifetime $\tau(L)$ in the radial diffusion equation. To our knowledge, there exists no general procedure to solve analytically such a problem involving a general nonuniform loss term. To overcome this difficulty, the idea is to approximate the nonuniform electron lifetime by a piecewise constant electron lifetime on M pieces, which enables to transform the full unsolvable eigenvalue problem to a more straightforward Sturm-Liouville problem with M interfaces. This is a generalization of an existing procedure for two interfaces Sturm-Liouville problem (e.g., *Cain and Meyer*, 2005). As we will show, we obtain a Sturm-Liouville problem with M interfaces that is solvable for a distribution function being continuous and having a continuous first spatial derivative. The initial condition, the two boundary conditions and the $2M - 2$ interface conditions, which connect the distribution function and its first spatial derivative at each side of the interface points, enable us to define a well-posed problem and to solve it analytically. The continuity of the second-order and higher-order spatial derivatives of the distribution function f breaks down contrary to the solutions f obtained by *Schulz and Newman* (1988) that are are continuous with all their derivatives being continuous (such functions are said to be C^∞). Furthermore, due to the piecewise-constant property of the electron lifetime, we will exhibit transient solutions that can be expressed by the combination of Bessel functions and modified Bessel functions, at the difference of the previous works (*Walt*, 1970; *Schulz*, 1986; *Schulz and Newman*, 1988) that only involved Bessel functions in the transient solution. Hence the present chapter details respectively 1- the mathematical method used to find the analytical solution on each subinterval, which is based on a separation of variables (L, t) and leads to an eigenfunction approach (e.g., *Schulz and Newman*, 1988) and 2- a general connection procedure between each interface to build a realistic solution on the full spatial domain.

As direct applications of this work, let us first mention that analytical solutions are preferable to "brute force" numerical ones, because they lead to a "more physical" interpretation of the mathematical expressions (equation, functional form of the solution) involved. The effects of changes in values and/or functional forms of parameters and coefficients can be better examined and visualized, which may lead to a better understanding of the physical assumptions made in the derivation. It also helps us better exploring the domain of validity of the solution in question. In particular, the consideration of a general piecewise-continuous lifetime in the analytical method presented here can be built to fit any of the recent data-driven lifetimes (e.g., *Gu et al.*, 2012; *Mourenas and Ripoll*, 2012; *Orlova and Shprits*, 2014; *Orlova et al.*, 2014, 2016). As emphasized in sections 3.5.2 and 3.7, the proposed analytical method could be an interesting alternative numerical method compared with its purely numerical counterpart to find the long-term evolution

of electrons in the Earth's radiation belts. It is moreover well adapted to simulating the whole dynamics of the magnetosphere of Jupiter (as mentioned by *Schulz and Newman* (1988)) and Saturn for which the radial transport is much weaker than in the Earth's radiation belts (e.g., *Baker and Goertz*, 1976; *Thomsen et al.*, 1977a,b; *Hood*, 1983) (see sections 3.5.3 and 3.7). Another application of this work is to give access to the physical timescales of the dynamics of the radial diffusion of particles in the radiation belts, as discussed for instance in *de Pater and Goertz* (1994).

3.2 An analytical recipe applied to the diffusion equation

We first briefly present the analytical method retained to solve the reduced Fokker-Planck equation (2.57). The approach is based on a separation of the time and space variables (L, t) that relies on an eigenfunction decomposition. Beyond the previous aforementioned works dedicated to the radial diffusion equation, the eigenfunction decomposition has also enabled to derive analytical solutions of more general problems related to space science, such as solving the Fokker-Planck equation in the velocity space with some applications to the polar wind and the solar wind (e.g., *Pierrard and Lemaire*, 1998; *Pierrard et al.*, 1999). For the case of interest in this chapter, it is useful to recall here some properties of a specific eigenvalue problem: the Sturm-Liouville problem.

3.2.1 Approximations with orthogonal projections

3.2.1.a Definition of an orthogonal projection

Let us consider a vector space, Ω, with the usual definition of the inner product $\langle f, g \rangle$ and the associated norm $\|f\| = \sqrt{\langle f, f \rangle}$. Two vectors f and g in a inner product space Ω are said orthogonal if $\langle f, g \rangle = 0$. Let us consider Ω_N, the subspace of the Ω inner product space such that Ω_N has the finite dimension N. Suppose that $\{\varphi_1, ..., \varphi_N\}$ is a basis of the Ω_N subspace.

We define the orthogonal projection Pf of f onto Ω_N as the vector $Pf \in \Omega_N$ such that the vector $f - Pf \in \Omega$ is orthogonal to every vector $g \in \Omega_N$, i.e. $\langle f - P_f, g \rangle = 0$. This definition is illustrated by a simple example in Figure 3.1. Now, let us emphasize some useful properties of the orthogonal projection.

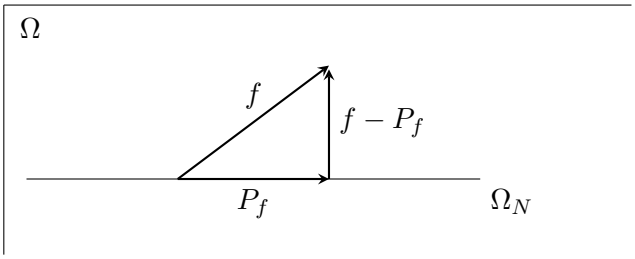

Figure 3.1 – A simple example of the geometric meaning of an orthogonal projection is illustrated. The Ω space is the plane (2 dimensional), and the Ω_N subspace is represented by the straight line (1 dimension). The vector f belongs to the Ω plane and is projected onto the Ω_N straight line, such that the vector $f - Pf \in \Omega$ is orthogonal to any element of Ω_N.

3.2.1.b Expressing the orthogonal projection

The projection Pf of f into Ω_N is a member of the Ω_N subspace, so that Pf can be written as a linear combination of the elements of the basis $\{\varphi_1, ..., \varphi_N\}$ of Ω_N

$$Pf = \sum_{n=1}^{N} \alpha_n \varphi_n, \tag{3.1}$$

for which the coordinates α_n of Pf have yet to be found. From the definition of the orthogonal projection, the vector $f - Pf$ is orthogonal to every element of Ω_N if and only if it is orthogonal to each of the basis element φ_n, i.e.

$$\langle f - Pf, \varphi_n \rangle = 0 \text{ for all } n \in [1, N].$$

Hence, from the usual properties of the inner product, the above equality becomes

$$\langle f, \varphi_n \rangle - \langle Pf, \varphi_n \rangle = 0$$

so that

$$\langle f, \varphi_n \rangle - \left\langle \sum_{m=1}^{N} \alpha_m \varphi_m, \varphi_n \right\rangle = 0 \Rightarrow \sum_{m=1}^{N} \alpha_m \langle \varphi_m, \varphi_n \rangle = \langle f, \varphi_n \rangle.$$

If the basis $\{\varphi_1, .., \varphi_N\}$ of Ω_N is supposed to be orthogonal, i.e. $\langle \varphi_m, \varphi_n \rangle = 0$ if $m \neq n$, we obtain

$$\sum_{m=1}^{N} \alpha_m \langle \varphi_m, \varphi_n \rangle = \alpha_n \langle \varphi_n, \varphi_n \rangle = \langle f, \varphi_n \rangle,$$

from which we can extract an expression of the coordinates α_n of the vector Pf in Ω_N such that

$$\alpha_n = \frac{\langle f, \varphi_n \rangle}{\langle \varphi_n, \varphi_n \rangle}, \tag{3.2}$$

which gives

$$Pf = \sum_{n=1}^{N} \frac{\langle f, \varphi_n \rangle}{\langle \varphi_n, \varphi_n \rangle} \varphi_n.$$

3.2.1.c Best approximation

Let Ω_N be a subspace of an inner product space Ω and suppose $f \in \Omega$. If $g \in \Omega_N$, then $\|f - Pf\| \leq \|f - g\|$ where Pf is the orthogonal projection of f onto Ω_M. Reciprocally, if $h \in \Omega_M$ is such that $\|f - h\| \leq \|f - g\|$ for all $g \in \Omega_N$, then $h = Pf$, the orthogonal projection of f onto Ω_N. This means that Pf is the best approximation of f in subspace Ω_N.

3.2.1.d Working in an appropriate vector space

In what follows, the study is made on the specific Ω space such that $\Omega \equiv \mathbb{L}_2([L_0, L_M], \sigma)$, for which $\mathbb{L}_2([L_0, L_M], \sigma)$ is the collection of all functions for which $|f|^2\sigma$ is integrable on the real interval $[L_0, L_M]$. The σ function is a so-called weight function, continuous on $[L_0, L_M]$, and such that $\sigma(L) \geq 0$ for all L, and $\sigma(L) = 0$ at a finite set of points.

The Ω vector space becomes an inner product space if we define the inner product $\langle f, g \rangle$ between two vectors f and g of Ω such that

$$\langle f, g \rangle = \int_{L_0}^{L_M} f(L) g(L) \sigma(L) \, \mathrm{d}L. \tag{3.3}$$

The restriction on $\sigma(L)$ guarantees that $\langle f, f \rangle > 0$ for $f \neq 0$. In the next paragraph, we relate the above defined mathematical quantities to the solution of a general Sturm-Liouville problem.

3.2.2 Sturm-Liouville problem

3.2.2.a Definition

A typical Sturm-Liouville problem related to a function, φ, that depends on a space variable L is given by a second order linear differential equation involving a general operator $\mathcal{L}$ of the form

$$\mathcal{L}(L)\varphi \equiv \Big(p(L)\varphi^{'}(L)\Big)^{'} - q(L)\varphi(L) = \lambda \sigma(L)\varphi(L) \tag{3.4}$$

for which the $p^{'}$, q and σ are continuous functions on a given interval $[L_0, L_M]$ (the prime symbol denotes the derivation with respect to L). The p function has to be nonnegative on $[L_0, L_M]$ and the σ function is positive except possibly at a finite number of points belonging to $[L_0, L_M]$. The latter function is the aforementioned weight function. We call by φ the functions that are solutions of (3.4), now referred as the eigenfunctions of the Sturm-Liouville problem. The parameter λ is the eigenvalue associated to the eigenfunction φ. The licit general boundary conditions associated to the eigenfunction φ can be written in the following general form (*Cain and Meyer*, 2005) (combination of Dirichlet and Neumann boundary conditions)

$$\begin{cases} p(L_0)\Big[a_1\varphi(L_0) - a_2\varphi^{'}(L_0)\Big] & = 0, \\ p(L_M)\Big[b_1\varphi(L_M) - b_2\varphi^{'}(L_M)\Big] & = 0 \end{cases}$$

for which $a_1 a_2 \geq 0$ with $a_1^2 + a_2^2 \neq 0$, and $b_1 b_2 \geq 0$ with $b_1^2 + b_2^2 \neq 0$.

3.2.2.b Properties of eigenvalues and eigenfunctions

The previously described Sturm-Liouville problem associated to the above boundary conditions has some useful properties that are summarized below.

1. The eigenvalues are real,
2. If $a_1/a_2 > 0$, $b_1/b_2 < 0$ and $q > 0$, the eigenvalues λ_n are all negative,
3. If the coefficients p and q of (3.4) are continuous and $p, \sigma > 0$ on $[L_0, L_M]$, then the successive eigenvalues λ_n (associated to the corresponding φ_n eigenfunctions) are decreasing and are such that $\lim_{n \to \infty} \lambda_n = -\infty$,
4. The eigenfunctions corresponding to distinct eigenvalues are orthogonal.

Proofs of properties 1, 2 and 4 are given in Appendix D.1. All eigenfunctions constitute an orthogonal basis of the inner product space $\mathbb{L}_2([L_0, L_M], \sigma)$. For any $f \in \mathbb{L}_2([L_0, L_M], \sigma)$, we have

$$\lim_{N\to\infty} ||f - P_N f|| = 0, \tag{3.5}$$

for which $P_N f$, defined from (3.1) and (3.2), is the orthogonal projection of f into $\Omega_N = \text{span}\{\varphi_1, ..., \varphi_N\}$, i.e. the subspace built on the N first eigenfunctions $\{\varphi_1, ..., \varphi_N\}$ of the Sturm-Liouville problem.

3.2.2.c Extension to a general formulation

Finally, the Sturm-Liouville problem (3.4) can be developed into

$$p(L)\varphi^{''}(L) + p^{'}(L)\varphi^{'}(L) - q(L)\varphi(L) = \lambda\sigma(L)\varphi(L), \tag{3.6}$$

such that any general eigenvalue problem of the form

$$\mathcal{L}(L)\varphi \equiv a(L)\varphi^{''}(L) + b(L)\varphi^{'}(L) + c(L)\varphi(L) = \lambda\varphi(L) \tag{3.7}$$

can be written as a Sturm-Liouville problem (3.4) if there exists σ, a weight function, such that

$$\left[a(L)\varphi^{''}(L) + b(L)\varphi^{'}(L) + c(L)\varphi(L)\right]\sigma(L) = \lambda\sigma(L)\varphi(L). \tag{3.8}$$

Equating (3.6) and (3.8), we have

$$a(L)\sigma(L) = p(L),$$

$$b(L)\sigma(L) = p^{'}(L).$$

Hence $(a\sigma)^{'} = b\sigma$. If $a(L) \neq 0$ on $[L_0, L_M]$, we can write

$$(a\sigma)^{'}(L) = \frac{b(L)}{a(L)}(a\sigma)(L)$$

and find the corresponding weight function σ for any $L_s \in [L_0, L_M]$ given by

$$\sigma(L) = \frac{1}{a(L)}\exp\left(\int_{L_s}^{L}\frac{b(s)}{a(s)}\mathrm{d}s\right). \tag{3.9}$$

To summarize, any general problem of the form (3.7) can be considered as a Sturm-Liouville problem with the inner product $\langle , \rangle$ associated to the σ weight function defined in (3.9).

3.2.3 Solving a diffusion problem step by step

Based on the above, we describe here a general analytical method used to solve a linear diffusion equation that involves a first partial derivative in time and a second partial derivative in space plus a linear source term in f^α with $\alpha = 1$. Let us call $\mathcal{L}$ the diffusion operator, and f the function of respectively the space and time variables (L, t) governed by a diffusion equation. The latter takes the form of

$$\mathcal{L}f = F,$$

for which F is any L-dependent function (independent of f). We assume that f obeys two inhomogeneous boundary conditions $f(L_0,t) = f_{L_0}(t)$ and $f(L_M,t) = f_{L_M}(t)$, and one initial condition such that $f(L,t=0) = f_0(L)$. We further assume that the whole diffusion operator $\mathcal{L}$ can be split into one time-component $\mathcal{L}_t$ and into one space-component $\mathcal{L}_L$ such that $\mathcal{L} = \mathcal{L}_t + \mathcal{L}_L$ (separation of variables). The time-operator involves a first-order derivative in order to fall into the category of a diffusion equation (it would be a second-order time derivative for the wave equations, out of the scope of the present work). The space-operator $\mathcal{L}_L$ involves partial derivatives of f with respect to L up to the second order.

The following describes the general formulation of the analytical resolution, and focuses particularly on two specific cases that both assume that $F(L,t) = 0$ and $f(L_0,t) = 0$. This first case involves a time-independent (static) outer boundary condition (i) and the second case is related to a time-dependent (dynamic) outer boundary condition (ii).

3.2.3.a Step 1: reduction to a homogeneous problem

The first step of the recipe is to find a w function that solves the same diffusion equation as f but with the two associated homogeneous boundary conditions $w(L_0,t) = w(L_M,t) = 0$. For this purpose, we should first find a third function v such that v satisfies the two boundary conditions imposed on f. In most case, the choice of the v function should be the simplest as possible and leading to the less amount of computation. Now, taking w as $w(L,t) = f(L,t) - v(L,t)$ yields

$$\mathcal{L}w = G(L,t),$$

with $G(L,t) = -\mathcal{L}v$. The initial condition is $w(L,t=0) = w_0(L) = f_0(L) - v(L,t=0)$, and the two boundary conditions are obviously $w(L_0,t) = w(L_M,t) = 0$.

(i) Case of a constant outer boundary condition

If we assume that $F(L,t) = 0$, and also that the inner and outer boundary conditions for f writes respectively $f(L_0,t) = 0$ and $f(L_M,t) = f_{L_M}$ (static boundary conditions), a relevant choice for the v function is $v(L,t) = f_\infty(L)$, for which $f_\infty(L)$ is the solution of the stationary problem ($\partial f/\partial t = 0$). Hence $w(L,t) = f(L,t) - f_\infty(L)$, such that the w function, referred in the following as the transient solution, is simply the deviation of the full solution from the steady solution. Then, $\mathcal{L}w = \mathcal{L}f - \mathcal{L}f_\infty = 0$, and so $G(L,t) = 0$. The initial condition for w writes therefore $w_0(L) = f_0(L) - f_\infty(L)$. This solution is developed in (*Loridan et al.*, 2017).

(ii) Case of a time-dependent outer boundary condition

We still state that $F(L,t) = 0$, but we now newly consider a time-dependent outer boundary condition such that $f(L_M,t) = h(t)f_{L_M}$, for which the h function carries the dynamical evolution of the outer boundary. We can choose the v function as $v(L,t) = h(t)f_\infty(L)$, with f_∞ being the steady solution as previously defined. In this case, the w function is such that $w(L,t) = f(L,t) - h(t)f_\infty(L)$, and $\mathcal{L}w = \mathcal{L}f - \mathcal{L}v = -f_\infty(L)\mathcal{L}_t h$, and so $G(L,t) = -f_\infty(L)\mathcal{L}_t h$. The initial condition for w writes therefore $w_0(L) = f_0(L) - h(t=0)f_\infty(L)$.

3.2.3.b Step 2: Sturm-Liouville problem

Once the whole problem in f has been restated into an homogeneous problem for w, we have to solve the Sturm-Liouville problem (or eigenvalue problem) for the N first eigenfunctions φ_n $(n = 1, .., N)$,

$$\begin{cases} \mathcal{L}_L\varphi = \lambda\varphi, \\ \varphi(L_0) = 0 \text{ and } \varphi(L_M) = 0. \end{cases} \tag{3.10}$$

The resolution of such eigenvalue problem leads to the full knowledge of the eigenfunctions φ_n and their corresponding eigenvalues λ_n (for $n \in [1, N]$).

3.2.3.c Step 3: approximating the homogeneous problem

As we have seen earlier, the subspace Ω_N built on the previously calculated eigenfunctions $\{\varphi_1(L), ..., \varphi_N(L)\}$ associated to the inner product defined by (3.3) and the weight function calculated in (3.9) is orthogonal. We now have to compute the best approximations of the initial condition w_0 and the G function onto the Ω_N subspace, i.e. their orthogonal projection on Ω_N defined in (3.1) and (3.2) (treating t as a parameter). The projection of G on Ω_N is then given by

$$P_N\, G(L,t) = \sum_{n=1}^{N} \gamma_n(t)\varphi_n(L),$$

with

$$\gamma_n(t) = \frac{\langle G(L,t), \varphi_n(L)\rangle}{\langle \varphi_n(L), \varphi_n(L)\rangle} \tag{3.11}$$

and the projection of the initial condition $w_0(L)$ is

$$P_N\, w_0(L) = \sum_{n=1}^{N} \widehat{\alpha}_n\varphi_n(L),$$

with

$$\widehat{\alpha}_n = \frac{\langle w_0(L), \varphi_n(L)\rangle}{\langle \varphi_n(L), \varphi_n(L)\rangle}. \tag{3.12}$$

The approximated functions $P_N G$ and $P_N w_0$ can be considered as the vectors in Ω_N closest to G and w_0 respectively. The homogeneous problem $\mathcal{L}w = G(L,t)$ can then be approximated by the following problem,

$$\begin{cases} \mathcal{L}w_N = P_N G, \\ w_N(L, t = 0) = P_N w_0(L). \end{cases} \tag{3.13}$$

The solution w_N of the above approximated problem belongs to Ω_N, so that the w_N function should have the form

$$w_N = \sum_{n=1}^{N} \alpha_n(t)\varphi_n(L). \tag{3.14}$$

The $\alpha_n(t)$ coefficients have still to be determined. Note that w_N can also be considered as the projection of the w function on the Ω_N subspace, i.e. $w_N(L,t) = P_N w(L,t)$.

(i) Case of a constant outer boundary condition

For a static outer boundary condition,

$$\widehat{\alpha}_n = \frac{\langle f_0(L) - f_\infty(L), \varphi_n(L)\rangle}{\langle \varphi_n(L), \varphi_n(L)\rangle},$$

and

$$\gamma_n(t) = 0.$$

(ii) Case of a time-dependent outer boundary condition

For a dynamic outer boundary condition (involving the time-dependent function $h(t)$),

$$\widehat{\alpha}_n = \frac{\langle f_0(L) - h(0) f_\infty(L), \varphi_n(L)\rangle}{\langle \varphi_n(L), \varphi_n(L)\rangle},$$

and introducing

$$\widehat{\gamma}_n = \frac{\langle f_\infty(L), \varphi_n(L)\rangle}{\langle \varphi_n(L), \varphi_n(L)\rangle},$$

we obtain

$$\gamma_n(t) = -\mathcal{L}_t h(t)\, \widehat{\gamma}_n.$$

3.2.3.d Step 4: Cauchy problem

From the approximated problem (3.5) above, $\mathcal{L} w_N = P_N G$ so that

$$\mathcal{L}\left[\sum_{n=1}^{N} \alpha_n(t)\varphi_n(L)\right] = \sum_{n=1}^{N} \gamma_n(t)\varphi_n(L).$$

Splitting the operator $\mathcal{L}$ into its temporal ($\mathcal{L}_t$) and spatial ($\mathcal{L}_L$) components leads to

$$\sum_{n=1}^{N} \left[\alpha_n(t)\mathcal{L}_L\varphi_n(L) + \varphi_n(L)\mathcal{L}_t\alpha_n(t) - \gamma_n(t)\varphi_n(L)\right] = 0.$$

Since $\mathcal{L}_L\varphi_n(L) = \lambda_n\varphi_n(L)$ we obtain

$$\sum_{n=1}^{N} \left[\lambda_n\alpha_n(t) + \mathcal{L}_t\alpha_n(t) - \gamma_n(t)\right]\varphi_n(L) = 0.$$

As the successive eigenfunctions φ_n are independent, it follows that $\alpha_n(t)$ is governed by the differential equation

$$\lambda_n\alpha_n(t) + \mathcal{L}_t\alpha_n(t) = \gamma_n(t).$$

The corresponding initial condition is extracted from $w_N(L, t=0) = P_N w_0(L)$, i.e.

$$\sum_{n=1}^{N} \alpha_n(0)\varphi_n(L) = \sum_{n=1}^{N} \widehat{\alpha}_n\varphi_n(L),$$

so that

$$\sum_{n=1}^{N} \left[\alpha_n(0) - \widehat{\alpha}_n\right] \varphi_n(L) = 0,$$

and, therefore, we obtain the full Cauchy problem for $\alpha_n(t)$

$$\begin{cases} \lambda_n \alpha_n(t) + \mathcal{L}_t \alpha_n(t) & = \gamma_n(t), \\ \alpha_n(0) & = \hat{\alpha}_n. \end{cases} \tag{3.15}$$

(i) Case of a constant outer boundary condition

For a static outer boundary condition, the Cauchy problem reduces to

$$\begin{cases} \lambda_n \alpha_n(t) + \mathcal{L}_t \alpha_n(t) & = 0, \\ \alpha_n(0) & = \hat{\alpha}_n. \end{cases} \tag{3.16}$$

(ii) Case of a time-dependent outer boundary condition

For a dynamic outer boundary condition, the Cauchy problem remains identical to the general formulation and its solution is given by (3.15) (since $\gamma_n(t) \neq 0$).

3.2.3.e Step 5: full solution

We are now able to build the transient solution w_N from (3.14). From property (3.5), the w_N function, which is the orthogonal projection on Ω_N of the transient solution w, converges to the true transient solution w when the dimension N of the Ω_N subspace tends to infinity. This means that

$$w(L,t) = \lim_{N \to \infty} w_N(L,t) = \sum_{n=1}^{\infty} \alpha_n(t) \varphi_n(L).$$

From the previous steps, the full solution writes, therefore, $f(L,t) = v(L,t) + w(L,t)$, i.e.

$$f(L,t) = v(L,t) + \sum_{n=1}^{\infty} \alpha_n(t) \varphi_n(L). \tag{3.17}$$

(i) Case of a constant outer boundary condition

For a static outer boundary condition, the full solution writes

$$f(L,t) = f_\infty(L) + \sum_{n=1}^{\infty} \alpha_n(t) \varphi_n(L)$$

as shown in (*Loridan et al.*, 2017).

(ii) Case of a time-dependent outer boundary condition

For a dynamic outer boundary condition, the full solution writes

$$f(L,t) = h(t) f_\infty(L) + \sum_{n=1}^{\infty} \alpha_n(t) \varphi_n(L).$$

3.3 The analytical solution of the radial diffusion equation

3.3.1 Framework of the study

As mentioned in the motivations, we now restrict our study to the reduced Fokker-Planck equation (2.57), that we recall here as

$$\frac{\partial f}{\partial t} = L^2 \frac{\partial}{\partial L}\left[\frac{D_{LL}}{L^2}\frac{\partial f}{\partial L}\right]_{\mu,K} - \frac{f}{\tau}. \tag{3.18}$$

In what follows, we will assume that the lifetime τ can be an arbitrary L-dependent function and that the radial diffusion coefficient is proportional to a fixed power n of L, such that $D_{LL} = D_0\, L^n$ $(n \geq 0)$. Under this assumption, the reduced Fokker-Planck equation of geomagnetically trapped particles between the outer boundary $L = L_M$ and the inner boundary $L = L_0$ becomes

$$\frac{\partial f}{\partial t} = D_0 L^n \frac{\partial^2 f}{\partial L^2} + \left[(n-2) D_0 L^{n-1}\right] \frac{\partial f}{\partial L} - \frac{f}{\tau}. \tag{3.19}$$

We will use Dirichlet boundary conditions given by $f(L_0, t) = f_{L_0} = 0$ and $f(L_M, t) = h(t) f_{L_M}$, where f_{L_0} and f_{L_M} are known constant values, independent of time, and $h(t)$ is a known time-dependent function that drives the dynamics of the outer boundary condition as emphasized previously. The invocation of the h function aims at generalizing the results obtained in (*Loridan et al.*, 2017), in which the h function is simply $h(t) \equiv 1$ for any t. We will also use a general initial condition for f given by $f(L, t = 0) = f_0(L)$, where $f_0(L)$ is a known function that is supposed to be continuous and to have continuous derivatives.

The dynamical radial diffusion equation (3.19) has been solved for static boundary conditions (i.e. when $h(t) \equiv 1$) and when the loss term τ is a constant value (e.g., *Schulz*, 1986). These results are recalled in Table 3.1 and will be used to verify that our solution remains valid in the limit of one constant lifetime. Note that even in this simplest case, the eigenvalues λ_k of the analytical solution are the zeros of a scalar function and cannot (in most cases) be expressed analytically, so that there is always a need to numerically compute the eigenvalues. Exceptions exist for $n = 2$ or $n = 4$, as discussed in the Appendices.

Nevertheless setting the electron lifetime τ to a fixed constant is a strong assumption on which we cannot rely, but it has been used in preliminary studies (e.g., *Brautigam and Albert*, 2000; *Shprits et al.*, 2005; *Tu et al.*, 2009) to quantify the effect of coupled transport and loss. The electron loss term is rather often set to be discontinuous at the plasmapause location L_{pp} (as defined by *Carpenter and Anderson* (1992) for example) and takes at least two different constant values inside and outside the plasmasphere to consider separately the effects induced by whistler mode chorus waves acting in the outer belt ($L > L_{pp}$) and the influence of whistler mode hiss waves occurring in the inner zone ($L < L_{pp}$). Therefore, considering in our study a piecewise-constant source term, split in two pieces, would be a good start to take this inhomogeneous behavior into account. This kind of approach is analogous to heat transfer problems focusing on the diffusion of temperature in two distinct materials with different conductivity. The solution is analytically tractable for such a Sturm-Liouville problem with two interfaces (e.g., *Cain and Meyer*, 2005). However, recent papers aiming at building more realistic lifetimes that strongly depend on both L-shell and energy (e.g., *Gu et al.*, 2012; *Mourenas and Ripoll*, 2012; *Orlova and Shprits*, 2014; *Orlova et al.*, 2014, 2016; *Ripoll et al.*, 2016a,

Table 3.1 – Functions, coefficients, and full solution involved when $\tau = \tau_0$ (uniform case) and $D_{LL} = D_0 L^n$, if $n \neq 2$.

$$\nu = \left|\frac{n-3}{n-2}\right|,\ p = \frac{n-2}{2},\ q = \frac{n-3}{2} \text{ and } \beta = \frac{2}{(n-2)\sqrt{\tau_0 D_0}}$$

Steady solution $f_\infty(L)$

$$f_\infty(L) = f_{L_M}\left(\frac{L_M}{L}\right)^q \left(\frac{I_\nu\left(\beta L_0^{-p}\right) K_\nu\left(\beta L^{-p}\right) - K_\nu\left(\beta L_0^{-p}\right) I_\nu\left(\beta L^{-p}\right)}{I_\nu\left(\beta L_0^{-p}\right) K_\nu\left(\beta L_M^{-p}\right) - K_\nu\left(\beta L_0^{-p}\right) I_\nu\left(\beta L_M^{-p}\right)}\right)$$

where I_ν and K_ν correspond to the modified Bessel function of order ν

Spatial and temporal components of the transient solution $w(L,t)$

From variable λ, $\Lambda(\lambda) = \frac{2}{n-2}\sqrt{\left|\frac{|\lambda| - \frac{1}{\tau_0}}{D_0}\right|}$

The eigenvalues λ_k (with integer $k \geq 1$) are the zeros of function $D(\lambda)$ with

$$D(\lambda) = J_\nu\left(\Lambda(\lambda) L_0^{-p}\right) Y_\nu\left(\Lambda(\lambda) L_M^{-p}\right) - J_\nu\left(\Lambda(\lambda) L_M^{-p}\right) Y_\nu\left(\Lambda(\lambda) L_0^{-p}\right)$$

where J_ν and Y_ν correspond to the Bessel function of order ν

$$\Lambda_k = \Lambda(\lambda_k)$$

Eigenfunctions

$$g_k(L) = L^{-q}\left[J_\nu\left(\Lambda_k L_0^{-p}\right) Y_\nu\left(\Lambda_k L^{-p}\right) - Y_\nu\left(\Lambda_k L_0^{-p}\right) J_\nu\left(\Lambda_k L^{-p}\right)\right]$$

Temporal functions

The $\alpha_k(t)$ function is defined in Table 3.2

Full solution $f(L,t) = w(L,t) + v(L,t)$

(i) Case of a constant outer boundary condition

$$f(L,t) = \sum_{k=1}^{\infty} \alpha_k(t) g_k(L) + f_\infty(L)$$

(ii) Case of a time-dependent outer boundary condition

$$f(L,t) = \sum_{k=1}^{\infty} \alpha_k(t) g_k(L) + h(t) f_\infty(L)$$

2017) motivated this study to consider a more general piecewise-continuous lifetime split to M pieces to approach such a complexity.

Bearing this in mind, let us split the closed interval $[L_0, L_M]$ into M subintervals denoted as $[L_{i-1}, L_i]$, for each integer i such that $1 \leq i \leq M$. On each subinterval $[L_{i-1}, L_i]$, we use the mathematical properties of the indicator function of a subset A

of $\mathbb{R}$, with $\mathbb{R}$ being the set of all real numbers. The indicator function of the subset $[L_{i-1}, L_i]$ of $[L_0, L_M]$ is defined by

$$\mathbb{1}_{[L_{i-1},L_i]}(L) = \begin{cases} 1 & \text{if } L \in [L_{i-1}, L_i] \\ 0 & \text{if } L \notin [L_{i-1}, L_i]. \end{cases}$$

From this definition, let us first define the function $\mathbb{1}_i(L)$ such that $\mathbb{1}_i(L) = \mathbb{1}_{[L_{i-1},L_i]}(L)$ if $i \in [2, M-1]$, $\mathbb{1}_1(L) = \mathbb{1}_{]-\infty,L_1]}(L)$ and $\mathbb{1}_M(L) = \mathbb{1}_{[L_{M-1},+\infty[}(L)$. We have set the interval limits of the function $\mathbb{1}_1(L)$ from $-\infty$ to L_1 and the interval limits of the function $\mathbb{1}_M(L)$ from L_{M-1} to $+\infty$ in order to avoid any abrupt slopes at both the boundary values L_0 and L_M (see Appendix D.2 for more details). We then define the piecewise-constant function $\tau(L)$ representing a discretization of the electron lifetime on the whole interval $[L_0, L_M]$, $\tau(L)^{-1} = \sum_{i=1}^{M} \mathbb{1}_i(L)\, \tau_i^{-1}$, where τ_i is set to be a constant electron lifetime on the subinterval $[L_{i-1}, L_i]$, for $i \in [1, M]$. Discontinuities (if any) should only occur at the intermediate interface points L_i, for $i \in [1, M-1]$. But numerical studies have shown that the fluxes derived from PSD functions solutions of (3.19) are always continuous functions with continuous derivatives even in the case of a model considering strongly discontinuous electron lifetimes without discontinuous initial injections (*Ripoll et al.*, 2016a). From this perspective, it is appropriate to look for a distribution function, f, continuous with continuous first spatial derivative on the interval $[L_0, L_M]$, i.e. $f \in C^1([L_0, L_M])$, such that f is a solution of (3.19) with the boundary and initial conditions defined above. This is due to the fact that the diffusion operator of (3.19) cannot lead to discontinuous solutions even with a discontinuous electron lifetime. This property of the solution has also been used to a lesser extent by *Thomsen et al.* (1977a,b), who worked on a steady problem with a piecewise-continuous lifetime split into 3 pieces. The continuity of the distribution function and its first spatial derivative at the two interface points gave them four interface conditions, in addition to the two boundary conditions, which enabled them to treat a well-posed stationary problem and therefore to calculate the corresponding steady distribution function.

The special form of our electron lifetimes allows us to consider a distribution function f defined on $[L_0, L_M]$ and written as $f(L,t) = \sum_{i=1}^{M} \mathbb{1}_i(L)\, f^i(L,t)$, where the function f^i is the restriction of the function f on the closed subinterval $[L_{i-1}, L_i]$. Continuity (of f and $\partial f/\partial L$) will be enforced at the interface. Instead of solving the single equation (3.19) in f involving the L-dependent lifetime τ, we solve analytically for the M equations involving f^i and a constant electron lifetime τ_i.

The continuity of f imposes the following interface condition expressed in $f^i(L,t)$ (for $i \in [1, M-1]$)

$$f^i(L_i, t) = f^{i+1}(L_i, t) \tag{3.20a}$$

and the continuity of the derivatives of f imposes at each interface

$$\frac{\partial f^i}{\partial L}(L_i, t) = \frac{\partial f^{i+1}}{\partial L}(L_i, t). \tag{3.20b}$$

The two boundary conditions for f correspond to $f^1(L_0, t) = 0$ and $f^M(L_M, t) = h(t) f_{L_M}$ and the initial condition gives $f^i(L, t=0) = f_0^i(L)$.

As we will see, the assumption for f to be continuous and having continuous derivatives is of major importance as it enables us to define a well-posed problem. As shown with details in Appendix D.2, using (3.19), the interface conditions (3.20a) and (3.20b), and the previous definitions of τ and f, it follows that each $f^i(L)$ satisfies

$$-\frac{\partial f^i}{\partial t} + D_0 L^n \frac{\partial^2 f^i}{\partial L^2} + (n-2) D_0 L^{n-1} \frac{\partial f^i}{\partial L} - \frac{f^i}{\tau_i} = 0. \tag{3.21}$$

Consequently, expressing the functions $f^i \in C^1([L_{i-1}, L_i])$ solutions of (3.21) on M subintervals leads to the knowledge of the function $f \in C^1([L_0, L_M])$ solution of (3.19).

3.3.2 The analytical expression

The complete solution of (3.19) is given by $f(L,t) = v(L,t) + w(L,t)$. The $v(L,t)$ function has to satisfy the two boundary conditions. For this purpose, we choose to write $v(L,t) = h(t)f_\infty(L)$ where $f_\infty(L)$ refers to the steady solution, and $h(t)$ is the time-dependent function imposed on the outer boundary condition. In the particular case for which the outer boundary condition does not depend in time, i.e. if $h(t) = 1$, the $v(L,t)$ function simply reduces to the steady solution $f_\infty(L)$. In this case, the $w(L,t)$ function carries all the time-dependence of the full solution and is referred as the "transient" solution, in opposition to the "steady" solution $f_\infty(L)$. We use this denomination even in the general case of a dynamic outer boundary condition. We use an eigenfunction expansion for $w(L,t)$ such that $w(L,t) = \sum_{k=1}^{\infty} \alpha_k(t) g_k(L)$ where each k-index represents the k^{th} eigenmode associated to the eigenfunction $g_k(L)$ with eigenvalue λ_k, and $\alpha_k(t)$ behaves like a decreasing temporal exponential function. Hence, we write the full solution as (using (3.17))

$$f(L,t) = v(L,t) + w(L,t) = h(t)f_\infty(L) + \sum_{k=1}^{\infty} \alpha_k(t) g_k(L). \tag{3.22}$$

The steady solution $f_\infty(L)$ and the eigenfunctions $g_k(L)$ related to the eigenvalue λ_k are defined over the M subintervals, such that $f_\infty(L) = \sum_{i=1}^{M} \mathbb{1}_i(L) f_\infty^i(L)$ and $g_k(L) = \sum_{i=1}^{M} \mathbb{1}_i(L) g_k^i(L)$. In this formulation, $f_\infty^i(L)$ is the solution of the steady problem

$$L^2 \frac{\mathrm{d}^2 f_\infty^i}{\mathrm{d}L^2} + (n-2)L \frac{\mathrm{d}f_\infty^i}{\mathrm{d}L} - \frac{1}{\tau_i D_0} L^{-(n-2)} f_\infty^i = 0 \tag{3.23}$$

and the eigenfunction $g_k^i(L)$ solves the eigenvalue problem given by (see (3.10))

$$L^2 \frac{\mathrm{d}^2 g_k^i}{\mathrm{d}L^2} + (n-2)L \frac{\mathrm{d}g_k^i}{\mathrm{d}L} - \left(\frac{\lambda_k + \frac{1}{\tau_i}}{D_0} \right) L^{-(n-2)} g_k^i = 0. \tag{3.24}$$

The latter equation is a Sturm-Liouville equation, that can be solved using the expressions of Appendix D.1.d. As mentioned before, the eigenvalues λ_k of the Sturm-Liouville problem are strictly negative, distinct, and decreasing such that $\lim_{k\to\infty} \lambda_k = -\infty$. As indicated, there is no direct notion of interface i in the definition of the eigenvalues λ_k. The value of the eigenvalue λ_k corresponding to the k^{th} eigenmode depends of course of the positions of the interfaces and the value of the electron lifetime on each interface, but it corresponds to a global parameter on the contrary to τ_i that is a local parameter in space. The eigenfunctions $g_k(L)$ corresponding to distinct eigenvalues are orthogonal in the sense that $\langle g_k, g_l \rangle = 0$ if $k \neq l$, for which the inner product $\langle , \rangle$ is defined in (3.3). The weight function $\sigma(L)$ involved in the inner product is calculated from equation (3.9), in which $a(L) = D_0 L^n$ and $b(L) = (n-2)D_0 L^{n-1}$, leading finally to $\sigma(L) = L^{-2}$. By extension the aforementioned condition of orthogonality writes

$$\langle g_k, g_l \rangle = \int_{L_0}^{L_M} g_k(L) g_l(L) L^{-2} \mathrm{d}L = 0 \text{ if } k \neq l.$$

Finally the temporal functions $\alpha_k(t)$ solve the ordinary differential equation (see (3.15))

$$\frac{\mathrm{d}\alpha_k}{\mathrm{d}t} + |\lambda_k|\,\alpha_k(t) = -\gamma_k(t). \tag{3.25}$$

The full solution is therefore

$$f(L,t) = h(t)\sum_{i=1}^{M} \mathbb{1}_i(L) f_\infty^i(L) + \sum_{k=1}^{\infty} \alpha_k(t) \left(\sum_{i=1}^{M} \mathbb{1}_i(L) g_k^i(L) \right). \tag{3.26}$$

The steps of mathematical resolution are explained in Appendix D.3 and D.4. We find a solution of the form

$$\begin{aligned} f(L,t) =& h(t)\sum_{i=1}^{M} \mathbb{1}_i(L) \left[A^i U^i(L) + B^i V^i(L) \right] \\ &+ \sum_{k=1}^{\infty} \left(\alpha_k(t) \sum_{i=1}^{M} \mathbb{1}_i(L) \left[A_k^i U_k^i(L) + B_k^i V_k^i(L) \right] \right). \end{aligned} \tag{3.27}$$

The steady part $f_\infty(L)$ of the solution is represented by the right hand side, first line of (3.27) and is defined as a combination of function $U^i(L)$ and $V^i(L)$. In the case for which $n \neq 2$, i.e. when the radial transport of particles is induced by fluctuations occurring in the Earth's electric field ($n = 6$) or magnetic field ($n = 10$), or if the radial transport is due to ionospheric dynamo fields near Jupiter or Saturn ($n = 3$), both functions $U^i(L)$ and $V^i(L)$ are expressed in terms of modified Bessel functions $I_\nu\left(\beta_i L^{-p}\right)$ and $K_\nu\left(\beta_i L^{-p}\right)$ of fractional order $\nu = |(n-3)/(n-2)|$ (see Appendix D.1.d). The U^i and V^i functions are given in Table 3.5. The argument of these modified Bessel functions is $\beta_i L^{-p}$, where β_i is a known constant defined by $\beta_i = 2(n-2)^{-1}(\tau_i D_0)^{-1/2}$, and the power p is $p = (n-2)/2$. The expressions for the A^i and B^i coefficients are given in Table 3.6 and depend on both functions $U^i(L)$ and $V^i(L)$ and their derivatives (with respect to L) $U^{i'}(L)$ and $V^{i'}(L)$ taken at the interface points. The steady solutions for the specific case $n = 2$ are given in Appendix D.5. This specific solution can be applied to the radial transport of protons due to ionospheric dynamo fields in the vicinity of Jupiter for example.

The transient part $w(L,t)$ of the solution $f(L,t)$ is the second line of the right hand side of (3.27), which is expressed as the product of a temporal function $\alpha_k(t)$ with the spatial eigenfunction $g_k^i(L)$ associated with the eigenvalue λ_k. The resolution of the Sturm-Liouville problem with interfaces has to be performed first to get both the eigenfunctions $g_k(L)$ on $[L_0, L_M]$ and their corresponding eigenvalues λ_k. The eigenvalues λ_k are then used to solve the temporal ordinary differential equation giving $\alpha_k(t)$, which solution is discussed below. If $n \neq 2$, both functions $U_k^i(L) = U^i(\lambda_k, L)$ and $V_k^i(L) = V^i(\lambda_k, L)$ are expressible by either Bessel functions $J_\nu\left(\Lambda_k^i L^{-p}\right)$ and $Y_\nu\left(\Lambda_k^i L^{-p}\right)$ or by modified Bessel functions $I_\nu\left(\Lambda_k^i L^{-p}\right)$ and $K_\nu\left(\Lambda_k^i L^{-p}\right)$ of fractional order ν, depending on the sign of $|\lambda_k| - 1/\tau_i$ (see Appendix D.1.d). This alternation between a smooth decaying function (represented by the Bessel functions J_ν and Y_ν, behaving for example like a sine function) and a fast decaying function (the modified Bessel functions I_ν and K_ν behaving more like a hyperbolic sine function) has no counterpart in the case of a constant lifetime over the entire domain $[L_0, L_M]$, as the two boundary conditions $g_k(L_0) = g_k(L_M) = 0$ impose the problem to have only oscillating eigenfunctions such as J_ν and Y_ν. The argument of the eigenfunctions g_k^i is $\Lambda_k^i L^{-p}$, where the wavelength Λ_k^i related to the subinterval

$[L_{i-1}, L_i]$ depends on the k^{th} eigenvalue λ_k such that $\Lambda_k^i = 2/(n-2)\left|(|\lambda_k| - \tau_i^{-1})/D_0\right|^{1/2}$. Note that contrary to the eigenvalues λ_k, there is a notion of interface in the definition of Λ_k^i as the lifetime τ_i is involved in its expression. Therefore, the expression of both the $U_k^i(L)$ and $V_k^i(L)$ functions, as well as both the A_k^i and B_k^i coefficients, and Λ_k^i, require the calculation of the eigenvalue λ_k. The eigenfunctions $g_k^i(L)$ are analytically defined from A_k^i, B_k^i, $U_k^i(L)$ and $V_k^i(L)$. Tables 3.5, 3.6 and 3.7 sum up all the definitions of the previous coefficients and functions to compute the transient component $w(L,t)$ of the solution including the definition of the eigenfunctions and eigenvalues. The temporal function $\alpha_k(t)$ behaves like a time-decreasing exponential function involving the coefficients $\hat{\alpha}_k$ that represent the initial condition of $\alpha_k(t)$ and the coefficients $\gamma_k(t)$ that carry the dynamical effects of the time-dependent outer boundary condition. Both coefficients $\hat{\alpha}_k$ and $\gamma_k(t)$ are calculated from (3.12) and (3.11) respectively and are given in Table 3.2. The full solution is thus expressed by (3.27) with its terms defined in Tables 3.5, 3.6, 3.7 and 3.2. The derivation of the full solution is detailed in D.3 and D.4. The full solutions for the specific case $n = 2$ are given in Appendix D.5.

Table 3.2 – Functions and coefficients involved in the ODE (3.25).

(i) Case of a constant outer boundary condition

$$\alpha_k(t) = \hat{\alpha}_k e^{-|\lambda_k|t}$$

$$\alpha_k(0) = \hat{\alpha}_k = \left(\int_{L_0}^{L_M} \left[f_0(L) - f_\infty(L)\right] g_k(L) L^{-2} dL\right) \Big/ \left(\int_{L_0}^{L_M} g_k^2(L) L^{-2} dL\right)$$

(ii) Case of a time-dependent outer boundary condition

$$\alpha_k(t) = \hat{\alpha}_k e^{-|\lambda_k|t} - \int_0^t e^{-|\lambda_k|(t-s)} \gamma_k(s)\, \mathrm{d}s$$

$$\alpha_k(0) = \hat{\alpha}_k = \left(\int_{L_0}^{L_M} \left[f_0(L) - h(0) f_\infty(L)\right] g_k(L) L^{-2} dL\right) \Big/ \left(\int_{L_0}^{L_M} g_k^2(L) L^{-2} dL\right)$$

$$\text{and} \qquad \gamma_k(t) = h'(t)\,\widehat{\gamma}_k = h'(t) \left(\int_{L_0}^{L_M} f_\infty(L) g_k(L) L^{-2} dL\right) \Big/ \left(\int_{L_0}^{L_M} g_k^2(L) L^{-2} dL\right)$$

3.4 Numerical solutions and verification of the analytical method

3.4.1 Analytical computations: method and parameters

In this section we compare the analytical solution (presented in (3.27) and Tables 3.5, 3.6, 3.7 and 3.2) with solutions (further referred as numerical solutions) obtained with a numerical code (see (*Ripoll et al.*, 2016a,b, 2017) and Chapter 4). The latter code is completely decorrelated from the analytical computations and will be discussed in 4.2.

3.4.1.a Analytical method

During the PhD, a new numerical code has been fully developed to compute the analytical solutions. This dedicated latter code, hereinafter referred as *analytical code* in opposition to the *numerical code* presented in Chapter 4, consists of two steps.

The first step is devoted to the calculation of the eigenvalues on a specified finite domain in λ. To properly perform the analytical solution, the successive eigenvalues λ_k are calculated by finding numerically all the zeros of the $D(\lambda)$ function as defined in Table 3.7 on the selected interval in λ. For this purpose, a Newton-Raphson method and a secant method, both applied to $D(\lambda) = 0$, have been numerically developed. They have proven to be in agreement with each other as they both give the same eigenvalues λ_k on the considered interval. One numerical difficulty was not to miss any zero λ_k of the $D(\lambda)$ function. To avoid such a problem, we checked that for each eigenmode, the number of space-oscillations of the corresponding eigenfunction $g_k(L)$ is in accordance with the number k of eigenvalue λ_k. Hence, in order to catch all the oscillations of the eigenfunction $g_k(L)$ up to a high number of eigenmodes (e.g. 1000), we first use an excessively resolved geometric L grid with 50000 L bins, uniformly distributed in logarithm space. It rapidly appears that our ability to properly separate one eigenmode to the other is only challenged for the very first eigenmodes (i.e. the smallest in absolute value). As a matter of fact, the determinant function presented in Figure 3.2 shows that the first eigenmodes are likely to be very close to each other, but the gap in λ between both modes widens as we move on to the higher modes. Hence, if the numerical Newton-Raphson method is accurate enough to discriminate the very first eigenmodes from their next counterparts, it will also be able to select all the eigenmodes without forgetting any of them. Once this verification has been made, we simply perform the analytical solution with a uniform geometric grid in L made of 1000 bins (as it is the case for the numerical Crank-Nicholson scheme presented in Chapter 4). In practice, this first calculation step has been parallelized over 1 node of 28 cores, for which one given core takes care of the eigenvalues related to one given chosen interval in λ. Since the distance between two eigenmodes increases with λ, the length of the intervals can be larger as we increase their first lower bound in λ.

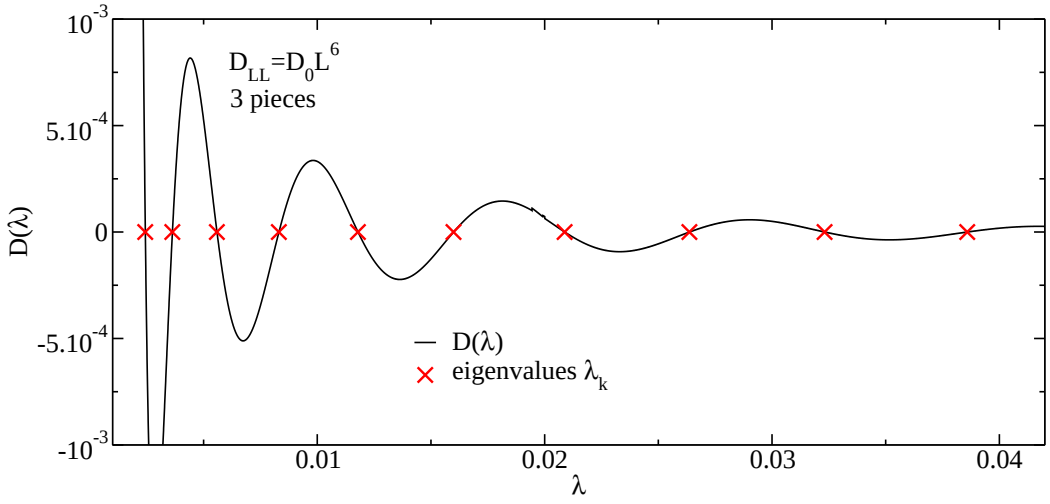

Figure 3.2 – Determinant function $D(\lambda)$ vs λ for which the interval $[L_0, L_M]$ has been split into 3 pieces. Each zero of the function corresponds to a successive eigenvalue λ_k (for $k \in [1, 10]$ in this figure) of the Sturm-Liouville problem (3.24).

Once all the eigenvalues over a reasonable range of λ have been calculated and stored, a second numerical step is started. It consists in computing the global solution $f(L, t)$

as the sum of the successive products between the $g_k(L)$ eigenfunctions and the $\alpha_k(t)$ temporal functions. The knowledge of the latter requires a prior numerical integration to account for the orthogonal projections involved in the $\hat{\alpha}_k$ and $\hat{\gamma}_k$ coefficients (see Table 3.2).

The computing time required to calculate one converged solution, starting from its pseudo steady state up to $t = 1$ day (including the computation of about 1000 eigenmodes, as emphasized in the next section), is about one hour.

3.4.1.b Parameters in use

In what follows, we consider a radial diffusion coefficient proportional to L^6 (e.g., *Schulz and Lanzerotti*, 1974; *Brautigam and Albert*, 2000; *Ukhorskiy and Sitnov*, 2008; *Ozeke et al.*, 2014; *Liu et al.*, 2016). For this specific case $n = 6$, we set $D_0 = 7.7 \times 10^{-6}$ s^{-1}, according to the value from *Ukhorskiy and Sitnov* (2008).

3.4.2 Accordance of the analytical solution with the numerical solution

To check the validity of our solutions, we compare the PSD given by its analytical expression (3.27) with the PSD computed from the numerical code detailed in Chapter 4 based on a Crank-Nicholson finite-difference scheme (with 1000 nodes equally spaced) intended to solve (3.19). We consider two different cases. The first case involves a static outer boundary condition ($h(t) \equiv 1$) and is further referred as *radial diffusion following a massive constant injection*. The second case involves a dynamic outer boundary condition and is referred as either increasing (*gradual injection*) or decreasing (*gradual dropout*) in time.

3.4.2.a Radial diffusion following a massive injection

Each set of figures presented here is related to a massive regular constant injection at the outer boundary, represented by a time-independent (constant) outer boundary condition $f(L_M, t) = f_{L_M}$, with $L_M = 5.5$ (here $h(t) \equiv 1$, case (i)). The constant value f_{L_M} is set to $f_{L_M} = 1.2 \times 10^{-4}$ $(c/MeV/cm)^3$, which is a typical PSD value at $L = 5.5$ during quiet times (corresponding for instance to 1 MeV electrons injected at $L = 5.5$ as taken in *Ripoll et al.* (2016a)), coming from the value of the energy-dependent flux at $L = 5.5$ and $E = 1$ MeV used in *Lyons and Thorne* (1973). The PSD is chosen to be expressed in $(c/MeV/cm)^3$ as it is common PSD units in magnetospheric physics (e.g., *Ni et al.*, 2009; *Tu et al.*, 2009, 2013; *Boyd et al.*, 2014). In this specific case, $h(t) = 1$, and the particular solution $v(L, t)$ reduces to the steady solution $f_\infty(L)$. The temporal functions are then simply given by $\alpha_k(t) = \hat{\alpha}_k e^{-|\lambda_k|t}$ (because $\gamma_k(t) = 0$). The initial condition is taken to be $f(L, t = 0) = 0$ so that we start from empty radiation belts. Such feature has been observed by *Baker et al.* (2014a), who highlighted a remarkable example of gradual inward radial diffusive transport of ultrarelativistic electrons from March 1st to 17th 2013, after the depletion of the radiation belts by the March 1st storm.

Results for which the lifetime τ is set to a constant τ_0 over the entire interval $[L_0, L_M]$ are presented in Figure 3.3 and Table 3.1. The analytical solutions (circle lines) fit perfectly well the numerical results (plain line), either for $\tau = 100$ days (left) or $\tau = 10$ days (right), with $D_0 = 7.7 \times 10^{-6}$ s^{-1}. The case $\tau_0 = 100$ days corresponds to the radial diffusion limit, i.e. for which losses are negligible in equation (3.19). The latter case is used to verify the method against formerly derived expressions (e.g., *Schulz*, 1986; *Schulz and Newman*, 1988) (see Table 3.1) as well as testing our piecewise method on the simplest case of one piece.

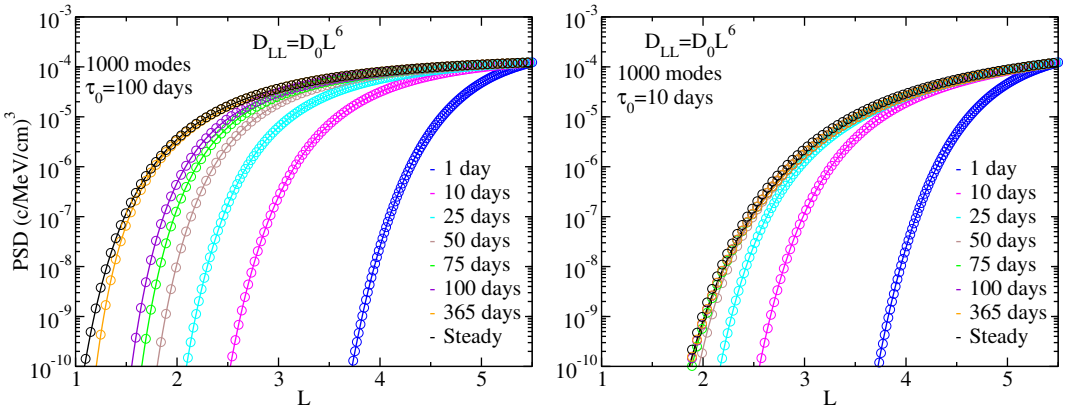

Figure 3.3 – Evolution of the PSD (in $(c/MeV/cm)^3$) vs L-shell for several times from one day to one year. Plain lines represent numerical results whereas circles represent analytical results (see Table 3.1). The electron lifetime τ_0 is set constant to 100 days (left) and 10 days (right) over the whole domain. The analytical computation of the transient function $w(L,t)$ stops at $N = 1000$ eigenmodes. There is a perfect correlation between the analytical and the numerical results.

Figure 3.3 emphasizes the role of the electron lifetime in the shape of the electron distribution in term of L-shells. A large electron lifetime (such as 100 days) corresponds to no pitch angle scattering from gyro-resonant interactions with VLF waves. In this case, electrons simply diffuse radially inward without being affected by VLF waves (Figure 3.3, left). If the electron lifetime is lower (i.e. 10 days), pitch angle scattering is no more negligible. By diffusing radially inward, particles are also likely to be brought to their bounce loss cone by gyro-resonant interactions with VLF waves and are consequently lost in the atmosphere before reaching the inner belt (Figure 3.3, right).

In Figure 3.4 we represent both analytical and numerical PSD solving (3.19) with a piecewise-constant electron lifetime, splitting regularly the interval $[L_0, L_M]$ into $M = 3$ parts (top-left) and $M = 10$ parts (top-right), for $D_{LL} \sim L^6$. Numerical solutions are plotted in plain lines whereas analytical solutions are presented in circle lines. The number of modes used for the analytical simulations is deliberately set to a very large number to ensure convergence. We choose $N = 1000$ eigenmodes (that point is discussed in the next section). We observe an excellent agreement between the analytical and the numerical solutions. Focusing on the 3-subinterval case, we clearly see 3 inflection points corresponding to the 3 interfaces of the electron lifetime, emphasizing that analytical and numerical PSD are indeed continuous with continuous derivatives in space and with discontinuous second derivative in space at the interface, which results to a change of convexity at the interface points. These plots fully justify the assumptions of continuity for both the distribution function (3.20a) and its first spatial derivative (3.20b). As such, it is important to note that the diffusion process described by (3.18) is a continuous process giving rise to a continuity in the PSD in spite of discontinuous electron lifetimes. Both Figures 3.3 and 3.4 prove that the proposed analytical solution is correct. As a matter of fact, the analytical expression of the full solution is non trivial and iterative. Therefore the numerical proof of the correctness of the solution was mandatory. Comparisons between analytical and numerical solutions also show the excellent accuracy of the second order (in space) Crank-Nicholson scheme (used here with 1000 points) which is commonly used in the literature (e.g., *Brautigam and Albert*, 2000; *Tu et al.*, 2009,

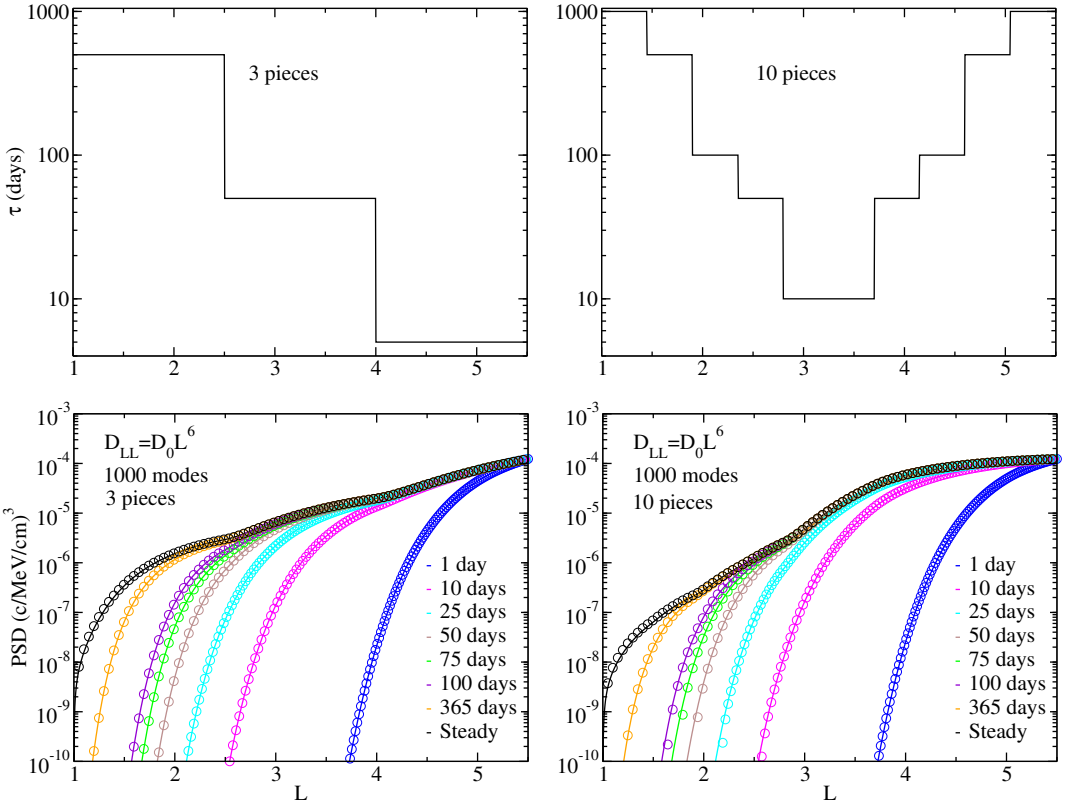

Figure 3.4 – Evolution of the PSD (in $(c/MeV/cm)^3$) vs L-shell for several given times, from one day to one year. Plain lines represent numerical results whereas circles represent analytical results (see (3.27) and Table 3.6, 3.7 and 3.2). The interval $[L_0, L_M]$ has been split into 3 pieces (left) and 10 pieces (right). The two top figures represent the piecewise-constant lifetime (in days) in use. The analytical results match well the numerical results. The discontinuities of the lifetime break the continuity of the second-order derivative in space of f and so impact the convexity of the distribution function. The latter remains continuous with continuous first-order derivative in space.

2013; *Ripoll et al.*, 2016a,b, 2017) as well as in Chapters 4, 5 and 6.

3.4.2.b Radial diffusion following a time-varying gradual injection or a gradual dropout

We generalize the previous result from the study in (*Loridan et al.*, 2017) by simulating either the inward radial diffusion after a gradual injection at the outer boundary condition or an outward radial diffusion following a gradual dropout. For both cases (corresponding to case (ii)) the outer boundary condition is now time-dependent contrary to the previous case (massive regular injection). As emphasized above, the "gradual" steady function $v(L,t)$ is $v(L,t) = h(t)f_\infty(L)$.

For the gradual dropout event, we set the initial condition as $f_0(L) = v(L,0) = h(t=0)f_\infty(L)$ and the outer boundary condition as $f(L_M,t) = v(L_M,t) = h(t)f_{L_M}$, with $h(t) = e^{-0.2t}$. For the gradual injection event, we set the initial condition as $f_0(L) = v(L,0) = h(t=0)f_\infty(L)$. The outer boundary condition is set to $f(L_M,t) = v(L_M,t) = h(t)f_{L_M}$, with $h(t) = \varepsilon e^{+0.2t}$, for which $\epsilon \ll 1$. The results obtained from both computations are presented in Figure 3.5 (left) for the gradual dropout and (right) for

the gradual injection. Figure 3.5 shows the accuracy of the analytical method compared to the numerical solutions. This verifies the correctness of terms in Tables 3.2, 3.5, 3.6, 3.7 and 3.2.

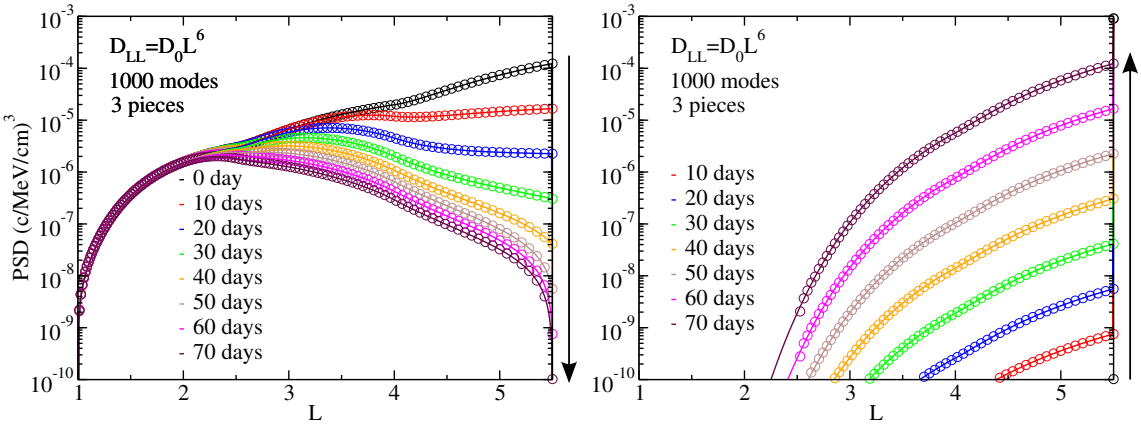

Figure 3.5 – Evolution of the PSD (in $(c/MeV/cm)^3$) vs L-shell for several given times, from 0 day to 80 days. As before, plain lines represent numerical results whereas circles represent analytical results. The interval $[L_0, L_M]$ has been split into 3 pieces. The panel on the left represents the evolution of the PSD following a gradual dropout, and the panel on the right represents the PSD inferred from a gradual injection.

The remaining discussion in this chapter only focuses on a time-independent outer boundary condition ($h(t) \equiv 1$) based on the previous massive-regular injection event.

3.4.3 Modeling any nonuniform lifetimes

With the analytical expressions given by (3.27) and Tables 3.5, 3.6, 3.7 and 3.2, we wish to put forward that we are able to calculate the PSD solving the radial diffusion equation for any given L-dependent lifetime, provided that we split the piecewise-constant lifetime τ over a sufficient number of subintervals. To confirm that this goal can be reached, we solve (3.19) for the particular case for which $\tau(L) = \tau_0 L^\xi$ for any real ξ. Steady analytical solutions have already been presented by *Haerendel* (1968) or *Schulz* (1986) for example. As far as we know, there exist no general procedure to calculate directly the time-dependent transient solution associated to the steady solutions presented in the aforementioned works. But for the specific power such that $\xi = 2 - n$ we are able to derive here analytically the full dynamical solution as given in Table 3.3. Here we choose the highly decreasing lifetime $\tau = \tau_0 L^{-4}$ corresponding to $n = 6$ for example. In Figure 3.6, we plot both numerical (plain lines) and analytical (circle lines) solutions for $D_{LL} = D_0 L^6$, and $\tau(L) = \tau_0 L^{-4}$ with $\tau_0 = 1000$ days (left), and the solutions (again, both numerical and analytical) given from a piecewise-constant lifetime τ divided into 25 pieces and built to match the values of $\tau_0 L^{-4}$ on each subinterval $[L_{i-1}, L_i]$, $\tau_i = \tau_0 L_i^{-4}$ for $i \in [1, M]$ (right). The agreement between the analytical and numerical solutions is again very good on both plots of Figure 3.6. Now comparing the plot on the left with the plot on the right, we observe that the solution taken from the discontinuous electron lifetime model (over 25 pieces) represents well the shape and the dynamics of the solution produced from the continuous loss term. There is, however, a peculiar difference occurring at $L < 1.7$ between the PSD obtained by the smooth lifetime $\tau(L) = \tau_0 L^{-4}$ on the right and the corresponding piecewise-constant lifetime on the left. The steady

solution obtained from the continuous lifetime (black curve on the bottom-left plot of Figure 3.6) is such that $f_\infty(L = 1.3) = 10^{-10}$ (c/MeV/cm)^3 whereas the steady solution obtained from the piecewise resolution (black curve on the bottom-right plot of Figure 3.6) reaches lower values, i.e. $f_\infty(L = 1.5) = 10^{-10}$ (c/MeV/cm)^3. As a matter of fact, the smooth lifetime plotted on the entire interval reaches higher values at small L than its piecewise-constant counterpart, which enables the PSD computed with the smooth lifetime to reach lower L-values. Otherwise the solutions generated with these two similar lifetimes look overall the same. Again, the correctness of the present method is numerically proven. Nothing would prevent us from matching an electron lifetime evolving as L^ξ, but now for any ξ power, with a piecewise-constant function over several subintervals, and then generalizing the historical works accomplished by *Haerendel* (1968) or *Baker and Goertz* (1976) (particularly the results presented in their Figure 4) by analytically performing the full dynamics, which goes beyond the scope of their calculated steady solutions. This comparison also illustrates that one can easily fit any L-dependent electron lifetime taken from the recent literature (e.g., *Gu et al.*, 2012; *Orlova et al.*, 2014; *Orlova and Shprits*, 2014; *Orlova et al.*, 2016) by a piecewise-constant function over 25 subintervals or more, and then exhibit analytically the full dynamics of such a complex solution with mathematical insight and understanding.

3.5 Convergence of the analytical solutions

During our numerical tests, we noticed that a large number of eigenmodes was often necessary to obtain convergent solutions at small times (10 days or below). As mentioned above, 500 modes were necessary to plot a solution at $t_0 = 1$ day for $D_{LL} \sim L^6$. This was also mentioned by *Schulz and Newman* (1988) but to a lesser extent. We also realized from our computations that the necessary number of modes at which the analytical solution converges to the numerical one increases with a decreasing snapshot time t_0, which is in agreement with *Schulz and Newman* (1988). The objective of the next subsection is to express analytically a characteristic decay time for the asymptotic modes. We also wish to simply but correctly put forward a criteria giving the necessary number of eigenmodes to compute an accurate solution at a given time t_0.

3.5.1 Estimation of the decaying timescale associated to one mode

The Sturm-Liouville problem characterizing the eigenvalue problem assures that the eigenvalues λ_k are all negatives (see Appendix D.1). Hence, the temporal functions $\alpha_k(t)$ solutions of the ordinary differential equation are expressed as $\alpha_k(t) = \alpha_k(0)e^{-|\lambda_k|t}$. We define

$$\tau_k^{\text{decay}} = 1/|\lambda_k| \tag{3.28}$$

as the characteristic decaying time associated with the k^{th} eigenmode, such that $\alpha_k(t) = \alpha_k(0)e^{-t/\tau_k^{\text{decay}}}$. From the relation associating Λ_k^i to λ_k we have, for $n \neq 2$, $\Lambda_k^i = 2/(n-2)\left|(1/\tau_k^{\text{decay}} - 1/\tau_i)/D_0\right|^{1/2}$. If we consider the case of a large number of eigenmodes N such that $|\lambda_N| \gg 1/\tau_i$, i.e. when $\tau_N^{\text{decay}} \ll \tau_i$, we have $\Lambda_N^i = 2/(n-2)/\sqrt{D_0\tau_N^{\text{decay}}}$. Expressions for Λ_N^i are tractable in the asymptotic limit when the number of modes is very large ($N \gg 1$). We indeed found for simple cases (from the expression of $D(\lambda)$ with $M = 1$, $M = 2$, or $M = 3$ pieces) that the wavelength Λ_N^i can be written in its asymptotic form as

$$\Lambda_N^i \sim \Lambda_N \sim N\pi\ (L_0 L_M)^p\ /\ \left(L_M^p - L_0^p\right) \tag{3.29}$$

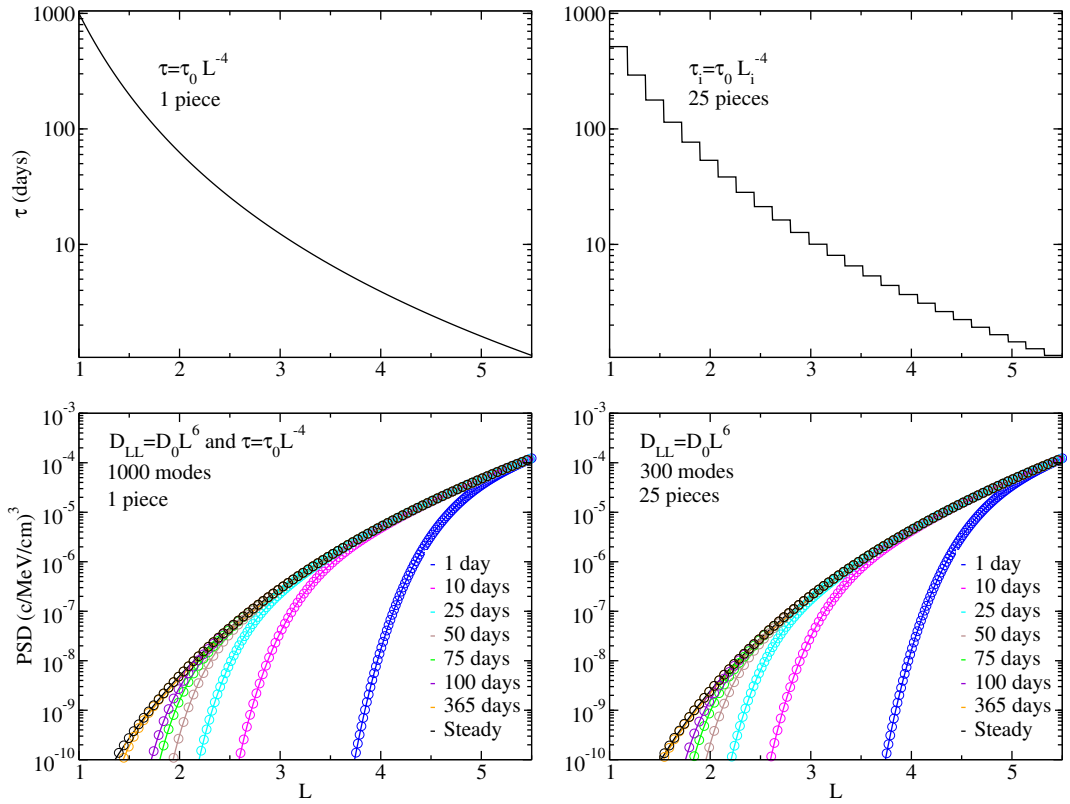

Figure 3.6 – Evolution of the PSD (in $(\mathrm{c/MeV/cm})^3$) vs L-shell for several times, from one day to one year. Plain lines represent numerical results whereas circles represent analytical results. The solution is plotted for $\tau = \tau_0 L^{-4}$ (top-left) over the entire interval $[L_0, L_M]$ (bottom-left). On the right the solution is computed for a piecewise-constant τ (with 25 pieces) matching the values of $\tau_0 L^{-4}$ (top). Differences between the distribution functions from the continuous lifetime (left) and the discontinuous one (right) are the most visible for the smallest values of L, where the solution is almost steady. This result highlights the capability to model any given nonuniform lifetime, providing that the discontinuous lifetime used in the analytical resolution is defined on a sufficient number of subintervals and correctly fits the physical nonuniform lifetime of interest.

with $p = (n-2)/2$ (*Abramowitz and Stegun*, 1964), which does not depend on the subinterval i or the number M of subintervals anymore. Supposing this result can be generalized for all integer $M \geq 1$, we equate the two last expressions for Λ_N^i to obtain

$$\tau_N^{\mathrm{decay}} \sim \frac{1}{D_0}\frac{1}{N^2\pi^2}\left(\frac{2}{n-2}\right)^2 \frac{\left(L_M^p - L_0^p\right)^2}{\left(L_0 L_M\right)^{2p}}. \tag{3.30}$$

A similar expression for $n = 2$ is written is Appendix D.5. From (3.30), the characteristic decaying time τ_N^{decay} associated with the N^{th} mode decreases as the power n of the diffusion coefficient increases, i.e. the time of evolution is reduced if the diffusion process goes stronger.

A characteristic decay time is often extracted from satellite data at various L-shell locations, trying to associate it to a single process, for instance a pitch angle diffusion, or multiple processes (e.g., *Meredith et al.*, 2006a,b; *Baker et al.*, 2007; *Borovsky and Denton*, 2009; *Fennell et al.*, 2013; *Ni et al.*, 2015; *Ripoll et al.*, 2016a). Here, it varies

Table 3.3 – Functions, coefficients, and full analytical solution involved when $\tau = \tau_0 L^{2-n}$ and $D_{LL} = D_0 L^n$, with $n \neq 2$. If $n = 2$, one can refer to Table 2.

$$\eta = \frac{1}{n-2}\sqrt{q^2 + \frac{1}{\tau_0 D_0}},\ p = \frac{n-2}{2},\ q = \frac{n-3}{2} \text{ and } r = \sqrt{q^2 + \frac{1}{\tau_0 D_0}}$$

Steady solution $f_\infty(L)$

$$f_\infty(L) = f_{L_M}\left(\frac{L_M}{L}\right)^{\frac{n-3}{2}+r}\left(\frac{L^{2r} - L_0^{2r}}{L_M^{2r} - L_0^{2r}}\right)$$

Spatial and temporal components of the transient solution $w(L,t)$

From variable λ, $\Lambda(\lambda) = \dfrac{2}{n-2}\sqrt{\dfrac{|\lambda|}{D_0}}$

The eigenvalues λ_k (with integer $k \geq 1$) are the zeros of function $D(\lambda)$ with

$$D(\lambda) = J_\eta\left(\Lambda(\lambda)L_0^{-p}\right)Y_\eta\left(\Lambda(\lambda)L_M^{-p}\right) - J_\eta\left(\Lambda(\lambda)L_M^{-p}\right)Y_\eta\left(\Lambda(\lambda)L_0^{-p}\right)$$

where J_ν and Y_ν correspond to the Bessel function of order ν

$$\Lambda_k = \Lambda(\lambda_k)$$

Eigenfunctions

$$g_k(L) = L^{-q}\left[J_\eta\left(\Lambda_k L_0^{-p}\right)Y_\eta\left(\Lambda_k L^{-p}\right) - Y_\eta\left(\Lambda_k L_0^{-p}\right)J_\eta\left(\Lambda_k L^{-p}\right)\right]$$

Temporal functions

$\alpha_k(t) = \hat{\alpha}_k e^{-|\lambda_k|t}$ where $\hat{\alpha}_k$ is defined in Table 3.2

Full solution $f(L,t) = w(L,t) + f_\infty(L)$

$$f(L,t) = \sum_{k=1}^{\infty}\alpha_k(t)g_k(L) + f_\infty(L)$$

asymptotically with $1/N^2$. We plot both τ_N^{decay} given by its general expression from (3.28) and its asymptotic form taken from (3.30) on Figure 3.7. Our expression can then help to better understand the theoretical meaning of decay times. But one does not want to confuse the characteristic decaying time associated with the k^{th} eigenmode, τ_k^{decay}, of radial diffusion with the electron lifetime τ_i occurring on subinterval i and associated to the electron loss only. The evolution of $\tau_k^{\text{decay}} = 1/|\lambda_k|$ and its asymptotic limit given by (3.30) as a function of the number of eigenmmodes k are shown in Figure 3.7. We clearly see that τ_k^{decay} converges to its asymptotic limit when $k \sim 50$ modes for $D_{LL} \sim L^6$, which proves the assumptions made in (3.29) on the form of the asymptotic limit of Λ_k^i for the general case.

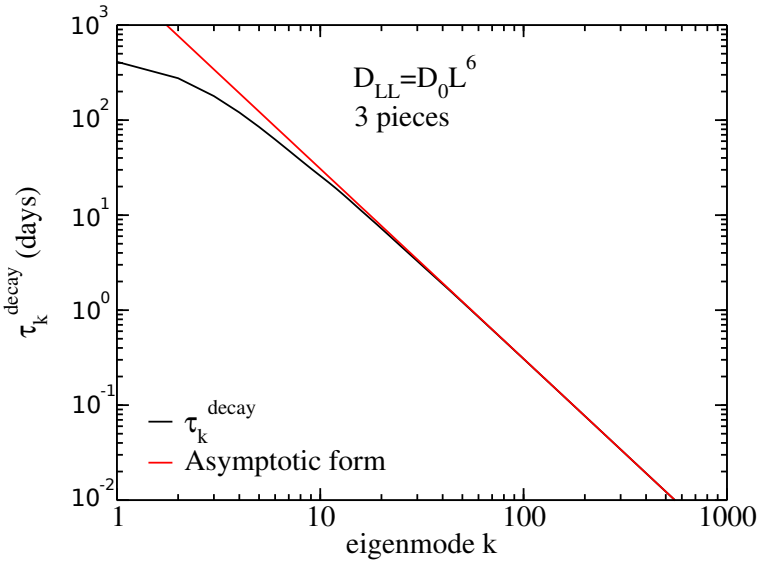

Figure 3.7 – Evolution of the characteristic decaying time τ_k^{decay} (black curve), in days, vs the number of eigenmodes k for $D_{LL} \sim L^6$, for the case of Figure 3.4 (left). As expected, the characteristic time decreases as the number of eigenmodes increases. The red curve represents the asymptotic form of the characteristic time given by (3.30). The evolution follows a power law in k^{-2} as shown in (3.30). The asymptotic limit is reached for $k \sim 50$ eigenmodes. One does not want to confuse the number of modes to reach the asymptotic limit and the number of modes to reach convergence. Convergence is generally reached at a much higher number of modes than the asymptotic limit.

3.5.2 A time-based criteria for the required mode number

In order to get an accurate analytical solution truncated at the N^{th} mode (i.e. with a sufficient number of modes, and such that $|\lambda_k| \gg 1/\tau_i$), we consider that the characteristic decaying time of the last N^{th} mode should be of the same order of magnitude as the fixed time t_0 at which we want to take a snapshot of the PSD f. This condition can be written as $\tau_N^{\text{decay}} \sim t_0$. From (3.30), we find that the required number of modes N_{t_0} at $t = t_0$ is

$$N_{t_0} \sim \left[\frac{2}{\pi(n-2)}\right]\left[\frac{L_M^p - L_0^p}{(L_0 L_M)^p}\right]\frac{1}{\sqrt{D_0 t_0}}. \tag{3.31}$$

The number of non-negligible terms to compute thus varies theoretically with the inverse of $\sqrt{D_0 t_0}$. Therefore, with small D_0 and t_0, N_{t_0} has to be large. For the case $n = 6$ et $D_0 = 7.7 \times 10^{-6}$, the number of required modes computed from (3.31) is $N_{t_0} \sim 55$ modes for $t_0 = 1$ day. *Schulz and Newman* (1988) have derived a similar expression of (3.31) (equation 31 in *Schulz and Newman* (1988)) from the relation $\tau_N^{\text{decay}} \leq t_0/5$. Their expression holds for intermediate values of the eigenmode number k ($k \leq 19$) and relies on the fact that $(L_0/L_1)^p \ll 1$, which is valid when p is large (which occurs when $n = 6$).

3.5.3 A space-based criteria for the required mode number

The criteria of convergence (3.31) previously derived relies on temporal considerations only and takes no account of the L-shell values. This has been made possible because both variables L and t are separated. This principle also indicates that one can

investigate further to highlight a space-based criteria for convergence. To understand it, we represent in Figure 3.8 some eigenfunctions corresponding to the case $D_{LL} \sim L^6$ for an electron lifetime split into 3 pieces. We notice that the eigenfunctions' oscillations spread easily over the entire interval $[L_0, L_M]$, from $L = L_0$ to $L = L_M$. For a given eigenmode number k, the corresponding eigenfunction is thus more likely to be flat in the outer domain, where L is close to $L_M = 5.5$, than in the inner domain for which L is close to $L_0 = 1.0$. If one does not calculate a sufficient number of eigenmodes, the summation of the eigenfunctions over the number of modes does not contribute to reach a convergent solution in the outer domain. Since the eigenfunctions $g_k(L)$ exhibit more and more oscillations over the outer domain as k increases, the last eigenfunction must have enough oscillations (i.e. enough zeros) to compensate the contribution of the lower modes eigenfunctions. For example in Figure 3.8, one has to push the superposition of the eigenfunctions up to 30 modes to obtain one oscillation over the outer domain $[3.5, 5.5]$. Let us link this observation to a second criteria for the convergence of the solutions. In its asymptotic limit, the $g_N(L)$ eigenfunction is written as

$$g_N(L) \sim L^{-(n-4)/4} \sin\left[\Lambda_N \left(L_0^{-p} - L^{-p}\right)\right],$$

with $\Lambda_N \sim N\pi \left(L_0 L_M\right)^p / \left(L_M^p - L_0^p\right)$ as before. The m^{th} zero $z_{N,m}$ of the $g_N(L)$ eigenfunction is such that $g_N(z_{N,m}) = 0 \Rightarrow \sin\left[\Lambda_N \left(L_0^{-p} - z_{N,m}^{-p}\right)\right] = 0$, leading to $z_{N,m} = \left(L_0^{-p} - m\pi/\Lambda_N\right)^{-1/p}$. We assume that the last eigenmode N corresponds to the $g_N(L)$ eigenfunction having at least N_z zeros belonging to $[L_A, L_B]$, where L_A and L_B are two given L-shells values taken from $[L_0, L_M]$ and such that $L_A < L_B$. Hence the m^{th} zero $z_{N,m}$ and the $(m+N_z)^{\text{th}}$ zero z_{m+N_z} of the last calculated eigenfunction $g_N(L)$ are included in subinterval $[L_A, L_B]$, giving the set of inequalities

$$\begin{cases} z_{N,m} & > L_A \\ z_{N,m+N_z} & < L_B. \end{cases}$$

We take the most restricting condition where the equality holds on both rows of the above system, which becomes a system of two equations with two unknowns N and m. Taking the asymptotic expression for Λ_N and solving for N we obtain

$$N_{[L_A,L_B]} \sim N_z \left[\frac{L_M^p - L_0^p}{(L_0 L_M)^p}\right] \left[\frac{(L_A L_B)^p}{L_B^p - L_A^p}\right]. \tag{3.32}$$

In practice, we choose the value L_B such that L_B=L_M and we will use the general space variable L to identify L_A. Hence we have $N_L \sim N_z \left[\left(L_M^p - L_0^p\right) / \left(L_M^p - L^p\right)\right] \left[L^p / L_0^p\right]$. Imposing the last eigenfunction $g_N(L)$ to have for example $N_z = 10$ zeros over the subinterval $[4.0, 5.5]$ leads to the computation of $N_{[4.0,5.5]} \sim 328$ eigenmodes for $D_{LL} \sim L^6$. These values for the space-based criteria are higher but still consistent with the one taken from the time-based criteria for the required number of modes.

3.5.4 Numerical convergence

Figure 3.9 shows the solution computed from $D_{LL} = D_0 L^6$ at $t_0 = 10$ days (left) and $t_0 = 1$ day (right) for different numbers of eigenmodes. The convergence of the analytical solution (circles) towards the numerical solution (black plain line) is reached for $N \sim 200$ modes for $t_0 = 1$ day and $N \sim 100$ modes for $t_0 = 10$ days (which is slightly higher than an evaluation of (3.31) and lower than (3.32)). In particular, the

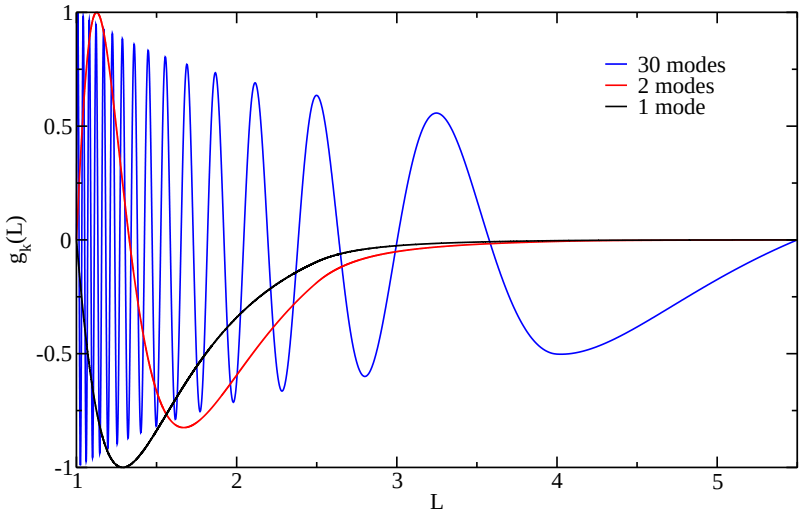

Figure 3.8 – Evolution of the eigenfunctions $g_k(L)$ vs L for 1, 2 and 30 eigenmodes. The electron lifetime τ used in this plot is the 3 pieces piecewise-constant function shown in Figure 3.4 (left). As the number of modes increases, the oscillations spread progressively from $L_0 = 1.0$ to $L_M = 5.5$. Solutions at small times differ strongly from the steady solution, even at L close to L_M. To capture their behavior, many eigenmodes are thus required to add the eigenfunctions' oscillations for L close to L_M and make the solution deviate substantially from the steady solution.

analytical solution approaches the numerical solution by moving back and forth around the numerical solution as the number of modes increases. More explicitly we see in Figure 3.9 (left) that the solution truncated at $N = 31$ modes overestimates the numerical solution and drops brutally at $L \approx 3.7$, while the solution obtained with $N = 51$ modes approaches the numerical solution but underestimating it this time, dropping before at $L = 4$. Abrupt drops of the analytical PSD is found to be an indicator of a too low number of computed modes. This back and forth motion of the analytical solution around the converged solution is due to the sign of the eigenfunctions which changes according to the eigenmode k, as shown in Figure 3.8. The larger the k^{th} mode is and the more oscillating the eigenfunctions are.

The analytical solution is built from the steady state (infinite time) to which modal components are subtracted back to access to the solution at a given time. A low number of modes gives access to large times, for which the solution is close to the steady solution. On the contrary, for small times, a large number of contributing modes has to be subtracted to the steady solution to build the full solution. Solutions at small times require therefore more effort than at large times. The approach is reversed with any explicit numerical schemes since they advance in time iteratively starting from $t = 0$ and moving towards the steady state. Numerical solutions at large times require more effort than at small times. In terms of error, numerical schemes propagate and increase the error with time, while analytically the opposite occurs as the error increases as the lack of modes becomes important, i.e. at small times.

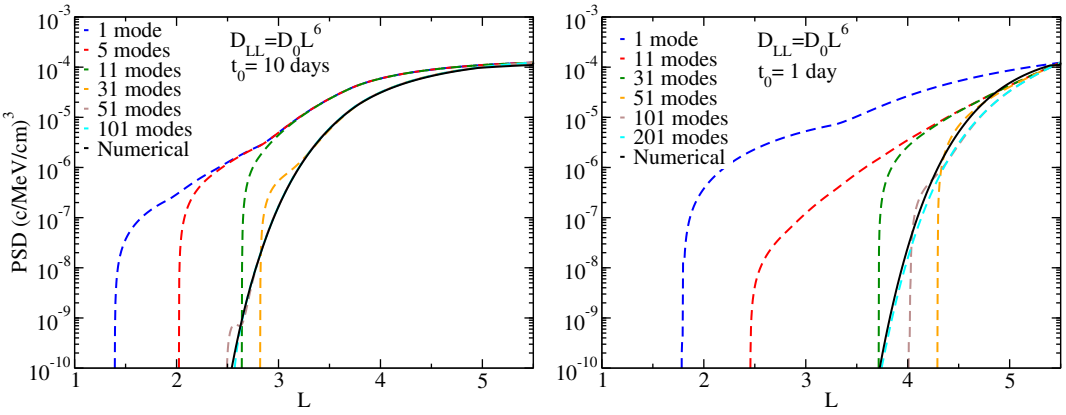

Figure 3.9 – Evolution of the analytical PSD (dashed lines, in $(c/MeV/cm)^3$) vs L-shell at $t_0 = 1$ day (left) and $t_0 = 10$ days (right), for several number of eigenmodes, for the case of Figure 3.4 (right). Plain lines represent the numerical solution to which the analytical solution should converge if there were enough eigenmodes. As shown, convergence is reached faster as the snapshot time t_0 is longer.

3.5.5 Evolution of the number of eigenmodes with the diffusion power

Focusing on the space-based convergence criteria exhibited above by (3.32), we have for a strong diffusion (i.e. for $p = (n-2)/2$ large), $N_L \sim N_z(L/L_0)^p$. Hence, for the same number of oscillations of the eigenfunctions between a given L and L_M, one would need a higher number of eigenmodes for a higher power n of the diffusion coefficient. In other words, if the diffusion transport goes stronger, the required number of eigenmodes to reach a convergent solution increases. To illustrate this phenomenon, let us impose (as before) $N_z = 10$ oscillations for the last eigenfunction $g_N(L)$ between $L = 4.0$ and $L_M = 5.5$. We then find that $N_{[4.0,5.5]} \sim 54$ eigenmodes for $D_{LL} \sim L^2$ (using (48) in Appendix D.5), $N_{[4.0,5.5]} \sim 78$ eigenmodes for $D_{LL} \sim L^3$, $N_{[4.0,5.5]} \sim 120$ eigenmodes for $D_{LL} \sim L^4$, $N_{[4.0,5.5]} \sim 328$ eigenmodes for $D_{LL} \sim L^6$ (as mentioned before) and $N_{[4.0,5.5]} \sim 3550$ eigenmodes for $D_{LL} \sim L^{10}$ (by using (3.32)). All these values support the need to compute more and more eigenvalues when the diffusion power increases. As a comment, the time-based criteria emphasized by (3.31) does not enable us to conclude on the evolution of the necessary number of eigenmodes vs the power n, because an increase of n (and so of p) in (3.31) compensates the associated decrease of $t_0 = \tau_N^{\text{decay}}$. The interesting comment we can make from (3.31) is that for a same snapshot time t_0, one would need a fewer eigenmode number N if the diffusion power is stronger, because the equilibrium state is reached faster, and so the solution at a given t_0 will be closer to the steady solution for a high power n than for a low power n.

3.6 An estimation of the time needed to reach the equilibrium state

We focus here on the time to reach an equilibrium state, as numerically calculated in *Ripoll et al.* (2016a) and in Chapter 4. We extract an estimation of the time t_{eq} to reach an equilibrium state (up to some ratio $\varepsilon \ll 1$), defined as the time to nearly reach the steady solution $f_\infty(L)$ of (3.18), i.e. t_{eq} is such that $|f(L, t_{eq}) - f_\infty(L)| = \varepsilon f_\infty(L) \Leftrightarrow |w(L, t_{eq})| = \varepsilon f_\infty(L)$. Expanding the transient component $w(L,t)$ up to the

N^{th} eigenmode, we obtain

$$t_{eq} \text{ such that } \left| \sum_{k=1}^{N} \hat{\alpha}_k e^{-t_{eq}/\tau_k^{\text{decay}}} g_k(L) \right| - \varepsilon f_\infty(L) = 0. \tag{3.33}$$

Equation (3.33) can be solved as such, searching for its zero, and gives an exact equilibrium time t_{eq}. In Figure 3.10 we compute the general equilibrium times (with $\varepsilon = 0.1$, i.e. a 10% difference between the steady solution and the solution at t_{eq}) from solving numerically (3.33) for the case $D_{LL} = D_0 L^6$, when the full domain is split over 3 subintervals (case of Figure 3.4). As we see in Figure 3.10, approximating the distribution function at the equilibrium time with its first eigenmode is valid only when the equilibrium time is large or equivalently when L is below 2. It is however necessary to account for an important number of eigenmodes when L is close to L_M since the equilibrium time is small and times of the dynamics are smaller.

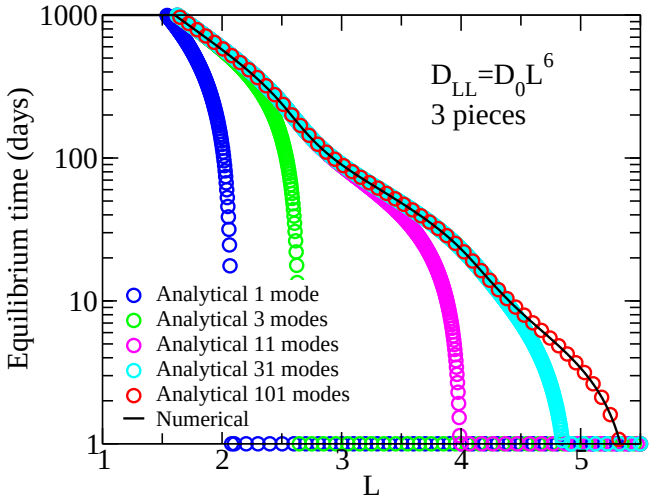

Figure 3.10 – Evolution of the equilibrium time (in days) vs L-shell for the case of Figure 3.4 (left). Plain lines represent the numerical equilibrium time whereas circle lines represent its analytical counterpart. A few modes compute only large equilibrium times that happen at low L-shells. By increasing the mode number we access to the larger L-shells. The minimum value of the equilibrium time has been set to 1 for readability.

As stated previously, the number of eigenmodes required to accurately approach the numerical solution decreases as time increases. Assuming the time to reach an equilibrium state is long enough to neglect all modes except the first one (which has to be true for small L values), we obtain $\left| \hat{\alpha}_1 e^{-t_{eq}/\tau_1^{\text{decay}}} g_1(L) \right| = \varepsilon f_\infty(L)$ and

$$t_{eq} \sim \tau_1^{\text{decay}} \ln \left| [\hat{\alpha}_1 g_1(L)] \,/\, [\varepsilon f_\infty(L)] \right|.$$

In the particular case of a radial diffusion coefficient $D_{LL} \sim L^4$ (larger n values and the specific case $n = 2$ will be addressed after) and for a constant electron lifetime over $[L_0, L_M]$, it is possible to determine analytically the time to reach equilibrium according to the above definition since the expressions for the coefficients $\hat{\alpha}_k$ become tractable. The expressions for t_{eq} are gathered in Table 3.4 for three different cases corresponding to three different initial conditions for the distribution function f.

Table 3.4 – Approximated equilibrium times for $\tau = \tau_0$ and $D_{LL} = D_0 L^4$

If $f(L, t=0) = 0$ and $f(L_M, t) = f_{L_M}$
$t_{\mathrm{eq}}(L) = \tau_1^{\mathrm{decay}} \ln\left(\left\lvert \frac{2}{\varepsilon\pi} \frac{1}{\left(1+\frac{\beta^2}{\Lambda_1^2}\right)} \sinh\left[\beta\left(L_0^{-1}-L_M^{-1}\right)\right] \frac{\sin\left[\Lambda_1\left(L_0^{-1}-L^{-1}\right)\right]}{\sinh\left[\beta\left(L_0^{-1}-L^{-1}\right)\right]} \right\rvert\right)$
If $f(L, t=0) = r f_\infty(L)$ and $f(L_M, t) = f_{L_M}$
$t_{\mathrm{eq}}(L) = \tau_1^{\mathrm{decay}} \ln\left(\left\lvert \frac{2\lvert r-1\rvert}{\varepsilon\pi} \frac{1}{\left(1+\frac{\beta^2}{\Lambda_1^2}\right)} \sinh\left[\beta\left(L_0^{-1}-L_M^{-1}\right)\right] \frac{\sin\left[\Lambda_1\left(L_0^{-1}-L^{-1}\right)\right]}{\sinh\left[\beta\left(L_0^{-1}-L^{-1}\right)\right]} \right\rvert\right)$
If $f(L, t=0) = f_0$ and $f(L_M, t) = f_{L_M}$
$t_{\mathrm{eq}}(L) = \tau_1^{\mathrm{decay}} \ln\left(\left\lvert \frac{2}{\varepsilon\pi} \left\lvert 2\frac{f_0}{f_{L_M}} - \frac{1}{\left(1+\frac{\beta^2}{\Lambda_1^2}\right)} \right\rvert \sinh\left[\beta\left(L_0^{-1}-L_M^{-1}\right)\right] \frac{\sin\left[\Lambda_1\left(L_0^{-1}-L^{-1}\right)\right]}{\sinh\left[\beta\left(L_0^{-1}-L^{-1}\right)\right]} \right\rvert\right)$

If $f_0(L) = 0$ or if $f_0 = r f_\infty(L)$ (with r is a given constant), corresponding to the case where the initial condition is proportional to the steady solution, the equilibrium time does not depend on the boundary condition f_{L_M}. It is however dependent on the position L_M of the boundary condition. This theoretical result, even if it only deals with the single case $n = 4$, is also in accordance with the simulations carried out in Chapter 4 and in (*Ripoll et al.*, 2016a), which show that the time to reach the equilibrium state weakly depends on the boundary conditions. Only the dependence to the boundary position is important. If the initial condition is now set to be a given constant ($f_0(L) = f_0$), the value of the boundary condition is involved in the equilibrium time expression, though it seems to only have a minor impact on the order of magnitude of its value. A particular case occurs when the initial state is twice the equilibrium state $f_0(L) = 2 f_\infty(L)$. As we see from Table 3.4, the time to reach the values of the equilibrium state when $r = 2$ is the same as when $r = 0$, i.e. it takes the same time to return to equilibrium from an empty magnetosphere than from a magnetosphere which density had artificially doubled. This result was indeed found and discussed in *Ripoll et al.* (2016a) and is detailed in Chapter 4. Let us call t_{eq1} the equilibrium time for which $f_0(L) = r f_\infty(L)$ and t_{eq2} the equilibrium time for which $f_0(L) = r f_\infty(L_M) = r f_{L_M}$. From Table 3.4, comparing t_{eq1} and t_{eq2} leads to the comparison between

$$Q_1 = \frac{r-1}{1+\dfrac{\beta^2}{\Lambda_1^2}} \qquad \text{and} \qquad Q_2 = 2r - \frac{1}{1+\dfrac{\beta^2}{\Lambda_1^2}},$$

which leads to evaluate the position of $2(1+\beta^2/\Lambda_1^2)$ with respect to 1. Since $\beta^2/\Lambda_1^2 > 0$ we always have $Q_2 > Q_1$ and therefore $t_{eq2} > t_{eq1}$. Hence we believe that the quasi-independence of the equilibrium time on the boundary conditions can be generalized for all power-law dependence of D_{LL} upon L ($n \geq 0$) and for more than only one piece.

3.7 Conclusions

Throughout this chapter we analytically solve the radial diffusion equation with a general nonuniform loss term in order to progress in our understanding of both mathematical properties and solutions involved in the dynamical radial transport of electrons in the radiation belts.

A reduced Fokker-Planck equation is used with constant first and second adiabatic invariants in the case where the radial diffusion coefficient is exactly proportional to a power law in L-shell, with a power $n \geq 0$. The solution is a distribution function composed of a steady-state (time-independent) term and a transient (time-varying) solution.

The steady state problem is first solved for a uniform loss term (1 piece), similarly to the fundamental historical results obtained by *Haerendel* (1968) or *Jentsch* (1984) in the study of the Earth's radiation belts. Our results are also in accordance with (*Baker and Goertz*, 1976; *Goertz et al.*, 1979), who focused their studies on Jupiter's magnetosphere, and with (*Hood*, 1983) for his work on the transport of protons in the vicinity of Saturn. Based on these results, the first purpose of this work is to generalize the study of the steady state case to a nonuniform loss term. To our knowledge, analytical expressions for the steady solution only exist for one specific space-dependent loss term, i.e. when the loss term evolves as a power law of the radial coordinate L (*Haerendel*, 1968). To bypass the difficulty of dealing with any general nonuniform loss term, we match any L-dependent electron losses $\tau(L)$ with a piecewise-constant function on M subintervals, i.e. setting a discretization of τ such that $\tau = \tau_i$ constant on each subinterval $i \in [1, M]$. The spatial continuity of the solution and the continuity of its first spatial derivative (seen numerically) give $2M - 2$ interface conditions that add up with the two boundary conditions, leading to a well-posed steady problem that is made of $2M$ equations for $2M$ unknowns. This procedure generalizes the method used by *Thomsen et al.* (1977a,b), who focused on a lesser extent to a piecewise constant electron lifetime split on 3 subintervals, for the diffusion of protons in Jupiter's magnetosphere. In the same context, the presented analytical method used to find the generalized steady solution might be confronted with satellites' data in order to point out new expressions for the radial diffusion coefficient related to Earth, Jupiter or Saturn. However, the question of whether or not the equilibrium state has been reached remains (*Ripoll et al.*, 2016a) and this work gives estimations of equilibrium timescales to answer it.

The resolution of the transient solution is much more complex compared to the steady-state problem, and falls under the eigenfunction expansion method that has already been detailed in previous papers for a uniform loss term (e.g., *Walt*, 1970; *Schulz*, 1986; *Schulz and Newman*, 1988). The procedure relies on the separation of the two variables in space (L) and time (t) (*Mei*, 1997) and leads to an ordinary differential equation in time (associated to the initial condition) and a second equation involving spatial derivatives (associated to the two boundary conditions). The second equation corresponds to a Sturm-Liouville problem, from which the associated eigenvalues λ_k and eigenfunctions $g_k(L)$ (for integer $k \geq 1$) can be calculated analytically for $n = 2$ or $n = 4$ and numerically otherwise. These mathematical steps have been successively performed to find some of the results presented by *Schulz* (1986) and *Schulz and Newman* (1988) for a uniform loss term. In the present case, the non uniformity of the loss term involved makes the analytical resolution of the Sturm-Liouville problem a challenging task to achieve, because there exists no analytical expressions for the eigenfunctions. As we have done before for the steady case, we address the issue of nonuniformity by transforming any nonuniform lifetime $\tau(L)$ to a discrete set of M different constant lifetimes τ_i on each of

the M subintervals. Based on the spatial continuity of the full solution and the continuity of its first spatial derivative, we show again that the global radial diffusion problem is well-posed. The global eigenvalue problem establishes a Sturm-Liouville problem with M interfaces, i.e. made of M equations occurring each on the single subinterval i and involving a constant electron lifetime τ_i. This problem can then be solved analytically such that the eigenfunctions become now tractable. The eigenvalues λ_k inherent to the system made of the M eigenvalue problems are calculated, either by analytical expressions (if $n = 2$ or $n = 4$) or by numerical computations ($n = 3$, 6, or 10, for example). As the electron lifetime changes from one domain to another, the eigenfunction $g_k^i(L)$ evolving on subinterval i alternates according to the sign of $|\lambda_k| - 1/\tau_i$ between a smooth decaying function, represented by the Bessel functions J_ν and Y_ν (behaving, for example, like a sine function) and a fast decaying function, represented by the modified Bessel functions I_ν and K_ν (behaving more like a hyperbolic sine function). This property has no equivalent when the electron lifetime is set constant over the whole interval $[L_0, L_M]$.

We find full agreement between our analytical solutions and our solutions provided by a numerical method, for a radial diffusion coefficient increasing with a power 6 with increasing L and different L-dependent loss terms (over 3, 10 and 25 pieces and different shapes). It proves the correctness of the approximations, methods, and solutions, and also the excellent accuracy of the second order in space Crank-Nicholson scheme used in the community for the numerical computations. Furthermore we put forward a strong correlation between the solutions derived from a particular electron lifetime $\tau = \tau_0 L^{2-n}$ and solutions derived with the corresponding piecewise-constant loss term (split over 25 pieces), showing that the presented method can be extended with a loss term built to fit any electron lifetimes, including the recently developed models of electron lifetimes from whistler mode hiss waves (e.g., *Orlova and Shprits*, 2014; *Orlova et al.*, 2016) and whistler mode chorus waves (e.g., *Gu et al.*, 2012; *Orlova et al.*, 2014).

Convergence of the analytical solutions to their numerical counterpart according to the number of eigenmodes is also discussed. In particular, we show that the number N of eigenmodes required to get an accurate snapshot of the solution at time t_0 is proportional to $1/\sqrt{D_0 t_0}$. When $D_{LL} \sim L^6$, more than a hundred eigenmodes can be required to get a solution at early times of about one day or less. For longer times (> 10 days), or times close to the steady state, the method is rather very fast, requiring only a few number of modes ($\sim 10 - 30$). The analytical method is not a serious concurrent to a finite-difference scheme as the computation of a large number of eigenmodes requires a lot of computing resources for small times, in particular if one wants to perform the computations with dynamical outer boundary conditions varying at the timescale of magnetospheric variability. However, we also show that the required number of eigenmodes to calculate decreases if the diffusive transport is weaker, i.e. if the power n decreases. The proposed analytical method may then be useful when dealing with radial diffusion in the magnetosphere of Jupiter or Saturn, for which the diffusion process is less significant than in the Earth's radiation belts, i.e. $2 \leq n \leq 4$ (*Brice and Mcdonough*, 1973; *Coroniti*, 1974; *Birmingham et al.*, 1974; *Thomsen et al.*, 1977a,b; *Hood*, 1983; *de Pater and Goertz*, 1990, 1994; *Woodfield et al.*, 2014). We finally give an analytical estimation of the time to reach an equilibrium state and emphasize that this time depends very slightly on the boundary conditions, but rather on the boundary condition location, and strongly on the initial condition (as also found numerically (*Ripoll et al.*, 2016a)). This so-called equilibrium time is of great interest because it quickly evaluates the evolution time of the diffusion process. One can imagine a new optimized hybrid computational method that uses the common numerical finite-difference schemes to derive the solution

at early times (i.e. times that are far below the estimated equilibrium time), and uses the presented analytical procedure to compute the solution at larger times (i.e. times around the estimated equilibrium time), taking effect of the benefits of both numerical and analytical processes. We also believe that the analytical solutions we presented can be applied to other fields of physics. It is possible that for other applications the power of the radial diffusion coefficient D_{LL} is not as stiff as in the Earth's magnetosphere. It would make therefore the analytical solution tractable with a lower number of eigenmodes ($< 10 - 20$) which would allow to find quickly an exact solution at any time (as soon as the source term is correctly discretized by M pieces, with M large).

3.8 Tables for the analytical solution

Table 3.5 – Functions $U^i(L)$ and $V^i(L)$ involved in the steady solution $f_\infty(L)$ and functions $\varphi^i(\lambda, L)$ and $\psi^i(\lambda, L)$ involved in the transient solution $w(L,t)$, for M pieces, with $n \neq 2$.

$$\nu = \left|\frac{n-3}{n-2}\right|,\ p = \frac{n-2}{2},\ q = \frac{n-3}{2},\ \beta_i = \frac{2}{(n-2)\sqrt{\tau_i D_0}} \text{ and from variable } \lambda,\ \Lambda^i(\lambda) = \frac{2}{n-2}\sqrt{\left|\frac{|\lambda| - 1/\tau_i}{D_0}\right|}$$

with $i \in [1, M]$ the pieces number

Functions involved in the steady solution $f_\infty(L)$

$$U^i(L) = L^{-q} I_\nu\left(\beta_i L^{-p}\right) \qquad V^i(L) = L^{-q} K_\nu\left(\beta_i L^{-p}\right)$$

Functions involved in the transient solution $w(L,t)$

$$\varphi^i(\lambda, L) = \begin{cases} L^{-q} J_\nu\left(\Lambda^i(\lambda) L^{-p}\right) & \text{if } |\lambda| > 1/\tau_i \\ L^{-q} I_\nu\left(\Lambda^i(\lambda) L^{-p}\right) & \text{if } |\lambda| < 1/\tau_i. \end{cases} \qquad \psi^i(\lambda, L) = \begin{cases} L^{-q} Y_\nu\left(\Lambda^i(\lambda) L^{-p}\right) & \text{if } |\lambda| > 1/\tau_i \\ L^{-q} K_\nu\left(\Lambda_k(\lambda) L^{-p}\right) & \text{if } |\lambda| < 1/\tau_i. \end{cases}$$

where J_ν, and Y_ν correspond to the Bessel functions of order ν and I_ν and K_ν correspond to the modified Bessel functions of order ν

Table 3.6 – Steady solution $f_\infty(L)$ of equation (3.18) and (3.23) for M pieces and $D_{LL} = D_0 L^n$. For the sake of concision, the derivative with respect to L is noted with a prime symbol " ' " in the following tables.

With $U^i(L)$ and $V^i(L)$ defined in Table 3.5,

$$F^1 = -\frac{V^1(L_0)}{U^1(L_0)},\ F^M = -\frac{V^M(L_M)}{U^M(L_M)} \text{ and } G^M = \frac{f(L_M)}{U^M(L_M)}$$

$$F^i = -\left(\frac{V^i(L_{i-1})}{U^i(L_{i-1})}\right)^2 \left(\frac{F^{i-1}U^{i-1}(L_{i-1}) + V^{i-1}(L_{i-1})}{V^i(L_{i-1})}\right)' \Bigg/ \left(\frac{F^{i-1}U^{i-1}(L_{i-1}) + V^{i-1}(L_{i-1})}{U^i(L_{i-1})}\right)' \qquad \text{for } i \in [2, M-1]$$

$$\begin{aligned} C_{M-1} = &\left[F^{M-1}U^{M-1}(L_{M-1}) + V^{M-1}(L_{M-1})\right] U^{M'}(L_{M-1}) \\ &- \left[F^{M-1}U^{M-1'}(L_{M-1}) + V^{M-1'}(L_{M-1})\right] U^M(L_{M-1}) \\ D_{M-1} = &\left[F^M U^M(L_{M-1}) + V^M(L_{M-1})\right] \left[F^{M-1}U^{M-1'}(L_{M-1}) + V^{M-1'}(L_{M-1})\right] \\ &- \left[F^M U^{M'}(L_{M-1}) + V^{M'}(L_{M-1})\right] \left[F^{M-1}U^{M-1}(L_{M-1}) + V^{M-1}(L_{M-1})\right] \end{aligned}$$

$$B^M = G^M \frac{C_{M-1}}{D_{M-1}} \qquad A^M = F^M B^M + G^M$$

$$B^i = \frac{A^{i+1}U^{i+1}(L_i) + B^{i+1}V^{i+1}(L_i)}{F^i U^i(L_i) + V^i(L_i)} \qquad A^i = F^i B^i \qquad \text{for } i \in [1, M-1]$$

Steady solution

$$f_\infty(L) = \sum_{i=1}^{M} \mathbb{1}_i(L) \left[A^i U^i(L) + B^i V^i(L)\right]$$

Table 3.7 – Transient component $w(L,t)$ of the full analytical solution for M pieces and $D_{LL} = D_0 L^n$.

From variable λ, $\Lambda^i(\lambda)$ has been defined in Table 3.5 with $i \in [1, M]$ the pieces number.

With $\varphi^i(\lambda, L)$ and $\psi^i(\lambda, L)$ defined in Table 3.5,

$$\mathcal{F}^1(\lambda) = -\frac{\psi^1(\lambda, L_0)}{\varphi^1(\lambda, L_0)} \quad \text{and} \quad \mathcal{F}^M(\lambda) = -\frac{\psi^M(\lambda, L_M)}{\varphi^M(\lambda, L_M)}$$

$$\mathcal{F}^i(\lambda) = -\left(\frac{\psi^i(\lambda, L_{i-1})}{\varphi^i(\lambda, L_{i-1})}\right)^2 \left(\frac{\mathcal{F}^{i-1}(\lambda)\varphi^{i-1}(\lambda, L_{i-1}) + \psi^{i-1}(\lambda, L_{i-1})}{\psi^i(\lambda, L_{i-1})}\right)' \Bigg/ \left(\frac{\mathcal{F}^{i-1}(\lambda)\varphi^{i-1}(\lambda, L_{i-1}) + \psi^{i-1}(\lambda, L_{i-1})}{\varphi^i(\lambda, L_{i-1})}\right)'$$

for $i \in [2, M-1]$

The eigenvalues λ_k (for each integer $k \geq 1$) are the zeros of the function $D(\lambda)$ with

$$D(\lambda) = \left[\mathcal{F}^{M-1}(\lambda)\varphi^{M-1'}(\lambda, L_{M-1}) + \psi^{M-1'}(\lambda, L_{M-1})\right]\left[\mathcal{F}^M(\lambda)\varphi^M(\lambda, L_{M-1}) + \psi^M(\lambda, L_{M-1})\right] - \left[\mathcal{F}^{M-1}(\lambda)\varphi^{M-1}(\lambda, L_{M-1}) + \psi^{M-1}(\lambda, L_{M-1})\right]\left[\mathcal{F}^M(\lambda)\varphi^{M'}(\lambda, L_{M-1}) + \psi^{M'}(\lambda, L_{M-1})\right]$$

$\Lambda_k^i = \Lambda^i(\lambda_k)$, $U_k^i(L) = \varphi^i(\lambda_k, L)$, $V_k^i(L) = \psi^i(\lambda_k, L)$ and $F_k^i = \mathcal{F}^i(\lambda_k)$

$B_k^M = 1$ or any nonzero arbitrary value

$$B_k^i = \frac{A_k^{i+1}U_k^{i+1}(L_i) + B_k^{i+1}V_k^{i+1}(L_i)}{F_k^i U_k^i(L_i) + V_k^i(L_i)}$$

$$A_k^M = F_k^M B_k^M$$

$$A_k^i = F_k^i B_k^i \qquad \text{for } i \in [1, M-1]$$

Eigenfunctions

$$g_k(L) = \sum_{i=1}^{M} \mathbb{1}_i(L)\left[A_k^i U_k^i(L) + B_k^i V_k^i(L)\right]$$

Full transient solution

$$w(L,t) = \sum_{k=1}^{\infty} \alpha_k(t)\left(\sum_{i=1}^{M} \mathbb{1}_i(L) g_k^i(L)\right)$$

where $\alpha_k(t)$ is defined in Table 3.2

Chapter 4

On the equilibrium structure of the radiation belts

One of the purposes of the previous chapter has been to characterizing the dynamical evolution of the PSD f towards its equilibrium structure for static and dynamic boundary conditions. However, it did not give any information on the dynamical behavior of the corresponding electron flux $j = p^2 f$ and on its long-term structure, which is considered to shape two radiation belts (one inner belt and one outer belt) separated by a slot region (*Lyons and Thorne*, 1973). From this perspective, the purpose of the present chapter is to analyze the dynamics of the unidirectional electron flux in a more realistic background, and relate it to the analytical properties derived above. The previously discussed notions are here complemented with numerical simulations of the reduced Fokker-Planck equation that enables us to uncover the radiation belts in a physical plane in L-shell and energy, following the historical study adopted by *Lyons and Thorne* (1973). In this chapter, we use realistic electron lifetimes derived from Coulomb collisions and interactions with whistler mode hiss and chorus waves respectively inside and outside the plasmasphere, as well as different models for the radial diffusion coefficient. The dynamical behavior is also dependent on the geomagnetic activity, which is represented by the value of the K_p geomagnetic index. During quiet times, we show that the equilibrium structure of the electron flux plotted in the (L, E) plane displays the same interesting "S shape" for the inner edge of the outer belt as recently observed by the Van Allen Probes (*Reeves et al.*, 2016). We also reveal that this particular shape is not inherent to the equilibrium state, and is also produced as the radiation belts dynamically evolve toward the equilibrium state when initialized to simulate the buildup after a massive dropout or to simulate loss (out of the magnetopause) due to outward radial diffusion from a saturated state. In particular, the slot region results from a depletion of electrons (atmospheric loss) induced by VLF wave-particle interactions. The shape of the slot region is sculpted by the dependence of the electron loss rate on both energy and L-shell. Finally, we put forwards some useful physical quantities that can be quickly derived to infer the shape of the fluxes and their equilibrium times. As mentioned in Chapter 3, this S shape is governed by the initial state of the belts, the property of the dynamics (diffusion coefficients), and the size of the domain of computation. Its structure in the (L, E) plane particularly shows that convergence to equilibrium requires hundreds of days in the inner belt and is practically reachable only for small selected regions in the (L, E) plane, challenging the usual view inspired by *Lyons and Thorne* (1973) of the two radiation belts at equilibrium.

The study of the present chapter has been the subject of a publication (*Ripoll et al.*, 2016a). Here we choose to additionally emphasize the implementation of the numerical model made during the PhD as well as the transformations in use to convert the adiabatic space (μ, K, L) into the physical space (E, α_0, L) made of energy, equatorial pitch angle and L-shell. This chapter is also an opportunity to reproduce and question the results obtained by *Lyons and Thorne* (1973). Making use of the results of (*Ripoll et al.*, 2016a), we will first compare the effects of different radial diffusion models and focus on the radial diffusion model of (*Ozeke et al.*, 2014) that gives the most relevant results. We emphasize here the dynamical structure of the radiation belts in both fluxes and PSD, while we only focused on electron fluxes in (*Ripoll et al.*, 2016a,b, 2017). As the radial diffusion coefficient is different from the one in use in (*Ripoll et al.*, 2016a), the maps showing the regions for which the equilibrium state is reached have been updated.

4.1 Framework of the study

The shape of the radiation belts has first been theoretically put forward by *Lyons and Thorne* (1973), whose study has become one of the linchpins of radiation belt physics

over the years. The equilibrium structure of the radiation belts, two belts separated by a slot region devoid of electron, was obtained by assuming a balance between atmspheric loss and radial diffusion. The loss term results from the interactions of electrons with plasmaspheric hiss waves that increase the electrons' pitch angles and make them reach higher latitudes until being lost in the atmosphere. Radial diffusion is induced by resonant interactions of electrons with ULF waves, breaking the conservation property of the third adiabatic invariant. This pleasant picture of steady radiation belts shows today its limitations as the outer belt is rather found to be very dynamic (with a timescale of a few hours).

The successive launches of satellite missions have also greatly improved our understanding of the physical properties of the radiation belts. The Combined Release and Radiation Effects Satellite (CRRES) mission operated during the 1990's uncovered the dynamics of fluxes down to the slot region (e.g., *Meredith et al.*, 2006a; *Shprits et al.*, 2005; *Kim et al.*, 2011; *Friedel et al.*, 1996; *Korth et al.*, 2000), while the Solar, Anomalous, and Magnetospheric Particle EXplorer (SAMPEX) mission showed the dynamics of fluxes in the slot region (e.g., *Baker et al.*, 2007; *Meredith et al.*, 2006a, 2009; *Selesnick*, 2015). The High Earth Orbiting (HEO) mission showed a quiet inner belt (e.g., *Shprits et al.*, 2015a; *Turner et al.*, 2013b; *Baker et al.*, 2014b; *Mann et al.*, 2016), and the Van Allen Probes missions highlighted, in some specific situations, the birth of a third belt (e.g., *Fennell et al.*, 2013; *Ripoll et al.*, 2014a,b), later referred as "remnant belt". The recently launched Van Allen Probes also revealed that the inner belt is devoid of high energy electron (*Fennell et al.*, 2015), such that the flux of electrons drops steeply above 800 keV, which is possibly explained by a physical barrier (*Baker et al.*, 2014b) made of vanishing radial transport and/or hiss scattering. In view of this tricky magnetospheric context, this chapter aims at discussing the physical relevancy of the equilibrium state of the radiation belts. If the equilibrium state proves to be relevant, it would enable us to quickly calculate the electron fluxes by approximating them by their steady (time-independent) states, by such, to give an accurate estimation of the radiation dose received by the orbiting satellites.

This chapter is dedicated to the computation of a large variety of solutions as a function of energy and L-shell, among which some of them can be directly compared with the recently observed "S shape" of the inner edge of the outer belt (*Reeves et al.*, 2016) (see Figure 4.1). Since the present work aims at discussing the equilibrium state of the belts (and also to be consistent with some of the results made on the previous chapter), no dynamic boundary conditions are used, which assumes that the magnetospheric conditions must be steady during the time of interest. We use some recently developed models of electron lifetimes due to pitch angle scattering from whistler mode hiss and chorus waves, which depend on energy and L-shell. To the best of our knowledge, the only past study that compared steady state and time-dependent solutions was done with a primitive electron lifetime model (constant values) in (*Shprits and Thorne*, 2004), not energy-dependent models computed from full diffusion coefficients that are key to reproduce a meaningful radiation belt structure. In particular, we compute the time-dependent solution and the time required to reach the equilibrium state as a function of (L, E) for two classes of problem: an injection of electrons into a magnetosphere devoid of electrons after a massive dropout and the decay of a saturated magnetosphere after massive injections.

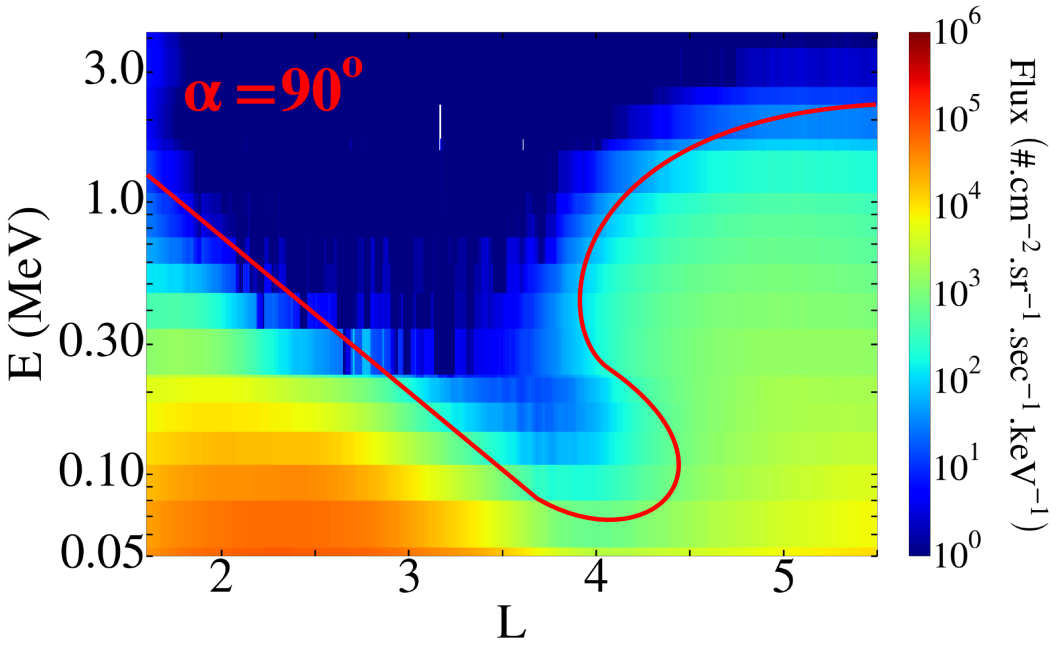

Figure 4.1 – Illustration of the S shape via the unidirectional electron flux versus energy and L-shell. The displayed outbound flux has been observed by the MagEIS instrument on board Van Allen Probe A on March 4, 2013, from 07:57 to 12:26 UT and corresponds to a 90 degrees local pitch angle. Adapted from *Reeves et al.* (2016).

4.2 Numerical code

Before focusing on the case of interest, let us take the opportunity to detail here the general *numerical code* used to produce the PSD and the electron fluxes for this study. This same code has also been successfully used in Chapters 5 and 6.

The model at stake is still the one dimensional reduced Fokker-Planck equation (2.57) that governs the evolution of the phase-averaged distribution function of electrons f, thereafter referred (abusively) as PSD,

$$\frac{\partial f}{\partial t} = L^2 \frac{\partial}{\partial L}\left[\frac{D_{LL}}{L^2}\frac{\partial f}{\partial L}\right]_{(\mu,K)} - \frac{f}{\tau}.$$

We recall that L is the Roederer's L value, equivalent to the equatorial radial distance in a dipole magnetic field. The diffusion coefficient that drives the radial diffusion and the lifetime that represents the losses from pitch angle scattering are respectively the D_{LL} and τ parameters. The radial diffusion process occurs at constant adiabatic invariants (μ, K), enabling the electrons to gain energy when they diffuse inward (betatron acceleration) and reciprocally for an outward radial diffusion.

4.2.1 Numerical scheme

The numerical scheme for discretizing the reduced Fokker-Planck equation (3.18) has been developed by *Bussutil* (2014). It is based on a semi-implicit β method (for $\beta \in [0, 1]$). A β parameter set to $\beta = 0.5$ yields to the Crank-Nicholson scheme, which is first order in time and second order in space. A parameter $\beta = 1$ corresponds to

the implicit Euler method, which has the advantage of being unconditionally stable. Equation (3.18) is solved with the Crank-Nicholson scheme ($\beta = 0.5$) for constant first and second invariants, with typically 1000 nodes equally spaced in L. Two stability conditions have to be verified to ensure the stability of the Crank-Nicholson numerical scheme. First, since we use a uniform grid in time, the gap between two successive times is determined by the timestep condition $\Delta t \leq 5/100\,\tau$. This condition preserves the algorithm from numerical instabilities, the timestep being controlled by the lifetime $\tau = \min_i \tau_i$. A second stability condition arises when $\beta \neq 1$, known as the Courant-Friedrichs-Lewy (CFL) condition. The diffusion operator requires that $\Delta t \leq (\Delta L)^2/(2D_{LL})$.

4.2.2 Electron lifetimes

The *numerical code* was first able to consider statistically-derived lifetime expressions (*Bussutil*, 2014). The latters were typically taking account of Coulomb collisions (*Lyons and Thorne*, 1973), whistler mode hiss (e.g., *Orlova et al.*, 2014) or chorus (e.g., *Orlova and Shprits*, 2014) waves. More recently, the work carried out during the PhD thesis enables to extend the code capability to consider event-specific and data-driven (time-dependent) electron lifetimes, such as the ones calculated in (*Ripoll et al.*, 2017). Since the latters are given by scattered points rather than being a given mathematical function (involving explicitely the L-shell, energy, or the K_p index), numerical interpolations and extrapolations are necessary to relate them to the (μ, K, L^*) reference grid.

4.2.3 Initial and boundary conditions

The reduced Fokker-Planck equation is usually associated with two boundary conditions at the inner boundary $L = L_0$ and outer boundary $L = L_M$, and one general initial condition that we call $f(\mu, L, t = 0) = f_0(\mu, L)$ for now. The specific use of static boundary conditions (such as the one considered in this chapter) has also been developed by (*Bussutil*, 2014). The generalization to dynamic and realistic boundary conditions has further been done during the present PhD thesis in the perspective of Chapters 5 and 6.

4.2.4 Transformations and magnetic fields

While the code solves the radial diffusion equation on a given grid in (μ, K, L), the lifetimes we use in our simulations depend directly on the energy E (and L-shells). Moreover, the fluxes derived from the obtained PSD, f, have to be plotted in the (E, α_0, L) space rather than the adiabatic space in order to compare them with satellites observations. Hence it is always necessary to relate in the code the coordinates (μ, K) with the new variables (E, α_0).

4.2.4.a Dipole magnetic field

The transformations initially implemented in the reduced Fokker-Planck code by *Bussutil* (2014) were relying on the centered dipole field topology. They are detailed as follow. Defining as before B_m as the magnetic field intensity at the mirror point and B_0 the equatorial magnetic intensity, we have from the conservation of the first invariant (2.24) $B_m = B_0/y_0^2$, with $y_0 = \sin(\alpha_0)$. For a dipole field, the approximation made on the expression of J from *Schulz and Lanzerotti* (1974) gives

$$J \approx 2pLR_E \left[2.76(1 - y_0) + 0.64\left(y_0 \ln(y_0) + 2y_0 - 2y_0^{1/2}\right)\right].$$

Since $K = \sqrt{B_m}/(2p)\, J = \sqrt{B_0}/(2py_0)\, J$, the transformation from (μ, K) to (E, α_0) (with the knowledge of the value $B_0(L) = B_E/L^3$, with B_E the equatorial magnetic field intensity at the Earth's surface) is written under the form of the following system

$$\begin{cases} \mu = f_1(p, y_0, L) = \dfrac{p^2 y_0 L^3}{2mB_E}, \\ \\ K = f_2(y_0, L) = \dfrac{R_E}{y_0}\sqrt{\dfrac{B_E}{L}}\left[2.76(1-y_0) + 0.64\left(y_0 \ln(y_0) + 2y_0 - 2y_0^{1/2}\right)\right]. \end{cases} \tag{4.1}$$

Knowing the values of μ and K, the new values of $p(\mu, K, L)$ and $y_0(K, L)$ are extracted from the above system by numerically performing a Newton-Raphson method. This formulation also emphasizes the dependence of the magnetic field geometry on the transformation from (μ, K) to (E, α_0). The relations between the physical space (E, α_0, L) and the initial invariant grid in (μ, K, L) are illustrated for a dipole field in Figure 4.2.

4.2.4.b Realistic magnetic fields

One important improvement of the *numerical code* relies on the consideration of more realistic magnetic field models and constituted a major step forward of this PhD thesis. If the magnetic field model is not a dipole, the approximation (4.1) made on the expression of K does not hold, and K has then to be computed numerically from its general integrand expression detailed in Chapter 2 rather than equation (4.1). More accurate computations could use for example the T89 magnetic field model (*Tsyganenko*, 1989) (see Chapter 6) or the Tsyganenko 04 storm time model (*Tsyganenko and Sitnov*, 2005) at large K_p (e.g., *Tu et al.*, 2014). Another example is the use the IGRF model (*Thébault et al.*, 2015) if the study is focused on the inner belt (see Chapter 7). In practice the transformations, which are time-dependent, are performed with the use of the LANLGeoMag library prior to any PSD calculation. More details about their implementation are given in Chapters 6 for the outer belt and 7 for the inner belt.

4.2.5 Parallelization

Another numerical development made during the PhD has been the mandatory optimization of the numerical calculations. In this context, the computation of the full PSD over a large and highly resolved adiabatic grid (built on the three invariants) is done in paralllel by using the High Performance Computing resources for the Research and Technology Computing Center (*CCRT - Centre de Calcul pour la Recherche et la Technologie*), with one core taking care of a very restricted grid in (μ, K), such that all the cores involved process the full range.

4.3 Revisiting the historical approach to uncover the radiation belts

4.3.1 Parameters into consideration

In the framework of the present study, we use a mesh made of 200 μ values logarithmically sampled from $\mu = 10^{-5}$ to 10^6 MeV/G, and all results are presented at the second invariant $K = 0.0$ $\mathrm{G}^{1/2} R_E$ (which corresponds to an electron population having an equatorial pitch angle α_0 of 90 degrees).

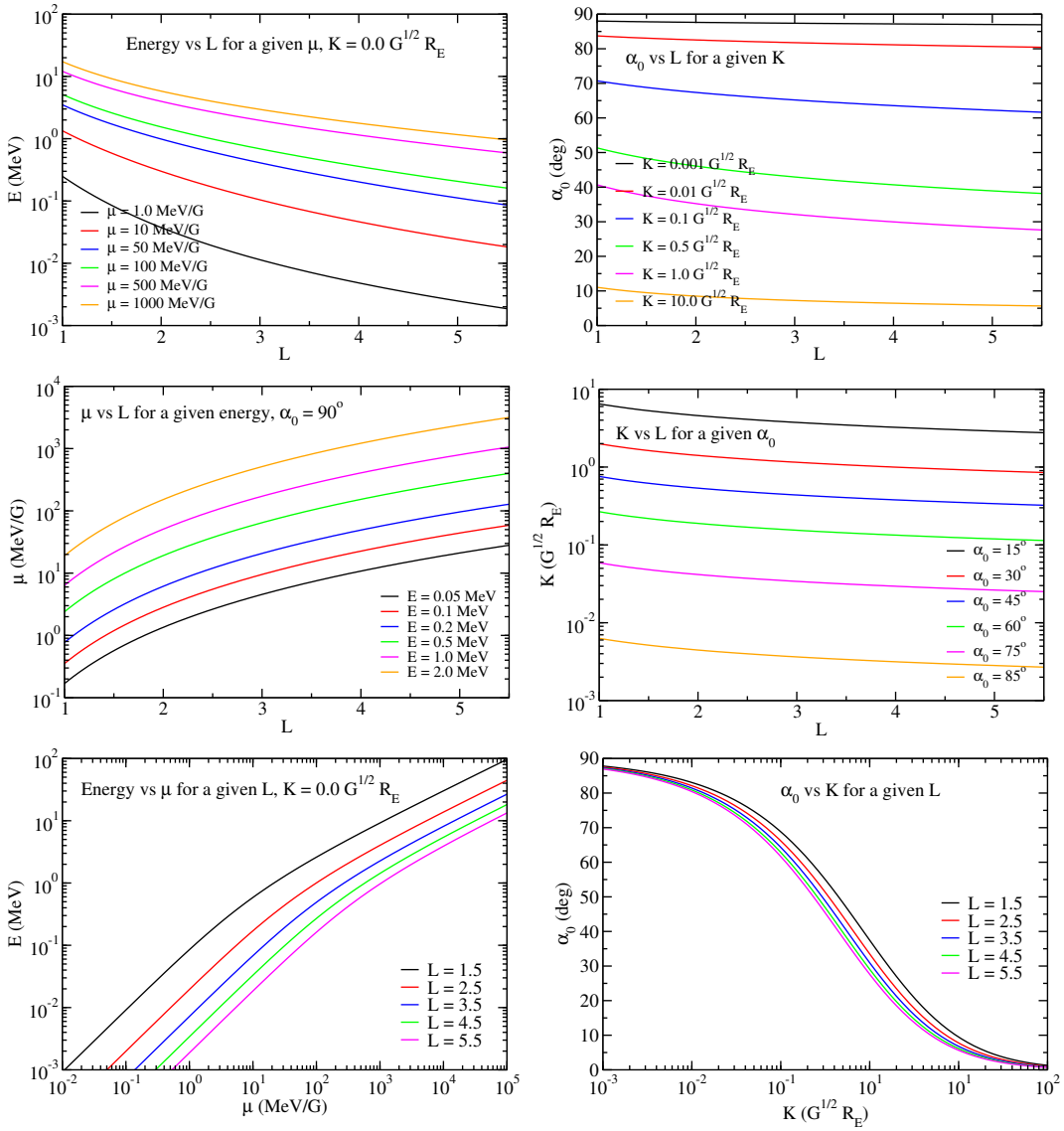

Figure 4.2 – The top-left panel represents the evolution of E versus L for several given μ, assuming $K = 0.0$ G$^{1/2}R_E$, while the top-right panel represents the evolution of α_0 versus L for several given K. The center-left panel shows the evolution of μ versus L for several given E, assuming $\alpha_0 = 90$ degrees, while the center-right panel shows the evolution of K versus L for several given α_0. For several different values of L, the bottom-left panel displays the evolution of E versus μ, assuming again $K = 0.0$ G$^{1/2}R_E$, while the bottom-right panel displays the evolution of α_0 versus K.

The outer boundary condition $f(\mu, K, L_M)$ at $L_M = 5.5$ is derived from the energy-dependent flux used in (*Lyons and Thorne*, 1973), which is given by

$$j(\mu, K, L_M) = \begin{cases} 1.163 \times 106 \exp(-0.05/0.2) & \text{if } E_{\min} < 0.05 \text{ MeV}, \\ 1.163 \times 106 \exp(-E(\mu, K, L_M)/0.2) & \text{otherwise.} \end{cases} \tag{4.2}$$

The flux j has the typical units of a flux #/(cm^2.s.sr.MeV) in the above formulation. Hence the outer boundary condition in PSD is $f(\mu, K, L_M) = j(\mu, K, L_M)/p^2(\mu, K, L_M)$.

The inner boundary condition is such that $f(\mu, K, L_0) = 0$ at $L_0 = 1.0$ (electron scattering in the dense atmosphere).

4.3.2 Radial transport and losses

In the present study, we first solve numerically the reduced Fokker-Planck equation (2.57) by considering the historical parameters used by *Lyons and Thorne* (1973). From this context the pitch angle diffusion processes are taken from Coulomb collisions and from wave particle interactions induced by whistler mode hiss waves, whose associated electron lifetimes are respectively denoted as τ_{col} and τ_{hiss}. The hiss model is activated inside the plasmapause, with the plasmapause location, L_{pp}, being determined from *Carpenter and Anderson* (1992) by

$$L_{pp} = 5.6 - 0.46 K_p^*,$$

for which the K_p^* index is defined as the maximum value of K_p during the last 24 hours. The global lifetime τ is such that $\tau = 1/(1/\tau_{\text{col}} + 1/\tau_{\text{hiss}})$ (see equation (2.58)) that includes all waves and Coulomb collisions. Writing such a mean time consists of assuming all processes are decoupled (see Chapter 2 and (*Ripoll et al.*, 2016a)), and the linear sum of each represents the global process, as explained when deriving equation (2.57) in Chapter 2. This sum is always positive and represents the sum of the inverse of each of the smallest eigenvalues (slowest decaying modes) associated with the pitch angle diffusion operator (*Walt*, 1970; *Lyons et al.*, 1972). The radial diffusion model is derived from the electrostatic diffusion coefficient D_{LL}^E of the historical *Lyons and Thorne* (1973) work that implicitly assumes $K_p = 1$. The aforementioned historical diffusion coefficient and electron lifetimes are presented in Figure 4.3.

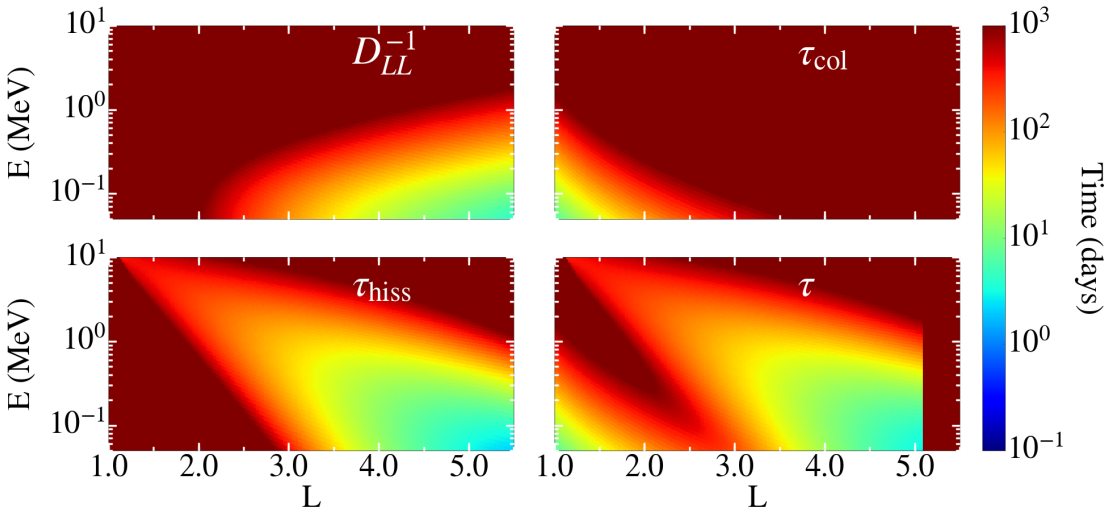

Figure 4.3 – Radial diffusion rate (top-left), lifetime due to Coulomb scattering (top-right), lifetimes due to whistler mode hiss waves (bottom-left), and harmonic sum of all lifetimes (bottom-right) in the (L-shell, Energy) plane, computed with the historical *Lyons and Thorne* (1973) model ($K_p = 1$).

4.3.3 Emergence of two radiation belts via steady solutions

Let us first mention that through this chapter we make a difference between the notion of steady state and equilibrium state. The steady state refers to the f_∞ solution of the reduced Fokker-Planck equation (2.57) that is obtained when the first partial derivative of f with respect to time vanishes. The equilibrium state, as we will see in the following sections, corresponds to an intermediate state for which the f solution is almost (up to a ε parameter that is discussed below) the steady f_∞ solution. Having these two conceptual notions in mind, we first perform the steady state solution f_∞ of the reduced Fokker-Planck equation. The computation does not need to proceed any time iteration, such that the steady solution is found very quickly. The obtained steady PSD are plotted in Figure 4.4 (left), showing a spread over the entire range in L-shell only for selected values of first adiabatic invariant μ. This spread depends on the outer boundary condition. The corresponding steady fluxes (right side of Figure 4.4) are obtained through the relation $j = p^2 f$ and by projection from the (L, μ) plane into the (L, E) plane according to the transformation given by (4.1), as emphasized by the two center panels of Figure 4.4, showing respectively the flux in the (L, μ) space (top) and the PSD in the (L, E) space (bottom). More precisely, changing the coordinate system from (μ, K, L) (Figure 4.4, left) to (E, α_0, L) affects the shape of the distribution function (Figure 4.4, bottom). On the other hand, converting the PSD in the (μ, K, L) space (Figure 4.4, left) into fluxes in the (μ, K, L) space brings a significant contribution in the inner region (Figure 4.4, top) as a consequence of betatron acceleration through inward radial diffusion. Combining both transformations (Figure 4.4, right) exhibits two radiation belts (outer and inner) separated by a slot region. The steady fluxes also illustrate the energy dependence of both the slot and the location of the belts (*Lyons and Thorne*, 1973).

Figure 4.4 (right) also provides the physical explanation for the existence of two radiation belts at equilibrium. High-energy electrons initially located at the outer boundary diffuse radially inward, but are subsequently scattered by VLF waves (and ultimately lost in the atmosphere for $L \sim 2 - 3$), preventing particles from reaching the inner belt. On the contrary, initially low-energy electrons at the outer boundary avoid the action of VLF waves and diffuse radially inward by gaining energy (through betatron acceleration) to fill the inner belt.

Providing equilibrium states in the (L, E) plane as in Figure 4.4 is very useful to compare with recent observations. In particular, we notice on the center-right panel of Figure 4.4 that the steady flux has a form of a rather rudimentary S-shape. A similar structure has been observed from the Van Allen Probes (*Reeves et al.*, 2016). Since our simulations at the equilibrium show a less pronounced S shape structure from what is currently observed, the historical parameters for radial transport and losses might not be accurate enough, and are left behind for the rest of the chapter. We now perform equilibrium solutions with more recent and relevant models, and see if we succeed to identify the aforementioned "S" feature.

Figure 4.5 complement the view by showing 1-D line cuts of the PSD versus L (left) for μ=3, 10, 30, 50, 300 and 300 MeV/G and fluxes versus L (right) for E=0.05, 0.1, 0.2, 0.5, 1 and 2 MeV.

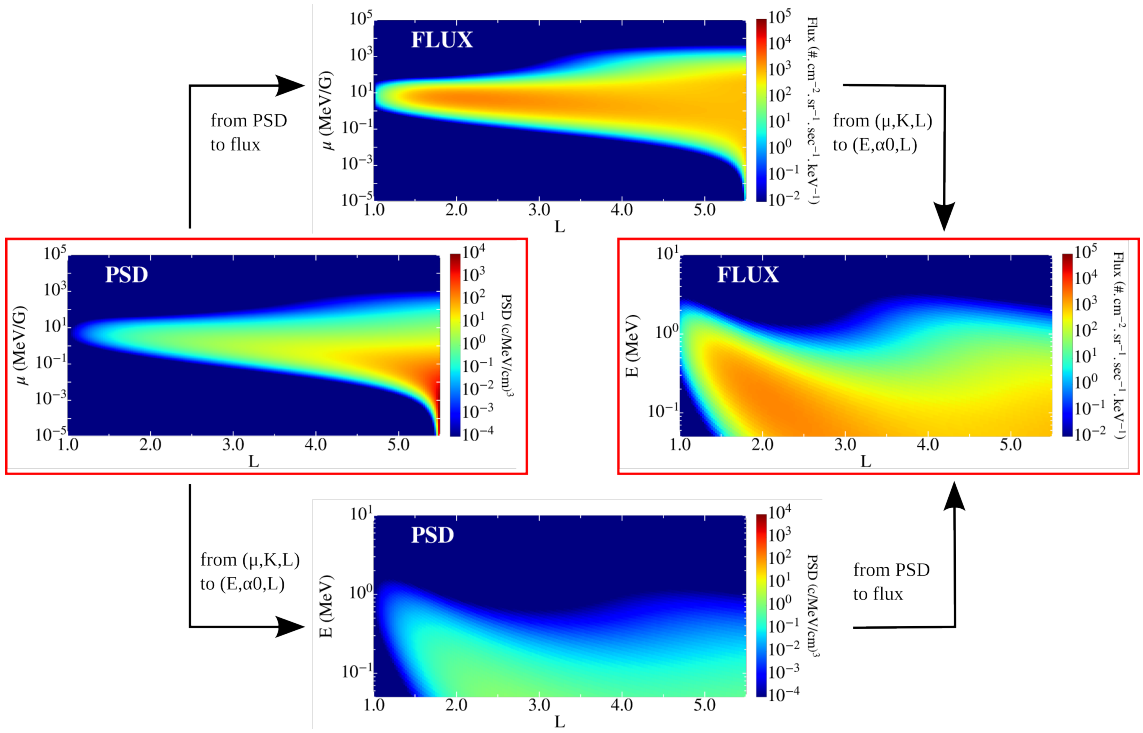

Figure 4.4 – Illustration of the transformation from the adiabatic space (μ, K, L) to the physical space (E, α_0, L). The left panel represents the steady PSD f_∞ solution of the steady reduced Fokker-Planck equation and computed for the parameters D_{LL}^E and τ depicted above, for $K = 0.0$ $G^{1/2}R_E$. From this solution, one can either compute the corresponding flux in the (μ, L) plane (top-center panel) or the corresponding PSD in the (L, E) plane (with $\alpha_0 = 90$ degrees, bottom-center panel). The desired flux in the (L, E) plane can therefore be obtained (right panel). Both paths are equivalent

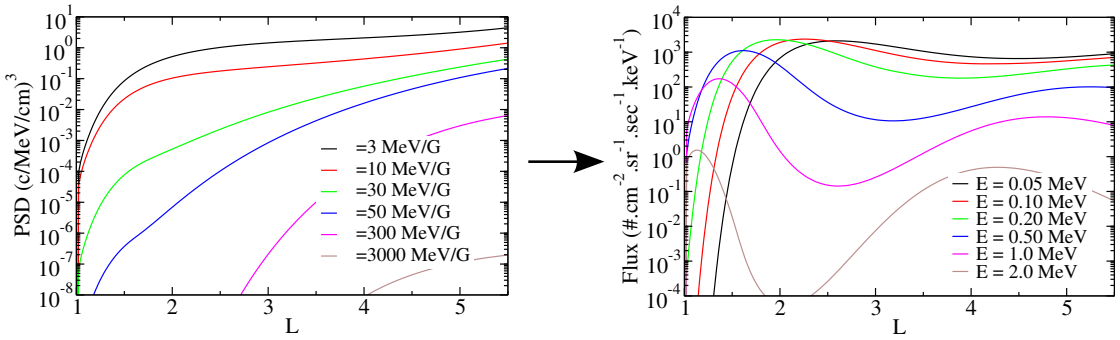

Figure 4.5 – The two panels represent respectively a cut of the PSD versus L plotted in Figure 4.4 for several values of μ (left) and a cut of the fluxes versus L at some chosen energies (right). The latter highlights the structure of two radiation belts separated by a slot region, particularly for energies above 500 keV, as shown in (*Lyons and Thorne*, 1973).

4.4 Reproducing the S shape structure of the equilibrium

4.4.1 Model in use

4.4.1.a Radial diffusion coefficients

We now solve equation (2.57) with three different expressions for the radial diffusion coefficient, which are plotted in Figures 4.6 and 4.7.

We use the well-known *Brautigam and Albert* (2000) radial diffusion coefficient. This model is composed of two components. The first is the D_{LL}^{E} (electrostatic) term from *Lyons and Thorne* (1973), but corrected with the K_p dependence introduced in (*Brautigam and Albert*, 2000),

$$D_{LL}^{E}(\mathrm{BA}) = 0.25 \times \left(\frac{cE_{rms}}{B_E}\right)^2 \left(\frac{T}{1+(\omega_d T/2)^2}\right) L^6$$

with $E_{rms} = 0.26 \times (K_p - 1) + 0.1$ (mV/m), $T = 0.75$ hours (exponential decay time) and for which ω_d is the electron drift frequency related to the dipole field expressed by equation (2.30). The latter is combined with the electromagnetic diffusion coefficient D_{LL}^{M} term of (*Brautigam and Albert*, 2000)

$$D_{LL}^{M}(\mathrm{BA}) = 10^{0.506K_p - 9.325}\, L^{10}.$$

It is referred as the $D_{LL}^{EM}(\mathrm{BA})$ model. The latter model is commonly used in most 3-D radiation belt simulations, as in the VERB-3D code (*Shprits et al.*, 2009; *Subbotin et al.*, 2010) or in LANL DREAM3D (*Tu et al.*, 2013). However, *Kim et al.* (2011) suggested that the radial diffusion coefficient from *Brautigam and Albert* (2000) might overestimate the electrostatic component D_{LL}^{E} at high K_p.

Hence, we use a second formulation that only uses the electromagnetic part of the radial diffusion coefficient of *Brautigam and Albert* (2000), further indicated as $D_{LL}^{M}(\mathrm{BA})$.

The third radial diffusion coefficient into consideration is the electric and magnetic radial diffusion coefficients obtained by *Ozeke et al.* (2014) based on statistical representations of ULF wave power. This model, indicated here as $D_{LL}^{EM}(\mathrm{O})$, is also widely used in radiation belts simulations (e.g., *Kim et al.*, 2016; *Li et al.*, 2016b; *Ma et al.*, 2016). The expressions for the electric and magnetic components are respectively (*Ozeke et al.*, 2014, equations (20) and (23))

$$D_{LL}^{E}(\mathrm{O}) = 2.16 \times 10^{-8}\, 10^{0.217L + 0.461K_p}\, L^6$$

and

$$D_{LL}^{M}(\mathrm{O}) = 6.62 \times 10^{-13}\, 10^{-0.0327L^2 + 0.625L - 0.0108K_p^2 + 0.499K_p}\, L^8.$$

As a last comment, let us keep in mind the concern that radial transport during individual events can exhibit large deviations from average transport rates because of nondiffusive character of the transport (e.g., *Ukhorskiy and Sitnov*, 2013; *Ukhorskiy et al.*, 2014) as well as substantial deviations due to impulsive transport for energies between tens and hundreds of keV (e.g., *Turner et al.*, 2015). It may then not be an appropriate model to accurately describe filling or emptying of the slot region in particular during active times.

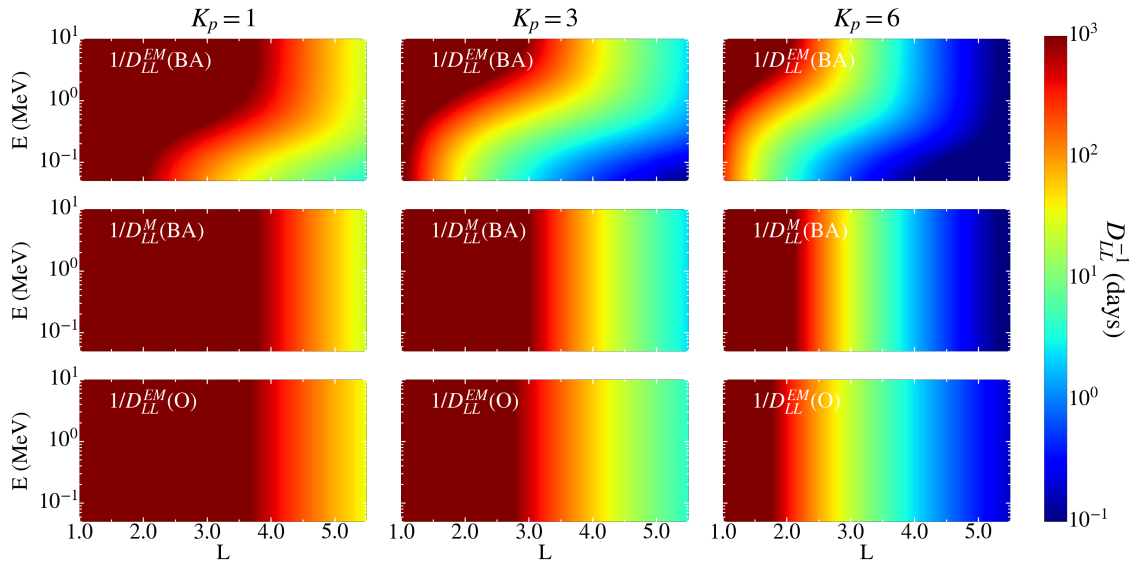

Figure 4.6 – Radial diffusion times (which are defined as the inverse of radial diffusion coefficients) plotted in the (L, E) plane for different geomagnetic indices $K_p = 1$ (first column), $K_p = 3$ (second column) and $K_p = 6$ (third column). The first row shows the radial diffusion time calculated from the radial diffusion coefficient D_{LL}^{EM}(BA) computed from *Brautigam and Albert* (2000), including its electrostatic and electromagnetic components. The second row shows the diffusion time that is only calculated from the electromagnetic part D_{LL}^{M}(BA) of the latter model. The third row shows the diffusion time induced by the radial diffusion coefficient D_{LL}^{EM}(O) from *Ozeke et al.* (2014) (with both electrostatic and electromagnetic components). Both D_{LL}^{M}(BA) and D_{LL}^{EM}(O) are comparable, while the D_{LL}^{EM}(BA) exhibits larger values.

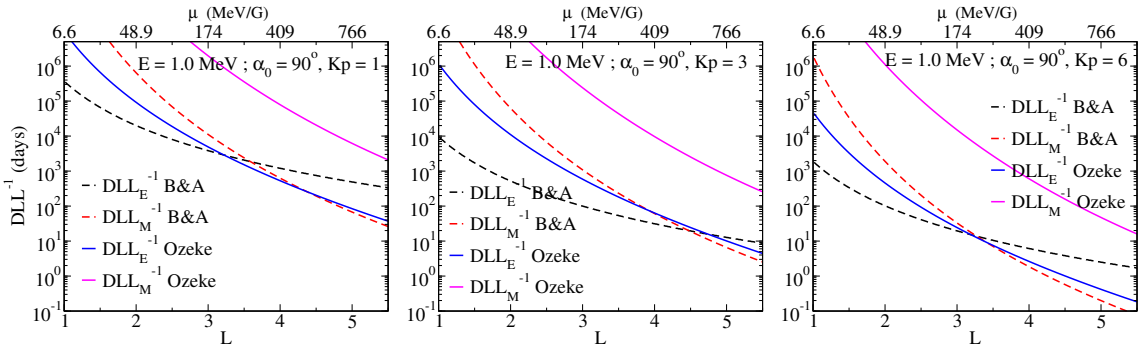

Figure 4.7 – Radial diffusion times, similarly to Figure 4.6, for $E = 1.0$ MeV, including the electrostatic and electromagnetic component of D_{LL}(BA) and the electric and magnetic componenets of D_{LL}(O). For high K_p values, the diffusion timescales can be as low as a few hours. Let us emphasize that there is no direct comparison to make between D_{LL}^{E}(BA) and D_{LL}^{E}(O) on the first hand, and D_{LL}^{M}(BA) and D_{LL}^{M}(O) on the other hand, since, as mentioned in Chapter 2, *Brautigam and Albert* (2000) separated the radial diffusion coefficient into one electrostatic part and one electromagnetic part whereas *Ozeke et al.* (2014) did a split into an electric part and a magnetic part.

4.4.1.b Electron lifetimes

In the present study, we consider three pitch angle diffusion processes, one from Coulomb collisions and two from whistler mode wave-particle interactions induced by both hiss and chorus waves.

The Coulomb collision lifetime is taken from *Lyons and Thorne* (1973) and assumes Coulomb pitch angle scattering and, to a lesser extent, some energy loss.

The hiss lifetime model is the full and K_p-dependent fit model derived from numerical simulations (*Orlova et al.*, 2014) using the Full Diffusion Code (*Shprits and Ni*, 2009; *Orlova et al.*, 2012) that is formulated similarly to *Albert* (2005) and *Glauert and Horne* (2005). The calculations include high-order resonances (*Ripoll and Mourenas*, 2012), and lifetimes were calculated using the method of (*Albert and Shprits*, 2009) that accounts for a deep minimum of hiss scattering rates at intermediate pitch angles. Note that the latter is extrapolated below $L = 3$. The magnetic field model underlying the lifetime model is a dipole field for hiss since they are confined within the plasmasphere and the T89 magnetic field model (*Tsyganenko*, 1989) for chorus waves as they act at higher L-shells, for which the geomagnetic topology differs significantly from the dipole model (cf. Chapter 6). The variation of hiss lifetimes with both energy and L-shell are in agreement with previous works (e.g., *Meredith et al.*, 2007).

Similarly, electron lifetimes from chorus waves are taken from the recent work of *Orlova and Shprits* (2014), in which fits are also derived from full numerical simulations of $D_{\alpha\alpha}$. An extrapolation is made for $E > 2$ MeV. As statistics at high K_p were limited, the model may slightly underestimate the scattering rates for the times when K_p exceeds ~ 4 but gives rather accurate results for long-term calculations.

The hiss model is activated within the plasmasphere while the chorus one is activated only outside the plasmasphere, with the plasmapause location being determined as before from *Carpenter and Anderson* (1992).

The global electron lifetime τ accounting for Coulomb collisions as well as interactions with whistler mode hiss and chorus waves is the harmonic average of the corresponding lifetimes, i.e. $\tau = 1/(1/\tau_{\text{col}} + 1/\tau_{\text{hiss}} + 1/\tau_{\text{chorus}})$ (cf equation (2.58)). A last model considers $\tau \to \infty$, which corresponds to no loss and radial diffusion only.

4.4.2 Steady PSD and fluxes

Thanks to the K_p dependent models, we are able to present steady state solutions for different geomagnetic conditions, although the steady state solution can only be physically achieved if the time to reach equilibrium is shorter than the timescale of the changes in geomagnetic activity. Quiet geomagnetic conditions $K_p \sim 1$ can last up to several weeks. Moderate geomagnetic conditions $K_p \sim 3$ show a more pronounced variability and can last at this level during several days. Active geomagnetic conditions $K_p \sim 6$ result from sudden impulses and abrupt release of energy caused by geomagnetic storms. The associated timescale is much shorter and is about a few hours.

As before, we first perform the steady state solution f_∞ of the reduced Fokker-Planck equation, from which the corresponding steady fluxes are extracted and plotted in the usual (L, E) space. Here, we notice an interesting pronounced S-shape form of the inner edge of the outer belt found for the steady state at low and moderate geomagnetic activity (K_p= 1 or 3), which is much closer to the feature observed from the Van Allen Probes (*Reeves et al.*, 2016). The so-called S-shape structure can be formed at moderately low K_p for energies between 300 keV and 2 MeV, in the same range of energy as observed. The shape of the slot is strongly influenced by the dependence of electron loss rate on

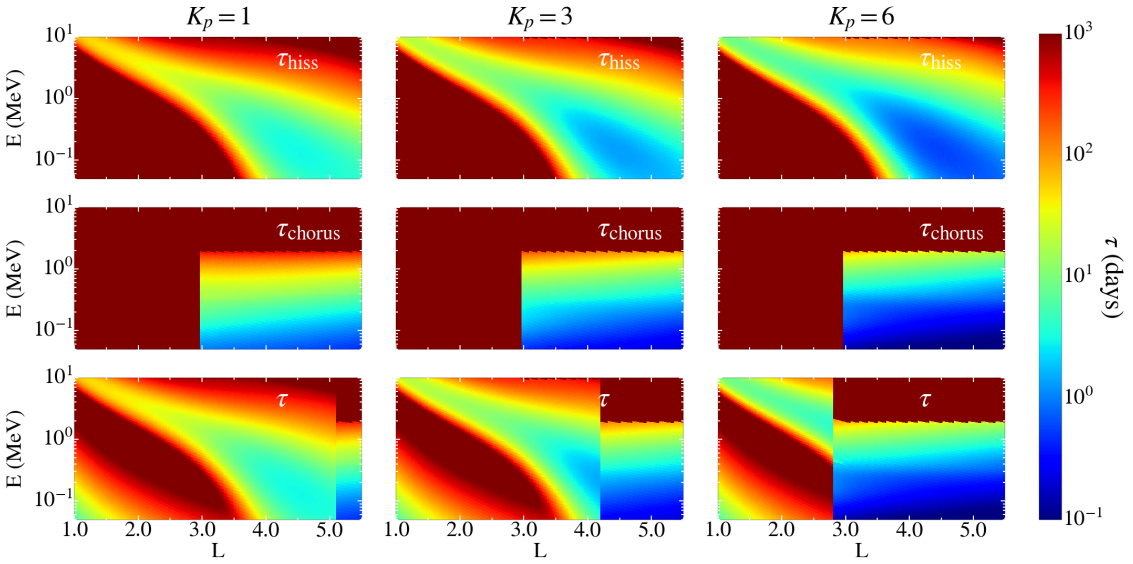

Figure 4.8 – Lifetimes models represented in the usual (L, E) plane for hiss waves (first row), chorus waves (second row) and with the combination of both waves in addition to Coulomb collisions (third row). The columns relate the lifetime models to the geomagnetic activity: $K_p = 1$ (first column), $K_p = 3$ (second column) and $K_p = 6$ (third column). The hiss lifetimes have been derived by *Orlova et al.* (2014) and the chorus lifetimes are taken from *Orlova and Shprits* (2014).

energy and L-shell (unless radial transport is either too weak or too strong and hides the loss as discussed below).

Since the hiss loss terms are quite similar between the original historical model from *Lyons and Thorne* (1973) (see Figure 4.3) and the model at stakes (Figure 4.8), although lower in the original model, we believe that the S-shape was not well produced by the original model (see Figure 4.4, right panel) due to the absence of the D_{LL}^{M} component in the radial diffusion coefficient, which causes the radial transport at large L-shells to be reduced. We recall that D_{LL}^{M} is considered a key aspect of the modeling of the outer belt dynamics (e.g., *Shprits et al.*, 2008b; *Tu et al.*, 2013).

The steady fluxes obtained from the D_{LL}^{EM}(BA) model (Figure 4.9, first row) exhibit a more pronounced enhancement than their counterparts performed from the D_{LL}^{M}(BA) model (Figure 4.9, second row) and the D_{LL}^{EM}(O) model (Figure 4.9, third row). In the D_{LL}^{EM}(BA) model, transport may indeed be too strong, as suggested in (*Kim et al.*, 2011), and incoming electrons fill up the slot. At low geomagnetic activity (first column of Figure 4.9), the S-shape is formed whatever the model into consideration. Its location encompasses rather high energies (between 300 keV and 2 Mev) in the D_{LL}^{EM}(BA) model (first column, top panel) compared with the D_{LL}^{M}(BA) and D_{LL}^{EM}(O) models (the two last panels of the first column), for which the S-shape is persistent between 100 keV and 2 MeV. Let us notice that even at this low K_p value, the D_{LL}^{EM}(BA) model brings high energy particles (about 1-2 MeV) in the inner belt, which is currently not observed (*Fennell et al.*, 2015) and therefore unphysical. Since the diffusion transport is weaker in the two last models, the electrons are not able to reach the inner belt. At higher geomagnetic activity ($K_p = 3$) the dynamics are controlled by fast radial transport that washes out the S shape at low energy (Figure 4.9, center-column) for the D_{LL}^{EM}(BA)

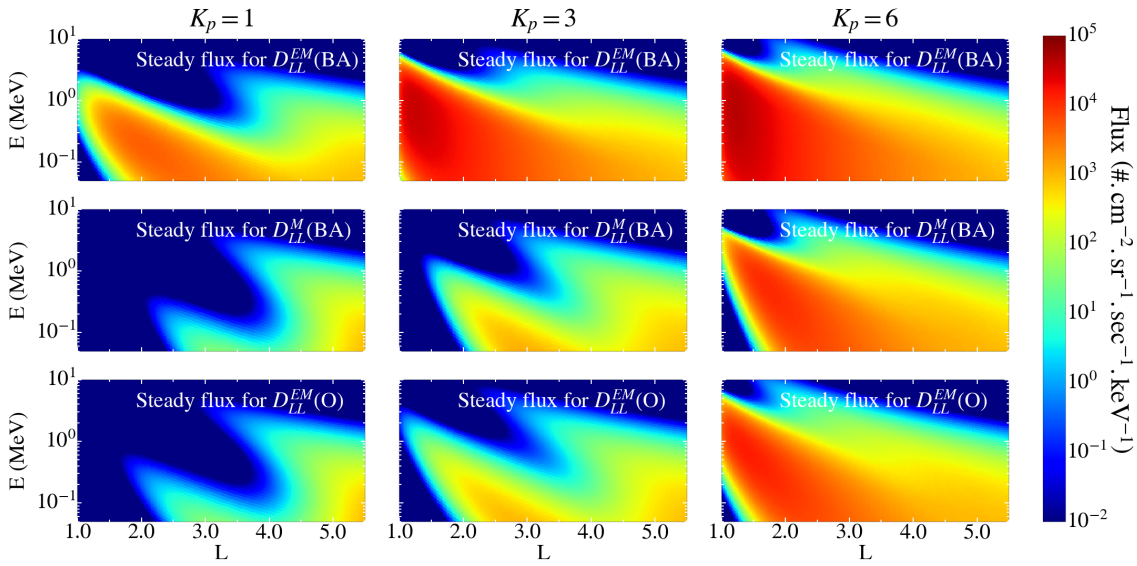

Figure 4.9 – Steady fluxes are represented with respect to L-shell and energy. The different rows correspond to the three different models of the radial diffusion coefficient taken into account: D_{LL}^{EM}(BA) (first row), D_{LL}^{EM}(BA) (second row) and D_{LL}^{EM}(BA) (third row). As before, the different columns (from left to right) correspond to K_p=1, 3 and 6 respectively.

model, showing a inner belt filled with high energy electrons. However, the S-shape persists for the D_{LL}^{M}(BA) and D_{LL}^{EM}(O) models. The electrons hardly reach the inner belt. At $K_p = 6$, the S shape is reduced and shifted up to very high energy and lower L-shells, remaining slightly visible at $E > 3$ MeV. It corresponds to L-shell and energy at which radial transport gets slow enough so that losses from waves can dig their slot. One can check that the energy range of the slot matches well the L-shells at which losses from hiss waves are strong, i.e., $L \sim 2$ for 3-4 MeV electrons and $L \sim 3$ for 1 MeV electrons (e.g., *Ripoll et al.*, 2014a,b, 2016a). If the inner belt is full of electrons covering the entire energy range for the first model, the inner belt is rather preserved from low energy electrons in the two last models, for which only electrons with energies about 1-3 MeV can penetrate. The last results are quite surprising because no observations stated such a behavior during high geomagnetic activity. In particular, it seems that considering a steady flux for high values of K_p is a doubtful approach in view of the recent observations (*Fennell et al.*, 2015).

The question we have to answer now is whether or not the equilibrium state is relevant. To do that, we perform in the next section the dynamical evolution of the electron fluxes and define a so-called equilibrium time for which the flux is considered close to its steady structure. If the equilibrium time is below the timescale variability of the geomagnetic conditions for K_p=1, 3 and 6, then the equilibrium state is relevant, otherwise it is not. In what follows, the numerical simulations are only performed with the radial diffusion coefficient D_{LL}^{EM}(O) from *Ozeke et al.* (2014). As mentioned above, this choice is justified with its steady solution at moderate K_p, showing that only a small part of high energy electrons can penetrate the inner belt, in accordance with the observations made by *Fennell et al.* (2015) and with the S shape predicted by (*Reeves et al.*, 2016).

4.5 Time to reach the equilibrium state for dynamical solutions

4.5.1 Definition

Similarly to what we have done in the previous section, we define the equilibrium time t_{eq} as the time required to nearly reach the value of the steady state solution, i.e. the first time t for which

$$|f(\mu, L, t) - f_\infty(\mu, L)| \,/\, |f_\infty(\mu, L)| < \varepsilon,$$

with $\varepsilon = 0.1$, limited to 365 days. The time taken for the PSD to first be included within 10% of the value of the equilibrium state shall be referred to as "time to equilibrium". Let us mention that the parameter t_{eq} is always defined because f_∞ is never zero due to the nonzero outer boundary condition at $L_M = 5.5$. For the specific (L, E) locations at which nothing evolves and for which the PSD remains below 10^{-20} $(\mathrm{c/cm/MeV})^3$, the equilibrium time t_{eq} is not plotted and the corresponding figures show therefore empty white regions. We present the dynamics and the time to reach equilibrium for two cases of interest in the next paragraphs.

4.5.2 Injection following a massive dropout

We first consider the case of a constant injection of electrons within an empty magnetosphere (i.e. when $f_0(\mu, L) = 0$), as if a massive dropout had occurred previously. The static outer boundary condition is still taken from (4.2). An example of a massive dropout is reported during the 17 March 2013 storm event (*Ukhorskiy et al.*, 2014). We now numerically solve the time-dependent reduced Fokker-Planck equation governing the evolution of the PSD in the (μ, L) plane. The results in PSD are presented in Figure 4.10 for K_p=1, 3 and 6 respectively in the first, second and third column at different times until 100 days (rows 1 to 4) and compared to the steady state (row 5). The very last row of Figure 4.10 represents the corresponding equilibrium time in the (μ, L) plane.

The dynamics of radial diffusion is faster with increasing geomagnetic activity, enabling the electron population to penetrate deeper in the inner belt. The calculated equilibrium times prove that it would require about 100 days to fill the inner belt. We now convert the obtained PSD into fluxes projected on the (L, E) space, which enables us to obtain the dynamics of the electron flux population in the radiation belts, as shown in Figure 4.11.

At $K_p = 1$ (left column of Figure 4.11) and $K_p = 3$ (middle column), the aforementioned S-shape structure starts forming after 10 days, which proves that this shape does not necessarily reflect an equilibrium state. We can also compare the dynamics of Figure 4.11 with the behavior of the fluxes induced by radial diffusion only (i.e. for which all the losses have been turned off) presented in Figure 4.12. The latter figure does not show any typical S-shape, which reveals that this specific feature (S-shape) is caused by atmospheric scattering with hiss waves.

As time evolves, this structure becomes an increasingly obvious feature, as observed from the Van Allen Probes during quiet storm recovery periods (*Reeves et al.*, 2016; *Ripoll et al.*, 2016b, 2017). The long-term (evolution times above 100 days) and the steady state solutions are highly wave-dependent, characterized by a wide slot region and an outer belt made of mostly low energy (below 500 keV) electrons. At $K_p = 1$, the inner belt is never filled with high energy electrons, which is consistent with the current observations form the Van Allen Probes. With the model in use, a "barrier" is indeed observed for

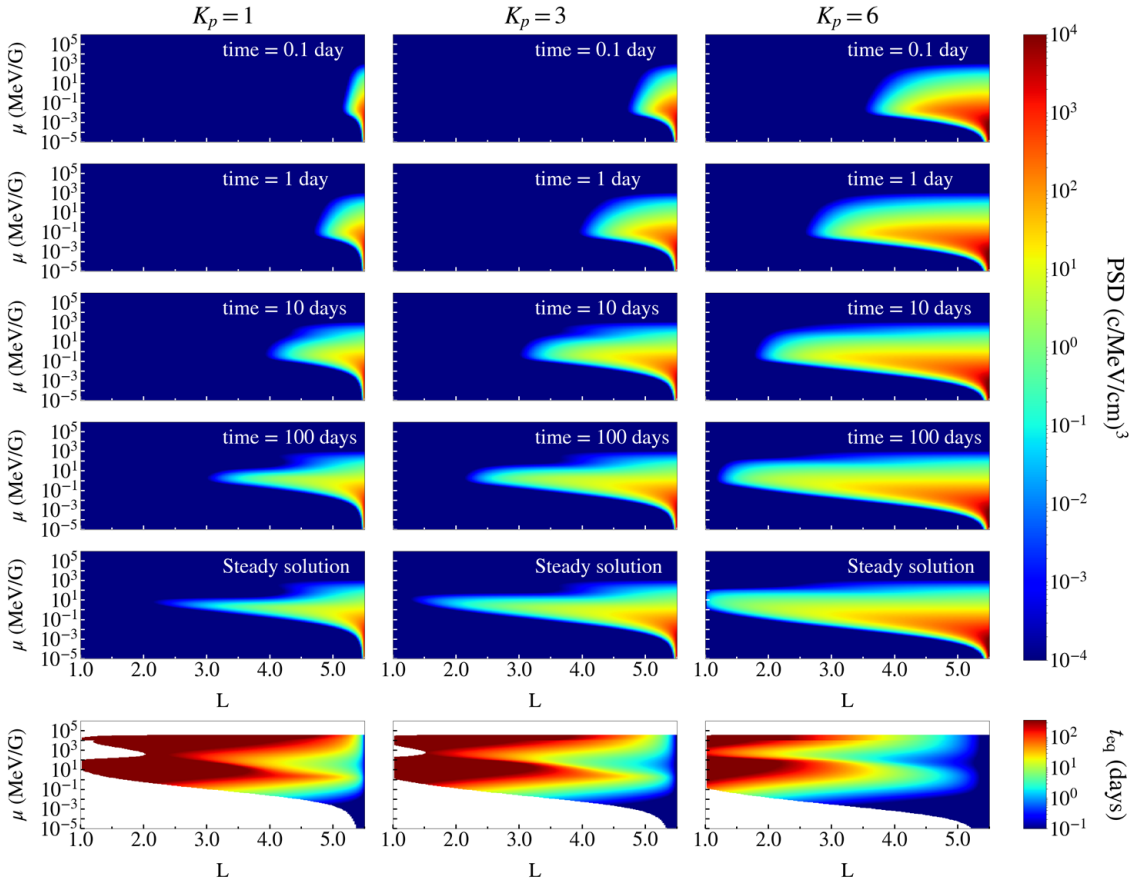

Figure 4.10 – Evolution of PSD versus time in the (μ, L) space for $K = 0$ (equatorial particles), snapshot in the successive rows at given times $t = 0.1$, 1, 10, 100 days. The fifth row corresponds to PSD at steady state (i.e. for which $t \to \infty$). The very last row depicts the necessary time to reach the aforementioned steady state (within 10% accuracy) in the (L, E) plane. This time is referred as "equilibrium time" t_{eq}. The three columns represent the three geomagnetic indices, from $K_p = 1$ (left) to $K_p = 3$ (middle) and $K_p = 6$ (right). We recall that the radial diffusion coefficient involved corresponds to the formulation of *Ozeke et al.* (2014), and both hiss and chorus waves are activated (inside and outside the plasmasphere respectively) and are derived from *Orlova et al.* (2014); *Orlova and Shprits* (2014).

ultrarelativistic energies (*Baker et al.*, 2014b). For $K_p = 3$, the S shape is not visible before the first 10 days of simulation. It would also require more than 100 days for high energy electrons to eventually get trapped into the inner belt. For $K_p = 6$, the slot region starts forming around 100 days. The long-term and steady solutions at large K_p build an inner belt that is constituted of electrons whose energy is above 1 MeV, which is not observed (*Fennell et al.*, 2015; *Baker et al.*, 2014b). This surprising result might be due to the fact that we have implicitly assumed that active conditions ($K_p \sim 6$) persist longer (on the timescale of 100 days) than they would in reality (timescale of a few hours). It may also result from inaccuracies in the lifetime models at large K_p ($K_p > 5$).

Figure 4.11 also represents the equilibrium time t_{eq} that we have defined above in the (L, E) plane. Such a description in terms of the equilibrium time helps us to find out which electrons have reached their equilibrium state, and for which ones we could infer

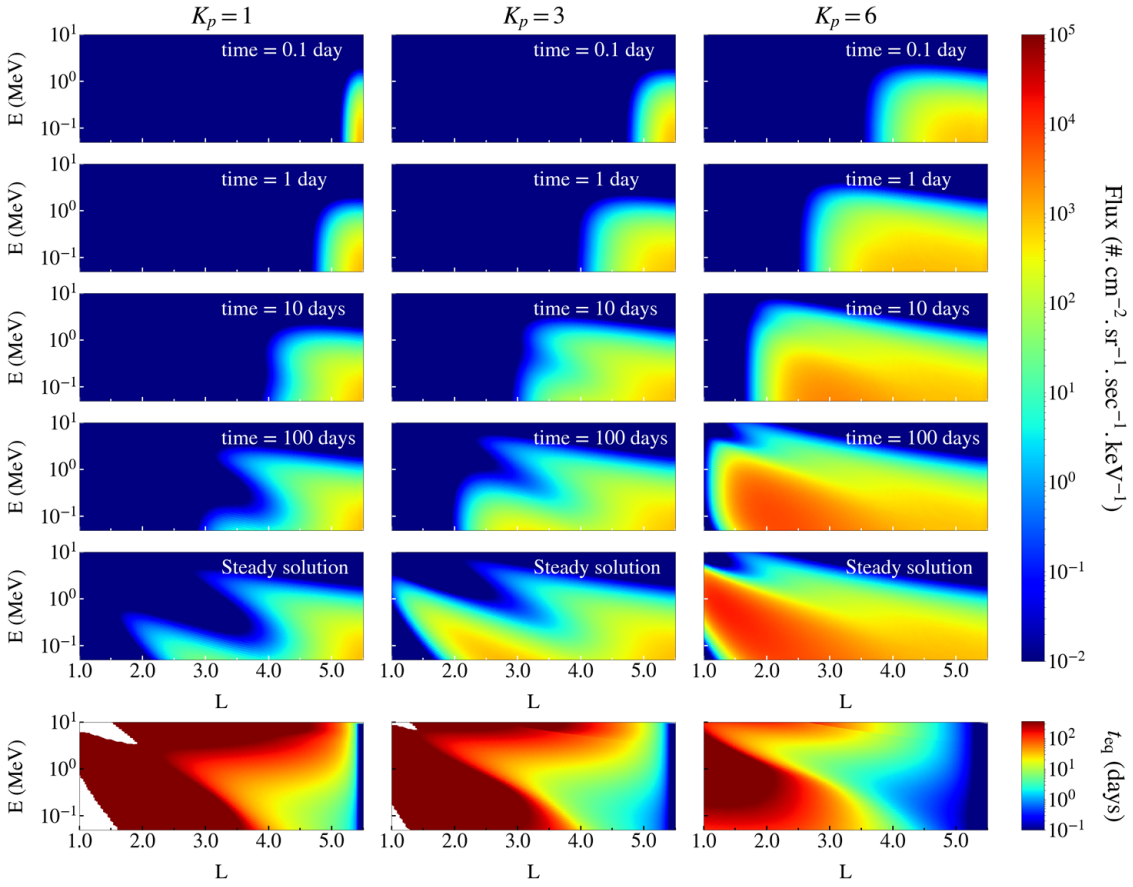

Figure 4.11 – Evolution of electron fluxes versus time in the (L, E) space, for $\alpha_0 = 90$ degrees, according to different times and geomagnetic activities (same as Figure 4.10). The last row represents the associated equilibrium times in the (L, E) space.

that wave scattering balances radial diffusion.

The equilibrium time depicted in the (L, E) space exhibits some small values (below 10 days) forming a narrow region inside which low losses, small diffusion, and large trapping prevail. Outside these regions, hundreds of days (or more) are needed to reach the PSD value of the equilibrium state. On the other hand, the prescribed boundary condition at $L_M = 5.5$ implies that the PSD of the dynamical solution reaches the PSD value of the equilibrium state almost immediately (as emphasized by the thin vertical blue line close to $L = 5.5$). If the boundary was pushed further out to L_M^{new}, the equilibrium time would be increased by the time it takes for the electron dynamics to propagate from L_M^{new} to $L_M = 5.5$. Increasing K_p shows that the faster the processes are, the less time is needed to reach the PSD value of the equilibrium state, which translates to smaller t_{eq} for larger K_p. In general, obtaining the PSD values of the equilibrium state at all L, as assumed in (*Lyons and Thorne*, 1973), is very unlikely to occur with the models in use. The equilibrium values may then be reached only for selected values of L, E, and K_p.

For $K_p = 1$, a prolonged geomagnetically quiet period may last for up to 10 days or longer. The equilibrium state could then be reached in 1 to 10-20 days that correspond to locations from blue to green-yellow color regions of Figure 4.11 (last row, first column). For such an extended quiet time, the source population is steady, and our simulations show that it is possible to reach equilibrium for L-shells above approximately 4 and

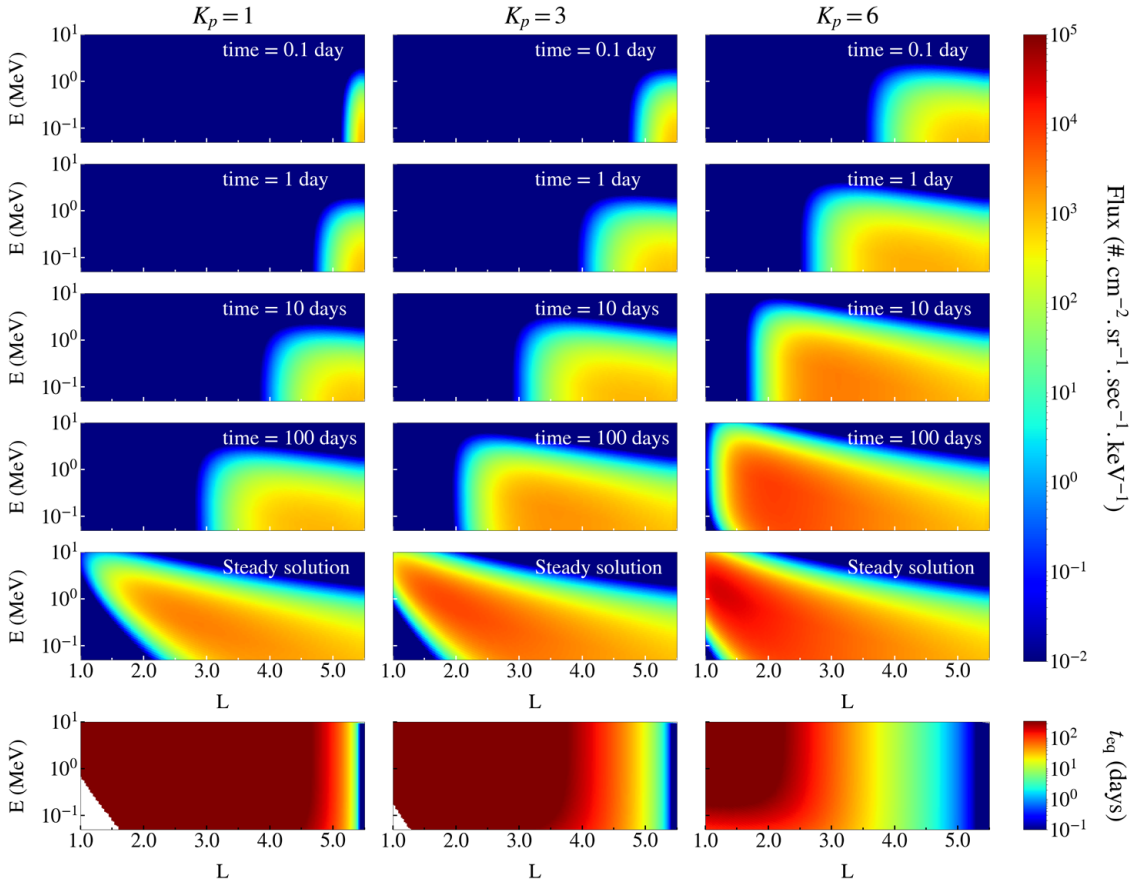

Figure 4.12 – Evolution of electron fluxes versus time in the (L, E) space, for $\alpha_0 = 90$ degrees, with no loss (radial diffusion only). The last row shows the corresponding equilibrium times. We notice a reasonably good agreement between the equilibrium times of the last row and the diffusion times $(1/D_{LL})$ of the last row of Figure 4.6, allowing us to think that there exists a strong correlation between the equilibrium time and the global evolution time of the system. This specific point is clarified and discussed in the next section.

energies below 600 keV. It corresponds to $E \sim 200$ keV starting as low as $L > 3.7$ for $K_p = 1$ or to $E < 400$ keV for $L > 4$ that we now list.

For $K_p = 3$, these elevated geomagnetic conditions may last for several days or even weeks, when solar wind activity is dominated by streams with high solar wind speed. Hence we assume that the value of the equilibrium state could be reached in 1 to 10-20 days in the blue to green regions. In this case, equilibrium may be reached for $L > 3$ for electrons with energies below ~ 600 keV. The dynamics of electrons at energies lower than approximately 100 keV during such disturbed conditions are most likely dominated by the convective transport (absent in the current modeling). For $L > 3.5$, the equilibrium state can be reached for energies between 200 keV and 1 MeV.

During storm time conditions ($K_p = 6$), seen during coronal mass ejection driven storms, the elevated K_p lasts from a few hours to a day. The duration of such elevated K_p is limited to the time of passage of the magnetic cloud and to the period when the magnetic field has a southward component (which is required to allow substorms to form on the night side, as depicted in Chapter 1). We choose then to look for the regions

for which t_{eq} is of the order of one day or below (i.e. the blue region) so as to identify regions in (L, E) where the value of the equilibrium state can feasibly be reached. Our calculations show that the value of the equilibrium state may be reached only for $L > 4$ and $E > 300$ keV, provided that the boundary is kept constant. However, dropouts due to loss to the magnetopause, outward transport, and injections that can be significant at $L > 4$ would most likely not allow for the values of the equilibrium state to be reached, except for, possibly, a very narrow region in energy and L-shell (i.e. $E \sim 400 - 500$ keV at $L = 4$).

Assuming that L-shells larger than 4 are often perturbed by daily injections, as one can witness looking at long time periods (for instance, HEO observations over many years at $L = 4$ (*Ripoll et al.*, 2014b)), we now restrict our interest to the regions below $L = 4$. Only small regions in (L, E) space can feasibly reach the value of the equilibrium state: $E \in [200, 300]$ keV for $L \in [3.7, 4]$ at $K_p = 1$, $E \in [0.6, 1]$ MeV for $L \in [3, 4]$ at $K_p = 3$, and $E \sim 300$ keV for $L \in [3.5, 4]$ at $K_p = 6$, assuming no new incoming electrons.

4.5.3 Decaying saturated belts

Finally, we look at the dynamic evolution of a saturated magnetosphere, following a massive injection, losing its electrons from both wave scattering and outward radial diffusion. For this purpose, we consider an initial condition higher than the steady state (the latter being imposed by the static boundary outer boundary condition (4.2)), such that $f_0(\mu, L) = r f_\infty(\mu, L)$, with r=2, 10 and 100. Again, the static outer boundary condition is built on (4.2). The dynamics are shown for $K_p = 3$ in Figure 4.13.

The time to decay to within 10% of the value of the unmodified equilibrium state is also plotted in Figure 4.13 for $K_p = 3$. In general, the saturated inner belt and inner slot regions take hundreds of days and more before reaching the value of the equilibrium state. If the initial state is close to the steady state ($f_0(L) = 2f_\infty(L)$), it is considered feasible to reach the value of the equilibrium state if t_{eq} is less than 10 days for $K_p = 3$. This occurs for a large domain (all energies between $L = 2$ and $L = 4$) when the initial state is only a slight modification of the equilibrium state (first column of Figure 4.13). Otherwise, with a saturated magnetosphere (by a factor 10 or more), there are small windows of (L, E) in which it is feasible to reach the values of the equilibrium state below $L = 4$, among which a triangular region at $K_p = 3$ along the line of dominant hiss scattering for $L \in [3.5, 4]$ that includes energies close to 1 MeV at $L = 3.5$ and energies close to $400 - 500$ keV at $L = 4$. At large L-shell ($L > 5$), outward radial diffusion is very efficient at removing an excess of electrons, and times to reach the equilibrium are quite small due to the proximity of the boundary condition.

We also look at a uniformly saturated magnetosphere, $f_0(\mu, L) = r f_\infty(\mu, L_M) =$ constant, with r=2, 10 and 100 as before. The dynamics and time to equilibrium are plotted in Figure 4.14. Solutions evolve similarly, with different shapes of the flux determined by the initial conditions. The time to reach the value of the equilibrium state is longer because the dependence of the initial condition on L is less similar to the equilibrium state, which is consistent with the previous analytical results presented in Table 3.4. However, its overall profile conserves the same shape.

Simulations of the evolution after fast massive injections ($f_0(L) = 100 f_\infty(L_M)$ and $f_0(L) = 100 f_\infty(L_M)$) clearly show that the time to reach equilibrium strongly depends on the initial condition. For typical increases by 2 orders of magnitude, our calculations show that the time to reach equilibrium is longer than the characteristic times of relatively constant geomagnetic conditions. The assumption of steady state is then likely to be invalid at all L-shells and energies. Finally, if one increases the flux boundary condition

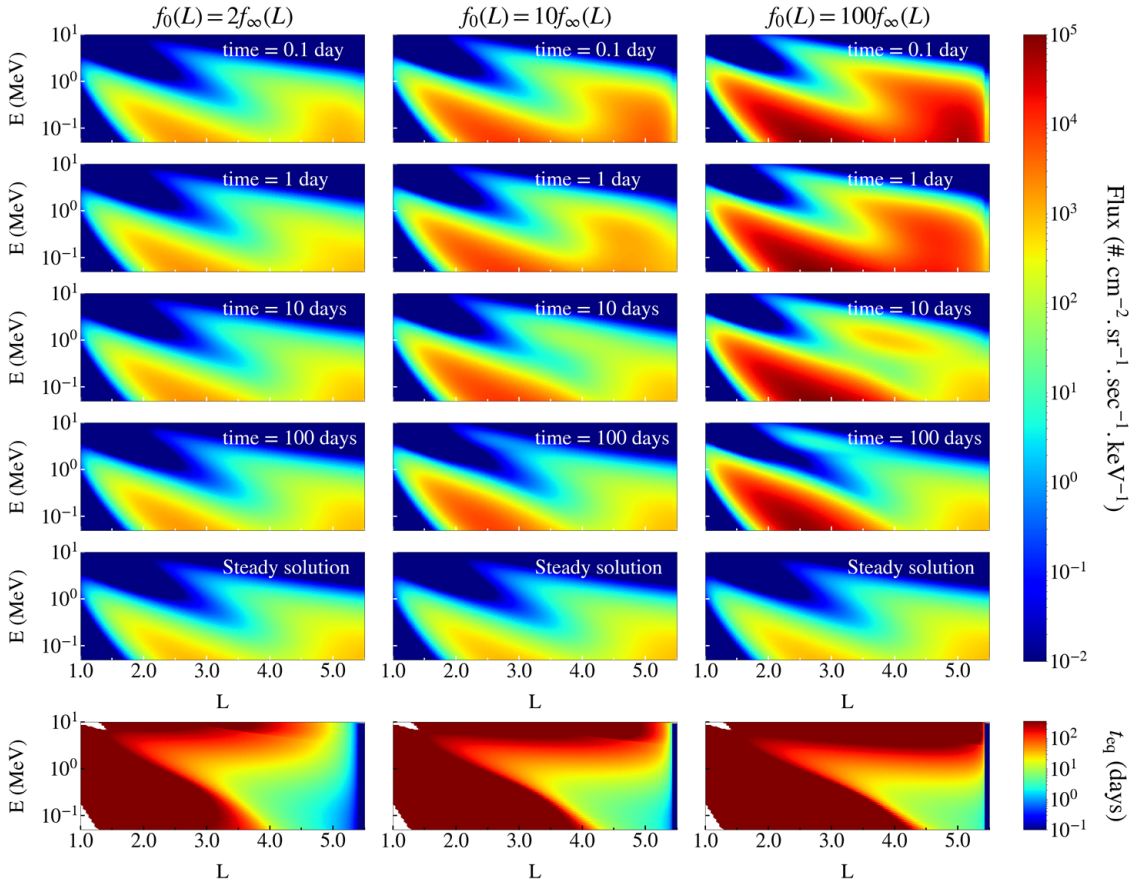

Figure 4.13 – Evolution of the electron fluxes in the (L, E) space for several days and computed for $K_p = 3$, respectively when the initial condition is 2 times the steady solution (left column), 10 times the steady solution (center) and 100 times the steady solution (right column). The last row depicts the associated equilibrium times, which are obviously higher when the initial condition is far from the steady state.

at L_M by a constant factor, then all fluxes are increased by that factor, but the timescales of the dynamics remain unchanged. Therefore, the time to reach equilibrium is not very sensitive to the boundary condition value itself, although it remains sensitive to the position of the boundary, as described in Table 3.4 in Chapter 3.

4.5.4 Properties of the equilibrium time

When the initial state is twice the equilibrium state, we check that it takes the same time to return to the value of the equilibrium state as it does when the initial state is an empty magnetosphere, i.e., the time to reach the values of the equilibrium state in Figure 4.13 is exactly the same as Figure 4.11, but slightly different from Figure 4.14. Results are reported in Figure 4.15 and are fully consistent with the derivation of the equilibrium time presented in Chapter 3 (particularly in Table 3.4).

As a last sensitivity test, we modified the criteria of the equilibrium time so that the value of the PSD only had to come within 50% of the value of the equilibrium state, rather than 10% as before. This test is performed to understand whether our 10% criterion could be too restrictive and leads to an overestimation of the times to reach

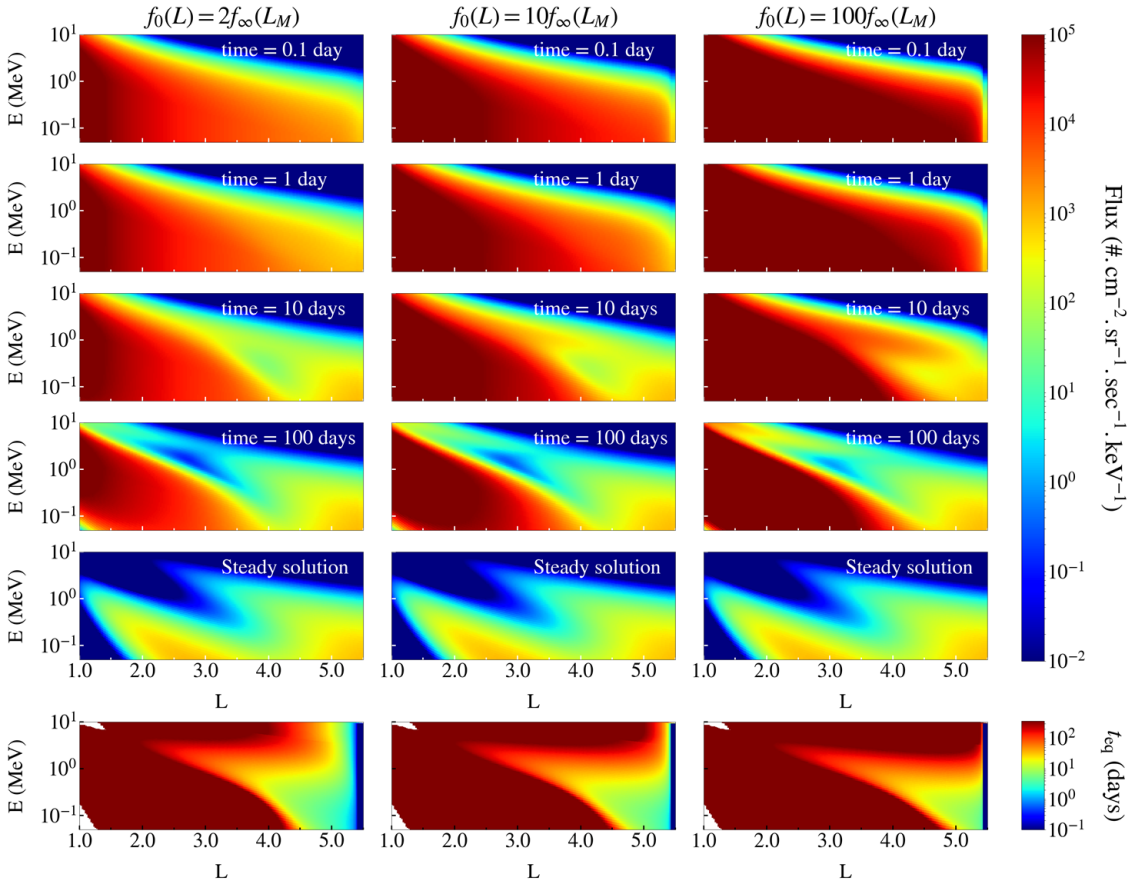

Figure 4.14 – Evolution of the electron fluxes in the (L, E) space for several days and computed for $K_p = 3$, respectively when the initial condition is uniform and equal to 2 times the steady solution at the outer boundary $L = L_M$ (left column), 10 times the steady solution at $L = L_M$ (center) and 100 times the steady solution at $L = L_M$ (right column). The last row depicts the associated equilibrium times.

the equilibrium state. Results are presented for $K_p = 3$ in Figure 4.16. We find that the time to reach the value of the equilibrium state conserves its characteristic shape. It is slightly reduced as expected, with the 10 days region being shifted inward by 0.5 L-shell or so. Regions where it is feasible to reach the value of the equilibrium state remain however quite similar.

4.6 Estimating the equilibrium time and the shape of the fluxes

As we have seen throughout this chapter, the equilibrium state is intrinsically linked with a balance between radial transport and losses (from pitch angle scattering). In this perspective, let us put forward two quantities that relate the radial transport with the losses. First, we define the ratio of both the characteristic time of radial diffusion ($\tau_D = 1/D_{LL}$) and pitch angle (τ), which is analogous to the Biot number (from Jean-Baptiste Biot, 1774-1862) in transitional heat transfer. That number compares conduction, here, radial diffusion, with forced convection, here, the f/τ loss term, with $1/\tau$ acting as a heat

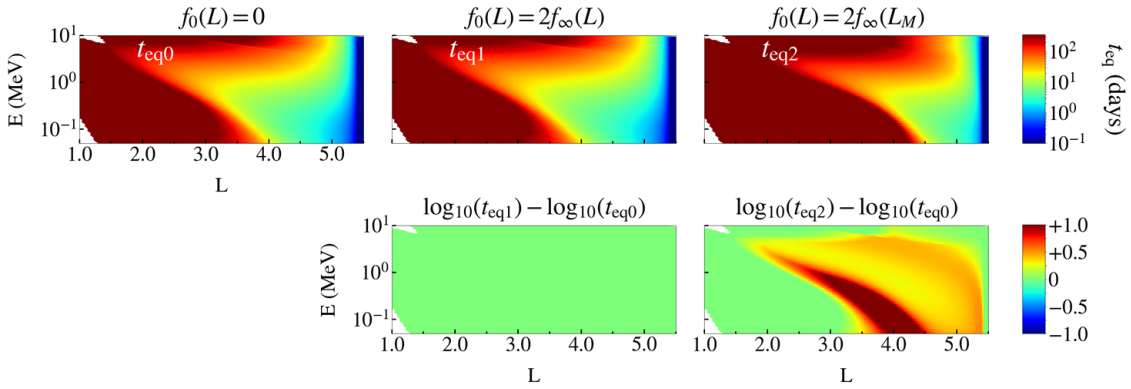

Figure 4.15 – The three top panels show the equilibrium time for $K_p = 3$ in the (L, E) space when the initial condition in PSD has been set to $f_0(L) = 0$ (empty magnetosphere, top-left, referred as t_{eq0}), when $f_0(L) = 2\,f_\infty(L)$ (top-center, referred as t_{eq1}) and when $f_0(L)$ is a constant value equal to $2\,f_\infty(L_M)$ (top-right, denoted t_{eq2}). The two bottom panels represent respectively the difference between $\log_{10}(t_{eq1})$ and $\log_{10}(t_{eq0})$ (bottom-center), and between $\log_{10}(t_{eq2})$ and $\log_{10}(t_{eq0})$ (bottom-left). As underlined in Chapter 3, there is no differences in equilibrium times between a flux that fills an initial empty magnetosphere and a flux that diffuses radially outward from a state that is initially exactly twice the equilibrium flux. However, there is some significant discrepancies in equilibrium times if the flux diffuses radially outward from a uniform state that is set to be twice the steady PSD value at the outer boundary. These results are fully consistent with the analytical estimations of the equilibrium times presented earlier in Table 3.4.

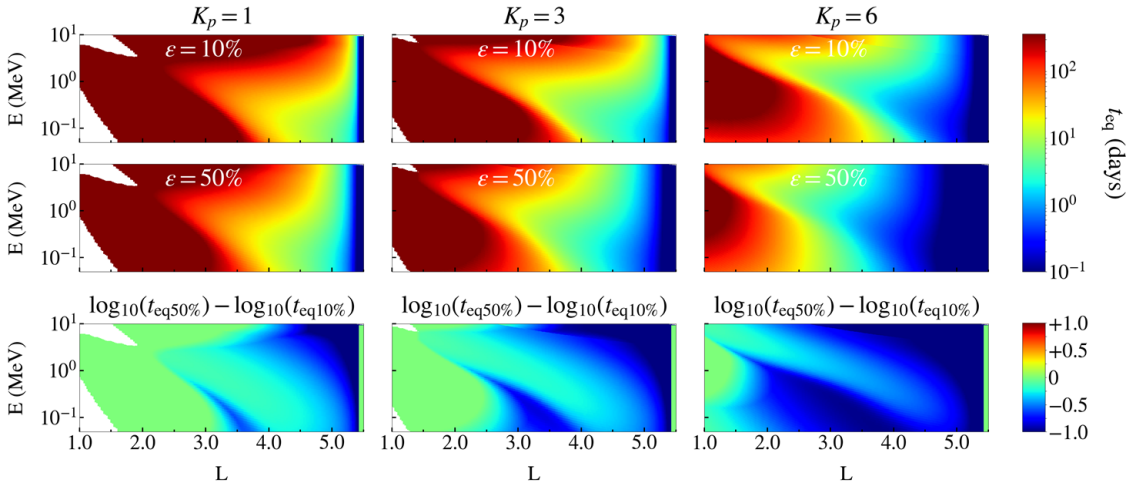

Figure 4.16 – The first row shows the equilibrium times, computed for $f_0(L) = 0$, when the convergence criterion is set to 10% for K_p=1, 3 and 6 (the three panels are identical to the equilibrium times displayed on the last row of Figure 4.11). The second row represent the equilibrium times inferred for a sensitivity test set to 50%. The last row represents the differences in $\log_{10}$ between both equilibrium times for each K_p.

transfer exchange coefficient relaxing f to zero. We also define the mean characteristic time τ_m as the harmonic average of all physical processes involved, $\tau_m = 1/(\tau^{-1} + \tau_D^{-1})$.

In Figure 4.17 we plot again the equilibrium times related to the three K_p at stake

(K_p=1, 3 and 6) starting from an empty initial condition (top) in view of the mean time (bottom). Both pictures show some very pronounced similarities in shape, indicating that the mean time is closely linked to the equilibrium time, and can be quickly estimated to predict if a given electron population has reached its steady state.

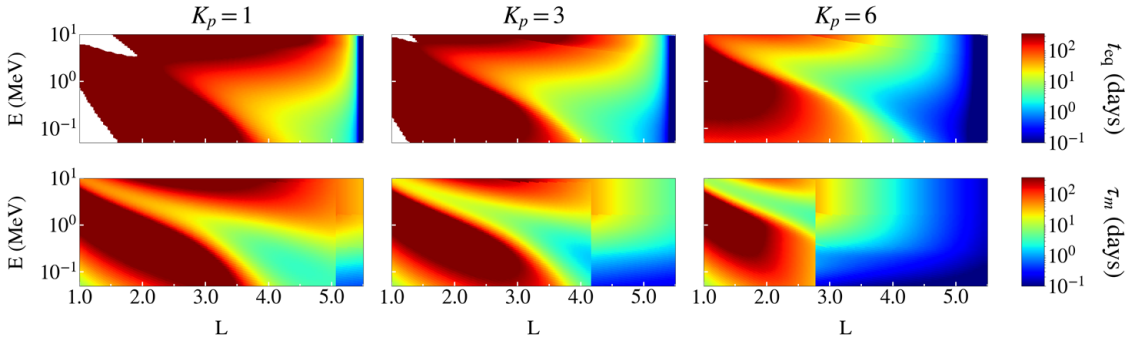

Figure 4.17 – The equilibrium times are represented in the usual (L, E) space on the first row, for different values of K_p. Below are plotted the corresponding mean times. As K_p increases, the equilibrium time t_{eq} and the mean time τ_m decrease in the same way.

Finally, the inverse Biot number, i.e. the ratio of loss over diffusion timescales (cf. Figure 4.18) gives a rough idea of the shape of the fluxes. Fluxes are large for large inverse Biot numbers; i.e. when diffusion is strong compared to scattering and reciprocally small for small inverse Biot numbers; i.e. when atmospheric scattering decays the fluxes.

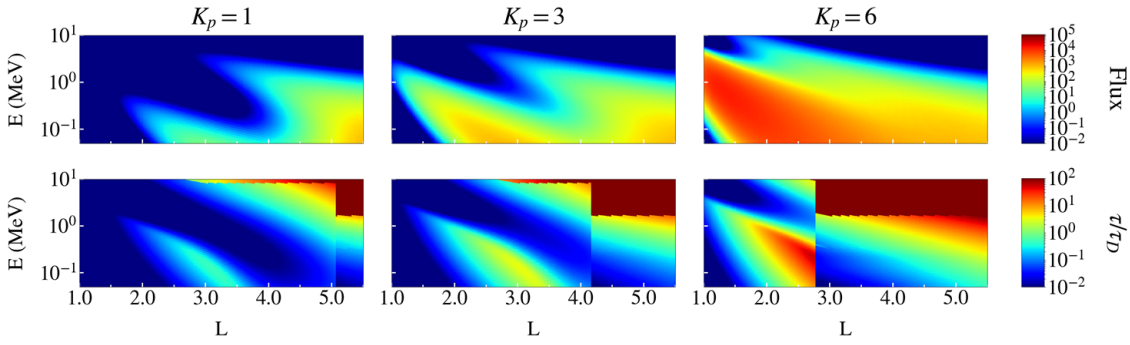

Figure 4.18 – The first row represents the steady fluxes for K_p=1, 3 and 6, while the second row displays the corresponding Biot number. Again the shapes of both quantities (steady fluxes and τ/τ_D) behave similarly when K_p increases.

4.7 Summary

In this chapter, we complement the study of (*Ripoll et al.*, 2016a) by reproducing the dynamics and the steady state (time-independent) of trapped electrons in the inner and outer radiation belts with a one dimensional radial diffusion equation (the reduced Fokker-Planck equation) associated with lifetimes from Coulomb collisions, whistler mode hiss and chorus waves that approximate the effects of electron scattering. The radial diffusion, hiss, and chorus processes are all K_p and energy-dependent. We first compute the equilibrium state presented either as PSD being a function of L-shell and μ, or as

fluxes being a function of L-shell and energy, in order to revisit the historical study carried out by (*Lyons and Thorne*, 1973). In particular, the steady electron flux obtained from this simulation shows a characteristic S shape in the (L, E) space, as observed by *Reeves et al.* (2016), suggesting specifically that this shape results from a balance between radial transport and losses induced by hiss waves.

We then compute additional steady solutions by using more recent models for both radial transport and wave scattering. The results lead to a more pronounced S shape, closer from what is currently observed from the Van Allen Probes. Among the different models, we select the radial diffusion coefficient from *Ozeke et al.* (2014), which proves to be the most accurate so far. Equilibrium electron flux profiles specifically follow the Biot number, for which large Biot numbers correspond to low fluxes and low Biot number to large fluxes.

Next, starting from different initial states of the PSD that simulate either a recently depleted or saturated inner magnetosphere, we compute the time-dependent PSD (and the corresponding flux) using academic inner and outer boundary conditions and, for each (L, E), we calculate the time that it takes for the PSD to first come within 10% of the value of the equilibrium state, which we call the equilibrium time. Focusing on the dynamics, the time-dependent flux plotted in the (L, E) plane at a given time at moderately low K_p presents a characteristic S shape near the inner edge of the outer belt, which appears to be similar to recent observations from the Van Allen Probes (*Reeves et al.*, 2016; *Ripoll et al.*, 2016b, 2017). This shape shows off at relatively early times such as 10 days, and is also persistent until obtaining the equilibrium state. These simulations confirm that this shape is due to the combination of radial transport and atmospheric loss, with a structure in the (L, E) plane dictated by the electron loss rate dependence in both energy and L-shell. As for the time to reach equilibrium, it proves to be a complex quantity that is governed by the initial state of the belts, the property of the dynamics (diffusion coefficients), and the size of the domain of computation. Its structure shows a rather complex form in the (L, E) plane, with trapping regions being localized in the inner belt and at high energy, where the dynamics are slower. In the same way the Biot number dictates the shape of the steady fluxes, the mean characteristic time of the dynamics imposes its signature on the shape of the equilibrium times. If the overall dynamical process is fast, the mean characteristic time is small and the time to reach equilibrium is the lowest. The latter has also to be compared to the timescale of the changes of the magnetospheric conditions in order to be a relevant physical quantity. If the time to reach equilibrium for a given (L, E) is less than the amount of time reasonable to suppose that a steady value of K_p could be observed, we propose that it is feasible to reach the equilibrium value at that particular (L, E) location, and we present regions in the (L, E) space for different K_p where the equilibrium state can be reached. It is shown that it is only feasible to reach the value of the equilibrium state for selected locations in energy, radial distance, and geomagnetic activity. While the periods when K_p stays relatively constant may be longer at very quiet geomagnetic conditions, the time to reach equilibrium is shown to be shorter during disturbed geomagnetic conditions ($K_p \geq 3$) when diffusion rates are higher. The time to reach equilibrium also tends to be shorter at higher L-shells, where radial diffusion is faster, but also at selected energies for which the electromagnetic waves provide most of the scattering.

For $K_p = 1$, as during extended solar minimum periods, our simulations show that it is possible to reach the value of the equilibrium state for L-shells above approximately 4 and energies below ~ 600 keV. For stable $K_p = 3$, as during high solar wind streams, the value of the equilibrium state may be reached for energies between 200 keV and 1 MeV

for $L > 3.5$. During storm time conditions, we show that the value of the equilibrium state may be reached only for $L > 4$ and $E > 300$ keV but, either magnetopause losses, outward transport, and/or injections would most likely not allow for the value of the equilibrium state to be reached, except for, possibly, a very narrow region in energy and L-shell. To summarize, restricting our interest to the deepest regions below $L = 4$ that are less disturbed by the outer belt dynamics, only small regions in (L, E) space can reach the value of the equilibrium state. These regions include $E \in [200, 300]$ keV for $L \in [3.7, 4]$ at $K_p = 1$, $E \in [0.6, 1]$ MeV for $L \in [3, 4]$ at $K_p = 3$, and $E \sim 300$ keV for $L \in [3.5, 4]$ at $K_p = 6$, assuming no new incoming electrons. At low or moderate K_p, we believe that it may be observable in nature for these energies after ~ 10 days of stable conditions. Simulations of the evolution after fast massive injections show that the time to reach the value of the equilibrium state is longer than times of relatively constant geomagnetic conditions, and thus, the assumption of steady state is then unlikely to be valid for entire belts at all radial distances and energies.

Finally, the present analysis challenges the historical guess of two well defined radiation belts at equilibrium for any L-shell of energy. It rather allows us to determine when the steady state assumption can be used to simplify the calculation of the state of the radiation belts, for instance, in space weather computations. The next chapter is focused on more realistic modeling of the dynamics of the radiation belts.

Chapter 5

Reproducing the outer belt dynamics during storm-recovery

So far we have derived an analytical solution of the reduced Fokker-Planck equation assuming either static or dynamic boundary conditions (Chapter 3), and we obtained a PSD that is a function of L-shell and time, with the first two adiabatic invariants (μ, K) treated as fixed parameters. The analytical solution has proven to be useful at emphasizing some properties of the radiation belts (such as the timescale of the dynamical evolution of the radial transport) (*Loridan et al.*, 2017) but has also been relevant to validate the numerical code that solves the reduced Fokker-Planck equation (*Ripoll et al.*, 2016a,b, 2017). The latter code has then been used to generalize the previous study for all μ and K (Chapter 4) and to illustrate the evolution of the shape of the electron fluxes in the (energy, L-shell) space, highlighting particularly the birth of a S shape (*Reeves et al.*, 2016) at a timescale of about 10 days. The boundary and initial conditions we used in Chapter 4 were rather academic and very generic, the purpose being the identification of the dynamical structure of the radiation belts.

Now we complement the previous studies by studying a specific event that occurred in March 2013. The period at stake is from March 4, 2013, to March 15, 2013, and represents storm recovery after the storm of March 1, 2013. The electron flux dropout occurring during this period has been particularly well observed by the Magnetic Electron and Ion Spectrometer (MagEIS) instrument on board the Van Allen Probes (*Blake et al.*, 2013). The measurements made by Radiation Belt Storm Probe (RBSP) A on its outbound orbits during this event led to both level 2 (L2) spin-averaged electron fluxes (FESA) and more recently to level 3 (L3) unidirectional differential electron fluxes (FEDU) data sets, which have been organized with respect to energy, L-shells and pitch angles for L3 data. These high resolution electron flux data are a great opportunity to further understand the physical processes at stake during a storm-recovery. The depletion of electrons occurring after the March 1, 2013, enhancement is thought to be a signature of whistler mode hiss waves that interact with the trapped radiation belt particles, which are pitch angle scattered and, thus, ultimately lost in the Earth's upper atmosphere. In this perspective, we especially consider the hiss-related pitch angle diffusion coefficient and its corresponding hiss lifetime that have been calculated by *Ripoll et al.* (2017) specifically for the studied period of March 2013. Both the pitch angle diffusion coefficient and hiss lifetime (that are spatially and temporally resolved) can respectively be incorporated either into a 3-D Fokker-Planck code or in a 1-D reduced Fokker-Planck equation.

Therefore, in order to quantify the impact of whistler mode hiss waves in the gradual formation of the slot region and the S shape observed in (*Reeves et al.*, 2016), we perform several numerical simulations that take into account realistic initial and time-dependent boundary conditions, as observed by the MagEIS instrument on board RBSP A. First, we focus on 1-D numerical solutions of omnidirectional fluxes coming from the integration of unidirectional fluxes uniformly distributed in pitch angle, which is equivalent to simulate an equatorially mirroring electron population. The computations are implemented for several different radial diffusion coefficients, by using either the aforementioned data-driven hiss lifetime but also by considering other different statistical electron lifetime models. A parametric study is made by using L2 omnidirectional flux data to compare the results related to each parameters. We particularly show that one of the best accuracy is obtained with the use of the event-specific lifetime. We then push further the analysis by generalizing the study to unidirectional fluxes that exhibit a nonuniform pitch angle distribution coming either from the L2 MagEIS data combined with an academic pitch angle distribution or from the L3 MagEIS data alone. In this purpose, we calculate both unidirectional and omnidirectional electron fluxes by using either a 1-D simulation (that solves the aforementioned reduced Fokker-Planck equation) or the VERB-3D code,

developed by the UCLA team since the last 10 years. VERB-3D is able to solve the full 3-D Fokker-Planck equation combining radial diffusion with pitch angle and energy diffusion (the two later being often referred as local diffusion). The data-driven pitch angle diffusion coefficients also derived in (*Ripoll et al.*, 2017) are directly implemented in these simulations.

Through these different calculations, we can explain the full S shape structure in energy and L-shell of the belts (*Reeves et al.*, 2016) and the slot formation by hiss scattering during storm recovery. We also numerically confirm the existence of an inner belt devoid of high energy electrons, as observed by *Fennell et al.* (2015). We emphasize the importance of implementing dynamical simulations over all energies and L-shells and the need for using data-driven and event-specific conditions to corroborate the observations. A final discussion is finally made about our ability to reproduce other storm-recovery events.

Sections 1 to 4 of the present chapter have been the subject of two previous publications (see *Ripoll et al.* (2016b, 2017)). We do not recall here the details of the computation of the event-specific pitch angle diffusion coefficient and lifetime, which are the substance of *Ripoll et al.* (2017). We however give a particular focus on the different Van Allen Probes data we use for the event and the assumptions made for the computations. The details of the different simulations are here formalized in a more comprehensive way, and the parametric study has been updated with the recently statistical indices derived in (*Morley*, 2016; *Morley et al.*, 2018) that are specifically devoted to study the radiation belts. Sections 5 and 6 are dedicated to the computation of realistic omnidirectional fluxes with the respective 1-D and 3-D codes. A particular care is taken on the distinction and the use of L2 or L3 electron flux data. Most of the computation presented here, as well as their related conclusions, are the subject of an imminent publication (*Ripoll et al.*, 2018, in print).

5.1 Presentation of the March 2013 storm-recovery

This chapter is dedicated to the computation of the energy-dependent structure of the radiation belts and the reformation of the slot region during the quiet recovery period following the 1 March 2013 storm. The period of March 2013 is specifically chosen because of the large interest its two storms (March 1 and March 17, 2013) have aroused in the literature (e.g., *Baker et al.*, 2014a; *Hudson et al.*, 2015; *Xiao et al.*, 2014; *Li et al.*, 2014b; *Boyd et al.*, 2014; *Yiqun et al.*, 2014; *Brito et al.*, 2015; *Reeves et al.*, 2016). The 1 March storm (*Baker et al.*, 2014a; *Li et al.*, 2014b; *Reeves et al.*, 2016) was associated with a high-speed solar wind stream that created strong erosion of the plasmasphere, down to $L = 3.3$, and resulted in strong outer belt flux dropout events followed by enhancements of relativistic electrons in the outer belt. After the storm, an extended period of 16 days of relatively quiet solar wind conditions was observed, ending with the next storm on 17 March 2013 (e.g., *Baker et al.*, 2014a; *Hudson et al.*, 2015; *Xiao et al.*, 2014; *Li et al.*, 2014b). The quiet solar wind conditions and the pitch angle homogeneous decay of outer belt electron fluxes between the two March 2013 storms is ideal for studying loss due to wave-particle scattering (e.g., *O'Brien et al.*, 2014; *Ripoll et al.*, 2016a, 2017), as we do here. As an example, the same interval in March was particularly simulated by *Li et al.* (2014b) at fixed first adiabatic invariant $\mu = 200$, 400, and 1000 MeV/G using recently developed statistical models for electron lifetimes due to pitch angle scattering from whistler mode hiss (*Orlova et al.*, 2014) and chorus (*Orlova and Shprits*, 2014) waves.

Rather than using statistical models, *Ripoll et al.* (2017) applied a data-driven, event-specific approach using lifetimes $\tau(E, L)$ computed from wave observations by the Electric and Magnetic Field Instrument Suite and Integrated Science (EMFISIS) waves instrument (*Kletzing et al.*, 2013) on board the Van Allen Probes satellites (*Mauk et al.*, 2013). They used wave observations made during the recovery period from 4 to 15 March 2013 to calculate electron lifetimes for this specific event at all energy (above 50 keV) for $1.8 \leq L \leq 6.0$. In the following computations, we assume that there are only two distinct operating processes: atmospheric losses due to scattering by whistler mode (VLF) waves and radial transport by radial diffusion (interaction with ULF waves). Local acceleration or any injections from the tail are neglected for this quiet interval between storms. Observations and computations are presented as a function of L-shell and energy (e.g., *Meredith et al.*, 2006a; *Ripoll et al.*, 2014a,b). Comparing the radiation belt response over a broad spectrum of energies and broad range of L-shells simultaneously as in (*Reeves et al.*, 2016) provides unprecedented opportunity for testing our understanding of physical processes in specific events.

5.2 Observations from the Van Allen Probes

The data used in this chapter are taken from measurements operated by the MagEIS instrument on board Van Allen Probe A. We recall that each RBSP spacecraft carries four MagEIS instruments, each covering a separate part of the energy spectrum and a wide range of pitch angles. The MagEIS instrument observes electrons and ions in the middle energy ranges (from $\sim$ 30 keV to 4 MeV for electrons and from $\sim$ 20 keV to 1 MeV for ions) (*Blake et al.*, 2013). Two sets of electron flux data have been made available from measurements from the MagEIS instrument: Level 2 (L2) and Level (L3) electron flux data. The L2 data include spin-averaged electron fluxes (FESA). These electron fluxes are however not resolved in pitch angle. The L3 data include pitch angle resolved electron fluxes (FEDU). The omnidirectional electron fluxes (FEDO) are not part of the L3 data, but will be in a future data release (they can still be calculated by integrating the L3 pitch angle distributions with respect to pitch angle, as done in the next sections). Let us mention that fluxes have been corrected for background contamination by ground-based post-processing (*Claudepierre et al.*, 2015; *Fennell et al.*, 2015).

Figure 5.1 illustrates the orbit of the Van Allen Probe A during March 4, 2013 (which is the first day of interest), from 07:00:00 to 13:00:00 UTC. The outbound orbit goes from 07:57:00 to 12:26:00 UTC, such that RBSP A takes approximatively 4:30 hours to cover each L-shell (from 1.1 to 6.1), and 9 hours to complete a full orbit. Let us mention that the satellite covers one given location at a given time, such that each L-shell value corresponds to one specific latitude λ that depends on the date considered. The latitudes of RBSP A provided in the Solar Magnetic (SM) coordinate system (*Russell*, 1971; *Hapgood*, 1992) and their corresponding L values can be found on `https://www.rbsp-ect.lanl.gov/data_pub/rbspa/MagEphem/definitive/2013/`. Since the measurements are made at different energy channels, the electron flux is typically rebuilt in the (L, E) space (e.g. *Reeves et al.*, 2016). There are 20 available energies from 30 keV to 4.2 MeV, 800 available L-shells from 1.6 to 6.1, as well as 11 available pitch angles from 8 to 172 degrees (courtesy of Mick Denton).

In this context, Figure 5.2 plots the electron fluxes as a function of L-shell and energy, for $L \in [1.6, 5.5]$ and $E \in [0.05, 4.2]$ MeV. Each panel represents the electron flux on outbound orbits for one pass of Van Allen Probe A, from 4 to 15 March 2013, as measured by the MagEIS instrument. More specifically, the first column represents the L2

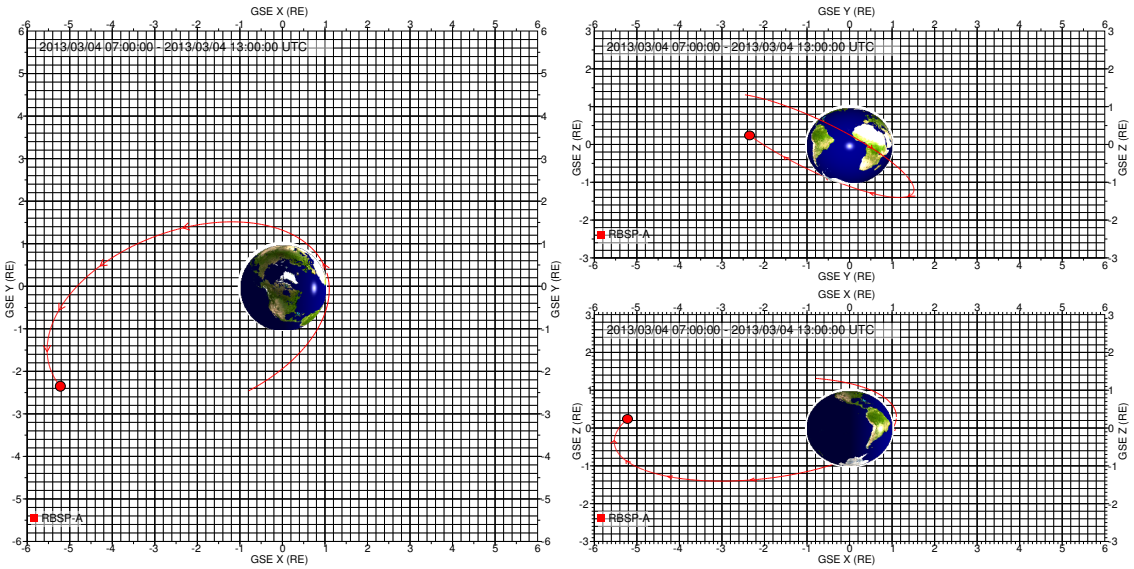

Figure 5.1 – Representation of the RBSP A orbit on March 4, 2013, from 07:00:00 to 13:00:00 UTC, in the GSE coordinate system. During this time interval, the satellite covers the entire L-shell range, from 1.1 to 6.1 R_E. The red arrows represent the position of the satellite at each hour. Source: http://rbspgway.jhuapl.edu/ExtendedMissionOrbit.

spin-averaged electron flux (FESA), whereas the next columns represent L3 unidirectional fluxes (FEDU) for a local pitch angle of 8, 25, 41, 57, 74, 90, 106, 123, 139, 155 and 172 degrees respectively. The blank regions that are present in most of the panels indicate a lack of data for the specified energy and L-shell. Let us recall that each panel corresponds to a timeline of approximately 4:30 hours, which is the time for the satellite to cover all L-shell. Figure 5.2 shows in more detail the evolution of the slot region in the recovery phase after the 1 March enhancement event.

The energy and L-dependent structure of the radiation belts seen in Figure 5.2 are characteristic of the quiescent state of the belts (*Reeves et al.*, 2016), providing all the specific features of the inner zone, slot region, and outer zone. Focusing on the L2 data (first column), the inner belt flux appears to be below background levels for $E > 800$ keV, consistent with observations of *Fennell et al.* (2015). The removal of the low-energy electrons (<100 keV) in the slot region ($3.5 < L < 5$) is particularly significant from 6 to 9 March. On March 9, a second tiny depletion becomes noticeable, removing the low-energy ($E \sim 100$ keV) electrons from the slot higher than $L = 5.2$. On March 11, there is a small incoming flux of low-energy electrons (< 130 keV) during a period of substorm activity that penetrates inside of $L \sim 5$ and strengthens the outer belt at these lower energies (e.g., *Turner et al.*, 2015). High-energy electrons ($E > 1$ MeV) did not penetrate below $L \sim 4$ during the 1 March storm and stayed above $L \sim 4$ during the first 15 days of March. During the ensuing period, the high-energy electron flux constantly decays. Let us mention that while each successive panels shows similar qualitative characteristics, the belts are still continually evolving. They are progressively separated by the enlarging slot region, until reaching the final feature of March 15, 2013, which is called an "S-shaped" structure (*Reeves et al.*, 2016, Figure 11), based on the shape of the flux distribution in the L-shell and energy maps.

Figure 5.2 – Snapshots of MagEIS measurements in the (Energy, L-shell) plane of the electrons flux plotted daily from 4 to 15 March 2013. The first column represents L2 omnidirectional electron flux data, and the next columns represent L3 unidirectional electron flux data for a respective local pitch angle α of 8, 25, 41, 57, 74, 90, 106, 123, 139, 155 and 172 degrees. On overall, we observe the slot forming between the belts during 12 days, with a removal of the lowest energy electrons along the outer edge of the inner belt and a progressive enlargement, which is started by a second depletion at $L \sim 5$ and $E \sim 100 - 200$ keV on 9 March.

The L3 corrected unidirectional electron fluxes (columns 2 to 13) show a very similar structure. However, they exhibit some discrepancies with the L2 data. We can separate the global time-evolution into two main parts (see for example the 90 degree-unidirectional fluxes in column 7, which presents the most significant values). A first gradual depletion of electrons occurs from March 4 to March 8, 2013, followed by a sharp low-energy enhancement at the outer boundary $L \sim 6$. From March 9 to March 15, 2013, the decaying process continues, leading to a less pronounced S shape, whose nose, made of high-energy electrons ($E \sim 2$ MeV) between 4.5 and 5.5 R_E, is constituted of residual electrons that have been removed by, perhaps, outward radial diffusion (losses out of the magnetopause) or scattering due to the action of (yet to define) electromagnetic waves (atmospheric loss). Another noticeable point is that there is no erratic structure coming from one particular pitch angle. On the contrary, the unidirectional fluxes seem to behave pretty much the same, no matter their pitch angle, leading to a very homogeneous distribution in pitch angle in the outer belt. We clearly see a smooth evolution in the pitch angle distribution (from column 2 to 12, at any time), the 90 degrees unidirectional flux exhibiting the maximal values.

In what follows, we suppose that the pitch angle distribution is symmetric with respect to 90 degrees. Hence we only focus on the pitch angles below 90 degrees, and we obtain the unidirectional averaged fluxes by averaging the jointly flux corresponding to two symmetric pitch angles (e.g. the averaged flux at 25 degrees is obtained by averaging the data at 25 degrees with the data at 155 degrees, and so on). The data (L2 and L3) are then interpolated and extrapolated over the range $1.6 \leq L \leq 5.5$ and 50 keV $\leq E \leq 4.2$ MeV.

5.3 Modeling pitch angle scattering from hiss waves

5.3.1 Pitch angle diffusion coefficient

The calculation of the pitch angle diffusion coefficient inferred from whistler mode hiss waves activity has been described in detailed in (*Ripoll et al.*, 2017) and is beyond the scope of the PhD thesis. Let us still briefly mention that time-resolved hiss effects are computed with an 8 hours temporal resolution using event specific in situ observations taken from the data of EMFISIS (*Kletzing et al.*, 2013) on board the Van Allen Probes A spacecraft (*Mauk et al.*, 2013). The measurements have been restricted to the right-hand polarized waves falling into the typical hiss frequency range of 50 Hz - 2 kHz. The calculation of the pitch angle diffusion coefficients is made in the framework of low frequency and dense plasma approximations (e.g., *Lyons et al.*, 1972). The data-driven pitch angle diffusion coefficients are bounce and drift-averaged. Ambient plasma density are taken from both EMFISIS and the Electric Field and Waves (EFW) (*Wygant et al.*, 2013) instruments. In (*Ripoll et al.*, 2017, Figure 2f), it is shown that the plasmasphere is widely extended from 4 to 15 March 2013, sometimes above $L = 5$, which is likely to favor long lasting whistler mode hiss wave activity.

The obtained time-averaged pitch-angle diffusion coefficients are plotted in Figure 5.3 for the periods of 4-10 March, 2013 and 11-15 March, 2013 (each row of Figure 5.3), at a given L-shell value (each column) in the common (E, α_0) space. These pitch angle diffusion coefficients can be compared with the one derived statistically in (*Subbotin et al.*, 2010, Figure 1) or in (*Kim et al.*, 2011, Figure 2). They both show a general similar trend.

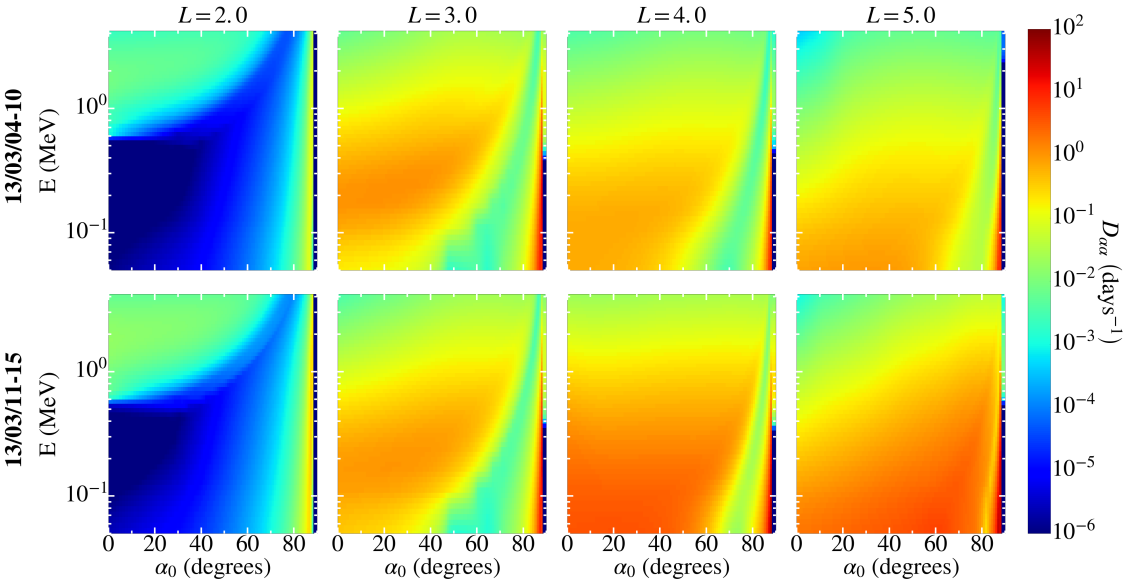

Figure 5.3 – Representation of the data-driven pitch angle diffusion coefficient $D_{\alpha\alpha}$ versus E and α_0. The first row represents the $D_{\alpha\alpha}$ computed for the period of March 4-10, 2013, and the second row displays the $D_{\alpha\alpha}$ calculated for the second period of March 11-15, 2013. Each column corresponds to a given L-shell, respectively L=2.0, 3.0, 4.0 and 5.0.

5.3.2 Electron lifetime

The lifetime corresponding to the calculated pitch angle diffusion coefficient is given by the lowest eigenvalue (in absolute value) associated to the full pitch angle diffusion operator, and is deduced from the pitch angle diffusion coefficient by using (*Lyons et al.*, 1972, equations 11-13). The full process is also described in (*Ripoll et al.*, 2017). The inverse of the computed lifetime, as well as the pitch angle diffusion coefficients, are represented in Figure 5.4 in the (L, E) space, for two different periods: one from March 4 to March 10, 2013 (first row), and the other from March 11 to March 15, 2013 (second row). We notice some important differences between the two considered periods, for both the inverse lifetime and the pitch angle diffusion coefficient. The second period seems to be much more favorable for the extension of hiss waves along a wider region in (L, E). We also clearly see the effect of the Landau resonance at $\alpha \sim 89$ degrees, whereas the lower pitch angle ($\alpha < 75$ degrees) are subjected to several cyclotron resonances (see *Ripoll et al.* (2017) for more details).

5.4 Model validation

The purpose of this section is to test the relevancy of the event-specific lifetime inferred from whistler mode hiss waves calculated by *Ripoll et al.* (2017) among other statistical lifetime models that are widely used in the literature. To achieve this goal, we use either the aforementioned data-driven lifetime model or other statistically-driven lifetime models among several different radial diffusion coefficients in a 1-D reduced Fokker-Planck code.

For now, we build the initial and the two time-dependent boundary conditions on the L2 spin-averaged flux data, and we restrict our study to a single pitch angle. From the

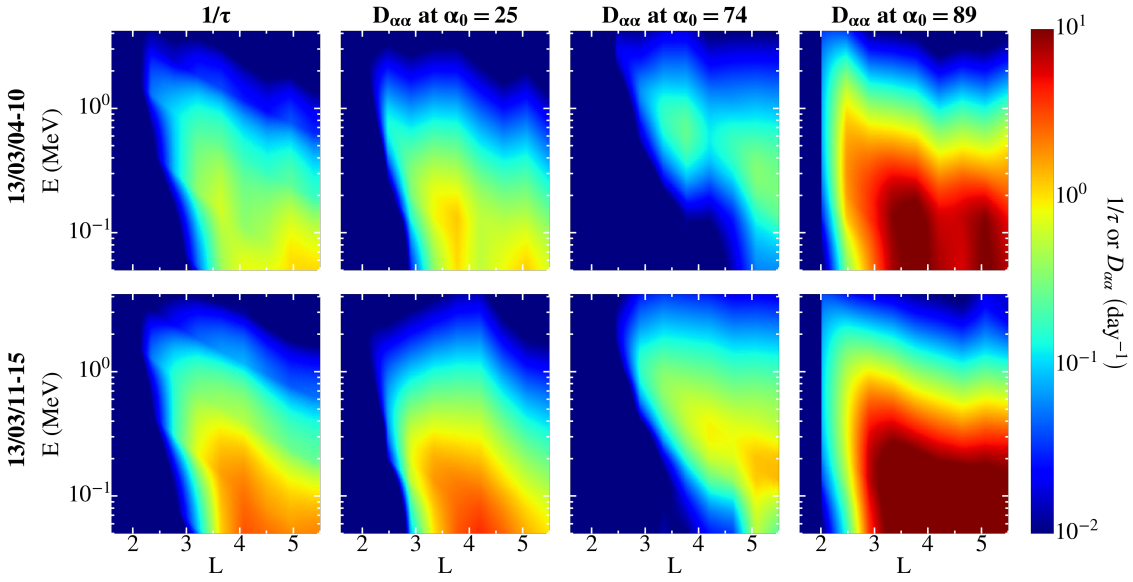

Figure 5.4 – Representation of the data-driven pitch angle diffusion coefficient $D_{\alpha\alpha}$ (columns 2 to 7, respectively for α_0=8, 25, 41, 57, 74 and 89 degrees) and the inverse of the corresponding lifetime $1/\tau$ (first column) for the period of 4-10 March 2013 (first row) and the period of 11-15 March 2013 (second row) in the usual (L, E) space. The high values of the pitch angle diffusion coefficient for $\alpha_0 < 70$ degrees are due to cyclotron resonances, whereas the abrupt increase at $\alpha_0 \sim 90$ degrees is an effect of the Landau resonance.

different simulated fluxes that we obtain (each set of results corresponds to one given lifetime and one given radial diffusion coefficient), we perform several statistical metrics (that compare the predicted fluxes with the L2 observations) in order to validate the accuracy of the data-driven lifetime. This validation step is necessary to justify the use of the event-specific lifetime from *Ripoll et al.* (2017) in the more complete simulations that are presented in sections 5.5 and 5.6.

5.4.1 Implementation of the simulations

We attempt here to reproduce the depletion of the radiation belts after the March 1, 2013 storm and the S shape feature of the electron fluxes through a 1-D model based on the reduced Fokker-Planck equation

$$\frac{\partial f}{\partial t} = L^2 \frac{\partial}{\partial L}\left[\frac{D_{LL}}{L^2}\frac{\partial f}{\partial L}\right]_{(\mu,K)} - \frac{f}{\tau},$$

in which D_{LL} is the radial diffusion coefficient (as one of the statistical radial diffusion coefficients described below) and τ is the electron lifetime, here written as a combination of a Coulomb scattering lifetime taken from *Lyons and Thorne* (1973) with a hiss lifetime model (either the aforementioned data-driven lifetime or another statistical hiss electron lifetime described below).

The reduced Fokker-Planck equation is classically solved for the phase-averaged distribution function f (or more commonly referred as PSD), which depends on the first

(μ), second (K) and third (L) invariants. Since radial diffusion occurs at constant μ and K, the two aforementioned invariants are treated as parameters. The μ grid is deduced from the energy grid available from the Van Allen Probes MagEIS flux data. The minimum value is $\mu_{\min} = 0.45$ MeV/G that corresponds to the minimum available energy $E_{\min} = 0.0315$ MeV at the $L_{\min} = 1.6$. The maximum value for μ is $\mu_{\max} = 15770$ MeV/G that is calculated at $L_{\max} = 5.5$ and $E_{\max} = 4.216$ MeV. The μ grid used to solve the reduced Fokker-Planck equation is composed of 200 cells, which are uniformly distributed in logarithmic space between $\mu_{\min}$ and $\mu_{\max}$. As mentioned before, we simply focus on the unidirectional flux at a single pitch angle. In this context, we set $K = 0.0$ $G^{1/2}R_E$, which corresponds to an equatorial pitch angle of 90 degrees, such that, in this section, the simulated unidirectional electron flux relates to a particle population that mirrors at the magnetic equator. The simulations also use a uniform grid in L with 200 cells equally spaced. We use a dipole magnetic field to perform the transformation between flux as a function of the (E, α_0, L) physical space and PSD in the (μ, K, L) adiabatic space. Chapter 6 will be devoted to the quantification of the effects a non dipole magnetic field.

5.4.2 Initial and boundary conditions

As stated earlier, we only consider the L2 differential electron flux data (FESA) available from the MagEIS instrument of RBSP A. Let us call J_{VAP} this Van Allen Probes observed flux. We can typically relate the measured spin-averaged differential flux J_{VAP} to the local differential, omnidirectional flux J_O registered at a given energy E, radial distance L, latitude λ_s and time t, such that (see section 2.7.4.b of Chapter 2)

$$J_{\text{VAP}}(E, L, \lambda_s, t) \equiv J_O(E, L, \lambda_s, t) = 4\pi \int_{x_s=0}^{x_s=x_{sLC}} j(E, x_s, L, \lambda_s, t)\, \mathrm{d}x_s,$$

for which $x_s = \cos(\alpha_s)$, the cosine of the local pitch angle α_s at a given point s of the field line. The integration is performed from $x_s = 0$ (a 90 degree local pitch angle) to $x_s = x_{sLC}$, which is the value of x_s at the bounce loss cone.

In the framework of this first study, whose purpose is to validate the accuracy of the data-driven lifetime τ compared with the other aforementioned formulations of electron lifetimes, we make the two following severe assumptions to simplify the calculations and reduce the amount of computational resources. We first assume that the omnidirectional flux measured at a local position of the field line (latitude λ_s) is equal to the omnidirectional flux measured at the equatorial point λ_0, i.e. that the satellite stays in a plane very close to the equatorial plane. This approximation is relatively accurate in view of the orbit taken by RBSP A (cf. Figure 5.1) that stays below 20 degrees in latitude. Hence $x_0 \approx x_s$ so that

$$J_O(E, L, \lambda_0, t) \approx 4\pi \int_{x_0=0}^{x_0=x_{0LC}} j(E, x_0, L, \lambda_0, t)\, \mathrm{d}x_0.$$

Then, we make the strong hypothesis of a uniform pitch angle distribution, i.e. considering the unidirectional flux has no dependence on the equatorial pitch angle α_0. If this approximation holds, $j(E, x_0, L, \lambda_0, t) \equiv j(E, L, \lambda_0, t)$, and therefore the omnidirectional flux writes

$$J_O(E, L, \lambda_0, t) \approx 4\pi x_{0LC} j(E, L, \lambda_0, t).$$

We now define

$$j_{\text{data}}(E, L, \lambda_0, t) = J_O(E, L, \lambda_0, t) = 4\pi x_{0LC} j(E, L, \lambda_0, t). \tag{5.1}$$

In this context, performing the omnidirectional flux is equivalent to calculating the unidirectional flux for any chosen equatorial pitch angle (modulo the $4\pi x_{0LC}$ factor) as emphasized by (5.1). Here, we focus on an equatorial pitch angle of 90 degrees that corresponds to an equatorially mirroring electron population. We can thus easily compute the initial PSD condition $f_0(\mu, K, L) = f(\mu, K, L, t = 0)$ and the inner and outer boundary conditions, respectively $f_{L_0}(\mu, K, t) = f(\mu, K, L_0, t)$ and $f_{L_M}(\mu, K, t) = f(\mu, K, L_M, t)$, from the assumed unidirectional flux $j_{\text{data}}(E, L, \lambda_0, t)$ after converting the latter into PSD and transforming the (E, α_0, L) space into the (μ, K, L) adiabatic space, as depicted in Chapter 4. The approximation of a uniform pitch angle distribution is discussed in the next sections.

5.4.3 Radial transport and losses

5.4.3.a Radial diffusion coefficients

We solve the reduced Fokker-Planck equation with four different expressions for the radial diffusion coefficient, which are plotted in Figure 5.5 for $K_p = 1$.

The first one is the diffusion coefficient obtained by *Ozeke et al.* (2014, equations (20) and (23)), which includes the electric and the magnetic components, indicated here as $D_{LL}(\text{O})$, and the second is he *Brautigam and Albert* (2000) radial diffusion coefficient, with notation $D_{LL}(\text{BA})$ (including the electrostatic and the electromagnetic components). Both models have been briefly described in Chapter 4, section 4.4.1.a. The third formulation corresponds to the electric radial diffusion coefficient obtained by *Liu et al.* (2016, equation (2)), indicated as $D_{LL}(\text{L})$, derived from 7 years of in situ electric field measurements by the Time History of Events and Macroscale Interactions during Substorms (THEMIS), whose expression is given by

$$D_{LL}(\text{L}) = 1.115 \times 10^{-6}\, 10^{0.281 K_p}\, L^{8.184}\, \mu^{-0.608}.$$

Finally, the last D_{LL} of the study is the radial diffusion coefficients from *Ali et al.* (2016, equations (14) and (15)), derived from 3 years of the magnetic field data and the electric field data respectively measured by EMFISIS and by the EFW instrument on board the Van Allen Probes. This radial diffusion coefficient is indicated as $D_{LL}(\text{A})$ and is the combination of the electric component

$$D^E_{LL}(\text{A}) = \exp\left(-16.951 + 0.181 K_p\, L + 1.982 L\right)$$

with the magnetic term

$$D^M_{LL}(\text{A}) = \exp\left(-16.253 + 0.224 K_p\, L + L\right).$$

All the mentioned radial diffusion coefficients are K_p dependent in the simulations.

From Figure 5.5, $D_{LL}(\text{A})$ has the lowest values of the considered radial diffusion models. It is thus supposed to trigger the weakest radial transport in the upcoming flux simulations. It is followed by the $D_{LL}(\text{O})$, whose values and shape are quite close to $D_{LL}(\text{A})$. On the other side, the $D_{LL}(\text{L})$ exhibits large values, and $D_{LL}(\text{BA})$ has the maximum intensity among the four models, particularly due to the consideration of its electrostatic component (see *Kim et al.* (2011) and Chapter 4).

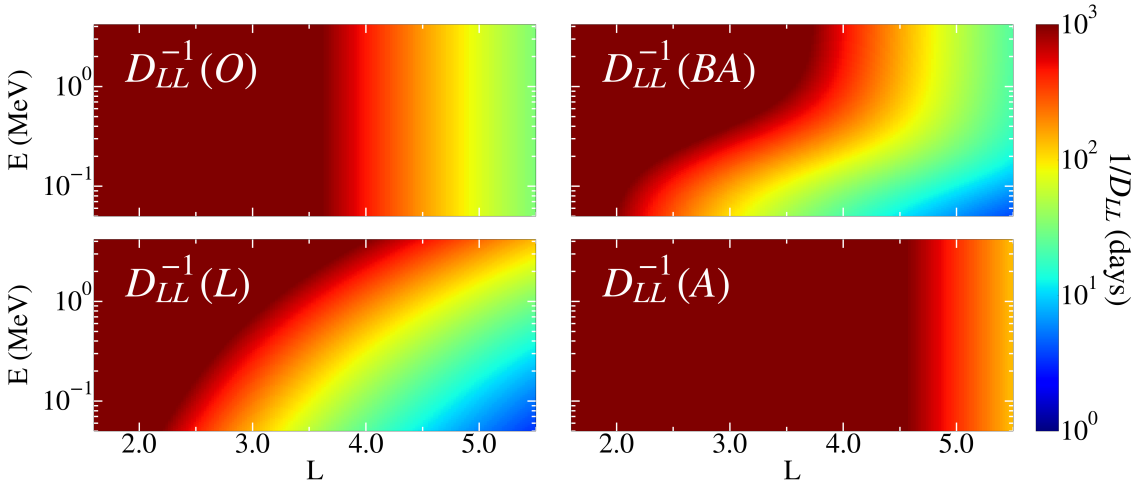

Figure 5.5 – The four radial diffusion coefficients plotted as $1/D_{LL}$ (in days) in the (L, E) plane derived by (top left) *Ozeke et al.* (2014) (D_{LL}(O)), (top right) *Brautigam and Albert* (2000) (D_{LL}(BA)), (bottom left) *Liu et al.* (2016) (D_{LL}(L)), and (bottom right) *Ali et al.* (2016) (D_{LL}(A)), for $K_p = 1$.

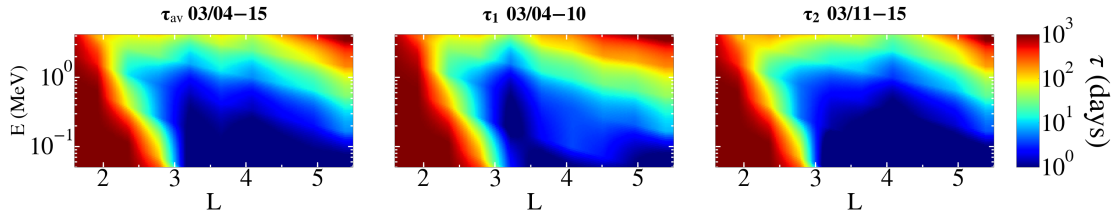

Figure 5.6 – Representation in the (L, E) space of the data-driven lifetime computed by *Ripoll et al.* (2017) that has been averaged for the full period of March 4 to March 15, 2013 (left), the lifetimes corresponding to the period of March 4-10, 2013 (center) and March 11-15, 2013 (right). Only the two latter are used in the following reduced Fokker-Planck simulation. The last two panels show that the lifetime corresponding to the last period is lower than its counterpart corresponding to the first period, from which we deduce that hiss waves are much more active during the second period than during the first one.

5.4.3.b Electron lifetimes

We also use five different lifetime models that have been derived from whistler mode hiss wave activity. The first model consists in the computed data-driven lifetimes taken from *Ripoll et al.* (2017) for the periods of 4-10 March, 2013 and for the period of 11-15 March, 2013. Both lifetimes are represented in Figure 5.6 (respectively τ_1 and τ_2 in the last two columns), in which the first panel illustrates the averaged lifetime τ_{av} over the whole event from March 4 to March 15, 2013. Let us mention that for the entire storm recovery event, the K_p is mostly constant between 1 and 2.

In the following 1-D simulations, we do not use the averaged lifetime but rather the lifetime corresponding to the first period (second column of Figure 5.6, 4-10 March) during the first 7 days of the simulations, and the lifetime corresponding to the second period (third column of 5.6, 11-15 March) for the next 5 days of the simulation. Both

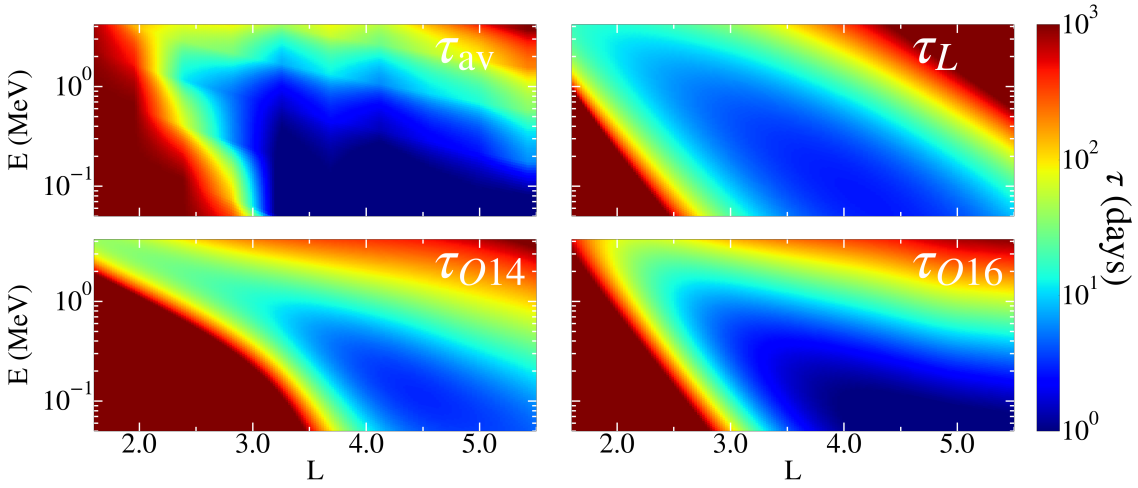

Figure 5.7 – The four electron lifetimes (in days) from interactions with hiss waves, plotted in the (L, E) plane. They are derived (top left) from averaging the pitch angle diffusion coefficients of *Ripoll et al.* (2017) taken from 4 to 15 March ($\tau_{\rm av}$), (top right) from *Lyons et al.* (1972) combined with the hiss wave amplitudes from *Orlova et al.* (2014) plotted for $K_p = 1$ ($\tau_{\rm L}$), (bottom left) from *Orlova et al.* (2014) (extrapolated below $L = 3$ and plotted for $K_p = 1$) using CRRES data ($\tau_{\rm O14}$), (bottom right) and from *Orlova et al.* (2016) (extrapolated above $L = 5$ and plotted for $K_p = 1$) using Van Allen Probes data ($\tau_{\rm O16}$). The latter model $\tau_{\rm O16}$ is rather close to the lifetime τ of this study (top left).

lifetimes are further referred as the single τ notation. The averaged lifetime $\tau_{\rm av}$ is only displayed in Figure 5.6 (first row) and Figure 5.7 (top left) in the purpose of comparison with the other statistical lifetimes that we use in our simulations.

The second model is the so-called statistical lifetime of the historical *Lyons et al.* (1972) model, which we associate with the wave amplitude B_w inferred for plasmaspheric hiss derived in (*Orlova et al.*, 2014, equation (1)) as a function of L and K_p. This lifetime, identified with the notation τ_L, is represented in Figure 5.7 (top right).

The third model is the lifetime $\tau_{\rm O14}$ derived in (*Orlova et al.*, 2014, equation (6)-(9)), based on electric field measurements from the Combined Release and Radiation Effects Satellite (CRRES) satellite and parametrized as a function of energy, L and K_p, as shown in Figure 5.7 (bottom left). Let us mention that the later lifetime is extrapolated below $L = 3$, as done in Chapter 4, section 4.4.1.b.

The fourth hiss lifetime $\tau_{\rm O16}$ is derived by *Orlova et al.* (2016) from statistical analysis of data taken from EMFISIS instrument on board the Van Allen Probes and is illustrated in Figure 5.7 (bottom right). It is extrapolated above $L = 5.5$. The latter model is rather close to the one derived inhere (Figure 5.7, top left), with some differences in the outer belt for $L > 4.5$ and $E < 500$ keV and in the inner slot region $L < 2.5$ and $E \sim 1$ MeV. In all cases, the hiss lifetime models are activated on the full spatial domain $L \in [1.6, 5.5]$ and no other wave is included in the reduced Fokker-Planck code.

The fifth model is the limit $\tau \to \infty$ that corresponds to no loss and radial diffusion only.

5.4.4 Numerical results

We represent the results of the simulations in four figures (Figures 5.8 to 5.11) corresponding each to one specific D_{LL} model, each taking account of the different lifetime models in use, respectively no lifetime (column 2), τ_{L} (column 3), τ_{O14} (column 4), τ_{O16} (column 5) and the event-driven τ (column 6). The first column in each figure represents the L2 spin-averaged electron flux (FESA) obtained from the Van Allen Probe A observations (cf. section 5.2). The latter has been interpolated in order to fill the empty regions (blank regions of Figure 5.4) characterizing a lack of data.

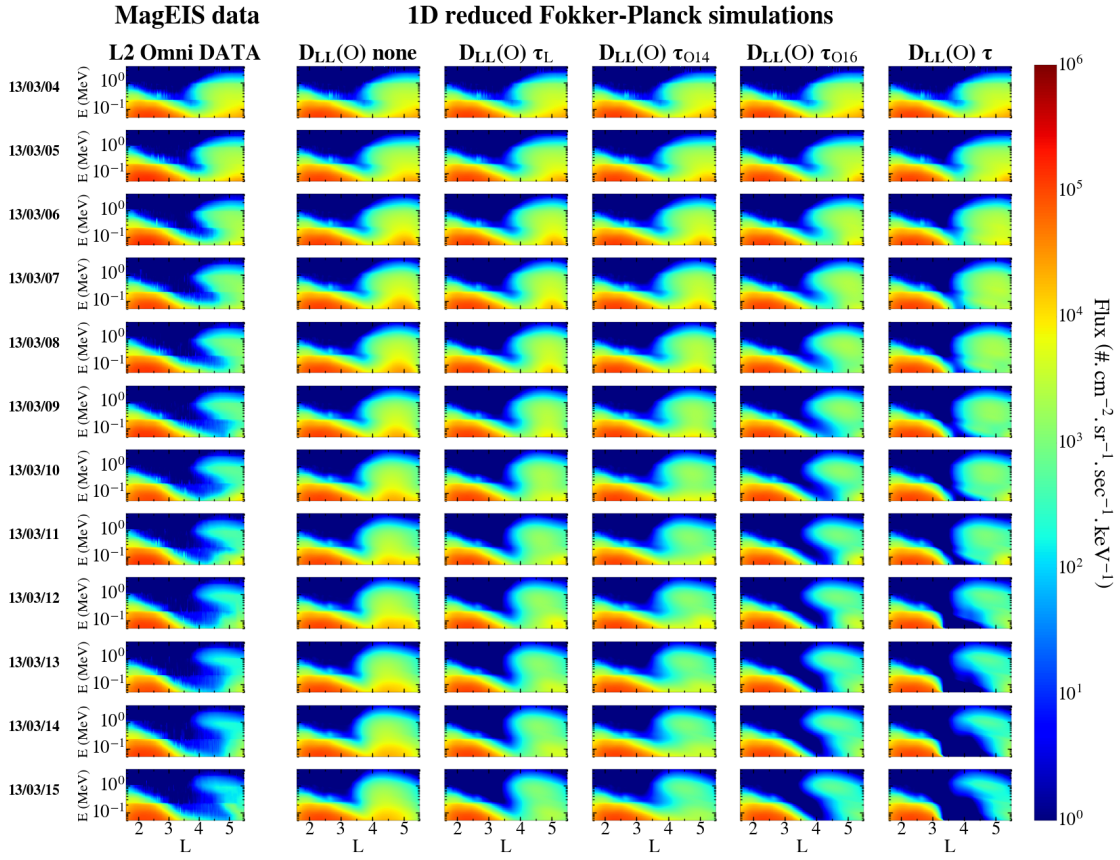

Figure 5.8 – Evolution of the equatorial unidirectional flux (as a model of the omnidirectional flux) in the (L, E) space, for the radial diffusion coefficient D_{LL}(O) from *Ozeke et al.* (2014). Each row represents a given day of March 2013, starting from March 4 (first row) to March 15 (last row). The first column displays the L2 omnidirectional flux data as observed by the Van Allen Probes (RBSP A). The next columns represent the results of our simulations from the reduced Fokker-Planck equation, with the respective use of no lifetime $\tau \to \infty$ such that only radial transport is activated (second column), τ_{L} (third column), τ_{O14} (fourth column), τ_{O16} (fifth column) and τ (last column).

Flux profiles obtained with the D_{LL} of *Ozeke et al.* (2014) (Figure 5.8) are close to those of *Ali et al.* (2016) (Figure 5.9) while both of the D_{LL} of *Liu et al.* (2016) (Figure 5.10) and *Brautigam and Albert* (2000) (Figure 5.11) are too strong to be compensated by the loss of any of the lifetime models used here, leading to a large overestimation of the flux in the slot region and in the outer belt. As we will see below, their best performance is obtained when they are coupled to the strongest loss brought by the

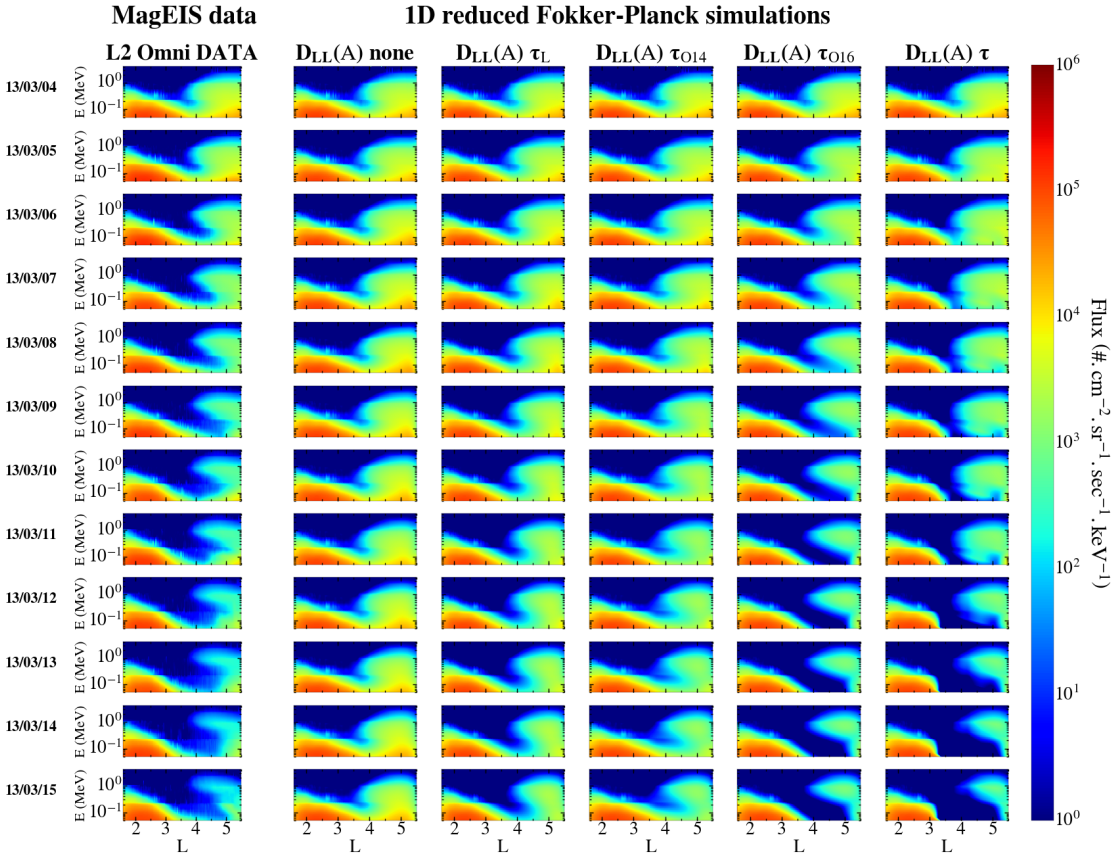

Figure 5.9 – Evolution of the equatorial unidirectional flux (as a model of the omnidirectional flux) in the (L, E) space, for the radial diffusion coefficient D_{LL}(A) from *Ali et al.* (2016). Each row represents a given day of March 2013, starting from March 4 (first row) to March 15 (last row). The first column displays the L2 omnidirectional flux data as observed by the Van Allen Probes (RBSP A). The next columns represent the results of our simulations from the reduced Fokker-Planck equation, with the respective use of no lifetime $\tau \to \infty$ such that only radial transport is activated (second column), τ_L (third column), τ_{O14} (fourth column), τ_{O16} (fifth column) and τ (last column).

Orlova et al. (2016) lifetime model. On the other hand, the D_{LL} of *Ali et al.* (2016) is the weakest and produces the widest slot because electrons do not diffuse inward enough from $L \sim 5-6$ and hiss waves scatter the initial electrons out. With this D_{LL}, the best appropriate lifetime models seem to be the ones with the weakest effect (either the *Orlova et al.* (2014) model or the *Lyons et al.* (1972) model).

The combination of the D_{LL} from *Ozeke et al.* (2014) and the event-specific lifetime τ reproduces the observations quite well (as emphasized below). There is overall a good reproduction of the dynamics of the slot region and radiation belts. Over the five first days there are gradual losses in the slot enlarging the region devoid of electrons. The clear correspondence between computed loss location and the observed slot digging dynamics strongly suggests that the two phenomena are connected. The inner belt is unaffected by hiss waves. Some discrepancies exist such as the overestimation of loss between $L = 4$ and $L = 5$ below 100 keV equivalent to the underestimation of new incoming electrons below 100 keV. There is also a qualitative and quantitative match between the computed loss

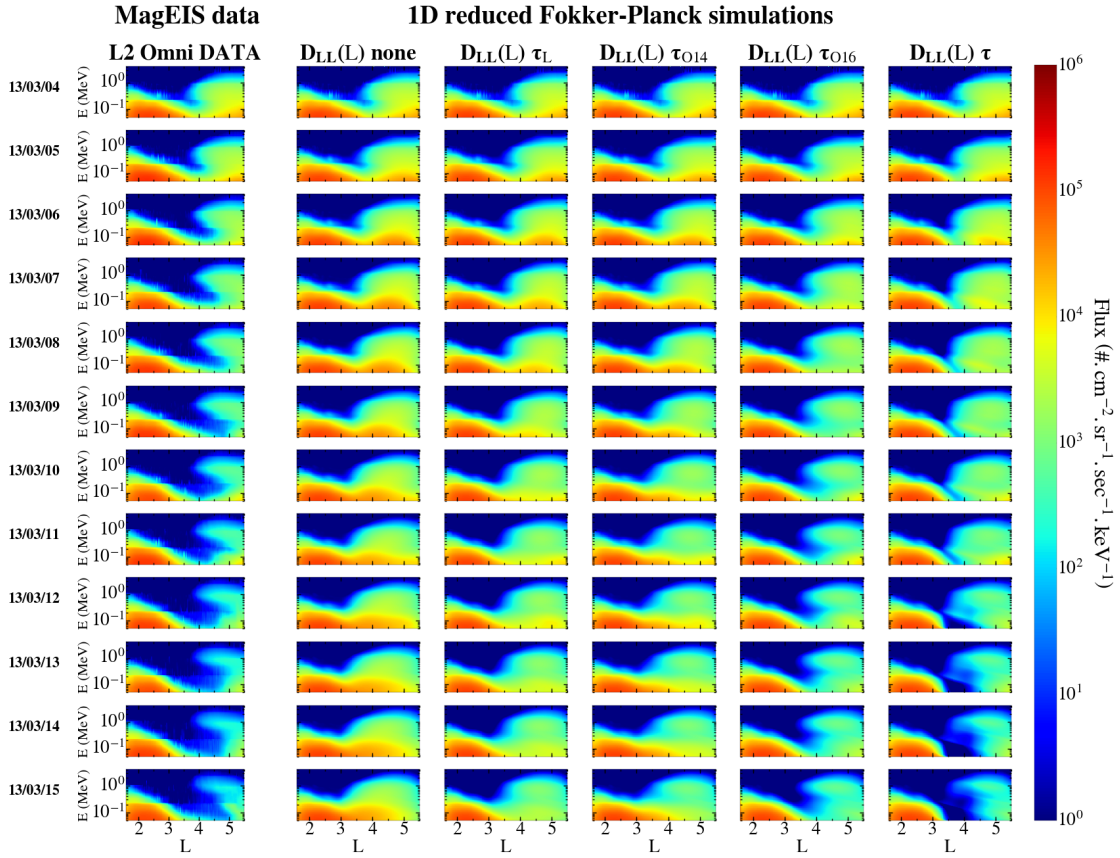

Figure 5.10 – Evolution of the equatorial unidirectional flux (as a model of the omnidirectional flux) in the (L, E) space, for the radial diffusion coefficient D_{LL}(L) from *Liu et al.* (2016). Each row represents a given day of March 2013, starting from March 4 (first row) to March 15 (last row). The first column displays the L2 omnidirectional flux data as observed by the Van Allen Probes (RBSP A). The next columns represent the results of our simulations from the reduced Fokker-Planck equation, with the respective use of no lifetime $\tau \to \infty$ such that only radial transport is activated (second column), τ_{L} (third column), τ_{O14} (fourth column), τ_{O16} (fifth column) and τ (last column).

from hiss and the slot location and enlargement. These results show that the lifetimes of this study are able to capture the loss dynamics in the slot and the structure of the observed radiation belts with a reasonable accuracy.

5.4.5 Accuracy of the data-driven model

We assess now the sensitivity of the variety of models by exploring the 20 different combinations of the 4 radial diffusion coefficients and 5 lifetime models presented above. In this perspective, we aim at quantifying the error made by the model compared with the data by using the statistical metrics defined in 2.9.

Table 5.1 indicates the global value of the MdAE, MdAPE, MdSA and MdLQ indices corresponding to each of the 20 different models, calculated over the entire ranges of L-shell, energy and time. Let us mention that the median function is taken over the sets of energy and L if we want to highlight the evolution of the model accuracy in time (see Figures 5.12 and 5.13). However, the median function can also be taken over all energies,

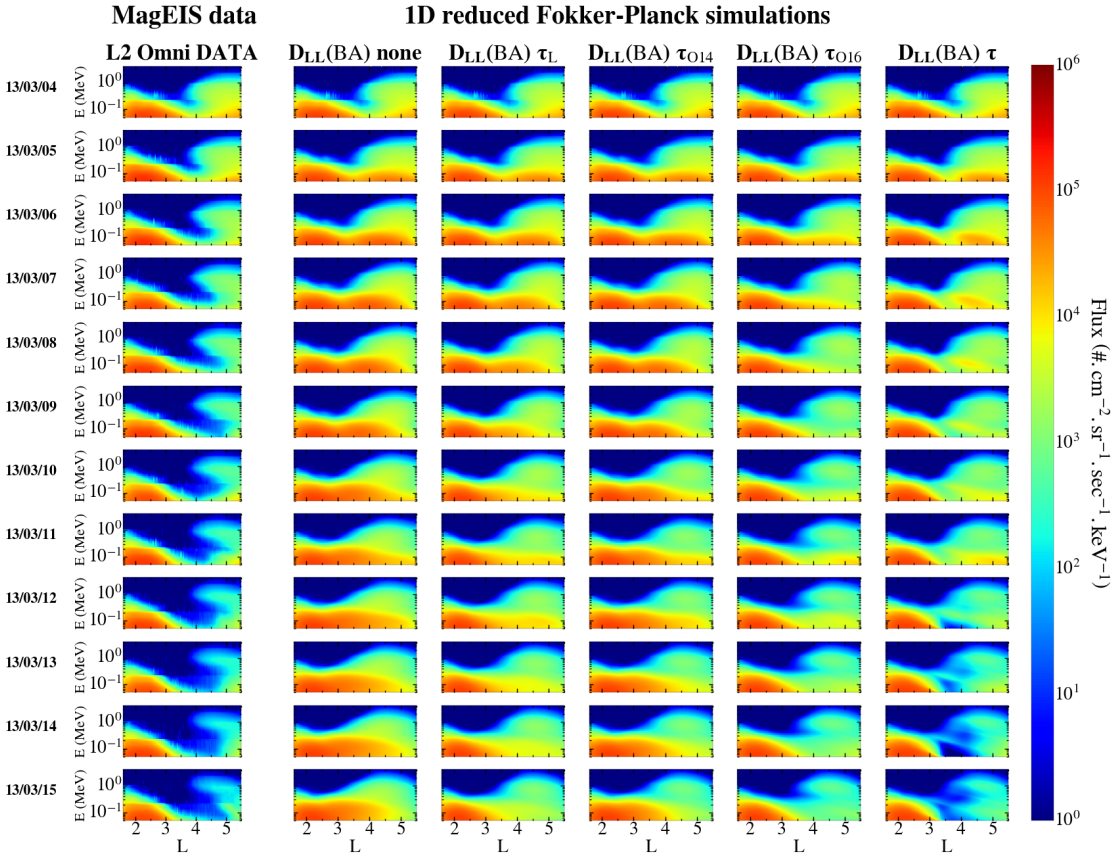

Figure 5.11 – Evolution of the equatorial unidirectional flux (as a model of the omnidirectional flux) in the (L, E) space, for the radial diffusion coefficient D_{LL}(BA) from *Brautigam and Albert* (2000). Each row represents a given day of March 2013, starting from March 4 (first row) to March 15 (last row). The first column displays the L2 omnidirectional flux data as observed by the Van Allen Probes (RBSP A). The next columns represent the results of our simulations from the reduced Fokker-Planck equation, with the respective use of no lifetime $\tau \to \infty$ such that only radial transport is activated (second column), τ_{L} (third column), τ_{O14} (fourth column), τ_{O16} (fifth column) and τ (last column).

L-shells and times when a global statistical quantity is desired to distil the full solution into a single quantitative number (see Table 5.1).

There is no best reproduction minimizing all error metrics emerging from Table 5.1. The best MdAE is obtained with D_{LL}(A) and τ_{O16} (MdAE=14), which has also the best MdAPE (MdAPE=44). The later result is consistent with the fact that the MdAPE index tends to favor underestimations, which is the case with the use of the weakest radial diffusion coefficient (D_{LL}(A)) and one of the smallest lifetime (τ_{O16}). The best MdLQ is reached for D_{LL}(O) and our event-driven lifetime τ (MdLQ $= 4.8 \times 10^{-4}$), while the best MdSA is for D_{LL}(L) and τ_{O16} (MdSA=64). We underestimate only twice the observations (MdLQ<0), with D_{LL}(A) combined with τ_{O16} or the event-driven τ. This result is expected since the radial diffusion coefficient from *Ali et al.* (2016) is the weakest of all the D_{LL} in use, and the two aforementioned lifetimes are the one having the most of whistler mode hiss effects embedded. The worst case scenario is achieved with

Table 5.1 – An Assessment of the models accuracy through the computation of four global error indices over the period of (March 4-15, 2013): the median absolute error, the median absolute percentage error, the median symmetric accuracy and the median log accuracy ratio. Each case is evaluated by a global grade, which can either be very poor (- -) or poor (-) if the data are not well reproduced, or either good (+) or very good (++) when the model accuracy is better.

	D_{LL}(O) (weak)	D_{LL}(A) (weak)	D_{LL}(L) (strong)	D_{LL}(BA) (strong)
none	MdAE = 108 MdAPE = 61 MdLQ = 1.8×10^{-1} MdSA = 92 - -	MdAE = 57 MdAPE = 48 MdLQ = 5.9×10^{-2} MdSA = 72 -	MdAE = 160 MdAPE = 53 MdLQ = 1.4×10^{-1} MdSA = 77 - -	MdAE = 280 MdAPE = 77 MdLQ = 2.4×10^{-1} MdSA = 97 - -
τ_{L}	MdAE = 59 MdAPE = 61 MdLQ = 6.2×10^{-2} MdSA = 104 -	MdAE = 25 MdAPE = 52 MdLQ = 1.9×10^{-4} MdSA = 86 ++	MdAE = 95 MdAPE = 57 MdLQ = 5.5×10^{-2} MdSA = 93 -	MdAE = 177 MdAPE = 69 MdLQ = 1.7×10^{-1} MdSA = 115 - -
τ_{O14}	MdAE = 76 MdAPE = 56 MdLQ = 1.4×10^{-1} MdSA = 85 -	MdAE = 36 MdAPE = 46 MdLQ = 2.5×10^{-2} MdSA = 70 +	MdAE = 110 MdAPE = 50 MdLQ = 1.1×10^{-1} MdSA = 72 - -	MdAE = 191 MdAPE = 68 MdLQ = 2.1×10^{-1} MdSA = 90 - -
τ_{O16}	MdAE = 25 MdAPE = 48 MdLQ = 9.8×10^{-3} MdSA = 71 ++	MdAE = 14 MdAPE = 44 MdLQ = -3.8×10^{-2} MdSA = 65 ++	MdAE = 43 MdAPE = 46 MdLQ = 5.5×10^{-2} MdSA = 64 +	MdAE = 94 MdAPE = 58 MdLQ = 1.5×10^{-1} MdSA = 81 -
τ	MdAE = 26 MdAPE = 52 MdLQ = 4.8×10^{-4} MdSA = 80 ++	MdAE = 16 MdAPE = 48 MdLQ = -5.4×10^{-2} MdSA = 75 ++	MdAE = 33 MdAPE = 46 MdLQ = 1.2×10^{-2} MdSA = 66 +	MdAE = 62 MdAPE = 54 MdLQ = 9.2×10^{-2} MdSA = 77 -

the combination of D_{LL}(BA) and no lifetime, which results in a severe overestimation (MdLQ $= 2.4 \times 10^{-1}$).

We focus now on the radial diffusion coefficient from *Ozeke et al.* (2014) (first column of Table 5.1) since Table 5.1 shows that this model performs the best. There is only small differences between the use of the event-driven τ (last row) and τ_{O16} (fourth row), for instance on the 8 March 13 for $L \in [4, 5]$ and $E < 200$ keV in Figure 5.8. Differences are mostly visible at large L-shells with, for instance, the shape of the outer belt being slightly different. Results are also close to observations, and the error indices are very close to the ones obtained with the lifetime model of this study (*Ripoll et al.*, 2017). Agreements with observations degrade with the use of the *Orlova et al.* (2014) model, and more with the one of the *Lyons et al.* (1972). Comparing the two latter models against each other shows the influence of the frequency and wave normal angle distributions (since wave amplitudes are the same and taken from *Orlova et al.* (2014)). In the *Orlova et al.* (2014) lifetime model, wave parameters come from CRRES measurements, while for *Lyons et al.* (1972) we use their theoretical fixed values. Differences are often minor as corroborated by the error indices of Table 5.1 (independently of the radial diffusion model).

As a complement to the analysis, we plot in Figure 5.12 the time evolution of four indices, MdAE (top-left), MdAPE (top-right), MdSA (bottom-left) and MdLQ (bottom-right) that have been calculated over the energy and L-shell ranges with the use of the D_{LL} of *Ozeke et al.* (2014) with the different lifetime models. It confirms the best accuracy is obtained with the event-driven lifetime model of this study ($t \geq 8$ days) and the lifetime derived by *Orlova et al.* (2016) (shorter times). The worst accuracy is obtained when hiss losses are omitted.

We also plot the evolution of the four error indices at fixed electron lifetime model in Figure 5.13 with the use of the one of this study and varying the radial diffusion coefficient model. In view of the diversity of the results obtained in Figure 5.13, it is rather difficult to choose which radial diffusion coefficient is the best combined with the lifetime τ. If the MdAE index argues in favor of D_{LL}(A), the three other indices (MdAPE, MdSA and MdLQ) exhibit pretty poor results, with the MdLQ metric emphasizing a severe underestimation (bottom-right panel). The radial diffusion coefficients D_{LL}(L) and D_{LL}(O) are also good candidates as they complement each other in overestimating (D_{LL}(L)) and underestimating (D_{LL}(O)) the observations. The worst accuracy is obtained when *Brautigam and Albert* (2000) is used, which is due to a large D_{LL}^{E}, (e.g., *Kim et al.*, 2011) see also the previous chapter.

Fluxes computed with the absence of hiss scattering (second column of all Figures 5.8 to 5.11 and Table 5.1) strongly indicate how important hiss waves are for the slot formation and, therefore, for the radiation belts energy structure we witness forming in March 2013. Without hiss scattering and with the fastest radial diffusion models, the slot is filled up by inward diffusion from the outer belt, particularly for E below 200 keV. Without hiss scattering and with the slowest radial diffusion models, the slot is not emptied at the observed rate. The absence of loss always gives the worst error accuracy in Table 5.1. Table 5.1 also shows how errors can be compensated; the lowest error for fast radial diffusion models is obtained with the strongest loss model, and vice versa, the lowest error for slow radial diffusion model is obtained with the weakest loss model. Determining which regime occurs in reality is dependent upon the accuracy of the method of computation of the loss rates and, equivalently, the radial diffusion coefficients. Here we provide evidence that the use of an event-specific approach, integrating as much as possible the actual wave and density measurements, provides a good determination of the accuracy of the loss rate model.

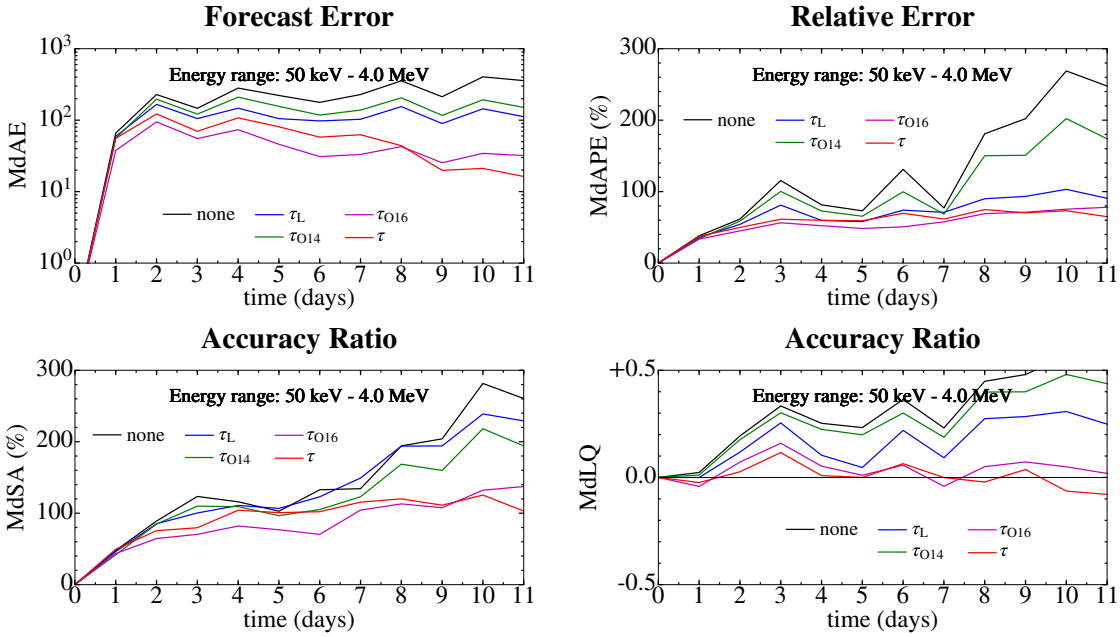

Figure 5.12 – An assessment of the models accuracy through the evolution during the 12 days of the event (4 to 15 March, 2013) of four global error indices: the median absolute error (MdAE, top-left), the median absolute percentage error (MdAPE, top-right), the median symmetric accuracy (MdSA, bottom-left) and the median log accuracy ratio (MdLQ, bottom-right). Best accuracy is obtained when the indices are zero, which occurs at $t = 0$ when the model uses the measured flux to initiate the computation. Computations are made at fixed radial diffusion coefficient (*Ozeke et al.*, 2014) and with five electron lifetime models: the one of this study (τ), (*Orlova et al.*, 2014) (τ_{O14}), (*Orlova et al.*, 2016) (τ_{O16}), (*Lyons et al.*, 1972) (τ_L), and none.

None of the results above shall disqualify any radial diffusion model in general since pitch angle diffusion is by construction necessary faster for some finite duration than lifetimes, leading to faster loss. Therefore, stronger radial diffusion models, as the one of *Brautigam and Albert* (2000) or *Liu et al.* (2016), could well be accurate when combined with pitch angle diffusion coefficients in a 3-D Fokker-Planck equation, which could favor stronger diffusion due to non-equilibrium pitch angle diffusion. This study only shows which radial diffusion coefficient and lifetime models are the most accurate when used within a 1-D reduced Fokker-Planck equation. However, the next section 5.6 will be devoted to test these models within a 3-D Fokker-Planck framework.

Finally, Figures 5.8 to 5.11 show the great diversity of solutions obtained according to the choice of models (both D_{LL} and τ), which argues in favor of more simulations (for different events) to confirm the findings of the current study. The good reproduction of the flux decay with the lifetime of this study gives also confidence in the pitch angle diffusion coefficients and a future capability to simulate finer effects with these coefficients used within a 3-D Fokker-Planck framework (e.g., *Tu et al.*, 2013; *Drozdov et al.*, 2015), such as, for instance, the formation of butterfly pitch angle distributions (*Zhao et al.*, 2014a,b; *Albert et al.*, 2016) and pitch angle dependent loss (e.g., *Yu et al.*, 2016).

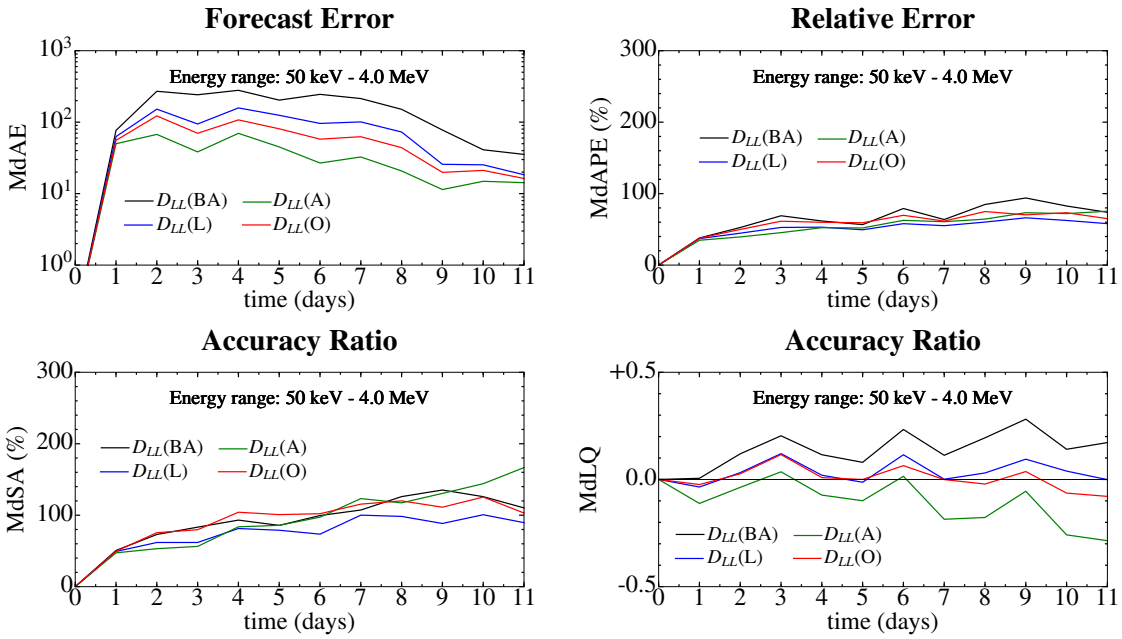

Figure 5.13 – An assessment of the models accuracy through the evolution during the 12 days of the event (4 to 15 March, 2013) of four global error indices: the median absolute error (MdAE, top-left), the median absolute percentage error (MdAPE, top-right), the median symmetric accuracy (MdSA, bottom-left) and the median log accuracy ratio (MdLQ, bottom-right). Best accuracy is obtained when the indices are zero, which occurs at $t = 0$ when the model uses the measured flux to initiate the computation. Computations are made at fixed electron lifetime model (the one of this study, τ (*Ripoll et al.*, 2017)) and for four radial diffusion models: $D_{LL}(BA)$ from *Brautigam and Albert* (2000), $D_{LL}(A)$ from *Ali et al.* (2016), $D_{LL}(L)$ from *Liu et al.* (2016) and $D_{LL}(O)$ from *Ozeke et al.* (2014).

5.5 One dimensional simulations of omnidirectional fluxes

In this section, in regard to the previous results, we only use the combination of the D_{LL} from *Ozeke et al.* (2014) with the event-specific lifetime model for hiss waves τ in one dimensional simulations that solve the reduced Fokker-Planck equation presented above. We here compute omnidirectional electron fluxes by no longer assuming a uniform pitch angle distribution for the PSD.

5.5.1 Pre-processing

We take directly advantage of the MagEIS L3 unidirectional electron flux data j_{VAP} (FEDU) at our disposal (see Figure 5.2, columns 2 to 12) to solve the reduced Fokker-Planck equation using the pitch angle resolved initial and boundary data. As the unidirectional fluxes from the Van Allen Probes are directly available for a given energy and (L, λ) couple, the transformation from the latter local unidirectional fluxes to equatorial unidirectional fluxes shall verify Liouville's theorem that states that the distribution function (or here the electron flux for an equipotential field line) should be conserved along dynamical path (see more details in Chapter 2), i.e.

$$j_{\mathrm{data}}(E, x_0, L, \lambda_0, t) = j_{\mathrm{VAP}}(E, x_s, L, \lambda_s, t), \tag{5.2}$$

with

$$x_0 = \sqrt{1 - \frac{B_0}{B_s}(1 - x_s^2)},$$

as imposed by the conservation of the first adiabatic invariant, for which B_0 is the magnetic field intensity at the equator, and B_s is the local magnetic field intensity. We should take a particular care at performing the transformation (5.2) from local flux to equatorial flux since, even at the relatively low latitudes taken by RBSP A during the March 2013 event ($|\lambda| < 15$ degrees), the equatorial pitch angle α_0 can be significantly lower than the local pitch angle α_s of the electron at latitude λ_s. In this context, Figure 5.14 represents the evolution of the so-called maximum available equatorial pitch angle $\alpha_{0,\max}$, i.e. the values of α_0 such that the electrons mirror at the latitude λ_s covered by RBSP A. In other words, $\alpha_{0,\max} = \arccos\left(\sqrt{1 - B_0/B_s}\right)$. We realize that at some days of the March 2013 event, the maximum available equatorial pitch angle can be significantly lower than the local pitch angle α_s. Performing transformation (5.2) requires the extrapolation of the unidirectional fluxes from $\alpha_0 = \alpha_{0,\max}$ to $\alpha_0 = 90$ degrees.

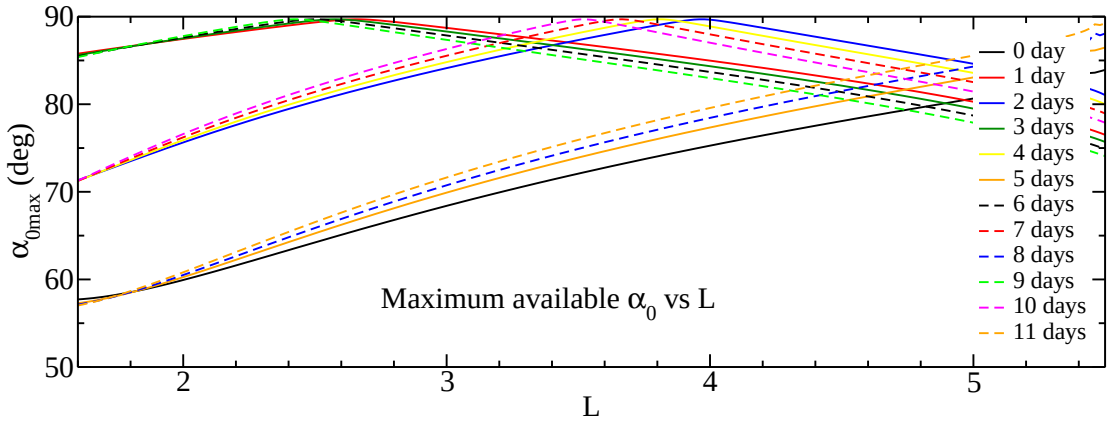

Figure 5.14 – For the outbound orbits of RBSP A considered in the March 2013 event, each latitude taken by Probe A corresponds to one value of L. At each latitude, we compute the so-called maximum available equatorial pitch angle $\alpha_{0,\max}$ that corresponds to a 90 degree local pitch angle α_s (electrons that mirror at λ_s), which verifies $x_s = \sqrt{1 - B_0/B_s}$. For t=0, 5, 8 and 11 days, the equatorial pitch angle corresponding to $\alpha_s = 90$ degrees can be as low as 57 degrees for $L \sim 1.6$.

As before, the equatorial unidirectional flux depicted in the (E, x_0, L) space is used to derive an initial condition and two boundary conditions in terms of a PSD written in the (μ, K, L) space. Figure 5.15 depicts the electron fluxes we use to set the initial condition and the two time-dependent boundary conditions in PSD. The first column represents, as before, the L2 spin-averaged electron fluxes (FESA) as observed by RBSP A on its outbound orbits during the March 2013 event. Columns 3 to 8 represent the L3 unidirectional electron fluxes (FEDU) measured by the satellite and translated using (5.2) at the equatorial pitch angles of 8, 25, 41, 57, 74 and 90 degrees respectively. The L3 unidirectional fluxes have been integrated with respect to local pitch angle to lead to the omnidirectional fluxes represented in the second column. Let us notice that these latter supposed "L3" omnidirectional fluxes (second column) are slightly different from their L2 counterparts (first column). The overall shape is conserved, but the L2 omnidirectional

fluxes exhibit a more significant enhancement at $L \sim 5.0 - 5.5$ for low energies (around 100 keV).

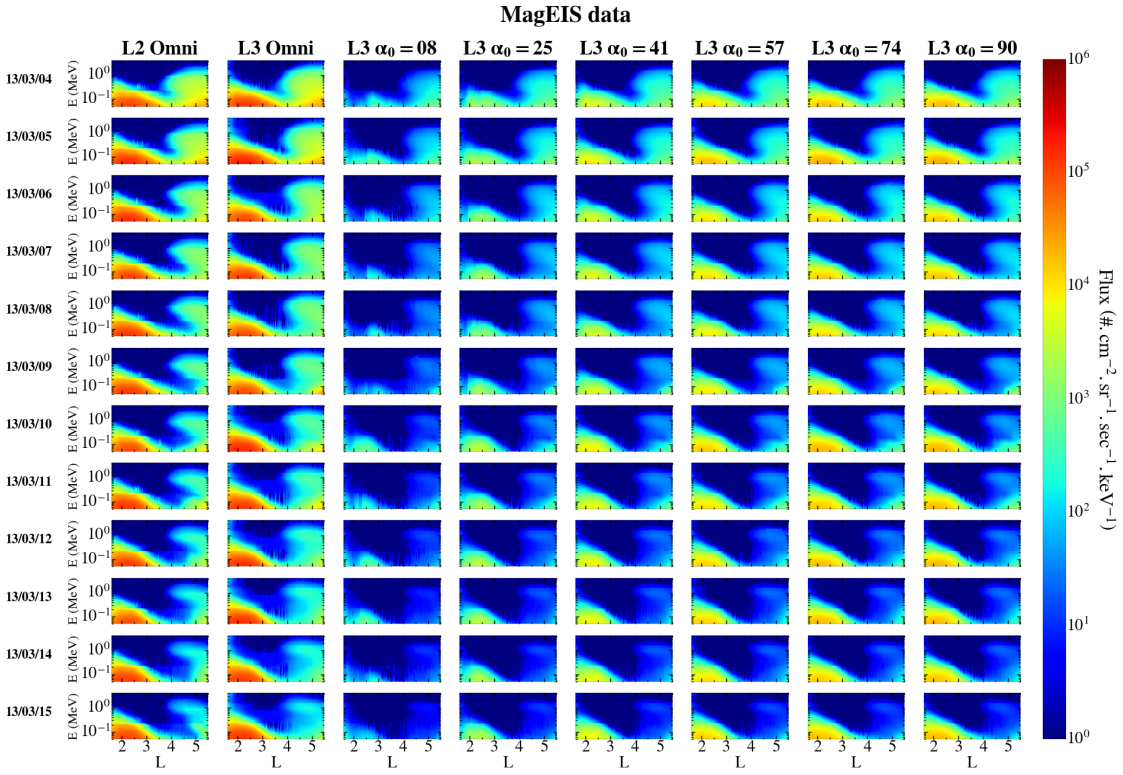

Figure 5.15 – Representation of the data taken from the Van Allen Probes (RBSPA A) for each day, starting from 4 March 2013 to 15 March 2013. Each row represents a snapshot of the electron flux in the (L, E) space at a given time. The first column displays the L2 omnidirectional fluxes measured from the Van Allen Probes. The second column shows the assumed L3 omnidirectional fluxes coming from the integration with respect to α_0 of the measured L3 unidirectional fluxes. The obtained L3 omnidirectional fluxes are rather close to the L2 omnidirectional fluxes of the first column, but some non negligible differences occur between both representations. In particular, the slot appears to be wider at low energies in the representation of the L2 omnidirectional fluxes. The next columns show the equatorial unidirectional fluxes derived from the measured local unidirectional fluxes. The corresponding equatorial pitch angles are respectively 8, 25, 41, 57, 74 and 90 degrees.

5.5.2 Results

The data shown above are used to set the initial condition and the two time-dependent boundary conditions in the (μ, K, L) space for the PSD. The numerical resolution of the reduced Fokker-Planck equation leads to the results presented in Figure 5.16 in the same format as before. The first column shows the omnidirectional flux data coming from the integration of the L3 unidirectional flux data (FEDU) with respect to pitch angle (previously presented in Figure 5.15, second column). Columns 3 to 8 depict the predicted equatorial unidirectional fluxes for an equatorial pitch angle of 8, 25, 41, 57, 74 and 90 degrees. The integration of the simulated unidirectional electron fluxes

results in the predicted omnidirectional illustrated by the second column of Figure 5.15. The accuracy of the model depends on how the predicted omnidirectional fluxes (second column) compare with the omnidirectional fluxes directly inferred from the MagEIS L3 data (first column).

We see from Figure 5.16 that the directional electron fluxes are depleted uniformly in pitch angle due to the lifetime used in the simulations.

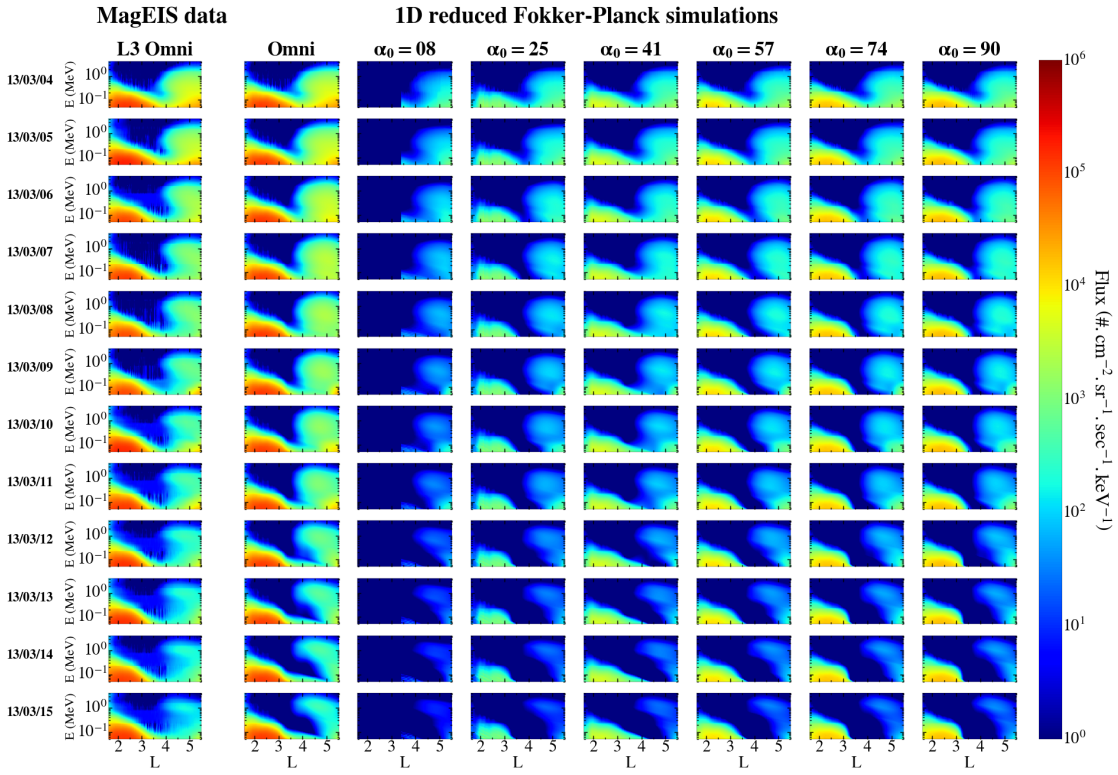

Figure 5.16 – 1-D simulations of electron fluxes in the (L, E) space evolving in time during the period of the 4-15 March 2013. The first column shows the L3 omnidirectional fluxes taken from the Van Allen Probes (MagEIS instrument on board RBSP A). The second column represents the simulated omnidirectional fluxes, calculated from the integration with respect to α_0 of the simulated unidirectional fluxes at each equatorial pitch angle. The next columns represent a snapshot of the calculated unidirectional flux in the (L, E) space for each day and for a respective equatorial pitch angle of 8, 25, 41, 57, 74 and 90 degrees.

5.6 Three dimensional simulations of omnidirectional fluxes

As already mentioned in Chapter 2, the single averaged lifetime τ of the reduced Fokker-Planck equation comes from the reduction of the pitch angle diffusion operator to its first and dominant eigenvalue. Such an approximation only holds if pitch angle scattering is fast compared with the timescale of radial diffusion, so that the full solution of pitch angle diffusion is always close to its equilibrium feature (a so-called long-term solution), and can be therefore written as a single exponential decaying function with time.

However, if electron fluxes exhibiting such a pure decay mode have indeed been observed (*O'Brien et al.*, 2014), it is rather hard to say whether or not the higher eigenmodes of the pitch angle diffusion operator can be neglected. In practice, quiet magnetic conditions combined with a gradual electron dropout are favorable for the relevancy of the aforementioned assumption, but the only way to find out is to compare side by side the results brought by the 1-D reduced Fokker-Planck equation with the ones obtained from the computation of a full pitch angle and radial diffusion code. In this section, we thus simulate the time-evolution of both unidirectional and omnidirectional electron fluxes in a more complete three-dimensional model (in E, α_0 and L) rather than the one-dimensional (in L) reduced Fokker-Planck equation. In this context, the data-driven pitch angle diffusion coefficients presented earlier are directly used in the Fokker-Planck equation that combines pitch angle diffusion occurring at constant energy and L-shell with the radial diffusion process that keeps the two first invariants μ and K unaltered. The code we use to perform the following computations is the Versatile Electron Radiation Belt (VERB) code that have been developed by the UCLA team since the last ten years (courtesy of Y. Shprits). The VERB-3D code is described in detail in (*Subbotin and Shprits*, 2009; *Subbotin et al.*, 2010; *Kim et al.*, 2011).

5.6.1 Model and parameters

5.6.1.a Fokker-Planck equation

The Fokker-Planck equation that governs the evolution of the phase-averaged distribution function f under combined radial diffusion and local (pitch angle and energy) diffusion is written as (e.g., *Schulz and Lanzerotti*, 1974; *Subbotin and Shprits*, 2009; *Subbotin et al.*, 2010; *Kim et al.*, 2011; *Tu et al.*, 2013)

$$\begin{aligned}\frac{\partial f}{\partial t} = {} & L^2 \frac{\partial}{\partial L}\left[\frac{D_{LL}}{L^2}\frac{\partial f}{\partial L}\right]_{(\mu,K)} \\ & + \frac{1}{T(\alpha_0)\sin(2\alpha_0)}\frac{\partial}{\partial \alpha_0}\left[T(\alpha_0)\sin(2\alpha_0)\, D_{\alpha_0\alpha_0}\frac{\partial f}{\partial \alpha_0}\right]_{(p,L)} + \frac{1}{p^2}\frac{\partial}{\partial p}\left[p^2\, D_{pp}\frac{\partial f}{\partial p}\right]_{(\alpha_0,L)} \\ & + \frac{1}{T(\alpha_0)\sin(2\alpha_0)}\left.\frac{\partial}{\partial \alpha_0}\right|_{(p,L)}\left[T(\alpha_0)\sin(2\alpha_0)\, D_{\alpha_0 p}\left.\frac{\partial f}{\partial p}\right|_{(\alpha_0,L)}\right] \\ & + \frac{1}{p^2}\left.\frac{\partial}{\partial p}\right|_{(\alpha_0,L)}\left[p^2\, D_{\alpha_0 p}\left.\frac{\partial f}{\partial \alpha_0}\right|_{(p,L)}\right], \end{aligned} \tag{5.3}$$

for which D_{LL}, $D_{\alpha_0\alpha_0}$ and D_{pp} are respectively the radial, the pitch angle and the momentum (equivalent to energy) diffusion coefficients. We have also included here the cross diffusion coefficients $D_{\alpha_0 p}$ in pitch angle and momentum. The $T(\alpha_0)$ function is the approximate normalized electron bounce period in a dipole field (as defined in Chapter 2), arising from the Jacobian transformation from the canonical adiabatic invariants (J_1, J_2, J_3) to the physical variables (p, α_0, L). Although the cross diffusion coefficients are generally known to have a non-negligible influence on the shape of the radiation belts (e.g., *Albert*, 2005; *Albert et al.*, 2009; *Subbotin et al.*, 2010; *Albert et al.*, 2016), they are neglected in the following because of the lack of event-specific model for the period of 4-15 March, 2013.

In this formulation, the pitch angle diffusion coefficient $D_{\alpha_0\alpha_0}$ and the energy diffusion coefficient D_{pp} only describe the interaction between electrons and whistler mode hiss waves. Since whistler mode hiss waves do not make electrons diffuse significantly in energy (e.g., *Shprits et al.*, 2008b; *Thorne*, 2010), we might be allowed to neglect any energy diffusion and their associated cross diffusion coefficients, and thus the Fokker-Planck equation (5.3) with only the radial and pitch angle diffusion operators should be accurate enough to describe the evolution of the electron fluxes during quiet times.

The radial and pitch angle Fokker-Planck equation is solved with the VERB-3D code (*Subbotin and Shprits*, 2009; *Subbotin et al.*, 2010; *Kim et al.*, 2011). It consists of an unconditionally stable implicit scheme (no stability conditions are imposed, contrary to the CFL imposed on our 1-D explicit reduced Fokker-Planck code). As explained in section 4.2, the code relies on two grids: a so-called radial diffusion grid in (μ, K, L) on which radial diffusion is solved, and on a so-called pitch angle and energy diffusion grid in (E, α_0, L) on which the pitch angle diffusion and energy diffusion is solved. At each time step, the PSD is interpolated between the two grids. In what follows, we refer to the simulations performed with the VERB-3D code as 3-D simulations, despite the fact that possible radial-local cross diffusion are ignored due to the use of the two independent grids.

5.6.1.b Diffusion coefficients

In the context of our simulations, we consider the radial diffusion coefficient $D_{LL}(\mathrm{O})$ of *Ozeke et al.* (2014) and the data-driven pitch angle diffusion coefficient $D_{\alpha_0\alpha_0}$ of section 5.3 that accounts for whistler mode hiss wave activity (presented above), interpolated on the pitch angle and energy diffusion grid of VERB-3D. The hiss activity is extended on the whole spatial domain (L-shells) rather than being constrained by an ad-hoc plasmapause model (the plasmapause being directly accounted by the electron density, which is used to compute the data-driven pitch angle diffusion coefficient).

As a preliminary estimation of the energy diffusion coefficient, we assume that D_{pp} can be computed as $D_{pp} = \left(D_{pp}^{\mathrm{O16}}/D_{\alpha_0\alpha_0}^{\mathrm{O16}}\right) D_{\alpha_0\alpha_0}$, for which $D_{\alpha_0\alpha_0}^{\mathrm{O16}}$ and D_{pp}^{O16} are respectively the pitch angle and energy diffusion coefficients derived from the whistler mode hiss wave activity by *Orlova et al.* (2016).

We first neglect the D_{pp} term and all the cross-terms in equation (5.3), such that only radial diffusion and pitch angle diffusion are taken into account.

5.6.1.c Grid parameters

We use 45 uniformly distributed bins in L-shell, going from $L = 1.6$ (inner boundary) to $L = 5.5$ (outer boundary). We also work with a uniform geometric grid in α_0 made of 100 bins, from 0.3 to 89.7 degrees, and with an energy grid with 100 bins uniformly distributed in logarithm space, going from 0.5 keV to 4.5 MeV.

The time step of our simulations is set to 0.1 hour. The logarithm of the PSD value between the radial diffusion grid and the pitch angle and energy diffusion grid are interpolated by using spline functions. Moreover, we choose to use the highly resolved (but computationally more costly) Lapack package for successive matrix inversion, and we use the Block method that solves for pitch angle and energy diffusion simultaneously. Let us mention that, as before, the magnetic field model into consideration is the dipole field.

5.6.1.d Initial and boundary conditions

The initial condition is the PSD on March 4, 2013 that has been performed from the L3 unidirectional fluxes measured by the MagEIS instrument, as we have done for the 1-D reduced Fokker-Planck code. Similarly, we consider for the inner and outer boundary conditions in L-shell the time-dependent PSD (at L_0 and L_M) computed directly from the L3 unidirectional flux data. The version of the VERB-3D code in use during this PhD thesis was only able to take account of static boundary conditions. Therefore, supplementary numerical developments have been required to include such dynamical boundary conditions in the 3-D model. This is done by a script file that successively runs the code with constant boundary conditions during a small time step of 3 hours, which means that these two boundary conditions in L are updated every 3 hours. We also consider a flat pitch angle distribution at $\alpha_{0,\max}$ (i.e. such that $\partial f/\partial\alpha_0|_{\alpha_{0,\max}} = 0$) and a zero PSD at $\alpha_{0,\min}$. The inner boundary condition in energy is set to a constant equal to the initial value at the initial state, i.e. $f(E_{\min}, \alpha_0, L, t) = f_0(E_{\min}, \alpha_0, L)$, whereas the outer boundary condition in energy is set to zero.

In the purpose of understanding the influence of the initial pitch angle distribution on the shape of the omnidirectional electron flux, we build pitch angle dependent initial and boundary conditions by implementing two different approaches. The first approach uses a combination of the available L2 spin-averaged electron flux observed by RBSP A (first column of Figure 5.2) with an empirical model of pitch angle distribution that depends on energy and L-shell. A second approach discards any empirical model for the pitch angle distribution and rather uses, as before, the whole set of available L3 unidirectional fluxes. Comparing the simulations related to each process enables us to identify the effects of the initial pitch angle distribution on the shape of the radiation belts up to 12 days.

5.6.2 Uniform pitch angle distribution

We can first simply consider a uniform pitch angle distribution as done in the previous section. The results are shown in Figure 5.17. This simple model is only used to quantify the benefits of using the more realistic nonuniform pitch angle distribution depicted in section 5.6.3.

5.6.3 Using MagEIS L2 omnidirectional flux data

5.6.3.a Deriving the corresponding MagEIS L2 unidirectional fluxes

First we assume that we know a priori the pitch angle distribution of the unidirectional fluxes. Let us call $\widetilde{j}(E, x_0, L)$ this presumably known normalized pitch angle distribution, that is also energy and L-dependent. The desired unidirectional flux writes therefore

$$j_{\text{data}}(E, x_0, L, \lambda_0, t) = A(E, L, \lambda_0, t)\,\widetilde{j}(E, x_0, L), \tag{5.4}$$

for which the factor A has to be determined and relates the theoretical unidirectional fluxes with the omnidirectional flux at our disposal. From equation (2.68) that enables us to calculate the omnidirectional flux at a given latitude λ_s according to the knowledge of the equatorial unidirectional flux we still have $J_{\text{VAP}}(E, L, \lambda_s, t) \equiv J_O(E, L, \lambda_s, t)$ with

$$J_O(E, L, \lambda_s, t) = 4\pi \frac{B_s}{B_0} \int_{x_0=\sqrt{1-B_0/B_s}}^{x_0=x_{0LC}} j_{\text{data}}(E, x_0, L, \lambda_0, t)\, \frac{x_0}{\sqrt{1 - \dfrac{B_s}{B_0}\left(1 - x_0^2\right)}}\, \mathrm{d}x_0,$$

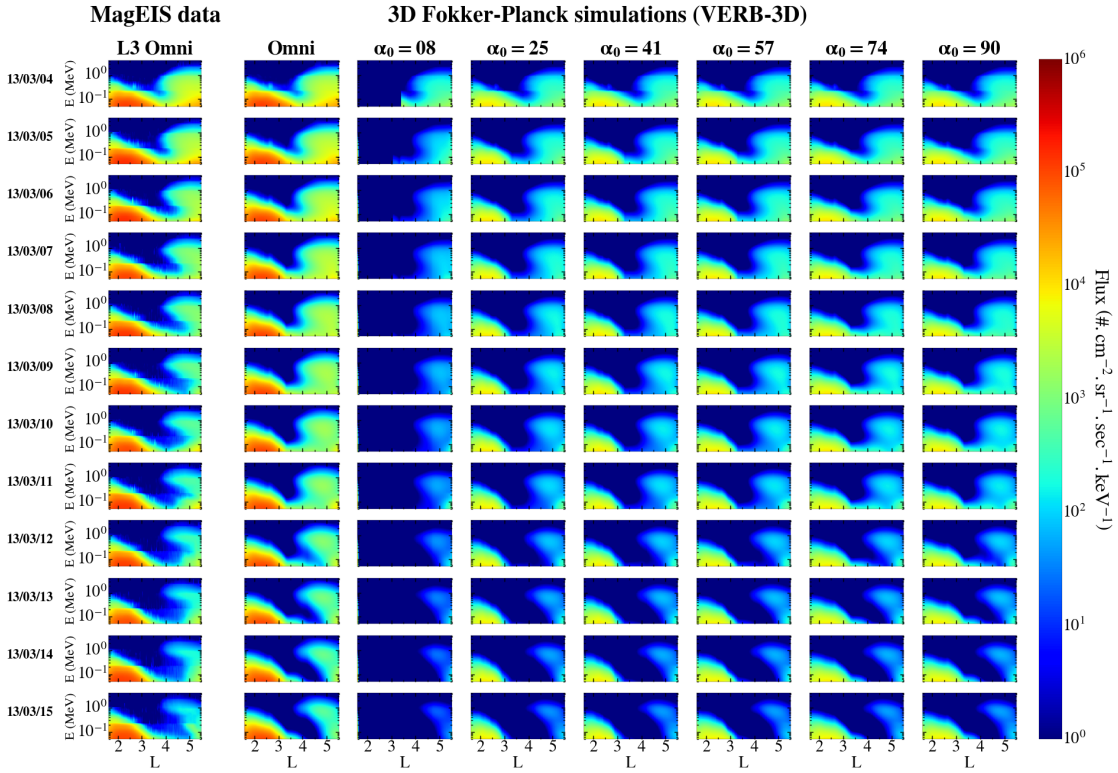

Figure 5.17 – 3-D simulations of electron fluxes in the (L, E) space evolving in time during the period of the 4-15 March 2013. The first column shows the L2 omnidirectional fluxes taken from the Van Allen Probes (MAGEIS instrument on board RBSP A). The second column represents the simulated omnidirectional fluxes, calculated from the integration with respect to α_0 of the simulated unidirectional fluxes at each equatorial pitch angle. The next columns represent a snapshot of the calculated unidirectional flux in the (L, E) space for each day and for a respective equatorial pitch angle of 8, 25, 41, 57, 74 and 90 degrees. The initial and boundary conditions have been set up directly from the omnidirectional fluxes of the first column and by considering a uniform pitch angle distribution.

which gives, with the use of (5.4),

$$J_O(E, L, \lambda_s, t) = 4\pi A(E, L, \lambda_0, t)\, \frac{B_s}{B_0} \int_{x_0=\sqrt{1-B_0/B_s}}^{x_0=x_{0LC}} \widetilde{j}_0(E, x_0, L)\, \frac{x_0}{\sqrt{1 - \frac{B_s}{B_0}\left(1 - x_0^2\right)}}\, \mathrm{d}x_0.$$

Let us denote by $\widetilde{J}_O(E, L, \lambda_s, t)$ the integration of the normalized theoretical flux with respect to x_0, such that

$$\widetilde{J}_O(E, L, \lambda_s, t) = 4\pi \frac{B_s}{B_0} \int_{x_0=\sqrt{1-B_0/B_s}}^{x_0=x_{0LC}} \widetilde{j}(E, x_0, L, \varphi_g, \lambda_0, \varphi_d, t)\, \frac{x_0}{\sqrt{1 - \frac{B_s}{B_0}\left(1 - x_0^2\right)}}\, \mathrm{d}x_0,$$

Then the factor $A(E, L, \lambda_0, t)$ can be extracted to gives

$$A(E, L, \lambda_0, t) = \frac{J_O(E, L, \lambda_s, t)}{\widetilde{J_O}(E, L, \lambda_s, t)}.$$

Equation (5.4) writes therefore

$$j_{\text{data}}(E, x_0, L, \lambda_0, t) = \frac{J_O(E, L, \lambda_s, t)}{\widetilde{J_O}(E, L, \lambda_s, t)} \widetilde{j}(E, x_0, L). \tag{5.5}$$

Empirical models of pitch angle distributions for electrons in the Earth's radiation belts are legion in the literature (*Vampola*, 1997; *Horne et al.*, 2003; *Gannon et al.*, 2007; *Xudong et al.*, 2011; *Zhao et al.*, 2014a,b; *Chen et al.*, 2014; *Ni et al.*, 2015; *Shi et al.*, 2016).

More specifically, *Chen et al.* (2014) adopted an empirical model, called the Relativistic Electron Pitch Angle Distribution (REPAD), to present statistical pictures of electron pitch angle distributions by using Legendre polynomials to fit long-term in situ directional fluxes observed near the magnetic equator from three missions: CRRES, POLAR, and LANL-97A. Such a sophisticated model is able to provide an accurate representation of magnetospheric electron distributions (allowing to cover the whole outer belt region), but relies on many input parameters, which results in increased complexity.

Shi et al. (2016) rather focused on the inner magnetosphere ($L < 6$), for which pitch angle distributions are supposed to be more likely to fit to a $\sin^n(\alpha)$ form (first-order fitting method). The power law index n has thus been quantified as a function of electron kinetic energy, MLT interval, and geomagnetic index K_p. Their statistical analysis of pitch angle distributions was based on the data from the MagEIS instrument on board the Van Allen Probes during the period from 1 October 2012 to 1 May 2015. In the purpose a using a simple model for the normalized pitch angle distribution $\widetilde{j}(E, x_0, L)$ that we use in the above formulation, we consider the latter statistical representation of *Shi et al.* (2016), and we use the MLT-averaged n values of *Shi et al.* (2016, their Figure 9, left column) corresponding to a quiet geomagnetic activity. Hence we have

$$\widetilde{j}(E, \alpha_0, L) = \sin^{n(E,L)}(\alpha_0),$$

or in terms of variable x_0,

$$\widetilde{j}(E, x_0, L) = \left(1 - x_0^2\right)^{n(E,L)/2}.$$

From the obtained equatorial unidirectional fluxes $j_{\text{data}}(E, x_0, L, \lambda_0, t)$, we easily derive the corresponding PSD as $f(E, x_0, L, t) = j_{\text{data}}(E, x_0, \lambda_0, L, t)/p^2$ and then perform the transformation from the (E, x_0, L) space to the adiabatic space (μ, K, L) as depicted in Chapter 4. From the data-derived PSD $f(\mu, K, L, t)$ we can extract the initial condition $f_0(\mu, K, L) = f(\mu, K, L, t = 0)$ and the respective inner and outer boundary conditions $f_{L_0}(\mu, K, t) = f(\mu, K, L_0, t)$ and $f_{L_M}(\mu, K, t) = f(\mu, K, L_M, t)$.

Figure 5.18 represents the electron fluxes that enable to produce the initial and boundary conditions required to solve the reduce Fokker-Planck equation. More specifically, the first column represents the L2 spin-averaged electron fluxes observed by RBSP A (also previously represented in Figure 5.2, first column), while the columns from 3 to 8 display the obtained unidirectional fluxes directly calculated from the L2 omnidirectional data fluxes according to relation (5.5). The second column represents the omnidirectional flux obtained by integrating the unidirectional fluxes with respect to the equatorial pitch

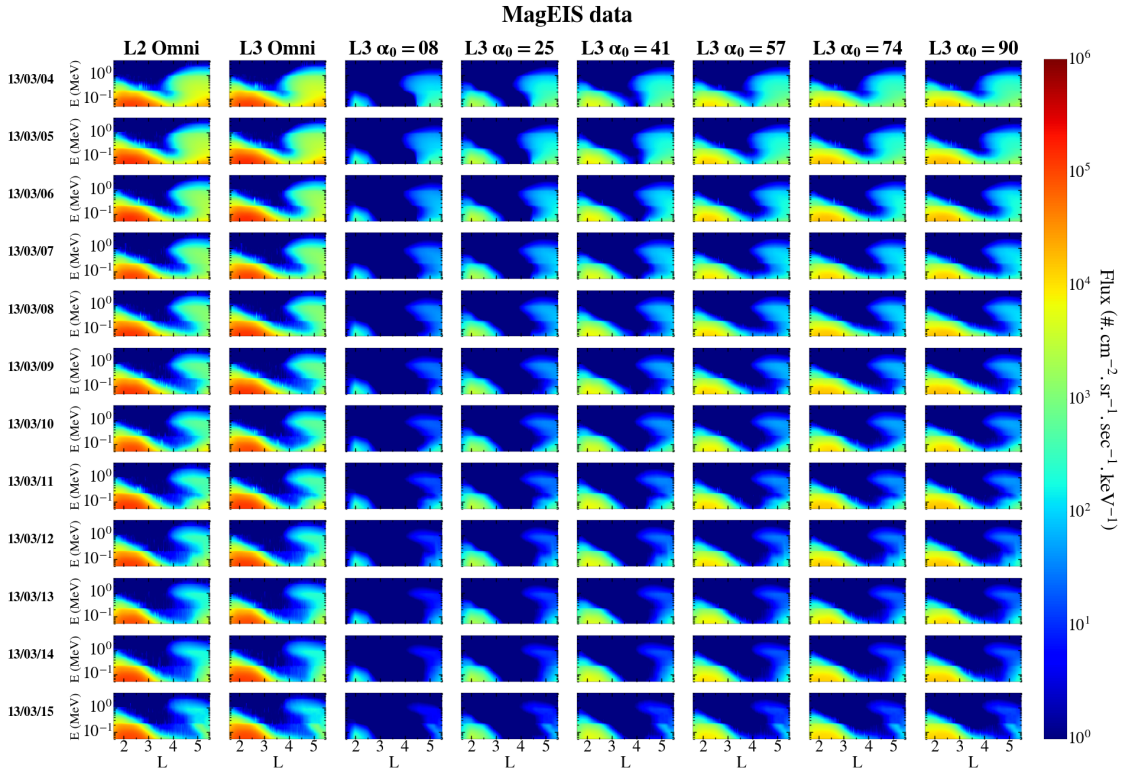

Figure 5.18 – Representation of the data taken from the Van Allen Probes (RBSPA A) for each day, starting from 4 March 2013 to 15 March 2013. Each row represents a snapshot of the electron flux in the (L, E) space at a given time. The first column displays the L2 omnidirectional fluxes measured from the Van Allen Probes. The second column shows the integration with respect to α_0 of the assumed unidirectional fluxes calculated according to the pitch angle distributions from *Shi et al.* (2016). The obtained omnidirectional fluxes have the exact same profile of the omnidirectional flux displayed in the first column. The next columns show the corresponding calculated unidirectional fluxes for a respective equatorial pitch angle of 8, 25, 41, 57, 74 and 90 degrees, according to the profiles predicted by *Shi et al.* (2016).

angle α_0 for each energy and couple (L, λ), according to (2.68). This way we verify that the obtained omnidirectional flux (column 2) equates, by construction as expected, the L2 omnidirectional flux measured by Van Allen Probe A (column 1).

It is also instructive to compare the observed L3 unidirectional fluxes in column 3 to 8 of 5.15 with the predicted unidirectional fluxes represented in Figure 5.18 (from column 3 to 8). Both observed and predicted unidirectional fluxes are very similar on March 4, 2013 for high equatorial pitch angles ($\alpha_0 \geq 57$ degrees). However the predicted unidirectional flux values are lower in the slot region for low pitch angles ($\alpha_0 \leq 41$ degrees).

5.6.3.b Results

Once the necessary data have been constructed, we can properly define the initial and boundary conditions to perform the numerical solution of the reduced Fokker-Planck equation with $D_{LL}(O)$ and τ. The results are presented in Figure 5.19.

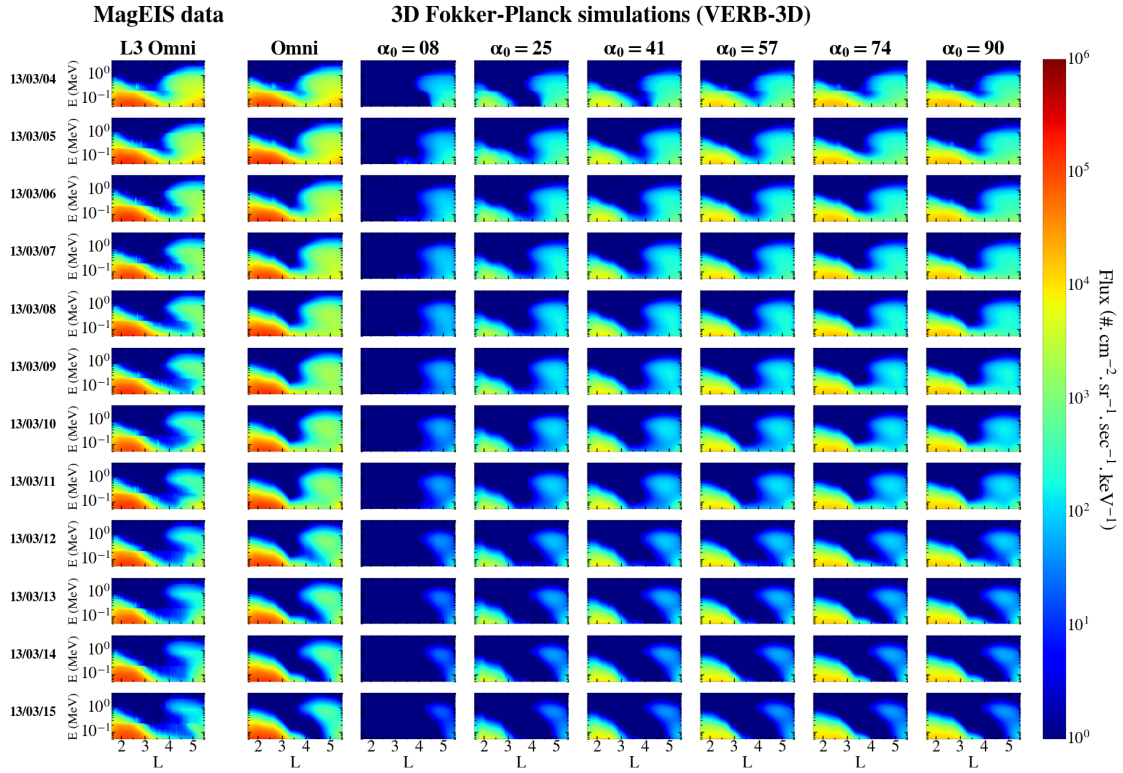

Figure 5.19 – 3-D simulations of electron fluxes in the (L, E) space evolving in time during the period of the 4-15 March 2013. The first column shows the L2 omnidirectional fluxes taken from the Van Allen Probes (MAGEIS instrument on board RBSP A). The second column represents the simulated omnidirectional fluxes, calculated from the integration with respect to α_0 of the simulated unidirectional fluxes at each equatorial pitch angle. The next columns represent a snapshot of the calculated unidirectional flux in the (L, E) space for each day and for a respective equatorial pitch angle of 8, 25, 41, 57, 74 and 90 degrees. The initial and boundary conditions have been set up directly from the omnidirectional fluxes of the first column and by considering the nonuniform pitch angle distribution given by the model of *Shi et al.* (2016).

At first sight, we do not see significant changes between the simulated omnidirectional flux integrated from nonuniform pitch angle distributions with the previously derived omnidirectional flux coming from a uniform distribution for the same set of parameters (see Figure 5.17, column 2). The electron flux decreases in the slot region is now a bit lower and takes a longer time. However, the computation of the global indices MdAE, MdAPE, MdLQ and MdSA given in Table 5.2 indicates that MdAE = 23 (versus MdAE = 22 for the uniform distribution), MdAPE = 41% (versus MdAPE = 46%), MdLQ = 2.3×10^{-2} (versus MdLQ = -9.6×10^{-4}) and MdSA = 52% (versus MdSA = 66%), which is slightly better than the indices related to the previous uniform case (see Table 5.2). This result indicates the importance of dealing with the unidirectional quantities to set the initial and boundary conditions of the whole problem for 3-D simulations.

5.6.3.c Comparison with the simulated unidirectional fluxes

We depict in Figure 5.20 the time-evolution of MdAE (top-left), MdAPE (top-right), MdSA (bottom-left) and MdLQ (bottom-right) for the electron fluxes simulated in the previous section (blue lines) and the fluxes predicted by combining the L2 flux data with the empirical model of pitch angle distributions inferred by *Shi et al.* (2016) (red lines).

We notice some tiny improvements coming from the last model compared with the previously simulated fluxes uniformly distributed in pitch angles. For example, considering an initial realistic pitch angle distribution leads to less overestimations than with a uniform distribution. Table 5.2 provides the global indices over the full period for both simulations, also highlighting a better prediction for the 3-D simulations based on the empirically derived ((*Shi et al.*, 2016)) nonuniform unidirectional flux data rather than the computations relying on the uniformly distributed (in pitch angles) unidirectional fluxes.

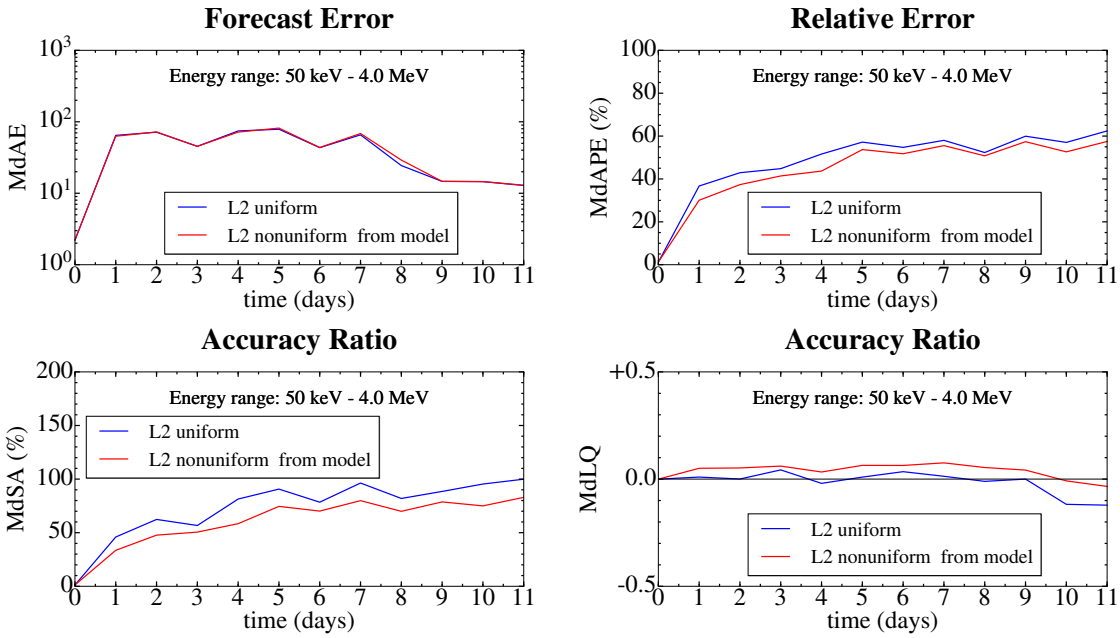

Figure 5.20 – Evolution of the median absolute error (MdAE, top-left), the median absolute percentage error (MdAPE, top-right), the median symmetric accuracy (MdSA, bottom-left) and the median log accuracy ratio (MdLQ, bottom-right) versus time for predicted omnidirectional fluxes calculated from a uniform pitch angle distribution (blue lines) and from the empirically-derived pitch angle distribution adopted by *Shi et al.* (2016) (red lines). The four panels indicate a better reproduction for an initial realistic distribution in pitch angles.

5.6.4 Using MagEIS L3 unidirectional flux data

5.6.4.a Results

Simulations of electron fluxes governed by radial and pitch angle diffusion are presented in Figure 5.21. As before, the reference omnidirectional flux observations are shown in the first column, and come from the integration (with respect to pitch angle) of

Table 5.2 – Global Median Absolute Error (MdAE), Median Absolute Percentage Error (MdAPE), Median Log Accuracy Ratio (MdLQ) and Median Symmetric Accuracy (MdSA) for the 3-D simulations computed with the L2-derived uniform distributions and the L2-derived nonuniform distributions. The indicated indices correspond to the omnidirectional electron fluxes and have been calculated over all available L-shells, energies and times.

	3-D simulations uniform distribution from L2 data	3-D simulations nonuniform distribution from L2 data and *Shi et al.* (2016)
MdAE	2.2×10^{1}	2.3×10^{1}
MdAPE	46%	41%
MdLQ	-9.6×10^{-4}	2.3×10^{-2}
MdSA	66%	52%

the L3 unidirectional fluxes measured by the MagEIS instrument. Columns 3 to 8 represent the simulated unidirectional fluxes, whose integration with respect to pitch angle leads to the predicted omnidirectional fluxes of the second column.

5.6.4.b Comparison between the L3 omnidirectional fluxes with the direct use of data or the use of a statistical formulation for the pitch angle distribution

We can also use the calculated L3 omnidirectional flux data to derive empirical unidirectional fluxes by using the approach of *Shi et al.* (2016) and compare them with the L3 unidirectional flux data. In Figure 5.22 we show the evolution of the omnidirectional and unidirectional electron fluxes whose initial and boundary conditions have been set up with the combination of the L3 omnidirectional data and the empirically derived pitch angle distributions from *Shi et al.* (2016).

We can compare the performance of our computations according to the data in use by the model (either the combination of L3 omnidirectional flux data with an empirical model of pitch angle distributions, or the direct use of the L3 unidirectional flux data). Figure 5.23 shows the evolution of the error metrics; the median absolute error (MdAE, top-left), the median absolute percentage error (MdAPE, top-right), the median symmetric accuracy (MdSA, bottom-left) and the median log accuracy ratio (MdLQ, bottom-right) versus time for the simulations coming from the pitch angle distributions calculated by (*Shi et al.*, 2016) combined with the L3 omnidirectional data (blue) and the one extracted directly from the L3 unidirectional data alone (red).

The statistics are very close to each other, but they exhibit a slight improvement when the L3 unidirectional flux data (red) are directly used to build the initial and boundary conditions. Table 5.3 provides the global indices over the full period for both simulations, also highlighting a better prediction for the 3-D simulations based on the realistic nonuniform unidirectional flux data. Still, differences are small enough so that we conclude that the *Shi et al.* (2016) model is accurate for quiet time periods lasting about 12 days when used in a 3-D Fokker-Planck model.

5.6.4.c Comparison between the L3 omnidirectional fluxes in 1-D and 3-D

As before, the simulations highlight an increasingly wider slot from March 4 to March 15, 2013, which is consistent with the observations. The results are also very close to the

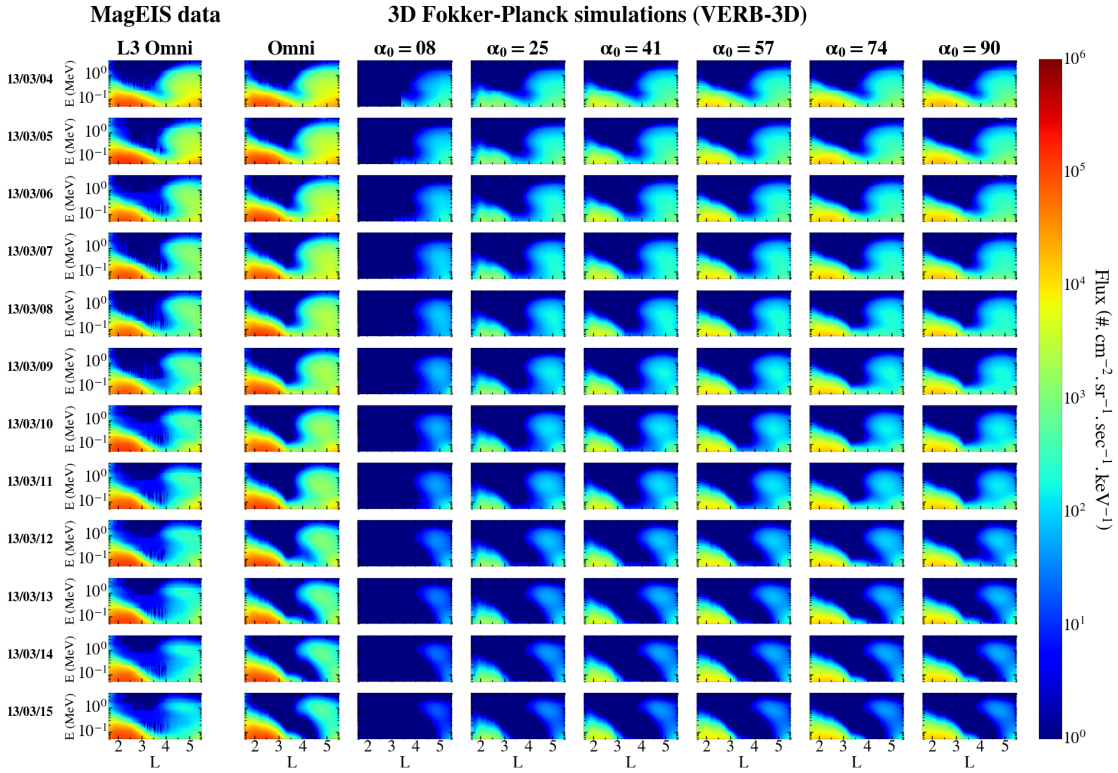

Figure 5.21 – 3-D simulations of electron fluxes in the (L, E) space evolving in time during the period of the 4-15 March 2013. The first column shows the L3 omnidirectional fluxes taken from the Van Allen Probes (MAGEIS instrument on board RBSP A). The second column represents the simulated omnidirectional fluxes, calculated from the integration with respect to α_0 of the simulated unidirectional fluxes at each equatorial pitch angle. The next columns represent a snapshot of the calculated unidirectional flux in the (L, E) space for each day and for a respective equatorial pitch angle of 8, 25, 41, 57, 74 and 90 degrees. The initial and boundary conditions have been set up directly from the nonuniform pitch angle distribution given by the L3 data of Figure 5.15.

Table 5.3 – Global Median Absolute Error (MdAE), Median Absolute Percentage Error (MdAPE), Median Log Accuracy Ratio (MdLQ) and Median Symmetric Accuracy (MdSA) for the 3-D simulations computed with the L3-derived nonuniform distributions from the empirical model of *Shi et al.* (2016) and the L3-derived nonuniform distributions from the L3 unidirectional flux data. The indicated indices correspond to the omnidirectional electron fluxes and have been calculated over all available L-shells, energies and times.

	3-D simulations nonuniform distribution from L3 data and *Shi et al.* (2016)	3-D simulations nonuniform distribution from L3 data
MdAE	4.3×10^{1}	3.9×10^{1}
MdAPE	62%	61%
MdLQ	2.0×10^{-2}	8.5×10^{-3}
MdSA	88%	87%

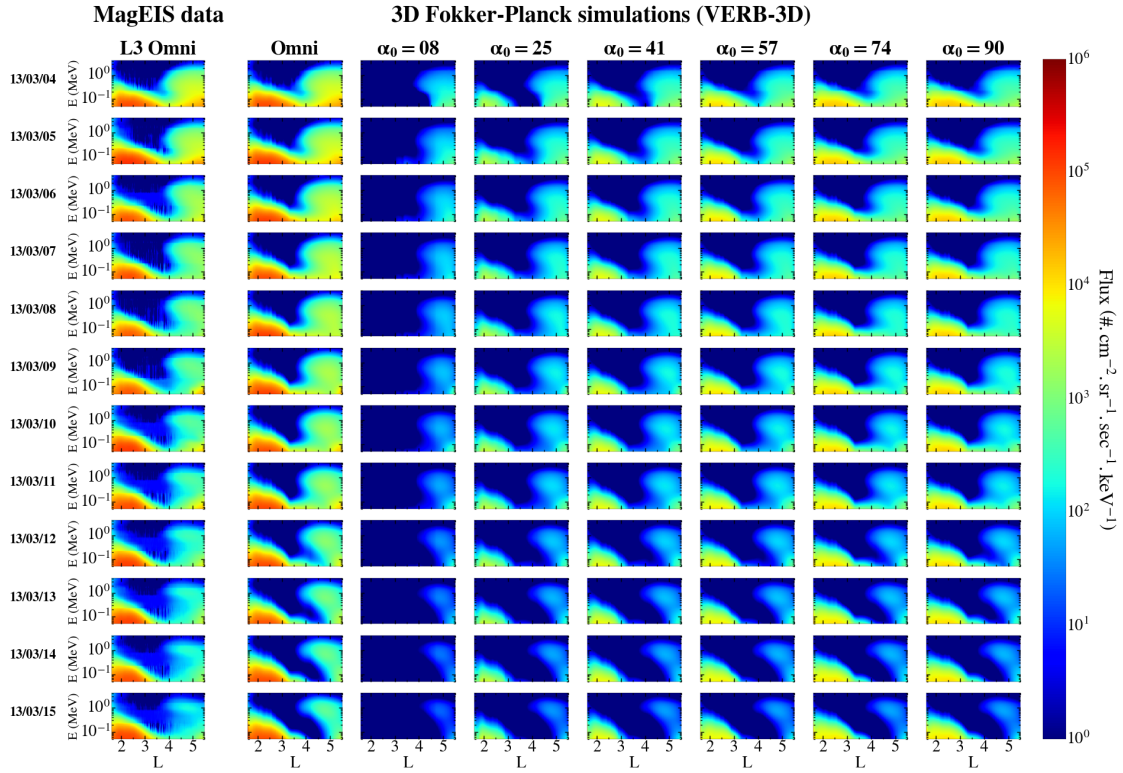

Figure 5.22 – 3-D simulations of electron fluxes in the (L, E) space evolving in time during the period of the 4-15 March 2013. The first column shows the L3 omnidirectional fluxes taken from the Van Allen Probes (MagEIS instrument on board RBSP A). The second column represents the simulated omnidirectional fluxes, calculated from the integration with respect to α_0 of the simulated unidirectional fluxes at each equatorial pitch angle. The next columns represent a snapshot of the calculated unidirectional flux, following the empirically-derived pitch angle distributions of *Shi et al.* (2016) combined with the L3 omnidirectional data, in the (L, E) space for each day and for a respective equatorial pitch angle of 8, 25, 41, 57, 74 and 90 degrees.

Table 5.4 – Global Median Absolute Error (MdAE), Median Absolute Percentage Error (MdAPE), Median Log Accuracy Ratio (MdLQ) and Median Symmetric Accuracy (MdSA) for the 1-D simulations computed with the L3-derived nonuniform distributions from the L3 unidirectional flux data and the 3-D simulations including radial and pitch angle diffusion. The indicated indices correspond to the omnidirectional electron fluxes and have been calculated over all available L-shells, energies and times.

	1-D simulations nonuniform distribution from L3 data	3-D simulations nonuniform distribution from L3 data
MdAE	5.0×10^{1}	3.9×10^{1}
MdAPE	67%	61%
MdLQ	-5.9×10^{-2}	8.5×10^{-3}
MdSA	100%	87%

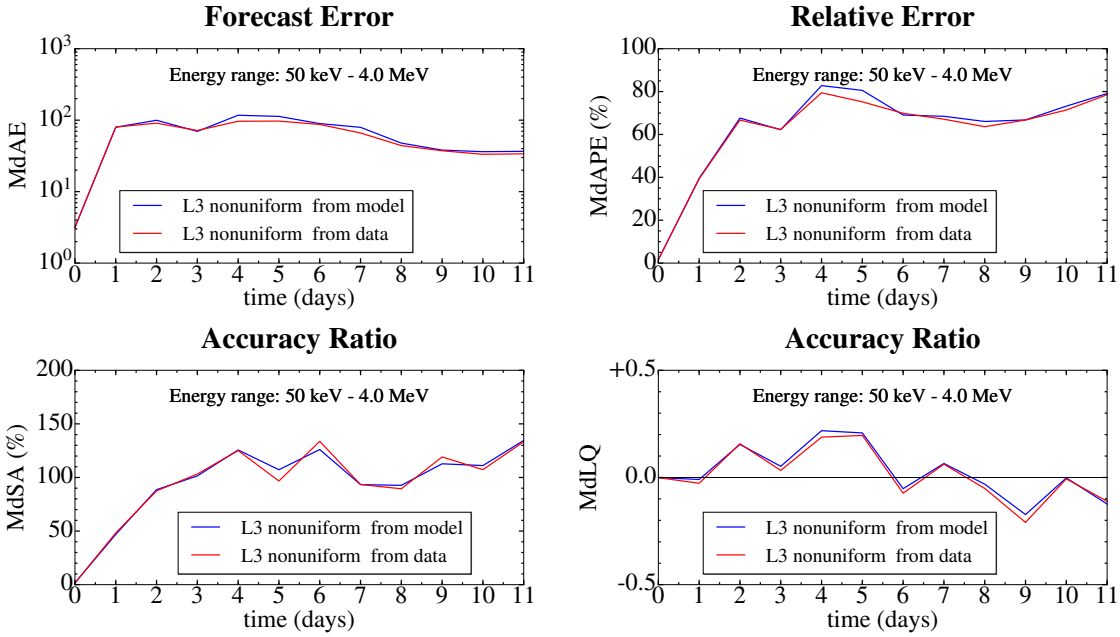

Figure 5.23 – The four panels represent respectively the median absolute error (MdAE, top-left), the median absolute percentage error (MdAPE, top-right), the median symmetric accuracy (MdSA, bottom-left) and the median log accuracy ratio (MdLQ, bottom-right) versus time for the simulated fluxes that are taken from the simulation that used the L3 electron flux data with the combination of the empirical pitch angle distribution calculated by *Shi et al.* (2016) (blue) and for the omnidirectional fluxes calculated with the use of the L3 unidirectional flux data (red).

fluxes obtained through the resolution of the reduced Fokker-Planck equation, indicating that approximating the pitch angle diffusion operator with its first eigenvalue is relevant in the context of this quiet March 2013 event. In what follow, we compare the accuracy of the 3-D model versus the 1-D model.

The accuracy of both 1-D and 3-D models are illustrated in Figure 5.24. The statistics related to the reduced Fokker-Planck model (blue) and the 3-D code (red) are shown in the four panels respectively for the MdAE (top-left), the MdAPE (top-right), the MdSA (bottom-left) and the MdLQ (bottom-right) indices. Speaking in terms of omnidirectional fluxes, the VERB-3D code performs solutions that are closer to the L3 omnidirectional flux data than with the 1-D code. The latter particularly exhibits a pronounced overestimation at early times ($t \leq 6$ days), contrary to its 3-D counterpart. Some noticeable oscillations characterize the evolution of the MdSA and MdLQ metrics versus time. These two latter metrics equivalently penalize the overestimations and the underestimations, contrary to MdAPE (that penalizes more heavily the overestimations) and MdAE (that penalizes the large errors), for which there is no such erratic variations. Hence the MdSA and MdLQ metrics are more likely to be sensitive to the noise levels and they consequently get contaminated by the measures of the (non physically significative) differences related to low-energy electrons of the slot region between data and simulations.

Table 5.4 provides the global indices over the full period for both simulations, also highlighting a better prediction for the 3-D radial and pitch angle computations. Still,

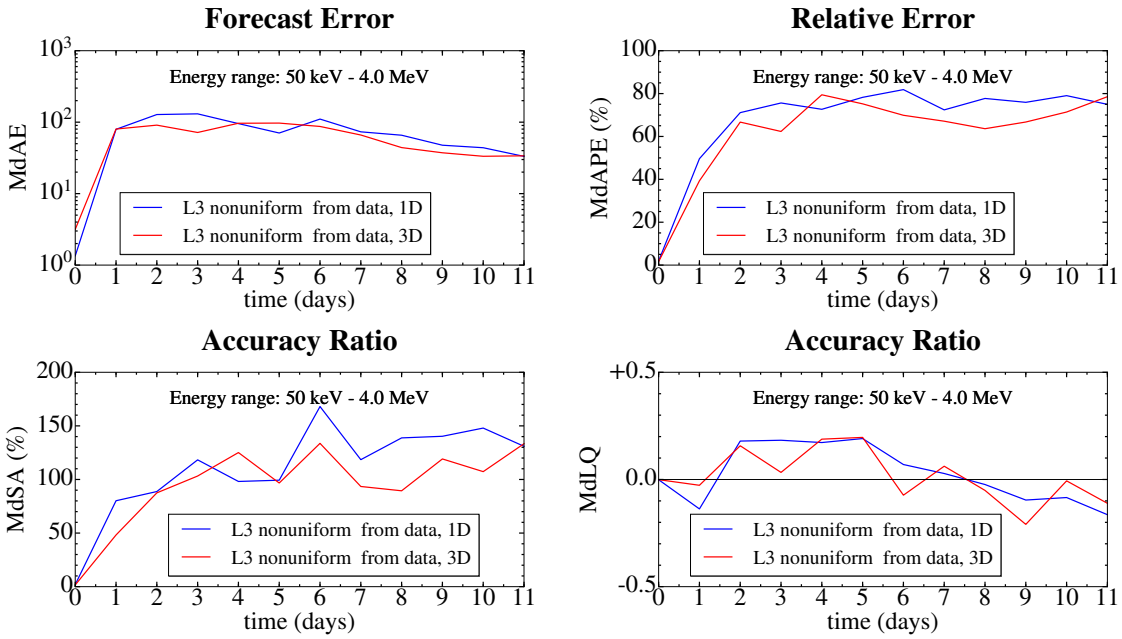

Figure 5.24 – The four panels represent respectively the median absolute error (MdAE, top-left), the median absolute percentage error (MdAPE, top-right), the median symmetric accuracy (MdSA, bottom-left) and the median log accuracy ratio (MdLQ, bottom-right) versus time for the simulated fluxes that are taken from the L3 unidirectional flux data computed with the reduced Fokker-Planck 1-D code (blue) and the VERB-3D code (red). The evolution of the median symmetric accuracy indicates that the fluxes obtained from the 3-D simulations are slightly closer to the data than the predicted omnidirectional fluxes performed with the 1-D code. The median log accuracy ratio exhibits a more pronounced overestimation at early times ($t \leq 6$ days) for the 1-D solutions.

both 1-D and 3-D codes are found to give an accurate representation of the event.

5.6.5 Influence of local acceleration

Here we consider the influence of the energy diffusion (D_{pp} term) in the Fokker-Planck equation (5.3), still neglecting the cross-term $D_{\alpha_0 p}$. Figure 5.25 represents the data-driven normalized energy diffusion coefficient D_{pp}/p^2 versus energy and L-shell for the two periods of March 4-10 and March 11-15, 2013. We recall that the energy diffusion coefficient has been calculated generically from the knowledge of the event-specific pitch angle diffusion coefficient $D_{\alpha_0\alpha_0}$ and the ratio $D_{pp}^{\mathrm{O16}}/D_{\alpha_0\alpha_0}^{\mathrm{O16}}$ of *Orlova et al.* (2016).

The intensity of the derived normalized energy diffusion coefficients is significantly lower than the intensity of the data-driven pitch angle diffusion coefficient (see Figure 5.3), confirming the fact that local acceleration is not the main driver process at stake during this March 2013 event. The corresponding simulations of omnidirectional fluxes based on the L3 nonuniform pitch angle distribution observed by the MagEIS instrument are displayed in Figure 5.26.

Figure 5.26 shows very similar results to the simulations implemented without energy diffusion (see Figure 5.21). A tiny difference is noticeable at low energy (below 100 keV) for $L \sim 3-4$, for which the latter simulation emphasizes a smoother decrease of electron flux than the computations accounting for radial and pitch angle diffusion only. Figure

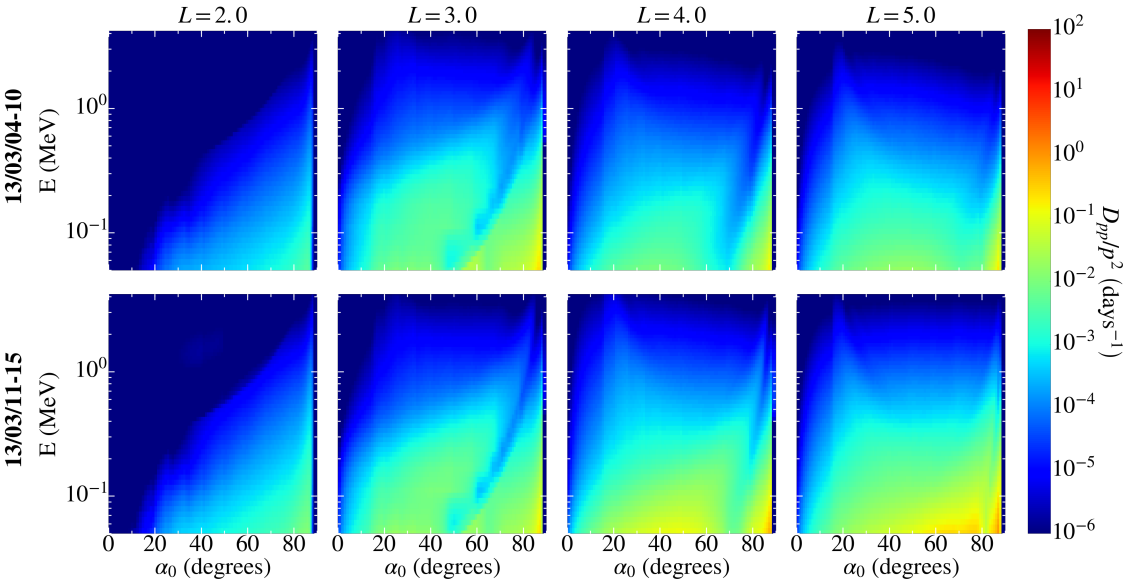

Figure 5.25 – Representation of the data-driven energy diffusion coefficient D_{pp}/p^2 versus E and α_0. The first row represents the D_{pp}/p^2 computed for the period of March 4-10, 2013, and the second row displays the D_{pp}/p^2 calculated for the second period of March 11-15, 2013. Each column corresponds to a given L-shell, respectively L=2.0, 3.0, 4.0 and 5.0.

5.27 represents the evolution of the four statistical metrics (MdAE, MdAPE, MdSA and MdLQ) versus time for the 3-D simulations corresponding to radial and pitch angle diffusion (blue) and radial, pitch angle and energy diffusion (red).

Table 5.5 provides the global indices over the full period for both simulations, also highlighting a better prediction for the radial and pitch angle computations.

Surprisingly, the pitch angle diffusion code reproduces the observations better than the combined energy and pitch angle diffusion code, since the median absolute error, the median percentage absolute error and the median symmetric accuracy are higher for the latest simulations. We also overestimate more the observations with the consideration of energy diffusion (as emphasized by the MdLQ metrics, bottom-right), which is likely to strengthen the electron fluxes at specific energies. This discrepancy may indicate that local acceleration by hiss waves is unlikely to occur, or might also be due to our rough calculation of the energy diffusion coefficient D_{pp}. Finally, differences are small enough that they may not be well reproducible We leave the full calculation of the event-specific energy diffusion coefficient for a future work.

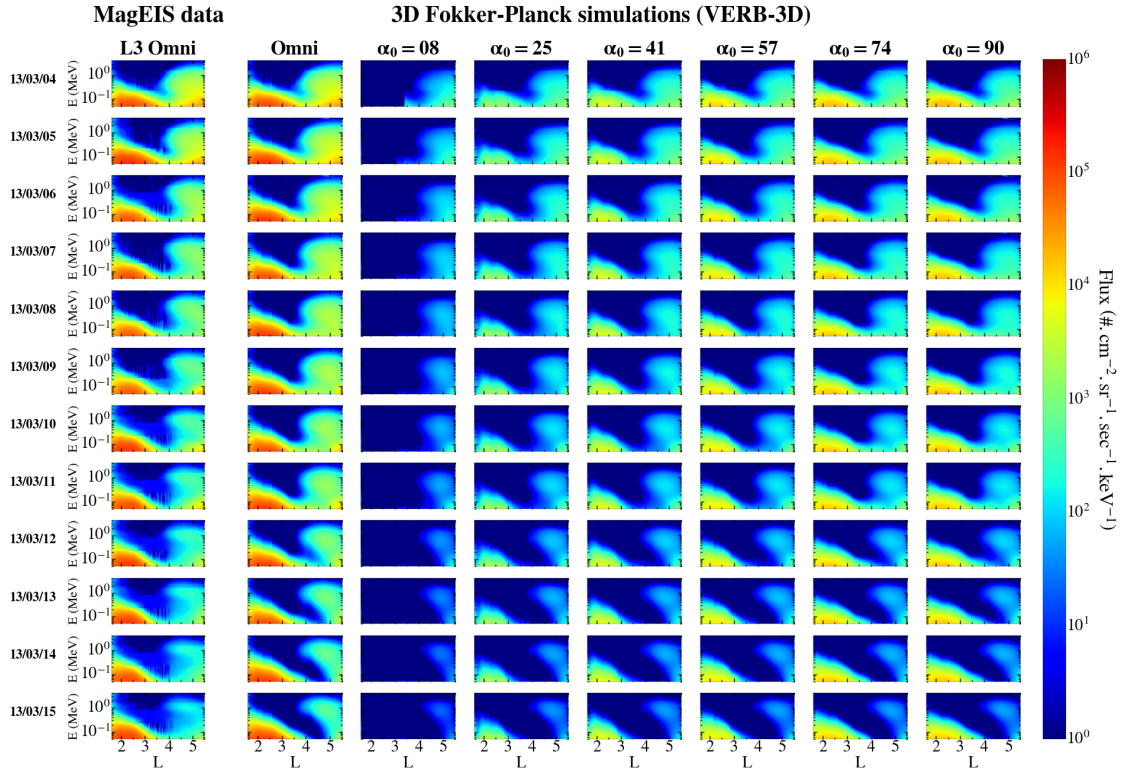

Figure 5.26 – 3-D simulations of electron fluxes in the (L, E) space evolving in time during the period of the 4-15 March 2013. The first column shows the L3 omnidirectional fluxes taken from the Van Allen Probes (MAGEIS instrument on board RBSP A). The second column represents the simulated omnidirectional fluxes, calculated from the integration with respect to α_0 of the simulated unidirectional fluxes at each equatorial pitch angle. The next columns represent a snapshot of the calculated unidirectional flux in the (L, E) space for each day and for a respective equatorial pitch angle of 8, 25, 41, 57, 74 and 90 degrees.

Table 5.5 – Global Median Absolute Error (MdAE), Median Absolute Percentage Error (MdAPE), Median Log Accuracy Ratio (MdLQ) and Median Symmetric Accuracy (MdSA) for the 3-D simulations including radial and pitch angle diffusion and the 3-D simulations including radial, pitch angle and energy diffusion. The indicated indices correspond to the omnidirectional electron fluxes and have been calculated over all available L-shells, energies and times.

	3-D simulations nonuniform distribution from L3 data pitch angle diffusion	3-D simulations nonuniform distribution from L3 data pitch angle and energy diffusion
MdAE	3.9×10^{1}	4.2×10^{1}
MdAPE	61%	64%
MdLQ	8.5×10^{-3}	2.7×10^{-2}
MdSA	87%	90%

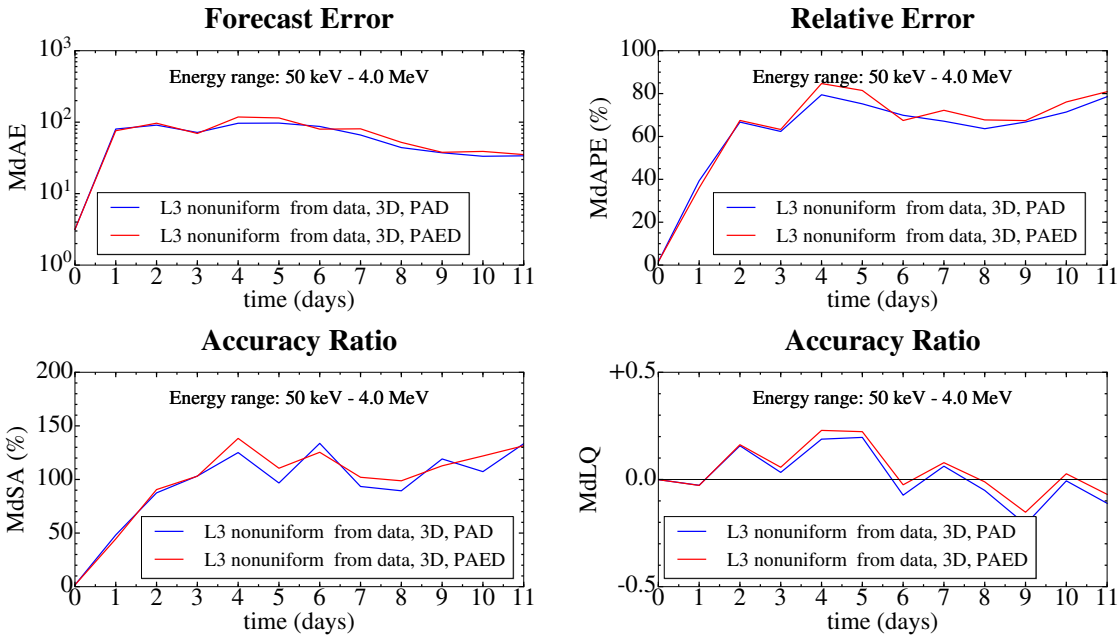

Figure 5.27 – The four panels represent respectively the median absolute error (MdAE, top-left), the median absolute percentage error (MdAPE, top-right), the median symmetric accuracy (MdSA, bottom-left) and the median log accuracy ratio (MdLQ, bottom-right) versus time for the simulated fluxes that are taken from the L3 unidirectional flux data computed with the 3-D code accounting for radial and pitch angle diffusion (blue) and the 3-D code that integrate the radial, pitch angle and energy diffusion (red).

5.7 Conclusions

This chapter shows one of the first attempts to reproduce the radiation belt dynamics over a broad spectrum of energies and L-shells simultaneously. In this context, we extensively study the storm-recovery of March 4-15, 2013, that took place between two storms largely studied (e.g., *Baker et al.*, 2014a; *Hudson et al.*, 2015; *Xiao et al.*, 2014; *Li et al.*, 2014b; *Boyd et al.*, 2014; *Yiqun et al.*, 2014; *Brito et al.*, 2015; *Reeves et al.*, 2016). The characteristics inherent to this storm-recovery (quiet solar wind conditions and steady decay observed in the electron flux) offer an unprecedented opportunity to quantify losses inferred by whistler mode hiss waves (sections 1, 2 and 3). Pitch angle diffusion coefficients and average electron lifetimes have been calculated in (*Ripoll et al.*, 2017) and computed from whistler-mode hiss wave scattering using hourly measurements from the EMFISIS instrument during the specific storm recovery phase in March 2013. Both the data-driven lifetime and pitch angle diffusion coefficient can be respectively embedded into a 1-D reduced Fokker-Planck code or into a 3-D Fokker-Planck model to assess for the behavior of the electron fluxes when subjected to the action of ULF waves (radial diffusion) and whistler mode hiss waves (pitch angle diffusion), and to be compared with observations. The flux data used in this chapter are taken from different measurements made by the MagEIS instrument on board the Van Allen Probe A. We consider both Level 2 (L2) and Level 3 (L3) data sets. The L2 data are made of spin-averaged electron fluxes (FESA), not resolved in pitch angle, whereas the recent L3 data account for pitch angle resolved electron fluxes (FEDU). The corresponding omnidirectional electron fluxes, (FEDO), which are not included in the L3 data at our

disposal, are deduced from the integration of the L3 unidirectional fluxes with respect to pitch angle. Both L2 and L3 fluxes exhibit a similar evolution, forming ultimately a S shape structure (*Reeves et al.*, 2016). The inner belt is also devoid of high-energy electrons (above 800 keV), which is consistent with the observations made by *Fennell et al.* (2015) with the ECT and MagEIS instruments on board the Van Allen Probes. Let us also mention that *Pierrard and Lopez Rosson* (2016) used the data provided by the Energetic Particle Telescope (EPT) on board the PROBA-V satellite to highlight the unusual penetration of MeV electrons in the inner belt during the big storm of March 2015. This observation, also supported by the background corrected Van Allen Probes data described in (*Claudepierre et al.*, 2017), does not contradict the conclusions drawn by *Fennell et al.* (2015) but rather suggests that the filling of the inner belt with high energy electrons (that can sometimes reach 1 MeV) is dependent on the storm intensity. Some discrepancies are also seen between the L2 and L3 structures, the latter showing a featureless S shape.

The observed electron fluxes are used to implement the initial condition and the dynamic boundary conditions for the PSD in our Fokker-Planck simulations. They are also obviously used to be compared with the predicted electron fluxes, so as to discriminate one parameter from the other and choose the best couple of radial diffusion coefficient and lifetime/pitch angle diffusion coefficient among the many available models of the rich literature of space weather forecasting. This validating step constitutes the substance of section 4. For this purpose we perform a 1-D reduced Fokker-Planck simulation for which we combine four different radial diffusion coefficients (*Ozeke et al.*, 2014; *Brautigam and Albert*, 2000; *Liu et al.*, 2016; *Ali et al.*, 2016), and four more different lifetime models (*Orlova et al.*, 2016, 2014; *Lyons et al.*, 1972) (and $\tau \rightarrow \infty$). The initial and boundary conditions are simply extracted from the observed L2 spin-averaged electron fluxes, by assuming a uniform distribution in pitch angle, and only the electron population mirroring at the magnetic equator ($\alpha_0 = 90$ degrees) is considered. A quantitative error assessment is performed for each model through the computation of four global error indices (the median absolute error, the median absolute percentage error, the median symmetric accuracy and the median log accuracy ratio, the two latter being derived in (*Morley*, 2016; *Morley et al.*, 2018)) to distil the qualitative flux comparisons into a single quantitative error assessment. One of the best agreements between observations and simulations is given by the radial diffusion coefficient from (*Ozeke et al.*, 2014) and the event-specific hiss lifetime from *Ripoll et al.* (2017). Results obtained with the *Orlova et al.* (2016) lifetime model turned out to be rather close to the observations as well. Loss models based on the Combined Release and Radiation Effects Satellite (CRRES) data (*Orlova et al.*, 2014) underestimate the loss. Results without hiss loss (with highest error indices) show how different would the energy structure be and how important these waves are for the Earth's radiation belts. The best reproduction of the observations thanks to the use of the ambient wave and plasma properties measured by the Van Allen Probes data (either dynamically (*Ripoll et al.*, 2017) or statistically (*Orlova et al.*, 2016)) shows how crucial these data will be at correctly reproducing the radiation belt dynamics in the next decades. Simulations show that hiss waves are indeed the main driver of loss in the slot region during quiet decay times. Combined with radial transport, they mainly sculpt the energy structure of the radiation belts, with a prevalent slot region dynamically forming a typical S shape of the inner edge of the outer belt, as described by *Reeves et al.* (2016) who asserted that this evolution is characteristic of periods following most (if not all) storms. Inward radial transport acts as a source mechanism and wave scattering by plasmaspheric hiss is a fundamental loss mechanism. The remainder of the study only

focuses on the best selected association of radial diffusion coefficient (*Ozeke et al.*, 2014) and lifetime (*Ripoll et al.*, 2017).

The two last sections aim at developing the aforementioned simulations by assuming a realistic pitch angle distribution for the electron fluxes, the purpose being the prediction of the unidirectional fluxes for all pitch angles and, ultimately, the calculation of the corresponding omnidirectional electron flux. The implementation of the initial and boundary conditions in PSD, needed for the computations, requires the extraction of the equatorial unidirectional fluxes from the MagEIS data. Two different approaches are adopted to collect the equatorial unidirectional fluxes. The first approach still sticks to the L2 spin-averaged electron fluxes observed by the MagEIS instrument on board RBSP A, but involves in addition a recently-derived empirical model of pitch angle distribution (*Shi et al.*, 2016) to obtain the shape of the equatorial unidirectional electron fluxes for all pitch angles. Once the initial and boundary conditions in PSD have been properly set up, the calculation of the unidirectional fluxes enables us to obtain an omnidirectional electron flux directly comparable with the L2 MagEIS data. The results are slightly improved in view of the calculations made in Section 4, highlighting the importance of taking into account a realistic initial condition in 3-D. The second approach directly uses the whole set of available L3 unidirectional fluxes (FEDU) of MagEIS measurements. With the use of Liouville's theorem, the corresponding equatorial unidirectional fluxes are directly deduced from the unidirectional fluxes observed locally by Van Allen Probe A. As before, we are then able to build the initial and boundary conditions to perform the simulation of unidirectional fluxes at all pitch angles, and, by integration, obtain the predicted omnidirectional flux. Again, the results compare pretty well with the data, showing a slot region gradually eaten by whistler mode hiss waves, and no high-energy electrons penetrating the inner belt.

The use of an averaged lifetime embedded into a so-called 1-D reduced Fokker-Planck equation assumes that pitch angle scattering is "fast enough" compared with the timescale of radial transport. In other words, pitch angle diffusion is implemented via its long-term solution, which is reduced to its first eigenvalue. Although such a single exponential decay of electron flux has been observed at $L = 5$ by (*O'Brien et al.*, 2014), assessing whether that approximation is true or not (for all energies and L-shells) would require many more simulations beyond the scope of this study. In this context, we include the full pitch angle diffusion operator within 3-D simulations (E, α_0, L). The code used to perform the computation is the Versatile Electron Radiation Belt (VERB) code (*Subbotin and Shprits*, 2009; *Subbotin et al.*, 2010; *Kim et al.*, 2011). Taking into account the L3 MagEIS data, we obtain some improvements in our results compared with the 1-D reduced Fokker-Planck simulations. The better accuracy of the electron fluxes is confirmed with the use of the dedicated metrics (the median absolute error, the median absolute percentage error, the median symmetric accuracy and the median log accuracy ratio), the latter proving that we overestimate the data less than previously. For example, the error made with the 1-D simulation is about 100%, which reduces to 87% with the use of the VERB-3D code.

In our latest simulations, there is still a significant remaining isolated region for $E \sim 1$ MeV and $4.0 < L < 5.0$ that is relatively preserved by the action of whistler mode hiss waves, contrary to the data showing that the same region is gradually depleted over time. Hence, this decrease in the flux intensity revealed by the data appears not to be an effect of hiss waves, and it is also not likely to be the result of whistler mode chorus waves that act beyond the plasmapause and at lower energies. Although the collapse of this pocket of electrons is still an open question, it might be an effect of EMIC waves,

which are known to cause the depletion of ultra relativistic electrons (e.g., *Shprits et al.*, 2008b; *Thorne*, 2010). For future works, it could be interesting to include the effect of EMIC waves in the presented simulations (via the calculation of a EMIC waves driven pitch angle diffusion coefficient) to verify if this high intensity region persists or not. It might also be instructive to simulate other similar events to further explore the effects and limitations of whistler mode hiss waves.

Chapter 6

Quantifying the influence of the magnetic field

Chapters 3 and 4 mainly focused on the general dynamics and shape of the radiation belts in a formal and academic framework, whereas Chapter 5 intended to reproduce a realistic storm recovery phase by using data-driven lifetime or pitch angle diffusion coefficient embedded respectively in a 1-D and a 3-D Fokker-Planck code. In this latter perspective, this chapter aims at reproducing a larger variety of geomagnetic events, and particularly periods of intense geomagnetic activity.

During geomagnetic storms, the magnetic field configuration is strongly shaped by solar activity. The magnetic field lines are indeed compressed by the solar wind on the dayside and reversely highly stretched out on the night side due to currents that build the magnetotail. In the present study we take the opportunity of discussing the use of different magnetic field models in numerical simulations.

We recall that the electron fluxes observed by the dedicated orbiting satellites are recorded as a function of local position and time, within a given range of energy and local pitch angle. The latter coordinate system can be converted into the so-called (E, α_0, L^*) physical space made of the energy, equatorial pitch angle and L-shell of an electron population. This observable physical space is opposed to the (μ, K, L^*) space built on the three adiabatic invariants, which is used for the theoretical purpose of calculating the electron phase space density in the radiation belts (cf. Chapter 2). In this study, we only focus on the effects of the magnetic field on the transformation between the (μ, K, L^*) adiabatic space and the equivalent (E, α_0, L^*) physical space. All other possible physical effects induced by the magnetic field configuration are not incorporated in the present study. Some of them will be the topic of Chapter 7.

The magnetic field model can have different uses through the entire process of simulating electron fluxes on the basis of satellites' observations. We indeed separate the simulation process into three different steps. The simulation first requires a pre-processing step to properly convert the electron fluxes observed by the satellite into phase space density as a function of the three adiabatic invariants. From the obtained phase space density, one initial condition and several boundary conditions are then extracted to feed the numerical code and run the phase space density as a solution of the Fokker-Planck equation. A last step consists at transforming the simulated phase space density back to electron fluxes in term of the (E, α_0, L^*) coordinates. The first and last steps are simply data processing. They both require a magnetic field model to properly perform the space transformations, which we refer to the *extrinsic* magnetic field model since these two steps are not part of the numerical resolution itself. The extrinsic field model can be chosen within a rich variety of available models in the literature. The second step of the numerical computation is also dependent on a magnetic field model, as different decoupled physical processes embedded in the Fokker-Planck equation may rely on different separate coordinate systems (cf. Chapters 2 and 4). The so-called *intrinsic* magnetic field used in this second step is usually (if not always) the dipole field for simplicity.

In this chapter we use for the first time a non-dipole intrinsic magnetic field in the numerical computation per se. For consistency, the same non-dipole field is also considered for the steps of pre-processing and post-processing (extrinsic field). The effects inherent to a realistic magnetic field are quantified and compared with the use of a pure dipole field, for each of the three simulating steps described above. The realistic field considered here is the combination of the International Geomagnetic Reference Field (IGRF) model that takes account of the magnetic field generated by the Earth's interior (*Thébault et al.*, 2015), with the magnetic field model from *Tsyganenko* (1989) (T89). The latter external field model takes account of a diversity of phenomena that originate from the Sun and that impact the Earth's own magnetic field. Focusing on two distinct events reported by

the Combined Release and Radiation Effects Satellite (CRRES), we particularly show that the effects of the magnetic field during the two processing steps are preponderant compared with the effects involved in the computing step. More specifically, we demonstrate that the use of a dipole field leads to inaccuracies in the reconstruction of the phase space density. The latter can exhibit artificial isolated peaks (*Selesnick and Blake*, 2000; *Green and Kivelson*, 2004) that can be interpreted as effects of in-situ acceleration by wave acceleration, which are not reproducible by our 1-D numerical code. The use of a realistic magnetic field smooths these non physical peaks, so that most of the PSD shape is rather seen as the result of radial diffusion, easily replicable by our simulations.

Chapter 6 is organized as follows. We first contextualize the study and detail the goals of the present works. We then describe the numerical implementation of the magnetic field (*Cunningham*, 2016) and we present the model used to solve the reduced Fokker-Planck equation. The results are detailed in the last two sections, which emphasize the differences that are obtained through the use of the two distinct magnetic field models via the calculation of electron unidirectional fluxes as well as omnidirectional and integral fluxes.

6.1 Contextualization of the study

6.1.1 Overview of the usual Fokker-Planck resolution strategy

The dipole field is the zero-order approximation of a curl vanishing magnetic field. It is axisymmetric and static in the sense that its geometric configuration does not depend on external time-dependent parameters. It also discards any effect brought by solar wind compression of magnetospheric currents. On the other hands, realistic magnetic field models depend on input physical parameters that are time-dependent. In this context, their numerical implementations can be computationally prohibitive.

We should also make the distinction between the magnetic field used for both steps of pre-processing (data) and post-processing (results) that we call the *extrinsic magnetic field*, and the magnetic field involved in the computation itself, which we refer as the *intrinsic magnetic field*. This differentiation is inherent to the whole adopted computing approach. The computations of electron fluxes written in the (E, α_0, L^*) space from satellite observations indeed commonly requires four successive steps that are depicted below.

- Step 1: data formatting
  The very first step consists at starting from the satellite's observations, which are commonly represented as local electron fluxes $j_{\text{data}}(E, \alpha, x(t))$ that depend on kinetic energy E, local pitch angle α and spacecraft orbital position $x(t)$ at time t, which are converted into equatorial fluxes $j_{\text{data}}(E, \alpha_0, L^*, t)$ written in the (E, α_0, L^*) space, indicated as

  $$j_{\text{data}}(E, \alpha, x(t)) \rightarrow j_{\text{data}}(E, \alpha_0, L^*, t).$$

  The transformation requires the knowledge of the magnetic field geometry.

- Step 2: pre-processing (data)
  A second step consists at converting the obtained equatorial electron fluxes into phase space density as a function of the three adiabatic invariants $f_{\text{data}}(\mu, K, L^*, t)$, written as

  $$j_{\text{data}}(E, \alpha_0, L^*, t) \rightarrow f_{\text{data}}(\mu, K, L^*, t),$$

which is the mapping from the unidirectional flux written in the physical space to the PSD in the adiabatic space. This is required to properly feed the numerical code with an initial condition and boundary conditions.

- Step 3: PSD computations within the Fokker-Planck equation
  The third step is the computation itself. The numerical code takes account of the initial and boundary conditions generated previously to calculate a simulated phase space density $f_{\text{model}}(\mu, K, L^*, t)$ in the adiabatic space, formalized as

  $$f_{\text{data}}(\mu, K, L^*, t) \rightarrow f_{\text{model}}(\mu, K, L^*, t).$$

  For reasons of simplicity and so as to keep the code within reasonable computational time, the intrinsic magnetic field considered for the transition between the physical space (e.g. processes related to local diffusion in pitch angle or in energy) and the adiabatic space (e.g. radial diffusion) is usually the dipole field. Moreover, the diffusion coefficients themselves are commonly pre-computed in a dipole field.

- Step 4: post-processing (model)
  This last requirement is the reverse process of step 2. The simulated phase space density is converted back to equatorial fluxes $j_{\text{model}}(E, \alpha_0, L^*)$ whose dynamics is depicted in the (E, α_0, L^*) space,

  $$f_{\text{model}}(\mu, K, L^*) \rightarrow j_{\text{model}}(E, \alpha_0, L^*),$$

  which is the mapping from the PSD written in the adiabatic space to the unidirectional flux in the physical space. This enables direct comparisons between the fluxes generated in step 2. For a sake of consistency, the magnetic field model used in the conversion should be the same as the one of step 2 (extrinsic field).

The method as well as these conversion steps (2, 3 and 4) that required the full understanding and control of the approaches described in Chapter 2 have been implemented in the code during the PhD. We now develop the different uses of the magnetic field respectively within the Fokker-Planck equation (step 3) and through the processing steps (steps 1, 2 and 4).

6.1.2 On the use of the magnetic field in the Fokker-Planck equation

The Fokker-Planck equation (2.51), as historically written by *Schulz and Lanzerotti* (1974), is a three dimensional diffusion equation written in the (J_1, J_2, J_3) adiabatic space that governs the evolution of the phase-averaged distribution function. As mentioned in Chapter 2, reducing the six-dimensional Vlasov equation to a three-dimensional Fokker-Planck equation by averaging over the phases of gyration, bounce and drift trajectories has an inherent cost, which translates into the preliminary effort of calculating the diffusion coefficients. The latter take account of the non-adiabatic effects induced by the interactions of a charged particle with electromagnetic waves of small amplitude, and they obviously have to be calculated prior to any attempt of solving the Fokker-Planck equation. The magnetic field geometry is involved in both the calculation of the adiabatic invariants and the implementation of the diffusion coefficients.

6.1.2.a Calculation of the adiabatic invariants

The numerical resolution of the Fokker-Planck equation is currently carried out with two different approaches.

A first approach explicitly separates radial diffusion from pitch angle and energy diffusion. This process is justified by the difference of timescale related to radial diffusion (violation of the third adiabatic invariant) and related to pitch angle and energy diffusion (violation of the first and second adiabatic invariants). Whereas radial diffusion conserves the first two adiabatic invariants, pitch angle diffusion typically conserves energy, and reciprocally, energy diffusion occurs at constant pitch angle. Consequently the complete Fokker-Planck equation can be split into these two main processes and involves therefore two competitive coordinate systems: the adiabatic space (μ, K, L^*) (equivalent to J_1, J_2 and J_3) used for radial diffusion and the physical space (E, α_0, L^*) appropriate for pitch angle and energy diffusion. In particular, the transformation from (J_1, J_2, J_3) to (E, α_0, L^*) materializes in the Fokker-Planck equation under a Jacobian term, whose calculation requires a magnetic field model, which is commonly the dipole field for simplicity. This first approach has been adopted in several 3-D codes, such as both the American UCLA Versatile Electron Radiation Belt (VERB-3-D) code (e.g., *Subbotin and Shprits*, 2009; *Shprits et al.*, 2009; *Subbotin et al.*, 2010; *Kim et al.*, 2011) and the LANL Dynamic Radiation Belt Environment Assimilation Model (DREAM-3-D) code (*Tu et al.*, 2013), or the British BAS Radiation Belt Model (BAS-RBM) code (*Glauert et al.*, 2014).

The second approach directly addresses the Fokker-Planck equation in its native invariant (μ, K, L^*) space, so that no Jacobian transformation arises in the equation itself. However, the related diffusion coefficients also write in the adiabatic space. Since the aforementioned space is inadequate to observations, the calculation of the adiabatic diffusion coefficients (i.e. in terms of adiabatic invariants) is a difficult task to achieve. Hence, it is easier and preferable to relate the adiabatic diffusion coefficients (D_{KK}, $D_{\mu\mu}$ or $D_{\mu K}$ and others) to those derived in the physical space ($D_{\alpha_0\alpha_0}$, D_{pp} or $D_{\alpha_0 p}$) by reversely using relation (2.53). Again, the conversion demands a magnetic field model, which is the dipole field in practice. This is for example how the French ONERA Salammbô code works (*Beutier et al.*, 1995). In both approaches, the magnetic field implicitly embedded in the Fokker-Planck equation (referred as the intrinsic field) is a dipole field.

6.1.2.b Implementation of the various diffusion coefficients

Beyond the consideration of the Fokker-Planck equation by itself, the calculation of the diffusion coefficients also requires the knowledge of the magnetic field.

The radial diffusion coefficient $D_{L^*L^*}$, which accounts for drift resonant interactions with ULF waves, is traditionally computed in the framework of a background dipole field, onto which small electromagnetic perturbations are added (*Fälthammar*, 1965; *Fälthammar*, 1968). Exceptions occur, although not yet commonly used by the scientific community. For example, *Cunningham* (2016) has presented a numerical recipe to calculate a radial diffusion coefficient that can assume any realistic magnetic field models for the background field. He specifically implemented a new radial diffusion coefficient based on the background magnetic field from *Tsyganenko* (1989)(referred as the T89 field). His conclusions supported the fact that the new realistic radial diffusion coefficients could be significantly larger than the coefficients computed with a dipole field, especially at large L-shells.

Similarly the energy and pitch angle diffusion coefficients, which represent the perturbations induced by gyro-resonant interactions with electromagnetic waves, are calculated within the framework of quasilinear theory (*Kennel and Engelmann*, 1966; *Lerche*, 1968). They are currently bounce-averaged in the dipole magnetic field before being implemented in the Fokker-Planck equation (*Lyons et al.*, 1972). Only a few works have performed the bounce integration in the framework of the T89 or the T01s (*Tsyganenko*

et al., 2003) magnetic fields (*Orlova and Shprits*, 2010; *Ni et al.*, 2011; *Orlova et al.*, 2012). To our knowledge, none of these recent diffusion coefficients have yet been incorporated into a Fokker-Planck equation.

6.1.2.c Summary

As stated above, the use of a non-dipole field for the numerical resolution of the Fokker-Planck equation (referred as step 3) is a challenging task to achieve. It would indeed require to

- update the (E, α_0, L^*) map at each time step according to the time-dependent input parameters needed by the magnetic field model,
- have the diffusion coefficients available for the magnetic field into consideration, making them also time-dependent.

As things stand, the numerical resolution of the Fokker-Planck equation is commonly performed with a dipole field (*Brautigam and Albert*, 2000; *Albert et al.*, 2009; *Subbotin and Shprits*, 2009; *Shprits et al.*, 2009; *Subbotin et al.*, 2010; *Kim et al.*, 2011; *Tu et al.*, 2013; *Glauert et al.*, 2014), the use of realistic magnetic fields being rather only involved in pre-processing or post-processing steps (steps 1,2 and 4) as detailed next.

6.1.3 Pre-processing and post-processing

6.1.3.a Processing steps in the existing litterature

The steps of pre-processing the data and post processing the results (steps 1, 2 and 4) can be accomplished with a large variety of magnetic fields.

Brautigam and Albert (2000) performed steps 1 and 2 from CRRES observations to provide phase space density as a function of the three adiabatic invariants. The data processing involved the combined IGRF model and the T89 magnetic field model. They implemented a reduced Fokker-Planck model to account for radial diffusion and pitch angle scattering by whistler mode hiss waves. The latter effect is represented by a loss term calculated in *Lyons et al.* (1972). They did not performed step 4 but rather directly compare the obtained PSD with the one generated by step 2. They specifically conclude that the model's inconsistency at high μ values (data underestimation) was due to local acceleration from wave particle acceleration, which was not addressed by their model.

Albert et al. (2009) formatted CRRES data by using the IGRF and the magnetic field from *Olson and Pfitzer* (1982) (referred as the OP77 field), and they run 3-D simulations with the BAS-RBM code that intricately uses a dipole field to the correspondence between the adiabatic space and the physical space. Again, step 4 was not executed.

Glauert et al. (2014) also took advantage of the BAS-RBM code and CRRES data to implement steps 1 to 4 with the use of the IGRF model and T89 field model for steps 1, 2 and 4, and the dipole field inherent to the 3-D code in step 3.

In the same perspective, the UCLA VERB-3-D (e.g., *Subbotin and Shprits*, 2009; *Shprits et al.*, 2009; *Subbotin et al.*, 2010; *Kim et al.*, 2011) code and the LANL DREAM-3-D code (e.g., *Tu et al.*, 2013; *Cunningham et al.*, 2018) are fed with PSD data derived from a variety of magnetic fields (step 2), but they still account for a dipole field when the space transformations are required through the resolution of the Fokker-Planck equation (step 3). The back transformation (step 4) is then done with the magnetic field of step 2. Other examples that take advantage of the new data released from the Van Allen Probes are also legion in the rich literature of the radiation belts.

6.1.3.b Influence of the extrinsic magnetic field

The influence of the magnetic field model through numerical simulations should not be taken lightly. The importance of the choice of the field model has for example been demonstrated by *Selesnick and Blake* (2000) and *Green and Kivelson* (2004). Their initial purpose was to identify the possible mechanisms of electron acceleration, which are known to shape the PSD accordingly. The presence of peaks in PSD at large L-shells ($L \sim 6$) is indeed commonly attributed to radial diffusion whereas isolated peaks located at intermediate L-shells ($L \sim 4$) are a signature of local energy diffusion.

In this perspective, *Selesnick and Blake* (2000) attempted to localize the source of PSD acceleration by looking at potential PSD positive gradients. Based on the observations from the High Sensitivity Telescope (HIST) on board the POLAR satellite, they convert the electron fluxes measured for several energies and local pitch angles into PSD as a function of L^* and time for $\mu = 200$ and 800 MeV/G and for $K = 1.0$ $G^{1/2}R_E$ (which are typically steps 1 and 2). The transformation process has been successively performed with four different magnetic field models: the IGRF model alone, the combined IGRF and T89 models, the combined IGRF and T96 (*Tsyganenko and Stern*, 1996) models and the combined IGRF and OP77 models. As a result, *Selesnick and Blake* (2000) did not find the emergence of a single specific region where acceleration occurs. They were subsequently not able to conciliate all of the aforementioned field models, the location of the peaks in PSD being highly sensitive to the magnetic field in use. They partly conclude that the T89 field was the most relevant field model among its counterparts.

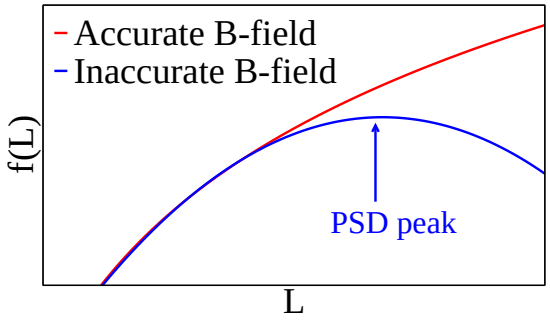

Figure 6.1 – Evolution of PSD versus L^* at a given μ and K, reconstructed from electron fluxes with the use of an accurate magnetic field (red) and with a inaccurate magnetic field (blue). The latter field can lead to an artificial PSD peak, which can be wrongly interpreted as an effect of outward radial diffusion or local acceleration. Adapted from (*Green and Kivelson*, 2004).

In a similar context, *Green and Kivelson* (2004) performed the pre-processing steps (steps 1 and 2 again) with the T96 field model so as to target the possible PSD enhancements depicted in the adiabatic space. In most cases, they were able to discriminate the external acceleration process due to inward radial diffusion (also called betatron acceleration) from the internal acceleration sources (also referred as local or in situ acceleration) induced by wave-particle interactions. However, they realized that modifying the magnetic field configuration (stretching of the field line by adapting the input parameters) could affect the PSD gradients and thus lead to contradictory results on the source of acceleration. They particularly show that a key aspect of the computations relies on the estimation of the second invariant K (and L^* in a lesser extent) from an initial grid built on energy E, local pitch angle α and the orbital positions of the POLAR satellite that

provided the flux observations. Inaccurate magnetic field models have proven to somewhat lead to artificial peaks in phase space density that could be wrongly interpreted as an effect of local acceleration (see Figure 6.1).

6.1.4 Purpose of the current work

The present chapter falls within the framework of the aforementioned studies in the sense that we aim at identifying the flux characteristics inherent to the magnetic field model. We also take this opportunity to quantify and explain the differences obtained with a realistic field compared with a dipole field. In this perspective, we implement, for the first time, a realistic intrinsic field within the resolution of the reduced Fokker-Planck equation itself (step 3). The realistic field is specifically used for the transformation between the adiabatic space (μ, K, L^*) and the physical space (E, α_0, L^*), the latter being potentially updated at each time step according to the temporal evolution of the geomagnetic activity. The radial diffusion coefficients as well as the lifetime accounting for pitch angle diffusion are taken from the literature and, therefore, computed with a dipole field. In addition, similarly to the previous works quoted above, we use the same realistic magnetic field for the two pre-processing and post-processing steps (steps 1, 2 and 4).

6.2 Data and model

In order to reach the presented objective, we attempt to reproduce two specific events that occurred in 1990 (end of September for the first one, mid-October for the second one) with either a dipole field or the combination of the IGRF and T89 field. The first event is relatively quiet and is specifically considered in the purpose of validating the computational steps of implementing a realistic field model. The second event constitutes the heart of the chapter and is devoted to prove the accuracy and the importance of the use of a realistic magnetic field model compared with a dipole field in both the computation of the Fokker-Planck equation and the processing steps. The use of data related to the October 1990 period is here relevant because this event, which is one of the strongest geomagnetic storm that has ever been recorded by satellites, has already been widely considered in the literature (e.g., *Brautigam and Albert*, 2000; *Albert et al.*, 2009). Our results (presented in section 6.5) can therefore be compared with these previous works.

6.2.1 CRRES data

6.2.1.a Data organization

The two events reported in this chapter (from September 24 to October 2, 1990 and from October 9 to October 15, 1990) have been recorded by the Medium Electron A (MEA) instrument on board the Combined Release and Radiation Effects Satellite (CRRES). The MEA instrument is a magnetic spectrometer based on 17 logarithmically spaced energy channels from 0.15 MeV to 1.58 MeV (*Vampola et al.*, 1992). Let us mention that the two lowest-energy channels (0.15 and 0.21 MeV) are often saturated during intense low-energy fluxes. The measure of the local magnetic field vector is used to determine the pitch angle associated with each individual spectrum, providing a complete set of electron differential unidirectional fluxes. The obtained local pitch angles are uniformly distributed over 17 bins, from 5 to 90 degrees. The unidirectional electron

fluxes for an energy of 1 MeV and a pitch angle of 45 degrees are represented in Figure 6.2 from August 15, 1990 (DOY=227) to October 15, 1990 (DOY=288). They are displayed as a function of time (horizontal axis) and L-shell (vertical axis, also referred as L^*). Let us mention that the L^* adiabatic invariant (Figure 6.2) has upstream been calculated with the T89 magnetic field model by the LANL team. More specifically, L^* has been computed every 10 min in accordance to the satellite radial position (r) and MLT location (φ) at time t with respect to the equatorial pitch angle (α_0) of the measured electron flux. As a result, we have been provided with the complete fluxes measured by CRRES as a function of L^*, time, energy and pitch angle (courtesy of G. Cunningham and W. Tu). Hence this study does not attempt to deal with the aforementioned step 1 of data formatting, and starts directly to step 2. The full period under consideration (two-month duration) has been subjected to relatively quiet event as well as geomagnetic storms (active events). Within this two-month period, we focus on the two shaded regions of Figure 6.2. The first region corresponds to a 9-day period from September 24 to October 2, 1990. The second region extends from October 9 to October 15, 1990, and is known to host a geomagnetic storm.

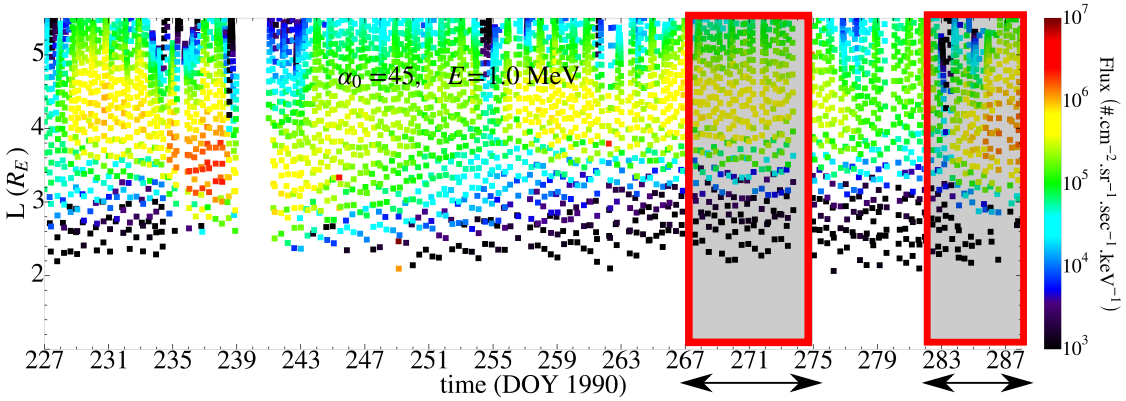

Figure 6.2 – Evolution of the electron unidirectional flux for $E = 1.0$ MeV and $\alpha_0 = 45$ degrees, during 62 days of 1990 from DOY=227 to DOY=288, 1990. The two shaded regions correspond respectively to 9 days of the quiet period (from DOY=267 to DOY=275) and to 7 days of the active period (from DOY 282 to DOY=288) at stake in this chapter.

6.2.1.b Preliminary interpolations and extrapolations

The unidirectional flux data are recorded versus L-shell and time on the CRRES orbit for each available energies and pitch angles. The first step is to transform the scattered available data into a usable Cartesian grid in (time, L-shell). For this purpose, the space and time variables have first to be decoupled. The decoupling process consists at targeting all the local maxima and minima of L^* over the entire time domain for each available energy and pitch angle. For a given maximum value in L^* we identify its corresponding time value and refer to it as the local initial time. Starting from this local initial time, we save all the following L^* values until a local minimum in L^* is reached (increasing times). The $N_{L_{\text{loc}}}$ found values of L^* are then stored to correspond to the given local initial time in question. Hence, for each local initial time, we have $N_{L_{\text{loc}}}$ different values of L^* covering a wide spectrum of L^* values, and so $N_{L_{\text{loc}}}$ corresponding values of electron flux that corresponds to the outbound orbits of the satellite. Then, for each local initial time we linearly interpolate the $\log_{10}$ values of the unidirectional

flux in L^* to cover a regular L-shell domain of reference (such that $1.0 \leq L \leq 5.5$). We repeat the same process for each time corresponding to a local minimum value in L^*, i.e. counting the next values until a local maximum is reached. Again, the $\log_{10}$ of the electron flux values, which now corresponds to the inbound orbits of the spacecraft, are interpolated linearly over the obtained scattered L^* values.

As a final procedure, the unidirectional electron fluxes are interpolated in time for each given energy and pitch angle. Let us mention that the satellite coverage is better for low energies and high pitch angles. The values of fluxes at these low energies and high pitch angles are subsequently extrapolated respectively to higher energies and lower pitch angles for each time and L-shell. Eventually, a last extrapolation in time and L-shell is done for each energy and pitch angle.

6.2.2 Model in use

6.2.2.a Fokker-Planck equation

We use as before the 1-D reduced Fokker-Planck equation that writes

$$\frac{\partial f}{\partial t} = L^2 \frac{\partial}{\partial L}\left[\frac{D_{LL}}{L^2}\frac{\partial f}{\partial L}\right]_{(\mu,K)} - \frac{f}{\tau},$$

with D_{LL} being the radial diffusion coefficient and τ being the electron lifetime that accounts for the electron losses due to pitch angle scattering. Pitch angle scattering can be caused either by the action of whistler mode hiss waves (inside the plasmapause) or by whistler mode chorus waves (outside the plasmapause). Any local acceleration due to whistler mode chorus waves is discarded in the above formulation.

We consider again the radial diffusion coefficient D_{LL} from *Ozeke et al.* (2014), which implicitly assumes a dipole background field. As for the electron lifetime, we implement the whistler mode hiss wave lifetime from *Orlova et al.* (2016) and the whistler mode chorus wave lifetime from *Orlova and Shprits* (2014). As mentioned above, whistler mode hiss waves are activated inside the plasmasphere, and whistler mode chorus waves outside the plasmasphere, the plasmapause location, L_{pp}, being defined from *Carpenter and Anderson* (1992), i.e. $L_{pp} = 5.6 - 0.46K_p^*$ where K_p^* is the maximum value of K_p during the last 24 hours.

The hiss lifetime from *Orlova et al.* (2016) have been calculated on the basis on the data provided by the Electric and Magnetic Field Instrument Suite and Integrated Science (EMFISIS) instrument on board the Van Allen Probes. It also specifically relies on the bounce-averaged pitch angle diffusion coefficient related to the action of whistler mode hiss waves, whose integration on the bounce path has been computed with a dipole field. In Chapter 5 we have shown that this model gives excellent results against observations, comparable to the event-specific model derived specifically, which constitutes a validation to our eyes and a good justification of its use here.

The chorus lifetime from *Orlova and Shprits* (2014) has, however, been derived from CRRES data, and has been obtained from the bounce averaged pitch angle diffusion coefficient corresponding whistler mode chorus waves. Contrary to the aforementioned electron hiss lifetime, the bounce averaging step has been performed with the use of the T89 magnetic field.

The computations use a uniform L^* grid made of 181 values between $L^*_{\min} = 1.0$ and $L^*_{\max} = 5.5$. The outer boundary is chosen at $L^*_{\max} = 5.5$ because it is a good compromise between data coverage and physical interpretations. The value of 5.5 R_E (near the

geostationary orbit) is indeed large enough to embrace most of the physical processes at stake in the radiation belts (electron acceleration and losses) and small enough to only keep the most reliable data from CRRES. Pushing the outer boundary further out would have been possible, but would have implied to treat an outer boundary mostly built on numerical extrapolations (due to a lack of CRRES data) at the expense of physical measurements. We use 18 μ values that are uniformly distributed in logarithm space, from $\mu_{\min} = 10^0$ MeV/G and $\mu_{\max} = 2 \times 10^3$ MeV/G. The K grid is also logarithmically sampled over 18 values from $K_{\min} = 10^{-2}$ $G^{1/2}R_E$ to $K_{\max} = 10^1$ $G^{1/2}R_E$.

6.2.2.b Magnetic field

The initial condition in PSD is extracted from the unidirectional fluxes provided by the MEA instrument on board CRRES. The conversion from the unidirectional flux $j(E, \alpha_0, L^*)$ at a given energy E, equatorial pitch angle α_0 and L^* into a PSD $f(\mu, K, L^*)$ at a given location in the adiabatic space is performed with two different models for the magnetic field. The first model is the dipole field and the second model is the combination of the IGRF model (internal field) and the T89 (external field) magnetic field.

As detailed in Chapter 2, the dipole field model represents the first dominant term in the expression of a curl-vanishing magnetic field that is composed of a succession of spherical harmonics (see the scalar potential expression (2.12) for example). The dipole magnetic environment is made of closed field lines and is symmetric with respect to the magnetic azimuth.

On the other hand, the second model used in this chapter is the combination of an internal field and an external field (not to be confused with what we called the intrinsic and extrinsic fields in section 6.1.1). The internal field model into consideration is the International Geomagnetic Reference Field (IGRF). This is a more complete description of the curl-vanishing magnetic model presented in Chapter 2, retaining in its description up to 13 spherical harmonics terms. In a such empirically-derived model, the property of azimuthal symmetry does not hold anymore. A characteristic indicator of the non symmetry of the IGRF model is the South Atlantic Anomaly feature presented in Chapter 2, which is a region of Earth where the magnetic intensity brutally drops, enabling high energy electrons to penetrate closer to Earth. We combine the internal IGRF model with an external magnetic field model in order to take account of the different currents flowing into the magnetosphere. We use here the so-called external T89 magnetic field model (*Tsyganenko*, 1989). It includes the day-night asymmetry produced by solar wind compression of the magnetosphere and stretching of field lines on the nightside due to the cross-tail current. The impact of the buildup of the ring current is also materialized by a reduction in magnetic field intensity. We also started with the T89 field because it only depends on the geomagnetic index K_p, giving six different states of the magnetosphere according to six domains in K_p, which makes the T89 field model relatively easy to implement.

6.3 Numerical implementation of the magnetic field model

6.3.1 Tools and libraries available

If the magnetic field is a dipole, the transformation between the adiabatic variables (μ, K, L^*) and the physical space (E, α_0, L) uses the semi-analytical expression of the normalized bounce period, as shown in Chapter 4. Note that the dipole field is axisymmetric, such that the longitude of the particle is never involved.

However, for a general magnetic field that is not axisymmetric, the variations with respect to the azimuth has to be properly addressed. The key point of the transformation is the correspondence between the adiabatic coordinates (L^*, K, φ) with the geometric coordinates (r, α_0, φ), where r is the radius position of the particle, α_0 the equatorial pitch angle and φ is the azimuth of the particle, both taken in the Geocentric Solar Magnetospheric (GSM) coordinates (*Russell*, 1971; *Hapgood*, 1992). This correspondence extensively uses the LANLGeoMag library, which is a collection of software (C and python) specifically dedicated to space science and space weather forecasting. The LANLGeoMag library is freely available here: `https://github.com/drsteve/LANLGeoMag/`.

The numerical FORTRAN code presented in Chapter 4 that has been developed by *Bussutil* (2014) and extended during the PhD solves the reduced Fokker-Planck equation and relies on an initial grid in (μ, L^*, K). From this given (μ, L^*, K) adiabatic space we need the realistic magnetic field to properly calculate the equivalent variables in the $(E, \langle\alpha_0\rangle, L^*)$ space, for which the $\langle..\rangle$ operator refers to a drift-average to discard the azimuthal dependence of the equatorial pitch angle α_0 (emphasized by the longitudinal φ variable). The transformation implemented here requires the intermediate step of knowing the geometric coordinates (r, α_0, φ) that enable to convert the (L^*, K, φ) coordinates into the (L^*, α_0, φ) coordinates. Reversely, the LANLGeoMag software (C code) enables us to perform the calculation of the adiabatic invariants and azimuth (L^*, K, φ) from a given set in (r, α_0, φ).

To conciliate both worlds (FORTRAN and C codes), we use the approach described in (*Cunningham*, 2016) to perform the correspondence from the adiabatic coordinates (L^*, K, φ) to the geometric coordinates (r, α_0, φ). His overall numerical strategy is summarized thereafter.

6.3.2 Numerical implementation

6.3.2.a Obtaining the particle's drift positions

The approach consists of setting an initial grid built on the equatorial pitch angle α_0 and on the spherical coordinates (r, θ, φ) for which θ is the colatitude and φ is the azimuth as before. From this grid, the local magnetic field intensity $B(r, \theta, \varphi)$ of the chosen magnetic field model is computed, as well as the equatorial magnetic field intensity $B_0(r, \varphi)$ and the intensity of the magnetic field at the mirror point $B_m(\alpha_0, r, \varphi) = B_0(r, \varphi)/\sin^2(\alpha_0)$. Any electron drift path keeps B_m (and K) constant such that the strength of the mirror point magnetic field does not depend on the longitude φ and simply writes $B_m(\alpha_0, r)$. The colatitude $\theta_m(\alpha_0, r, \varphi)$ at the mirror point is also such that $B(r, \theta_m, \varphi) = B_m(\alpha_0, r)$. With the use of the LANLGeoMag software, the second adiabatic invariant corresponding to B_m at r_0 and φ_0 is calculated as

$$K(\alpha_0, r_0, \varphi_0) = \int_{\theta_m^s}^{\theta_m^n} \sqrt{B_m(\alpha_0, r_0) - B(r_0, \theta, \varphi_0)}\, \frac{\mathrm{d}s}{\mathrm{d}\theta} \mathrm{d}\theta,$$

for which the $\mathrm{d}s/\mathrm{d}\theta$ term is numerically computed from the bounce path increment δs resulting from a small variation in colatitude $\delta\theta$.

Starting at a given r_0 and φ_0 and keeping both B_m and K constant while going through all azimuth enables us to find the drift path $\Gamma_{(\varphi)}$. The third adiabatic invariant

associated to the aforementioned drift path is

$$\Phi(\alpha_0, r_0, \varphi_0) = \oint_{\Gamma_{(r_0,\varphi_0,\alpha_0)}} \boldsymbol{A} \cdot \mathrm{d}\boldsymbol{l} = \iint_{\Sigma_{(r_0,\varphi_0,\alpha_0)}} \boldsymbol{B} \cdot \mathrm{d}\boldsymbol{S}$$

for which $\boldsymbol{A}$ is the potential vector and $\Gamma_{(r_0,\varphi_0,\alpha_0)}$ is the drift path (covering the point $r = r_0$ for $\varphi = \varphi_0$) that corresponds to the constant (B_m, K) couple. Similarly, $\boldsymbol{B}$ is the magnetic field and $\Sigma_{(r_0,\varphi_0,\alpha_0)}$ refers to the surface enclosed by the drift shell. Hence, the Roederer L^* value can be generated as

$$L^*(\alpha_0, r_0, \varphi_0) = \frac{2\pi R_E^2 B_E}{\Phi(\alpha_0, r_0, \varphi_0)}.$$

Thus, the transformation from the Cartesian grid $(\alpha_0, r, \varphi)_{\text{Cartesian}}$ to the scattered locations $(K, L^*, \varphi)_{\text{scattered}}$ can be performed. Defining now a new Cartesian grid in the adiabatic coordinates $(K, L^*, \varphi)_{\text{Cartesian}}$, it is possible to reciprocally obtain the corresponding scattered coordinates $(\alpha_0, r, \varphi)_{\text{scattered}}$ by interpolating $(K, L^*, \varphi)_{\text{scattered}}$ onto $(K, L^*, \varphi)_{\text{Cartesian}}$. This final step produces an accurate new grid in $(\alpha_0, r, \varphi)_{\text{scattered}}$ providing that the initial grid $(\alpha_0, r, \varphi)_{\text{Cartesian}}$ has an acceptable resolution. Both the radial distance $r(L^*, K, \varphi)$ and the equatorial pitch angle $\alpha_0(L^*, K, \varphi)$ are thus functions of the adiabatic invariants K and L^* as well as the longitude φ.

6.3.2.b Particle's energy and drift-averaging

From a given field line identified by (L^*, φ), and a specified value for K, we compute the magnetic field intensity $B_m(K, L^*)$ at the mirror point (conserved along a drift shell by definition). Hence, for each given μ value, we derive the momentum p such that $p(\mu, K, L^*) = \sqrt{2m_0\mu B_m}$. Then, the kinetic energy E is calculated as $E(\mu, K, L^*) = \sqrt{p^2c^2 + m_0^2c^4} - m_0c^2$, from which we can successively compute the relativistic factor $\gamma(\mu, K, L^*) = 1 + E/(m_0c^2)$ and the β factor such that $\beta(\mu, K, L^*) = \sqrt{1 - 1/\gamma^2}$ in order to obtain the electron velocity $v(\mu, K, L^*) = \beta c$. A last step requires to average the equatorial pitch angle over each given drift shell to remove any azimuth dependence. The drift-averaging process, as given by equation (2.32), is not trivial, and requires first the calculation of the bounce path $S_b(K, L^*, \varphi)$ given by

$$S_b(K, L^*, \varphi) = \int_{s_1}^{s_2} \frac{\mathrm{d}s}{\sqrt{1 - B(s)/B_m}}.$$

The integration exhibits a singularity at the mirror point, which can be removed by an appropriate change of variable as provided by *Orlova and Shprits* (2011). Using their approach, the bounce path S_b is calculated for each field line and leads to the knowledge of the bounce period $\tau_b(\mu, K, L^*, \varphi)$ defined as

$$\tau_b(\mu, K, L^*, \varphi) = \frac{2}{v} S_b$$

for which $v = p/(\gamma m_0)$ is the electron velocity. Let us define $\boldsymbol{e}_0$ the unit vector that points in the direction of the magnetic field and $\hat{\boldsymbol{\varphi}}$ the unit vector pointing in the azimuthal direction. We use the J notation to refer to the second adiabatic invariant, and we set

$I = J/(2p)$. Then, we can compute the drift frequency $\omega_d(\mu, K, L^*, \varphi)$ from equation (2.31) as

$$\omega_d = \frac{2p}{qr_0\tau_b B_0} \left(\boldsymbol{\nabla}_0 I \times \boldsymbol{e}_0\right) \cdot \hat{\boldsymbol{\varphi}},$$

for which q is the particle's charge. The associated drift period $\tau_d(\mu, K, L^*)$ is also calculated as

$$\tau_d = \int_{\varphi=0}^{\varphi=2\pi} \frac{1}{\omega_d} \mathrm{d}\varphi.$$

We can finally average the equatorial pitch angle over the azimuth, with the use of (2.32), to obtain $\langle\alpha_0\rangle_\varphi(K, L^*)$ as

$$\langle\alpha_0\rangle_\varphi = \frac{1}{\tau_d} \int_{\varphi=0}^{\varphi=2\pi} \frac{1}{\omega_d} \alpha_0(\varphi)\, \mathrm{d}\varphi,$$

which is the last derivation step to transform the Cartesian adiabatic space (μ, K, L^*) into the physical space $(E, \langle\alpha_0\rangle, L^*)$.

For each specific given adiabatic set in (μ, K, L^*), the dipole field simply generates a unique couple (E, α_0), whereas the combined IGRF model and T89 field model produce six different $(E, \langle\alpha_0\rangle)$ couples according to the six possible configurations of the T89 magnetic field, going from quiet geomagnetic activity $K_p \sim 0$ to a highly perturbed magnetic field $K_p \geq 6$. In practice, the six conversion tables relating the adiabatic invariants with the physical coordinates are generated only once at the very first step of the numerical calculation. The choice of a specific magnetic configuration is updated during the numerical resolution of the reduced Fokker-Planck equation, according to the time-dependent value of K_p, by picking up in the appropriate conversion table.

6.3.2.c Grid resolution

The Cartesian grid made of the spherical coordinates (r, θ, φ) is specifically built on 300 bins for radius r uniformly distributed from $r_{\min} = 1.025$ to $r_{\max} = 6.525$. The colatitude θ represents 200 points between the two mirror points of the field line into consideration, from which we have built the B_m bins uniformly distributed in logarithm space. The azimuth φ coordinate is defined over 24 values between 0 and 2π, corresponding to one value per MLT (15 degrees in azimuth).

As before, the adiabatic invariant grid (μ, K, L^*) exactly matches the adiabatic grid detailed above used for the resolution of the Fokker-Planck equation, with a geometric μ grid made of 18 μ bins uniformly distributed in logarithm space from $\mu_{\min} = 10^0$ MeV/G and $\mu_{\max} = 2 \times 10^3$ MeV/G, a K grid that is also logarithmically sampled over 18 values from $K_{\min} = 10^{-2}$ $\mathrm{G}^{1/2}R_E$ to $K_{\max} = 10^1$ $\mathrm{G}^{1/2}R_E$ and a uniform L^* grid of 181 values between $L^*_{\min} = 1.0$ and $L^*_{\max} = 5.5$.

6.4 Verification step: focusing on a quiet geomagnetic event

A verification process is required to ensure the good numerical implementation of the non dipole magnetic field. The approach is split into two points.

First, we assure that the computation of a centered dipole field using the combination of the approach of *Cunningham* (2016) and the LANLGeoMag software is similar to the

use of a centered dipole field with the use of the semi-analytical transformations detailed in Chapter 4. This early verification has been done successfully and is not detailed here. Since the study is focused on the outer radiation belt, we did not try to compare the results between the use of a centered dipole field and an eccentric dipole field (also implemented in the LANLGeoMag software). It could have however been interesting to do so to emphasize the impact of the offset dipole field, which is linked to the South Atlantic Anomaly.

The second step consists in checking that a realistic field in a quiet time gives similar results to those obtained with a dipole field, at least for $L \leq 5$.

6.4.1 Data and magnetic field

6.4.1.a Data

We focus here on the 9-days event from September 24 to October 2, 1990. To our knowledge, this specific period has never been simulated as a whole. The chosen event is relatively quiet, as emphasized by Figure 6.3 that shows the evolution of the geomagnetic index K_p over time. The K_p index is never above the value of 4, which argue in favor of a reasonably steady period. The physical processes that are expected to take place are outward radial transport and pitch angle scattering.

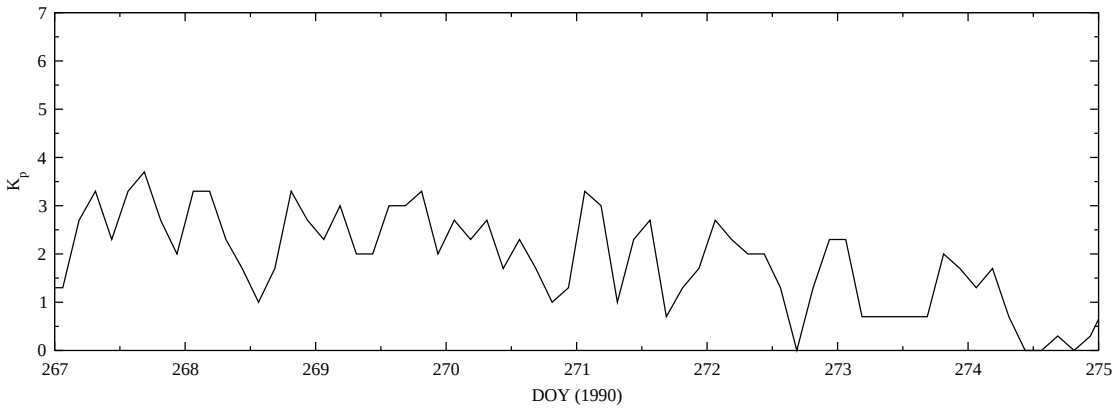

Figure 6.3 – Evolution of the geomagnetic index K_p during the period going from DOY=267 to DOY=275.

The CRRES data are displayed in Figure 6.4 (top panel), emphasizing the different orbits taken by the satellite during the whole period. These flux data are used to build the initial condition and the inner ($L = 1.0$) and outer ($L = 5.5$) boundary conditions for the reduced Fokker-Planck equation, and also are essential to test the accuracy of the simulation. For this purpose, the scattered data (top panel) have to be properly interpolated and extrapolated, following the procedure detailed in section 6.2.1.b. The obtained data are shown in Figure 6.4 (bottom panel).

The gap that extends from DOY=274 to DOY=275 is a signature of a lack of data provided by the satellite. It seems however well recovered after implementing the successive steps of decoupling the space and time variables, interpolating over L and time and extrapolating over L and time.

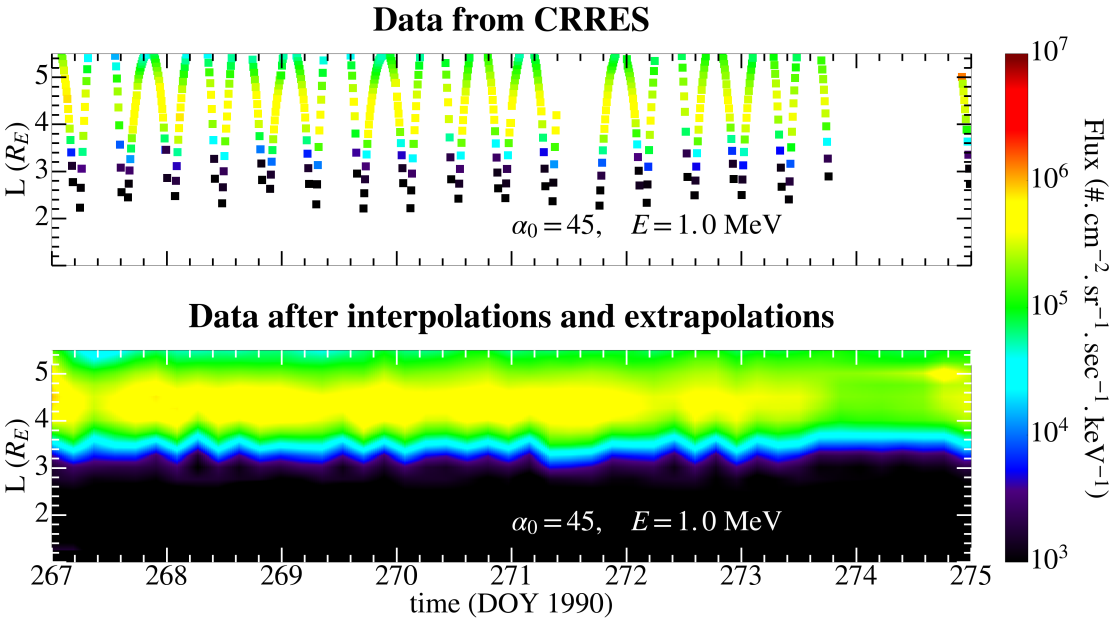

Figure 6.4 – Illustration of the decoupling process carried on the unidirectional electron fluxes measured by the MEA instrument on board CRRES (top) to obtain the usable interpolated and extrapolated unidirectional fluxes (bottom). The electron population of the two panels is represented for $E = 1.0$ MeV and $\alpha = 45$ degrees, for $1.0 \leq L^* \leq 5.5$ from September 24 (DOY=267) to October 2 (DOY=275), 1990.

6.4.1.b Magnetic field

Figure 6.5 displays two configurations of the magnetic field according to the model in use in the GSM coordinate system (the x-axis points to the Sun). The left panel represents the magnetic field lines for a dipole field, whereas the right panel represents the magnetic field lines calculated for the combination of the IGRF (internal field) with the T89 (external field), for a fixed K_p around 2, which is a rather representative value of K_p for the event at stake. The field lines for both models correspond to different values of L^*, respectively $L^* = 2$, 3, 4 and 5 R_E, which characterize a specific drift path for the electrons. As raised in Chapter 2, the L^* value for a dipole field (also commonly and simply referred as L) corresponds exactly to the equatorial radial distance of the electron population, whereas the L^* value for a non dipole field represents the equatorial radial distance at which the electron population would end up if all non adiabatic effects were abruptly turned off (*Roederer and Zhang*, 2014).

These two different interpretations are clearly visible in Figure 6.5, for which the location of the dipole field lines perfectly match the equatorial radial distance (modulo the tiny tilt angle). On the other side, the magnetic field lines in the T89 configuration are (not significantly but surely) stretched out on the night side. For example, a L^* value of 5 rather corresponds to an equatorial radial distance of x $\sim$ 6 on the night side. The effect of the IGRF model compared with the dipole field (internal part of the field, around $L \sim 1.5$) is not visible at the spatial scale of Figure 6.5. Overall, the differences from both magnetic models are barely noticeable due to the weak geomagnetic activity ($K_p = 2$) chosen to plot the T89 field lines.

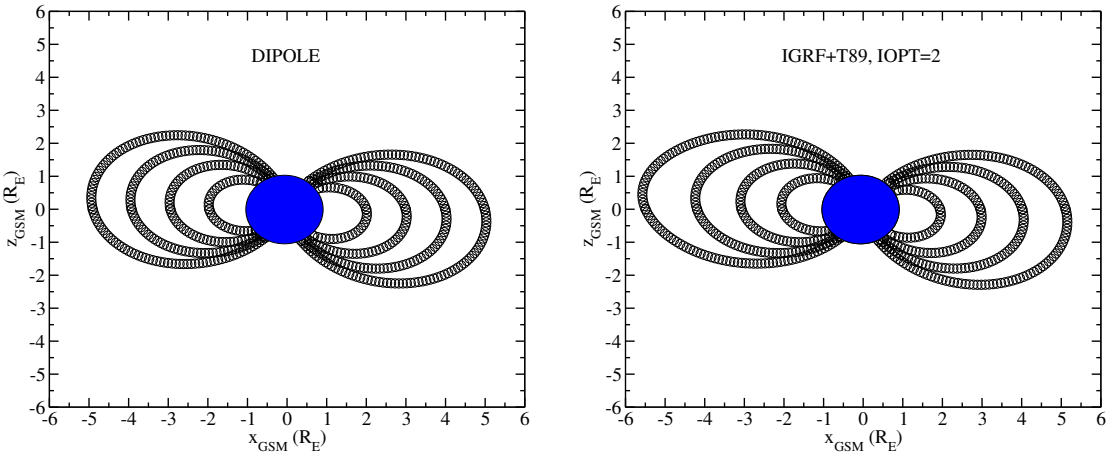

Figure 6.5 – Magnetic field lines for the dipole field (left) and the combination of the IGRF model and T89 field model (right), the latter being selected at $K_p = 2$. The field lines are plotted in the GSM Cartesian coordinates, such that the solar wind comes from the positive x (i.e. the (Ox) axis points sunwards, in the MLT 12 direction). They correspond to $L^* = 2, 3, 4$ and 5 for a 90 degrees pitch angle electron population at MLT=00 (negative x) and MLT=12 (positive x).

6.4.2 Preliminary results

6.4.2.a Simulations of differential unidirectional fluxes

The initial and boundary conditions of the PSD are given by unidirectional fluxes observed by the MEA instrument on board CRRES. As mentioned above, the transformation from flux to PSD (step 2: pre-processing the data) is implemented with either the dipole field (Figure 6.6, top-left) or the combined IGRF and T89 field (Figure 6.6, bottom-left). The numerical resolution of the Fokker-Planck equation (step 3) relies on the adiabatic grid in (μ, K, L^*). The simulated PSD are provided in Figure 6.6 for a dipole field (top-right) and the IGRF and T89 field (bottom-right). The data and simulations are shown for $\mu = 210$ MeV/G and $K = 0.11$ G$^{1/2}R_E$. The white line represents the location of the plasmapause calculated from (*Carpenter and Anderson*, 1992).

Although not striking, discrepancies are already noticeable in the reconstructed PSD data (left column of Figure 6.6) according to the magnetic field model at stake. The data-derived PSD performed with the IGRF and T89 field exhibits more significant enhancements than its counterpart calculated with the dipole field. The cause of this enhancements will be discussed in the next section, for which the differences between both PSD are more prominent. As shown by Figure 6.6, the simulations (right column of Figure 6.6) consistently preserve these deviations between both magnetic models.

Once the PSD have been simulated, the final transformation from PSD in the adiabatic space to unidirectional fluxes in the physical space is implemented to give a direct comparison with the CRRES observations (step 4: post-processing). Again, the transformation uses either the geometry of the dipole field or the geometry inherent to the IGRF and the T89 field. Figure 6.7 displays the unidirectional fluxes in physical space for $\alpha_0 = 45$ degrees and $E = 1.0$ MeV, which are respectively the flux measured by the MEA instrument after interpolation and extrapolation over the whole domain of interest (top), the corresponding flux obtained with the simulations involving a dipole field

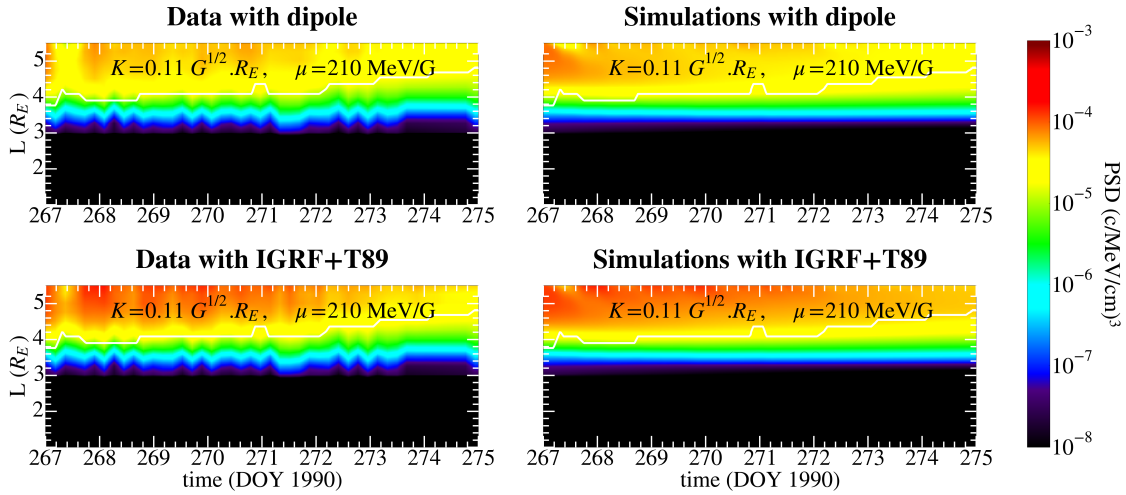

Figure 6.6 – PSD versus time (horizontal axis) and L^* (vertical axis) for $\mu = 210$ MeV/G and $K = 0.03$ G$^{1/2}R_E$. The two panels on the left represent, respectively, the PSD data extracted from the unidirectional fluxes provided by the MEA instrument with a dipole field (top-left) and with the combination of the IGRF and the T89 field (bottom-left). The PSD simulated with the 1-D reduced Fokker-Planck code are represented on the right panel, respectively for a dipole field (top-right) and for the IGRF and T89 field (bottom-right).

(center), and the flux given by the use of the IGRF and T89 field (bottom).

As expected, we do not see here any remarkable differences between the simulations performed with the dipole field and with the realistic field (IGRF and T89). The data are also pretty well reproduced by both simulations, testifying the ability of the numerical code to accurately reproduce electron fluxes for quiet geomagnetic events (*Ripoll et al.*, 2016b, 2017). To quantify the relevancy of both models (dipole and the combined IGRF and T89), Figure 6.8 aims at giving an estimation of the accuracy of the models performed either with the dipole field (blue lines) or the IGRF and T89 field (red lines), taken at $\alpha_0 = 45$ degrees and $E = 1.0$ MeV. More specifically, the first panel represents the evolution of the Median Absolute Error (MdAE) versus time for both simulations (top-left), the second panel (top-right) displays the Median Absolute Percentage Error (MdAPE), the third panel (bottom-left) depicts the evolution of the Median Symmetric Accuracy (MdSA), while the last panel (bottom-right) emphasizes the overestimation (positive values) or underestimation (negative values) of both models compared with the observation through the Median Log Accuracy Ratio (MdLQ). The two latter metrics have been put forwards by *Morley* (2016); *Morley et al.* (2018). All those four metrics have been extensively presented in section 2.9 and used in Chapter 5.

All the metrics indicate a very good reproduction for both the dipole and the combination of the IGRF and T89 field models, with a MdAE that does not exceed 10^4 #.cm^{-2}.sr^{-1}.sec^{-1}.keV^{-1}, which represents only a few percent of the average flux value that lies around 10^6 #.cm^{-2}.sr^{-1}.sec^{-1}.keV^{-1}. Similarly, the MdAPE, the MdSA and the MdLQ confirm the model accuracy, with, for instance, a MdAPE that only reaches 20% in worst cases, a MdSA around 100% and a MdLQ below 0.2 in absolute value. This last statistical index is the most able to put forward the discrepancies between the dipole and the T89 field, as the T89 field tends to overestimate the observation whereas the dipole field is more likely to underestimate them. Let us recall that overestima-

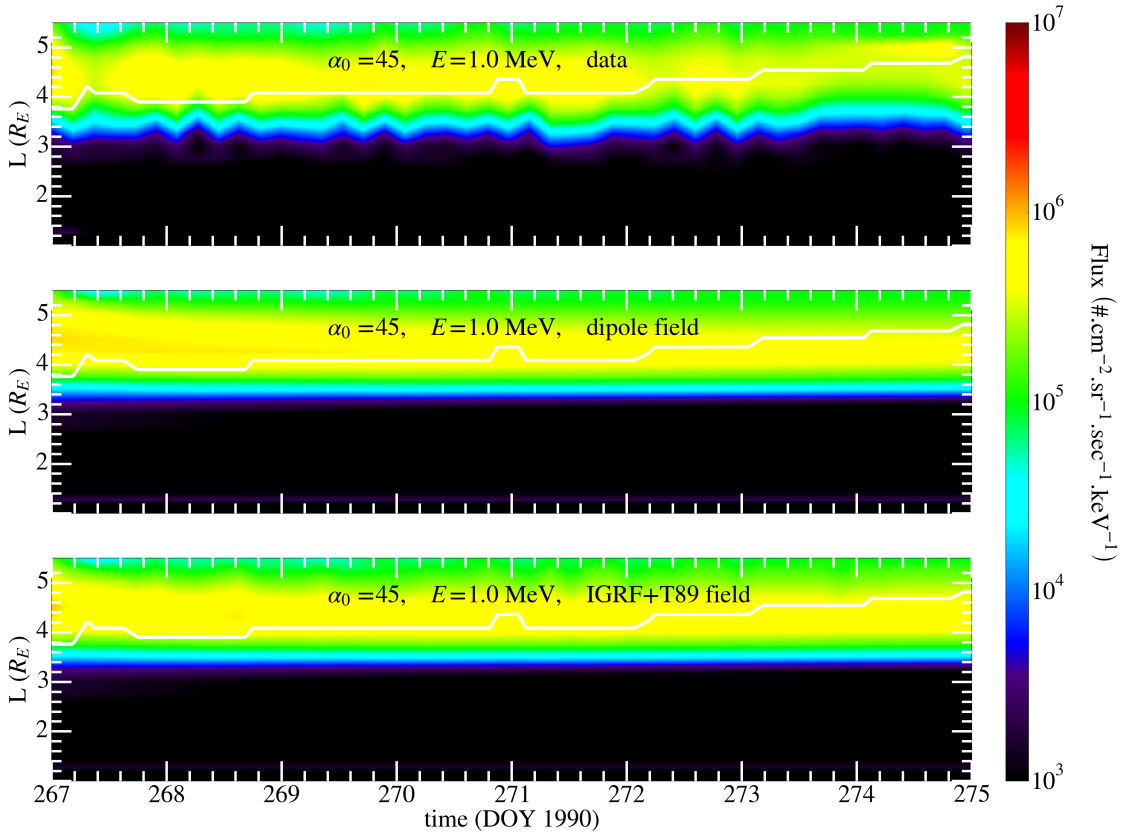

Figure 6.7 – Representation of the unidirectional electron flux at the energy of 1.0 MeV and a given equatorial pitch angle of 45 degrees. The top panel describes the evolution of the fluxes data recorded by CRRES, after interpolation and extrapolation on a Cartesian grid in L and time. The second row indicates the simulated flux obtained with the use of the dipole field model, and the last row illustrates the predicted electron fluxes coming from the implementation of the combined IGRF model and T89 magnetic field model. The white line represents the location of the plasmapause.

tions bring a prevalent error penalty on the MdAPE metric (see Chapter 5 and (*Morley*, 2016)), such that the larger MdAPE values displayed for the T89 field should not make us necessarily discriminate the T89 model. Beyond the overall satisfactory reproduction of the observations, there is no major impact of the T89 field model in the presented simulations.

6.4.2.b Simulations of differential omnidirectional fluxes

Knowing that the CRRES spacecraft nearly lies in the equatorial plane, we can approximate the local pitch angle by the equatorial pitch angle and the local flux by the equatorial flux. This assumption enables us to simply compute, at each energy, the differential omnidirectional electron fluxes by integrating in pitch angle the equatorial unidirectional fluxes $j(E, \alpha_0, L, t)$. The total omnidirectional flux J_O at energy E, L-shell L, latitude λ and time t is here calculated along a dipole field line and is given by

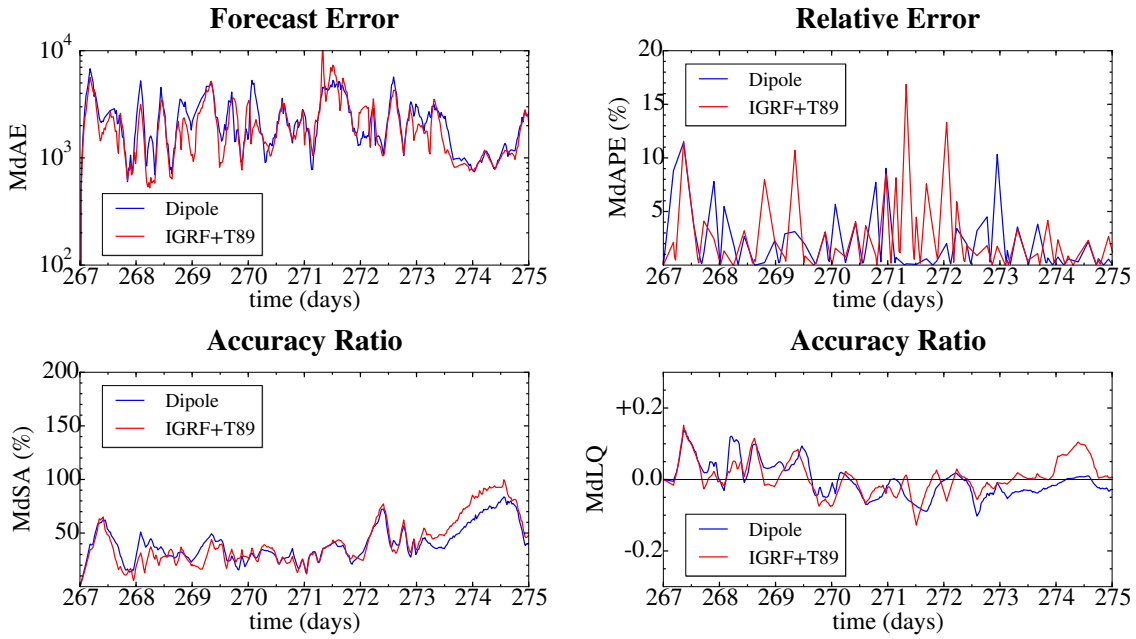

Figure 6.8 – Evolution of the Median Absolute Error (MdAE, top-left), the Median Absolute Percentage Error (MdAPE, top-right), Median Symmetric Accuracy (MdSA, bottom-left) and Median Log Accuracy Ratio (MdLQ, bottom-right) versus time for an unidirectional electron flux at $E = 1.0$ MeV and $\alpha = 45$ degrees (see also Figure 6.7).

(see equation (2.68) and (*Roederer*, 1970))

$$J_O(E, L, \lambda, t) = 4\pi \frac{B(\lambda, L)}{B_0(L)} \int_{x_{01}(L,\lambda)}^{x_{0LC}(L)} j(E, x_0, L, t) \frac{x_0}{\sqrt{1 - \frac{B(\lambda, L)}{B_0(L)}\left(1 - x_0^2\right)}} \mathrm{d}x_0.$$

for which $x_0 = \cos(\alpha_0)$. The intensity $B_0(L)$ of the equatorial magnetic field is related to the field line identified by its radial position L, whereas $B(\lambda, L)$ is the intensity of the magnetic field at latitude λ for the field line at L. The lower bound of the integrand is $x_{01}(L, \lambda) = \sqrt{1 - B_0(L)/B(\lambda, L)}$ and the upper bound of the integrand corresponds to the equatorial loss cone $x_{0LC}(L) = \sqrt{1 - B_0(L)/B_L(L)}$, for which $B_L(L)$ is the magnetic intensity for field line L at an altitude of 120 km above the Earth's surface.

Figures 6.24, 6.25 and 6.26 gathered at the end of this chapter represent respectively the omnidirectional fluxes every day during 9 days, for three energies, E=0.5, 1.0 and 1.5 MeV. The first row of each figure displays the observations taken from the MEA instrument on board CRRES. The second row shows the simulations computed with a dipole field, and the last row exhibits the simulations obtained with the combination of the IGRF model and T89 field model. In these figures, the omnidirectional electron fluxes (data and both simulations) have been projected onto dipole field lines, with the Earth represented at the center of each panel (black sphere). Since the electron fluxes (as well as the phase space density) have no azimuthal dependence, it makes sense to map them onto dipole field lines that are symmetric around the dipole axis. It also enable us to easily compare the intensity of electron fluxes for each L-shell (field line location).

For each of the three illustrated energies, the omnidirectional fluxes taken from CR-

RES measurements (first row of Figures 6.24, 6.25 and 6.26) exhibit a gradual depletion of the outer belt, mostly due to outward radial diffusion as we witness the decrease of the flux at $L = 5.5$ during the first three days of the period. Both models give qualitatively the same omnidirectional fluxes for $E = 0.5$, 1.0 and 1.5 MeV, which also show a progressive depletion of the outer belt. They both qualitatively compare quite well with the data. The computations performed with the combined IGRF model and T89 field model slightly overestimate the observations at $E = 1.0$ MeV.

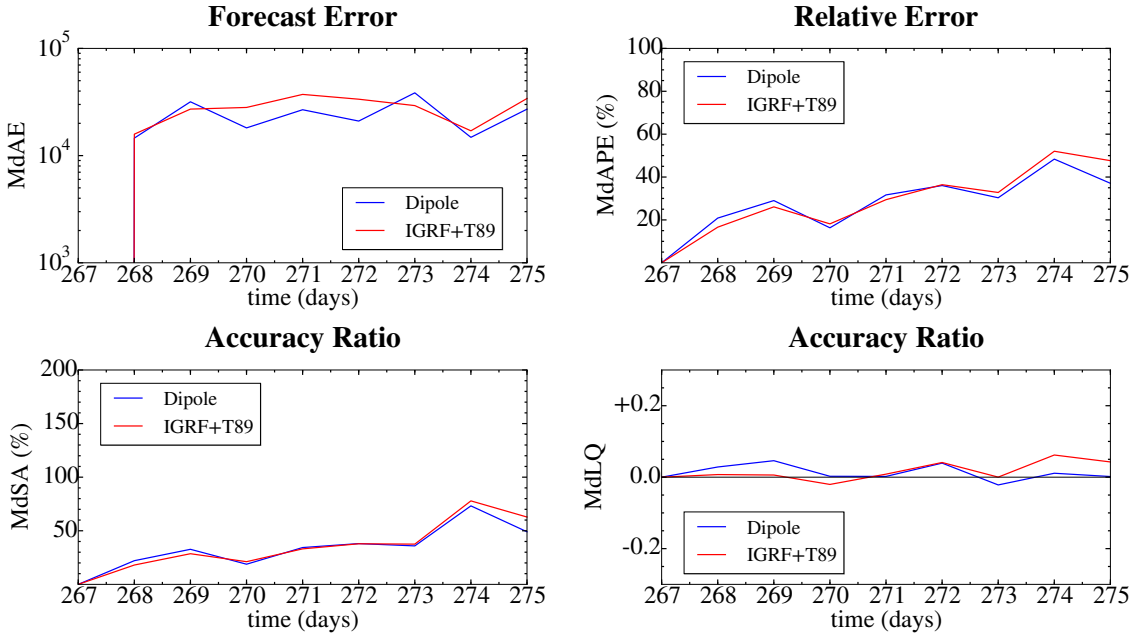

Figure 6.9 – Evolution of the Median Absolute Error (MdAE, top-left), the Median Absolute Percentage Error (MdAPE, top-right), Median Symmetric Accuracy (MdSA, bottom-left) and Median Log Accuracy Ratio (MdLQ, bottom-right) versus time for an omnidirectional electron flux at $E = 1.0$ MeV (see also Figure 6.25).

The accuracy of the two models is emphasized by Figure 6.9, which represents the Median Absolute Error (top-left), the Median Absolute Percentage Error (top-right), the Median Symmetric Accuracy (bottom-left) and the Median Log Accuracy Ratio (bottom-right) taken for the omnidirectional fluxes (data and simulations) at $E = 1.0$ MeV (see Figure 6.25). The different statistics confirm the good reproduction of the observations for both magnetic field models. No significant discrepancy seems to emerge between both models, which, again, testify in favor of the good numerical implementation of the realistic magnetic field model, as well as its weak effects on radiation belts during quiet times.

Table 6.1 provides the global indices over the full period for both simulations (dipole and T89 magnetic field). The metrics related to the omnidirectional fluxes are calculated over the energies $E = 0.2$, 0.5, 1.0, 1.5, 2.0 and 4.0 MeV, for $1.6 < L^* < 5.5$, consistently with Chapter 5. It highlights a (slightly) better prediction with the use of the T89 magnetic field.

The error metrics indicate the same accuracy for both the dipole and the T89 models. Let us mention that the MdAPE and the MdSA metrics are here below the results obtained in the 1-D reduced Fokker-Planck simulations with the data-driven lifetime of

Table 6.1 – Global Median Absolute Error (MdAE), Median Absolute Percentage Error (MdAPE), Median Log Accuracy Ratio (MdLQ) and Median Symmetric Accuracy (MdSA) for the 1-D reduced Fokker-Planck simulations including the dipole magnetic field and the T89 magnetic field. The indicated indices correspond to the omnidirectional electron fluxes and have been calculated over all available L-shells, energies and times.

	1-D simulations, dipole field	1-D simulations, IGRF+T89 field
MdAE	4.7×10^4	3.7×10^4
MdAPE	29%	27%
MdSA	32%	31%

Chapter 5 (see Table 5.4, left column, with MdAPE = 67% and MdSA = 100%). This can be explained because of the quiet properties of the event at stake compared with the March 2013 storm-recovery of Chapter 5 that exhibits a more significant dropout.

6.4.2.c Simulations of integral omnidirectional fluxes

We use the opportunity of having electron fluxes covering a wide range of pitch angles and energies to calculate the total integral omnidirectional electron flux J_{IO}, given by

$$J_{IO}(L, \lambda, t) = \int_{E_1}^{E_2} J_O(E, L, \lambda, t)\, \mathrm{d}E.$$

The integral omnidirectional flux is derived from the previous omnidirectional fluxes that are integrated from $E_1 = 0.15$ MeV to $E_2 = 1.58$ MeV (complete set of available energies). It represents a global number of electrons going through a surface of unit area per unit time, and is therefore expressed as $\#.\mathrm{cm}^{-2}.\mathrm{sec}^{-1}$.

Figure 6.27 represents the integral omnidirectional fluxes. As before, they have been projected onto dipole field lines from $L = 1.0$ to 5.5 Earth radii. The first row displays the observations taken from the MEA instrument on board CRRES. The second row shows the simulations computed with a dipole field, and the last row exhibits the simulations obtained with the combination of the IGRF model and T89 field model. The reconstructed integral omnidirectional flux data show a gradual electron depletion from DOY=267 to 271, followed by a steady state until the end of the event (DOY=275). If both simulations take also account of the overall depletion, their dynamics is slightly faster than currently observed. The electron losses occurred quicker, from DOY=267 to DOY=269, and the quiescent state rather starts at DOY=270.

In Figure 6.10 we plot the evolution versus time of the four statistical indices (same format as before) related to the integral omnidirectional electron fluxes. As expected, the two models are comparable. The combined IGRF model and T89 field model only tend to overestimate the data more significantly than the dipole field. The error made on the integral omnidirectional fluxes are about 50-60% (well below a factor of 2) in both cases (dipole and T89 field), which indicates an accurate reproduction.

6.4.3 Summary

The last sections prove the accuracy of the predictions of differential unidirectional fluxes, differential omnidirectional fluxes and integral omnidirectional fluxes, whatever the magnetic field model used in the computations, as soon as conditions are quiet

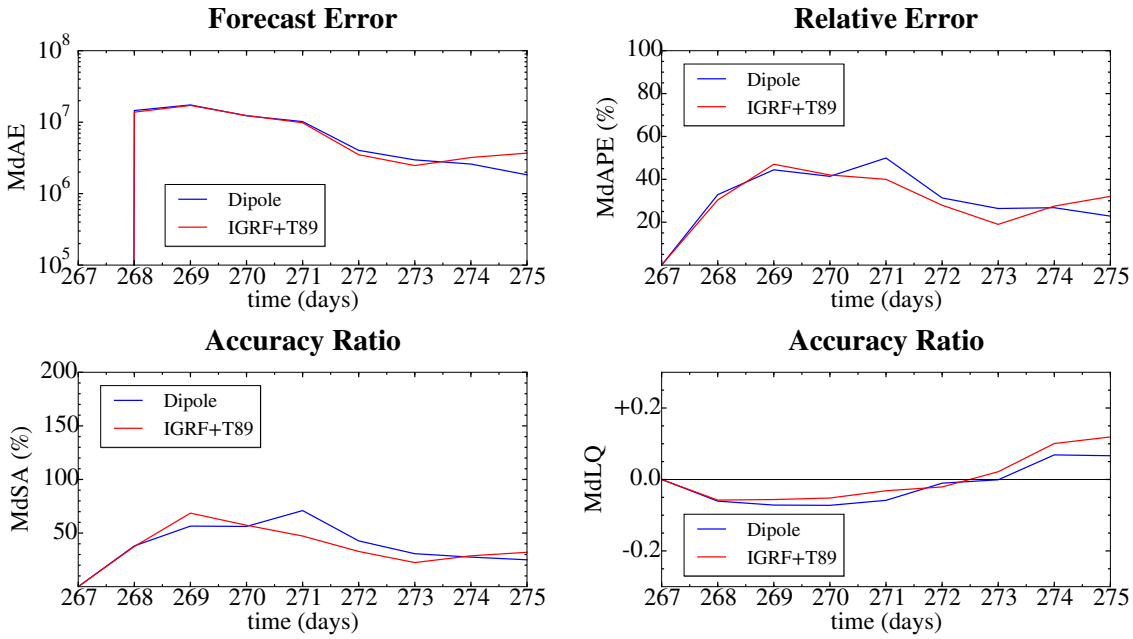

Figure 6.10 – Evolution of the Median Absolute Error (MdAE, top-left), the Median Absolute Percentage Error (MdAPE, top-right), Median Symmetric Accuracy (MdSA, bottom-left) and Median Log Accuracy Ratio (MdLQ, bottom-right) versus time for the integral electron flux (see also Figure 6.27).

enough. Since the event considered was relatively quiet, any local acceleration process (that originates from energy diffusion) is unlikely to occur, and the reduced Fokker-Planck equation appeared to be pretty well adapted. This confirms the results of Chapter 5 and our published results (*Ripoll et al.*, 2016b, 2017). Now that the implementation has been tested and validated for this academic quiet event, the next step is to attempt the reproduction of an active event and to quantify the effects of the magnetic field geometry.

6.5 Simulating a geomagnetic active period

6.5.1 Framework of the study

6.5.1.a Data

In this section, we focus on the period going from October 9 to October 15, 1990, which is also known as the October storm (1990). This specific event has been devoted to a large interest from the space weather community (e.g., *Brautigam and Albert*, 2000; *Albert et al.*, 2009). The corresponding CRRES data are displayed in Figure 6.11 (top of each subpanel), emphasizing again the different orbits taken by the satellite during the whole period. Starting on October 10, 1990 (DOY = 283), the electron fluxes at 1.0 MeV are subjected to a dramatic decrease by more than two orders of magnitude. The electron depletion lasts during about 18 hours, and is followed by a significant increase in electron fluxes. This strong enhancement is remarkable at intermediate L-shells ($L^* \sim 4$) and is predominant after October 11, 1990 (DOY = 284), showing an outer radiation belt that is gradually replenished until October 15, 1990 (DOY = 288).

These flux data are used to build the initial condition and the inner ($L = 1.0$) and

outer ($L = 5.5$) boundary conditions for the reduced Fokker-Planck equation and to test the accuracy of the simulation. For this purpose, the scattered data (top panel) have to be properly interpolated and extrapolated, as shown in Figure 6.11 (bottom subpanels).

The period from October 9 to October 15, 1990, is much more active than the previous quiet event, as highlighted by the K_p evolution in Figure 6.12. Such high K_p values would affect the strength of radial transport through the K_p-dependent radial diffusion coefficient from *Ozeke et al.* (2014). By comparing the K_p evolution in Figure 6.12 with the flux observed in Figure 6.11, we notice that the massive electron flux dropout occurring at $t = 283$ DOY corresponds to the time for which K_p is maximal and reaches the value of 6. On the contrary, the strong electron enhancement from $t = 286$ to $t = 288$ relates to a gradual decrease of geomagnetic activity, with a moderate K_p around the value of 3.

6.5.1.b Flux dropouts

The flux dropouts are the reflections of electron losses. The latter are caused by two distinct phenomena. The first is the combination between magnetopause shadowing and outward radial diffusion, which brings the electron beyond the magnetopause. The second is related to pitch angle diffusion (breaking the two first adiabatic invariants) inferred from gyro-resonant interactions between the electrons and VLF (mainly whistler mode hiss) waves. The progressive decrease of electron pitch angle makes them reach the bounce loss cone and precipitate into the atmosphere. The rapid electron decrease and its low energy-dependence is more likely to suggest electron losses in the outer space (outward radial diffusion) rather than electron precipitation.

6.5.1.c Flux enhancements

Flux enhancements characterize the process of electron acceleration. Restricting to the Fokker-Planck model, electron acceleration can be modeled by two diffusive processes. Inward radial diffusion (violation of the third adiabatic invariant only, keeping the two other constant) is due to drift resonant interactions between the electrons and ULF waves and results to betatron acceleration, as the electrons diffuse toward regions of higher magnetic intensity. Energy diffusion (breaking of the two first adiabatic invariants) is inferred from gyro-resonant interactions between the electrons and VLF (mainly whistler mode chorus) waves and results to in-situ acceleration. Simulations are required to distinguish between those two competitive processes.

6.5.1.d Magnetic field

Figure 6.13 displays two configurations of the magnetic field according to the model in use.

As before, the left panel represents the magnetic field lines for a dipole field, whereas the right panel represents the magnetic field lines calculated for the combination of the IGRF (internal field) with the T89 (external field). The latter model is shown for $K_p = 5$, which is a typical representative K_p for the event at stake. We here notice significant differences between both models, in particular the magnetic field lines are substantially stretched out on the night side for the IGRF and T89 magnetic field models. For example, on the night side, the field lines corresponding to $L^* = 4$ reaches equatorial radial distance above Earth's radii above 5 and the field lines related to $L^* = 6$ are stretched beyond 6 Earth radii. This is expected since the T89 model accounts for both

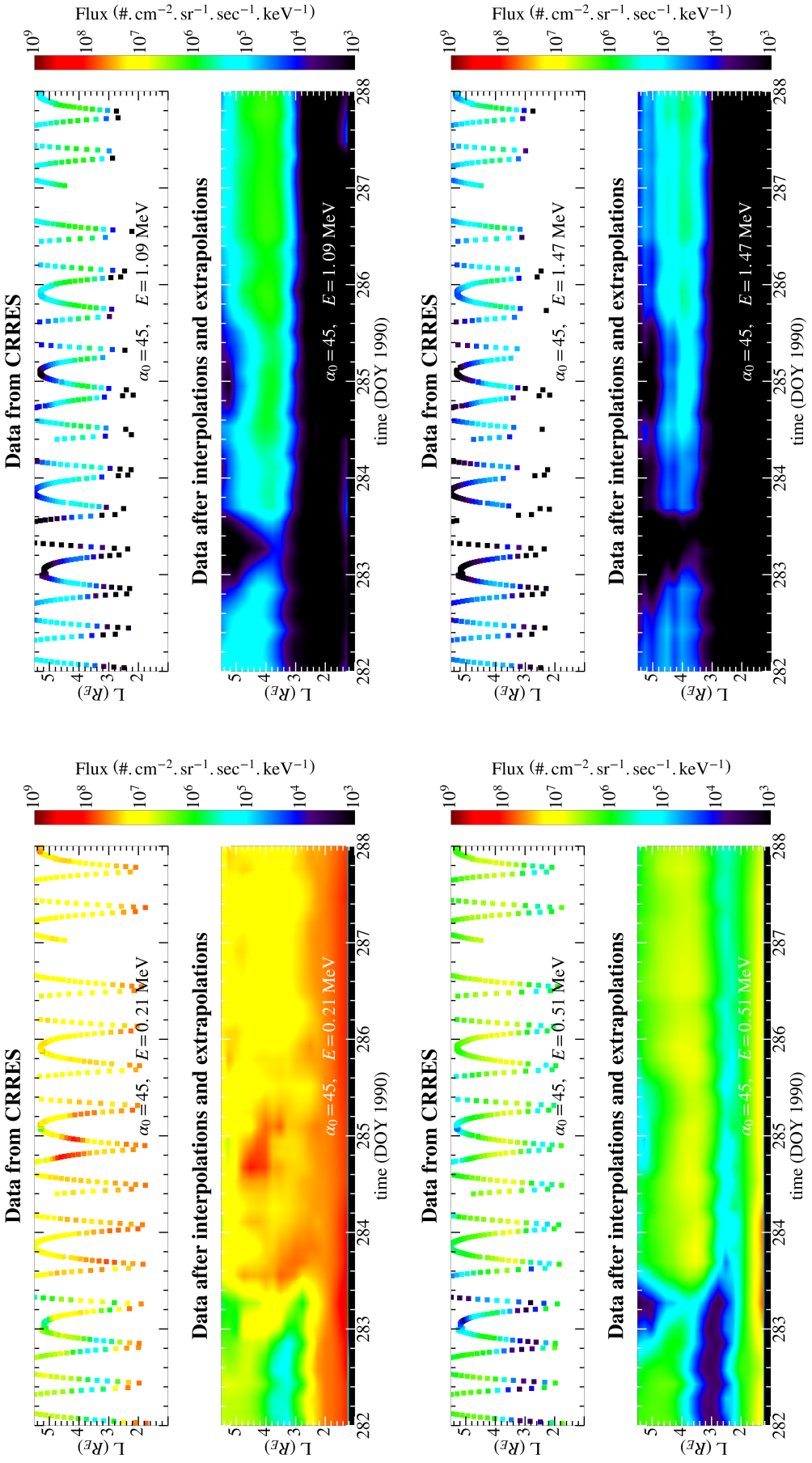

Figure 6.11 – Illustration of the decoupling process carried on the unidirectional electron fluxes measured by the MEA instrument on board CRRES (top of each four panel) to obtain the usable interpolated and extrapolated unidirectional fluxes (bottom of each four panel). The electron population is represented from October 9 (DOY=282) to October 15 (DOY=288), 1990, for $\alpha = 45$ degrees and $E = 0.2$ MeV (top-left), $E = 0.5$ MeV (bottom-left), $E = 1.0$ MeV (top-right) and $E = 1.5$ MeV (bottom-right).

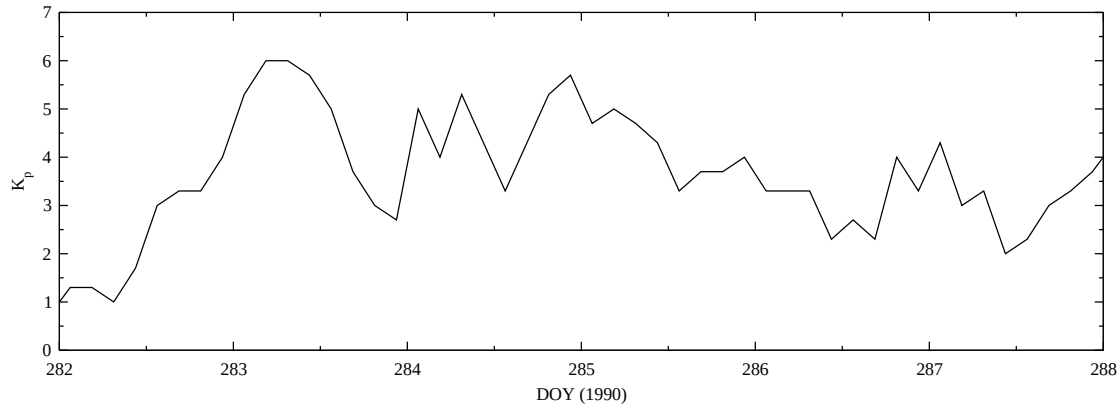

Figure 6.12 – Evolution of the geomagnetic index K_p during the October 1990 storm period going from DOY=282 to DOY=288.

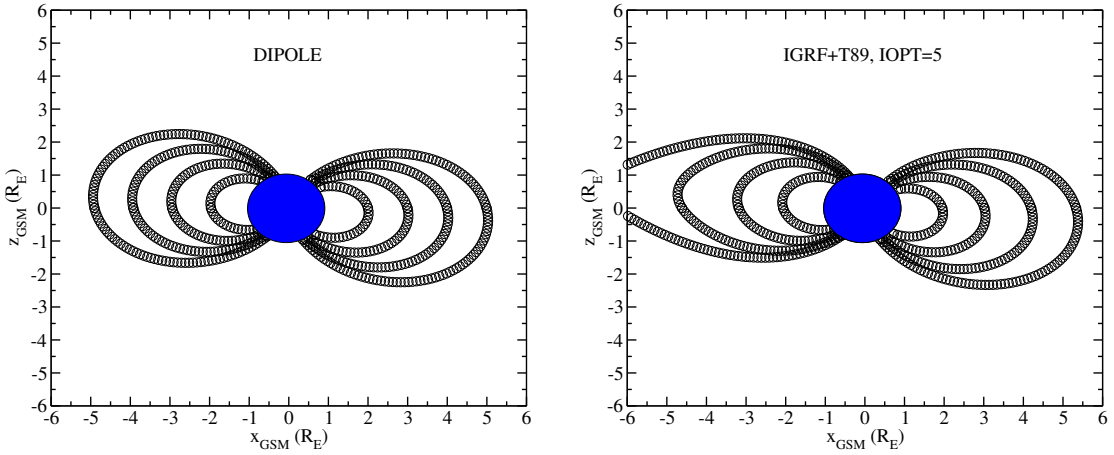

Figure 6.13 – Magnetic field lines for the dipole field (left) and the combination of the IGRF model and T89 field model (right), the latter being selected at $K_p = 5$. The field lines are plotted in the GSM Cartesian coordinates. The solar wind comes from the right. They correspond to $L^* = 2, 3, 4$ and 5 for a 90 degrees pitch angle electron population at MLT=00 (negative x) and MLT=12 (positive x).

field lines compression by solar wind on the day side and for the effects of cross-tail currents that stretch out the field lines on the night side.

6.5.2 Pre-processing

The PSD used to build the initial and boundary conditions results from the unidirectional fluxes observed by CRRES with either the dipole field (Figure 6.14, top) or the combined IGRF and T89 field models (Figure 6.14, bottom).

The PSD extracted from the observed electron fluxes (Figure 6.14) exhibits significantly higher values for the T89 field (bottom) than for a dipole field (top), up to two order of magnitude at large L-shells ($L^* > 5.0$), contrary to the previous quiet event. Let us briefly discuss here the physical reasons for such enhanced PSD for the T89 field

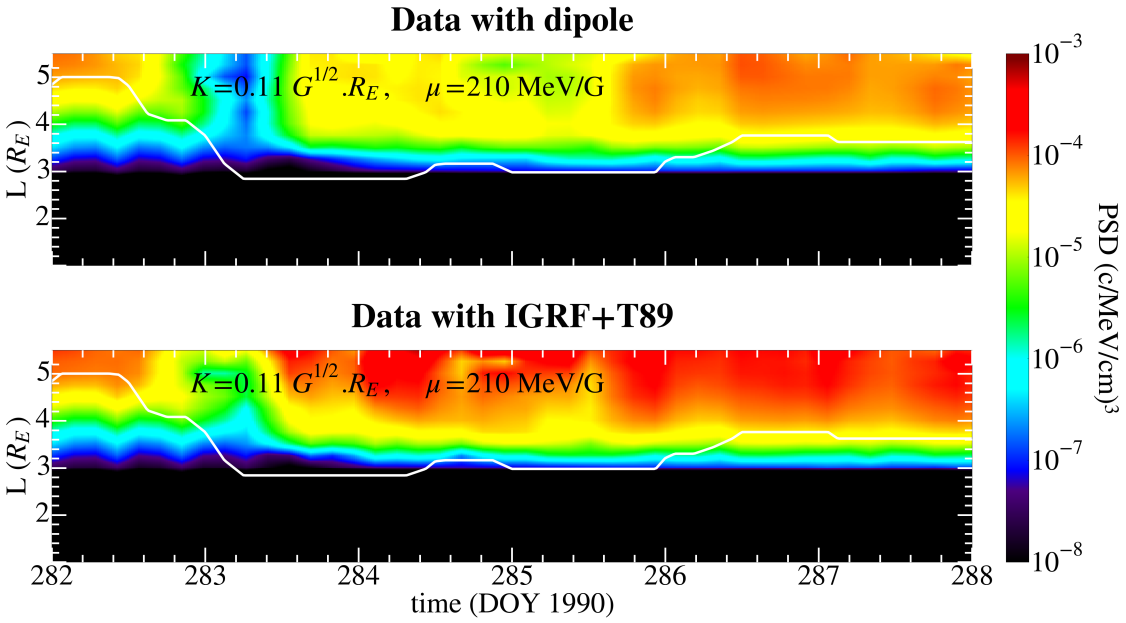

Figure 6.14 – Representation of PSD versus time (horizontal axis) and L^* (vertical axis) for $\mu = 210$ MeV/G and $K = 0.03$ G$^{1/2}R_E$. The two panels represent respectively the PSD data extracted from the unidirectional fluxes provided by the MEA instrument with a dipole field (top) and with the combination of the IGRF and the T89 field (bottom). The white line represents the location of the plasmapause calculated from (*Carpenter and Anderson*, 1992).

compared with their counterparts obtained with a dipole field (that are here significantly underestimated).

We remind that the strategy of resolution relies on a given set of (E, α_0, L^*). We attempt to explain the differences occurring on the reconstructed PSD by quantifying the obtained values for the first invariant μ and the second invariant K (as emphasized by *Green and Kivelson* (2004) for K), according to the field model, and their impact on the PSD.

6.5.2.a Estimation of K for both models

First, the second invariant K can be roughly estimated as $K \sim \sqrt{B_m - B_0}s$, i.e. $K \sim \sqrt{B_m}\cos(\alpha_0)s$, for which s is the length of the electron bounce path, B_m the magnetic field intensity at the mirror point and B_0 the equatorial magnetic field intensity. Since the T89 magnetic field exhibits stretched field lines on the night side contrary to the symmetric dipole field ($s_{\mathrm{T89}} > s_{\mathrm{DIP}}$), we have for a unique given value of α_0,

$$K_{\mathrm{T89}} > K_{\mathrm{DIP}}$$

for which K_{DIP} is the second invariant K computed with the dipole field and K_{T89} is the second invariant computed with the combined IGRF model and T89 field model.

6.5.2.b Estimation of μ for both models

Let us consider an electron population that mirrors at the magnetic equator (i.e. such that $\alpha_0 = 90$ degrees). In this case, $B_0 = B_m$ and the first adiabatic invariant writes

$\mu = p^2/(2m_0B_0)$. For a fixed value of momentum p (which is equivalent to set a given value for energy), the difference between μ_{T89} and μ_{DIP} would arise from a discrepancy in the value of B_0. Let us raise here the important point that the equatorial magnetic field intensities for both fields are not evaluated at the same geometric location in space, but rather at the same L^* value. In Appendix E, we demonstrate that for a same value of L^*, the intensity of the equatorial field for the non-symmetric simplified Mead field model is lower than for a dipole field (see equation (53)). Even if the simplified Mead field considered in Appendix E does not include all the effects embedded in the T89 field, we strongly believe that the T89 field has the same global characteristics as the non-symmetric Mead field. This is supported by the work led by *Lejosne* (2013), who adapted with a good accuracy the two available parameters of the Mead field to fit the behavior of the T89 field according to the appropriate value of K_p. From these results, we may conclude that at the same value of L^* for both the dipole field and the T89 field ($L^*_{\mathrm{T89}} = L_{\mathrm{DIP}}$), the magnetic field intensity of the T89 field is lower than the intensity of the dipole field, i.e. $B_0^{\mathrm{T89}} < B_0^{\mathrm{DIP}}$, which leads to

$$\mu_{\mathrm{T89}} > \mu_{\mathrm{DIP}}$$

for which the first adiabatic invariants μ_{DIP} and μ_{T89} are calculated respectively with the dipole field and the T89 field.

6.5.2.c Mathematical assessment of the impact of the magnetic field model on the phase space density

The generic form of the phase space density f obtained as a solution of the reduced Fokker-Planck equation, which has been derived in Chapter 3 and in (*Loridan et al.*, 2017), writes

$$f(\mu, K, L^*, t) = u(\mu)v(K)\sum_{k=1}^{\infty}\alpha_k(t)g_k(L^*),$$

for which $g_k(L^*)$ are the eigenfunctions related to radial transport, the $\alpha_k(t)$ functions governs the temporal evolution, and the $u(\mu)$ and $v(K)$ functions are respectively the distribution in μ and K. Both distributions $u(\mu)$ and $v(K)$ can be considered as steady at the timescale of radial diffusion. Since $K_{T89} > K_{\mathrm{DIP}}$, the $v_{T89}(K)$ distribution related to the T89 field is shifted towards the higher K values compared with the $v_{\mathrm{DIP}}(K)$ distribution related to the dipole field. Similarly, from $\mu_{\mathrm{T89}} > \mu_{\mathrm{DIP}}$, we also end up with a $u_{\mathrm{T89}}(\mu)$ distribution that stands in a region of larger μ compared with the $u_{\mathrm{DIP}}(\mu)$ distribution. Furthermore, observations from satellites attest the fact that both distributions $u(\mu)$ and $v(K)$ are respectively decreasing with respect to μ and K. Hence we conclude that for a same value of μ, $u_{\mathrm{T89}}(\mu) > u_{\mathrm{DIP}}(\mu)$ and $v_{\mathrm{T89}}(K) > v_{\mathrm{DIP}}(K)$. This shift is illustrated for both distributions in Figure 6.15 in the same way as in (*Green and Kivelson*, 2004). From these two contributing steps we conclude that

$$f_{\mathrm{dipole}}(\mu, K, L^*, t) < f_{\mathrm{T89}}(\mu, K, L^*, t),$$

which is fully consistent with the previous results of Figure 6.14.

We also notice in Figure 6.14 that isolated regions of enhanced PSD appear at some time intervals (between $t = 285$ and $t = 287$ DOY for example) for the dipole-case. For the T89-case, the overall PSD looks smoother in time. Since the large values of K_p result in a magnetic configuration with more stretched field lines for the T89 field, the transformation from (E, α_0, L^*) to (μ, K, L^*) would more severely impact the PSD

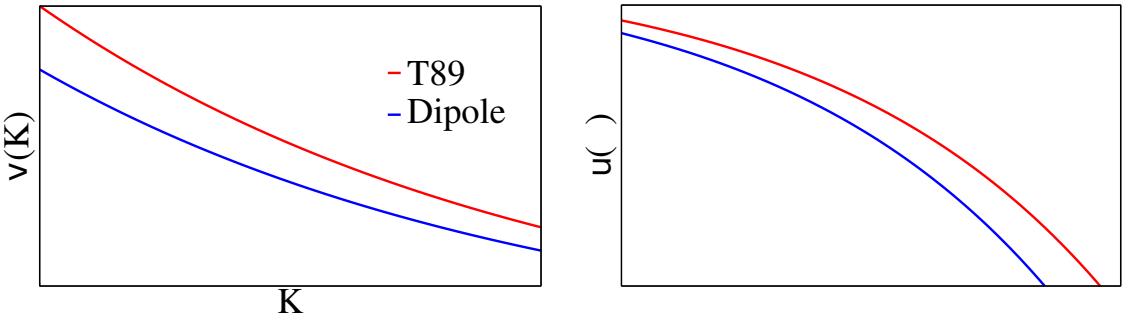

Figure 6.15 – Typical evolution of the electron K-distribution $v(K)$ versus K (left) and typical evolution of the electron μ-distribution $u(\mu)$ versus μ (right). Both distributions are commonly decreasing functions, such that they are constantly underestimated when considered within the framework of a dipole field.

values (in the T89 magnetic field model). The latter would therefore be strongly enhanced compared with a dipole field during such disturbed times, as illustrated by Figure 6.15. Then, the PSD values at large K_p increase more significantly than the ones of low K_p. Overall, the T89 field tends to balance the PSD value outside the isolated islands with the one within the islands, which get melted in the ambient PSD. No well-defined enhanced regions in T89-based PSD can be seen anymore, contrary to its dipole-counterpart which is no more balanced in time by the variations in K_p.

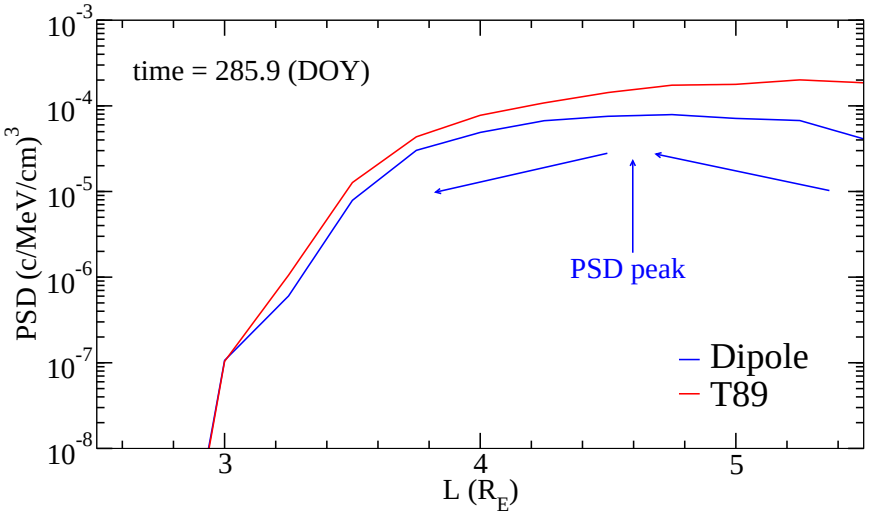

Figure 6.16 – Cut of Figure 6.14 at $t = 285.9$. If the PSD related to the T89 magnetic field (red) is decreasing (monotonic gradient), which is a clue for inward radial diffusion, the PSD built with the use of the dipole field (blue) exhibits a maximum at $L^* \sim 4.6$. This peak is rather due to the numerical inaccuracies of the dipole topology at high L-shells and should not be interpreted as an effect of local acceleration or outward radial diffusion.

Beyond the fact that the PSD obtained with the realistic field exhibits larger values than the ones obtained with the dipole field, the two data set represented in Figure 6.14 are somewhat contradictory as they illustrate the effects of different physical processes.

The PSD data derived with a dipole field (top-panel of Figure 6.14) show a massive dropout at $t = 283$, which is followed by moderate and regular injections. In particular, we notice the presence at $t = 286$ of an isolated island of electrons between $L^* = 4.0$ and $L^* = 5.2$ (see Figure 6.14 and Figure 6.16). This high density region cannot result from outward radial diffusion because there was no such a high density region at the outer boundary at earlier times. Hence this so-called peak in PSD could be thought as the result of in-situ electron acceleration by interaction with electromagnetic waves as commonly observed. Other similar features are also observable at larger times, for example at $t = 287$ or $t = 288$, which correspond to the least active times ($K_p \sim 3$) of the event (see Figure 6.12). We are unable to test and reproduce such local acceleration by simulations because energy diffusion cannot be modeled in the 1-D reduced Fokker-Planck equation.

The PSD data taken from the T89 field (bottom-panel of Figure 6.14) give, however, a glimpse of a very different structure. First, the dropout of $t = 283$ is not as strong as identified in the dipole case. More important, we do not locate any isolated high density region in the realistic case (see Figure 6.16).

By comparing the two data sets of Figure 6.14, we conclude that the peaks observed in the PSD computed with the dipole field are purely numerical artefacts that do not represent local acceleration. This contamination is induced by the inaccuracies of the dipole field and is mainly removed when a more realistic magnetic field is considered. This important impact of the magnetic field model is in agreement with *Green and Kivelson* (2004), who notice that imperfect magnetic field models might create artificial peaks in PSD. They attributed these unnatural features to inaccuracies in the calculations of the second invariant K.

6.5.3 PSD computations

6.5.3.a Radial diffusion or local acceleration?

The simulation results are represented in Figure 6.17. The two top panels represent respectively the reconstructed PSD data (same as in Figure 6.17) with the dipole field (top-left) and the corresponding simulated PSD (top-right). The two bottom panels similarly represent the PSD (data for the bottom-left panel, simulations for the bottom-right panel) corresponding to the combined IGRF model and T89 field model.

As expected, we obtain a better agreement with the use of the T89 field than with a dipole field. With the use of a dipole field, we are left with the apparent need to include the effects of in-situ acceleration, which are believed to be non-physical and completely artificial as explained above. The 1-D simulation thus results in a poor reproduction and significantly underestimates the reconstructed observations, particularly in the region where the local artificial enhancements appear, from $t = 284$ to $t = 288$, with L^* lying between 4.0 and 5.0 R_E. With the use of the T89 field however, the PSD data are likely to be shaped by radial diffusion only, and the 1-D simulation is accurate enough to capture the effects of radial transport and to reproduce rather correctly the PSD data. We draw attention that this effect of discriminating radial transport from local acceleration is only due to the way the PSD are reconstructed from the flux observations. This is thus inherent to the pre-processing steps (steps 1 and 2). Let us have a look now at the effects of the intrinsic magnetic field model during the computations per se via the loss term mapping.

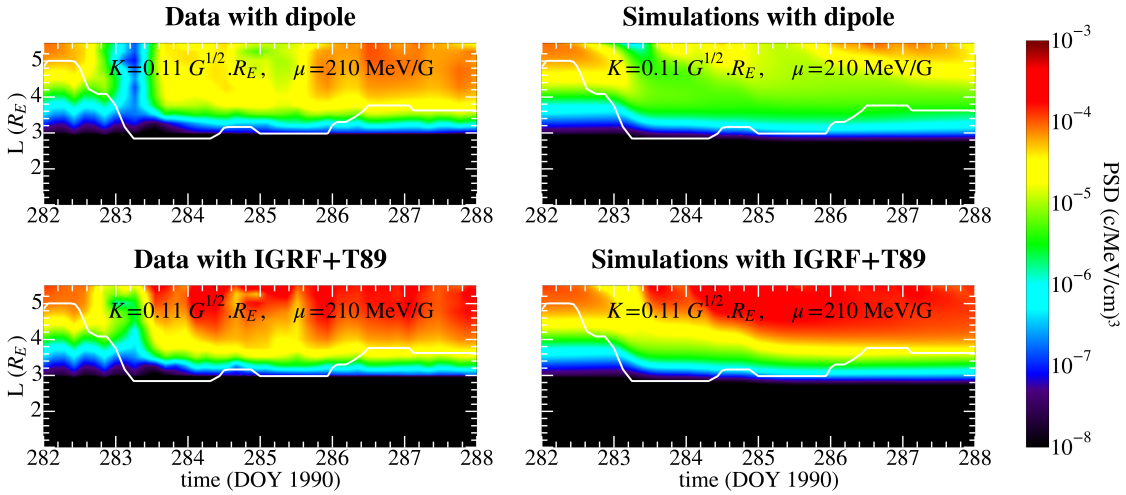

Figure 6.17 – Representation of PSD versus time (horizontal axis) and L^* (vertical axis) for $\mu = 210$ MeV/G and $K = 0.11$ G$^{1/2}R_E$. The two panels on the left represent respectively the PSD data extracted from the unidirectional fluxes provided by the MEA instrument with a dipole field (top-left) and with the combination of the IGRF and the T89 field (bottom-left). The simulated PSD corresponding to the initial and boundary conditions of the left panel are represented on the right panel, respectively for a dipole field (top-right) and for the IGRF and T89 field (bottom-right).

6.5.3.b Impact of the magnetic field model on the loss term mapping

The electron lifetime τ included in the reduced Fokker-Planck equation depends on the particle energy and L-shell. Since the computations are carried out for fixed values in the adiabatic space, the value of the lifetime involved at a given triplet (μ, K, L^*) is different between the case of a dipole field and the case of the T89 field. It results that the lifetime $\tau(E, L) \equiv \tau(E(\mu, K, L), L) \equiv \tau(\mu, K, L)$ scatters electrons on different regions of the (μ, K, L^*) space according to the magnetic field model.

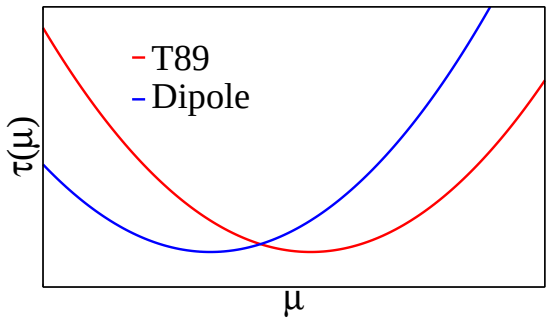

Figure 6.18 – Typical evolution of the electron lifetime $\tau(\mu)$ for a given value of K and L^*. As the lifetime roughly behaves like a quadratic function of μ, the use of a T89 magnetic field leads to higher lifetimes below a threshold μ and lower lifetimes above the threshold. The latter corresponds to $\tau_{\mathrm{T89}}(\mu) = \tau_{\mathrm{DIP}}(\mu)$.

Since the dependence in K of τ is an artefact that only comes from the energy dependence, it can be neglected. As for the dependence in the first invariant μ, the

electron lifetimes can typically be approximated by a quadratic function of μ, being a decreasing function of μ at low μ values and being an increasing function of μ at larger values of μ. The shift between μ_{DIP} and μ_{T89} then leads to a higher T89-lifetime for small μ values and to a lower T89-lifetime large μ values compared with a lifetime that has been transformed with a dipole model. This effect is emphasized in Figure 6.18.

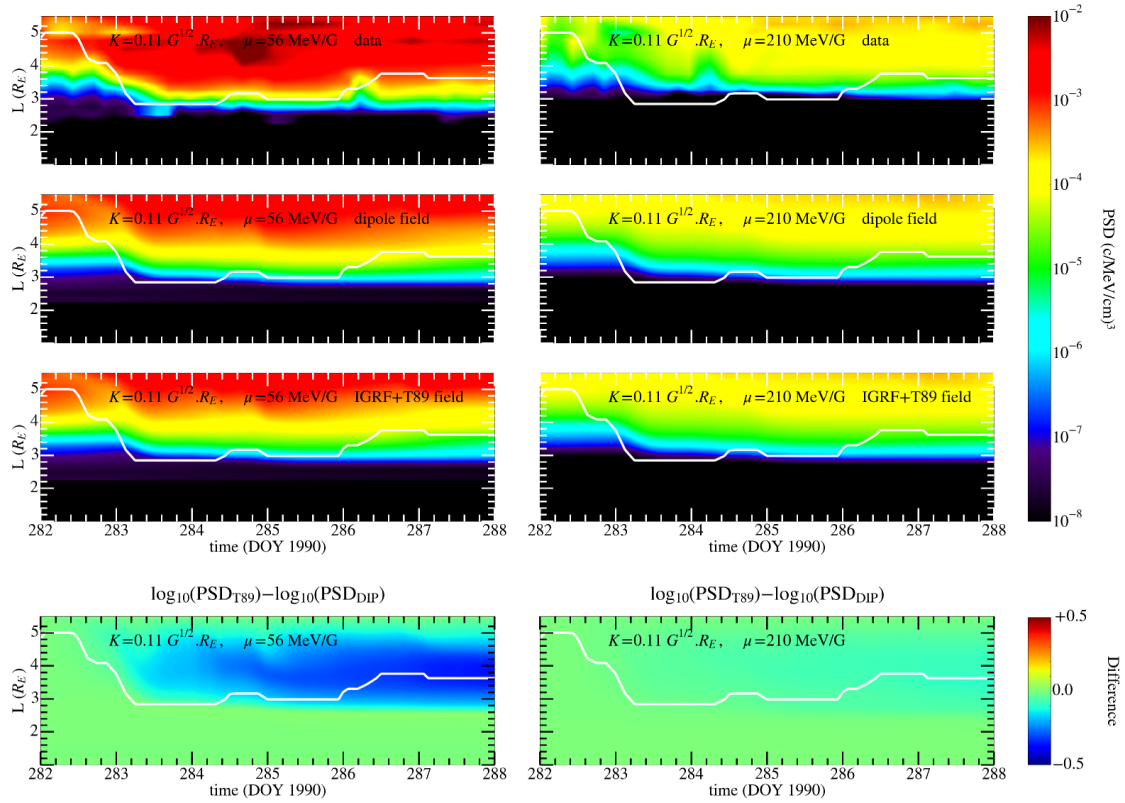

Figure 6.19 – From one unique given PSD for $\mu = 56$ MeV/G (top-left) and $\mu = 210$ MeV/G (top right) that brings the boundary and initial conditions, we simulate the PSD with either a dipole field (second row, left panel for $\mu = 56$ MeV/G and second row, right panel for $\mu = 210$ MeV/G) and the IGRF model and T89 field model (third row, left panel for $\mu = 56$ MeV/G and third row, right panel for $\mu = 210$ MeV/G). The log ratio of the PSD simulated with the T89 field over the one obtained with the dipole field is shown on the last row. For $\mu = 56$ MeV/G, the ratio reaches $10^{-0.5}$, such that the PSD obtained with the T89 field is about 3 times lower than its dipolar counterpart for L between 3 and 5. The ratio approaches 1 when μ increases, making the difference between both PSD rather negligible compared with the differences up to 10^2 brought by the data pre-processing.

In order to evaluate the importance of this shift in lifetime between a dipole field and the T89 field, we have run the simulations with the two magnetic fields by using the same initial and boundary conditions in PSD. We display the resulting simulated PSD in Figure 6.19.

The threshold μ value corresponding to the same lifetime value for the dipole model and the T89 model is found to be $\mu \sim 20$ MeV/G, which is too low to be involved in the computation of 1 MeV electron flux (see Figure 4.2 for example). Thus the resulting T89-lifetime is lower than its dipole counterpart. The results of Figure 6.19 show that the

PSD computed with the T89 field are, in the worst case, approximatively 3 times lower ($10^{0.5}$) than the dipole lifetime for $\mu = 56$ MeV/G. We have checked that this ratio tends to 1 (i.e. same PSD for both dipole and T89 field) as we increase the value of μ. This is explained because even if the difference should increase between the two lifetimes (dipole and T89) as μ increases, the simulated PSD are not impacted by such high lifetime values at high μ (an electron lifetime above 100 days has no effect compared with radial diffusion). This suggests that the shift in lifetime during the numerical resolution of the Fokker-Planck equation only has a minor contribution, that can certainly be neglected compared with the effects of pre-processing described above. It does not mean that in a full 3-D code the inherent shift in pitch angle, energy and mixed diffusion coefficients can be neglected. Further computations would be required to quantify these effects and compare them with the ones occurring in data processing.

6.5.4 Post-processing and differential unidirectional fluxes

Converting the predicted PSD back to unidirectional fluxes (step 4: post-processing) leads to higher electron fluxes in a T89 field. Figure 6.20 shows the temporal evolution of the electron fluxes for $E = 1.0$ MeV, respectively the observations (top) and the predictions with the dipole field (center) and the T89 field (bottom). As emphasized, the predicted fluxes are closer to the observations when performed with the T89 field.

The electron flux shows larger enhancements from $t = 285$ when calculated with the T89 field compared with the dipole field, which is more consistent with CRRES observations. As a matter of fact, in the dipole case, these enhancements are seen as an effect of local acceleration, which cannot be modeled with the 1-D code. In the T89 case, however, these enhancements are simply considered as an artefact effect of outward radial diffusion, which can be captured by the 1-D code, resulting to a better prediction. There is still some non negligible enhancements in the data that have not been reproduced by the numerical simulations, which are probably due this time to local acceleration as highlighted by *Albert et al.* (2009). We recall that the purpose here is not to achieve the best possible reproduction (which reaches the limit of the presented 1-D code) but rather to quantify the inaccuracy of the 1-D model and to open the debate on the impact of the magnetic field geometry on the electron fluxes.

In Figure 6.21 we plot, as in the previous section, the accuracy of both simulations performed with either the dipole field or the T89 field through the calculation of the Median Absolute Error (MdAE, top-left), the Median Absolute Percentage Error (MdAPE, top-right), Median Symmetric Accuracy (MdSA, bottom-left) and Median Log Accuracy Ratio (MdLQ, bottom-right). All of them depict an obvious improvement when the realistic field is used for comparison to the dipole field. The dipole model dramatically underestimates the data (as illustrated by the MdLQ, bottom-right panel). According to the MdAPE metric (top-right panel), the simulations computed with the T89 field seem, at some specific given times, less accurate than the one taken from a dipole field, for example, for $t = 284$ DOY. We nevertheless recall that overestimations are more heavily penalized than underestimations in the MdAPE metric, so that the aforementioned lack of consistency illustrated for the T89 field by the MdAPE might not be physically significant.

If the use of a realistic field significantly enhances the performance of our simulations, the errors are still substantially higher than the predictions related to the previous quiet event, which irremediably brings us to the conclusion that other physical aspects that have been neglected might occur, such as local acceleration by wave particle interactions. For example, the MdAE almost reaches 10^5 $\#.\mathrm{cm}^{-2}.\mathrm{sr}^{-1}.\mathrm{sec}^{-1}.\mathrm{keV}^{-1}$, compared with

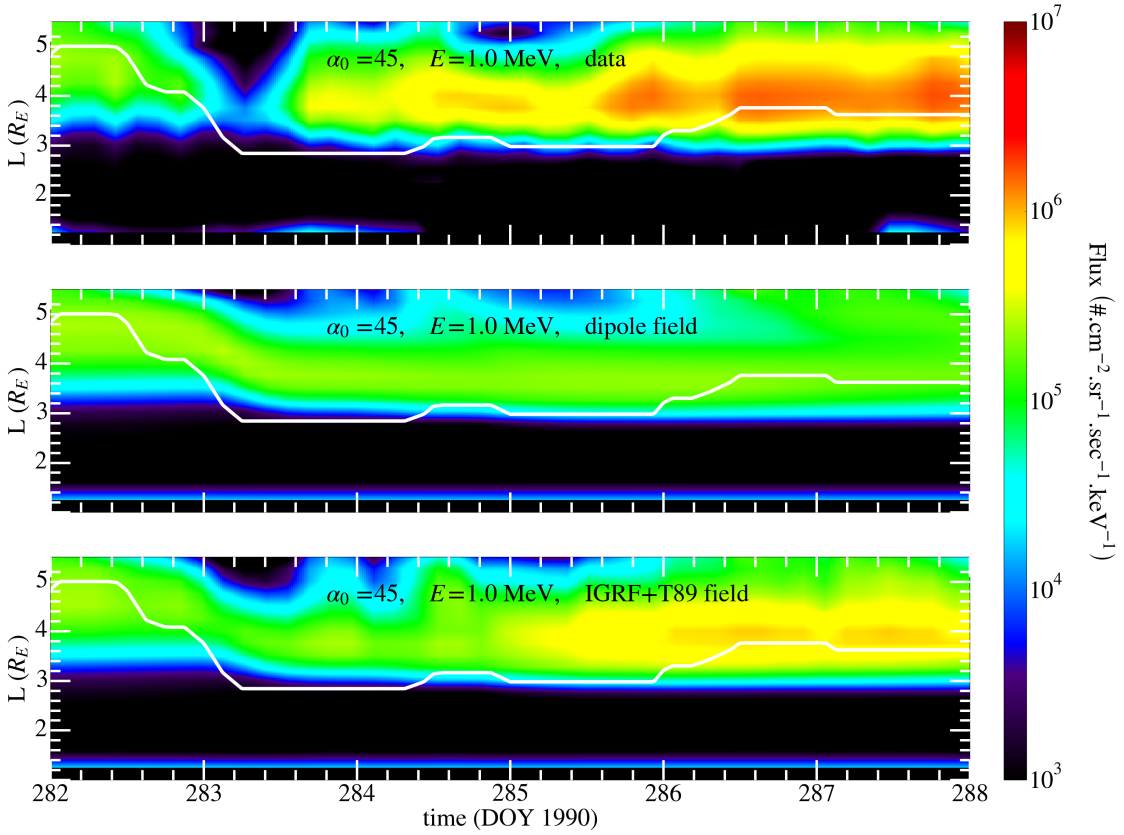

Figure 6.20 – Representation of the unidirectional electron flux at the energy of 1.0 MeV and a given equatorial pitch angle of 45 degrees. The top panel describes the evolution of the fluxes data recorded by CRRES, after interpolation and extrapolation on a Cartesian grid in (time, L-shell). The second row indicates the simulated flux obtained with the use of the dipole field model, and the last row illustrates the predicted electron fluxes coming from the implementation, for the 1990 October storm, of the combined IGRF and T89 magnetic field models. The use of the T89 magnetic field brings a clear improvement.

the value of 10^4 in the quiet case. The MdAPE can also exhibits values up to 30% (constrained only to 20% for the quiet event), as well as the MdSA that is equal to 200% in the worst cases (100% in the previous study). The MdLQ metric is able to reach the value of 0.5 (in absolute value) at the difference of the previous scenario for which the MdLQ (in absolute value) was always lower than 0.2.

6.5.5 Simulations of differential omnidirectional fluxes

In the same perspective of the previous section, we compute the omnidirectional electron fluxes for $E = 0.5$, 1.0 and 1.5 MeV, as depicted in Figures 6.28, 6.29 and 6.30 respectively. The first row of each figure displays the observations taken from the MEA instrument on board CRRES. The second row shows the simulations computed with a dipole field and the last row exhibits the simulations obtained with the combination of the IGRF model and T89 field model.

The presented omnidirectional fluxes derived from CRRES data (first row of Figures 6.28, 6.29 and 6.30) clearly emphasize the massive electron dropout that occurs at $t = 283$

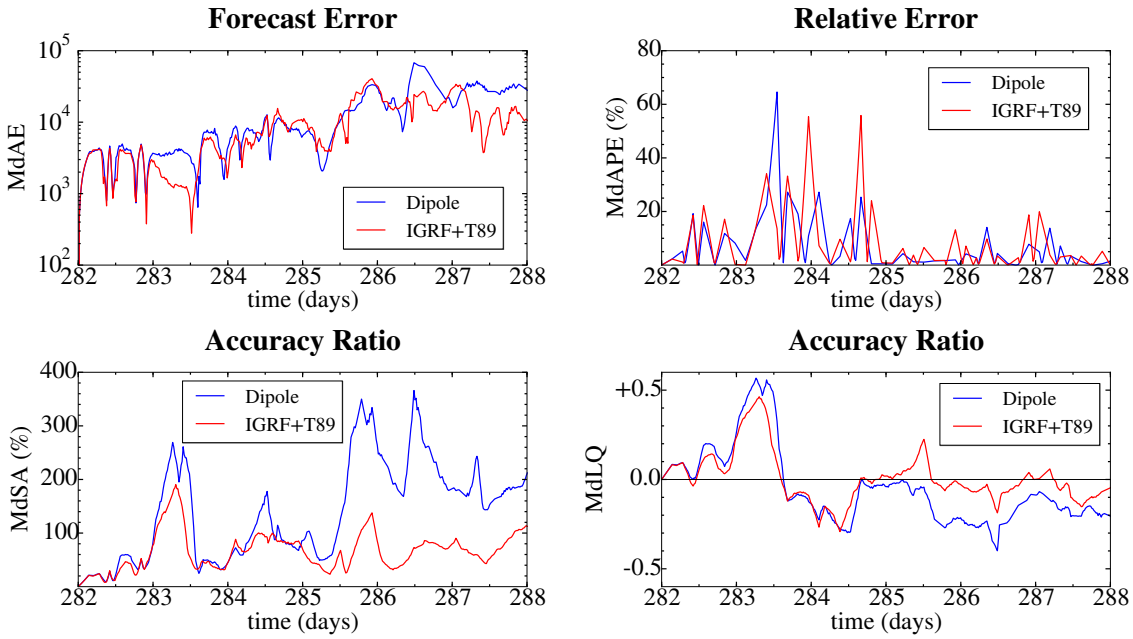

Figure 6.21 – Evolution of the Median Absolute Error (MdAE, top-left), the Median Absolute Percentage Error (MdAPE, top-right), Median Symmetric Accuracy (MdSA, bottom-left) and Median Log Accuracy Ratio (MdLQ, bottom-right) versus time for an unidirectional electron flux at $E = 1.0$ MeV and $\alpha = 45$ degrees (see also Figure 6.20).

illustrated by a decrease of more than one order of magnitude in the omnidirectional electron fluxes. Similarly, the gradual strong enhancement is clearly indicated from $t = 284$, especially for $E = 1.0$ MeV and 1.5 MeV. Focusing on the 1.0 MeV omnidirectional fluxes (Figure 6.29), the simulations computed with a dipole field (second row) hardly manage to reproduced the dramatic dropout of $t = 283$. During the following times, the electron enhancement is also rather weak compared with the data. The numerical code cannot reproduce such enhancements that would be (most of the time wrongly) assimilated to an effect of local acceleration. The simulations related to the T89 field (third row) have a better agreement compared with the data. If the strength of the electron massive dropout is still underestimated, the model is able to reproduce more accurately the gradual enhancement from $t = 284$. In the view of the T89 field, this flux increase is solved by the model as an effect of radial diffusion rather than local acceleration, leading to the wrong interpretation of local acceleration (itself opening therefore the way to the use of local acceleration models to correct the model deficiency and reach better agreement between simulations and observations). The differences between the dipole and the T89 simulations can reach more than 2 orders of magnitude at $t = 288$, which is considerable.

As before, we present in Figure 6.22 the statistical indices related to the omnidirectional fluxes at $E = 1.0$ MeV. They show a better data reproduction when the realistic field is considered. The MdLQ metric (bottom-left) particularly emphasizes the data underestimation inherent to the dipole field simulations. Except for the MdAE index, all the other statistical indices (MdAPE, MDSA and MdLQ) presented in Figure 6.22 confirm the necessity of considering a realistic magnetic field in reproducing the observations.

Table 6.2 provides the global indices over the full period for both simulations (dipole and T89 magnetic field). The metrics are related to the omnidirectional fluxes and are

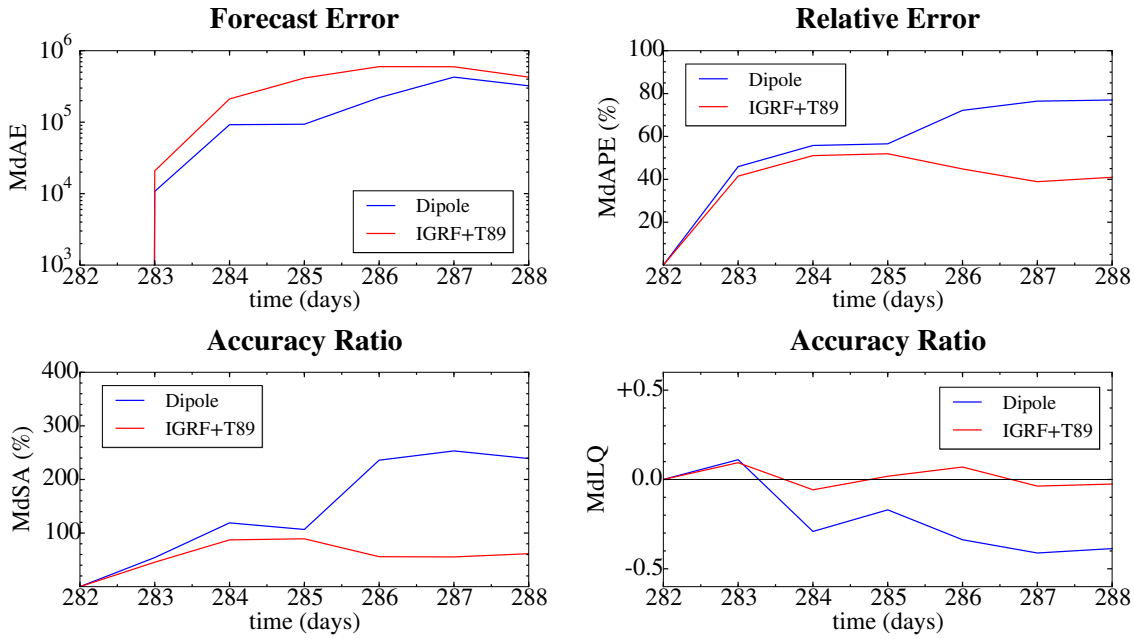

Figure 6.22 – Evolution of the Median Absolute Error (MdAE, top-left), the Median Absolute Percentage Error (MdAPE, top-right), Median Symmetric Accuracy (MdSA, bottom-left) and Median Log Accuracy Ratio (MdLQ, bottom-right) versus time for an omnidirectional electron flux at $E = 1.0$ MeV (see also Figure 6.29).

calculated over the energies $E = 0.2$, 0.5, 1.0, 1.5, 2.0 and 4.0 MeV, for $1.6 < L^* < 5.5$, consistently with Chapter 5. It highlights a (slightly) better prediction with the use of the T89 magnetic field.

Table 6.2 – Global Median Absolute Error (MdAE), Median Absolute Percentage Error (MdAPE), Median Log Accuracy Ratio (MdLQ) and Median Symmetric Accuracy (MdSA) for the 1-D reduced Fokker-Planck simulations including the dipole magnetic field and the T89 magnetic field. The indicated indices correspond to the omnidirectional electron fluxes and have been calculated over all available L-shells, energies and times.

	1-D simulations, dipole field	1-D simulations, IGRF+T89 field
MdAE	8.1×10^4	1.4×10^5
MdAPE	71%	60%
MdSA	195%	98%

The simulations performed with the T89 field model are substantially closer to the CRRES data than the one obtained with the dipole field. The T89 error metrics are similar to the one obtained with the 1-D reduced Fokker-Planck code in Chapter 5 with the data-driven lifetime related to the storm-recovery of March 2013 (see Table 5.4, left column, showing that MdAPE = 67% and MdSA = 100%). The metrics related to the dipole field (MdAPE = 71% and MdSA = 195% in Table 6.2) emphasize a relatively poor data reproduction in view of the results obtained in Chapter 5 and Table 6.1. All of this confirm the significant improvement brought by the use of a realistic field model during active geomagnetic events.

6.5.6 Simulations of integral omnidirectional fluxes

Figure 6.31 represents the integral omnidirectional fluxes on the magnetic field lines. Again, the first row displays the observations taken from the MEA instrument on board CRRES. The second row shows the simulations computed with a dipole field, and the last row exhibits the simulations obtained with the combination of the IGRF model and T89 magnetic field model.

The CRRES integral flux data emphasize no more electron dropout at $t = 283$, which is unexpected. The electron dropout, which is believed to be due to magnetopause shadowing combined with outward radial diffusion (*Shprits et al.*, 2006), is indeed significant at energies higher than 0.5 MeV, but less pronounced at lower energies and absent at very low energies such as $E \sim 200$ keV. *Turner et al.* (2012) inferred that at those low energies, the electron losses due to magnetopause shadowing are balanced by substorm injections and enhanced convection from a source in the plasma sheet. Only the strong electron enhancement is preserved under the lens of integral electron flux from $t = 284$. On the other side, both simulations slightly put forward the electron dropout at $t = 283$. The gradual enhancement during the following time is, as expected, substantially underestimated by the dipole simulations, but also underestimated by the T89 simulations. We believe it is still due to additional effects of local acceleration that are neglected by the reduced Fokker-Planck code (*Albert et al.*, 2009).

It is also important to mention that the accuracy of the computation of the integral fluxes is questionable in view of the few number of available energies and pitch angles for the measured electron fluxes (17 energies and 17 pitch angles). The integration relies on several interpolations ($\log_{10}$-based) made on pitch angles and energies (cf. Chapter 5), which makes it certainly very sensitive to the numerical interpolation method by itself.

Finally, Figure 6.23 shows the four statistical metrics computed with the integral fluxes: MdAE (top-left), MdAPE (top-right), MdSA (bottom-left) and MdLQ (bottom-right).

The statistics confirm the accuracy of the T89 field model compared with the dipole field model in all of the four cases. However, the use of the T89 field does not remove all the difficulties encountered by the dipole field. We realize that the error made on such an active event are significantly higher than the ones made on the previous studies of the quiet period. For example the MdAE was mostly below 10^7 in the quiet case, whereas it reaches a constant value of 3×10^7 in the present case. Similarly, the MdAPE was mostly lower than 60% in the quiet case, the latter value is constantly reached for the October 1990 active event. The MdSA for the T89 field is around 150% in this study, while the same metric exhibited values below 100% in the previous case. The most striking difference between the two studies is emphasized by the MdLQ metrics, which displays a systematic data underestimation, even with the T89 field.

If the results related to the September 1990 event demonstrated our ability to accurately reproduce the electron fluxes during quiet geomagnetic periods, the present study is more circumspect since the best obtained results (that correspond to the use of the T89 field) are less accurate than the one presented with the use of a dipole field during the quiet period. There is obviously still room from improvements. The T89 magnetic field model is still a rather crude model among more advanced and accurate magnetic field topologies that are specifically dedicated to account for geomagnetic storms. The use a different magnetic field will therefore change the results accordingly. For future prospects, the first challenge would be to carry the same study with a more realistic magnetic field (the TS04 model for example (*Tsyganenko and Sitnov*, 2005)) and see if some more possible unphysical acceleration effects can be removed. If so, 1-D simula-

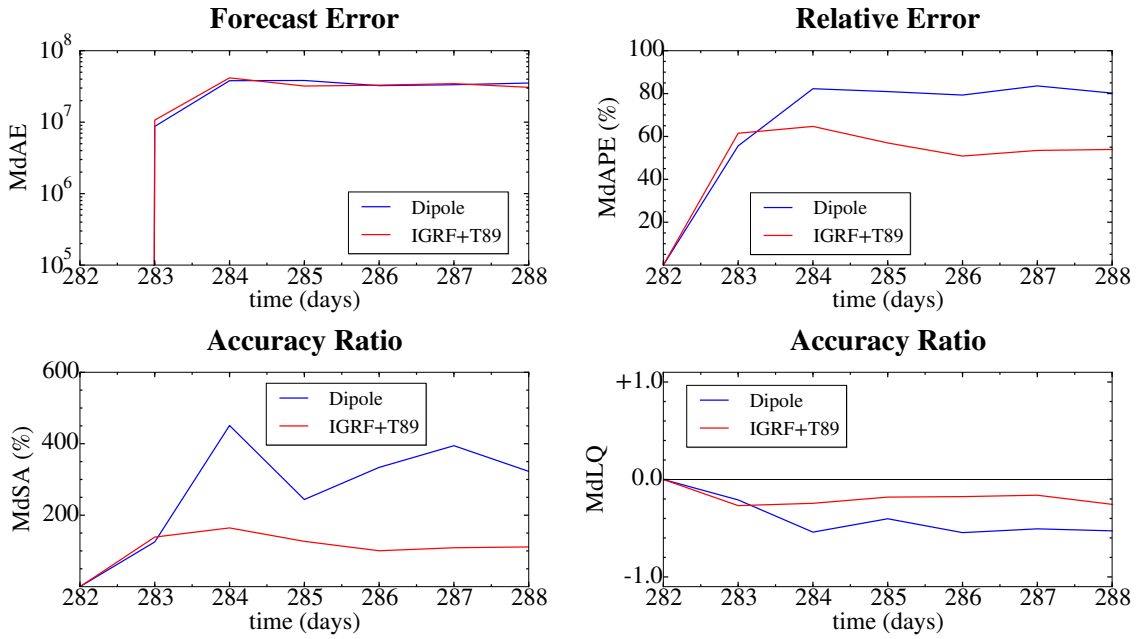

Figure 6.23 – Evolution of the Median Absolute Error (MdAE, top-left), the Median Absolute Percentage Error (MdAPE, top-right), Median Symmetric Accuracy (MdSA, bottom-left) and Median Log Accuracy Ratio (MdLQ, bottom-right) versus time for the integral electron flux for the 1990 October storm (see also Figure 6.31).

tions could still be relevant for reproducing active events. One other next option would be to compute the same event with a full 3-D code, as done by (*Albert et al.*, 2009), with the additional complete implementation of non dipolar transformations (present in the Jacobian terms for example) combined with the inclusion of potential non dipolar diffusion coefficients within the resolution of the Fokker-Planck equation, which is a great challenge that has yet to be achieved.

6.6 Discussion

This chapter intends to discuss the influence of the magnetic field model in the computation of electron fluxes. In order to reproduce the dynamics of electron fluxes within the radiation belts, there is always a need to relate the physical space (E, α_0, L^*) appropriate for observations with the adiabatic space (μ, K, L^*) suitable for theoretical purposes. The impact of the magnetic field geometry mostly manifests into the transformation between the two aforementioned coordinate systems. The transformation is invoked either during the steps of pre-processing the data and post-processing the results or during the step dedicated to the numerical resolution of the Fokker Planck equation. To our knowledge, most of the theoretical studies that have been done so far only considered a realistic magnetic field model through the two pre- and post-processing steps and rather used a dipole field during the computation step itself for reasons of simplicity.

In the present chapter, we evaluate the impacts inherent to a realistic field by including a combination of the IGRF model and T89 field model into each steps of the simulation process (including the computational step) and by comparing the results with those obtained with a dipole field. After describing the numerical implementation in a

general framework, we test the new model on two different specific events that have been recorded by CRRES during year 1990. The first chosen event goes from September 24 to October 2, 1990. It is a typically quiet period whose results serve as checking the good implementation as well as confirming our ability to accurately reproduce such rather steady event. The second chosen event goes from October 9 to October 15, 1990. This period follows a geomagnetic storm and exhibits a remarkable geomagnetic activity. It also has the advantage of being widely studied over the past 20 years (*Brautigam and Albert*, 2000; *Albert et al.*, 2009), which enables us to compare our results with their conclusions and evaluate the increasing level of maturity of the model over 20 years.

We show that if the effects inherent to the non symmetry of the magnetic field are minor through the simulation of quiet geomagnetic events, they may lead to dramatic differences compared with a dipole field. More specifically, the strong enhancements of electron fluxes observed by CRRES are interpreted as local acceleration when the dipole field is used (*Selesnick and Blake*, 2000; *Green and Kivelson*, 2004). With a realistic field however, most of these local PSD peaks vanish, attesting for their artificial numerical origin rather than being a physical source. With such corrected data sets, most of the acceleration processes can be described by radial transport and are thus better reproduced by the simulations. The simulations obtained with a dipole field lead to an error of about 200%, whereas the use of the T89 field model brings an error slightly less than 100%, which indicates that the accuracy has been improved by a factor of 2. The accuracy obtained with the T89 field model is also comparable with the accuracy emphasized in Chapter 5 related to the reproduction of a storm-recovery with the use of a data-driven lifetime.

One remaining issue this chapter does not address is related to the origin of high energy electrons at the outer boundary $L^* = 5.5$, which is still an open question. The electrons might come from substorm-related injections from the magnetotail or from higher L-shells electrons that have been transported inward and got energized via betatron acceleration (radial diffusion). They could have also been locally accelerated from wave-particle interaction at $L^* \sim 5.5$, before being transported inward to lower L-shells. Because of the lack of CRRES data above $L^* = 5.5$, it is difficult to discriminate one process from the other, the two being potentially occurring at the same time. For example *Schiller et al.* (2014) and *Boyd et al.* (2018) used the correlation of data provided by the Van Allen Probes and the Time History of Events and Macroscale Interactions during Substorms (THEMIS) satellite to build PSD profiles over a larger range of L-shells (up to $L^* = 7.5$). They both showed evidence of electrons being locally accelerated in the vicinity of the Van Allen Probes apogee (around $L^* = 5.5$) and transported inward to lower L-shells.

For future prospects, the same study can be pushed further with the use of a more recent magnetic field, such as the TS04 model (*Tsyganenko and Sitnov*, 2005) for example. Such work will be the topic of a future publication (*Loridan et al.*, 2018, in preparation). It could also be very instructive to simulate other strong geomagnetic storms with the described approach. It would enable to further understand how the use of a more realistic field model (T89 or TS04 for example) affects the data reproduction and to see if the same specific effects (removal of artificial PSD peaks, if any) can also be identified for other geomagnetic storms. The 17 March 2015 storm would be a good candidate for such investigations. Known to be one of the strongest event of the last decades, it has been well recorded by the Van Allen Probes (*Baker et al.*, 2016) and by the European PROBA-V satellite (*Pierrard and Lopez Rosson*, 2016) and has already been the topic of numerical simulations (*Li et al.*, 2016b).

We also state that the intrinsic use of a realistic magnetic field during the process of numerically solving the Fokker-Planck equation has only a minor effect compared with the impact of the extrinsic field used in the processing steps. However, we should re-evaluate this step by implementing diffusion coefficients that are consistent with the magnetic field, i.e. diffusion coefficients that have been initially calculated with the use of the same intrinsic non-dipole field, but, this step remains rare (*Orlova and Shprits*, 2010; *Ni et al.*, 2011; *Orlova et al.*, 2012) and not yet mature. Furthermore, in the perspective of solving the full Fokker-Planck equation, the latter should be written with the use of realistic Jacobian to account for the transformation between the (μ, K, L^*) adiabatic space and the (E, α_0, L^*) physical space, which requires much more work and a considerable amount of computational resources.

In this chapter, we only investigated the effects of the magnetic field geometry through the transformation between (μ, K, L^*) and (E, α_0, L^*). A realistic configuration of the magnetic field also produces other physical effects that can materialize in supplementary terms in the Fokker-Planck equation. For example, the asymmetry of the magnetic field can cause anomalous diffusion at large L-shell when combined with pitch angle diffusion due to wave-particle interactions (also known as anomalous radial diffusion (*O'Brien*, 2014, 2015; *Zheng et al.*, 2016)). The asymmetry of the magnetic field, combined with pitch angle scattering due to Coulomb collisions in the upper atmosphere, also produces neoclassical radial diffusion at very low L-shells (*Roederer et al.*, 1973; *Cunningham et al.*, 2018). We pursue our study of the effect of the magnetic field in the next final chapter through the study of neoclassical diffusion that originates from the non-symmetric nature of the magnetic field.

Figure 6.24 – Snapshots of the omnidirectional flux at $E = 0.5$ MeV from DOY=267 to DOY=275. The first row represents the omnidirectional electron flux data observed by the MEA instrument on board CRRES. The second row displays the predicted omnidirectional fluxes implemented with a dipole field, and the last row displays the predicted omnidirectional fluxes implemented with the combination of the IGRF model and the T89 field model. Note that the omnidirectional fluxes have been mapped onto dipole field lines to compare more easily the flux intensity between the different models at a given L^* (which does not correspond to the same geographic locations between the dipole field and the T89 field).

Figure 6.25 – Snapshots of the omnidirectional flux at $E = 1.0$ MeV from DOY=267 to DOY=275. The first row represents the omnidirectional electron flux data observed by the MEA instrument on board CRRES. The second row displays the predicted omnidirectional fluxes implemented with a dipole field, and the last row displays the predicted omnidirectional fluxes implemented with the combination of the IGRF model and the T89 field model. Note that the omnidirectional fluxes have been mapped onto dipole field lines to compare more easily the flux intensity between the different models at a given L^* (which does not correspond to the same geographic locations between the dipole field and the T89 field).

Figure 6.26 – Snapshots of the omnidirectional flux at $E = 1.5$ MeV from DOY=267 to DOY=275. The first row represents the omnidirectional electron flux data observed by the MEA instrument on board CRRES. The second row displays the predicted omnidirectional fluxes implemented with a dipole field, and the last row displays the predicted omnidirectional fluxes implemented with the combination of the IGRF model and the T89 field model. Note that the omnidirectional fluxes have been mapped onto dipole field lines to compare more easily the flux intensity between the different models at a given L^* (which does not correspond to the same geographic locations between the dipole field and the T89 field).

Figure 6.27 – Snapshots of the integral flux from DOY=267 to DOY=275. The first row represents the integral electron flux data observed by the MEA instrument on board CRRES. The second row displays the predicted integral fluxes implemented with a dipole field, and the last row displays the predicted integral fluxes implemented with the combination of the IGRF model and the T89 field model. Note that the integral fluxes have been mapped onto dipole field lines to compare more easily the flux intensity between the different models at a given L^* (which does not correspond to the same geographic locations between the dipole field and the T89 field).

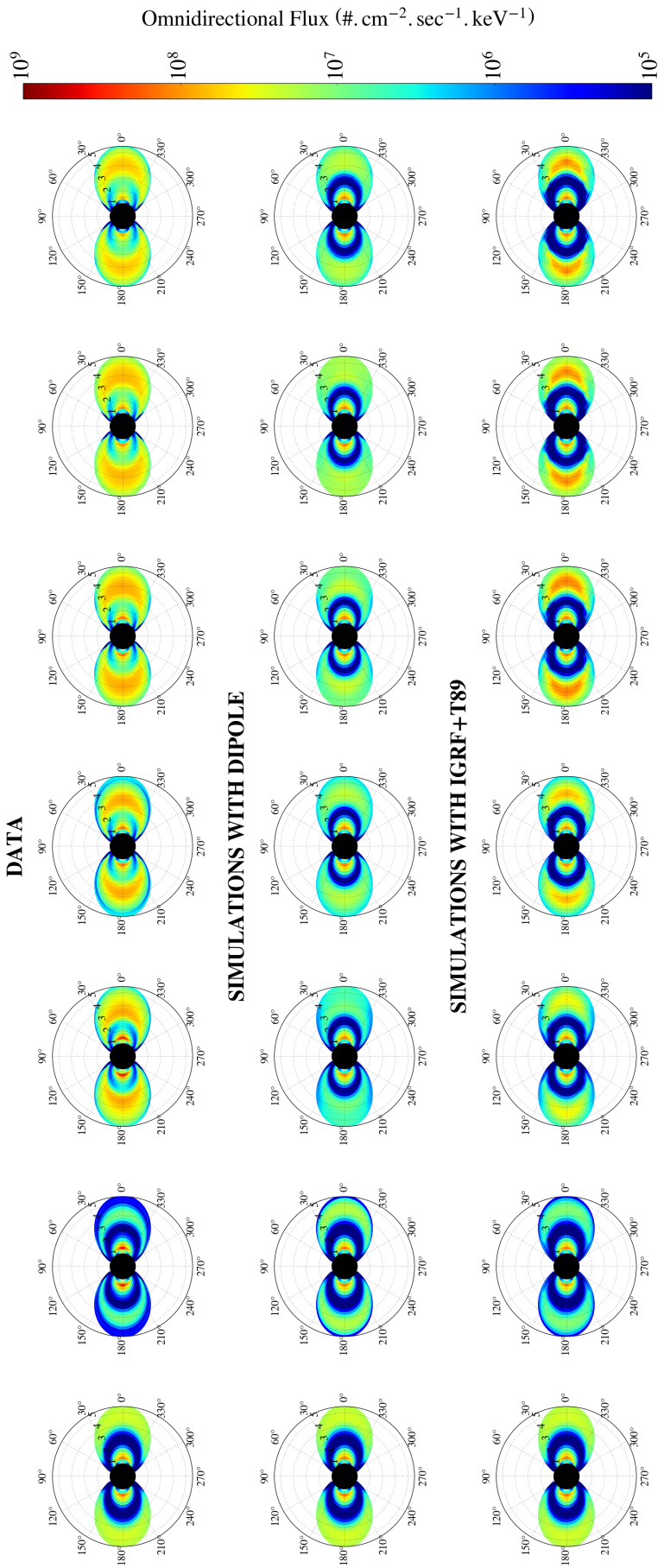

Figure 6.28 – Snapshots of the omnidirectional flux at $E = 0.5$ MeV from DOY=282 to DOY=288. The first row represents the omnidirectional electron flux data observed by the MEA instrument on board CRRES. The second row displays the predicted omnidirectional fluxes implemented with a dipole field, and the last row displays the predicted omnidirectional fluxes implemented with the combination of the IGRF model and the T89 field model. Note that the omnidirectional fluxes have been mapped onto dipole field lines to compare more easily the flux intensity between the different models at a given L^* (which does not correspond to the same geographic locations between the dipole field and the T89 field).

Figure 6.29 – Snapshots of the omnidirectional flux at $E = 1.0$ MeV from DOY=282 to DOY=288. The first row represents the omnidirectional electron flux data observed by the MEA instrument on board CRRES. The second row displays the predicted omnidirectional fluxes implemented with a dipole field, and the last row displays the predicted omnidirectional fluxes implemented with the combination of the IGRF model and the T89 field model. Note that the omnidirectional fluxes have been mapped onto dipole field lines to compare more easily the flux intensity between the different models at a given L^* (which does not correspond to the same geographic locations between the dipole field and the T89 field).

Figure 6.30 – Snapshots of the omnidirectional flux at $E = 1.5$ MeV from DOY=282 to DOY=288. The first row represents the omnidirectional electron flux data observed by the MEA instrument on board CRRES. The second row displays the predicted omnidirectional fluxes implemented with a dipole field, and the last row displays the predicted omnidirectional fluxes implemented with the combination of the IGRF model and the T89 field model. Note that the omnidirectional fluxes have been mapped onto dipole field lines to compare more easily the flux intensity between the different models at a given L^* (which does not correspond to the same geographic locations between the dipole field and the T89 field).

Figure 6.31 – Snapshots of the integral flux from DOY=282 to DOY=288. The first row represents the integral electron flux data observed by the MEA instrument on board CRRES. The second row displays the predicted integral fluxes implemented with a dipole field, and the last row displays the predicted integral fluxes implemented with the combination of the IGRF model and the T89 field model. Note that the integral fluxes have been mapped onto dipole field lines to compare more easily the flux intensity between the different models at a given L^* (which does not correspond to the same geographic locations between the dipole field and the T89 field).

Chapter 7

Computation of neoclassical radial diffusion coefficients

The Earth's magnetic field is constantly affected either by secular variations that originate from the Earth's interior (over timescales of several years) or by solar activity that shapes the field lines at large L-shells (on shorter timescales of about a few days). Such perturbations manifest in asymmetries that develop into the magnetic field topology. Chapter 6 brought an insight of the impact of those asymmetries on the outer radiation belt. We have particularly seen how these perturbations can affect the way of conciliating theory and observations. Relating spacecraft data to the (μ, K, L^*) adiabatic world is very sensitive to the magnetic field model used in the computations. If the latter is too rough, severe inaccuracies in the calculations of the electron phase space density are reported (see Chapter 6 and (*Selesnick and Blake*, 2000; *Green and Kivelson*, 2004)). These aforementioned discrepancies are the result of a purely mathematical transformation between the two different coordinate systems (μ, K, L^*) and (E, α_0, L^*) themselves the results of misunderstanding and misrepresenting the magnetic field.

This impact is, however, only a glimpse of the importance of considering realistic magnetic fields compared with the dipole paradigm. Going now deeper into the physics of the radiation belts, the present chapter aims at emphasizing the emergence of hidden diffusive processes due to the natural irregularity of the Earth's magnetic field. As we will see, the asymmetry of non dipole fields can also bring into its wake supplementary diffusion terms in the Fokker-Planck equation. The latter ones can more specifically take the form of an extra radial diffusion coefficient, which is commonly the resultant of two different physical effects. The first effect is inherent to the asymmetries of the Earth's magnetic field and makes particles of different equatorial pitch angles populate different drift shells. This is the so-called drift-shell splitting effect. The second phenomenon is pitch angle diffusion of electrons. Such diffusion occurs when the particles are subjected to gyro-resonant interactions with the small amplitude electromagnetic waves that commonly propagate within the magnetosphere. Pitch angle diffusion can also be induced at very low L-shells ($L < 1.5$) by Coulomb collisions of electrons with the molecules of the Earth's upper atmosphere. Combined together, scattering of electrons (pitch angle diffusion) makes their pitch angle decrease and thus makes the electrons drift along different drift shells (drift-shell splitting), which in turn makes them diffuse radially.

When the pitch angle diffusion process is due to wave particle interactions (large L-shells), such additional radial diffusion is referred as anomalous radial diffusion (e.g., *O'Brien*, 2014, 2015). If, on the other side, the origin of pitch angle diffusion is attributed to atmospheric Coulomb collisions of electrons with heavier molecules constituting the upper atmosphere (low L-shells), we speak of neoclassical radial diffusion (*Cunningham et al.*, 2018), in reference to the physics of laboratory plasma tokamaks (e.g., *Balescu*, 1988). In this chapter, which is exclusively focused on neoclassical diffusion, we estimate the neoclassical radial diffusion coefficient by coupling both processes of drift-shell splitting and Coulomb collisions. We show that the radial diffusion term that arises from the numerical calculations decreases with increasing L-shells, in agreement with empirical studies made in the late 1960's. The obtained quantitative result therefore supports the importance of neoclassical diffusion and its influence on the dynamics of the inner belt at very low L-shells.

The work detailed in the present chapter has been initiated during a project made under the mentorship of G. Cunningham at the Los Alamos Space Weather Summer School in 2016. The previously obtained results are the topic of this chapter and can also be found in the summer school report (*Loridan et al.*, 2016). We here more specifically contextualize the aforementioned study and take the opportunity to improve it with updated figures.

This work also served as a steppingstone for the study led by G. Cunninghamn, which materialized a year later in a publication dedicated to computing neoclassical diffusion and its effects on trapped electrons over three years (*Cunningham et al.*, 2018). This article explicitly used both drift-averaged pitch angle diffusion coefficient accounting for Coulomb collision and the derived associated neoclassical radial diffusion coefficient into a 2-D Fokker-Planck equation in (α_0, L^*). The latter code, coupled with a 1-D advection equation in momentum p that models energy loss due to inelastic collisions, enabled to reproduce with acceptable accuracy the observations made in 1964 (see (*Cunningham et al.*, 2018) for more details). These further simulations, which have been performed by G. Cunningham after the summer school, are out of the scope of the PhD thesis and are therefore not detailed in the present chapter, which is limited to the derivation and first estimations of the neoclassical radial diffusion coefficients.

7.1 Introduction

7.1.1 Historical observations

Newkirk and Walt (1968), and, then, *Farley* (1969), studied the electron flux in the upper atmosphere following the Starfish nuclear detonation in 1962. As pointed out by *Imhof et al.* (1967), they realized that the decay rate of the low L-shell electrons was surprisingly much slower than what was predicted by the atmospheric scattering theory of *Walt and MacDonald* (1964). This discrepancy between theory and observations was attributed to additional radial diffusion from an unknown process. Based on these observations, they empirically derived the expression for the radial diffusion coefficient in the narrow region $L < 1.5$, for a constant first adiabatic invariant and for equatorially mirroring particles (i.e. for $K = 0.0$ $\mathrm{G}^{1/2}R_E$). These studies both showed a surprising radial diffusion coefficient that strongly decreases with increasing L, as shown in Figure 7.1.

This sharp behavior at radial distances below 1.3 Earth radius differs strongly from the radial diffusion coefficients calculated a few years earlier by *Fälthammar* (1965). His theoretical radial diffusion coefficient indeed reversely increases as a power law with respect to L-shell. This so-called conventional radial diffusion coefficient, which has been derived under the framework of drift-resonant interactions between electrons and ultra low-frequency (ULF) electromagnetic waves at constant first and second adiabatic invariants (μ, K), has later been extended by *Schulz and Lanzerotti* (1974) and updated with the use of wave measurements by *Brautigam and Albert* (2000) and *Ozeke et al.* (2014). All of the aforementioned work confirmed the typical trend of the radial diffusion coefficient with an increase in L^6 or L^{10} and were thus unable to explain the observations made in the 1960's. If the observations have been a first clue that suggests the existence of neoclassical diffusion, *Selesnick* (2012) also pointed out that the radial diffusion coefficient needed to explain the observed decay rates of electrons in the atmosphere during year 2009 should be 10 times larger than the one inferred from drift resonance interactions with ULF waves.

7.1.2 Physical interpretation

A physical explanation of extra radial diffusion due to the combined effect of pitch angle diffusion and drift-shell splitting of electron has first been theoretically formalized by *Roederer et al.* (1973) as an attempt to understand some of the surprising observations made during the 1960's by *Newkirk and Walt* (1968) and *Farley* (1969) of high density

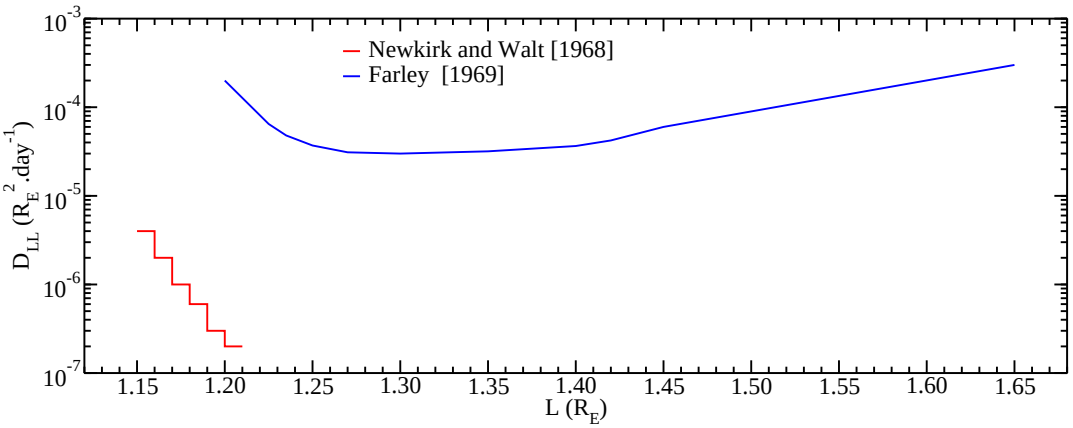

Figure 7.1 – Evolution of the radial diffusion coefficient versus L-shell, taken from *Newkirk and Walt* (1968) (red) and *Farley* (1969) (blue), for $K \sim 0.0$ G$^{1/2}R_E$. The electron energy studied by *Newkirk and Walt* (1968) is above 1.6 MeV, while *Farley* (1969) focused on electrons having an energy of 1 MeV at $L^* = 1.65$. We also notice that the values of the radial diffusion coefficient taken from *Farley* (1969) are two orders of magnitude above the values obtained by *Newkirk and Walt* (1968). As mentioned by *Walt* (1971), this discrepancy is due to the fact that *Farley* (1969) took only into account the losses due to atmosphere collision, which makes his values an upper limit for the radial diffusion coefficient. As mentioned below, the decreasing trend of such inferred radial diffusion coefficients with increasing L-shell contradicts the more recent radial diffusion coefficients inferred from ULF waves activity that increase with increasing L-shells (*Brautigam and Albert*, 2000; *Ozeke et al.*, 2014).

electrons in the upper atmosphere. If *Roederer et al.* (1973) roughly estimated a typical radial diffusion coefficient of 10^{-7} day^{-1} consistent with the observations of *Newkirk and Walt* (1968), the early paper of *Roederer et al.* (1973) was intended to be complemented by a supplementary study including a comprehensive model of the pitch angle diffusion coefficient for atmospheric scattering. However, no such subsequent article has ever been published.

The combination of drift-shell splitting and pitch angle scattering can more generally disrupt our physical understanding of the radiation belts at wider scales, specifically at higher L-shells for which pitch angle diffusion is inferred from wave-particle interaction. More recently, *O'Brien* (2014) numerically calculated the anomalous diffusion coefficients in the (K, L^*) space, including cross-terms, arising from pitch angle scattering by whistler mode chorus waves combined with drift-shell splitting near geostationary orbit. He particularly draws attention to the fact that the new inferred anomalous coefficients could be as important as their conventional counterparts. In the following, *O'Brien* (2015) generalized his previous work in the (μ, K, L^*) space and mathematically formalized the emergence of the anomalous diffusion coefficients emanating from both pitch angle and energy diffusion. *Zheng et al.* (2016) also evaluated the influence of such anomalous diffusion coefficients on 3-D Fokker-Planck simulations of PSD, highlighting on a relatively significant impact of the cross diffusion coefficients.

7.2 Theoretical formulation

7.2.1 Adiabatic space and drift-averaging

7.2.1.a Transformation into the adiabatic space

We consider a situation in which the only interaction that occurs is pitch angle scattering from Coulomb collisions between electrons with ions and neutrals. Because the ions and neutrals are massive compared to the electron, the interaction is nearly elastic, i.e. the energy of the electron is nearly constant. The only physical process involved is electron scattering due to Coulomb collisions. Let us consider the associated bounce-averaged pitch angle diffusion coefficient $D_{\alpha_0\alpha_0}$. In order to solve the phase space density that results from pitch angle diffusion, the aforementioned bounce-averaged pitch angle diffusion coefficient should be drift-averaged before being included in the Fokker-Planck equation (*O'Brien*, 2015). The equatorial pitch angle α_0 is not an invariant over the drift path because it carries an azimuthal dependence (except when the magnetic field is approximated by a dipole field). Hence, in preparation for drift-averaging, the (p, α_0, L^*) variables have to be converted into the corresponding (μ, K, L^*) invariant coordinates.

The equation expressing the transformation from the diffusion coefficient $D_{Y_iY_j}$ written for the (Y_1, Y_2, Y_3) variables to the diffusion coefficient $D_{X_kX_l}$ written in the new (X_1, X_2, X_3) variables is (see (2.53))

$$D_{Y_iY_j} = \sum_{k=1}^{3} \frac{\partial Y_i}{\partial X_k} \sum_{l=1}^{3} D_{X_kX_l} \frac{\partial Y_j}{\partial X_l},$$

for which, in our case, the (X_1, X_2, X_3) space refers to the (E, α_0, L^*) physical space and the (Y_1, Y_2, Y_3) space refers to the (μ, K, L^*) adiabatic space. One can also express the above equation into its tensorial form. For this purpose we introduce the $\underline{\underline{D}}(\mu, K, L^*, \varphi)$ diffusion tensor written in the (μ, K, L^*, φ) space (where φ refers to the magnetic longitude as before). With this notation, the above equation reduces to

$$\underline{\underline{D}}(\mu, K, L^*, \varphi) = \begin{pmatrix} D_{\mu\mu} & D_{\mu K} & D_{\mu L^*} \\ D_{\mu K} & D_{KK} & D_{KL^*} \\ D_{\mu L^*} & D_{LK} & D_{L^*L^*} \end{pmatrix} = \begin{pmatrix} \frac{\partial \mu}{\partial \alpha_0} \\ \frac{\partial K}{\partial \alpha_0} \\ \frac{\partial L^*}{\partial \alpha_0} \end{pmatrix} \cdot D_{\alpha_0\alpha_0} \cdot \begin{pmatrix} \frac{\partial \mu}{\partial \alpha_0} & \frac{\partial K}{\partial \alpha_0} & \frac{\partial L^*}{\partial \alpha_0} \end{pmatrix}.$$

The components of the diffusion tensor write therefore

$$\begin{cases} D_{\mu\mu} = \left(\frac{\partial \mu}{\partial \alpha_0}\right)^2 D_{\alpha_0\alpha_0} & \text{and} \quad D_{KK} = \left(\frac{\partial K}{\partial \alpha_0}\right)^2 D_{\alpha_0\alpha_0}, \\ D_{\mu K} = \left(\frac{\partial \mu}{\partial \alpha_0}\right)\left(\frac{\partial K}{\partial \alpha_0}\right) D_{\alpha_0\alpha_0} & \text{and} \quad D_{KL^*} = \left(\frac{\partial K}{\partial \alpha_0}\right)\left(\frac{\partial L^*}{\partial \alpha_0}\right) D_{\alpha_0\alpha_0}, \\ D_{\mu L^*} = \left(\frac{\partial \mu}{\partial \alpha_0}\right)\left(\frac{\partial L^*}{\partial \alpha_0}\right) D_{\alpha_0\alpha_0} & \text{and} \quad D_{L^*L^*} = \left(\frac{\partial L^*}{\partial \alpha_0}\right)^2 D_{\alpha_0\alpha_0}. \end{cases}$$

We realize that an a priori single process of pitch angle diffusion occurring at constant energy leads to diffusion in all directions of the (μ, K, L^*) invariant space.

7.2.1.b Drift-averaging

Once the components of the diffusion tensor have been obtained in the standard (K, L^*, φ) space, the drift-averaging integration, referred as the $\langle .. \rangle_d$ operator

$$\langle .. \rangle_d = \frac{1}{\tau_d} \int_{\varphi=0}^{\varphi=2\pi} \frac{1}{\omega_d} (..) \, \mathrm{d}\varphi$$

can effectively be performed (see also equation (2.32) of Chapter 2). We simply obtain

$$\begin{cases} \widetilde{D}_{\mu\mu} = \left\langle \left(\dfrac{\partial \mu}{\partial \alpha_0} \right)^2 D_{\alpha_0\alpha_0} \right\rangle_d & \text{and} \quad \widetilde{D}_{KK} = \left\langle \left(\dfrac{\partial K}{\partial \alpha_0} \right)^2 D_{\alpha_0\alpha_0} \right\rangle_d , \\ \widetilde{D}_{\mu K} = \left\langle \left(\dfrac{\partial \mu}{\partial \alpha_0} \right) \left(\dfrac{\partial K}{\partial \alpha_0} \right) D_{\alpha_0\alpha_0} \right\rangle_d & \text{and} \quad \widetilde{D}_{KL^*} = \left\langle \left(\dfrac{\partial K}{\partial \alpha_0} \right) \left(\dfrac{\partial L^*}{\partial \alpha_0} \right) D_{\alpha_0\alpha_0} \right\rangle_d , \\ \widetilde{D}_{\mu L^*} = \left\langle \left(\dfrac{\partial \mu}{\partial \alpha_0} \right) \left(\dfrac{\partial L^*}{\partial \alpha_0} \right) D_{\alpha_0\alpha_0} \right\rangle_d & \text{and} \quad \widetilde{D}_{L^*L^*} = \left\langle \left(\dfrac{\partial L^*}{\partial \alpha_0} \right)^2 D_{\alpha_0\alpha_0} \right\rangle_d , \end{cases}$$

for which the upper tilde symbol refers to the drift-averaged computed in the (μ, K, L^*) space. The above expressions are consistent with the expressions derived by *O'Brien* (2015).

The neoclassical radial diffusion coefficient $\widetilde{D}_{LL}$ appears as we have changed the system of coordinates, highlighting the impact of both processes of drift-shell splitting (emphasized by the $\partial L^*/\partial \alpha_0$ term) and pitch angle diffusion (given by the $D_{\alpha_0\alpha_0}$ bounce-averaged diffusion coefficient) (*O'Brien*, 2015).

7.2.1.c Related Fokker-Planck equation

As a comment, the Fokker-Planck equation used to solve pitch angle diffusion combined with drift-shell splitting effects writes in the (μ, K, L^*) space

$$\frac{\partial f}{\partial t} = \frac{1}{G_{XY}} \sum_{i=1}^{3} \frac{\partial}{\partial Y_i} \left[\sum_{j=1}^{3} G_{XY} \, D_{Y_i Y_j} \, \frac{\partial f}{\partial Y_j} \right] \tag{7.1}$$

with $(Y_1, Y_2, Y_3) = (\mu, K, L^*)$ and for which

$$G_{XY} = G(J_1, J_2, J_3; \mu, K, L^*) = 8\sqrt{2}\pi^2 m_0^{3/2} R_E^2 B_E \frac{\sqrt{\mu}}{L^2}$$

is the Jacobian transformation from the (J_1, J_2, J_3) adiabatic invariant to the related (μ, K, L^*) coordinates. For an axisymmetric magnetic field (such as a dipole field), L^* does not depend on the equatorial pitch angle, and so the drift-shell splitting term $\partial L^*/\partial \alpha_0$ is zero, leading to vanishing cross diffusion coefficients $D_{\mu L^*} = 0$, $D_{KL^*} = 0$ and $D_{L^*L^*} = 0$, and reducing the Fokker-Planck equation (7.1) to only 3 diffusive terms (initially 9 terms). The Fokker Planck equation (7.1) requires a lot of computational effort to be solved as it is a 3-D diffusion equation. It can be easier to relate it into the native (p, α_0, L) physical space, as we will see below.

7.2.2 Projection into the physical space

7.2.2.a Physical space and dipole field

The final step requires to go back to the original physical coordinates (α_0, L^*) to obtain the $\underline{\underline{\widehat{D}}}(\alpha_0, L)$ drift-averaged diffusion tensor. Let us mention that the α_0 variable is now considered in a dipole field rather than in a realistic field in order to remove its azimuthal dependence along the drift path. Consistently with the dipole framework, the new L^* variables now writes as the dipole L. The transformation of the diffusion tensor back into the (p, α_0, L) space reduces to

$$\underline{\underline{\widehat{D}}}(\alpha_0, L) = \begin{pmatrix} \widehat{D}_{\alpha_0\alpha_0} & \widehat{D}_{\alpha_0 L} \\ \widehat{D}_{L\alpha_0} & \widehat{D}_{LL} \end{pmatrix} = \begin{pmatrix} \frac{\partial \alpha_0}{\partial K} & \frac{\partial \alpha_0}{\partial L^*} \\ \frac{\partial L}{\partial K} & \frac{\partial L}{\partial L^*} \end{pmatrix} \cdot \begin{pmatrix} \widetilde{D}_{KK} & \widetilde{D}_{KL^*} \\ \widetilde{D}_{KL^*} & \widetilde{D}_{L^*L^*} \end{pmatrix} \cdot \begin{pmatrix} \frac{\partial \alpha_0}{\partial K} & \frac{\partial L}{\partial K} \\ \frac{\partial \alpha_0}{\partial L^*} & \frac{\partial L}{\partial L^*} \end{pmatrix}.$$

After formal calculations, and taking account that the differential terms $\partial\alpha_0/\partial L^*$ and $\partial L/\partial K$ are zeros by definition and $\partial L/\partial L^* = 1$, the new drift-averaged $\widehat{D}_{\alpha_0\alpha_0}$ pitch angle diffusion coefficient expressed in the (α_0, L^*) space writes

$$\widehat{D}_{\alpha_0\alpha_0} = \left(\frac{\partial \alpha_0}{\partial K}\right)^2 \widetilde{D}_{KK} = \left(\frac{\partial \alpha_0}{\partial K}\right)^2 \left\langle \left(\frac{\partial K}{\partial \alpha_0}\right)^2 D_{\alpha_0\alpha_0} \right\rangle_d,$$

the new drift-averaged $\widehat{D}_{\alpha_0 L}$ cross diffusion coefficient is

$$\widehat{D}_{\alpha_0 L} = \left(\frac{\partial \alpha_0}{\partial K}\right) \widetilde{D}_{KL^*} = \left(\frac{\partial \alpha_0}{\partial K}\right) \left\langle \left(\frac{\partial K}{\partial \alpha_0}\right) \left(\frac{\partial L^*}{\partial \alpha_0}\right) D_{\alpha_0\alpha_0} \right\rangle_d$$

and the so-called neoclassical (drift-averaged) $\widehat{D}_{LL}$ radial diffusion coefficient is obtained as

$$\widehat{D}_{LL} = \widetilde{D}_{L^*L^*} = \left\langle \left(\frac{\partial L^*}{\partial \alpha_0}\right)^2 D_{\alpha_0\alpha_0} \right\rangle_d. \tag{7.2}$$

Since the energy is conserved during elastic Coulomb collisions, $\widehat{D}_{pp} = 0$, $\widehat{D}_{p\alpha_0} = 0$ and $\widehat{D}_{pL} = 0$.

7.2.2.b Related Fokker-Planck equation

The new Fokker-Planck equation used to solve radial diffusion inferred from pitch angle diffusion with drift-shell splitting effects writes

$$\begin{aligned} \frac{\partial f}{\partial t} = &\frac{1}{G_2}\frac{\partial}{\partial \alpha_0}\left[G_2 \widehat{D}_{\alpha_0\alpha_0}\frac{\partial f}{\partial \alpha_0}\right] + \frac{1}{G_2}\frac{\partial}{\partial L}\left[G_2 \widehat{D}_{L^*L^*}\frac{\partial f}{\partial L}\right] \\ &+ \frac{1}{G_2}\frac{\partial}{\partial \alpha_0}\left[G_2 \widehat{D}_{\alpha_0 L}\frac{\partial f}{\partial L}\right] + \frac{1}{G_2}\frac{\partial}{\partial L}\left[G_2 \widehat{D}_{\alpha_0 L}\frac{\partial f}{\partial \alpha_0}\right] \end{aligned} \tag{7.3}$$

with

$$G_2(J_1, J_2, J_3; p, \alpha_0, L) = \frac{8\pi^2 R_E^2 B_E}{L^2}\left(\frac{p^2}{B_m^{3/2}}\left|\frac{\partial K}{\partial \alpha_0}\right|\right),$$

which can be calculated in a non dipole field, the $\partial K/\partial\alpha_0$ term being numerically quantified. Note that equation (7.3) is formally a 2-D equation, equivalent to equation (7.1).

In (*Cunningham et al.*, 2018), this 2-D Fokker-Planck equation has been coupled and solved with a 1-D energy advection equation. In the case of a dipole field, the previous Fokker-Planck equation simply reduces to

$$\frac{\partial f}{\partial t} = \frac{1}{G_2}\frac{\partial}{\partial \alpha_0}\left[G_2 \widehat{D}_{\alpha_0\alpha_0}\frac{\partial f}{\partial \alpha_0}\right]$$

with $\widehat{D}_{\alpha_0\alpha_0} = D_{\alpha_0\alpha_0}$. Non-dipole fields bring supplementary terms in the Fokker-Planck equation (one single pitch angle diffusion term that develop into 4 diffusive terms), impacting significantly the physical processes at stakes contrary to the effects investigated in Chapter 6. Quantifying properly the supplementary diffusion coefficients is thus crucial but hard to do if one does not have the capability of accounting for realistic magnetic fields (cf. Chapter 6).

7.3 Drift-shell splitting effects

We first evaluate the drift-shell splitting term $\partial L^*/\partial \alpha_0$ involved in the expression of the neoclassical radial diffusion coefficient (7.2).

7.3.1 Magnetic field

The magnetic field in use to study drift-shell splitting effects below $L^* < 1.5$ is the IGRF model presented in Chapter 2. The non symmetry of IGRF induces azimuthal variations for the equatorial pitch angle, and thus for the particle bounce path and drift frequency. This is emphasized in Figure 7.2, which illustrates the evolution of the equatorial pitch angle (top-left) and bounce path (top-right) versus geographic longitude, for $K = 0.065$, 0.080 and 0.100 $\mathrm{G}^{1/2}R_E$ at $L^* = 1.2$ R_E. Plain lines represent the calculations made with the IGRF model whereas the dot lines correspond to the dipole field. Figure 7.2 also illustrates the azimuthal evolution of the electron drift frequency ω_d (bottom) for $E = 0.27$, 0.55, 1.03 and 1.52 MeV, for $L^* = 1.2$ R_E and $K = 0.080$ $\mathrm{G}^{1/2}R_E$. These snapshots have been calculated for the date of December 8, 1964, to refer to the observations of electron fluxes made by *Newkirk and Walt* (1968).

Let us notice that the bounce path peak at longitude $\varphi = 310$ degrees (Figure 7.2, top-right) corresponds to the location of the South Atlantic Anomaly. If the differences between a dipole field and the IGRF model do not seem to be significant at first sight, they still lead to dramatic discrepancies for the computation of the bounce-averaged pitch angle diffusion coefficient, as we will see below.

7.3.2 Methodology of the numerical approach

The first step of the study is to compute accurately the drift-shell splitting term $\partial L^*/\partial \alpha_0$. In Chapter 6, we described the numerical approach of *Cunningham* (2016) to find all the closed drift shells on a target Cartesian grid (K, L^*). More exhaustively, from a given numerical invariant grid (L^*_i, K_j, φ_k), the process consisted in computing the corresponding coordinate $(r_{i,j,k}, \alpha_{0i,j,k}, \varphi_{i,j,k})$ populated by the particle. Then, any new coordinate (r, α_0, φ) can be reversely associated with a specific drift-shell using the reference set $(r_{i,j,k}, \alpha_{0i,j,k}, \varphi_{i,j,k})$ by linear interpolation.

Hence, by choosing $r = r_{i,j,k}$, $\varphi = \varphi_{i,j,k}$ (so that both the radius and longitude are kept constant during the transformation) and adding a slight increment $\delta\alpha_0$ to $\alpha_{0i,j,k}$ such that $\alpha_0 = \alpha_{0i,j,k} + \delta\alpha_0$, we are able to find the corresponding new L^* value $L^*_i + \delta L^*_{i,j,k}$,

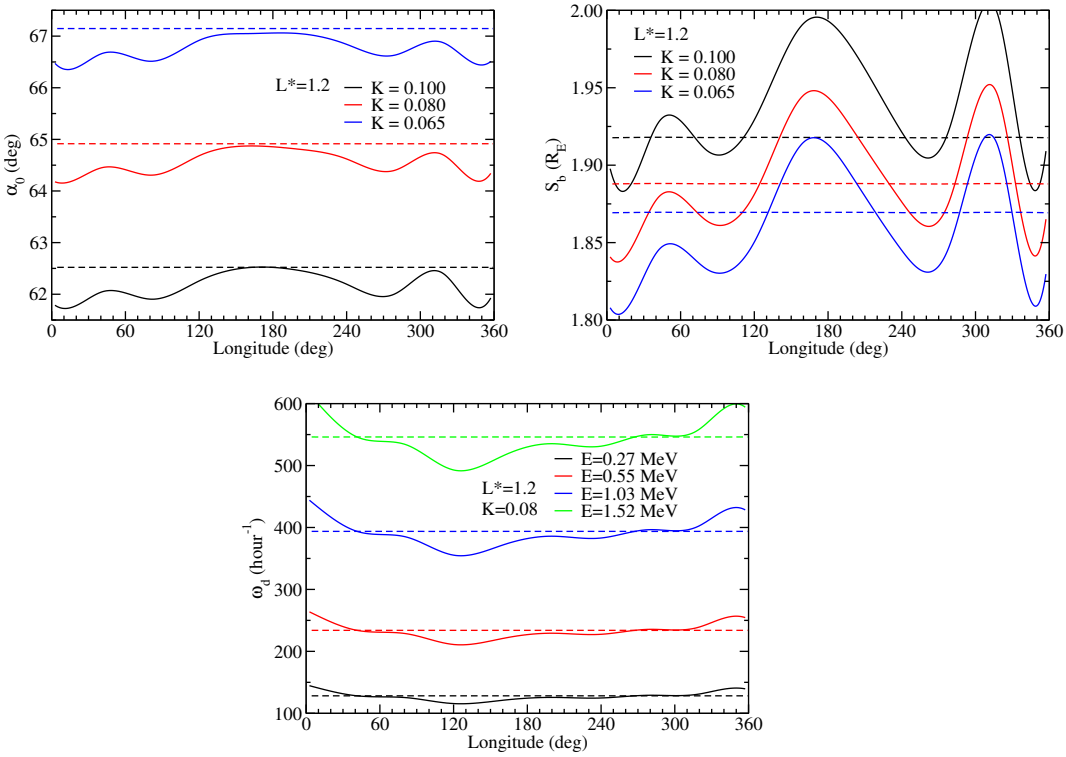

Figure 7.2 – Evolution of the equatorial pitch angle (top-left) and the bounce path (top-right) versus geographic longitude for $K = 0.065$, 0.080 and 0.100 $G^{1/2}R_E$ at $L^* = 1.2\ R_E$ and evolution of the electron drift frequency ω_d (bottom) versus geographic longitude for $E = 0.27$, 0.55, 1.03 and 1.52 MeV, at $L^* = 1.2\ R_E$ and $K = 0.080\ G^{1/2}R_E$. Plain lines represent the calculations made with the IGRF model whereas the dot lines correspond to the dipole field.

for which $\delta L^*_{i,j,k}$ is the change of the radial invariant due to the variation in equatorial pitch angle. The transformation process is illustrated by relation (7.4) that writes

$$\left\{\begin{array}{l} r_{i,j,k} \\ \alpha_{0i,j,k} \\ \varphi_{i,j,k} \end{array}\right. \Rightarrow \left\{\begin{array}{l} L^*_i \\ K_j \\ \varphi_k \end{array}\right. \quad \text{and} \quad \left\{\begin{array}{l} r_{i,j,k} \\ \alpha_{0i,j,k} + \delta\alpha_0 \\ \varphi_{i,j,k} \end{array}\right. \Rightarrow \left\{\begin{array}{l} L^*_i + \delta L^*_{i,j,k} \\ K_j + \delta K_{i,j,k} \\ \varphi_k. \end{array}\right. \tag{7.4}$$

The desired quantity $\delta L^*/\delta\alpha_0$, as a function of (L^*, K, φ), is finally deduced.

The calculations use a grid in L^* that is uniformly distributed over 150 bins ($i \in [1, 100]$) between $L^*_{\min} = 1.05$ and $L^*_{\max} = 1.55$, a grid in K logarithmically sampled over 100 values ($j \in [1, 100]$) from $K_{\min} = 10^{-3}$ to $K_{\max} = 10^0\ G^{1/2}R_E$, as well as azimuth values built on the 24 MLT values ($k \in [1, 24]$).

7.3.3 Challenges and results

7.3.3.a Numerical challenges

The first challenge arising from this methodology is how to choose the best $\delta\alpha_0$ to represent the derivative of L^* with respect to α_0. As a matter of fact, if the $\delta\alpha_0$ parameter is too small, the numerical $\delta L^*/\delta\alpha_0$ tends to zero, and if $\delta\alpha_0$ is too large, we lose the mathematical meaning of the derivative of a function at any given point (the slope of

the tangent of the function at this localized point). To deal with such a problem, we compute the values of the radial invariant $L^*_i + \delta L^*_{i,j,k}$ corresponding to the equatorial pitch angle $\alpha_{0i,j,k} + \delta\alpha_0$, for several values of $\delta\alpha_0$, at fixed radius and longitude. This step gives us a L^* function evolving with respect to α_0. We then apply several spline interpolations of the L^* function over points separated by different $\delta\alpha_0$ values. Figure 7.3 (left) shows the differences occurring on the slope of L^* with respect to equatorial pitch angle according to the chosen interpolated points. The $\delta L^*/\delta\alpha_0$ function evolving with the $\delta\alpha_0$ parameter is thus created. From that, a region where $\delta L^*/\delta\alpha_0$ is approximately constant with respect to $\delta\alpha_0$ should emerge. This plateau region gives us an admissible range for $\delta\alpha_0$. From our study, we conclude that $\delta\alpha_0 = 0.03$ radian (i.e. $\delta\alpha_0 \sim 1.8°$) is a good value that gives an accurate derivative of L^* with respect to the equatorial pitch angle to quantify the drift-shell splitting effect. Figure 7.3 (right) illustrates the difficulty of finding an admissible range of $\delta\alpha_0$ to accurately compute $\delta L^*/\delta\alpha_0$. This step has been significantly improved in (*Cunningham et al.*, 2018).

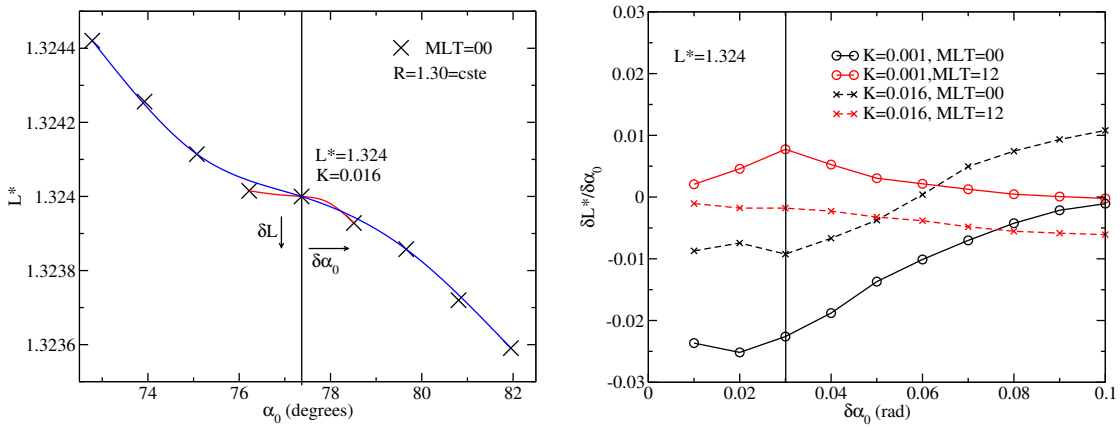

Figure 7.3 – Effects of spline interpolations on the value of $\delta L^*/\delta\alpha_0$ (left). The red curve corresponds to the spline interpolation on all the available points in L^*. Hence the local slope value of the function is close to zero. As for the blue curve, the interpolation is made on one point over two. The slope is in this case clearly negative. The right panel shows the evolution of $\delta L^*/\delta\alpha_0$ versus $\delta\alpha_0$ for a fixed L^*, K and φ. A plateau region hardly emerges around $\delta\alpha_0 = 0.03$ radian, highlighting the difficulty of finding a single $\delta\alpha_0$ value for all cases.

7.3.3.b Results

From this numerical method, we are able to compute the drift-shell splitting quantity $\delta L^*/\delta\alpha_0$ for any given (L^*, K, φ) parameters. Our numerical study leads us to a drift-shell splitting term $|\delta L^*/\delta\alpha_0|$ of about 10^{-2} Earth radius per radian.

As illustrated in Figure 7.4, the evolution of the $\delta L^*/\delta\alpha_0$ function with L^*, at a given K and φ, is characterized by many oscillations (black curve). We think this behavior is due to the spherical harmonics expansion in the IGRF model. A spline regression (red curve) can be done to get the global trend of the $\delta L^*/\delta\alpha_0$ function.

Figure 7.5 represents the evolution of $\delta L^*/\delta\alpha_0$ versus longitude at $L^* = 1.2$, respectively for $K = 0.016$, 0.062, and 0.080 $G^{1/2}R_E$. We notice a strong azimuthal variation of the drift shell-splitting term. The maximum intensity of $\delta L^*/\delta\alpha_0$ (in absolute value) cor-

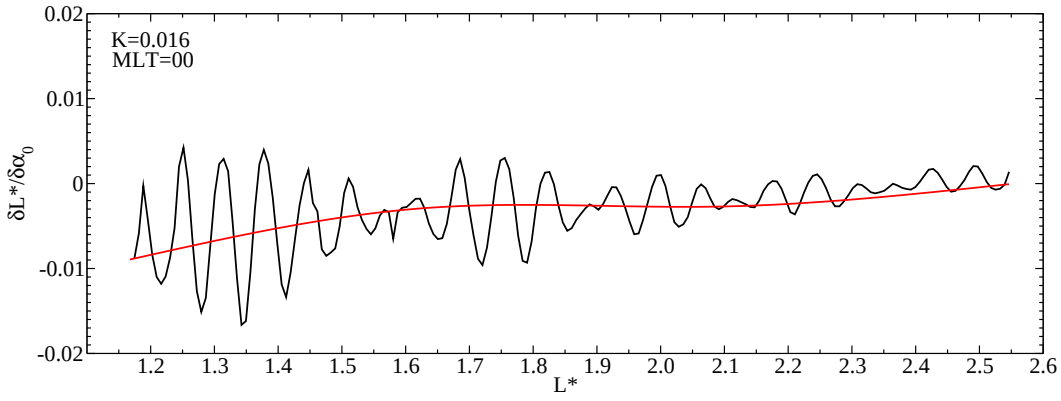

Figure 7.4 – Evolution of $\delta L^*/\delta\alpha_0$ versus L^*, for $K = 0.016$ $G^{1/2}R_E$ and MLT=00 (midnight). The black line represents the untreated computed values of $\delta L^*/\delta\alpha_0$ at each L^* location, and the red line is the results of a spline interpolation so as to obtain the general trend.

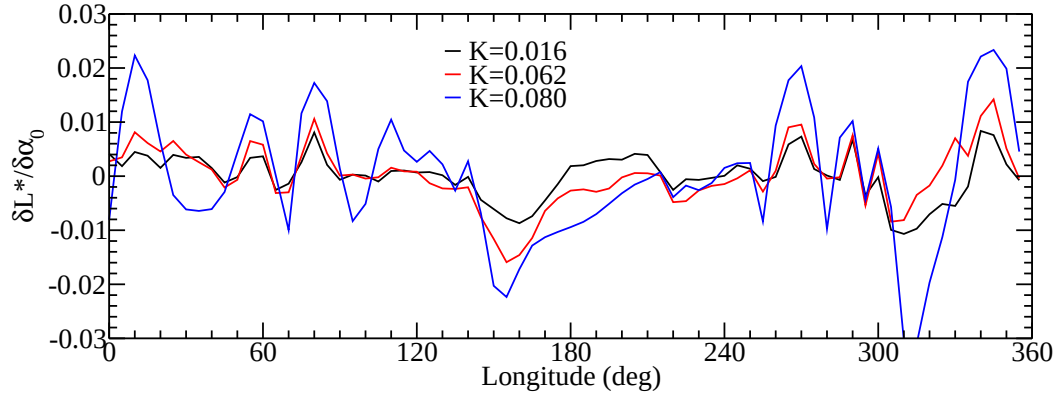

Figure 7.5 – Evolution of $\delta L^*/\delta\alpha_0$ versus longitude at $L^* = 1.2$ for $K = 0.016$ (black), 0.062 (blue), and 0.080 (red) $G^{1/2}R_E$.

responds to $\varphi \sim 310$ degrees, which relates to the region of the South Atlantic Anomaly. Let us mention that the azimuthal evolution of the drift-shell splitting term is in good agreement with (*Cunningham et al.*, 2018, Figure (2a)) despite the shortcomings of the numerical method adopted here.

For an illustrative purpose, we also plot in Figure 7.6 the evolution of the drift-average of the $(\delta L^*/\delta\alpha_0)^2$ local quantity as a function of L^*, for $K = 0.800$, 0.620, 0.405, 0.265, 0.062, 0.016 and 0.004 $G^{1/2}R_E$. Let us mention that the $\left\langle (\delta L^*/\delta\alpha_0)^2 \right\rangle$ term is not used in the computation of the neoclassical radial diffusion coefficient as $D_{L^*L^*}$ is the drift averaged of the whole quantity $(\delta L^*/\delta\alpha_0)^2 D_{\alpha_0\alpha_0}$. We still notice that the drift-shell splitting quantity is maximal at the lowest L-shell, for which the irregularities of the magnetic field (IGRF) are predominant.

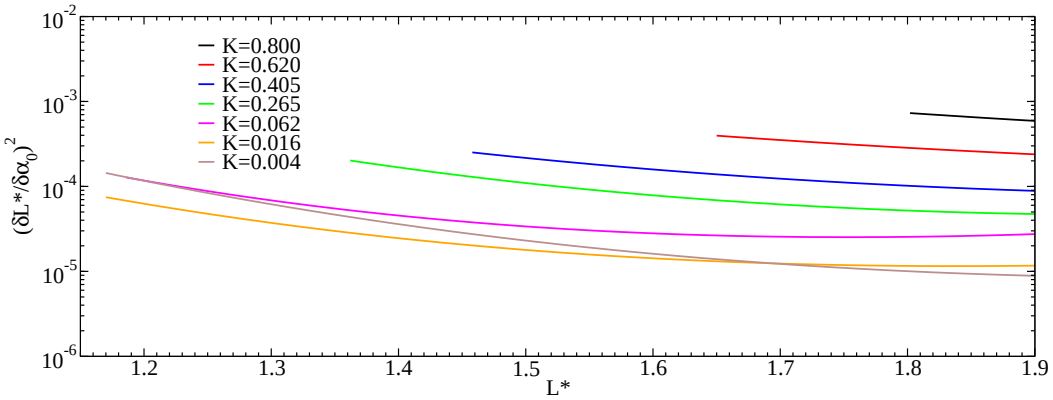

Figure 7.6 – Evolution of $\left\langle (\delta L^*/\delta\alpha_0)^2 \right\rangle$ versus L^* for K = 0.800, 0.620, 0.405, 0.265, 0.062, 0.016 and 0.004 $\mathrm{G}^{1/2}R_E$.

7.4 Atmospheric Coulomb scattering effects

To quantify the effects due to atmospheric pitch angle scattering from Coulomb collisions of electrons with ions and neutrals invoked in (7.2), we use the pitch angle diffusion coefficient formulation of *Selesnick* (2012) given by

$$D_{x_0x_0} = \frac{2\pi r_e^2 m_0^3 c^4 y_0^2 \gamma}{p^3 x_0^3} \left\langle \left(\frac{B_0}{B} - y_0^2 \right) \left[n_e \lambda_e + \sum_i n_i Q_i^2 \left(\lambda_p - \lambda_{ni} \right) + \sum_j n_j Z_j^2 \lambda_{n_j} \right] \right\rangle_b \tag{7.5}$$

for which $x_0 = \cos(\alpha_0)$ and $y_0 = \sin(\alpha_0)$. The parameter $r_e = e^2/(4\pi\epsilon_0 m_0 c^2)$ is the classical electron radius and γ the Lorentz factor related to the local electron velocity v.

Notation n_e states for the electron number density, which is given by the empirical formula

$$n_e = 21400 \times 10^{-R_E(1+h/R_E)/3}.$$

The densities n_j of the neutral species (He, O, N2, O2, Ar, H and N) are given by the MSIS (Mass Spectrometer Incoherent Scatter Radar) model (*Picone et al.*, 2002), which is included in the LANLGeoMag library, with AP=4 and $F_{10.7} = 100$. Notation n_i corresponds to the ion number density. For the purpose of this study, we intentionally do not take the ion number density into account, contrary to *Cunningham et al.* (2018). The densities at stakes are illustrated versus altitude in Figure 7.7.

Parameters Q_i and Z_j involved in (7.5) are respectively the charge state of the ion i and the atomic number of the neutral species j. Given the Debye length $\lambda_D = \sqrt{kT/\left(8\pi n_e e^2\right)}$ and the reduced mass $m_r = m_0/2$, we have $\lambda_{e/p} = \ln\left[(m_r v \lambda_D)/\hbar\right]$ and $\lambda_{ni} = \ln\left[\beta\gamma/\left(2.05\alpha_f Z_i^{1/3}\right)\right]$ with $\beta = v/c$ and $\alpha_f = 1/137$, the fine structure constant. As before, B is the intensity of the local magnetic field and B_0 is the equatorial magnetic field intensity.

In order to compute the pitch angle diffusion coefficient in a non-dipole magnetic field, we first have to express the local diffusion coefficient at each point of a given field line, and then apply the integration over each bounce path, as in (*Selesnick*, 2012) (see

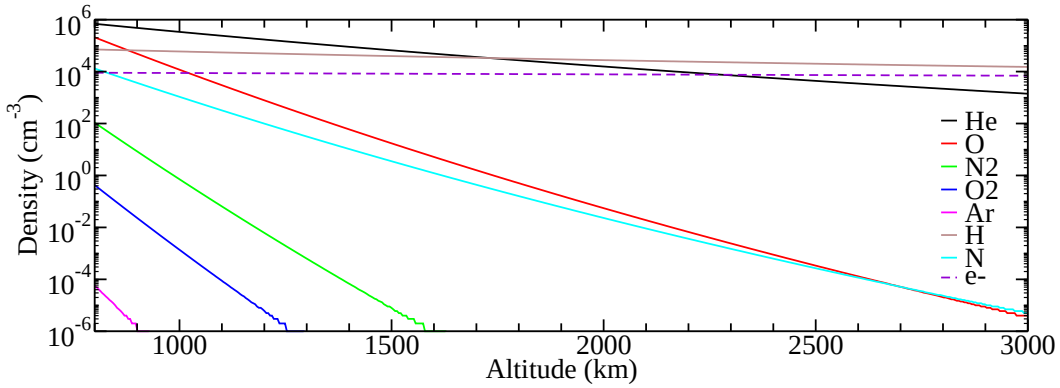

Figure 7.7 – Neutrals (He, O, N2, O2, Ar, H and N) and electron densities versus altitude. The density of neutrals is calculated from the MSIS model (*Picone et al.*, 2002), whereas the electron density is taken from the empirical formula shown in the text.

also equation (2.29) of Chapter 2)

$$\langle .. \rangle_b = \frac{1}{S_b} \int_{s_m}^{n_m} \frac{(..)}{\cos(\alpha)} \mathrm{d}s,$$

for which S_b is the half-bounce path length. Similarly to the bounce integration performed in Chapter 6, we use the approach of *Orlova and Shprits* (2011) to discard the singularity that appears at the mirror point. The x_0 diffusion coefficient is converted into the needed pitch angle diffusion coefficient by the relation $D_{\alpha_0\alpha_0} = D_{x_0x_0}/y_0^2$.

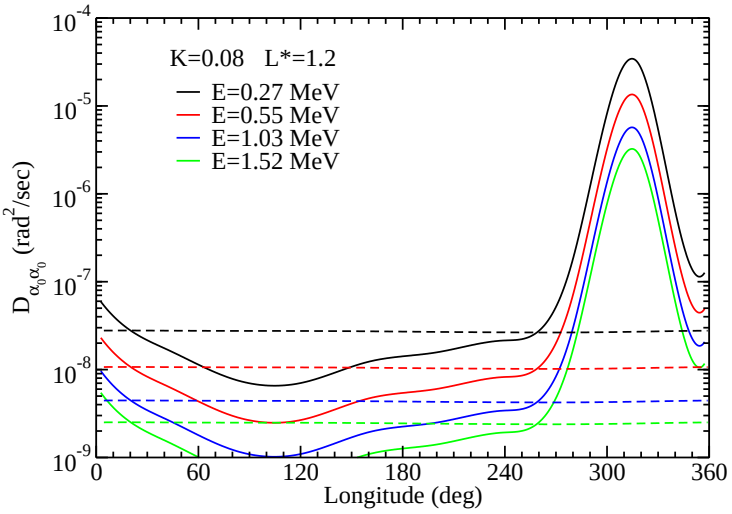

Figure 7.8 – Evolution of bounce-averaged pitch angle diffusion coefficient $D_{\alpha_0\alpha_0}$ versus geographic longitude φ at $K = 0.08$ G$^{1/2}R_E$ at $L^* = 1.2$ for $E = 270$ keV, 550 keV, 1.03 MeV and 1.52 MeV. The plain lines represent the $D_{\alpha_0\alpha_0}$ computed with the IGRF model whereas the dot lines represent the $D_{\alpha_0\alpha_0}$ computed with the dipole field model.

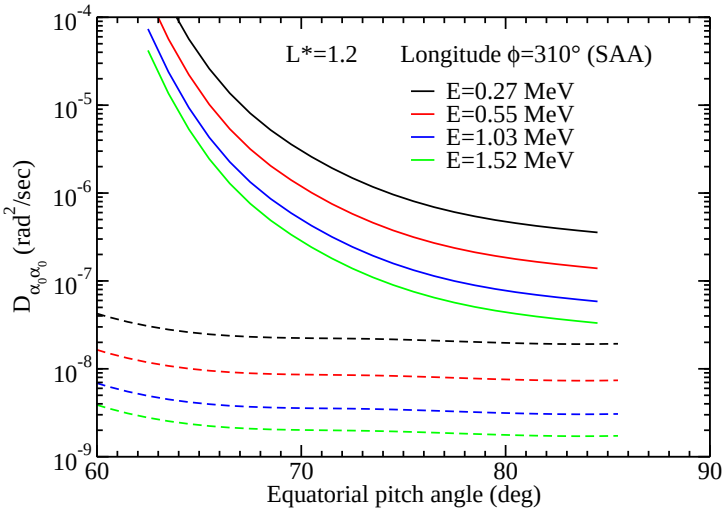

Figure 7.9 – Evolution of bounce-averaged pitch angle diffusion coefficient $D_{\alpha_0\alpha_0}$ versus equatorial pitch angle α_0 for $\varphi = 310$ degrees (right) at $L^* = 1.2$ for $E = 270$ keV, 550 keV, 1.03 MeV and 1.52 MeV. The plain lines represent the $D_{\alpha_0\alpha_0}$ computed with the IGRF model whereas the dot lines represent the $D_{\alpha_0\alpha_0}$ computed with the dipole field model.

In this work, we focus on the particular date of December 8, 1964. Figure 7.8 shows the evolution of the bounce-averaged pitch angle diffusion coefficient $D_{\alpha_0\alpha_0}$ with respect to geographic longitude φ for $K = 0.08$ G$^{1/2}R_E$ at various energies $E = 0.27$, 0.55, 1.03 and 1.52 MeV. A peak of almost 4 orders of magnitude is visible in the vicinity of the South Atlantic Anomaly ($\varphi \sim 310$ degrees). This is consistent with (*Selesnick*, 2012, Figure 4) and (*Cunningham et al.*, 2018, Figure 3). Figure 7.9 depicts the behavior of the drift-averaged pitch angle diffusion coefficient $\langle D_{\alpha_0\alpha_0} \rangle$ versus equatorial pitch angle α_0. The global trend of the obtained curves can be compared with the results obtained in (*Selesnick et al.*, 2013, Figure 6) and in (*Cunningham et al.*, 2018, Figure 4a).

7.5 Quantification of anomalous radial diffusion

7.5.1 Results

After drift-averaging the local (i.e. the bounce-averaged) radial diffusion coefficient $(\partial L^*/\partial\alpha_0)^2 D_{\alpha_0\alpha_0}$, we obtain the neoclassical radial diffusion coefficient $D_{L^*L^*}$ expressed by (7.2). In the present work, we use again a spline regression over $D_{L^*L^*}$ in order to capture its global trend and to avoid non-physical noise that goes along the calculation of the $\delta L^*/\delta\alpha_0$ term. The evolution of the anomalous radial diffusion coefficient $D_{L^*L^*}$ with respect to L^* is represented below in Figure 7.10, for $K = 0.01$ G$^{1/2}R_E$ (nearly equatorial particles) and several values of μ.

Other simulations have been made for different values of K, as presented in Figure 7.11. For smaller equatorial pitch angles, electrons are likely to be in the loss cone at small L^* values, for example at $L^* < 1.3$ for $\alpha_0 \sim 43°$. The above results theoretically support the empirically-derived negative slopes shown in Figure 7.1 as observed by *Newkirk and*

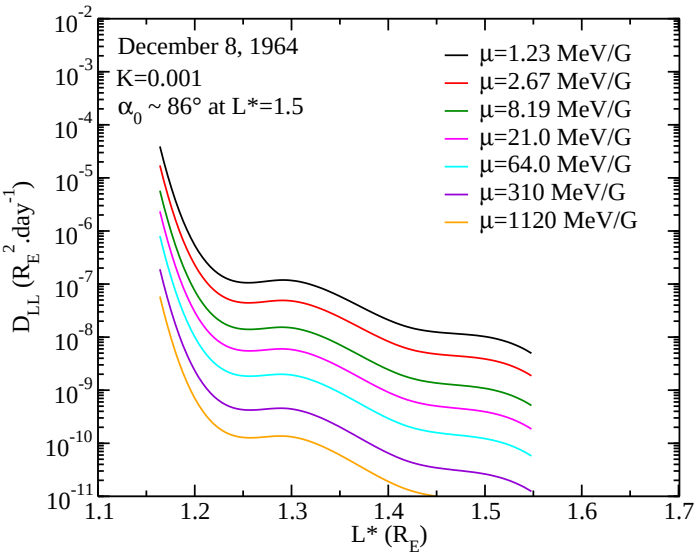

Figure 7.10 – Evolution of the anomalous radial diffusion term $D_{L^*L^*}$ versus L^* for $K = 0.001$ $G^{1/2}R_E$ and different values of the first adiabatic invariant μ. The indicated values for first adiabatic invariant μ (taken in ascending order) in the legend correspond respectively to energies of $E = 0.1$, 0.2, 0.5, 1.0, 2.0, 5.0 and 10 MeV at $L^* = 1.5$.

Walt (1968) and *Farley* (1969). We notice that for the lowest equatorial pitch angles, the impact of spline interpolations are visible on the computation of the radial diffusion coefficient, as illustrated by the slope variations of Figure 7.11 (bottom-right), for which a global trend is more difficult to grasp.

Neoclassical radial diffusion coefficients have also been obtained for another date (March 8, 2010, not shown), which confirms the negative slope of the radial diffusion coefficient at low L-shells. It suggests that this trend is not a local feature but might rather be a general property inherent to neoclassical diffusion.

7.5.2 Comparison with the empirically-derived diffusion coefficients

As stated before, *Farley* (1969) focused on a radial diffusion coefficient $D_{L^*L^*}(\mu, L^*)$ for $K = 0.0$ $G^{1/2}R_E$ such that μ corresponds to $E = 1.0$ MeV at $L^* = 1.65$, which gives $\mu \sim 28$ MeV/G from the IGRF model. However, the values obtained by *Farley* (1969) can be considered as an upper limit for the radial diffusion coefficient (*Walt*, 1971) and are two order of magnitude higher than the values obtained from our calculations, which makes the comparison with our anomalous radial diffusion term difficult. As for *Newkirk and Walt* (1968), they obtained average values of the radial diffusion coefficient for electrons above the threshold energy of 1.6 MeV rather than a $D_{L^*L^*}(\mu, K = 0, L^*)$ expressed at a fixed μ. We can nevertheless relate our D_{LL} calculation with the radial diffusion coefficient described by *Newkirk and Walt* (1968). As shown in Figure 7.10, the radial diffusion coefficient falls abruptly when μ increases for $L^* \in [1.15, 1.21]$. In this narrow interval of L^*, we can also consider that the energy does not vary much for a fixed μ (for instance $\mu = 21$ MeV/G corresponds to $E = 1.53$ MeV at $L^* = 1.21$ and $E = 1.66$ MeV at $L^* = 1.15$), and so the radial diffusion coefficient should also strongly decrease when the energy increases. Furthermore, for these high energies ($E > 2$ MeV),

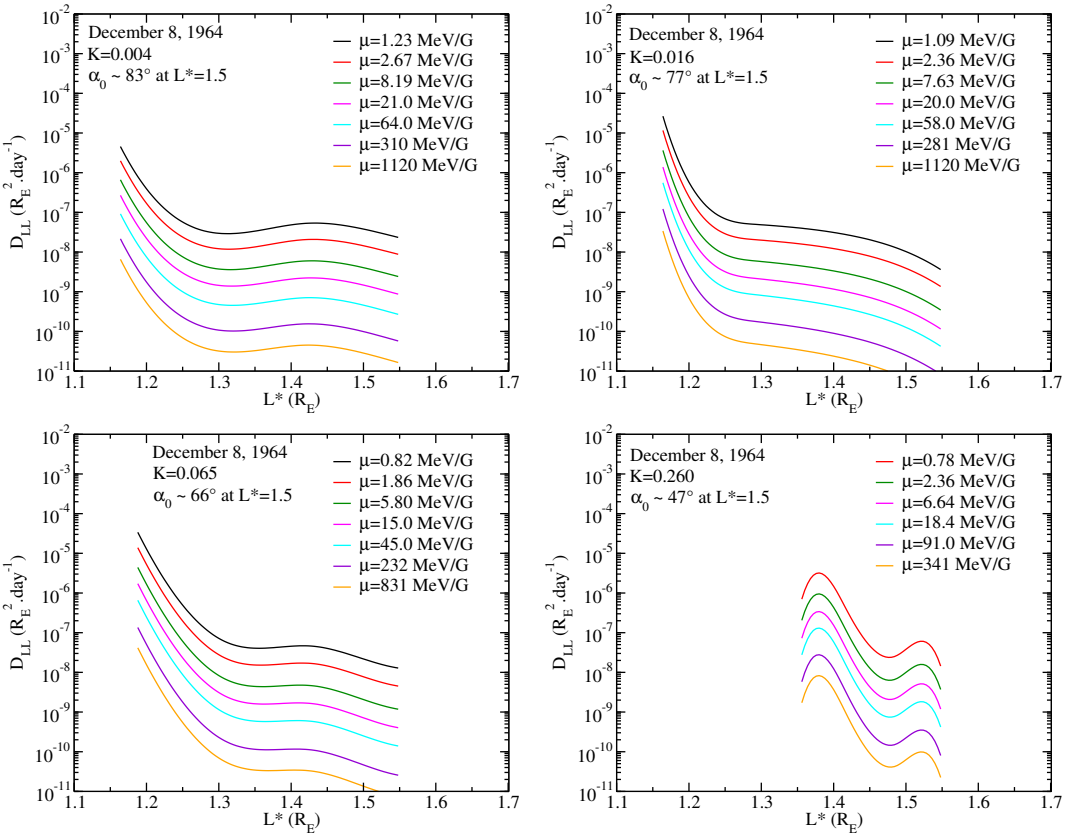

Figure 7.11 – Evolution of the anomalous radial diffusion term $D_{L^*L^*}$ vs L^* for $K = 0.004$ (top-left), $K = 0.016$ (top-right), $K = 0.065$ (bottom-left) and $K = 0.260$ $\mathrm{G}^{1/2}R_E$ (bottom-right) with different values of the first adiabatic invariant μ. Again, the indicated values for first adiabatic invariant μ (taken in ascending order) correspond respectively to energies of $E = 0.1$, 0.2, 0.5, 1.0, 2.0, 5.0 and 10 MeV at $L^* = 1.5$ for $K = 0.004$, $K = 0.016$ and $K = 0.065$ $\mathrm{G}^{1/2}R_E$. For the last case $K = 0.260$ $\mathrm{G}^{1/2}R_E$, the values for μ (taken in ascending order) correspond respectively to energies of $E = 0.2$, 0.5, 1.0, 2.0, 5.0 and 10 MeV at $L^* = 1.5$.

the distribution function should decrease with increasing energies, leading to the fact that the radial diffusion coefficient evaluated for energies higher than 1.6 MeV should approximatively have the same behavior and the same order of magnitude as our $D_{L^*L^*}$ at $E = 1.6$ MeV, i.e. for $\mu \sim 21$ MeV/G. The comparison between the empirically-derived diffusion coefficient from *Newkirk and Walt* (1968) and the diffusion coefficient taken from our computations is shown in Figure 7.12.

The orders of magnitude of the radial diffusion coefficients shown in Figure 7.12 are consistent with the empirical results from *Newkirk and Walt* (1968), with $D_{L^*L^*}$ taking values between 10^{-5} and 10^{-7} R_E^2/day for $L^* \in [1.15, 1.20]$. The simulations exhibit a sharper slope from the radial diffusion coefficient empirically derived by *Newkirk and Walt* (1968). In (*Cunningham et al.*, 2018) the illustration of the neoclassical radial diffusion coefficient relies on a different format in order to be closer to the conditions of the historical observations (*Imhof et al.*, 1967; *Newkirk and Walt*, 1968). This leads to a neoclassical radial diffusion coefficient that better matches the empirical estimation of *Newkirk and Walt* (1968).

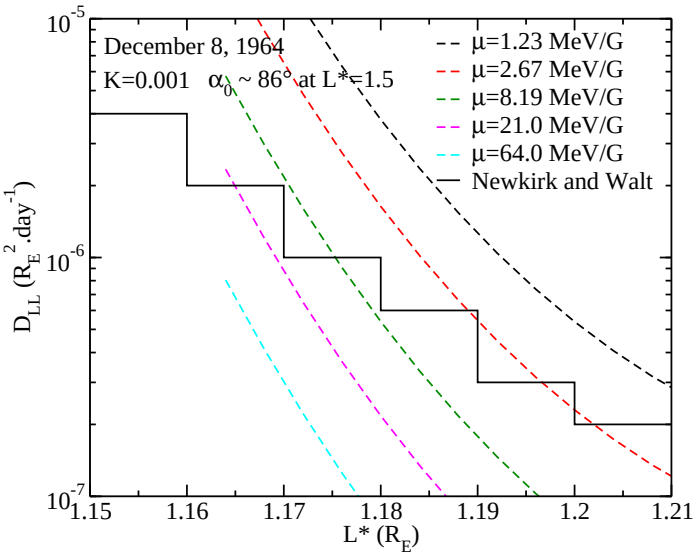

Figure 7.12 – Evolution of the anomalous radial diffusion term $D_{L^*L^*}$ taken from our computations (dashed line) vs L^* for $K = 0.001$ and different values of the first adiabatic invariant μ, compared with the results obtained by *Newkirk and Walt* (1968) (solid line). The purple curve corresponding to $\mu = 21$ MeV/G is not the closest curve to the values of *Newkirk and Walt* (1968), indicating that (among other issues) we might have underestimated the values of the drift-shell splitting term $\delta L^*/\delta\alpha_0$.

7.6 Conclusions

Throughout this work we have emphasized some significant effects brought by the irregular spatial nature of the geomagnetic field. We have specifically investigated and quantified the resulting physical processes thought to produce additional radial diffusion at low L-shell values. *Roederer et al.* (1973) worked on an interpretation of the surprising empirical radial diffusion coefficients obtained by *Newkirk and Walt* (1968) and *Farley* (1969), which exhibit a significant drop as the L-shell increases, up to $L = 1.5$. At low L-shell values, a particle trapped in the Earth magnetic field experiences a pitch angle diffusion induced by atmospheric scattering. As the magnetic field is intrinsically asymmetric, a change in pitch angle will end up in a change in drift-shell due to the drift-shell splitting effects, leading to additional and non-negligible radial diffusion at such low L-shells compared with radial diffusion usually inferred from interactions with ULF waves. Hence we use the formalism of *O'Brien* (2015) to highlight an anomalous radial diffusion coefficient. The drift-shell splitting effect is represented by the variation of the radial invariant L^* with respect to the equatorial pitch angle. This term has been computed for all (L^*, K, φ) by using the numerical routines discussed in (*Cunningham*, 2016) and based on the LANLGeoMag library. If some improvements have been done in (*Cunningham et al.*, 2018) to better quantify the drift-shell splitting term $\delta L^*/\delta\alpha_0$, the calculated drift-shell splitting term is thought to be relevant. The atmospheric scattering effect is computed from the pitch angle diffusion coefficient $D_{x_0x_0}$ from atmospheric Coulomb scattering derived from *Selesnick* (2012). In this perspective, we use the MSIS model, implemented in the LANLGeoMag library, to find the density profile of the neutral species. Moreover, an integration of the local $D_{x_0x_0}$ over the bounce path taken in the

IGRF model has also been required. From all of these steps, we put forward a drift-averaged neoclassical radial diffusion coefficient at very low L^* values, expressed in terms of μ, K and L^*.

The final obtained results are promising as they show the same global decreasing trend as observed by *Newkirk and Walt* (1968) and *Farley* (1969) in the late 1960's. Investigating this process for different atmospheric conditions and at different dates in order to confirm the importance of this unusual transport would be worthwhile. We also plan to assess for which electron energy and pitch angle the extra radial diffusion becomes significant and whether or not it can become a dominant mode of transport at low L-shell. More generally, this study also supports the conclusions drawn by *O'Brien* (2015), which state that accurately modeling the effects of drift-shell splitting, combined with pitch angle and energy diffusion, is crucial to unveil some yet hidden properties of the inner and outer radiation belts.

Conclusions

This PhD thesis addresses some issues that are inherent to the study of the radiation belts. It merely focuses on radial transport and atmospheric losses of electrons in the outer radiation belts. We recall that the radiation belts constitute the prime trapping region of the magnetosphere. It is also the privileged place where electromagnetic waves of different nature thrive, which makes the radiation belts a natural laboratory adapted to cold plasma physics and appropriate to observe and analyze wave-particle interactions.

Particles energization by betatron acceleration (radial diffusion inferred from resonant interactions with ULF waves) or local acceleration (energy diffusion inferred from resonant interactions with VLF waves) can result in critical breakdowns to some of the so many orbiting satellites, which are at the frontline of geomagnetic storms. One recorded 450 known satellites at the geostationary orbit in 2018 according to `http://www.satsig.net/sslist.htm`. The study of radiation belts is thus crucial for satellite protection. As things stand, the most powerful event that has ever been recorded is the Carrington event (reported in 1859) mentioned in Chapter 1. If a geomagnetic storm of such intensity had to occur again, it would undoubtedly cause much severe damages, impacting essential services of our modern society. Geomagnetic storms, which arise from solar activity, are however still barely predictable. More theoretical and computational efforts are indeed needed, as well as more satellite observations to confront numerical predictions with reality.

Main achievements of this PhD thesis study

The general objective of the present PhD thesis was to better understand the dynamics of the high-energy electrons trapped in the outer radiation belt. It has thus been the opportunity to improve the capability of the CEA in-house code to reproduce realistic geomagnetic events in a predictive way. In this perspective, the accuracy of our simulations has been quantified with the use of various dedicated error metrics (see Chapter 5 and 6) applied between our models and satellite observations (from CRRES and from the newly released L3 Van Allen Probes data). More specifically, the analytical method developed in Chapter 3 has been a first step to highlight the effects of radial diffusion (inward and outward) and pitch angle scattering for different geomagnetic contexts (massive or gradual injection and depletion). The possibility of taking account of realistic geomagnetic conditions, initiated in Chapter 4, reaches its pinnacle in Chapter 5, in which we have been able to reproduce the depletion of the outer belt during a storm-recovery, for a large range of pitch angles, energies and L-shells. The specific focus on a storm-time event (Chapter 6) underlines the importance of dealing with a realistic magnetic field model. This effect is one of the major keypoint addressed during the PhD. The influence of the magnetic field has also been investigated in the inner belt (Chapter 7) and enables us to unveil a new hidden diffusive phenomenon. Let us briefly summarize the related main achievements associated to each chapter.

Finding the analytical solution of the reduced Fokker-Planck equation

The first step of the thesis has been to analytically characterize the phase-averaged distribution function inferred for the reduced Fokker-Planck equation that governs the transport and loss of electrons within the radiation belts. In this perspective, we have generalized some previous fundamental works (e.g., *Haerendel*, 1968; *Walt*, 1970; *Thomsen et al.*, 1977a,b; *Schulz*, 1986; *Jentsch*, 1984; *Schulz and Newman*, 1988; *Hood*, 1983)

by considering a nonuniform loss term, for which no analytical solution had ever been calculated.

The analytical method relies on an original technique that consists of fitting the nonuniform lifetime by a piecewise constant function. The whole solution has then been split on several subintervals involving each a different constant lifetime. Each related solution is calculated via an eigenfunction approach (e.g., *Mei*, 1997). The last step of the procedure has been to reconstruct the global distribution function by merging all the obtained separate solutions. The connection on the whole domain is based on the continuity properties of the finale solution. Finding the numerous eigenvalues as well as performing the various orthogonal projections on the eigenfunction basis have required to develop a new numerical code dedicated to generate the full analytical solution during the PhD. The correctness of the obtained solution has been verified by comparing the latter with the results obtained from numerical simulations.

We have also given an analytical estimation of the time to reach an equilibrium state, for which its dependence upon the initial conditions has been investigated. This so-called equilibrium time is of great interest because it quickly gives an evaluation of the evolution time of the diffusion processes at stake.

We have finally demonstrated that the convergence of the proposed analytical solution is reached all the more quickly as the diffusion power is weak (≤ 4) and as the snapshot time is small. The proposed analytical method is useful when applied to the magnetosphere of Jupiter or Saturn, for which the diffusion process is less steep than in the Earth's radiation belts (*Hood*, 1983; *Woodfield et al.*, 2014). New optimized hybrid computational methods can also be implemented, taking advantage of the common numerical finite-difference schemes to derive the solution at early times and using rather the presented analytical procedure to compute the solution at larger times. Moreover we extracted small regions in the (L, E) plane where equilibrium solutions are likely to occur. These results have been published in (*Loridan et al.*, 2017).

Characterizing the dynamical structure and timescale of the radiation belts

The analytical results have been completed by numerical studies. The latter relies on a inhouse (CEA) reduced Fokker-Planck code based on a finite difference scheme, which includes the parts related to the dynamic treatment of the boundary conditions as well as the realistic (dynamic) magnetic field developed during the PhD. The inherent dynamics is shaped by radial diffusion induced by drift-resonant interactions with ULF waves, as well as losses, either induced by electron Coulomb collisions in the atmosphere or gyro-resonant interactions with VLF waves, respectively whistler mode hiss waves (inside the plasmasphere) and whistler mode chorus waves (outside the plasmasphere).

We have been able to illustrate the electron flux dynamics in a highly resolved grid in energy and L-shells. In particular, long-time solutions have emphasized a characteristic S shape of the inner edge of the outer radiation belt that has recently been observed by the Van Allen Probes (*Reeves et al.*, 2016). We demonstrate that this pronounced feature is dictated by the so-called Biot number, which is the ratio of the electron lifetime (related to losses inferred from pitch angle diffusion) over the characteristic time of radial transport.

We have also put forwards the time for which the electron fluxes approach their alleged equilibrium state, using different initial conditions, and have proven that this typical time is governed by the mean characteristic time, defined as the harmonic average of the radial and pitch angle diffusion times. These results agree with the theoretical

estimates of (*Loridan et al.*, 2017) (cf. Chapter 3).

Finally, we have built a map illustrating the reachable equilibrium states in the energy and L-shell plane. The equilibrium state is considered physically relevant if the associated equilibrium time is lower than the timescale of the changes of the magnetospheric conditions. Based on this criteria, we have shown that the assumption of steady state is unlikely to be valid for the entire radiation belts, except at some rare radial distances and energies, becoming even more hypothetical if the geomagnetic activity increases. These results have been published in (*Ripoll et al.*, 2016a).

Understanding electron scattering during storm-recovery

We have then taken the opportunity to improve the previous results by solving a realistic event. In this context, we have studied the storm-recovery of March 4-15, 2013, that took place between two main storms on the 1st and 17th of March 2013. The physical properties inherent to this storm-recovery (quiet solar wind conditions) offer an unprecedented opportunity to quantify losses inferred by whistler mode hiss waves.

We have specifically used a data-driven pitch angle diffusion coefficient and electron lifetimes (their computation have been made in a previous work that is not part of the thesis (*Ripoll et al.*, 2017)). Both the event-specific lifetime and pitch angle diffusion coefficient have been respectively included into the CEA 1-D reduced Fokker-Planck code and into a pre-existing 3-D Fokker-Planck model (VERB-3D) (*Subbotin and Shprits*, 2009; *Subbotin et al.*, 2010; *Kim et al.*, 2011) to assess for the behavior of the electron unidirectional and omnidirectional fluxes when subjected to the action of ULF waves (radial diffusion) and VLF whistler mode hiss waves (pitch angle diffusion).

The simulation results have been compared with both L2 (spin-averaged) data and L3 (pitch angle resolved) data taken from Van Allen Probe A. Comparison of different models with the use of dedicated error metrics (*Morley*, 2016; *Morley et al.*, 2018) have validated the accuracy of the data-driven lifetime and pitch angle diffusion coefficient, which attests for the need of using event-specific conditions to corroborate the observations. The importance of the initial pitch angle distribution has also been emphasized in the 3-D simulations. This work has enabled us to demonstrate that whistler mode hiss waves are responsible for the electron depletion in the slot region and the gradual formation of the observed S shape outer belt electron flux, which makes such plasmaspheric VLF waves a main contributor of electron losses within the radiation belts. These results have been published in (*Ripoll et al.*, 2016b, 2017). Results describing the 3-D structure (L, energy, pitch angle) of the radiation belts will be published in 2018 (*Ripoll et al.*, 2018, in print).

Investigating the impact of the Earth's magnetic field in the outer belt during a geomagnetic storm

If the electron fluxes have been previously well reproduced during the quiet storm-recovery, simulating a geomagnetic storm is more challenging. Effects of in-situ acceleration might arise and a particular care on the magnetic field topology is needed. During geomagnetic storms, the magnetic field in the outer belt is known to be significantly distorted by the solar wind, such that the question of the impact of the magnetic field topology on the outer belt dynamics arises.

In this context, we have generalized the use of a dipole field by developing the numerical implementation of a realistic field model, by taking advantage of the existing dedicated LANLGeoMag library, through all the steps of the reduced Fokker-Planck

code (pre-processing, computation, and post-processing). After validating the new implementation by reproducing another quiet event of year 1990, we have performed the solutions of the reduced Fokker-Planck equation in the framework of the geomagnetic storm that occurred from October 9 to October 15, 1990 (e.g., *Brautigam and Albert*, 2000; *Albert et al.*, 2009).

With the use of CRRES observations, the magnetic field model is shown to strongly affect the way of conciliating theory with observations (processing steps). More specifically, the use of a dipole field leads to misleading interpretations on the local enhancements (wrongly attributed to local acceleration) displayed by the electron distribution function (*Green and Kivelson*, 2004), resulting in inaccurate simulations results. The consideration of a realistic field enables us instead to smooth the previous artificial peaks. With such corrected data sets, most of the acceleration processes can be described by radial transport and are thus better reproduced by the simulations. This crucial importance of the field geometry is emphasized with the calculation of unidirectional, omnidirectional, and integral electron fluxes and is quantified thanks to dedicated metrics. These presented outcomes will be the topic of a forthcoming publication (*Loridan et al.*, 2018, in preparation).

Emphasizing the emergence of hidden diffusive transport in the inner belt

Finally, a different aspect of the importance of the magnetic field topology has also been put forward in the closest vicinity of the Earth.

The spatial asymmetry of the magnetic field is at the origin of drift-shell splitting, which makes electrons of different pitch angles populate different drift shells (*Roederer et al.*, 1973). This effect is particularly pronounced in the outer belt for $L > 7$. When pitch angle diffusion is involved along with drift-shell splitting, additional radial diffusion at very low L-shells occurs: this is the so-called neoclassical radial diffusion.

We have thus quantified the neoclassical radial diffusion coefficient by numerically coupling the effects of drift-shell splitting (represented by the variation of the third adiabatic invariant with pitch angle) with pitch angle diffusion (represented by an existing pitch angle diffusion coefficient that accounts for atmospheric Coulomb scattering of electrons in the atmosphere).

The obtained neoclassical radial diffusion coefficient has been characterized by a typical decreasing trend, which is consistent with empirical radial diffusion coefficients derived from observations made in the late 1960's (*Newkirk and Walt*, 1968; *Farley*, 1969). Such results pave the way for investigating more new hidden diffusive processes that can emerge from the natural irregularity of the Earth's magnetic field. These results have been published in (*Cunningham et al.*, 2018).

Discussion

The aforementioned results have all been obtained by considering that the conditions required for diffusion (Fokker-Planck equation) are physically satisfied within the radiation belts. These assumptions, mainly the guiding center approximation and the validity of quasilinear theory, can be discussed and debated.

Assumptions made for the theoretical framework

Let us first recall some of the important assumptions that have been made to simplify the complex theoretical framework of the study of the radiation belts.

(i) Guiding center approximation

The three motions of an electron trapped into a nonuniform magnetic field (gyration, bounce, and drift motions) have first been emphasized under the framework of the guiding center approximation (*Northrop*, 1963a) and has been described and explained in Chapter 2. The guiding center approximation consists at representing the particle motion by its gyro-averaged trajectory, i.e. the trajectory of the point around which the particle gyrates (the so-called guiding center) (e.g., *Roederer*, 1970; *Cary and Brizard*, 2009). It supposes that there exists a frame of reference in which the particle's motion is nearly circular around the magnetic field line. The guiding center approximation holds as long as the two adiabatic conditions are satisfied, which state respectively that the magnetic field varies slightly along the cyclotron trajectory and changes slightly during a cyclotron period. For a 1 MeV electron, the latter period is about 0.02 ms at $L = 2$ and about 0.7 ms at $L = 6$. The guiding center approximations are typically verified within the electron radiation belts. Equations of motion related to the guiding center can then be derived by averaging over the gyro-period and by expanding the Lorentz equation about the guiding center, as depicted in (*Northrop*, 1963a; *Roederer*, 1970; *Roederer and Zhang*, 2014) and in Chapter 2.

(ii) Quasilinear theory and related assumptions

Quasilinear theory is used to relate the Fokker-Planck diffusion equation governing the phase-averaged distribution function with the Vlasov equation describing the evolution of the electron density in phase space (*Kennel and Engelmann*, 1966; *Lerche*, 1968). It is commonly adopted for the computation of pitch angle, momentum, and radial diffusion coefficients (*Fälthammar*, 1965; *Lyons et al.*, 1971, 1972; *Lyons*, 1974a,b; *Albert*, 2005; *Glauert and Horne*, 2005).

Quasilinear theory basically describes the evolution of the phase space density in response to small-amplitude electromagnetic waves (*Fälthammar*, 1965; *Kennel and Engelmann*, 1966; *Lerche*, 1968). It mainly implies broadband waves as well as the fact that the amplitude of the electromagnetic waves proliferating in the magnetosphere are small (i.e. a few nT) compared with the amplitude of the ambient Earth magnetic field (hundreds of nT). The theory consists of splitting the distribution function as well as the magnetic and electric fields into a spatially homogeneous component and a small rapidly fluctuating part (*Kennel and Engelmann*, 1966; *Lerche*, 1968). The separation assumes a homogeneous and collisionless plasma immersed in a nearly uniform and static magnetic field (in the sense of the adiabatic conditions). Generally speaking, no static electric field is considered for high energy electrons.

The full derivation is carried out by expanding the Vlasov equation (also known as the collisionless Boltzmann equation) for the presumed particle distribution either in the canonical space (*Kennel and Engelmann*, 1966; *Lerche*, 1968) or in the action-angle coordinate system (*Ukhorskiy and Sitnov*, 2013). It leads to a so-called quasilinear diffusion equation for the gyro-averaged slow evolution of the distribution function. The latter equation can be assimilated to the Fokker-Planck equation with respect to pitch angle and momentum, which enables to highlight tractable expressions for the involved diffusion coefficients that represent the effect of small-amplitude waves.

Let us mention that such physical description via a single diffusion equation prevents any retroaction of the electron dynamics on the magnetic field that governs it (no self consistent wave-particles interactions), which makes sense since the amplitude of the electromagnetic perturbation has been considered small compared with the ambient magnetic field. Deviations from diffusive transport are discussed below.

Limitations

All the assumptions inherent to quasilinear theory and more generally related to the reduction of the whole system to a Fokker-Planck diffusion equation can however be broken in the context of radiation belt dynamics.

(i) Breaking the adiabatic conditions

The guiding center approximation can fail for protons and ions (*Ukhorskiy et al.*, 2018), for which the cyclotron gyroradius is much larger and the cyclotron motion much slower, see (2.2) and (2.1). As discussed in (*Sergeev et al.*, 1983), the radius of curvature of a given field line in the magnetotail can be small enough to violate condition (2.2), resulting in a rapid scattering in electron's pitch angle that materializes by a rapid electron depletion in the atmosphere. This effect is known to be the current sheet scattering.

(ii) Large-amplitude and narrow-band electromagnetic perturbations

First, large-amplitude waves, whose impact cannot be described by quasilinear theory, can be produced during large geomagnetic storms induced by coronal mass ejections. An example of such significant perturbations has first been reported in (*Wygant et al.*, 1994), which focused on fast magnetosonic waves whose amplitude exceeded 300 mV/m. This study showed that such active event could result in the energization of inner-belt electrons up to 10 MeV during a timescale much lower than the drift period. Investigating properly the effects associated to those waves would require a complete kinetic description of the phase space density through the Vlasov equation, since the dependences on the phases of motions are no longer negligible. Large-amplitude (200 mV/m) whistler mode chorus waves have also been recently observed (*Cattell et al.*, 2008; *Cully et al.*, 2008; *Kellogg et al.*, 2010; *Wilson et al.*, 2011) and can potentially trigger nonlinear effects that are out of the scope of quasilinear theory. Even if the limits of applications of quasilinear theory are not yet clearly defined (*Albert*, 2010), results brought by the Fokker-Planck modeling should be further confirmed by other approaches, such as test particle simulations, and more validated with satellites' observations.

In the meantime, nonlinear theories have emerged to describe the interactions with large amplitude and narrow-band electromagnetic waves and have proven to be a useful alternative to explore beyond the limits imposed by quasilinear diffusion (e.g., *Albert*, 2002; *Bortnik et al.*, 2008b; *Tao et al.*, 2012; *Albert et al.*, 2013).

(iii) Peculiarities due to drift motion

As mentioned in Chapter 2 (section 2.4.5.b), drifting particles can be brought to the drift loss cone and be lost either in the atmosphere or beyond the magnetopause. Such losses are azimuth-dependent and cannot be accurately quantified via a phase-averaged distribution function governed by a Fokker-Planck description.

The consistency of a description in terms of the adiabatic invariants also shows its limits under the process of magnetopause shadowing. For example, the third adiabatic

invariant L^* is defined only inside the last closed drift shell. Beyond this boundary, the particles are transported across the magnetopause and are lost into interplanetary space. If the latter effect is not commonly implemented in classical diffusion codes, some recent works have explicitly taken magnetopause shadowing into account (e.g., *Yu et al.*, 2013). The inherent impact of magnetopause shadowing on global electron losses has yet to be better understood (*Turner et al.*, 2013a). This effect is particularly important during storms for which the magnetopause can be brought inward down to geostationary orbits (e.g., *Olifer et al.*, 2018).

In the same context, the electron trajectory in the dayside can be subjected to geometrical peculiarities. In the vicinity of magnetopause currents, a given magnetic field line can exhibit two localized minima in the field intensity. This bifurcation results in perturbed electron orbits that are called Shabansky orbits (*Shabansky*, 1971) and sometimes referred as drift-orbit bifurcations. Dayside particles can such be trapped on the same equatorial side in high-latitude regions. The second adiabatic invariant is likely to be violated under such Shabansky orbits. Moreover drift-orbit bifurcations can also produce PSD peaks as the ones mentioned in Chapter 6, as shown from global test-particles simulations (*Ukhorskiy and Sitnov*, 2013; *Ukhorskiy et al.*, 2014).

(iv) Intrinsic non diffusive phenomena

Some other important effects cannot be described through the lens of diffusive transport because of their advective nature. The energy loss induced by inelastic collisions of electrons with the neutrals of the upper atmosphere is typically described by an advection equation that is coupled to the standard Fokker-Planck equation (*Cunningham et al.*, 2018). More generally, collisional behaviors are depicted by friction terms that are added to the Fokker-Planck equation (*Schulz and Lanzerotti*, 1974). The presence of such non-stochastic effects leads to a non-vanishing total time derivative for the phase space density, contrary to what is inferred in Liouville's theorem. In the worst-case scenario, the complete Boltzmann equation should be solved instead of the collisionless Vlasov equation.

Significant deviations from diffusive transport can occur in the outer radiation belt. For example, ULF wave oscillations induced by global magnetospheric compressions can break the global picture of radial diffusion (*Ukhorskiy and Sitnov*, 2008, 2013; *Sorathia et al.*, 2017, 2018). More specifically, it has been shown that over the timescale by which particle ensembles spread over the entire system, persistent phase correlations are still at stake, which contradicts the efficient phase mixing process required for the diffusion conditions to be valid (*Ukhorskiy and Sitnov*, 2008).

Perspectives

The Van Allen Probes offer the opportunity of reproducing more specific events, such as the ones chosen for the Geospace Environment Modeling (GEM) challenges. The GEM challenges are selected events whose properties (satellites data, wave activity measurements, model inputs) are shared with the scientific community. The available tools enable scientists of various laboratories to test different models (diffusive models, test particle simulations) and to subsequently quantitatively assess the importance of transport, losses, and acceleration processes within the radiation belts. The current GEM challenges mainly focus on radiation belt dropout (e.g., *Tu et al.*, 2013) and radiation belt buildup (e.g., *Ma et al.*, 2018), which are two types of problems not yet simulated in this work but soon reachable after the progress we made these last years. If whistler

mode hiss waves have been shown in Chapter 5 to be the main driver for the loss of relativistic electrons in the slot region during quiet times, some questions remain on their capability to scatter ultrarelativistic electrons in the inner outer belt at $L \sim 4$. It has rather recently been suggested that only EMIC waves were able to account for the depletion of ultrarelativistic electrons (e.g., *Shprits et al.*, 2018). Including the effects of EMIC waves in the reduced Fokker-Planck code could be a significant step forward to quantify the influence of EMIC waves on the high-energy electrons.

The present study, particularly the work presented in Chapter 6, can also be generalized to cover a wider range of realistic magnetic field topologies. This would pave the way for an accurate calculation of the last closed drift shell and, then, better estimate the losses induced by magnetopause shadowing in addition to atmospheric scattering.

As discussed in the limitation section just given above as well as in Chapters 6 and 7, the implementation of non-dipole fields put in light the importance of the azimuthal variation of the magnetic field geometry. In this context, as a long-term perspective, it could be interesting to generalize the Fokker-Planck description by taking account of the azimuth-dependence of the phase space density so as to combine azimuthal advection with diffusion. This objective, which has been initiated in (*Shprits et al.*, 2015b; *Aseev et al.*, 2016) with the development of the so-called VERB-4D code, remains an outstanding challenge. It might enable to produce MLT electron distribution and to better estimate the impacts of electromagnetic waves or some collisional effects that take place at the South Atlantic Anomaly, which are localized in azimuth.

Looking a few years back, most of the theoretical basis of the underlying physics of radiation belts have been mainly built during the 1960's (particle motion, adiabatic invariants, quasilinear theory, diffusion coefficients) (*Northrop*, 1963a; *Fälthammar*, 1965; *Kennel and Engelmann*, 1966; *Lerche*, 1968) and 1970's (Fokker-Planck diffusion equation) (*Roederer*, 1970; *Schulz and Lanzerotti*, 1974). The studies carried out during the following years have rather been devoted to use, develop numerically, and test these theories, with, today, more concrete and direct applications of these well-established pioneering theories. The joint development of numerical codes and simulations along with the spread of more trustful satellite observations are the seedbed for the birth of new fruitful physical theories and for an enrichment in our understanding of the physics of the radiation belts.

Appendices

A Some useful elements of relativistic dynamics and electromagnetism

A.1 Relativistic dynamics

In this section, we define the few relations that are constantly used in a Fokker-Planck code to relate together velocity, momentum and energy (total, inertial and kinetic). We first define the well-known relativistic factor γ as

$$\gamma = \frac{1}{\sqrt{1 - v^2/c^2}}, \tag{6}$$

for which v is the particle's velocity and c is the speed of light. The particle's total energy E_{total} is given by

$$E_{\text{total}} = mc^2 = E + m_0c^2, \tag{7}$$

for which m_0 is the particle's rest mass and $m = \gamma m_0$ is the particle's relativistic mass. The particle's kinetic energy is referred as E. From above, the kinetic energy can be written as $E = m_0c^2(\gamma - 1)$. The particle's relativistic momentum p is also defined as $p = mv = \gamma m_0 v$. Hence we find that

$$\gamma = \frac{1}{\sqrt{1 - p^2/(\gamma m_0 c)^2}} \Leftrightarrow \gamma = \sqrt{1 + \frac{p^2}{m_0^2c^2}}.$$

From (7) and the above expression for γ we obtain

$$E_{\text{total}}^2 = m^2c^4 \Leftrightarrow \left(E + m_0c^2\right)^2 = p^2c^2 + m_0^2c^4.$$

Reversely, the above expression enables to write the particle's momentum p as

$$p = \frac{1}{c}\sqrt{(E + m_0c^2)^2 - m_0^2c^4}.$$

We can also express γ as

$$\gamma = \sqrt{1 + \frac{p^2}{m_0^2c^2}} = \sqrt{1 + \frac{\left(E + m_0c^2\right)^2 - m_0^2c^4}{m_0^2c^4}},$$

i.e.

$$\gamma = 1 + \frac{E}{m_0c^2}. \tag{8}$$

Equating (6) and (8) enables to express the particle's velocity v as a function of its kinetic energy E

$$v = c\sqrt{1 - \frac{1}{\left(1 + \frac{E}{m_0c^2}\right)^2}}. \tag{9}$$

A.2 Vector calculus

Let us consider a scalar quantity ψ and a vector $\boldsymbol{u}$.

A.2.a Differential operators

Divergence

The divergence of vector $\boldsymbol{u}$ is a scalar quantity indicated as $\boldsymbol{\nabla} \cdot \boldsymbol{u}$, which results in Cartesian coordinates

$$\boldsymbol{\nabla} \cdot \boldsymbol{u} = \frac{\partial u_x}{\partial x} + \frac{\partial u_y}{\partial y} + \frac{\partial u_z}{\partial z}.$$

Curl

The curl of vector $\boldsymbol{u}$ is a vector indicated as $\boldsymbol{\nabla} \times \boldsymbol{u}$, which results in Cartesian coordinates

$$\boldsymbol{\nabla} \times \boldsymbol{u} = \begin{pmatrix} \dfrac{\partial u_z}{\partial y} - \dfrac{\partial u_y}{\partial z} \\ \dfrac{\partial u_x}{\partial z} - \dfrac{\partial u_z}{\partial x} \\ \dfrac{\partial u_y}{\partial x} - \dfrac{\partial u_x}{\partial y} \end{pmatrix}.$$

Gradient

The gradient vector of scalar ψ is indicated as $\boldsymbol{\nabla}\psi$, which results in Cartesian coordinates

$$\boldsymbol{\nabla}\psi = \begin{pmatrix} \dfrac{\partial \psi}{\partial x} \\ \dfrac{\partial \psi}{\partial y} \\ \dfrac{\partial \psi}{\partial z} \end{pmatrix}.$$

The gradient tensor of the vector $\boldsymbol{u}$ is the tensor product of the gradient operator $\boldsymbol{\nabla}$ and $\boldsymbol{u}$. It is indicated as $\boldsymbol{\nabla} \otimes \boldsymbol{u}$, which gives in Cartesian coordinates

$$\boldsymbol{\nabla} \otimes \boldsymbol{u} = \begin{pmatrix} \dfrac{\partial u_x}{\partial x} & \dfrac{\partial u_y}{\partial x} & \dfrac{\partial u_z}{\partial x} \\ \dfrac{\partial u_x}{\partial y} & \dfrac{\partial u_y}{\partial y} & \dfrac{\partial u_z}{\partial y} \\ \dfrac{\partial u_x}{\partial z} & \dfrac{\partial u_y}{\partial z} & \dfrac{\partial u_z}{\partial z} \end{pmatrix}.$$

The so-called convective derivative of vector $\boldsymbol{u}$ represents the variation of this quantity induced by the displacement of a field frozen in time. It is related to the velocity field $\boldsymbol{V}$

and is indicated as $(\boldsymbol{V}\cdot\boldsymbol{\nabla})\,\boldsymbol{u}$. In Cartesian coordinates, it leads to

$$(\boldsymbol{V}\cdot\boldsymbol{\nabla})\,\boldsymbol{u} = \begin{pmatrix} V_x\dfrac{\partial u_x}{\partial x} + V_y\dfrac{\partial u_x}{\partial y} + V_z\dfrac{\partial u_x}{\partial z} \\ V_x\dfrac{\partial u_y}{\partial x} + V_y\dfrac{\partial u_y}{\partial y} + V_z\dfrac{\partial u_y}{\partial z} \\ V_x\dfrac{\partial u_z}{\partial x} + V_y\dfrac{\partial u_z}{\partial y} + V_z\dfrac{\partial u_z}{\partial z} \end{pmatrix}.$$

A.2.b Useful theorems

Stokes theorem

Stoke's theorem states that the integral of the curl of $\boldsymbol{u}$ over the surface Σ enclosed by the contour Γ is equal to the line integral of $\boldsymbol{u}$ over its boundary Γ, i.e.

$$\iint_{\Sigma} (\boldsymbol{\nabla}\times\boldsymbol{u})\cdot\mathrm{d}\boldsymbol{S} = \oint_{\Gamma} \boldsymbol{u}\cdot\mathrm{d}\boldsymbol{l}. \tag{10}$$

Divergence theorem

The divergence theorem states that the integral of the divergence of $\boldsymbol{u}$ over the volume Ω inside the closed surface Σ is equal to the outward flux of $\boldsymbol{u}$ through Σ, i.e.

$$\iiint_{\Omega} (\boldsymbol{\nabla}\cdot\boldsymbol{u})\,\mathrm{d}\mathcal{V} = \oiint_{\Sigma} \boldsymbol{u}\cdot\mathrm{d}\boldsymbol{S}. \tag{11}$$

A.3 Some basis of electromagnetism

A.3.a Maxwell's equations and charge conservation

Here we write some basic elements of electromagnetism based on (*Jackson*, 1975). The four Maxwell's equations constitute the backbone of electromagnetism. They are referred as the Maxwell-Gauss equation

$$\boldsymbol{\nabla}\cdot\boldsymbol{\mathcal{E}} = \frac{\rho}{\epsilon_0}, \tag{12}$$

the Maxwell-Faraday equation

$$\boldsymbol{\nabla}\times\boldsymbol{\mathcal{E}} = -\frac{\partial\boldsymbol{B}}{\partial t}, \tag{13}$$

the Maxwell-Flux equation

$$\boldsymbol{\nabla}\cdot\boldsymbol{B} = 0 \tag{14}$$

and the Maxwell-Ampere equation

$$\boldsymbol{\nabla}\times\boldsymbol{B} = \mu_0\boldsymbol{\mathcal{J}} + \mu_0\epsilon_0\frac{\partial\boldsymbol{\mathcal{E}}}{\partial t}, \tag{15}$$

for which $\boldsymbol{\mathcal{E}}$ and $\boldsymbol{B}$ are respectively the electric and magnetic fields, ρ is the charge density and $\boldsymbol{\mathcal{J}}$ is the current density.

Along with the Maxwell's equations, the conservation of charge writes

$$\frac{\partial \rho}{\partial t} + \boldsymbol{\nabla} \cdot \boldsymbol{\mathcal{J}} = 0. \tag{16}$$

A.3.b Electric and magnetic potentials

The magnetic potential is defined from $\boldsymbol{\nabla} \cdot \boldsymbol{B} = 0$, such that there exists a vector $\boldsymbol{\mathcal{A}}$ verifying

$$\boldsymbol{B} = \boldsymbol{\nabla} \times \boldsymbol{\mathcal{A}}. \tag{17}$$

The static Maxwell-Faraday equation writes $\boldsymbol{\nabla} \times \boldsymbol{\mathcal{E}} = 0$, from which a scalar potential V is such that

$$\boldsymbol{\mathcal{E}} = -\boldsymbol{\nabla} V. \tag{18}$$

Generalizing the previous result to the dynamical case, Maxwell-Faraday equation is $\boldsymbol{\nabla} \times \boldsymbol{\mathcal{E}} = -\partial \boldsymbol{B}/\partial t = -\boldsymbol{\nabla} \times \partial \boldsymbol{\mathcal{A}}/\partial t$, i.e.

$$\boldsymbol{\nabla} \times \left(\boldsymbol{\mathcal{E}} + \frac{\partial \boldsymbol{\mathcal{A}}}{\partial t} \right) = \boldsymbol{0},$$

such that

$$\boldsymbol{\mathcal{E}} + \frac{\partial \boldsymbol{\mathcal{A}}}{\partial t} = -\boldsymbol{\nabla} V,$$

which leads to

$$\boldsymbol{\mathcal{E}} = -\boldsymbol{\nabla} V - \frac{\partial \boldsymbol{\mathcal{A}}}{\partial t}.$$

Equations (12) and (18) lead to the Poisson's equation that governs the spatial evolution of static electric potential V,

$$\nabla^2 V + \frac{\rho}{\epsilon_0} = 0. \tag{19}$$

Equivalently, the static equation (15) combined with (17) leads to

$$\boldsymbol{\nabla} \times (\boldsymbol{\nabla} \times \boldsymbol{\mathcal{A}}) = \mu_0 \boldsymbol{\mathcal{J}},$$

i.e.

$$\boldsymbol{\nabla} (\boldsymbol{\nabla} \cdot \boldsymbol{\mathcal{A}}) - \nabla^2 \boldsymbol{\mathcal{A}} = \mu_0 \boldsymbol{\mathcal{J}}.$$

By imposing $\boldsymbol{\nabla} \cdot \boldsymbol{\mathcal{A}} = 0$ (the Lorentz gauge), we end up with the following Poisson's equation for $\boldsymbol{\mathcal{A}}$

$$\nabla^2 \boldsymbol{A} + \mu_0 \boldsymbol{\mathcal{J}} = \boldsymbol{0}. \tag{20}$$

A.3.c Conductive media

In a conductive media, the current density is linked to the electric field via a local Ohm's law

$$\boldsymbol{\mathcal{J}} = \sigma \boldsymbol{\mathcal{E}}, \tag{21}$$

for which σ is the media conductivity. The conductivity can be quantified by invoking a Drude model of electrons.

B Particle motion

B.1 First order Taylor expansion

The aim of this section is to calculate each of the terms involved in (2.7), which we recall here,

$$q\,\langle \boldsymbol{\mathcal{E}} \rangle + q\,\langle \boldsymbol{V} \times \boldsymbol{B} \rangle + q\,\langle \boldsymbol{v}^* \times \boldsymbol{B} \rangle + \langle \boldsymbol{F} \rangle - m \left\langle \frac{\mathrm{d}\boldsymbol{V}}{\mathrm{d}t} \right\rangle = 0, \tag{22}$$

for which the $\langle .. \rangle$ operator denotes the average (2.27) over the gyromotion. To do that, we follow the approach of (*Roederer and Zhang*, 2014).

The radial vector $\boldsymbol{r}$ in the original frame of reference is simply the sum of the radial vector $\boldsymbol{r_c}$ linking the center of the original frame of reference with the guiding center system point, with the Larmor radius vector $\boldsymbol{\rho_c}$ that links the guiding center system with the particle position, i.e.

$$\boldsymbol{r} = \boldsymbol{r_c} + \boldsymbol{\rho_c},$$

for which $\rho_c \ll r_c$. The first order expansion of any space-dependent vector quantity $\boldsymbol{P}$ writes

$$\boldsymbol{P}(\boldsymbol{r}) = \boldsymbol{P}(\boldsymbol{r_c} + \boldsymbol{\rho_c}) = \boldsymbol{P}(\boldsymbol{r_c}) + \boldsymbol{\delta P} = \boldsymbol{P}(\boldsymbol{r_c}) + \boldsymbol{\nabla} \otimes \boldsymbol{P}|^T \boldsymbol{\rho_c}.$$

In the moving guiding center system, the Larmor radius vector writes

$$\boldsymbol{\rho_c} = \begin{pmatrix} \rho_c \cos(\varphi) \\ \rho_c \sin(\varphi) \\ 0 \end{pmatrix}.$$

The first term of (22) is $\langle \boldsymbol{\mathcal{E}}(\boldsymbol{r}) \rangle = \langle \boldsymbol{\mathcal{E}}(\boldsymbol{r_c}) \rangle + \langle \boldsymbol{\delta \mathcal{E}} \rangle$ with

$$\boldsymbol{\delta \mathcal{E}} = \begin{pmatrix} \delta \mathcal{E}_x \\ \\ \delta \mathcal{E}_y \\ \\ \delta \mathcal{E}_z \end{pmatrix} = \begin{pmatrix} \dfrac{\partial \mathcal{E}_x}{\partial x} \rho_c \cos(\varphi) + \dfrac{\partial \mathcal{E}_x}{\partial y} \rho_c \sin(\varphi) \\ \\ \dfrac{\partial \mathcal{E}_y}{\partial x} \rho_c \cos(\varphi) + \dfrac{\partial \mathcal{E}_y}{\partial y} \rho_c \sin(\varphi) \\ \\ \dfrac{\partial \mathcal{E}_z}{\partial x} \rho_c \cos(\varphi) + \dfrac{\partial \mathcal{E}_z}{\partial y} \rho_c \sin(\varphi) \end{pmatrix},$$

so that $\langle \boldsymbol{\delta \mathcal{E}} \rangle = \boldsymbol{0}$, leading to

$$\langle \boldsymbol{\mathcal{E}}(\boldsymbol{r}) \rangle = \langle \boldsymbol{\mathcal{E}}(\boldsymbol{r_c}) \rangle = \boldsymbol{\mathcal{E}}(\boldsymbol{r_c}).$$

The second term of (22) is $\langle \boldsymbol{F}(\boldsymbol{r}) \rangle = \langle \boldsymbol{F}(\boldsymbol{r_c}) \rangle + \langle \boldsymbol{\delta F} \rangle$. Similarly to the previous case, we obtain $\langle \boldsymbol{\delta F} \rangle = \boldsymbol{0}$ so that

$$\langle \boldsymbol{F}(\boldsymbol{r}) \rangle = \langle \boldsymbol{F}(\boldsymbol{r_c}) \rangle = \boldsymbol{F}(\boldsymbol{r_c})$$

The third term of (22) contains $\langle \boldsymbol{V}(\boldsymbol{r}) \rangle = \langle \boldsymbol{V}(\boldsymbol{r_c}) \rangle + \langle \boldsymbol{\delta V} \rangle$, which, as before, leads to $\langle \boldsymbol{\delta V} \rangle = \boldsymbol{0}$, so that

$$\langle \boldsymbol{V}(\boldsymbol{r}) \rangle = \langle \boldsymbol{V}(\boldsymbol{r_c}) \rangle = \boldsymbol{V}(\boldsymbol{r_c}).$$

The last term of (22) is

$$\langle q\boldsymbol{v}^* \times \boldsymbol{B}(\boldsymbol{r}) \rangle = \langle q\boldsymbol{v}^* \times \boldsymbol{B}(\boldsymbol{r_c}) \rangle + \langle q\boldsymbol{v}^* \times \delta \boldsymbol{B} \rangle = q\,\langle \boldsymbol{v}^* \rangle \times \boldsymbol{B}(\boldsymbol{r_c}) + \langle q\boldsymbol{v}^* \times \delta \boldsymbol{B} \rangle.$$

Since $\langle \boldsymbol{v}^* \rangle = 0$, we obtain $\langle q\boldsymbol{v}^* \times \boldsymbol{B}(\boldsymbol{r}) \rangle = \langle q\boldsymbol{v}^* \times \delta\boldsymbol{B} \rangle$. The latter writes

$$\langle q\boldsymbol{v}^* \times \delta\boldsymbol{B} \rangle = q \left\langle \boldsymbol{v}^* \times \left(\boldsymbol{\nabla} \otimes \boldsymbol{B}|^T \boldsymbol{\rho_c} \right) \right\rangle .$$

We have on the first hand

$$\boldsymbol{v}^* = \boldsymbol{v}_\perp^* = \begin{pmatrix} \dfrac{q}{|q|} v_\perp^* \sin(\varphi) \\ -\dfrac{q}{|q|} v_\perp^* \cos(\varphi) \\ 0 \end{pmatrix}$$

in which the ratio $q/|q|$ enables us to put forward the effect of the sign of the electric charge. We have on the other hand

$$\boldsymbol{\delta B} = \begin{pmatrix} \delta B_x \\ \\ \delta B_y \\ \\ \delta B_z \end{pmatrix} = \begin{pmatrix} \dfrac{\partial B_x}{\partial x} \rho_c \cos(\varphi) + \dfrac{\partial B_x}{\partial y} \rho_c \sin(\varphi) \\ \\ \dfrac{\partial B_y}{\partial x} \rho_c \cos(\varphi) + \dfrac{\partial B_y}{\partial y} \rho_c \sin(\varphi) \\ \\ \dfrac{\partial B_z}{\partial x} \rho_c \cos(\varphi) + \dfrac{\partial B_z}{\partial y} \rho_c \sin(\varphi). \end{pmatrix},$$

Combining the fact that

$$\begin{cases} \dfrac{\partial B_x}{\partial z} & = 0, \\ \\ \dfrac{\partial B_y}{\partial z} & = -\dfrac{B}{R_c}, \\ \\ \dfrac{\partial B_z}{\partial z} & = \dfrac{\partial B}{\partial s}. \end{cases}$$

with Maxwell-Flux equation $\boldsymbol{\nabla} \cdot \boldsymbol{B} = 0$ (14), we obtain

$$\frac{\partial B_x}{\partial x} + \frac{\partial B_y}{\partial y} + \frac{\partial B_z}{\partial z} = 0 \Rightarrow \frac{\partial B_y}{\partial y} = -\left(\frac{\partial B}{\partial s} + \frac{\partial B_x}{\partial x} \right).$$

Hence $\boldsymbol{\delta B}$ becomes

$$\begin{cases} \delta B_x & = \dfrac{\partial B_x}{\partial x} \rho_c \cos(\varphi) + \dfrac{\partial B_x}{\partial y} \rho_c \sin(\varphi), \\ \\ \delta B_y & = \dfrac{\partial B_y}{\partial x} \rho_c \cos(\varphi) - \left(\dfrac{\partial B}{\partial s} + \dfrac{\partial B_x}{\partial x} \right) \rho_c \sin(\varphi), \\ \\ \delta B_z & = \dfrac{\partial B_z}{\partial x} \rho_c \cos(\varphi) + \dfrac{\partial B_z}{\partial y} \rho_c \sin(\varphi). \end{cases}$$

Computing

$$\boldsymbol{v}^* \times \boldsymbol{\delta B} = \begin{pmatrix} \frac{q}{|q|} v_\perp^* \sin(\varphi) \\ -\frac{q}{|q|} v_\perp^* \cos(\varphi) \\ 0 \end{pmatrix} \times \begin{pmatrix} \frac{\partial B_x}{\partial x}\rho_c \cos(\varphi) + \frac{\partial B_x}{\partial y}\rho_c \sin(\varphi) \\ \frac{\partial B_y}{\partial x}\rho_c \cos(\varphi) - \left(\frac{\partial B}{\partial s} + \frac{\partial B_x}{\partial x}\right)\rho_c \sin(\varphi) \\ \frac{\partial B_z}{\partial x}\rho_c \cos(\varphi) + \frac{\partial B_z}{\partial y}\rho_c \sin(\varphi) \end{pmatrix}$$

and averaging over the gyro-phase leads to

$$q \langle \boldsymbol{v}^* \times \boldsymbol{\delta B} \rangle = -\frac{1}{2}|q| v_\perp^* \rho_c \boldsymbol{\nabla} B_z.$$

Since $\rho_c = \dfrac{m v_\perp^*}{|q|B}$, we simply obtain

$$q \langle \boldsymbol{v}^* \times \boldsymbol{\delta B} \rangle = -\mathscr{M} \boldsymbol{\nabla} B_z.$$

Decomposing the gradient operator into its perpendicular and parallel component $\boldsymbol{\nabla} = \boldsymbol{\nabla}_\perp + \boldsymbol{\nabla}_\parallel$, we emphasize the gradient $\boldsymbol{B}$ force

$$\boldsymbol{f}_\perp = -\mathscr{M} \boldsymbol{\nabla}_\perp B_z$$

and the mirror force

$$\boldsymbol{f}_\parallel = -\mathscr{M} \boldsymbol{\nabla}_\parallel B_z.$$

At the guiding center point (and not at the particle actual position), equation (22) reduces to

$$q \boldsymbol{\mathcal{E}} + q \boldsymbol{V} \times \boldsymbol{B} - \mathscr{M} \boldsymbol{\nabla} B + \boldsymbol{F} - m \frac{\mathrm{d}\boldsymbol{V}}{\mathrm{d}t} = 0.$$

B.2 Drift motion

The previous equation is satisfied for (*Roederer and Zhang*, 2014)

$$\boldsymbol{V} = \left(q\boldsymbol{\mathcal{E}} + \boldsymbol{F} - \mathscr{M} \boldsymbol{\nabla} B - m \frac{\mathrm{d}\boldsymbol{V}}{\mathrm{d}t} \right) \times \frac{\boldsymbol{B}}{qB^2}.$$

We also notice that

$$\begin{cases} \boldsymbol{V}_\perp &= \left(q\boldsymbol{\mathcal{E}} + \boldsymbol{F} - \mathscr{M} \boldsymbol{\nabla} B - m \dfrac{\mathrm{d}\boldsymbol{V}}{\mathrm{d}t} \right) \times \dfrac{\boldsymbol{B}}{qB^2}, \\ \boldsymbol{V}_\parallel &= \boldsymbol{v}_\parallel. \end{cases}$$

To express the drift velocity, we still need to find an expression for the inertial force drift $\boldsymbol{F_i} = m\mathrm{d}\boldsymbol{V}/\mathrm{d}t$. Since

$$\boldsymbol{V} = \boldsymbol{V}_\parallel + \boldsymbol{V}_\perp,$$

we have

$$\frac{\mathrm{d}\boldsymbol{V}}{\mathrm{d}t} = \frac{\mathrm{d}}{\mathrm{d}t}\left(\boldsymbol{V}_{\parallel} + \boldsymbol{V}_{\perp}\right) = \frac{\mathrm{d}}{\mathrm{d}t}\left(v_{\parallel}\boldsymbol{e} + \boldsymbol{V}_{\perp}\right) = \frac{\mathrm{d}v_{\parallel}}{\mathrm{d}t}\boldsymbol{e} + v_{\parallel}\frac{\mathrm{d}\boldsymbol{e}}{\mathrm{d}t} + \frac{\mathrm{d}\boldsymbol{V}_{\perp}}{\mathrm{d}t}. \tag{23}$$

We recall that the time derivative is the total variation per unit time as seen by the particle during its motion (fluid mechanics approach). The local derivative of a quantity represents the time variation of this quantity for a given fixed point in space. The convective derivative of a quantity represents the variation of this quantity induced by the displacement for a field frozen in time. Hence *Roederer and Zhang* (2014) obtained

$$\begin{aligned}\frac{\mathrm{d}\boldsymbol{V}}{\mathrm{d}t} &= \frac{\mathrm{d}v_{\parallel}}{\mathrm{d}t}\boldsymbol{e} + v_{\parallel}\left[\frac{\partial \boldsymbol{e}}{\partial t} + \left(\boldsymbol{V}\cdot\boldsymbol{\nabla}\right)\boldsymbol{e}\right] + \frac{\mathrm{d}\boldsymbol{V}_{\perp}}{\mathrm{d}t} \\ &= \frac{\mathrm{d}v_{\parallel}}{\mathrm{d}t}\boldsymbol{e} + v_{\parallel}\left[\frac{\partial \boldsymbol{e}}{\partial t} + \left(\boldsymbol{v}_{\parallel}\cdot\boldsymbol{\nabla}\right)\boldsymbol{e} + \left(\boldsymbol{V}_{\perp}\cdot\boldsymbol{\nabla}\right)\boldsymbol{e}\right] + \frac{\mathrm{d}\boldsymbol{V}_{\perp}}{\mathrm{d}t}.\end{aligned}$$

Since $\left(\boldsymbol{v}_{\parallel}\cdot\boldsymbol{\nabla}\right)\boldsymbol{e} = v_{\parallel}\,\partial\boldsymbol{e}/\partial s$, we have

$$\boldsymbol{F_i} = m\frac{\mathrm{d}\boldsymbol{V}}{\mathrm{d}t} = m\left(\frac{\mathrm{d}v_{\parallel}}{\mathrm{d}t}\boldsymbol{e} + v_{\parallel}^2\frac{\partial \boldsymbol{e}}{\partial s} + v_{\parallel}\left(\boldsymbol{V}_{\perp}\cdot\boldsymbol{\nabla}\right)\boldsymbol{e} + v_{\parallel}\frac{\partial \boldsymbol{e}}{\partial t} + \frac{\mathrm{d}\boldsymbol{V}_{\perp}}{\mathrm{d}t}\right).$$

In what follows, *Roederer and Zhang* (2014) considered that

$$\left(\boldsymbol{V}_{\perp}\cdot\boldsymbol{\nabla}\right)\boldsymbol{e} \sim \left(\boldsymbol{U}_{\perp}\cdot\boldsymbol{\nabla}\right)\boldsymbol{e}$$

and

$$\frac{\mathrm{d}\boldsymbol{V}_{\perp}}{\mathrm{d}t} \sim \frac{\mathrm{d}\boldsymbol{U}_{\perp}}{\mathrm{d}t}.$$

By taking the expression that we have found for the transverse drift velocity

$$\boldsymbol{V}_{\perp} = \left(q\boldsymbol{\mathcal{E}} + \boldsymbol{F} - \mathscr{M}\,\boldsymbol{\nabla}B - m\frac{\mathrm{d}\boldsymbol{V}}{\mathrm{d}t}\right)\times\frac{\boldsymbol{B}}{qB^2} = \frac{\boldsymbol{e}}{qB}\times\left(-q\boldsymbol{\mathcal{E}} - \boldsymbol{F} + \mathscr{M}\,\boldsymbol{\nabla}B + m\frac{\mathrm{d}\boldsymbol{V}}{\mathrm{d}t}\right),$$

and by combining it to the approximated expression giving the inertial force, we obtain (cancelling all parallel components)

$$\boldsymbol{V}_{\perp} = \frac{\boldsymbol{e}}{qB}\times\left(-q\boldsymbol{\mathcal{E}} - \boldsymbol{F} + \mathscr{M}\,\boldsymbol{\nabla}_{\perp}B + mv_{\parallel}^2\frac{\partial \boldsymbol{e}}{\partial s} + mv_{\parallel}\frac{\partial \boldsymbol{e}}{\partial t} + mv_{\parallel}\left(\boldsymbol{U}\cdot\boldsymbol{\nabla}\right)\boldsymbol{e} + m\frac{\mathrm{d}\boldsymbol{U}}{\mathrm{d}t}\right).$$

Using the expression of the magnetic moment $\mathscr{M} = \dfrac{mv_{\perp}^{*2}}{2B}$, we end up with the full expression for the drift velocity

$$\boldsymbol{V}_{\perp} = \frac{\boldsymbol{B}}{qB^2}\times\left(-q\boldsymbol{\mathcal{E}} - \boldsymbol{F} + \frac{mv_{\perp}^{*2}}{2B}\boldsymbol{\nabla}_{\perp}B + mv_{\parallel}^2\frac{\partial \boldsymbol{e}}{\partial s} + mv_{\parallel}\frac{\partial \boldsymbol{e}}{\partial t} + mv_{\parallel}\left(\boldsymbol{U}\cdot\boldsymbol{\nabla}\right)\boldsymbol{e} + m\frac{\mathrm{d}\boldsymbol{U}}{\mathrm{d}t}\right),$$

which is equivalent to equation (2.9).

B.3 Deriving the parallel equation of motion

We recall the equation (2.8)

$$m\frac{\mathrm{d}\boldsymbol{V}}{\mathrm{d}t} = q\boldsymbol{\mathcal{E}} + \boldsymbol{F} + q\boldsymbol{V}\times\boldsymbol{B} - \mathscr{M}\,\boldsymbol{\nabla}B. \tag{24}$$

Following (*Roederer and Zhang*, 2014), we draw a particular attention to the fact that

$$\begin{cases} v_{\parallel} &= \boldsymbol{V}\cdot\boldsymbol{e} = \dfrac{\mathrm{d}s}{\mathrm{d}t}, \\ \dfrac{\mathrm{d}v_{\parallel}}{\mathrm{d}t} &= \dfrac{\mathrm{d}}{\mathrm{d}t}(\boldsymbol{V}\cdot\boldsymbol{e}) = \dfrac{\mathrm{d}\boldsymbol{V}}{\mathrm{d}t}\cdot\boldsymbol{e} + \boldsymbol{V}\cdot\dfrac{\mathrm{d}\boldsymbol{e}}{\mathrm{d}t} = a_{\parallel} + \boldsymbol{V}_{\perp}\cdot\dfrac{\mathrm{d}\boldsymbol{e}}{\mathrm{d}t} = \dfrac{\mathrm{d}^2 s}{\mathrm{d}s^2} \end{cases} \tag{25}$$

We have from (24)

$$m\frac{\mathrm{d}\boldsymbol{V}}{\mathrm{d}t}\cdot\boldsymbol{e} = ma_{\parallel} = (q\boldsymbol{\mathcal{E}} + \boldsymbol{F} + q\boldsymbol{V}\times\boldsymbol{B} - \mathscr{M}\,\boldsymbol{\nabla}B)\cdot\boldsymbol{e} = q\mathcal{E}_{\parallel} + F_{\parallel} - \mathscr{M}\,\nabla_{\parallel}B,$$

so that

$$ma_{\parallel} = q\mathcal{E}_{\parallel} + F_{\parallel} - \mathscr{M}\frac{\partial B}{\partial s}. \tag{26}$$

On the other hand, equation (25) gives the parallel acceleration component $a_{\parallel}$ as

$$\begin{aligned} a_{\parallel} &= \frac{\mathrm{d}v_{\parallel}}{\mathrm{d}t} - \boldsymbol{V}_{\perp}\cdot\frac{\mathrm{d}\boldsymbol{e}}{\mathrm{d}t} \\ &= \frac{\mathrm{d}v_{\parallel}}{\mathrm{d}t} - \boldsymbol{V}_{\perp}\cdot\left[\frac{\partial\boldsymbol{e}}{\partial t} + (\boldsymbol{V}\cdot\boldsymbol{\nabla})\,\boldsymbol{e}\right] \\ &= \frac{\mathrm{d}v_{\parallel}}{\mathrm{d}t} - \boldsymbol{V}_{\perp}\cdot\left[\frac{\partial\boldsymbol{e}}{\partial t} + \left((\boldsymbol{v}_{\parallel} + \boldsymbol{V}_{\perp})\cdot\boldsymbol{\nabla}\right)\boldsymbol{e}\right], \end{aligned}$$

so that

$$ma_{\parallel} = m\frac{\mathrm{d}v_{\parallel}}{\mathrm{d}t} - mv_{\parallel}\boldsymbol{V}_{\perp}\frac{\partial\boldsymbol{e}}{\partial s} - m\boldsymbol{V}_{\perp}\cdot\frac{\partial\boldsymbol{e}}{\partial t} - m\boldsymbol{V}_{\perp}\cdot(\boldsymbol{V}_{\perp}\cdot\boldsymbol{\nabla})\,\boldsymbol{e}. \tag{27}$$

Using both equations (26) and (27) giving $a_{\parallel}$ we obtain the equation of the parallel motion of the guiding center (2.10) as given in (*Roederer and Zhang*, 2014)

$$m\frac{\mathrm{d}v_{\parallel}}{\mathrm{d}t} = q\mathcal{E}_{\parallel} + F_{\parallel} - \mathscr{M}\frac{\partial B}{\partial s} + mv_{\parallel}\boldsymbol{V}_{\perp}\cdot\frac{\partial\boldsymbol{e}}{\partial s} + m\boldsymbol{V}_{\perp}\cdot\frac{\partial\boldsymbol{e}}{\partial t} + m\boldsymbol{V}_{\perp}\cdot(\boldsymbol{V}_{\perp}\cdot\boldsymbol{\nabla})\,\boldsymbol{e}. \tag{28}$$

This equation is equivalent to equation (2.10) that is used in Chapter 2 to characterize the electron bounce motion along a magnetic field line.

C Adiabatic invariants and Fokker-Planck equation

C.1 Derivation of the Fokker-Planck equation

Let us focus on the specific case for which only the third adiabatic invariant Φ is violated. It happens when the particle is subjected to electromagnetic perturbation induced by ultra low frequency (ULF) waves, i.e. if the frequency of the waves is of the same order of magnitude of the drift frequency f_d (*Kellogg*, 1959). For this situation, the relevant distribution function is $f_\Phi(\Phi, t)$, or, to say it differently, $(2\pi)^3 f_\Phi(\Phi, t)\,\delta\Phi$ represents the number of particles per unit μ and J at time t.

C.1.a Probability function

Let Δt be a time increment long enough for a particle to suffer a large number of displacements but still short enough to violate the third adiabatic invariant, $\Delta t \sim \tau_d$. There is a nonzero probability that a particle having coordinate $\Phi - \varphi$ at time t will end up at position Φ at the time $t + \Delta t$, for which φ and Δt are small increments in the third adiabatic invariant and time respectively. Using the same notation as in (*Chandrasekhar*, 1943; *Haerendel*, 1968), we name such probability function

$$\Psi\left(\Phi_{t+\Delta t} = \Phi / \Phi_t = \Phi - \varphi, t, \varphi\right) = \Psi\left(\Phi - \varphi, \varphi, t\right).$$

As the time increment Δt is fixed, the Ψ probability function only depends on the current time t as well as the target position Φ and the length of the space increment φ. As any probability function, the Ψ probability function has to be normalized such that

$$\int_{\Phi-\text{space}} \Psi \, \mathrm{d}\varphi = 1.$$

The above normalization simply states that, for a particle being at position Φ at time $t + \Delta t$, the probability that at previous time t the particle was located at any point of the entire Φ-space is 1.

C.1.b Discrete case

In a general discrete case, the law of total probability states that the probability $P\left(X_{t+1} = k\right)$ of reaching position k at time $t + 1$ is given by

$$P\left(X_{t+1} = k\right) = \sum_i P\left(X_{t+1} = k \cap X_t = i\right),$$

i.e.

$$P\left(X_{t+1} = k\right) = \sum_i P\left(X_{t+1} = k / X_t = i\right) P\left(X_t = i\right),$$

for which $P\left(X_{t+1} = k / X_t = i\right)$ is the conditional probability of reaching position k at time $t + 1$ given that the position is i at the previous time. In the above expression, the summation is carried on the space of all possible positions i. The $P\left(X_{t+1} = k\right)$ term can be seen as a discrete distribution at time $t + 1$, as well as the $P\left(X_{t+1} = k \cap X_t = i\right)$ term represents the discrete distribution at the previous time t. The conditional term $P\left(X_{t+1} = k / X_t = i\right)$ can be interpreted as a transition probability between position i and position k.

C.1.c Continuous case

Now coming back to the continuous case of interest, the equivalent total law of probability writes (e.g., *Chandrasekhar*, 1943; *Roederer*, 1970; *Roederer and Zhang*, 2014)

$$f\left(\Phi_{t+\Delta t}=\Phi\right)=\int\limits_{\Phi-\text{space}}\Psi\left(\Phi_{t+\Delta t}=\Phi/\Phi_t=\Phi-\varphi\right)f\left(\Phi_t=\Phi-\varphi\right)\,\mathrm{d}\varphi,$$

for which $f\left(\Phi_{t+\Delta t}=\Phi\right)$ is the distribution for Φ at time $t+\Delta t$, $\Psi\left(\Phi_{t+\Delta t}=\Phi/\Phi_t=\Phi-\varphi\right)$ is the transition probability to have Φ at $t+\Delta t$ starting from $\Phi-\varphi$ at t and $f\left(\Phi_t=\Phi-\varphi\right)$ is the distribution for $\Phi-\varphi$ at time t. We write the above expression in a more familiar way to obtain

$$f\left(\Phi,t+\Delta t\right)=\int\limits_{\Phi-\text{space}}\Psi\left(\Phi-\varphi,\varphi,t\right)f\left(\Phi-\varphi,t\right)\,\mathrm{d}\varphi. \tag{29}$$

Following (*Roederer and Zhang*, 2014), we now use a Taylor expansion to develop each term of the above equation, which gives

$$f\left(\Phi,t+\Delta t\right)=f\left(\Phi,t\right)+\Delta t\,\frac{\partial f}{\partial t}\left(\Phi,t\right)$$

as a first order expansion in time,

$$f\left(\Phi-\varphi,t\right)=f\left(\Phi,t\right)-\varphi\,\frac{\partial f}{\partial\Phi}\left(\Phi,t\right)+\frac{\varphi^2}{2}\,\frac{\partial^2 f}{\partial\Phi^2}\left(\Phi,t\right)$$

as a second order expansion in Φ, and

$$\Psi\left(\Phi-\varphi,\varphi,t\right)=\Psi\left(\Phi,\varphi,t\right)-\varphi\,\frac{\partial\Psi}{\partial\Phi}\left(\Phi,\varphi,t\right)+\frac{\varphi^2}{2}\,\frac{\partial^2\Psi}{\partial\Phi^2}\left(\Phi,\varphi,t\right)$$

as a second order expansion in Φ. Equation (29) therefore becomes

$$\begin{aligned}f\left(\Phi,t\right)+\Delta t\,\frac{\partial f}{\partial t}\left(\Phi,t\right)=\int\limits_{\Phi-\text{space}}&\left[\Psi\left(\Phi,\varphi,t\right)-\varphi\,\frac{\partial\Psi}{\partial\Phi}\left(\Phi,\varphi,t\right)+\frac{\varphi^2}{2}\,\frac{\partial^2\Psi}{\partial\Phi^2}\left(\Phi,\varphi,t\right)\right]\\&\times\left[f\left(\Phi,t\right)-\varphi\,\frac{\partial f}{\partial\Phi}\left(\Phi,t\right)+\frac{\varphi^2}{2}\,\frac{\partial^2 f}{\partial\Phi^2}\left(\Phi,t\right)\right]\,\mathrm{d}\varphi.\end{aligned}$$

We can develop everything to obtain

$$\begin{aligned}&f\left(\Phi,t\right)+\Delta t\,\frac{\partial f}{\partial t}\left(\Phi,t\right)\\&=\int\limits_{\Phi-\text{space}}\Psi\left(\Phi,\varphi,t\right)f\left(\Phi,t\right)\,\mathrm{d}\varphi-\int\limits_{\Phi-\text{space}}\Psi\left(\Phi,\varphi,t\right)\varphi\,\frac{\partial f}{\partial\Phi}\left(\Phi,t\right)\,\mathrm{d}\varphi\\&+\int\limits_{\Phi-\text{space}}\Psi\left(\Phi,\varphi,t\right)\frac{\varphi^2}{2}\,\frac{\partial^2 f}{\partial\Phi^2}\left(\Phi,t\right)\,\mathrm{d}\varphi-\int\limits_{\Phi-\text{space}}\varphi\,\frac{\partial\Psi}{\partial\Phi}\left(\Phi,\varphi,t\right)f\left(\Phi,t\right)\,\mathrm{d}\varphi\\&+\int\limits_{\Phi-\text{space}}\varphi^2\frac{\partial\Psi}{\partial\Phi}\left(\Phi,\varphi,t\right)\frac{\partial f}{\partial\Phi}\left(\Phi,t\right)\,\mathrm{d}\varphi+\int\limits_{\Phi-\text{space}}\frac{\varphi^2}{2}\,\frac{\partial^2\Psi}{\partial\Phi^2}\left(\Phi,\varphi,t\right)f\left(\Phi,t\right)\,\mathrm{d}\varphi.\end{aligned}$$

We can extract from the integrands all the quantities that do no depend on the φ variable (including the partial derivative operator with respect to Φ), which leads to

$$\begin{aligned}
&f(\Phi,t)+\Delta t\,\frac{\partial f}{\partial t}(\Phi,t)\\
=&f(\Phi,t)\int_{\Phi-\text{space}}\Psi(\Phi,\varphi,t)\,\mathrm{d}\varphi-\frac{\partial f}{\partial\Phi}(\Phi,t)\int_{\Phi-\text{space}}\varphi\,\Psi(\Phi,\varphi,t)\,\mathrm{d}\varphi\\
+&\frac{1}{2}\frac{\partial^2 f}{\partial\Phi^2}(\Phi,t)\int_{\Phi-\text{space}}\varphi^2\,\Psi(\Phi,\varphi,t)\,\mathrm{d}\varphi-f(\Phi,t)\,\frac{\partial}{\partial\Phi}\left[\int_{\Phi-\text{space}}\varphi\,\Psi(\Phi,\varphi,t)\,\mathrm{d}\varphi\right]\\
+&\frac{\partial f}{\partial\Phi}(\Phi,t)\,\frac{\partial}{\partial\Phi}\left[\int_{\Phi-\text{space}}\varphi^2\Psi(\Phi,\varphi,t)\,\mathrm{d}\varphi\right]+\frac{1}{2}f(\Phi,t)\,\frac{\partial^2}{\partial\Phi^2}\left[\int_{\Phi-\text{space}}\varphi^2\,\Psi(\Phi,\varphi,t)\,\mathrm{d}\varphi\right].
\end{aligned}$$

By taking the first order diffusion coefficient as (*Roederer and Zhang*, 2014)

$$\Pi_\Phi=\frac{\langle\Delta\Phi\rangle}{\Delta t}=\frac{1}{\Delta t}\int_{\Phi-\text{space}}\varphi\Psi\,\mathrm{d}\varphi$$

and the second order diffusion coefficient as (*Roederer and Zhang*, 2014)

$$\Pi_{\Phi\Phi}=\frac{\langle\Delta(\Phi)^2\rangle}{\Delta t}=\frac{1}{\Delta t}\int_{\Phi-\text{space}}\varphi^2\Psi\,\mathrm{d}\varphi,$$

we end up with

$$\frac{\partial f}{\partial t}=-\Pi_\Phi\frac{\partial f}{\partial\Phi}-\frac{\mathrm{d}\Pi_\Phi}{\mathrm{d}\Phi}f+\frac{1}{2}\Pi_{\Phi\Phi}\frac{\partial^2 f}{\partial\Phi^2}+\frac{\mathrm{d}\Pi_{\Phi\Phi}}{\mathrm{d}\Phi}\frac{\partial f}{\partial\Phi}+\frac{1}{2}\frac{\mathrm{d}^2\Pi_{\Phi\Phi}}{\mathrm{d}\Phi^2}f.$$

to finally obtain

$$\frac{\partial f}{\partial t}=-\frac{\partial}{\partial\Phi}\left[\Pi_\Phi f\right]+\frac{1}{2}\frac{\partial^2}{\partial\Phi^2}\left[\Pi_{\Phi\Phi}f\right]. \tag{30}$$

It has been shown (*Fälthammar*, 1966; *Haerendel*, 1968) that it is possible to relate the first order diffusion coefficient Π_Φ with the second order diffusion coefficient $\Pi_{\Phi\Phi}$. Here we rather follow the straightforward approach carried out in (*Roederer and Zhang*, 2014). For this purpose, let us consider a uniform distribution function, such that

$$\frac{\partial f}{\partial t}=\frac{\partial}{\partial\Phi}\left[-\Pi_\Phi f+\frac{1}{2}\frac{\partial}{\partial\Phi}\left[\Pi_{\Phi\Phi}f\right]\right]=0,$$

i.e.

$$-\Pi_\Phi+\frac{1}{2}\frac{\partial}{\partial\Phi}\left[\Pi_{\Phi\Phi}\right]=0,$$

Hence both coefficients are related according to the following relation

$$\Pi_\Phi=\frac{1}{2}\frac{\mathrm{d}\Pi_{\Phi\Phi}}{\mathrm{d}\Phi}.$$

Going back to (30) we have,

$$\frac{\partial f}{\partial t} = -\frac{\partial}{\partial \Phi}\left[\frac{1}{2}\frac{\mathrm{d}\Pi_{\Phi\Phi}}{\mathrm{d}\Phi} f\right] + \frac{1}{2}\frac{\partial^2}{\partial \Phi^2}\left[\Pi_{\Phi\Phi} f\right],$$

$$\frac{\partial f}{\partial t} = -\frac{\partial}{\partial \Phi}\left[\frac{1}{2}\frac{\partial}{\partial \Phi}(\Pi_{\Phi\Phi} f) - \frac{1}{2}\Pi_{\Phi\Phi}\frac{\partial f}{\partial \Phi}\right] + \frac{1}{2}\frac{\partial^2}{\partial \Phi^2}\left[\Pi_{\Phi\Phi} f\right],$$

from which we deduce the 1-D Fokker-Planck equation, written as

$$\frac{\partial f}{\partial t} = \frac{1}{2}\frac{\partial}{\partial \Phi}\left[\Pi_{\Phi\Phi}\frac{\partial f}{\partial \Phi}\right].$$

Taking $D_{\Phi\Phi} = \frac{1}{2}\Pi_{\Phi\Phi}$ we finally obtain (*Roederer and Zhang*, 2014)

$$\frac{\partial f}{\partial t} = \frac{\partial}{\partial \Phi}\left[D_{\Phi\Phi}\frac{\partial f}{\partial \Phi}\right]. \tag{31}$$

C.2 Some useful Jacobian transformations

This section is devoted to the derivation of the most useful Jacobian determinants that are considered in radiation belt physics. Since the adiabatic invariants are not directly appropriate to relate theory with observations, the computation of the Jacobian determinants is necessary to build more convenient noncanonical Fokker-Planck equations. This section gathers the Jacobian transformations available in (*Roederer*, 1970; *Schulz and Lanzerotti*, 1974; *Subbotin and Shprits*, 2012).

C.2.a Transformations within the invariant space

Such transformations do not require the knowledge of a specific magnetic field, so that the expressions presented below are very general.

(i) From (J_1, J_2, J_3) to (μ, J, Φ)

Since $J_1 = \dfrac{2\pi m_0 \mu}{q}$, $J_2 = J$ and $J_3 = q\Phi$, we simply obtain

$$G = \begin{vmatrix} \dfrac{\partial J_1}{\partial \mu} & \dfrac{\partial J_1}{\partial J} & \dfrac{\partial J_1}{\partial \Phi} \\ \dfrac{\partial J_2}{\partial \mu} & \dfrac{\partial J_2}{\partial J} & \dfrac{\partial J_2}{\partial \Phi} \\ \dfrac{\partial J_3}{\partial \mu} & \dfrac{\partial J_3}{\partial J} & \dfrac{\partial J_3}{\partial \Phi} \end{vmatrix} = \begin{vmatrix} 2\pi\dfrac{m_0}{q} & 0 & 0 \\ 0 & 1 & 0 \\ 0 & 0 & q \end{vmatrix}$$

i.e.

$$G(J_1, J_2, J_3; \mu, J, \Phi) = 2\pi m_0.$$

(ii) From (μ, J, Φ) to (μ, K, L^*)

Since $J = 2\sqrt{2m_0\mu}K$ and $\Phi = \dfrac{2\pi R_E^2 B_E}{L^*}$ we obtain

$$G = \begin{vmatrix} \dfrac{\partial\mu}{\partial\mu} & \dfrac{\partial\mu}{\partial K} & \dfrac{\partial\mu}{\partial L^*} \\ \dfrac{\partial J}{\partial\mu} & \dfrac{\partial J}{\partial K} & \dfrac{\partial J}{\partial L^*} \\ \dfrac{\partial\Phi}{\partial\mu} & \dfrac{\partial\Phi}{\partial K} & \dfrac{\partial\Phi}{\partial L^*} \end{vmatrix} = \begin{vmatrix} 1 & 0 & 0 \\ \dfrac{K\sqrt{2m_0}}{\sqrt{\mu}} & 2\sqrt{2m_0\mu} & 0 \\ 0 & 0 & \dfrac{2\pi R_E^2 B_E}{L^{*2}} \end{vmatrix}$$

so that

$$G(\mu, J, \Phi; \mu, K, L^*) = 4\sqrt{2}\pi B_E \frac{R_E^2}{L^{*2}}\sqrt{m_0\mu}.$$

(iii) From (J_1, J_2, J_3) to (μ, K, L^*)

We deduce $G(J_1, J_2, J_3; \mu, K, L^*)$ as

$$\begin{aligned} G(J_1, J_2, J_3; \mu, K, L^*) &= G(J_1, J_2, J_3; \mu, J, \Phi) \times G(\mu, J, \Phi; \mu, K, L^*) \\ &= 8\sqrt{2}\pi^2 B_E \frac{R_E^2}{L^{*2}} m_0^{3/2}\sqrt{\mu}. \end{aligned}$$

(iv) From Φ to L^*

We simply have

$$G(\Phi; L^*) = \frac{2\pi R_E^2 B_E}{L^{*2}}.$$

C.2.b Transformation from the adiabatic space to the physical space

The transformations from the adiabatic space to the physical space require the use of a magnetic field model. In practice (as discussed in Chapter 6) the centered dipole field is used because of its associated semi-analytical expressions.

(i) From (μ, J) to (p, x_0)

In a dipole field, we recall that $\mu = \dfrac{p^2 y_0^2 L^3}{2m_0 B_E}$ and $J = 2pLR_E Y(y_0)$, so that

$$G = \begin{vmatrix} \dfrac{\partial\mu}{\partial p} & \dfrac{\partial\mu}{\partial x_0} \\ \dfrac{\partial J}{\partial p} & \dfrac{\partial J}{\partial x_0} \end{vmatrix} = \begin{vmatrix} \gamma\dfrac{py_0^2L^3}{m_0B_E} & -x_0\dfrac{p^2L^3}{m_0B_E} \\ 2LR_EY(y_0) & -2pLR_E\dfrac{x_0}{y_0}Y'(y_0) \end{vmatrix}.$$

Knowing that $Y(y_0) - y_0Y'(y_0) = 2T(y_0)$ we finally find

$$G(\mu, J; p, x_0) = \frac{4p^2L^4}{m_0}\left(\frac{R_E}{B_E}\right)x_0T(y_0).$$

(ii) From (μ, J) to (E, x_0)
We simply use the fact that $p\,\mathrm{d}p = \gamma m_0\,\mathrm{d}E$ (cf equation (2.61)), so

$$\begin{aligned} G(\mu, J; E, x_0) &= \frac{\mathrm{d}p}{\mathrm{d}E} G(\mu, J; p, x_0) \\ &= \frac{\gamma m_0}{p} G(\mu, J; p, x_0), \end{aligned}$$

i.e.

$$G(\mu, J; E, x_0) = 4\gamma p L^4 \left(\frac{R_E}{B_E}\right) x_0 T(y_0).$$

(iii) From (μ, J) to (p, α_0)
The previous results lead to

$$\begin{aligned} G(\mu, J; p, \alpha_0) &= \frac{\mathrm{d}x_0}{\mathrm{d}\alpha_0} G(\mu, J; p, x_0) \\ &= y_0\, G(\mu, J; p, x_0), \end{aligned}$$

i.e.

$$\begin{aligned} G(\mu, J; p, \alpha_0) &= \frac{4p^2 L^4}{m_0} \left(\frac{R_E}{B_E}\right) \cos(\alpha_0) \sin(\alpha_0) T(y_0) \\ &= \frac{2p^2 L^4}{m_0} \left(\frac{R_E}{B_E}\right) \sin(2\alpha_0) T(y_0). \end{aligned}$$

(iv) From (μ, J) to (E, α_0)
Again it is straightforward to have

$$\begin{aligned} G(\mu, J; E, \alpha_0) &= \frac{\mathrm{d}x_0}{\mathrm{d}\alpha_0} G(\mu, J; E, x_0) \\ &= y_0\, G(\mu, J; E, x_0), \end{aligned}$$

i.e.

$$\begin{aligned} G(\mu, J; E, \alpha_0) &= 4\gamma p L^4 \left(\frac{R_E}{B_E}\right) \cos(\alpha_0) \sin(\alpha_0) T(y_0) \\ &= 2\gamma p L^4 \left(\frac{R_E}{B_E}\right) \sin(2\alpha_0) T(y_0). \end{aligned}$$

(v) From (μ, J, Φ) to (p, x_0, L)
Using the same idea as before, we obtain

$$\begin{aligned} G(\mu, J, \Phi; p, x_0, L) &= G(\Phi; L^*) \times G(\mu, J; p, x_0) \\ &= \frac{2\pi R_E^2 B_E}{L^{*2}} \times G(\mu, J; p, x_0), \end{aligned}$$

i.e.

$$G(\mu, J, \Phi; p, x_0, L) = \frac{8\pi R_E^3}{m_0} p^2 L^2 x_0 T(y_0).$$

(vi) From (μ, J, Φ) to (E, x_0, L)
Again

$$\begin{aligned} G(\mu, J, \Phi; E, x_0, L) &= G(\Phi; L^*) \times G(\mu, J; E, x_0) \\ &= \frac{2\pi R_E^2 B_E}{L^{*2}} \times G(\mu, J; E, x_0), \end{aligned}$$

so that

$$G(\mu, J, \Phi; E, x_0, L) = 8\pi\gamma p L^2 R_E^3 x_0 T(y_0).$$

(vii) From (μ, J, Φ) to (p, α_0, L)

$$\begin{aligned} G(\mu, J, \Phi; p, \alpha_0, L) &= G(\Phi; L^*) \times G(\mu, J; p, \alpha_0) \\ &= \frac{2\pi R_E^2 B_E}{L^{*2}} \times G(\mu, J; p, \alpha_0), \end{aligned}$$

i.e.

$$\begin{aligned} G(\mu, J, \Phi; p, \alpha_0, L) &= \frac{8\pi R_E^3}{m_0} p^2 \sin(\alpha_0) \cos(\alpha_0) L^2 T(\alpha_0) \\ &= \frac{4\pi R_E^3}{m_0} p^2 \sin(2\alpha_0) L^2 T(\alpha_0). \end{aligned}$$

(viii) From (μ, J, Φ) to (E, α_0, L)

$$\begin{aligned} G(\mu, J, \Phi; E, \alpha_0, L) &= G(\Phi; L^*) \times G(\mu, J; E, \alpha_0) \\ &= \frac{2\pi R_E^2 B_E}{L^{*2}} \times G(\mu, J; E, \alpha_0), \end{aligned}$$

i.e.

$$\begin{aligned} G(\mu, J, \Phi; E, \alpha_0, L) &= 8\pi R_E^3 \gamma p \sin(\alpha_0) \cos(\alpha_0) L^2 T(\alpha_0) \\ &= 4\pi R_E^3 \gamma p \sin(2\alpha_0) L^2 T(\alpha_0). \end{aligned}$$

D On the analytical solution of the diffusion equation

D.1 Properties of a Sturm-Liouville problem

Before giving some proofs of the enumerated properties of the eigenvalues and eigenfunctions of the Sturm-Liouville problem

$$\mathcal{L}\varphi \equiv \left(p\varphi^{'}\right)^{'} - q\varphi = \lambda\sigma\varphi,$$

let us first emphasize two useful identities.

D.1.a Identities

Here we follow the properties derived in (*Cain and Meyer*, 2005).

Lagrange's identity

Let φ and ψ be two functions that satisfy the Sturm-Liouville problem. Then the Lagrange identities states that

$$\varphi\mathcal{L}\psi - \psi\mathcal{L}\varphi = \left[p(\varphi\psi^{'} - \psi\varphi^{'})\right]^{'}.$$

Proof:

$$\begin{aligned}
\varphi\mathcal{L}\psi - \psi\mathcal{L}\varphi &= \varphi\left[\left(p\psi^{'}\right)^{'} - q\psi\right] - \psi\left[\left(p\varphi^{'}\right)^{'} - q\varphi\right] \\
&= \varphi\left(p\psi^{'}\right)^{'} - \psi\left(p\varphi^{'}\right)^{'} \\
&= \varphi\left(p^{'}\psi^{'} + p\psi^{''}\right) - \psi\left(p^{'}\varphi^{'} - p\varphi^{''}\right) \\
&= p^{'}\varphi\psi^{'} + p\varphi\psi^{''} - p^{'}\psi\varphi^{'} - p\psi\varphi^{''} \\
&= p^{'}\varphi\psi^{'} + p\varphi^{'}\psi^{'} + p\varphi\psi^{''} - p^{'}\psi\varphi^{'} - p\psi^{'}\varphi^{'} - p\psi\varphi^{''} \\
&= \left(p\varphi\psi^{'}\right)^{'} - \left(p\psi\varphi^{'}\right)^{'} \\
&= \left[p(\varphi\psi^{'} - \psi\varphi^{'})\right]^{'}.
\end{aligned}$$

Green's identity

The Green's identity is simply the integrand form of the Laplace's identity, yielding to

$$\int_{L_0}^{L_M} (\varphi\mathcal{L}\psi - \psi\mathcal{L}\varphi)\ \mathrm{d}L = \left[p(\varphi\psi^{'} - \psi\varphi^{'})\right]_{L_0}^{L_M}.$$

D.1.b Eigenvalues

The eigenvalues of the Sturm-Liouville problem are real

Proof: the Strum-Liouville problem related to the solution φ asserts that φ verifies $\mathcal{L}\varphi = \lambda\sigma\varphi$ for the φ function, and its complex conjugate $\bar{\varphi}$ verifies $\mathcal{L}\bar{\varphi} = \bar{\lambda}\sigma\bar{\varphi}$. Hence

$$\bar{\varphi}\mathcal{L}\varphi - \varphi\mathcal{L}\bar{\varphi} = (\lambda - \bar{\lambda})\sigma|\varphi|^2,$$

and after integrating the above equality we obtain

$$\int_{L_0}^{L_M} [\bar{\varphi}\mathcal{L}\varphi - \varphi\mathcal{L}\bar{\varphi}] \, \mathrm{d}L = (\lambda - \bar{\lambda}) \int_{L_0}^{L_M} \sigma|\varphi|^2 \, \mathrm{d}L.$$

By using the Green's identity on the left-hand side, we end up with

$$\left[p(\bar{\varphi}\varphi^{'} - \varphi\bar{\varphi}^{'})\right]_{L_0}^{L_M} = (\lambda - \bar{\lambda}) \int_{L_0}^{L_M} \sigma|\varphi|^2 \, \mathrm{d}L.$$

From the boundary conditions, the left-hand side term vanishes, so that

$$(\lambda - \bar{\lambda}) \int_{L_0}^{L_M} \sigma|\varphi|^2 \, \mathrm{d}L = 0,$$

i.e. $\lambda = \bar{\lambda}$. Hence the eigenvalues are real.

Rayleigh Quotient and positivity

Starting from the Sturm-Liouville problem itself, $\mathcal{L}\varphi = \lambda\sigma\varphi$, we can multiply both sides by the complex conjugate $\overline{\varphi}$ of eigenfunction φ to obtain

$$\overline{\varphi}(x)\mathcal{L}\varphi = \lambda\sigma|\varphi|^2,$$

i.e.

$$\int_{L_0}^{L_M} \bar{\varphi}\mathcal{L}\varphi \, \mathrm{d}L = \lambda \int_{L_0}^{L_M} \sigma|\varphi|^2 \, \mathrm{d}L.$$

Hence, from the definition of the $\mathcal{L}$ operator we have

$$\int_{L_0}^{L_M} \bar{\varphi} \left[\left(p\varphi^{'}\right)^{'} - q\varphi \right] \, \mathrm{d}L = \lambda \int_{L_0}^{L_M} \sigma|\varphi|^2 \, \mathrm{d}L,$$

so that

$$\int_{L_0}^{L_M} \bar{\varphi} \left(p\varphi^{'}\right)^{'} \, \mathrm{d}L - \int_{L_0}^{L_M} q|\varphi|^2 \, \mathrm{d}L = \lambda \int_{L_0}^{L_M} \sigma|\varphi|^2 \, \mathrm{d}L.$$

The integration by parts of the first term of the above equation yields

$$\left[\bar{\varphi}p\varphi^{'}\right]_{L_0}^{L_M} - \int_{L_0}^{L_M} \bar{\varphi}^{'}p\varphi^{'} \, \mathrm{d}L - \int_{L_0}^{L_M} q|\varphi|^2 \, \mathrm{d}L = \lambda \int_{L_0}^{L_M} \sigma|\varphi|^2 \, \mathrm{d}L,$$

i.e.

$$\left[p\bar{\varphi}\varphi^{'}\right]_{L_0}^{L_M} - \int_{L_0}^{L_M} p|\varphi^{'}|^2 \, \mathrm{d}L - \int_{L_0}^{L_M} q|\varphi|^2 \, \mathrm{d}L = \lambda \int_{L_0}^{L_M} \sigma|\varphi|^2 \, \mathrm{d}L.$$

Hence

$$\lambda = \frac{\left[p\bar{\varphi}\varphi^{'}\right]_{L_0}^{L_M} - \int_{L_0}^{L_M}\left[p|\varphi^{'}|^2 + q|\varphi|^2\right]\,\mathrm{d}L}{\int_{L_0}^{L_M}\sigma|\varphi|^2\,\mathrm{d}L},$$

which is called the Rayleigh quotient. Expanding the first term leads to

$$\lambda = \frac{p(L_M)\bar{\varphi}(L_M)\varphi^{'}(L_M) - p(L_0)\bar{\varphi}(L_0)\varphi^{'}(L_0) - \int_{L_0}^{L_M}\left[p|\varphi^{'}|^2 + q|\varphi|^2\right]\,\mathrm{d}L}{\int_{L_0}^{L_M}\sigma|\varphi|^2\,\mathrm{d}L},$$

and considering the boundary conditions, we obtain

$$\lambda = \frac{p(L_M)\left(\frac{b_1}{b_2}\right)|\varphi(L_M)|^2 - p(L_0)\left(\frac{a_1}{a_2}\right)|\varphi(L_0)|^2 - \int_{L_0}^{L_M}\left[p|\varphi^{'}|^2 + q|\varphi|^2\right]\,\mathrm{d}L}{\int_{L_0}^{L_M}\sigma|\varphi|^2\,\mathrm{d}L}.$$

From above, we conclude that if $a_1/a_2 > 0$, $b_1/b_2 < 0$ and $q > 0$, the eigenvalues λ_n are all negative.

D.1.c Eigenfunctions

The eigenfunctions that correspond to distinct eigenvalues are orthogonal

Proof: let us consider two different eigenfunctions φ_m and φ_n solutions of the Sturm Liouville problem, corresponding to the two distinct eigenvalues λ_n and λ_m,

$$\begin{cases} \mathcal{L}\varphi_n = \lambda_n\sigma\varphi_n, \\ \\ \mathcal{L}\varphi_m = \lambda_m\sigma\varphi_m. \end{cases}$$

Multiplying both equalities by the respective counterpart eigenfunction leads to

$$\begin{cases} \varphi_m\mathcal{L}\varphi_n = \lambda_n\sigma\varphi_m\varphi_n, \\ \\ \varphi_n\mathcal{L}\varphi_m = \lambda_m\sigma\varphi_n\varphi_m. \end{cases}$$

Subtracting one equality by the other, and integrating in the interval $[L_0, L_M]$ yields

$$\int_{L_0}^{L_M}\left[\varphi_m\mathcal{L}\varphi_n - \varphi_n\mathcal{L}\varphi_m\right]\,\mathrm{d}L = (\lambda_n - \lambda_m)\int_{L_0}^{L_M}\varphi_m\varphi_n\,\mathrm{d}L,$$

so that

$$\int_{L_0}^{L_M}\varphi_m\left[\left(p\varphi_n^{'}\right)^{'} - q\varphi_n\right]\,\mathrm{d}L - \int_{L_0}^{L_M}\varphi_n\left[\left(p\varphi_m^{'}\right)^{'} - q\varphi_m\right]\,\mathrm{d}L = (\lambda_n - \lambda_m)\int_{L_0}^{L_M}\varphi_m\varphi_n\,\mathrm{d}L,$$

and after removing the cancelling terms we obtain

$$\int_{L_0}^{L_M}\varphi_m\left(p\varphi_n^{'}\right)^{'}\,\mathrm{d}L - \int_{L_0}^{L_M}\varphi_n\left(p\varphi_m^{'}\right)^{'}\,\mathrm{d}L = (\lambda_n - \lambda_m)\int_{L_0}^{L_M}\varphi_m\varphi_n\,\mathrm{d}L.$$

We now integrate by parts the two terms in the right-hand side of the above equation to obtain

$$\left[\varphi_m p \varphi_n^{'}\right]_{L_0}^{L_M} - \int_{L_0}^{L_M} \varphi_m^{'} p \varphi_n^{'} \, \mathrm{d}L - \left[\varphi_n p \varphi_m^{'}\right]_{L_0}^{L_M} + \int_{L_0}^{L_M} \varphi_n^{'} p \varphi_m^{'} \, \mathrm{d}L = (\lambda_n - \lambda_m) \int_{L_0}^{L_M} \varphi_m \varphi_n \, \mathrm{d}L.$$

The first and third terms cancel, as for the second and fourth term, so that the expression on right-hand side vanishes, and the above equation simply reduces to

$$(\lambda_n - \lambda_m) \int_{L_0}^{L_M} \varphi_m \varphi_n \, \mathrm{d}L = 0.$$

Since we made the assumption that λ_m and λ_n are distinct eigenvalues, we end up with

$$\langle \varphi_n, \varphi_m \rangle = 0,$$

which means that the eigenfunctions corresponding to distinct eigenvalues are orthogonal.

D.1.d Solution of a specific Sturm-Liouville problem

We consider the following general equation

$$x^2 u^{''} + x \left[a + 2bx^p\right] u^{'} + \left[c + dx^{2q} + b(a + p - 1)x^p + b^2 x^{2p}\right] u = 0, \tag{32}$$

for which $(1 - a)^2 \geq 4c$ and $d, p, q \neq 0$. Setting

$$\alpha = \frac{1 - a}{2}, \qquad \beta = \frac{b}{p}, \qquad \Lambda = \frac{\sqrt{|d|}}{|q|}, \qquad \nu = \frac{\sqrt{(1 - a)^2 - 4c}}{2q},$$

the corresponding solutions are summarized in the Table below (*Cain and Meyer*, 2005)

$d > 0$ (Bessel functions)	$u(L) = L^{\alpha} e^{-\beta L^p} \left[c_1 J_{\nu}\left(\Lambda L^q\right) + c_2 Y_{\nu}\left(\Lambda L^q\right)\right]$
$d < 0$ (Modified Bessel functions)	$u(L) = L^{\alpha} e^{-\beta L^p} \left[c_1 I_{\nu}\left(\Lambda L^q\right) + c_2 K_{\nu}\left(\Lambda L^q\right)\right]$

for which the coefficients c_1 and c_2 are determined thanks to the boundary conditions.

D.2 Decomposition in space and identification to the global problem

In this section, we prove, following (*Loridan et al.*, 2017), that solving the equation governing the evolution of the distribution function $f(L, t)$ on the whole domain $[L_0, L_M]$ with a piecewise-constant loss term is equivalent to solve M radial diffusion equations, each one governing the evolution of $f^i(L, t)$ on subinterval $[L_{i-1}, L_i]$ with a constant loss term τ_i along with interface conditions.

Let us first define the radial diffusion operator $\mathcal{L}$ by

$$\mathcal{L} \equiv -\frac{\partial}{\partial t} + D_0 L^n \frac{\partial^2}{\partial L^2} + (n - 2) D_0 L^{n-1} \frac{\partial}{\partial L} - \frac{1}{\tau}$$

and suppose that $f(L,t)$ verifies $\mathcal{L}f = 0$ on the whole domain $[L_0, L_M]$. Now, let us assume $f(L,t)$ to be defined as $f(L,t) = \sum_{i=1}^{M} \mathbb{1}_i(L)\, f^i(L,t)$, where

$$\mathbb{1}_i(L) = \begin{cases} \mathbb{1}_{]-\infty, L_1]}(L) & \text{if } i = 1, \\ \mathbb{1}_{[L_{i-1}, L_i]}(L) & \text{if } i \in [2, M-1], \\ \mathbb{1}_{[L_{M-1}, +\infty[}(L) & \text{if } i = M, \end{cases}$$

with $\mathbb{1}_A(L)$ representing the indicator function of a subset A of $\mathbb{R}$. As mentioned in the main text, we have set the interval limits of the function $\mathbb{1}_i(L)$ at $-\infty$ to $+\infty$ to avoid any abrupt slopes at both the boundary values L_0 and L_M. The differentiation of f with respect to variable t simply gives

$$\frac{\partial f}{\partial t}(L,t) = \sum_{i=1}^{M} \mathbb{1}_i(L)\, \frac{\partial f^i}{\partial t}(L,t).$$

The differentiation with respect to L gives

$$\begin{aligned} \frac{\partial f}{\partial L}(L,t) = &- \delta(L - L_1)\, f^1(L,t) + \delta(L - L_{M-1})\, f^M(L,t) \\ &+ \sum_{i=2}^{M-1} \left[\delta(L - L_{i-1}) - \delta(L - L_i)\right]\, f^i(L,t) + \sum_{i=1}^{M} \mathbb{1}_i(L)\, \frac{\partial f^i}{\partial L}(L,t), \end{aligned}$$

where $\delta(L)$ corresponds to the common delta Dirac function. Using the continuity at the interface condition (3.20a) allows us to cancel the interface terms and to obtain $\frac{\partial f}{\partial L}(L,t) = \sum_{i=1}^{M} \mathbb{1}_i(L)\, \frac{\partial f^i}{\partial L}(L,t)$. Similarly, the second order derivative reads

$$\begin{aligned} \frac{\partial^2 f}{\partial L^2}(L,t) = &- \delta(L - L_1)\, \frac{\partial f^1}{\partial L}(L,t) + \delta(L - L_{M-1})\, \frac{\partial f^M}{\partial L}(L,t) \\ &+ \sum_{i=2}^{M-1} \left[\delta(L - L_{i-1}) - \delta(L - L_i)\right]\, \frac{\partial f^i}{\partial L}(L,t) + \sum_{i=1}^{M} \mathbb{1}_i(L)\, \frac{\partial^2 f^i}{\partial L^2}(L,t), \end{aligned}$$

and using the interface condition (3.20b) we obtain $\frac{\partial^2 f}{\partial L^2}(L,t) = \sum_{i=1}^{M} \mathbb{1}_i(L)\, \frac{\partial^2 f^i}{\partial L^2}(L,t)$. The last term f/τ can also be written as

$$\begin{aligned} \frac{f(L,t)}{\tau(L)} &= \left(\sum_{i=1}^{M} \mathbb{1}_i(L)\, f^i(L,t)\right) \left(\sum_{l=1}^{M} \mathbb{1}_l(L)\, \frac{1}{\tau_l}\right) \\ &= \sum_{i=1}^{M}\sum_{l=1}^{M} \mathbb{1}_i(L)\mathbb{1}_l(L)\, \frac{f^i(L,t)}{\tau_l} = \sum_{i=1}^{M}\sum_{l=1}^{M} \delta_{i,l}\, \mathbb{1}_i(L)\, \frac{f^i(L,t)}{\tau_l} = \sum_{i=1}^{M} \mathbb{1}_i(L) \frac{f^i(L,t)}{\tau_i} \end{aligned}$$

where $\delta_{i,l}$ is the common Kronecker delta symbol. Combining all terms together (loss-term, first-order differentiation with respect to t and L, second-order differentiation with respect to L) gives $\mathcal{L}f = \sum_{i=1}^{M} \mathbb{1}_i(L)\mathcal{L}f^i$. Since $\mathcal{L}f = 0$ and all subintervals are disjoint to each other except at the interface points, we deduce that $\mathcal{L}f^i = 0$ on the subinterval $[L_{i-1}, L_i]$, i.e.

$$-\frac{\partial f^i}{\partial t} + D_0 L^n \frac{\partial^2 f^i}{\partial L^2} + (n-2) D_0 L^{n-1} \frac{\partial f^i}{\partial L} - \frac{f^i}{\tau_i} = 0.$$

Consequently, the solution, f, of the global radial diffusion equation (3.19) involving a piecewise-constant electron lifetime τ, being continuous with continuous derivatives, is expressible as the superposition of the solutions, f_i, solved on each subinterval related to a constant electron lifetime τ_i, as soon as continuity (of f and $\partial f/\partial L$) is enforced at the interface. This property is essential in Chapter 3 and in the article of (*Loridan et al.*, 2017) as it allows the decomposition of the Sturm-Liouville problem into M subproblems.

D.3 Solving for the steady solution

In this section we derive the full steady solution $f_\infty(L)$ for $n \neq 2$ (*Loridan et al.*, 2017). Let $f^i_\infty(L)$ be the steady solution of the radial diffusion problem on a subinterval $[L_{i-1}, L_i]$ such that

$$D_0 L^n \frac{\mathrm{d}^2 f^i_\infty}{\mathrm{d}L^2} + (n-2) D_0 L^{n-1} \frac{\mathrm{d}f^i_\infty}{\mathrm{d}L} - \frac{1}{\tau_i} f^i_\infty = 0,$$

with interface conditions ($i \in [1, M]$)

$$f^i_\infty(L_i) = f^{i+1}_\infty(L_i) \tag{33a}$$

$$\frac{\mathrm{d}f^i_\infty}{\mathrm{d}L}(L_i) = \frac{\mathrm{d}f^{i+1}_\infty}{\mathrm{d}L}(L_i), \tag{33b}$$

and two boundary conditions

$$f^1_\infty(L_0) = 0, \tag{34a}$$

$$f^M_\infty(L_M) = f_{L_M}. \tag{34b}$$

Taking $\beta_i = \dfrac{2}{(n-2)\sqrt{\tau_i D_0}}$, $\nu = \left|\dfrac{n-3}{n-2}\right|$, $p = \dfrac{n-2}{2}$ and $q = \dfrac{n-3}{2}$, the solution is tractable and can be expressed in terms of modified Bessel functions I_ν and K_ν of fractional order ν, (*Mei*, 1997). We write it under the form

$$f^i_\infty(L) = L^{-q}\left[A^i I_\nu\left(\beta_i L^{-p}\right) + B^i K_\nu\left(\beta_i L^{-p}\right)\right]$$

where A^i and B^i are two constants determined by the interface condition (equations (33a) and (33b)) and boundary conditions (see (34a) and (34b)). To facilitate readability, we note $U^i(L) = L^{-q} I_\nu\left(\beta_i L^{-p}\right)$ and $V^i(L) = L^{-q} K_\nu\left(\beta_i L^{-p}\right)$ so that $f^i_\infty(L) = A^i U^i(L) + B^i V^i(L)$.

The functional form we use for the steady solution, expressed in terms of modified Bessel functions I_ν and K_ν is consistent with previous formulations (e.g., *Haerendel*, 1968; *Schulz*, 1986; *Schulz and Newman*, 1988). If the order ν is not an integer (which happens in most cases, for example if $n = 6$ or $n = 10$), the steady solution can also be expressed in terms of $I_{+\nu}$ and $I_{-\nu}$. Since $I_{-\nu}(x) = I_\nu(x) + 2\sin(\nu\pi)/\pi K_\nu(x)$, any solution $u(x) = AI_\nu(x) + BK_\nu(x)$ can also be written $u(x) = CI_{+\nu}(x) + DI_{-\nu}(x)$, with $C = A - \pi B/(2\sin(\nu\pi))$ and $D = \pi/(2\sin(\nu\pi))B$.

The system formed by (34a), (33a), (33b) and (34b) could be written with a matrix representation as $\sum_{l=1}^{2M} \mathbb{G}^{il} X^l = F^i$ such that $\mathbb{G}X = F$. We could obtain the coefficients $\left(X^{2i-1}, X^{2i}\right) \equiv \left(A^i, B^i\right)$ by performing numerically the operation $X = \mathbb{G}^{-1} F$. However a better method found here is to solve directly this system by hand, taking one equation after another, as described in the next subsection.

The first boundary condition $f^1_\infty(L_0) = 0$ leads to

$$A^1 U^1(L_0) + B^1 V^1(L_0) = 0$$

so that $A^1 = F^1 B^1$ with $F^1 = -V^1(L_0)/U^1(L_0)$. Therefore

$$f_\infty^1(L) = \left[F^1 U^1(L) + V^1(L)\right] B^1.$$

The second boundary condition $f_\infty^M(L_M) = f_{L_M}$ leads to

$$A^M U^M(L_M) + B^M V^M(L_M) = f_{L_M}$$

so that $A^M = F^M B^M + G^M$ with $F^M = -V^M(L_M)/U^M(L_M)$ and $G^M = f(L_M)/U^M(L_M)$. Therefore

$$f_\infty^M(L) = \left[F^M U^M(L) + V^M(L)\right] B^M + G^M U^M(L).$$

Successively, starting from the expression of $f_\infty^1(L)$ we obtain by using respectively the interface conditions $f_\infty^i(L_i) = f_\infty^{i+1}(L_i)$

$$\left[F^i U^i(L_i) + V^i(L_i)\right] B^i = A^{i+1} U^{i+1}(L_i) + B^{i+1} V^{i+1}(L_i).$$

Moreover using the second interface condition $\dfrac{\mathrm{d}f_\infty^i}{\mathrm{d}L}(L_i, t) = \dfrac{\mathrm{d}f_\infty^{i+1}}{\mathrm{d}L}(L_i, t)$ one gets for L_i ($i \in [1, M-2]$)

$$\left[F^i U^{i'}(L_i) + V^{i'}(L_i)\right] B^i = A^{i+1} U^{i+1'}(L_i) + B^{i+1} V^{i+1'}(L_i).$$

Combining the two previous equations gives a closed-form expression for B^i

$$B^i = \frac{A^{i+1} U^{i+1}(L_i) + B^{i+1} V^{i+1}(L_i)}{F^i U^i(L_i) + V^i(L_i)} = \frac{A^{i+1} U^{i+1'}(L_i) + B^{i+1} V^{i+1'}(L_i)}{F^i U^{i'}(L_i) + V^{i'}(L_i)}, \tag{35}$$

which leads to $A^{i+1} = F^{i+1} B^{i+1}$ with

$$F^{i+1} = -\left(\frac{V^{i+1}(L_i)}{U^{i+1}(L_i)}\right)^2 \frac{\left(\dfrac{F^i U^i(L_i) + V^i(L_i)}{V^{i+1}(L_i)}\right)'}{\left(\dfrac{F^i U^i(L_i) + V^i(L_i)}{U^{i+1}(L_i)}\right)'}. \tag{36}$$

In order to close the system, we write the two interface conditions at L_{M-1}, by using the same method and the expression giving $f_\infty^M(L)$. It gives the two following equations

$$\begin{aligned} &\left[F^{M-1} U^{M-1}(L_{M-1}) + V^{M-1}(L_{M-1})\right] B^{M-1} \\ &= \left[F^M U^M(L_{M-1}) + V^M(L_{M-1})\right] B^M + G^M U^M(L_{M-1}) \end{aligned}$$

and

$$\begin{aligned} &\left[F^{M-1} U^{M-1'}(L_{M-1}) + V^{M-1'}(L^{M-1})\right] B^{M-1} \\ &= \left[F^M U^{M'}(L_{M-1}) + V^{M'}(L_{M-1})\right] B^M + G^M U^{M'}(L_{M-1}). \end{aligned}$$

Combining together the two previous equations to equate B_{M-1}, it gives an expression for B_M,

$$B^M = G^M \frac{C_{M-1}}{D_{M-1}}, \tag{37}$$

with

$$\begin{aligned} C_{M-1} = &\left[F^{M-1} U^{M-1}(L_{M-1}) + V^{M-1}(L_{M-1})\right] U^{M'}(L_{M-1}) \\ &- \left[F^{M-1} U^{M-1'}(L_{M-1}) + V^{M-1'}(L_{M-1})\right] U^M(L_{M-1}) \end{aligned}$$

and

$$D_{M-1} = \left[F^M U^M(L_{M-1}) + V^M(L_{M-1})\right]\left[F^{M-1}U^{M-1'}(L_{M-1}) + V^{M-1'}(L_{M-1})\right] - \left[F^M U^{M'}(L_{M-1}) + V^{M'}(L_{M-1})\right]\left[F^{M-1}U^{M-1}(L_{M-1}) + V^{M-1}(L_{M-1})\right].$$

One understands that the solution is built analytically and is iteratively coupled from one equation to the other, passing successively from one interval to another. First we are able to calculate the coefficients F_1, F_i from (36), F_M and G_M. Second, from (37), the coefficient B^M is found and so we obtain A^M. Using (35) we recursively obtain all the B^i and deduce all the A^i, for $i \in [1, M-1]$.

D.4 Solving for the dynamic solution

In this section we derive the full transient solution $w(L,t)$ for any $n \neq 2$ (*Loridan et al.*, 2017). Instead of solving the main problem for the PSD, $f(L,t)$, we perform a translation and solve now the problem relatively to the function $w(L,t) = f(L,t) - f_\infty(L)$, which has the convenient property to be zero at the two boundary conditions by construction, i.e. $w(L_0,t) = w(L_M,t) = 0$. The initial condition becomes $w(L,0) = w_0(L) = f_0(L) - f_\infty(L)$. Taking the radial diffusion operator $\mathcal{L}$ defined above, the problem can be restated for $w(L,t)$ as $\mathcal{L}w = \mathcal{L}f - \mathcal{L}f_\infty = 0$ which satisfies the above homogeneous set of boundary conditions at $L = L_0$ and $L = L_M$. The partial differential equation $\mathcal{L}w = 0$ can be written in the form $\mathcal{L}w(L,t) = \mathcal{L}_1(L)w + \mathcal{L}_2(t)w$, in which $\mathcal{L}_1$ denotes the terms involving the spatial derivatives

$$\mathcal{L}_1(L)w = D_0 L^n \frac{\partial^2 w}{\partial L^2} + (n-2)D_0 L^{n-1}\frac{\partial w}{\partial L} - \frac{1}{\tau}w,$$

and $\mathcal{L}_2$ denotes the terms involving the temporal derivatives

$$\mathcal{L}_2(t)w = -\frac{\partial w}{\partial t}.$$

The form of $\mathcal{L}w = 0$ suggests a time-dependant solution $w(L,t) = \sum_{k=1}^{\infty} \alpha_k(t) g_k(L)$ in which $g_k(L)$ are the eigenfunctions of the operator $\mathcal{L}_1(L)$ corresponding respectively to the eigenvalues λ_k, i.e. $\mathcal{L}_1 g_k(L) = \lambda_k g_k(L)$. The $\alpha_k(t)$ are the expansion coefficients verifying the ordinary differential equation $\lambda_k \alpha_k(t) + \mathcal{L}_2 \alpha_k(t) = \gamma_k(t)$, for which the coefficient $\gamma_k(t)$ is defined in Table 3.2. This last ordinary differential equation with respect to t can be written as $\lambda_k\, \alpha_k - \mathrm{d}\alpha_k/\mathrm{d}t = \gamma_k(t)$, with the initial condition $\alpha_k(0) = \hat{\alpha}_k$, leading to the solution

$$\alpha_k(t) = \hat{\alpha}_k e^{-|\lambda_k| t} - \int_0^t e^{-|\lambda_k|(t-s)} \gamma_k(s)\, \mathrm{d}s, \tag{38}$$

where the coefficient $\hat{\alpha}_k$ is the usual expression given in Table 3.2. From this expression, one understand that the successive eigenvalues λ_k have to be negative to assure the stability of the solution. With a mathematical point of view, the Sturm-Liouville theory applying to the eigenvalue problem states that the eigenvalues λ_k are indeed negative (e.g., *Mei*, 1997).

On $[L_{i-1}, L_i]$, the eigenvalue problem $\mathcal{L}_1 g_k(L) = \lambda_k g_k(L)$ can be written as

$$D_0 L^n \frac{\mathrm{d}^2 g_k^i}{\mathrm{d}L^2} + \left[(n-2)D_0 L^{n-1}\right]\frac{\mathrm{d}g_k^i}{\mathrm{d}L} - \frac{1}{\tau_i} g_k^i = \lambda_k\, g_k^i.$$

The continuity at the interfaces has to be enforced such that

$$g_k^i(L_i) = g_k^{i+1}(L_i) \tag{39a}$$

$$\frac{\mathrm{d}g_k^i}{\mathrm{d}L}(L_i) = \frac{\mathrm{d}g_k^{i+1}}{\mathrm{d}L}(L_i), \tag{39b}$$

combined with two boundary conditions

$$g_k^1(L_0) = 0 \tag{40a}$$

$$g_k^M(L_M) = 0. \tag{40b}$$

If $|\lambda_k| > \dfrac{1}{\tau_i}$, the eigenvalue problem is

$$L^2\frac{\mathrm{d}^2 g_k^i}{\mathrm{d}L^2} + (n-2)L\frac{\mathrm{d}g_k^i}{\mathrm{d}L} + \left(\frac{|\lambda_k| - \frac{1}{\tau_i}}{D_0}\right) L^{-(n-2)}\, g_k^i = 0.$$

Taking $\Lambda_k^i = 2/(n-2)\left[(|\lambda_k| - \tau_i^{-1})/D_0\right]^{1/2}$, the solution can be expressed in terms of Bessel functions J_ν and Y_ν of fractional order ν (*Mei*, 1997), similarly to the standard case with a constant source term such that

$$g_k^i(L) = L^{-q}\left[A_k^i J_\nu\left(\Lambda_k^i L^{-p}\right) + B_k^i Y_\nu\left(\Lambda_k^i L^{-p}\right)\right]. \tag{41}$$

But if $|\lambda_k| < \dfrac{1}{\tau_i}$, the eigenvalue problem has to be written as

$$L^2\frac{\mathrm{d}^2 g_k^i}{\mathrm{d}L^2} + (n-2)L\frac{\mathrm{d}g_k^i}{\mathrm{d}L} - \left(\frac{\frac{1}{\tau_i} - |\lambda_k|}{D_0}\right) L^{-(n-2)}\, g_k^i = 0.$$

Taking $\Lambda_k^i = 2/(n-2)\left[(\tau_i^{-1} - |\lambda_k|)/D_0\right]^{1/2}$, the solution can be expressed in terms of modified Bessel functions of order ν, I_ν and K_ν,

$$g_k^i(L) = L^{-q}\left[A_k^i I_\nu\left(\Lambda_k^i L^{-p}\right) + B_k^i K_\nu\left(\Lambda_k^i L^{-p}\right)\right]. \tag{42}$$

Then, the global eigenfunction is built from the superposition of modified Bessel functions I_ν, K_ν and Bessel functions J_ν, Y_ν over each subinterval $[L_{i-1}, L_i]$ (as shown in Appendix D.2). For the particular case of $D_{LL} \sim L^4$ (and its asymptotic form as well), the eigenfunctions (41) and (42) show an alternation between both sine and hyperbolic sine functions, as shown in Table 1.

The functional form we use for the transient solution (with Bessel functions J_ν and Y_ν or modified Bessel functions I_ν and K_ν) is, again, consistent with previous formulations (e.g., *Haerendel*, 1968; *Schulz*, 1986; *Schulz and Newman*, 1988). If the order ν is not an integer (e.g. if $n = 6$ or $n = 10$), the eigenfunctions expressed in terms of the modified Bessel functions I_ν and K_ν can also be expressed in terms of $I_{+\nu}$ and $I_{-\nu}$. Similarly the eigenfunctions expressed in terms of the Bessel functions J_ν and Y_ν can also be written with $J_{+\nu}$ and $J_{-\nu}$. Since $I_{-\nu}(x) = I_\nu(x) + 2\sin(\nu\pi)/\pi K_\nu(x)$ and $J_{-\nu}(x) = \cos(\nu\pi)J_\nu(x) - \sin(\nu\pi)Y_\nu(x)$ when ν is not an integer, any solution $u(x) = AI_\nu(x) + BK_\nu(x)$ can also be written $u(x) = CI_{+\nu}(x) + DI_{-\nu}(x)$, with $C = A - \pi B/(2\sin(\nu\pi))$ and $D = \pi/(2\sin(\nu\pi))B$ (as mentioned before in Appendix D.3). Similarly, any solution $v(x) = AJ_\nu(x) + BY_\nu(x)$ can be expressed as $v(x) = CJ_{+\nu}(x) + DJ_{-\nu}(x)$ with $C = A + \cot(\nu\pi)B$ and $D = -B/sin(\nu\pi)$.

Table 1 – Functions, coefficients, and full solution involved when $\tau = \tau_0$ (uniform case) and $D_{LL} = D_0 L^4$, from (*Loridan et al.*, 2017).

$$\nu = \frac{1}{2},\ p = 1,\ q = \frac{1}{2} \text{ and } \beta = \frac{1}{\sqrt{\tau_0 D_0}}$$

Steady solution $f_\infty(L)$

$$f_\infty(L) = f_{L_M} \frac{\sinh\left[\beta\left(L_0^{-1} - L^{-1}\right)\right]}{\sinh\left[\beta\left(L_0^{-1} - L_M^{-1}\right)\right]}$$

Spatial and temporal components of the transient solution $w(L,t)$

$$\text{From variable } \lambda,\ \Lambda(\lambda) = \sqrt{\left|\frac{|\lambda| - \frac{1}{\tau_0}}{D_0}\right|}$$

The eigenvalues λ_k (with integer $k \geq 1$) are the zeros of function $D(\lambda)$ with

$$D(\lambda) = \sin\left[\Lambda(\lambda)\left(L_0^{-1} - L_M^{-1}\right)\right]$$

$$\Lambda_k = \Lambda(\lambda_k) = \frac{k\pi}{L_0^{-1} - L_M^{-1}}$$

Eigenfunctions

$$g_k(L) = \sin\left[\Lambda_k\left(L_0^{-1} - L^{-1}\right)\right]$$

Temporal functions

(i) Case of a constant outer boundary condition

$\alpha_k(t) = \hat{\alpha}_k e^{-|\lambda_k| t}$ where $\hat{\alpha}_k$ is defined in Table 3.2

(ii) Case of a time-dependent outer boundary condition

$$\alpha_k(t) = \hat{\alpha}_k e^{-|\lambda_k| t} - \int_0^t e^{-|\lambda_k|(t-s)} \gamma_k(s)\,\mathrm{d}s \text{ where } \hat{\alpha}_k \text{ and } \gamma_k(t) \text{ are defined in Table 3.2}$$

Full solution $f(L,t) = w(L,t) + f_\infty(L)$

$$f(L,t) = \sum_{k=1}^{\infty} \alpha_k(t) g_k(L) + f_\infty(L)$$

The system formed by (40a), (39a), (39b) and (40b) could be written with a matrix representation as $\sum_{l=1}^{2M} \mathbb{G}_k^{il} X_k^l = 0$ such that $\mathbb{G}_k X_k = 0$. Solutions $\left(X_k^{2i-1}, X_k^{2i}\right) \equiv \left(A_k^i, B_k^i\right)$ are non trivial if, and only if, $\det(\mathbb{G}_k) = 0$. The eigenvalues λ_k are such that $\det(\mathbb{G}_k) = 0$ and the N first eigenvalues can be computed. However we prefer finding the solutions by solving analytically the system step by step as explained now.

In the above expressions, the wavelength Λ_k^i and the coefficients A_k^i and B_k^i depend on the eigenvalue λ_k. This dependence is written by the subscript k in the above expressions. Therefore we first have to find all the eigenvalues λ_k, corresponding to the k^{th} mode to

be able to have a closed-form expression for Λ_k^i, A_k^i and B_k^i. This has to be done over $[L_0, L_M]$. Let us search the eigenvalues λ_k taken from the global variable λ and let us consider the following λ-dependent quantities, $\Lambda^i(\lambda) = 2/(n-2)\left|(|\lambda| - \tau_i^{-1})/D_0\right|^{1/2}$ and $g^i(\lambda, L) = \mathcal{A}^i(\lambda)\varphi^i(\lambda, L) + \mathcal{B}^i(\lambda)\psi^i(\lambda, L)$ with

$$\varphi^i(\lambda, L) = \begin{cases} L^{-q} J_\nu\left(\Lambda^i(\lambda) L^{-p}\right) & \text{if } |\lambda| > \dfrac{1}{\tau_i} \\ L^{-q} I_\nu\left(\Lambda^i(\lambda) L^{-p}\right) & \text{if } |\lambda| < \dfrac{1}{\tau_i} \end{cases}$$

and

$$\psi^i(\lambda, L) = \begin{cases} L^{-q} Y_\nu\left(\Lambda^i(\lambda) L^{-p}\right) & \text{if } |\lambda| > \dfrac{1}{\tau_i} \\ L^{-q} K_\nu\left(\Lambda^i(\lambda) L^{-p}\right) & \text{if } |\lambda| < \dfrac{1}{\tau_i} \end{cases}$$

such that $g^i(\lambda, L) = \mathcal{A}^i(\lambda)\varphi^i(\lambda, L) + \mathcal{B}^i(\lambda)\psi^i(\lambda, L)$ defined on $[L_0, L_M]$. Note that when $\lambda = \lambda_k$, it follows $\Lambda^i(\lambda) = \Lambda_k^i$ and $g^i(\lambda_k, L) = g_k^i(L)$.

Note that variable λ is introduced artificially in order to catch the eigenvalues λ_k and has not a physical meaning. In what follows, for both function $\varphi(\lambda, L)$ and $\psi(\lambda, L)$, we will note abusively the derivative with respect to variable L with a prime symbol, instead of a partial derivative, since it is the only derivative involved for the resolution of eigenvalues λ_k. By definition, $\varphi^{i'}(\lambda, L) \equiv \left.\dfrac{\partial \varphi^i}{\partial L}\right|_{(\lambda, L)}$ and $\psi^{i'}(\lambda, L) \equiv \left.\dfrac{\partial \psi^i}{\partial L}\right|_{(\lambda, L)}$. This notation is done for a sake of conciseness.

The boundary condition at L_0 gives $g^1(\lambda, L_0) = 0$ so that

$$\mathcal{A}^1(\lambda)\varphi^1(\lambda, L_0) + \mathcal{B}^1(\lambda)\psi^1(\lambda, L_0) = 0,$$

leading to $\mathcal{A}^1(\lambda) = \mathcal{F}^1(\lambda)\mathcal{B}^1(\lambda)$ with $\mathcal{F}^1(\lambda) = -\psi^1(\lambda, L_0)/\varphi^1(\lambda, L_0)$, which gives

$$g^1(\lambda, L) = \left[\mathcal{F}^1(\lambda)\varphi^1(\lambda, L) + \psi^1(\lambda, L)\right]\mathcal{B}^1(\lambda).$$

The second boundary condition at L_M is written as $g^M(\lambda, L_M) = 0$ and leads to

$$\mathcal{A}^M(\lambda)\varphi^M(\lambda, L_M) + \mathcal{B}^M(\lambda)\psi^M(\lambda, L_M) = 0,$$

so that $\mathcal{A}^M(\lambda) = \mathcal{F}^M(\lambda)\mathcal{B}^M(\lambda)$ with $\mathcal{F}^M(\lambda) = -\psi^M(\lambda, L_M)/\varphi^M(\lambda, L_M)$ and then

$$g^M(\lambda, L) = \left[\mathcal{F}^M(\lambda)\varphi^M(\lambda, L) + \psi^M(\lambda, L)\right]\mathcal{B}^M(\lambda).$$

Similarly to Appendix D.3 we use respectively the interface conditions $g^i(\lambda, L_i) = g_k^{i+1}(\lambda, L_i)$ to obtain

$$\left[\mathcal{F}^i(\lambda)\varphi^i(\lambda, L_i) + \psi^i(\lambda, L_i)\right]\mathcal{B}^i(\lambda) = \mathcal{A}^{i+1}(\lambda)\varphi^{i+1}(\lambda, L_i) + \mathcal{B}^{i+1}(\lambda)\psi^{i+1}(\lambda, L_i)$$

and $\left.\dfrac{\partial g^i}{\partial L}\right|_{(\lambda, L_i)} = \left.\dfrac{\partial g^{i+1}}{\partial L}\right|_{(\lambda, L_i)}$ for L_i ($i \in [1, M-2]$) to obtain

$$\left(\mathcal{F}^i(\lambda)\varphi^{i'}(\lambda, L_i) + \psi^{i'}(\lambda, L_i)\right)\mathcal{B}^i(\lambda) = \mathcal{A}^{i+1}(\lambda)\varphi^{i+1'}(\lambda, L_i) + \mathcal{B}^{i+1}(\lambda)\psi^{i+1'}(\lambda, L_i).$$

It gives a closed-form expression for $\mathcal{B}^i(\lambda)$

$$\begin{aligned}\mathcal{B}^i(\lambda) &= \frac{\mathcal{A}^{i+1}(\lambda)\varphi^{i+1}(\lambda, L_i) + \mathcal{B}^{i+1}(\lambda)\psi^{i+1}(\lambda, L_i)}{\mathcal{F}^i(\lambda)\varphi^i(\lambda, L_i) + \psi^i(\lambda, L_i)} \\ &= \frac{\mathcal{A}^{i+1}(\lambda)\varphi^{i+1'}(\lambda, L_i) + \mathcal{B}^{i+1}(\lambda)\psi^{i+1'}(\lambda, L_i)}{\mathcal{F}^i(\lambda)\varphi^{i'}(\lambda, L_i) + \psi^{i'}(\lambda, L_i)},\end{aligned} \tag{43}$$

which leads to $\mathcal{A}^{i+1}(\lambda) = \mathcal{F}^{i+1}(\lambda)\mathcal{B}^{i+1}(\lambda)$ with

$$\mathcal{F}^{i+1}(\lambda) = -\left(\frac{\psi^{i+1}(\lambda, L_i)}{\varphi^{i+1}(\lambda, L_i)}\right)^2 \frac{\left(\dfrac{\mathcal{F}^i(\lambda)\varphi^i(\lambda, L_i) + \psi^i(\lambda, L_i)}{\psi^{i+1}(\lambda, L_i)}\right)'}{\left(\dfrac{\mathcal{F}^i(\lambda)\varphi^i(\lambda, L_i) + \psi^i(\lambda, L_i)}{\varphi^{i+1}(\lambda, L_i)}\right)'}. \tag{44}$$

Similarly we obtain from the two interface conditions at L_{M-1}, by using the same method above with the expression giving $g^M(\lambda, L)$

$$\begin{aligned}&\mathcal{B}^M(\lambda)\left(\frac{\mathcal{F}^M(\lambda)\varphi^M(\lambda, L_{M-1}) + \psi^M(\lambda, L_{M-1})}{\mathcal{F}^{M-1}(\lambda)\varphi^{M-1}(\lambda, L_{M-1}) + \psi^{M-1}(\lambda, L_{M-1})}\right) \\ -&\mathcal{B}^M(\lambda)\left(\frac{\mathcal{F}^M(\lambda)\varphi^{M'}(\lambda, L_{M-1}) + \psi^{M'}(\lambda, L_{M-1})}{\mathcal{F}^{M-1}(\lambda)\varphi^{M-1'}(\lambda, L_{M-1}) + \psi^{M-1'}(\lambda, L_{M-1})}\right) = 0.\end{aligned} \tag{45}$$

Solutions are non trivial if $\mathcal{B}^M(\lambda) \neq 0$, so that the following expression has to be satisfied

$$\begin{aligned}&\frac{\mathcal{F}^M(\lambda)\varphi^M(\lambda, L_{M-1}) + \psi^M(\lambda, L_{M-1})}{\mathcal{F}^{M-1}(\lambda)\varphi^{M-1}(\lambda, L_{M-1}) + \psi^{M-1}(\lambda, L_{M-1})} \\ -&\frac{\mathcal{F}^M(\lambda)\varphi^{M'}(\lambda, L_{M-1}) + \psi^{M'}(\lambda, L_{M-1})}{\mathcal{F}^{M-1}(\lambda)\varphi^{M-1'}(\lambda, L_{M-1}) + \psi^{M-1'}(\lambda, L_{M-1})} = 0.\end{aligned}$$

Hence the eigenvalues λ_k are the roots of the determinant

$$\begin{aligned}D(\lambda) = &\Big[\mathcal{F}^{M-1}(\lambda)\varphi^{M-1'}(\lambda, L_{M-1}) + \psi^{M-1'}(\lambda, L_{M-1})\Big] \\ &\Big[\mathcal{F}^M(\lambda)\varphi^M(\lambda, L_{M-1}) + \psi^M(\lambda, L_{M-1})\Big] \\ -&\Big[\mathcal{F}^{M-1}(\lambda)\varphi^{M-1}(\lambda, L_{M-1}) + \psi^{M-1}(\lambda, L_{M-1})\Big] \\ &\Big[\mathcal{F}^M(\lambda)\varphi^{M'}(\lambda, L_{M-1}) + \psi^{M'}(\lambda, L_{M-1})\Big].\end{aligned} \tag{46}$$

Therefore we can compute all the eigenvalues λ_k by finding the zeros of the function $D(\lambda)$. This step has to be performed numerically to obtain the first N zeros of function $D(\lambda)$, which is numerically costly when a large number of eigenmodes is required.

The second step of the resolution of the eigenvalue problem is to determine the coefficients A_k^i and B_k^i involved in the expressions (41) giving the eigenfunction $g_k^i(L)$. First, coefficients $F_k^i = \mathcal{F}^i(\lambda_k)$ (recursively from $i = M$ to 1) are computed from (44). Then we can take for coefficient $B_k^M = \mathcal{B}^M(\lambda_k)$ any nonzero real value, which makes sense because everything will be normalized afterwards. Note that because the two boundary conditions are zero (homogeneous), the expression for B_k^M is different from the steady case (37). Once this is done, we can deduce $A_k^M = \mathcal{A}^M(\lambda_k)$. And recursively from $i = M - 1$ to 1 (43) gives $B_k^i = \mathcal{B}^i(\lambda_k)$, and then finally $A_k^i = \mathcal{A}^i(\lambda_k)$.

The whole described procedure is used by the numerical algorithm involved in (*Loridan et al.*, 2017) and in Chapter 3.

D.5 Solutions when $n = 2$

In this section we present the solution obtained for which $D_{LL} = D_0 L^2$ (i.e. $n = 2$) (*Loridan et al.*, 2017). This case corresponds to a radial transport induced by the ionospheric dynamo fields of Jupiter (e.g., *Baker and Goertz*, 1976). The expressions of the obtained solutions are very similar to the one written in the main text corresponding to a power $n = 4$ (Table 1). The steady and transient solutions for $n = 2$ and uniform case are detailed in Table 2, with the time-dependent functions $\alpha_k(t)$ defined in Table 3.2. The steady solution for M pieces is presented in Table 3.6 with the function $U^i(L)$ and $V^i(L)$ given in Table 3. The transient solution is given by Table 3.7, using the definitions of Table 3 and the expressions of $\alpha_k(t)$ in Table 3.2.

In order to extract a convergence criteria for the specific case $n = 2$, we find the closed-form expression $\Lambda_N = N\pi/\ln(L_M/L_0)$, leading to

$$\tau_N^{\text{decay}} \sim \frac{1}{D_0}\frac{1}{N^2\pi^2}\left[\ln\left(L_M/L_0\right)\right]^2,$$

and from which we find the number of eigenmodes to calculate in order to obtain an accurate solution at a given time t_0,

$$N_{t_0} \sim \frac{1}{\pi}\ln\left(L_M/L_0\right)\frac{1}{\sqrt{D_0 t_0}} \tag{47}$$

and the number of modes to calculate so that the last eigenfunction cancels N_z times between L_A and L_B,

$$N_{[L_A,L_B]} \sim N_z \frac{\ln\left(L_M/L_0\right)}{\ln\left(L_B/L_A\right)}. \tag{48}$$

Finally we are also able to give a closed-form expression for the time t_{eq} to reach an equilibrium state (up to a ratio $\epsilon \ll 1$), given in Table 4, since the analytical expressions for coefficients $\hat{\alpha}_k$ are tractable.

Table 2 – Functions, coefficients, and full solution involved when $\tau = \tau_0$ (uniform case) and $D_{LL} = D_0 L^2$, from (*Loridan et al.*, 2017)

$$\beta = \frac{1}{2}\sqrt{1 + \frac{4}{\tau_0 D_0}}$$

Steady solution $f_\infty(L)$

$$f_\infty(L) = f_{L_M} \left(\frac{L}{L_M}\right)^{1/2} \left(\frac{\sinh\left[\beta \ln(L/L_0)\right]}{\sinh\left[\beta \ln(L_M/L_0)\right]}\right)$$

Spatial and temporal components of the transient solution $w(L,t)$

$$\text{From variable } \lambda,\ \Lambda(\lambda) = \frac{1}{2}\sqrt{\left|1 + 4\frac{1/\tau_0 - |\lambda|}{D_0}\right|}$$

The eigenvalues λ_k (with integer $k \geq 1$) are the zeros of function $D(\lambda)$ with

$$D(\lambda) = \sin\left[\Lambda(\lambda) \ln(L_M/L_0)\right]$$

$$\Lambda_k = \Lambda(\lambda_k) = \frac{k\pi}{\ln(L_M/L_0)}$$

Eigenfunctions

$$g_k(L) = L^{1/2} \sin\left[\Lambda_k \ln(L/L_0)\right]$$

Temporal functions

(i) Case of a constant outer boundary condition

$\alpha_k(t) = \hat{\alpha}_k e^{-|\lambda_k| t}$ where $\hat{\alpha}_k$ is defined in Table 3.2

(ii) Case of a time-dependent outer boundary condition

$\alpha_k(t) = \hat{\alpha}_k e^{-|\lambda_k| t} - \int_0^t e^{-|\lambda_k|(t-s)} \gamma_k(s)\, \mathrm{d}s$ where $\hat{\alpha}_k$ and $\gamma_k(t)$ are defined in Table 3.2

Full solution $f(L,t) = w(L,t) + f_\infty(L)$

$$f(L,t) = \sum_{k=1}^{\infty} \alpha_k(t) g_k(L) + f_\infty(L)$$

Table 3 – Functions $U^i(L)$ and $V^i(L)$ involved in the steady solution $f_\infty(L)$ and functions $\varphi^i(\lambda, L)$ and $\psi^i(\lambda, L)$ involved in the transient solution $w(L,t)$, for M pieces, with $n = 2$, from (*Loridan et al.*, 2017).

$$\beta_i = \frac{1}{2}\sqrt{1 + \frac{4}{\tau_i D_0}} \text{ and from variable } \lambda,\ \Lambda^i(\lambda) = \frac{1}{2}\sqrt{\left|1 + 4\frac{1/\tau_i - |\lambda|}{D_0}\right|} \text{ with } i \in [1, M] \text{ the pieces number}$$

Functions involved in the steady solution $f_\infty(L)$

$$U^i(L) = L^{1/2}\cosh\left[\beta_i \ln(L)\right] \qquad V^i(L) = L^{1/2}\sinh\left[\beta_i \ln(L)\right]$$

Functions involved in the transient solution $w(L,t)$

$$\varphi^i(\lambda, L) = \begin{cases} L^{1/2}\cos\left[\Lambda^i(\lambda)\ln(L)\right] & \text{if } |\lambda| > 1/\tau_i + D_0/4 \\ L^{1/2}\cosh\left[\Lambda^i(\lambda)\ln(L)\right] & \text{if } |\lambda| < 1/\tau_i + D_0/4. \end{cases} \qquad \psi^i(\lambda, L) = \begin{cases} L^{1/2}\sin\left[\Lambda^i(\lambda)\ln(L)\right] & \text{if } |\lambda| > 1/\tau_i + D_0/4 \\ L^{1/2}\sinh\left[\Lambda^i(\lambda)\ln(L)\right] & \text{if } |\lambda| < 1/\tau_i + D_0/4. \end{cases}$$

Table 4 – Approximated equilibrium times for $\tau = \tau_0$ and $D_{LL} = D_0 L^2$, from (*Loridan et al.*, 2017)

If $f(L, t=0) = 0$ and $f(L_M, t) = f_{L_M}$

$$t_{\rm eq}(L) = \tau_1^{\rm decay} \ln\left(\left|\frac{2}{\varepsilon\pi}\frac{1}{\left(1+\frac{\beta^2}{\Lambda_1^2}\right)}\sinh\left[\beta\ln(L_M/L_0)\right]\frac{\sin\left[\Lambda_1\ln(L/L_0)\right]}{\sinh\left[\beta\ln(L/L_0)\right]}\right|\right)$$

If $f(L, t=0) = r f_\infty(L)$ and $f(L_M, t) = f_{L_M}$

$$t_{\rm eq}(L) = \tau_1^{\rm decay} \ln\left(\left|\frac{2|r-1|}{\varepsilon\pi}\frac{1}{\left(1+\frac{\beta^2}{\Lambda_1^2}\right)}\sinh\left[\beta\ln(L_M/L_0)\right]\frac{\sin\left[\Lambda_1\ln(L/L_0)\right]}{\sinh\left[\beta\ln(L/L_0)\right]}\right|\right)$$

If $f(L, t=0) = f_0$ and $f(L_M, t) = f_{L_M}$

$$t_{\rm eq}(L) = \tau_1^{\rm decay} \ln\left(\left|\frac{2}{\varepsilon\pi}\left|2\frac{f_0}{f_{L_M}} - \frac{1}{\left(1+\frac{\beta^2}{\Lambda_1^2}\right)}\right|\sinh\left[\beta\ln(L_M/L_0)\right]\frac{\sin\left[\Lambda_1\ln(L/L_0)\right]}{\sinh\left[\beta\ln(L/L_0)\right]}\right|\right)$$

E Properties of the non-symmetric Mead field

The purpose of this section is to compare, for a given third invariant L^*, the equatorial magnetic field intensity for the simplified asymmetric Mead field with the intensity of the symmetric dipole field. We also take the opportunity of generalizing some concepts emphasized in Chapter 2 for a simple asymmetric field.

E.1 Definition of the Mead field

The Mead field is the superposition of a static background field with a small time-dependent external contribution, which typically models the effects of magnetopause currents (also referred as Chapman-Ferraro currents) (*Mead*, 1964). In the present formulation, the magnetic perturbation is derived from the external magnetic scalar potential ψ_e (spherical harmonic expansion) given by (2.16) (Chapter 2) up to the first order in radial distance r. Such first-order expansion has been considered by *Fälthammar* (1968). The resulting magnetic field (background dipole field and external contribution) in spherical coordinates can be written as (*Mead*, 1964; *Fälthammar*, 1968; *Lejosne*, 2013)

$$\begin{cases} B_r = -2B_E \left(\dfrac{R_E}{r}\right)^3 \cos(\theta) - S(t)\cos(\theta) - A(t) r \sin(2\theta)\cos(\varphi) \\ B_\theta = -B_E \left(\dfrac{R_E}{r}\right)^3 \sin(\theta) + S(t)\sin(\theta) - A(t) r \cos(2\theta)\cos(\varphi) \\ B_\varphi = A(t) r \cos(\theta)\sin(\varphi), \end{cases}$$

for which $\varphi = 0$ corresponds to MLT=0 (midnight). As emphasized by *Fälthammar* (1968), the use of the unspecified time-dependent parameters $A(t)$ and $S(t)$ enables to work in a very general and adaptive framework. The S parameter has been shown to drive the temporal magnetic field variations symmetrically, whereas the A quantity relates to an asymmetric coefficient that shapes the field lines according to their longitudinal position (*Fälthammar*, 1968; *Lejosne*, 2013).

Since the external magnetic contributions are considered small compared with the ambient dipole field, let us define

$$\varepsilon_1(r) = \frac{S(t) r^3}{B_E R_E^3} \ll 1$$

and

$$\varepsilon_2(r) = \frac{A(t) r^4}{B_E R_E^3} \ll 1,$$

such that the magnetic field writes

$$\begin{cases} B_r = -2B_E \left(\dfrac{R_E}{r}\right)^3 \cos(\theta) \left[1 + \dfrac{1}{2}\varepsilon_1(r) + \varepsilon_2(r)\sin(\theta)\cos(\varphi)\right] \\ B_\theta = -B_E \left(\dfrac{R_E}{r}\right)^3 \sin(\theta) \left[1 - \varepsilon_1(r) - \varepsilon_2(r)\left(\dfrac{2\sin^2(\theta) - 1}{\sin(\theta)}\right)\cos(\varphi)\right] \\ B_\varphi = B_E \left(\dfrac{R_E}{r}\right)^3 \varepsilon_2(r)\cos(\theta)\sin(\varphi). \end{cases}$$

For $\theta = \pi/2$, at the magnetic equator, we obtain

$$\boldsymbol{B} = B_\theta(r,\varphi)\hat{\boldsymbol{\theta}} = -B_E \left(\frac{R_E}{r}\right)^3 \left[1-\varepsilon_1(r) - \varepsilon_2(r)\cos(\varphi)\right] \hat{\boldsymbol{\theta}} \tag{49}$$

and the equatorial magnetic field intensity is

$$B_0(r,\varphi) = B_E \left(\frac{R_E}{r}\right)^3 \left[1-\varepsilon_1(r) - \varepsilon_2(r)\cos(\varphi)\right]. \tag{50}$$

E.2 Drift path

Since our purpose is to estimate the equatorial magnetic field intensity with respect to the third adiabatic invariant L^*, we first have to express the electron drift path in the asymmetric Mead field. For equatorially mirroring particles (i.e. $B_m = B_0$), the drift path starting at (r_0, φ_0) is such that $B_0(r,\varphi) = B_0(r_0,\varphi_0)$, so

$$B_E \left(\frac{R_E}{r}\right)^3 \left[1-\varepsilon_1(r) - \varepsilon_2(r)\cos(\varphi)\right] = B_E \left(\frac{R_E}{r_0}\right)^3 \left[1-\varepsilon_1(r_0) - \varepsilon_2(r_0)\cos(\varphi_0)\right],$$

which gives, as in (*Lejosne*, 2013),

$$r(\varphi; r_0, \varphi_0) = r_0 \left(1 - \frac{1}{3}\varepsilon_2(r_0)\left[\cos(\varphi) - \cos(\varphi_0)\right]\right) \tag{51}$$

with $r_0 = r(\varphi_0)$.

E.3 Calculation of the third adiabatic invariant

As mentioned in Chapter 2, the magnetic flux can be calculated either with the use of the magnetic field $\boldsymbol{B}$ or with the magnetic potential vector $\boldsymbol{\mathcal{A}}$.

E.3.a Computation with the magnetic field

As stated in Chapter 2, the magnetic flux is computed as the sum of the internal magnetic contribution integrated over the plane lying outside the drift path with the external contribution calculated inside the drift shell,

$$\Phi(r_0,\varphi_0) = \iint_{\Sigma} \boldsymbol{B}\cdot\mathbf{d}\boldsymbol{S} = \iint_{\Sigma_{\text{int}}} \boldsymbol{B}_{\text{int}}\cdot\mathbf{d}\boldsymbol{S}_{\text{int}} + \iint_{\Sigma_{\text{ext}}} \boldsymbol{B}_{\text{ext}}\cdot\mathbf{d}\boldsymbol{S}_{\text{ext}}$$

with $\mathbf{d}\boldsymbol{S}_{\text{int}} = \mathrm{d}S\,\hat{\boldsymbol{\theta}}$ and $\mathbf{d}\boldsymbol{S}_{\text{ext}} = -\mathrm{d}S\,\hat{\boldsymbol{\theta}}$. Hence the magnetic flux writes

$$\begin{aligned}
\Phi(r_0,\varphi_0) &= \int_0^{2\pi}\int_{r(\varphi)}^{+\infty} B_{\text{int}\,\theta}(r,\varphi) r\,\mathrm{d}r\mathrm{d}\varphi - \int_0^{2\pi}\int_0^{r(\varphi)} B_{\text{ext}\,\theta}(r,\varphi) r\,\mathrm{d}r\mathrm{d}\varphi \\
&= -\int_0^{2\pi}\int_{r(\varphi)}^{+\infty} B_E\left(\frac{R_E}{r}\right)^3 r\mathrm{d}r\mathrm{d}\varphi - \int_0^{2\pi}\int_0^{r(\varphi)} \left[S(t) + A(t) r\cos(\varphi)\right] r\mathrm{d}r\mathrm{d}\varphi \\
&= -\int_0^{2\pi} \frac{B_E R_E^3}{r(\varphi)}\mathrm{d}\varphi - \int_0^{2\pi}\left(\frac{S(t)}{2} r^2(\varphi) + \frac{A(t)}{3} r^3(\varphi)\cos(\varphi)\right)\mathrm{d}\varphi.
\end{aligned}$$

Hence, by using the expression (51) for the drift path we obtain

$$\Phi(r_0,\varphi_0) = -\frac{B_E R_E^3}{r_0}\int_0^{2\pi}\left(1+\frac{1}{3}\varepsilon_2(r_0)\left[\cos(\varphi)-\cos(\varphi_0)\right]\right)\mathrm{d}\varphi$$
$$-\frac{S(t)}{2}\int_0^{2\pi} r_0^2\left(1-\frac{2}{3}\varepsilon_2(r_0)\left[\cos(\varphi)-\cos(\varphi_0)\right]\right)\mathrm{d}\varphi$$
$$-\frac{A(t)}{3}\int_0^{2\pi} r_0^3\left(1-\varepsilon_2(r_0)\left[\cos(\varphi)-\cos(\varphi_0)\right]\right)\cos(\varphi)\,\mathrm{d}\varphi.$$

The integration eventually leads to

$$\Phi(r_0,\varphi_0) = -\frac{2\pi B_E R_E^3}{r_0}\left(1+\frac{1}{2}\varepsilon_1(r_0)-\frac{1}{3}\varepsilon_2(r_0)\cos(\varphi_0)\right),$$

which is consistent with (*Lejosne*, 2013).

Hence the expression of L^* is derived as

$$L^*(r_0,\varphi_0) = -\frac{2\pi R_E^2 B_E}{\Phi(r_0,\varphi_0)}$$

i.e.

$$L^*(r_0,\varphi_0) = \frac{r_0}{R_E}\left(1-\frac{1}{2}\varepsilon_1(r_0)+\frac{1}{3}\varepsilon_2(r_0)\cos(\varphi_0)\right), \tag{52}$$

which is the particular case corresponding to $\alpha_0 = 90$ degrees of the L^* invariant derived in (*Roederer and Zhang*, 2014, equation (3.42)).

E.3.b Computation with the magnetic vector potential

It can also be instructive to obtain the above expression for L^* with the use of the magnetic vector potential $\boldsymbol{\mathcal{A}}$ rather than the magnetic field $\boldsymbol{B}$. The magnetic vector potential $\boldsymbol{\mathcal{A}}$ associated to the Mead field is given by (*Lejosne*, 2013)

$$\begin{cases} \mathcal{A}_r = -\dfrac{A(t)}{7}r^2\sin(\theta)\sin(\varphi) \\ \mathcal{A}_\theta = \dfrac{2A(t)}{7}r^2\cos(\theta)\sin(\varphi) \\ \mathcal{A}_\varphi = -\dfrac{B_E R_E^2}{r^2}\sin(\theta) - \dfrac{S(t)}{2}r\sin(\theta) + \dfrac{2A(t)}{21}r^2\left(3-7\sin^2(\theta)\right)\cos(\varphi), \end{cases}$$

which is equivalent to

$$\begin{cases} \mathcal{A}_r = -\dfrac{1}{7}B_E\left(\dfrac{R_E^3}{r^2}\right)\varepsilon_2(r)\sin(\theta)\sin(\varphi) \\ \mathcal{A}_\theta = \dfrac{2}{7}B_E\left(\dfrac{R_E^3}{r^2}\right)\varepsilon_2(r)\cos(\theta)\sin(\varphi) \\ \mathcal{A}_\varphi = -B_E\left(\dfrac{R_E^2}{r^2}\right)\left[\sin(\theta)+\dfrac{1}{2}\varepsilon_1(r)\sin(\theta)-\dfrac{2}{21}\varepsilon_2(r)\left(3-7\sin^2(\theta)\right)\cos(\varphi)\right]. \end{cases}$$

For $\theta = \pi/2$ we obtain

$$\boldsymbol{\mathcal{A}} = \mathcal{A}_r(r,\varphi)\hat{\boldsymbol{r}} + \mathcal{A}_\varphi(r,\varphi)\hat{\boldsymbol{\varphi}}$$

with

$$\mathcal{A}_\varphi(r,\varphi) = -B_E \frac{R_E^3}{r^2}\left[1 + \frac{1}{2}\varepsilon_1(r) + \frac{8}{21}\varepsilon_2(r)\cos(\varphi)\right].$$

The magnetic flux can be computed as

$$\Phi(r_0,\varphi_0) = \oint_\Gamma \boldsymbol{\mathcal{A}}\cdot\mathbf{d}\boldsymbol{l} = -\int_0^{2\pi} \mathcal{A}_\varphi(r(\varphi),\varphi)\, r(\varphi)\,\mathrm{d}\varphi,$$

which results in

$$\Phi(r_0,\varphi_0) = -\frac{2\pi B_E R_E^3}{r_0}\left(1 + \frac{1}{2}\varepsilon_1(r_0) - \frac{1}{3}\varepsilon_2(r_0)\cos(\varphi_0)\right)$$

as before.

Let us mention that the magnetic vector potential $\boldsymbol{\mathcal{A}}$ can be calculated from the knowledge of the magnetic field $\boldsymbol{B}$. It first consists at calculating the induced electric field $\boldsymbol{\mathcal{E}} = -\boldsymbol{v}\times\boldsymbol{B}$ (assuming frozen field lines as mentioned in Chapter 2, section 2.3.2.a). The velocity $\boldsymbol{v}$ is the velocity of the ionospheric plasma that rotates with the Earth. Its expression is obtained by deriving the field line equations for the Mead field (see (*Cunningham*, 2016) for example), and then by calculating their derivative with respect to time. Since $\boldsymbol{\mathcal{E}} = -\partial\boldsymbol{\mathcal{A}}/\partial t$, the expression of the magnetic potential $\boldsymbol{\mathcal{A}}$ is obtained (*Fälthammar*, 1968).

E.4 Equatorial Mead field intensity with respect to L^*

For a dipole field, the third invariant is equivalent to the normalized equatorial radial distance, i.e.

$$L = \frac{r_0^{\mathrm{DIP}}}{R_E},$$

with r_0^{DIP} the equatorial radial distance of the particle at any longitude φ_0 in the dipole field. As for the Mead field, the third adiabatic invariant is expressed with (52) as

$$L^* = \frac{r^{\mathrm{MEAD}}(\varphi_0)}{R_E}\left(1 - \frac{1}{2}\varepsilon_1(r_0) + \frac{1}{3}\varepsilon_2(r_0)\cos(\varphi_0)\right),$$

for which $r^{\mathrm{MEAD}}(\varphi_0)$ is the equatorial radial distance at the given longitude φ_0 in the Mead field. Imposing $L = L^*$, $r^{\mathrm{MEAD}}(\varphi_0)$ should verify

$$r^{\mathrm{MEAD}}(\varphi_0) = r_0^{\mathrm{DIP}}\left(1 + \frac{1}{2}\varepsilon_1(r_0) - \frac{1}{3}\varepsilon_2(r_0)\cos(\varphi_0)\right).$$

From (51) the drift contour of the particle, starting at $r^{\mathrm{MEAD}}(\varphi_0)$ at $\varphi = \varphi_0$, is such that

$$\begin{aligned} r(\varphi) &= r^{\mathrm{MEAD}}(\varphi_0)\left(1 - \frac{1}{3}\varepsilon_2(r_0)\left[\cos(\varphi) - \cos(\varphi_0)\right]\right) \\ &= r_0^{\mathrm{DIP}}\left(1+\frac{1}{2}\varepsilon_1(r_0) - \frac{1}{3}\varepsilon_2(r_0)\cos(\varphi_0)\right)\left(1 - \frac{1}{3}\varepsilon_2(r_0)\left[\cos(\varphi) - \cos(\varphi_0)\right]\right) \\ &= r_0^{\mathrm{DIP}}\left(1+\frac{1}{2}\varepsilon_1(r_0) - \frac{1}{3}\varepsilon_2(r_0)\cos(\varphi)\right). \end{aligned}$$

We now evaluate the equatorial Mead field intensity from (50) as

$$\begin{aligned} B_0^{\mathrm{MEAD}}(L^*) &= B_E\left(\frac{R_E}{r(\varphi)}\right)^3\left[1-\varepsilon_1(r_0) - \varepsilon_2(r_0)\cos(\varphi)\right] \\ &= B_E\left(\frac{R_E}{r_0^{\mathrm{DIP}}}\right)^3\left(1-\frac{3}{2}\varepsilon_1(r_0) + \varepsilon_2(r_0)\cos(\varphi)\right)\left[1-\varepsilon_1(r_0) - \varepsilon_2(r_0)\cos(\varphi)\right], \end{aligned}$$

so that

$$B_0^{\mathrm{MEAD}}(L^*) = \left(1-\frac{5}{2}\varepsilon_1(r_0)\right) B_0^{\mathrm{DIP}}(L^*), \tag{53}$$

with $B_0^{\mathrm{DIP}}(L^*) = B_E/L^3 = B_E\left(R_E/r_0^{\mathrm{DIP}}\right)^3$. The fact that B_0^{MEAD} does not depend on longitude φ is not a surprise since we have assumed $\alpha_0 = 90$ degrees, such that $B_0 = B_m$, which is constant along the drift shell. The above equation shows that for a same given L^* value, the equatorial magnetic intensity of the Mead field is always lower than the equatorial magnetic intensity of the dipole field. This property is extended to the T89 field in Chapter 6 to show that $B_0^{\mathrm{T89}} < B_0^{\mathrm{DIP}}$, and subsequently, for a given energy and equatorial pitch angle, $\mu_{\mathrm{T89}} > \mu_{\mathrm{DIP}}$.

Scientific communications

Articles in international peer-reviewed journals

V. Loridan, J.-F. Ripoll, W. Tu, and G. S. Cunningham (2018, in preparation), On the use of different magnetic field models for the major storm of October 1990, *Journal of Geophysical Research: Space Physics*.

J.-F. Ripoll, **V. Loridan**, M. H. Denton, G. S. Cunningham, G. D. Reeves, O. Santolík, J. F. Fennell, D. L. Turner, A. Y. Drozdov, J. S. Cervantes Villa, Y. Y. Shprits, S. A. Thaller, W. S. Kurth, C. A. Kletzing, M. G. Henderson, and A. Y. Ukhorskiy (2018), Observations and Fokker-Planck simulations of the L-shell, energy, and pitch-angle structure of Earth's electron radiation belts during quiet times, *Journal of Geophysical Research: Space Physics*.

G. S. Cunningham, **V. Loridan**, J.-F. Ripoll, and M. Schulz (2018), Neoclassical diffusion of radiation-belt electrons across very low L-shells, *Journal of Geophysical Research: Space Physics*.

J.-F. Ripoll, O. Santolík, G. D. Reeves, W. S. Kurth, M. H. Denton, **V. Loridan**, S. A. Thaller, C. A. Kletzing, and D. L. Turner (2017), Effects of whistler mode hiss waves in March 2013, *Journal of Geophysical Research: Space Physics*.

V. Loridan, J.-F. Ripoll, and F. de Vuyst (2017), The analytical solution of the transient radial diffusion equation with a nonuniform loss term, *Journal of Geophysical Research: Space Physics*.

J.-F. Ripoll, **V. Loridan**, G. S. Cunningham, G. D. Reeves, and Y. Y. Shprits (2016), On the time needed to reach an equilibrium structure of the radiation belts, *Journal of Geophysical Research: Space Physics*.

J.-F. Ripoll, G. D. Reeves, G. S. Cunningham, **V. Loridan**, M. Denton, O. Santolík, W. S. Kurth, C. A. Kletzing, D. L. Turner, M. G. Henderson, and A. Y. Ukhorskiy (2016), Reproducing the observed energy-dependent structure of Earth's electron radiation belts during storm recovery with an event-specific diffusion model, *Geophysical Research Letters*.

Oral scientific contributions

V. Loridan, Modélisation de la dynamique des électrons de forte énergie piégés dans la ceinture externe de la magnétosphère terrestre, *Séminaire du département de physique, CEA*, Bruyères-le-Châtel, France, 2018.

V. Loridan, Modélisation de la dynamique des électrons de forte énergie piégés dans la ceinture externe de la magnétosphère terrestre, *Journée des doctorants 2018*, Bruyères-le-Châtel, France, 2018.

V. Loridan, Modélisation de la dynamique des électrons de forte énergie piégés dans la ceinture externe de la magnétosphère terrestre, *Séminaire interne, CEA*, Bruyères-le-Châtel, France, 2017.

V. Loridan, Modélisation de la dynamique des électrons de forte énergie piégés dans la ceinture externe de la magnétosphère terrestre, *Séminaire des doctorants du CMLA 2017*, Cachan, France, 2017.

V. Loridan, G. S, Cunningham, and J.-F. Ripoll, Anomalous radial diffusion at low L shell due to the combined effects of drift shell splitting and atmospheric pitch-angle scattering, *Los Alamos Space Weather Summer School*, Los Alamos, USA, 2016.

V. Loridan, J.-F. Ripoll, W. Tu, G. S. Cunningham, Influence of radial diffusion coefficient models on the predictions of the belts dynamics, *International Workshop on Energetic Particle Processes of the Near-Earth Space*, Paris, France, 2015.

Posters

V. Loridan, J.-F. Ripoll, M. H. Denton, O. Santolík, S. A. Thaller, A. Y. Drozdov, Y. Y. Shprits, G. S. Cunningham, G. D. Reeves, and S. K. Morley, Assessing the consistency of data-driven whistler mode hiss wave scattering effects during storm-recovery via dedicated error metrics, *American Geophysical Union, Fall Meeting*, Washington D.C., USA, 2018, upcoming.

V. Loridan, and J.-F. Ripoll, Quantifying the influence of the magnetic field on the radiation belts during quiet and active periods, *American Geophysical Union, Chapman Conference*, Cascais, Portugal, 2018.

V. Loridan, J.-F. Ripoll, and F. de Vuyst, The analytical solution of the transient radial diffusion equation with a nonuniform loss term, *American Geophysical Union, Fall Meeting*, New-Orleans, USA, 2017.

V. Loridan, Modélisation de la dynamique des électrons de forte énergie piégés dans la ceinture externe de la magnétosphère terrestre, *Journée des doctorants 2017*, Bruyères-le-Châtel, France, 2017.

Bibliography

Abramowitz, M., and I. A. Stegun (1964), *Handbook of mathematical functions with formulas, graphs, and mathematical tables*, *National Bureau of Standards Applied Mathematics Series*, vol. 55, xiv+1046 pp., For sale by the Superintendent of Documents, U.S. Government Printing Office, Washington, D.C.

Albert, J. M. (2002), Nonlinear interaction of outer zone electrons with VLF waves, *Geophysical Research Letters*, *29*(8), 116–1–116–3, doi:10.1029/2001GL013941.

Albert, J. M. (2005), Evaluation of quasi-linear diffusion coefficients for whistler mode waves in a plasma with arbitrary density ratio, *Journal of Geophysical Research: Space Physics*, *110*(A3), doi:10.1029/2004JA010844.

Albert, J. M. (2010), Diffusion by one wave and by many waves, *Journal of Geophysical Research: Space Physics*, *115*(A3), doi:10.1029/2009JA014732.

Albert, J. M., and Y. Y. Shprits (2009), Estimates of lifetimes against pitch angle diffusion, *Journal of Atmospheric and Solar-Terrestrial Physics*, *71*(16), 1647 – 1652, doi:http://dx.doi.org/10.1016/j.jastp.2008.07.004, toward an Integrated View of Inner Magnetosphere and Radiation Belts.

Albert, J. M., N. P. Meredith, and R. B. Horne (2009), Three-dimensional diffusion simulation of outer radiation belt electrons during the 9 October 1990 magnetic storm, *Journal of Geophysical Research: Space Physics*, *114*(A9), doi:10.1029/2009JA014336.

Albert, J. M., X. Tao, and J. Bortnik (2013), *Aspects of Nonlinear Wave-Particle Interactions*, pp. 255–264, American Geophysical Union (AGU), doi:10.1029/2012GM001324.

Albert, J. M., M. J. Starks, R. B. Horne, N. P. Meredith, and S. A. Glauert (2016), Quasi-linear simulations of inner radiation belt electron pitch angle and energy distributions, *Geophysical Research Letters*, *43*(6), 2381–2388, doi:10.1002/2016GL067938.

Ali, A. F., D. M. Malaspina, S. R. Elkington, A. N. Jaynes, A. A. Chan, J. Wygant, and C. A. Kletzing (2016), Electric and magnetic radial diffusion coefficients using the Van Allen probes data, *Journal of Geophysical Research: Space Physics*, *121*(10), 9586–9607, doi:10.1002/2016JA023002.

Aseev, N. A., Y. Y. Shprits, A. Y. Drozdov, and A. C. Kellerman (2016), Numerical applications of the advective-diffusive codes for the inner magnetosphere, *Space Weather*, *14*(11), 993–1010, doi:10.1002/2016SW001484.

Baker, D. N., and C. K. Goertz (1976), Radial diffusion in Jupiter's magnetosphere, *Journal of Geophysical Research*, *81*(28), 5215–5219, doi:10.1029/JA081i028p05215.

Baker, D. N., S. Kanekal, J. B. Blake, B. Klecker, and G. Rostoker (1994), Satellite anomalies linked to electron increase in the magnetosphere, *Eos, Transactions American Geophysical Union*, *75*(35), 401–405, doi:10.1029/94EO01038.

Baker, D. N., S. G. Kanekal, X. Li, S. P. Monk, J. Goldstein, and J. L. Burch (2004), An extreme distortion of the Van Allen belt arising from the 'Halloween' solar storm in 2003, *Nature*, *423*, 878.

Baker, D. N., S. G. Kanekal, R. B. Horne, N. P. Meredith, and S. A. Glauert (2007), Low-altitude measurements of 2-6 MeV electron trapping lifetimes at $1.5 \leq L \leq 2.5$, *Geophysical Research Letters*, *34*(20), doi:10.1029/2007GL031007, l20110.

Baker, D. N., A. N. Jaynes, X. Li, M. G. Henderson, S. G. Kanekal, G. D. Reeves, H. E. Spence, S. G. Claudepierre, J. F. Fennell, M. K. Hudson, R. M. Thorne, J. C. Foster, P. J. Erickson, D. M. Malaspina, J. R. Wygant, A. Boyd, C. A. Kletzing, A. Drozdov, and Y. Y. Shprits (2014a), Gradual diffusion and punctuated phase space density enhancements of highly relativistic electrons: Van Allen Probes observations, *Geophysical Research Letters*, *41*(5), 1351–1358, doi:10.1002/2013GL058942.

Baker, D. N., A. Jaynes, V. C. Hoxie, R. M. Thorne, J. C. Foster, X. Li, J. Fennell, J. Wygant, S. Kanekal, P. J. Erickson, W. S. Kurth, W. Li, Q. Ma, Q. G. Schiller, L. Blum, D. Malaspina, A. J. Gerrard, and L. J. Lanzerotti (2014b), An impenetrable barrier to ultrarelativistic electrons in the Van Allen radiation belts., *Nature*, *515 7528*, 531–4.

Baker, D. N., A. N. Jaynes, S. G. Kanekal, J. C. Foster, P. J. Erickson, J. F. Fennell, J. B. Blake, H. Zhao, X. Li, S. R. Elkington, M. G. Henderson, G. D. Reeves, H. E. Spence, C. A. Kletzing, and J. R. Wygant (2016), Highly relativistic radiation belt electron acceleration, transport, and loss: Large solar storm events of March and June 2015, *Journal of Geophysical Research: Space Physics*, *121*(7), 6647–6660, doi:10.1002/2016JA022502.

Balescu, R. (1988), *Transport Processes in Plasmas: Neoclassical Transport Theory*, Transport Processes in Plasmas, North-Holland.

Baumjohann, W., and R. A. Treumann (1996), *Basic space plasma physics*, Imperial Coll., London.

Baumjohann, W., M. Blanc, A. Fedorov, and K.-H. Glassmeier (2010), Current Systems in Planetary Magnetospheres and Ionospheres, *Space Science Reviews*, *152*(1), 99–134, doi:10.1007/s11214-010-9629-z.

Beutier, T., D. Boscher, and M. France (1995), SALAMMBO: A three-dimensional simulation of the proton radiation belt, *Journal of Geophysical Research: Space Physics*, *100*(A9), 17,181–17,188, doi:10.1029/94JA02728.

Birmingham, T., W. Hess, T. Northrop, R. Baxter, and M. Lojko (1974), The electron diffusion coeffcient in Jupiter's magnetosphere, *Journal of Geophysical Research*, *79*(1), 87–97, doi:10.1029/JA079i001p00087.

Blake, J. B., P. A. Carranza, S. G. Claudepierre, J. H. Clemmons, W. R. Crain, Y. Dotan, J. F. Fennell, F. H. Fuentes, R. M. Galvan, J. S. George, M. G. Henderson, M. Lalic, A. Y. Lin, M. D. Looper, D. J. Mabry, J. E. Mazur, B. McCarthy, C. Q. Nguyen,

T. P. O'Brien, M. A. Perez, M. T. Redding, J. L. Roeder, D. J. Salvaggio, G. A. Sorensen, H. E. Spence, S. Yi, and M. P. Zakrzewski (2013), The Magnetic Electron Ion Spectrometer (MagEIS) Instruments Aboard the Radiation Belt Storm Probes (RBSP) Spacecraft, *Space Science Reviews*, *179*(1), 383–421, doi:10.1007/s11214-013-9991-8.

Bolduc, L. (2002), GIC observations and studies in the Hydro-Québec power system, *Journal of Atmospheric and Solar-Terrestrial Physics*, *64*(16), 1793 – 1802, doi:https://doi.org/10.1016/S1364-6826(02)00128-1, space Weather Effects on Technological Systems.

Borovsky, J. E., and M. H. Denton (2009), Electron loss rates from the outer radiation belt caused by the filling of the outer plasmasphere: The calm before the storm, *Journal of Geophysical Research: Space Physics*, *114*(A11), doi:10.1029/2009JA014063, a11203.

Bortnik, J., R. M. Thorne, and N. P. Meredith (2008a), The unexpected origin of plasmaspheric hiss from discrete chorus emissions, *Nature*, *452*.

Bortnik, J., R. M. Thorne, and U. S. Inan (2008b), Nonlinear interaction of energetic electrons with large amplitude chorus, *Geophysical Research Letters*, *35*(21), doi:10.1029/2008GL035500.

Bowers, K. J., B. J. Albright, B. Bergen, L. Yin, K. J. Barker, and D. J. Kerbyson (2008a), 0.374 Pflop/s Trillion-particle Kinetic Modeling of Laser Plasma Interaction on Roadrunner, in *Proceedings of the 2008 ACM/IEEE Conference on Supercomputing*, SC '08, pp. 63:1–63:11, IEEE Press, Piscataway, NJ, USA.

Bowers, K. J., B. J. Albright, L. Yin, B. Bergen, and T. J. T. Kwan (2008b), Ultrahigh performance three-dimensional electromagnetic relativistic kinetic plasma simulation, *Physics of Plasmas*, *15*(5), 055,703, doi:10.1063/1.2840133.

Bowers, K. J., B. J. Albright, L. Yin, W. Daughton, V. Roytershteyn, B. Bergen, and T. J. T. Kwan (2009), Advances in petascale kinetic plasma simulation with VPIC and Roadrunner, *Journal of Physics: Conference Series*, *180*(1), 012,055.

Boyd, A. J., H. E. Spence, S. G. Claudepierre, J. F. Fennell, J. B. Blake, D. N. Baker, G. D. Reeves, and D. L. Turner (2014), Quantifying the radiation belt seed population in the 17 March 2013 electron acceleration event, *Geophysical Research Letters*, *41*(7), 2275–2281, doi:10.1002/2014GL059626.

Boyd, A. J., D. L. Turner, G. D. Reeves, H. E. Spence, D. N. Baker, and J. B. Blake (2018), What Causes Radiation Belt Enhancements: A Survey of the Van Allen Probes Era, *Geophysical Research Letters*, *45*(11), 5253–5259, doi:10.1029/2018GL077699.

Brautigam, D. H., and J. M. Albert (2000), Radial diffusion analysis of outer radiation belt electrons during the October 9, 1990, magnetic storm, *Journal of Geophysical Research: Space Physics*, *105*(A1), 291–309, doi:10.1029/1999JA900344.

Brice, N., and T. R. Mcdonough (1973), Jupiter's radiation belts, *Icarus*, *18*(2), 206 – 219, doi:http://dx.doi.org/10.1016/0019-1035(73)90204-2.

Brito, T., M. K. Hudson, B. Kress, J. Paral, A. Halford, R. Millan, and M. Usanova (2015), Simulation of ULF wave-modulated radiation belt electron precipitation during the 17 March 2013 storm, *Journal of Geophysical Research: Space Physics*, *120*(5), 3444–3461, doi:10.1002/2014JA020838.

Bussutil, E. (2014), Dynamique des électrons piégés dans les ceintures de Van Allen, *Tech. rep.*, CEA, Master thesis directed by J.-F. Ripoll.

Cain, G., and G. Meyer (2005), *Separation of Variables for Partial Differential Equations: An Eigenfunction Approach*, Studies in Advanced Mathematics, CRC Press.

Carpenter, D. L. (1963), Whistler evidence of a 'knee' in the magnetospheric ionization density profile, *Journal of Geophysical Research*, *68*(6), 1675–1682, doi: 10.1029/JZ068i006p01675.

Carpenter, D. L., and R. R. Anderson (1992), An ISEE/whistler model of equatorial electron density in the magnetosphere, *Journal of Geophysical Research: Space Physics*, *97*(A2), 1097–1108, doi:10.1029/91JA01548.

Cary, J. R., and A. J. Brizard (2009), Hamiltonian theory of guiding-center motion, *Rev. Mod. Phys.*, *81*, 693–738, doi:10.1103/RevModPhys.81.693.

Cattell, C., J. R. Wygant, K. Goetz, K. Kersten, P. J. Kellogg, T. von Rosenvinge, S. D. Bale, I. Roth, M. Temerin, M. K. Hudson, R. A. Mewaldt, M. Wiedenbeck, M. Maksimovic, R. Ergun, M. Acuna, and C. T. Russell (2008), Discovery of very large amplitude whistler-mode waves in Earth's radiation belts, *Geophysical Research Letters*, *35*(1), doi:10.1029/2007GL032009.

Chandrasekhar, S. (1943), Stochastic Problems in Physics and Astronomy, *Rev. Mod. Phys.*, *15*, 1–89, doi:10.1103/RevModPhys.15.1.

Chandrasekhar, S. (1960), *Plasma Physics: A Course Given by S. Chandrasekhar at the University of Chicago*, University of Chicago Press.

Chappell, C. R., M. M. Huddleston, T. E. Moore, B. L. Giles, and D. C. Delcourt (2008), Observations of the warm plasma cloak and an explanation of its formation in the magnetosphere, *Journal of Geophysical Research: Space Physics*, *113*(A9), doi: 10.1029/2007JA012945.

Chen, Y., R. H. W. Friedel, M. G. Henderson, S. G. Claudepierre, S. K. Morley, and H. E. Spence (2014), REPAD: An empirical model of pitch angle distributions for energetic electrons in the Earth's outer radiation belt, *Journal of Geophysical Research: Space Physics*, *119*(3), 1693–1708, doi:10.1002/2013JA019431.

Claudepierre, S. G., T. P. O'Brien, J. B. Blake, J. F. Fennell, J. L. Roeder, J. H. Clemmons, M. D. Looper, J. E. Mazur, T. M. Mulligan, H. E. Spence, G. D. Reeves, R. H. W. Friedel, M. G. Henderson, and B. A. Larsen (2015), A background correction algorithm for Van Allen Probes MagEIS electron flux measurements, *Journal of Geophysical Research: Space Physics*, *120*(7), 5703–5727, doi:10.1002/2015JA021171.

Claudepierre, S. G., T. P. O'Brien, J. F. Fennell, J. B. Blake, J. H. Clemmons, M. D. Looper, J. E. Mazur, J. L. Roeder, D. L. Turner, G. D. Reeves, and H. E. Spence (2017), The hidden dynamics of relativistic electrons (0.7âĂŞ1.5 MeV) in the inner zone and slot region, *Journal of Geophysical Research: Space Physics*, *122*(3), 3127–3144, doi:10.1002/2016JA023719.

Coroniti, F. V. (1974), Energetic Electrons in Jupiter's Magnetosphere, *The Astrophysical Journal Supplement Series*, *27*, 261, doi:10.1086/190296.

Courtillot, V., and J.-L. Le Mouel (1988), Time Variations of the Earth's Magnetic Field: From Daily to Secular, *Annual Review of Earth and Planetary Sciences*, *16*, 389–476.

Cully, C. M., J. W. Bonnell, and R. E. Ergun (2008), THEMIS observations of long-lived regions of large-amplitude whistler waves in the inner magnetosphere, *Geophysical Research Letters*, *35*(17), doi:10.1029/2008GL033643.

Cunningham, G. S. (2016), Radial diffusion of radiation belt particles in nondipolar magnetic fields, *Journal of Geophysical Research: Space Physics*, *121*(6), 5149–5171, doi:10.1002/2015JA021981, 2015JA021981.

Cunningham, G. S., V. Loridan, J.-F. Ripoll, and M. Schulz (2018), Neoclassical Diffusion of Radiation-Belt Electrons Across Very Low L-Shells, *Journal of Geophysical Research: Space Physics*, *123*(4), 2884–2901, doi:10.1002/2017JA024931.

Davidson, G. T. (1976), An improved empirical description of the bounce motion of trapped particles, *Journal of Geophysical Research*, *81*(22), 4029–4030, doi:10.1029/JA081i022p04029.

de Pater, I., and C. K. Goertz (1990), Radial diffusion models of energetic electrons and Jupiter's synchrotron radiation: 1. Steady state solution, *Journal of Geophysical Research: Space Physics*, *95*(A1), 39–50, doi:10.1029/JA095iA01p00039.

de Pater, I., and C. K. Goertz (1994), Radial diffusion models of energetic electrons and Jupiter's synchrotron radiation: 2. Time variability, *Journal of Geophysical Research: Space Physics*, *99*(A2), 2271–2287, doi:10.1029/93JA02097.

Degeling, A. W., L. G. Ozeke, R. Rankin, I. R. Mann, and K. Kabin (2008), Drift resonant generation of peaked relativistic electron distributions by Pc 5 ULF waves, *Journal of Geophysical Research: Space Physics*, *113*(A2), doi:10.1029/2007JA012411.

Drozdov, A. Y., Y. Y. Shprits, K. G. Orlova, A. C. Kellerman, D. A. Subbotin, D. N. Baker, H. E. Spence, and G. D. Reeves (2015), Energetic, relativistic, and ultrarelativistic electrons: Comparison of long-term VERB code simulations with Van Allen Probes measurements, *Journal of Geophysical Research: Space Physics*, *120*(5), 3574–3587, doi:10.1002/2014JA020637.

Ebihara, Y., and Y. Miyoshi (2011), *Dynamic Inner Magnetosphere: A Tutorial and Recent Advances*, pp. 145–187, Springer Netherlands, Dordrecht, doi:10.1007/978-94-007-0501-2_9.

Engebretson, M. J., J. L. Posch, J. R. Wygant, C. A. Kletzing, M. R. Lessard, C.-L. Huang, H. E. Spence, C. W. Smith, H. J. Singer, Y. Omura, R. B. Horne, G. D. Reeves, D. N. Baker, M. Gkioulidou, K. Oksavik, I. R. Mann, T. . Raita, and K. Shiokawa (2015), Van Allen probes, NOAA, GOES, and ground observations of an intense EMIC wave event extending over 12 h in magnetic local time, *Journal of Geophysical Research: Space Physics*, *120*(7), 5465–5488, doi:10.1002/2015JA021227.

Engebretson, M. J., J. L. Posch, D. J. Braun, W. Li, Q. Ma, A. C. Kellerman, C.-L. Huang, S. G. Kanekal, C. A. Kletzing, J. R. Wygant, H. E. Spence, D. N. Baker, J. F. Fennell, V. Angelopoulos, H. J. Singer, M. R. Lessard, R. B. Horne, T. Raita, K. Shiokawa, R. Rakhmatulin, E. Dmitriev, and E. Ermakova (2018), EMIC Wave Events During the Four GEM QARBM Challenge Intervals, *Journal of Geophysical Research: Space Physics*, *0*(0), doi:10.1029/2018JA025505.

Fälthammar, C.-G. (1965), Effects of time-dependent electric fields on geomagnetically trapped radiation, *Journal of Geophysical Research*, *70*(11), 2503–2516, doi:10.1029/JZ070i011p02503.

Fälthammar, C.-G. (1966), On the transport of trapped particles in the outer magnetosphere, *Journal of Geophysical Research*, *71*(5), 1487–1491, doi:10.1029/JZ071i005p01487.

Fälthammar, C.-G. (1968), Radial Diffusion by Violation of the Third Adiabatic Invariant, in *Earth's Particles and Fields*, edited by B. M. McCormac, p. 157.

Farley, T. A. (1969), Radial diffusion of starfish electrons, *Journal of Geophysical Research*, *74*(14), 3591–3600, doi:10.1029/JA074i014p03591.

Farley, T. A., and N. L. Sanders (1962), Pitch angle distributions and mirror point densities in the outer radiation zone, *Journal of Geophysical Research*, *67*(6), 2159–2168, doi:10.1029/JZ067i006p02159.

Fennell, J. F., S. Kanekal, and J. L. Roeder (2013), *Storm Responses of Radiation Belts During Solar Cycle 23: HEO Satellite Observations*, pp. 371–384, American Geophysical Union (AGU), doi:10.1029/2012GM001356.

Fennell, J. F., S. G. Claudepierre, J. B. Blake, T. P. O'Brien, J. H. Clemmons, D. N. Baker, H. E. Spence, and G. D. Reeves (2015), Van Allen Probes show that the inner radiation zone contains no MeV electrons: ECT/MagEIS data, *Geophysical Research Letters*, *42*(5), 1283–1289, doi:10.1002/2014GL062874.

Friedel, R., G. Reeves, and T. Obara (2002), Relativistic electron dynamics in the inner magnetosphere - a review, *Journal of Atmospheric and Solar-Terrestrial Physics*, *64*(2), 265 – 282, doi:https://doi.org/10.1016/S1364-6826(01)00088-8, sTEP-Results, Applications and Modelling Phase (S-RAMP).

Friedel, R. H. W., A. Korth, and G. Kremser (1996), Substorm onsets observed by CRRES: Determination of energetic particle source regions, *Journal of Geophysical Research: Space Physics*, *101*(A6), 13,137–13,154, doi:10.1029/96JA00399.

Gannon, J. L., X. Li, and D. Heynderickx (2007), Pitch angle distribution analysis of radiation belt electrons based on Combined Release and Radiation Effects Satellite Medium Electrons A data, *Journal of Geophysical Research: Space Physics*, *112*(A5), doi:10.1029/2005JA011565.

Glauert, S. A., and R. B. Horne (2005), Calculation of pitch angle and energy diffusion coefficients with the PADIE code, *Journal of Geophysical Research: Space Physics*, *110*(A4), doi:10.1029/2004JA010851.

Glauert, S. A., R. B. Horne, and N. P. Meredith (2014), Three-dimensional electron radiation belt simulations using the BAS Radiation Belt Model with new diffusion models for chorus, plasmaspheric hiss, and lightning-generated whistlers, *Journal of Geophysical Research: Space Physics*, *119*(1), 268–289, doi:10.1002/2013JA019281.

Goertz, C. K., J. A. Van Allen, and M. F. Thomsen (1979), Further observational support for the lossy radial diffusion model of the inner Jovian magnetosphere, *Journal of Geophysical Research: Space Physics*, *84*(A1), 87–92, doi:10.1029/JA084iA01p00087.

Gombosi, T. I., G. Tóth, D. L. D. Zeeuw, K. C. Hansen, K. Kabin, and K. G. Powell (2002), Semirelativistic Magnetohydrodynamics and Physics-Based Convergence Acceleration, *Journal of Computational Physics*, *177*(1), 176 – 205, doi:https://doi.org/10.1006/jcph.2002.7009.

Green, J. C., and M. G. Kivelson (2004), Relativistic electrons in the outer radiation belt: Differentiating between acceleration mechanisms, *Journal of Geophysical Research: Space Physics*, *109*(A3), doi:10.1029/2003JA010153.

Green, J. C., T. G. Onsager, T. P. O'Brien, and D. N. Baker (2004), Testing loss mechanisms capable of rapidly depleting relativistic electron flux in the Earth's outer radiation belt, *Journal of Geophysical Research: Space Physics*, *109*(A12), doi:10.1029/2004JA010579.

Gu, X., Y. Y. Shprits, and B. Ni (2012), Parameterized lifetime of radiation belt electrons interacting with lower-band and upper-band oblique chorus waves, *Geophysical Research Letters*, *39*(15), doi:10.1029/2012GL052519, l15102.

Haerendel, G. (1968), Diffusion Theory of Trapped Particles and the Observed Proton Distribution, in *Earth's Particles and Fields*, edited by B. M. McCormac, p. 171.

Hapgood, M. A. (1992), Space physics coordinate transformations - A user guide, *Planetary and Space Science*, *40*, 711–717, doi:10.1016/0032-0633(92)90012-D.

Hess, W. N. (1968), *The radiation belt and magnetosphere*.

Hood, L. L. (1983), Radial diffusion in Saturn's radiation belts: A modeling analysis assuming satellite and ring E absorption, *Journal of Geophysical Research: Space Physics*, *88*(A2), 808–818, doi:10.1029/JA088iA02p00808.

Horne, R. B., N. P. Meredith, R. M. Thorne, D. Heynderickx, R. H. A. Iles, and R. R. Anderson (2003), Evolution of energetic electron pitch angle distributions during storm time electron acceleration to megaelectronvolt energies, *Journal of Geophysical Research: Space Physics*, *108*(A1), SMP 11–1–SMP 11–13, doi:10.1029/2001JA009165.

Horne, R. B., R. M. Thorne, Y. Y. Shprits, N. P. Meredith, S. A. lauert, A. J. Smith, S. G. Kanekal, D. N. Baker, M. J. Engebretson, J. L. Posch, M. Spasojevic, U. S. Inan, J. S. Pickett, and P. M. E. Decreau (2005), Wave acceleration of electrons in the Van Allen radiation belts, *Nature*, *437*, 227.

Hudson, M. K., J. Paral, B. T. Kress, M. Wiltberger, D. N. Baker, J. C. Foster, D. L. Turner, and J. R. Wygant (2015), Modeling CME-shock-driven storms in 2012-2013: MHD test particle simulations, *Journal of Geophysical Research: Space Physics*, *120*(2), 1168–1181, doi:10.1002/2014JA020833.

Imhof, W. L., J. B. Reagan, and R. V. Smith (1967), Long-term study of electrons trapped on low L shells, *Journal of Geophysical Research*, *72*(9), 2371–2377, doi:10.1029/JZ072i009p02371.

Jackson, J. D. (1975), *Classical Electrodynamics*, second ed., Wiley, New York.

Jentsch, V. (1984), The radial distribution of radiation belt protons: Approximate solution of the steady state transport equation at arbitrary pitch angle, *Journal of Geophysical Research: Space Physics*, *89*(A3), 1527–1539, doi:10.1029/JA089iA03p01527.

Jordanova, V. K., Y. S. Miyoshi, S. Zaharia, M. F. Thomsen, G. D. Reeves, D. S. Evans, C. G. Mouikis, and J. F. Fennell (2006), Kinetic simulations of ring current evolution during the Geospace Environment Modeling challenge events, *Journal of Geophysical Research: Space Physics*, *111*(A11), doi:10.1029/2006JA011644.

Jordanova, V. K., S. Zaharia, and D. T. Welling (2010), Comparative study of ring current development using empirical, dipolar, and self-consistent magnetic field simulations, *Journal of Geophysical Research: Space Physics*, *115*(A12), doi:10.1029/2010JA015671.

Kaufmann, R. (1965), Conservation of the first and second adiabatic invariants, *Journal of Geophysical Research*, *70*.

Kellogg, P. J. (1959), Van Allen Radiation of Solar Origin, *Nature*, *183*, 1295–1297, doi:10.1038/1831295a0.

Kellogg, P. J., C. A. Cattell, K. Goetz, S. J. Monson, and L. B. Wilson (2010), Electron trapping and charge transport by large amplitude whistlers, *Geophysical Research Letters*, *37*(20), doi:10.1029/2010GL044845.

Kennel, C. F., and F. Engelmann (1966), Velocity Space Diffusion from Weak Plasma Turbulence in a Magnetic Field, *The Physics of Fluids*, *9*(12), 2377–2388, doi:10.1063/1.1761629.

Kersten, T., R. B. Horne, S. A. Glauert, N. P. Meredith, B. J. Fraser, and R. S. Grew (2014), Electron losses from the radiation belts caused by EMIC waves, *Journal of Geophysical Research: Space Physics*, *119*(11), 8820–8837, doi:10.1002/2014JA020366.

Kim, H.-J., and A. A. Chan (1997), Fully adiabatic changes in storm time relativistic electron fluxes, *Journal of Geophysical Research: Space Physics*, *102*(A10), 22,107–22,116, doi:10.1029/97JA01814.

Kim, K. C., D.-Y. Lee, H.-J. Kim, L. R. Lyons, E. S. Lee, M. K. Öztürk, and C. R. Choi (2008), Numerical calculations of relativistic electron drift loss effect, *Journal of Geophysical Research: Space Physics*, *113*(A9), doi:10.1029/2007JA013011.

Kim, K.-C., Y. Shprits, D. Subbotin, and B. Ni (2011), Understanding the dynamic evolution of the relativistic electron slot region including radial and pitch angle diffusion, *Journal of Geophysical Research: Space Physics*, *116*(A10), doi:10.1029/2011JA016684.

Kim, K.-C., Y. Y. Shprits, and J. B. Blake (2016), Fast injection of the relativistic electrons into the inner zone and the formation of the split-zone structure during the Bastille Day storm in July 2000, *Journal of Geophysical Research: Space Physics*, *121*(9), 8329–8342, doi:10.1002/2015JA022072.

Kletzing, C. A., W. S. Kurth, M. Acuna, R. J. MacDowall, R. B. Torbert, T. Averkamp, D. Bodet, S. R. Bounds, M. Chutter, J. Connerney, D. Crawford, J. S. Dolan, R. Dvorsky, G. B. Hospodarsky, J. Howard, V. Jordanova, R. A. Johnson, D. L. Kirchner, B. Mokrzycki, G. Needell, J. Odom, D. Mark, R. Pfaff, J. R. Phillips, C. W. Piker, S. L. Remington, D. Rowland, O. Santolík, R. Schnurr, D. Sheppard, C. W. Smith, R. M. Thorne, and J. Tyler (2013), The Electric and Magnetic Field Instrument Suite and Integrated Science (EMFISIS) on RBSP, *Space Science Reviews*, *179*(1), 127–181, doi:10.1007/s11214-013-9993-6.

Korth, A., R. H. W. Friedel, C. G. Mouikis, J. F. Fennell, J. R. Wygant, and H. Korth (2000), Comprehensive particle and field observations of magnetic storms at different local times from the CRRES spacecraft, *Journal of Geophysical Research: Space Physics*, *105*(A8), 18,729–18,740, doi:10.1029/1999JA000430.

Kruskal, M. (1962), Asymptotic Theory of Hamiltonian and other Systems with all Solutions Nearly Periodic, *Journal of Mathematical Physics*, *3*(4), 806–828, doi:10.1063/1.1724285.

Lam, H.-L., D. H. Boteler, B. Burlton, and J. Evans (2012), Anik-E1 and E2 satellite failures of January 1994 revisited, *Space Weather*, *10*(10), doi:10.1029/2012SW000811.

Lanzerotti, L. J. (2007), *Space weather effects on communications*, pp. 247–268, Springer Berlin Heidelberg, Berlin, Heidelberg, doi:10.1007/978-3-540-34578-7_9.

Lavraud, B., H. Réme, M. W. Dunlop, J.-M. Bosqued, I. Dandouras, J.-A. Sauvaud, A. Keiling, T. D. Phan, R. Lundin, P. J. Cargill, C. P. Escoubet, C. W. Carlson, J. P. McFadden, G. K. Parks, E. Moebius, L. M. Kistler, E. Amata, M.-B. Bavassano-Cattaneo, A. Korth, B. Klecker, and A. Balogh (2005), *Cluster Observes the High-Altitude Cusp Region*, pp. 135–175, Springer Netherlands, Dordrecht, doi:10.1007/1-4020-3605-1_6.

Lavraud, B., C. Foullon, C. J. Farrugia, and J. P. Eastwood (2011), *The magnetopause, its boundary layers and pathways to the magnetotail*, pp. 3–28, Springer Netherlands, Dordrecht, doi:10.1007/978-94-007-0501-2_1.

Lejosne, S. (2013), Modélisation du phénomène de diffusion radiale au sein des ceintures de radiation terrestres par technique de changement d'échelle, Ph.D. thesis, thèse de doctorat dirigée par Boscher, Daniel et Maget, Vincent Astrophysique, sciences de l'espace, planétologie Toulouse, ISAE 2013.

Lerche, I. (1968), Quasilinear Theory of Resonant Diffusion in a Magneto-Active, Relativistic Plasma, *The Physics of Fluids*, *11*(8), 1720–1727, doi:10.1063/1.1692186.

Li, W., R. M. Thorne, Q. Ma, B. Ni, J. Bortnik, D. N. Baker, H. E. Spence, G. D. Reeves, S. G. Kanekal, J. C. Green, C. A. Kletzing, W. S. Kurth, G. B. Hospodarsky, J. B. Blake, J. F. Fennell, and S. G. Claudepierre (2014a), Radiation belt electron acceleration by chorus waves during the 17 March 2013 storm, *Journal of Geophysical Research: Space Physics*, *119*(6), 4681–4693, doi:10.1002/2014JA019945.

Li, W., Q. Ma, R. M. Thorne, J. Bortnik, C. A. Kletzing, W. S. Kurth, G. B. Hospodarsky, and Y. Nishimura (2015), Statistical properties of plasmaspheric hiss derived from Van Allen Probes data and their effects on radiation belt electron dynamics, *Journal of Geophysical Research: Space Physics*, *120*(5), 3393–3405, doi:10.1002/2015JA021048.

Li, W., O. Santolík, J. Bortnik, R. M. Thorne, C. A. Kletzing, W. S. Kurth, and G. B. Hospodarsky (2016a), New chorus wave properties near the equator from Van Allen Probes wave observations, *Geophysical Research Letters*, *43*(10), 4725–4735, doi:10.1002/2016GL068780.

Li, W., Q. Ma, R. M. Thorne, J. Bortnik, X.-J. Zhang, J. Li, D. N. Baker, G. D. Reeves, H. E. Spence, C. A. Kletzing, W. S. Kurth, G. B. Hospodarsky, J. B. Blake,

J. F. Fennell, S. G. Kanekal, V. Angelopoulos, J. C. Green, and J. Goldstein (2016b), Radiation belt electron acceleration during the 17 March 2015 geomagnetic storm: Observations and simulations, *Journal of Geophysical Research: Space Physics*, *121*(6), 5520–5536, doi:10.1002/2016JA022400.

Li, X., D. N. Baker, M. Temerin, T. E. Cayton, E. G. D. Reeves, R. A. Christensen, J. B. Blake, M. D. Looper, R. Nakamura, and S. G. Kanekal (1997), Multisatellite observations of the outer zone electron variation during the November 3-4, 1993, magnetic storm, *Journal of Geophysical Research: Space Physics*, *102*(A7), 14,123–14,140, doi:10.1029/97JA01101.

Li, Z., M. Hudson, A. Jaynes, A. Boyd, D. Malaspina, S. Thaller, J. Wygant, and M. Henderson (2014b), Modeling gradual diffusion changes in radiation belt electron phase space density for the March 2013 Van Allen Probes case study, *Journal of Geophysical Research: Space Physics*, *119*(10), 8396–8403, doi:10.1002/2014JA020359.

Liu, W., W. Tu, X. Li, T. Sarris, Y. Khotyaintsev, H. Fu, H. Zhang, and Q. Shi (2016), On the calculation of electric diffusion coefficient of radiation belt electrons with in situ electric field measurements by THEMIS, *Geophysical Research Letters*, *43*(3), 1023–1030, doi:10.1002/2015GL067398, 2015GL067398.

Loridan, V., G. S. Cunningham, and J.-F. Ripoll (2016), Anomalous radial diffusion at low L shell due to the combined effects of drift-shell splitting and atmospheric pitch angle scattering, in *2016 Los Alamos Space Weather Summer School Research Reports*, edited by M. Cowee, pp. 35–45.

Loridan, V., J.-F. Ripoll, and F. de Vuyst (2017), The analytical solution of the transient radial diffusion equation with a nonuniform loss term, *Journal of Geophysical Research: Space Physics*, *122*(6), 5979–6006, doi:10.1002/2017JA023868.

Loridan, V., J.-F. Ripoll, W. Tu, and G. S. Cunningham (2018, in preparation), On the use of different magnetic field models for the major storm of October 1990, *Journal of Geophysical Research: Space Physics*.

Love, J. J., and K. J. Remick (2007), *Magnetic Indices*, pp. 509–512, Springer Netherlands, Dordrecht, doi:10.1007/978-1-4020-4423-6_178.

Lyons, L. R. (1974a), General relations for resonant particle diffusion in pitch angle and energy, *Journal of Plasma Physics*, *12*(1), 45–49, doi:10.1017/S0022377800024910.

Lyons, L. R. (1974b), Pitch angle and energy diffusion coefficients from resonant interactions with ion-cyclotron and whistler waves, *Journal of Plasma Physics*, *12*(3), 417–432, doi:10.1017/S002237780002537X.

Lyons, L. R., and R. M. Thorne (1973), Equilibrium structure of radiation belt electrons, *Journal of Geophysical Research*, *78*(13), 2142–2149, doi:10.1029/JA078i013p02142.

Lyons, L. R., R. M. Thorne, and C. F. Kennel (1971), Electron pitch-angle diffusion driven by oblique whistler-mode turbulence, *Journal of Plasma Physics*, *6*(3), 589–606, doi:10.1017/S0022377800006310.

Lyons, L. R., R. M. Thorne, and C. F. Kennel (1972), Pitch-angle diffusion of radiation belt electrons within the plasmasphere, *Journal of Geophysical Research*, *77*(19), 3455–3474, doi:10.1029/JA077i019p03455.

Ma, Q., W. Li, R. M. Thorne, Y. Nishimura, X.-J. Zhang, G. D. Reeves, C. A. Kletzing, W. S. Kurth, G. B. Hospodarsky, M. G. Henderson, H. E. Spence, D. N. Baker, J. B. Blake, J. F. Fennell, and V. Angelopoulos (2016), Simulation of energy-dependent electron diffusion processes in the Earth's outer radiation belt, *Journal of Geophysical Research: Space Physics*, *121*(5), 4217–4231, doi:10.1002/2016JA022507.

Ma, Q., W. Li, J. Bortnik, R. M. Thorne, X. Chu, L. G. Ozeke, G. D. Reeves, C. Kletzing, W. Kurth, G. Hospodarsky, M. Engebretson, H. Spence, D. N. Baker, J. B. Blake, J. F. Fennell, and S. Claudepierre (2018), Quantitative Evaluation of Radial Diffusion and Local Acceleration Processes During GEM Challenge Events, *123*.

Malaspina, D. M., J.-F. Ripoll, X. Chu, G. Hospodarsky, and J. Wygant (2018), Variation in plasmaspheric hiss wave power with plasma density, *Geophysical Research Letters*, *45*(18), 9417–9426, doi:10.1029/2018GL078564.

Mann, I. R., L. G. Ozeke, K. R. Murphy, S. G. Claudepierre, D. L. Turner, D. N. Baker, I. J. Rae, A. Kale, D. K. Milling, A. J. Boyd, H. E. Spence, G. D. Reeves, H. J. Singer, S. Dimitrakoudis, I. A. Daglis, and F. Honary (2016), Explaining the dynamics of the ultra-relativistic third Van Allen radiation belt., *Nature Physics*, *12*, 978.

Mauk, B. H., N. J. Fox, S. G. Kanekal, R. L. Kessel, D. G. Sibeck, and A. Ukhorskiy (2013), Science Objectives and Rationale for the Radiation Belt Storm Probes Mission, *Space Science Reviews*, *179*(1), 3–27, doi:10.1007/s11214-012-9908-y.

McCormac, B. M. (Ed.) (1969), *Particles and Fields in the Magnetosphere*, Astrophysics and Space Science Library, Springer.

McIlwain, C. E. (1961), Coordinates for mapping the distribution of magnetically trapped particles, *Journal of Geophysical Research*, *66*(11), 3681–3691, doi:10.1029/JZ066i011p03681.

McIlwain, C. E. (1966a), Magnetic Coordinates, in *Radiation Trapped in the Earth's Magnetic Field*, edited by B. M. McCormac, pp. 45–61, Springer Netherlands, Dordrecht.

McIlwain, C. E. (1966b), Ring current effects on trapped particles, *Journal of Geophysical Research*, *71*(15), 3623–3628, doi:10.1029/JZ071i015p03623.

Mead, G. D. (1964), Deformation of the geomagnetic field by the solar wind, *Journal of Geophysical Research*, *69*(7), 1181–1195, doi:10.1029/JZ069i007p01181.

Mei, C. (1997), *Mathematical Analysis in Engineering: How to Use the Basic Tools*, Cambridge University Press.

Meredith, N. P., R. B. Horne, R. M. Thorne, D. Summers, and R. R. Anderson (2004), Substorm dependence of plasmaspheric hiss, *Journal of Geophysical Research: Space Physics*, *109*(A6), doi:10.1029/2004JA010387.

Meredith, N. P., R. B. Horne, S. A. Glauert, R. M. Thorne, D. Summers, J. M. Albert, and R. R. Anderson (2006a), Energetic outer zone electron loss timescales during low geomagnetic activity, *Journal of Geophysical Research: Space Physics*, *111*(A5), doi:10.1029/2005JA011516, a05212.

Meredith, N. P., R. B. Horne, M. A. Clilverd, D. Horsfall, R. M. Thorne, and R. R. Anderson (2006b), Origins of plasmaspheric hiss, *Journal of Geophysical Research: Space Physics*, *111*(A9), doi:10.1029/2006JA011707, a09217.

Meredith, N. P., R. B. Horne, S. A. Glauert, and R. R. Anderson (2007), Slot region electron loss timescales due to plasmaspheric hiss and lightning-generated whistlers, *Journal of Geophysical Research: Space Physics*, *112*(A8), doi:10.1029/2007JA012413.

Meredith, N. P., R. B. Horne, S. A. Glauert, D. N. Baker, S. G. Kanekal, and J. M. Albert (2009), Relativistic electron loss timescales in the slot region, *Journal of Geophysical Research: Space Physics*, *114*(A3), doi:10.1029/2008JA013889.

Meyer-Vernet, N. (2007), *Basics of the Solar Wind*, Cambridge Atmospheric and Space Science Series, Cambridge University Press, doi:10.1017/CBO9780511535765.

Millan, R., and R. Thorne (2007), Review of radiation belt relativistic electron losses, *Journal of Atmospheric and Solar-Terrestrial Physics*, *69*(3), 362 – 377, doi:https://doi.org/10.1016/j.jastp.2006.06.019, global Aspects of Magnetosphere-Ionosphere Coupling.

Millan, R. M., and D. N. Baker (2012), Acceleration of Particles to High Energies in Earth's Radiation Belts, *Space Science Reviews*, *173*(1), 103–131, doi:10.1007/s11214-012-9941-x.

Miyoshi, Y., A. Morioka, H. Misawa, T. Obara, T. Nagai, and Y. Kasahara (2003), Rebuilding process of the outer radiation belt during the 3 November 1993 magnetic storm: NOAA and Exos-D observations, *Journal of Geophysical Research: Space Physics*, *108*(A1), SMP 3–1–SMP 3–15, doi:10.1029/2001JA007542.

Morley, S. K. (2016), Alternatives to accuracy and bias metrics based on percentage errors for radiation belt modeling applications, doi:10.2172/1260362.

Morley, S. K., T. V. Brito, and D. T. Welling (2018), Measures of Model Performance Based On the Log Accuracy Ratio, *Space Weather*, *16*(1), 69–88, doi:10.1002/2017SW001669.

Mourenas, D., and J.-F. Ripoll (2012), Analytical estimates of quasi-linear diffusion coefficients and electron lifetimes in the inner radiation belt, *Journal of Geophysical Research: Space Physics*, *117*(A1), doi:10.1029/2011JA016985, a01204.

Mozer, F. S. (1973), Electric fields and plasma convection in the plasmasphere, *Reviews of Geophysics*, *11*(3), 755–765, doi:10.1029/RG011i003p00755.

Newkirk, L. L., and M. Walt (1968), Radial diffusion coefficient for electrons at low L values, *Journal of Geophysical Research*, *73*(3), 1013–1017, doi:10.1029/JA073i003p01013.

Ni, B., Y. Shprits, T. Nagai, R. Thorne, Y. Chen, D. Kondrashov, and H.-j. Kim (2009), Reanalyses of the radiation belt electron phase space density using nearly equatorial CRRES and polar-orbiting Akebono satellite observations, *Journal of Geophysical Research: Space Physics*, *114*(A5), doi:10.1029/2008JA013933, a05208.

Ni, B., R. M. Thorne, Y. Y. Shprits, K. G. Orlova, and N. P. Meredith (2011), Chorus-driven resonant scattering of diffuse auroral electrons in nondipolar magnetic fields, *Journal of Geophysical Research: Space Physics*, *116*(A6), doi:10.1029/2011JA016453.

Ni, B., Z. Zou, X. Gu, C. Zhou, R. M. Thorne, J. Bortnik, R. Shi, Z. Zhao, D. N. Baker, S. G. Kanekal, H. E. Spence, G. D. Reeves, and X. Li (2015), Variability of the pitch angle distribution of radiation belt ultrarelativistic electrons during and following intense geomagnetic storms: Van Allen Probes observations, *Journal of Geophysical Research: Space Physics*, *120*(6), 4863–4876, doi:10.1002/2015JA021065, 2015JA021065.

Northrop, T. G. (1963a), *The adiabatic motion of charged particles*, Interscience, New York.

Northrop, T. G. (1963b), Adiabatic charged-particle motion, *Reviews of Geophysics*, *1*(3), 283–304, doi:10.1029/RG001i003p00283.

Northrop, T. G., and E. Teller (1960), Stability of the Adiabatic Motion of Charged Particles in the Earth's Field, *Physical Review*, *117*, 215–225, doi:10.1103/PhysRev.117.215.

O'Brien, T. P. (2014), Breaking all the invariants: Anomalous electron radiation belt diffusion by pitch angle scattering in the presence of split magnetic drift shells, *Geophysical Research Letters*, *41*(2), 216–222, doi:10.1002/2013GL058712.

O'Brien, T. P. (2015), The activity and radial dependence of anomalous diffusion by pitch angle scattering on split magnetic drift shells, *Journal of Geophysical Research: Space Physics*, *120*(1), 328–343, doi:10.1002/2014JA020422, 2014JA020422.

O'Brien, T. P., S. G. Claudepierre, J. B. Blake, J. F. Fennell, J. H. Clemmons, J. L. Roeder, H. E. Spence, G. D. Reeves, and D. N. Baker (2014), An empirically observed pitch-angle diffusion eigenmode in the Earth's electron belt near $L^* = 5.0$, *Geophysical Research Letters*, *41*(2), 251–258, doi:10.1002/2013GL058713, 2013GL058713.

Olifer, L., I. R. Mann, S. K. Morley, L. G. Ozeke, and D. Choi (2018), On the Role of Last Closed Drift Shell Dynamics in Driving Fast Losses and Van Allen Radiation Belt Extinction, *Journal of Geophysical Research: Space Physics*, *123*(5), 3692–3703, doi:10.1029/2018JA025190.

Olson, W. P., and K. A. Pfitzer (1982), A dynamic model of the magnetospheric magnetic and electric fields for July 29, 1977, *Journal of Geophysical Research: Space Physics*, *87*(A8), 5943–5948, doi:10.1029/JA087iA08p05943.

Orlova, K., and Y. Shprits (2014), Model of lifetimes of the outer radiation belt electrons in a realistic magnetic field using realistic chorus wave parameters, *Journal of Geophysical Research: Space Physics*, *119*(2), 770–780, doi:10.1002/2013JA019596, 2013JA019596.

Orlova, K., M. Spasojevic, and Y. Shprits (2014), Activity-dependent global model of electron loss inside the plasmasphere, *Geophysical Research Letters*, *41*(11), 3744–3751, doi:10.1002/2014GL060100, 2014GL060100.

Orlova, K., Y. Shprits, and M. Spasojevic (2016), New global loss model of energetic and relativistic electrons based on Van Allen Probes measurements, *Journal of Geophysical Research: Space Physics*, *121*(2), 1308–1314, doi:10.1002/2015JA021878, 2015JA021878.

Orlova, K. G., and Y. Y. Shprits (2010), Dependence of pitch-angle scattering rates and loss timescales on the magnetic field model, *Geophysical Research Letters*, *37*(5), doi:10.1029/2009GL041639.

Orlova, K. G., and Y. Y. Shprits (2011), On the bounce-averaging of scattering rates and the calculation of bounce period, *Physics of Plasmas*, *18*(9), 092,904, doi:10.1063/1.3638137.

Orlova, K. G., Y. Y. Shprits, and B. Ni (2012), Bounce-averaged diffusion coefficients due to resonant interaction of the outer radiation belt electrons with oblique chorus waves computed in a realistic magnetic field model, *Journal of Geophysical Research: Space Physics*, *117*(A7), doi:10.1029/2012JA017591.

Ozeke, L. G., I. R. Mann, K. R. Murphy, I. Jonathan Rae, and D. K. Milling (2014), Analytic expressions for ULF wave radiation belt radial diffusion coefficients, *Journal of Geophysical Research: Space Physics*, *119*(3), 1587–1605, doi:10.1002/2013JA019204, 2013JA019204.

Parker, E. N. (1991), Space plasma and its origin at the sun, *Physics of Fluids B: Plasma Physics*, *3*(8), 2367–2373, doi:10.1063/1.859605.

Picone, J. M., A. E. Hedin, D. P. Drob, and A. C. Aikin (2002), NRLMSISE-00 empirical model of the atmosphere: Statistical comparisons and scientific issues, *Journal of Geophysical Research: Space Physics*, *107*(A12), SIA 15–1–SIA 15–16, doi:10.1029/2002JA009430.

Pierrard, V., and J. Lemaire (1998), A collisional kinetic model of the polar wind, *Journal of Geophysical Research: Space Physics*, *103*(A6), 11,701–11,709, doi:10.1029/98JA00628.

Pierrard, V., and G. Lopez Rosson (2016), The effects of the big storm events in the first half of 2015 on the radiation belts observed by EPT/PROBA-V, *Annales Geophysicae*, *34*(1), 75–84, doi:10.5194/angeo-34-75-2016.

Pierrard, V., M. Maksimovic, and J. Lemaire (1999), Electron velocity distribution functions from the solar wind to the corona, *Journal of Geophysical Research: Space Physics*, *104*(A8), 17,021–17,032, doi:10.1029/1999JA900169.

Powell, K. G., P. L. Roe, T. J. Linde, T. I. Gombosi, and D. L. D. Zeeuw (1999), A Solution-Adaptive Upwind Scheme for Ideal Magnetohydrodynamics, *Journal of Computational Physics*, *154*(2), 284 – 309, doi:https://doi.org/10.1006/jcph.1999.6299.

Ray, E. C. (1960), On the theory of protons trapped in the Earth's magnetic field, *Journal of Geophysical Research*, *65*(4), 1125–1134, doi:10.1029/JZ065i004p01125.

Reeves, G. D., K. L. McAdams, R. H. W. Friedel, and T. P. O'Brien (2003), Acceleration and loss of relativistic electrons during geomagnetic storms, *Geophysical Research Letters*, *30*(10), doi:10.1029/2002GL016513.

Reeves, G. D., R. H. W. Friedel, B. A. Larsen, R. M. Skoug, H. O. Funsten, S. G. Claudepierre, J. F. Fennell, D. L. Turner, M. H. Denton, H. E. Spence, J. B. Blake, and D. N. Baker (2016), Energy-dependent dynamics of keV to MeV electrons in the inner zone, outer zone, and slot regions, *Journal of Geophysical Research: Space Physics*, *121*(1), 397–412, doi:10.1002/2015JA021569, 2015JA021569.

Richardson, I. G. (2013), What in the solar wind does the earth react to?, *AIP Conference Proceedings*, *1539*(1), 370–375, doi:10.1063/1.4811063.

Ripoll, J.-F., and D. Mourenas (2012), *High-Energy Electron Diffusion by Resonant Interactions with Whistler Mode Hiss*, pp. 281–290, American Geophysical Union (AGU), doi:10.1029/2012GM001309.

Ripoll, J.-F., J. M. Albert, and G. S. Cunningham (2014a), Electron lifetimes from narrowband wave-particle interactions within the plasmasphere, *Journal of Geophysical Research: Space Physics*, *119*(11), 8858–8880, doi:10.1002/2014JA020217.

Ripoll, J.-F., Y. Chen, J. F. Fennell, and R. H. W. Friedel (2014b), On long decays of electrons in the vicinity of the slot region observed by HEO3, *Journal of Geophysical Research: Space Physics*, *120*(1), 460–478, doi:10.1002/2014JA020449, 2014JA020449.

Ripoll, J.-F., V. Loridan, G. S. Cunningham, G. D. Reeves, and Y. Y. Shprits (2016a), On the time needed to reach an equilibrium structure of the radiation belts, *Journal of Geophysical Research: Space Physics*, *121*(8), 7684–7698, doi:10.1002/2015JA022207, 2015JA022207.

Ripoll, J.-F., G. D. Reeves, G. S. Cunningham, V. Loridan, M. Denton, O. Santolík, W. S. Kurth, C. A. Kletzing, D. L. Turner, M. G. Henderson, and A. Y. Ukhorskiy (2016b), Reproducing the observed energy-dependent structure of Earth's electron radiation belts during storm recovery with an event-specific diffusion model, *Geophysical Research Letters*, *43*(11), 5616–5625, doi:10.1002/2016GL068869, 2016GL068869.

Ripoll, J.-F., O. Santolík, G. D. Reeves, W. S. Kurth, M. H. Denton, V. Loridan, S. A. Thaller, C. A. Kletzing, and D. L. Turner (2017), Effects of whistler mode hiss waves in March 2013, *Journal of Geophysical Research: Space Physics*, *122*(7), 7433–7462, doi:10.1002/2017JA024139.

Ripoll, J.-F., V. Loridan, M. H. Denton, G. S. Cunningham, G. D. Reeves, O. Santolík, J. F. Fennell, D. L. Turner, A. Y. Drozdov, J. S. Cervantes Villa, Y. Y. Shprits, S. A. Thaller, W. S. Kurth, C. A. Kletzing, M. G. Henderson, and A. Y. Ukhorskiy (2018, in print), Observations and Fokker-Planck simulations of the L-shell, energy, and pitch-angle structure of Earth's electron radiation belts during quiet times, *Journal of Geophysical Research: Space Physics*.

Roederer, J. (1970), *Dynamics of geomagnetically trapped radiation*, Physics and chemistry in space, Springer-Verlag.

Roederer, J., and H. Zhang (2014), *Dynamics of Magnetically Trapped Particles: Foundations of the Physics of Radiation Belts and Space Plasmas*, Astrophysics and Space Science Library, Springer Berlin Heidelberg.

Roederer, J. G., and S. Lejosne (2018), Coordinates for Representing Radiation Belt Particle Flux, *Journal of Geophysical Research: Space Physics*, *123*(2), 1381–1387, doi:10.1002/2017JA025053.

Roederer, J. G., H. H. Hilton, and M. Schulz (1973), Drift shell splitting by internal geomagnetic multipoles, *Journal of Geophysical Research*, *78*(1), 133–144, doi:10.1029/JA078i001p00133.

Russell, C. T. (1971), Geophysical coordinate transformations., *Cosmic Electrodynamics*, *2*, 184–196.

Saikin, A. A., J.-C. Zhang, C. W. Smith, H. E. Spence, R. B. Torbert, and C. A. Kletzing (2016), The dependence on geomagnetic conditions and solar wind dynamic pressure of the spatial distributions of EMIC waves observed by the Van Allen Probes, *Journal of Geophysical Research: Space Physics*, *121*(5), 4362–4377, doi:10.1002/2016JA022523.

Saito, S., Y. Miyoshi, and K. Seki (2010), A split in the outer radiation belt by magnetopause shadowing: Test particle simulations, *Journal of Geophysical Research: Space Physics*, *115*(A8), doi:10.1029/2009JA014738.

Sandel, B. R., and M. H. Denton (2007), Global view of refilling of the plasmasphere, *Geophysical Research Letters*, *34*(17), doi:10.1029/2007GL030669.

Santolík, O., D. A. Gurnett, J. S. Pickett, M. Parrot, and N. Cornilleau-Wehrlin (2004), A microscopic and nanoscopic view of storm-time chorus on 31 March 2001, *Geophysical Research Letters*, *31*(2), doi:10.1029/2003GL018757.

Schiller, Q., X. Li, L. Blum, W. Tu, D. L. Turner, and J. B. Blake (2014), A nonstorm time enhancement of relativistic electrons in the outer radiation belt, *Geophysical Research Letters*, *41*(1), 7–12, doi:10.1002/2013GL058485.

Schulz, M. (1986), Eigenfunction Methods in Magnetospheric Radial-Diffusion Theory, in *Ion Acceleration in the Magnetosphere and Ionosphere*, edited by T. Chang, M. K. Hudson, J. R. Jasperse, R. G. Johnson, P. M. Kintner, and M. Schulz, pp. 158–163, American Geophysical Union, Washington, D. C., doi:10.1029/GM038p0158.

Schulz, M., and L. Lanzerotti (1974), *Particle diffusion in the radiation belts*, Physics and chemistry in space, Springer-Verlag.

Schulz, M., and A. L. Newman (1988), Eigenfunctions of the magnetospheric radial-diffusion operator, *Physica Scripta*, *37*(4), 632.

Selesnick, R. S. (2012), Atmospheric scattering and decay of inner radiation belt electrons, *Journal of Geophysical Research: Space Physics*, *117*(A8), doi:10.1029/2012JA017793, a08218.

Selesnick, R. S. (2015), Measurement of inner radiation belt electrons with kinetic energy above 1 MeV, *Journal of Geophysical Research: Space Physics*, *120*(10), 8339–8349, doi:10.1002/2015JA021387.

Selesnick, R. S., and J. B. Blake (2000), On the source location of radiation belt relativistic electrons, *Journal of Geophysical Research: Space Physics*, *105*(A2), 2607–2624, doi:10.1029/1999JA900445.

Selesnick, R. S., J. M. Albert, and M. J. Starks (2013), Influence of a ground-based VLF radio transmitter on the inner electron radiation belt, *Journal of Geophysical Research: Space Physics*, *118*(2), 628–635, doi:10.1002/jgra.50095.

Sergeev, V., E. Sazhina, N. Tsyganenko, J. Lundblad, and F. Søraas (1983), Pitch-angle scattering of energetic protons in the magnetotail current sheet as the dominant source of their isotropic precipitation into the nightside ionosphere, *Planetary and Space Science*, *31*(10), 1147 – 1155, doi:https://doi.org/10.1016/0032-0633(83)90103-4.

Shabansky, V. P. (1971), Some processes in the magnetosphere, *Space Science Reviews*, *12*(3), 299–418, doi:10.1007/BF00165511.

Shi, R., D. Summers, B. Ni, J. F. Fennell, J. B. Blake, H. E. Spence, and G. D. Reeves (2016), Survey of radiation belt energetic electron pitch angle distributions based on the Van Allen Probes MagEIS measurements, *Journal of Geophysical Research: Space Physics*, *121*(2), 1078–1090, doi:10.1002/2015JA021724.

Shprits, Y. Y., and B. Ni (2009), Dependence of the quasi-linear scattering rates on the wave normal distribution of chorus waves, *Journal of Geophysical Research: Space Physics*, *114*(A11), doi:10.1029/2009JA014223.

Shprits, Y. Y., and R. M. Thorne (2004), Time dependent radial diffusion modeling of relativistic electrons with realistic loss rates, *Geophysical Research Letters*, *31*(8), doi:10.1029/2004GL019591.

Shprits, Y. Y., R. M. Thorne, G. D. Reeves, and R. Friedel (2005), Radial diffusion modeling with empirical lifetimes: comparison with CRRES observations, *Annales Geophysicae*, *23*(4), 1467–1471.

Shprits, Y. Y., R. M. Thorne, R. Friedel, G. D. Reeves, J. Fennell, D. N. Baker, and S. G. Kanekal (2006), Outward radial diffusion driven by losses at magnetopause, *Journal of Geophysical Research: Space Physics*, *111*(A11), doi:10.1029/2006JA011657, a11214.

Shprits, Y. Y., S. R. Elkington, N. P. Meredith, and D. A. Subbotin (2008a), Review of modeling of losses and sources of relativistic electrons in the outer radiation belt I: Radial transport, *Journal of Atmospheric and Solar-Terrestrial Physics*, *70*(14), 1679 – 1693, doi:http://dx.doi.org/10.1016/j.jastp.2008.06.008, dynamic Variability of Earth's Radiation BeltsAGU Fall Meeting.

Shprits, Y. Y., D. A. Subbotin, N. P. Meredith, and S. R. Elkington (2008b), Review of modeling of losses and sources of relativistic electrons in the outer radiation belt II: Local acceleration and loss, *Journal of Atmospheric and Solar-Terrestrial Physics*, *70*(14), 1694 – 1713, doi:http://dx.doi.org/10.1016/j.jastp.2008.06.014, dynamic Variability of Earth's Radiation BeltsAGU Fall Meeting.

Shprits, Y. Y., D. Subbotin, and B. Ni (2009), Evolution of electron fluxes in the outer radiation belt computed with the VERB code, *Journal of Geophysical Research: Space Physics*, *114*(A11), doi:10.1029/2008JA013784.

Shprits, Y. Y., D. Subbotin, A. Drozdov, M. E. Usanova, A. Kellerman, K. Orlova, D. N. Baker, D. L. Turner, and K.-C. Kim (2015a), Unusual stable trapping of the ultrarelativistic electrons in the Van Allen radiation belts, *Nature Physics*, *9*, 699, doi:10.1029/2008JA013784.

Shprits, Y. Y., A. C. Kellerman, A. Y. Drozdov, H. E. Spence, G. D. Reeves, and D. N. Baker (2015b), Combined convective and diffusive simulations: VERB-4D comparison with 17 March 2013 Van Allen Probes observations, *Geophysical Research Letters*, *42*(22), 9600–9608, doi:10.1002/2015GL065230.

Shprits, Y. Y., A. Y. Drozdov, M. Spasojevic, A. C. Kellerman, M. E. Usanova, M. J. Engebretson, O. V. Agapitov, I. S. Zhelavskaya, T. J. Raita, H. E. Spence, D. N. Baker, H. Zhu, and N. A. Aseev (2016), Wave-induced loss of ultra-relativistic electrons in the Van Allen radiation belts, *Nature Communications*, *7*(102), 9600–9608, doi:10.1038/ncomms12883.

Shprits, Y. Y., R. B. Horne, A. C. Kellerman, and A. Y. Drozdov (2018), The dynamics of Van Allen belts revisited, *Nature Physics*, *14*(102), 9600–9608, doi:10.1038/nphys4350.

Sorathia, K. A., V. G. Merkin, A. Y. Ukhorskiy, B. H. Mauk, and D. G. Sibeck (2017), Energetic particle loss through the magnetopause: A combined global MHD and test-particle study, *Journal of Geophysical Research: Space Physics*, *122*(9), 9329–9343, doi:10.1002/2017JA024268.

Sorathia, K. A., A. Y. Ukhorskiy, V. G. Merkin, J. F. Fennell, and S. G. Claudepierre (2018), Modeling the Depletion and Recovery of the Outer Radiation Belt During a Geomagnetic Storm: Combined MHD and Test Particle Simulations, *Journal of Geophysical Research: Space Physics*, *0*(ja), doi:10.1029/2018JA025506.

Stix, T. H. (1962), *The Theory of Plasma Waves*, New York: McGraw-Hill.

Subbotin, D., Y. Shprits, and B. Ni (2010), Three-dimensional VERB radiation belt simulations including mixed diffusion, *Journal of Geophysical Research: Space Physics*, *115*(A3), doi:10.1029/2009JA015070.

Subbotin, D. A., and Y. Y. Shprits (2009), Three-dimensional modeling of the radiation belts using the versatile electron radiation belt (VERB) code, *Space Weather*, *7*(10), 1–15, doi:10.1029/2008SW000452.

Subbotin, D. A., and Y. Y. Shprits (2012), Three-dimensional radiation belt simulations in terms of adiabatic invariants using a single numerical grid, *Journal of Geophysical Research: Space Physics*, *117*(A5), doi:10.1029/2011JA017467.

Takahashi, K., R. E. Denton, W. Kurth, C. Kletzing, J. Wygant, J. Bonnell, L. Dai, K. Min, C. W. Smith, and R. MacDowall (2014), Externally driven plasmaspheric ULF waves observed by the Van Allen Probes, *Journal of Geophysical Research: Space Physics*, *120*(1), 526–552, doi:10.1002/2014JA020373.

Tao, X., J. Bortnik, R. M. Thorne, J. M. Albert, and W. Li (2012), Effects of amplitude modulation on nonlinear interactions between electrons and chorus waves, *Geophysical Research Letters*, *39*(6), doi:10.1029/2012GL051202.

Thébault, E., C. C. Finlay, C. D. Beggan, P. Alken, J. Aubert, O. Barrois, F. Bertrand, T. Bondar, A. Boness, L. Brocco, E. Canet, A. Chambodut, A. Chulliat, P. Coïsson, F. Civet, A. Du, A. Fournier, I. Fratter, N. Gillet, B. Hamilton, M. Hamoudi, G. Hulot, T. Jager, M. Korte, W. Kuang, X. Lalanne, B. Langlais, J.-M. Léger, V. Lesur, F. J. Lowes, S. Macmillan, M. Mandea, C. Manoj, S. Maus, N. Olsen, V. Petrov, V. Ridley, M. Rother, T. J. Sabaka, D. Saturnino, R. Schachtschneider, O. Sirol, A. Tangborn, A. Thomson, L. Tøffner-Clausen, P. Vigneron, I. Wardinski, and T. Zvereva (2015), International Geomagnetic Reference Field: the 12th generation, *Earth, Planets and Space*, *67*(1), 79, doi:10.1186/s40623-015-0228-9.

Thomsen, M. F., C. K. Goertz, and J. A. Van Allen (1977a), A determination of the L dependence of the radial diffusion coefficient for protons in Jupiter's inner magnetosphere, *Journal of Geophysical Research*, *82*(25), 3655–3658, doi:10.1029/JA082i025p03655.

Thomsen, M. F., C. K. Goertz, and J. A. Van Allen (1977b), On determining magnetospheric diffusion coefficients from the observed effects of Jupiter's satellite Io, *Journal of Geophysical Research*, *82*(35), 5541–5550, doi:10.1029/JA082i035p05541.

Thorne, R. M. (1972), The Importance of Wave Particle Interactions in the Magnetosphere, in *Critical Problems of Magnetospheric Physics*, edited by E. R. Dyer, p. 211.

Thorne, R. M. (2010), Radiation belt dynamics: The importance of wave-particle interactions, *Geophysical Research Letters*, *37*(22), doi:10.1029/2010GL044990.

Thorne, R. M., T. P. O'Brien, Y. Y. Shprits, D. Summers, and R. B. Horne (2005), Timescale for MeV electron microburst loss during geomagnetic storms, *Journal of Geophysical Research: Space Physics*, *110*(A9), doi:10.1029/2004JA010882.

Thorne, R. M., W. Li, B. Ni, Q. Ma, J. Bortnik, L. Chen, D. N. Baker, H. E. Spence, G. D. Reeves, M. G. Henderson, C. A. Kletzing, W. S. Kurth, G. B. Hospodarsky, J. B. Blake, J. F. Fennell, S. G. Claudepierre, and S. G. Kanekal (2013), Rapid local acceleration of relativistic radiation-belt electrons by magnetospheric chorus, *Nature*, *504*, 411, doi:10.1038/nature12889.

Tsyganenko, N. A. (1989), A magnetospheric magnetic field model with a warped tail current sheet, *Planetary and Space Science*, *37*(1), 5 – 20, doi:https://doi.org/10.1016/0032-0633(89)90066-4.

Tsyganenko, N. A., and M. I. Sitnov (2005), Modeling the dynamics of the inner magnetosphere during strong geomagnetic storms, *Journal of Geophysical Research: Space Physics*, *110*(A3), doi:10.1029/2004JA010798.

Tsyganenko, N. A., and M. I. Sitnov (2007), Magnetospheric configurations from a high-resolution data-based magnetic field model, *Journal of Geophysical Research: Space Physics*, *112*(A6), doi:10.1029/2007JA012260.

Tsyganenko, N. A., and D. P. Stern (1996), Modeling the global magnetic field of the large-scale Birkeland current systems, *Journal of Geophysical Research: Space Physics*, *101*(A12), 27,187–27,198, doi:10.1029/96JA02735.

Tsyganenko, N. A., H. J. Singer, and J. C. Kasper (2003), Storm-time distortion of the inner magnetosphere: How severe can it get?, *Journal of Geophysical Research: Space Physics*, *108*(A5), doi:10.1029/2002JA009808.

Tu, W., X. Li, Y. Chen, G. D. Reeves, and M. Temerin (2009), Storm-dependent radiation belt electron dynamics, *Journal of Geophysical Research: Space Physics*, *114*(A2), doi:10.1029/2008JA013480, a02217.

Tu, W., G. S. Cunningham, Y. Chen, M. G. Henderson, E. Camporeale, and G. D. Reeves (2013), Modeling radiation belt electron dynamics during GEM challenge intervals with the DREAM3D diffusion model, *Journal of Geophysical Research: Space Physics*, *118*(10), 6197–6211, doi:10.1002/jgra.50560, 2013JA019063.

Tu, W., G. S. Cunningham, Y. Chen, S. K. Morley, G. D. Reeves, J. B. Blake, D. N. Baker, and H. Spence (2014), Event-specific chorus wave and electron seed population models in DREAM3D using the Van Allen Probes, *Geophysical Research Letters*, *41*(5), 1359–1366, doi:10.1002/2013GL058819.

Turner, D. L., Y. Shprits, M. Hartinger, and V. Angelopoulos (2012), Explaining sudden losses of outer radiation belt electrons during geomagnetic storms, *Nature Physics*, *8*, 208–212, doi:10.1038/nphys2185.

Turner, D. L., S. K. Morley, Y. Miyoshi, B. Ni, and C.-L. Huang (2013a), *Outer Radiation Belt Flux Dropouts: Current Understanding and Unresolved Questions*, pp. 195–212, American Geophysical Union (AGU), doi:10.1029/2012GM001310.

Turner, D. L., V. Angelopoulos, W. Li, M. D. Hartinger, M. Usanova, I. R. Mann, J. Bortnik, and Y. Shprits (2013b), On the storm-time evolution of relativistic electron phase space density in Earth's outer radiation belt, *Journal of Geophysical Research: Space Physics*, *118*(5), 2196–2212, doi:10.1002/jgra.50151.

Turner, D. L., S. G. Claudepierre, J. F. Fennell, T. P. O'Brien, J. B. Blake, C. Lemon, M. Gkioulidou, K. Takahashi, G. D. Reeves, S. Thaller, A. Breneman, J. R. Wygant, W. Li, A. Runov, and V. Angelopoulos (2015), Energetic electron injections deep into the inner magnetosphere associated with substorm activity, *Geophysical Research Letters*, *42*(7), 2079–2087, doi:10.1002/2015GL063225.

Ukhorskiy, A. Y., and M. I. Sitnov (2008), Radial transport in the outer radiation belt due to global magnetospheric compressions, *Journal of Atmospheric and Solar-Terrestrial Physics*, *70*(14), 1714 – 1726, doi:http://dx.doi.org/10.1016/j.jastp.2008.07.018.

Ukhorskiy, A. Y., and M. I. Sitnov (2013), Dynamics of Radiation Belt Particles, *Space Science Reviews*, *179*(1), 545–578, doi:10.1007/s11214-012-9938-5.

Ukhorskiy, A. Y., M. I. Sitnov, R. M. Millan, and B. T. Kress (2011), The role of drift orbit bifurcations in energization and loss of electrons in the outer radiation belt, *Journal of Geophysical Research: Space Physics*, *116*(A9), doi:10.1029/2011JA016623.

Ukhorskiy, A. Y., M. I. Sitnov, R. M. Millan, B. T. Kress, and D. C. Smith (2014), Enhanced radial transport and energization of radiation belt electrons due to drift orbit bifurcations, *Journal of Geophysical Research: Space Physics*, *119*(1), 163–170, doi:10.1002/2013JA019315.

Ukhorskiy, A. Y., K. A. Sorathia, V. G. Merkin, M. I. Sitnov, D. G. Mitchell, and M. Gkioulidou (2018), Ion Trapping and Acceleration at Dipolarization Fronts: High-Resolution MHD/Test-Particle Simulations, *Journal of Geophysical Research: Space Physics*, *0*(ja), doi:10.1029/2018JA025370.

Usanova, M. E., A. Drozdov, K. Orlova, I. R. Mann, Y. Shprits, M. T. Robertson, D. L. Turner, D. K. Milling, A. Kale, D. N. Baker, S. A. Thaller, G. D. Reeves, H. E. Spence, C. Kletzing, and J. Wygant (2014), Effect of EMIC waves on relativistic and ultra-relativistic electron populations: Ground-based and Van Allen Probes observations, *Geophysical Research Letters*, *41*(5), 1375–1381, doi:10.1002/2013GL059024.

Vampola, A. L. (1997), Outer zone energetic electron environment update, in *Conference on the High Energy Radiation Background in Space. Workshop Record*, pp. 128–136, doi:10.1109/CHERBS.1997.660263.

Vampola, A. L., J. V. Osborn, and B. M. Johnson (1992), CRRES magnetic electron spectrometer AFGL-701-5A (MEA), *Journal of Spacecraft and Rockets*, *29*, 592–595, doi:10.2514/3.25504.

Van Allen, J., and L. Frank (1959), Radiation Measurements to 658,300 km. with Pioneer IV, *Nature*, *184*, 219–224, doi:10.1038/184219a0.

Van Allen, J. A. (1959), The geomagnetically trapped corpuscular radiation, *Journal of Geophysical Research*, *64*(11), 1683–1689, doi:10.1029/JZ064i011p01683.

Vette, J. (1966), Models of the trapped radiation environment, Volume I: Inner zone protons and electron, *Tech. rep.*, NASA SP-3024, Washington, D.C.

Walt, M. (1970), Radial Diffusion of Trapped Particles, in *Particles and Fields in the Magnetosphere*, edited by B. M. McCormac, p. 410, Springer Netherlands, Dordrecht.

Walt, M. (1971), Radial diffusion of trapped particles and some of its consequences, *Reviews of Geophysics*, *9*(1), 11–25, doi:10.1029/RG009i001p00011.

Walt, M. (1994), *Introduction to Geomagnetically Trapped Radiation*, Cambridge Atmospheric and Space Science Series, Cambridge University Press, doi:10.1017/CBO9780511524981.

Walt, M., and W. M. MacDonald (1964), The influence of the Earth's atmosphere on geomagnetically trapped particles, *Reviews of Geophysics*, *2*(4), 543–577, doi:10.1029/RG002i004p00543.

Welling, D. T., V. K. Jordanova, S. G. Zaharia, A. Glocer, and G. Toth (2011), The effects of dynamic ionospheric outflow on the ring current, *Journal of Geophysical Research: Space Physics*, *116*(A2), doi:10.1029/2010JA015642.

Wilson, L. B., C. A. Cattell, P. J. Kellogg, J. R. Wygant, K. Goetz, A. Breneman, and K. Kersten (2011), The properties of large amplitude whistler mode waves in the magnetosphere: Propagation and relationship with geomagnetic activity, *Geophysical Research Letters*, *38*(17), doi:10.1029/2011GL048671.

Woodfield, E. E., R. B. Horne, S. A. Glauert, J. D. Menietti, and Y. Y. Shprits (2014), The origin of Jupiter's radiation belts, *Journal of Geophysical Research: Space Physics*, *119*(5), 3490–3502, doi:10.1002/2014JA019891.

Wygant, J., F. Mozer, M. Temerin, J. Blake, N. Maynard, H. Singer, and M. Smiddy (1994), Large amplitude electric and magnetic field signatures in the inner magnetosphere during injection of 15 MeV electron drift echoes, *Geophysical Research Letters*, *21*(16), 1739–1742, doi:10.1029/94GL00375.

Wygant, J. R., J. W. Bonnell, K. Goetz, R. E. Ergun, F. S. Mozer, S. D. Bale, M. Ludlam, P. Turin, P. R. Harvey, R. Hochmann, K. Harps, G. Dalton, J. McCauley, W. Rachelson, D. Gordon, B. Donakowski, C. Shultz, C. Smith, M. Diaz-Aguado, J. Fischer, S. Heavner, P. Berg, D. M. Malsapina, M. K. Bolton, M. Hudson, R. J. Strangeway, D. N. Baker, X. Li, J. Albert, J. C. Foster, C. C. Chaston, I. Mann, E. Donovan, C. M. Cully, C. A. Cattell, V. Krasnoselskikh, K. Kersten, A. Brenneman, and J. B. Tao (2013), The Electric Field and Waves Instruments on the Radiation Belt Storm Probes Mission, *Space Science Reviews*, *179*(1), 183–220, doi:10.1007/s11214-013-0013-7.

Xiao, F., C. Yang, Z. He, Z. Su, Q. Zhou, Y. He, C. A. Kletzing, W. S. Kurth, G. B. Hospodarsky, H. E. Spence, G. D. Reeves, H. O. Funsten, J. B. Blake, D. N. Baker, and J. R. Wygant (2014), Chorus acceleration of radiation belt relativistic electrons during March 2013 geomagnetic storm, *Journal of Geophysical Research: Space Physics*, *119*(5), 3325–3332, doi:10.1002/2014JA019822.

Xu, F., and J. E. Borovsky (2015), A new four-plasma categorization scheme for the solar wind, *Journal of Geophysical Research: Space Physics*, *120*(1), 70–100, doi:10.1002/2014JA020412.

Xudong, G., Z. Zhengyu, N. Binbin, S. Yuri, and Z. Chen (2011), Statistical analysis of pitch angle distribution of radiation belt energetic electrons near the geostationary orbit: CRRES observations, *Journal of Geophysical Research: Space Physics*, *116*(A1), doi:10.1029/2010JA016052.

Yiqun, Y., J. Vania, W. Dan, L. Brian, C. S. G., and K. Craig (2014), The role of ring current particle injections: Global simulations and Van Allen Probes observations during 17 March 2013 storm, *Geophysical Research Letters*, *41*(4), 1126–1132, doi:10.1002/2014GL059322.

Yu, Y., J. Koller, and S. K. Morley (2013), Quantifying the effect of magnetopause shadowing on electron radiation belt dropouts, *Annales Geophysicae*, *31*(11), 1929–1939, doi:10.5194/angeo-31-1929-2013.

Yu, Y., V. K. Jordanova, A. J. Ridley, J. M. Albert, R. B. Horne, and C. A. Jeffery (2016), A new ionospheric electron precipitation module coupled with RAM-SCB within the geospace general circulation model, *Journal of Geophysical Research: Space Physics*, *121*(9), 8554–8575, doi:10.1002/2016JA022585.

Zaharia, S., V. K. Jordanova, M. F. Thomsen, and G. D. Reeves (2006), Self-consistent modeling of magnetic fields and plasmas in the inner magnetosphere: Application to a geomagnetic storm, *Journal of Geophysical Research: Space Physics*, *111*(A11), doi:10.1029/2006JA011619.

Zeeuw, D. L. D., T. I. Gombosi, C. P. T. Groth, K. G. Powell, and Q. F. Stout (2000), An adaptive MHD method for global space weather simulations, *IEEE Transactions on Plasma Science*, *28*(6), 1956–1965, doi:10.1109/27.902224.

Zhao, H., X. Li, J. B. Blake, J. F. Fennell, S. G. Claudepierre, D. N. Baker, A. N. Jaynes, and D. M. Malaspina (2014a), Characteristics of pitch angle distributions of hundreds of keV electrons in the slot region and inner radiation belt, *Journal of Geophysical Research: Space Physics*, *119*(12), 9543–9557, doi:10.1002/2014JA020386.

Zhao, H., X. Li, J. B. Blake, J. F. Fennell, S. G. Claudepierre, D. N. Baker, A. N. Jaynes, D. M. Malaspina, and S. G. Kanekal (2014b), Peculiar pitch angle distribution of relativistic electrons in the inner radiation belt and slot region, *Geophysical Research Letters*, *41*(7), 2250–2257, doi:10.1002/2014GL059725.

Zheng, L., A. A. Chan, T. P. O'Brien, W. Tu, G. S. Cunningham, J. M. Albert, and S. R. Elkington (2016), Effects of magnetic drift shell splitting on electron diffusion in the radiation belts, *Journal of Geophysical Research: Space Physics*, *121*(12), 11,985–12,000, doi:10.1002/2016JA023438.

université PARIS-SACLAY | École doctorale de mathématiques Hadamard (EDMH)

Titre : Modélisation physique et numérique de la dynamique des électrons de haute énergie piégés dans la ceinture de radiation externe de la magnétosphère terrestre

Mots clefs : Ceintures de radiation, Équation de Fokker-Planck, Diffusion radiale, Temps de vie de l'électron, Champ magnétique non dipolaire, Invariants adiabatiques

Résumé : Les satellites sont vulnérables aux particules de haute énergie piégées dans les ceintures de Van Allen. Afin d'en assurer la protection, il est nécessaire de prédire avec précision la dynamique des électrons au sein de la magnétosphère.
Dans un premier temps nous proposons une méthode originale de résolution analytique de l'équation de Fokker-Planck réduite qui modélise le transport et les pertes des électrons de la magnétosphère interne. La résolution repose sur une technique de décomposition spectrale. Si la solution analytique s'avère utile pour mettre en exergue certaines propriétés physiques des ceintures de radiation, elle est également pertinente pour valider le code numérique de résolution de l'équation de Fokker-Planck réduite, développé en partie durant la thèse. Ce dernier nous amène à généraliser l'étude précédente en illustrant l'évolution des flux d'électrons pour diverses énergies et positions. Nous prouvons notamment que la structure des ceintures de radiation ainsi que leurs temps d'évolution ne dépendent que de quelques facteurs bien choisis. Dans la perspective de reproduire un événement particulier de retour au calme après un orage magnétique, mesuré par les satellites de la NASA dédiés aux ceintures de radiation, nous sommes en mesure de simuler la précipitation des électrons dans l'atmosphère terrestre causée par les interactions avec les ondes électromagnétiques de la magnétosphère. L'utilisation de conditions bâties sur des données empiriques et spécifiques à la période en question nous permet de corroborer les flux observés. Enfin, l'influence du champ magnétique terrestre sur la dynamique des ceintures de radiation est étudiée sous divers aspects. Nous nous concentrons sur la ceinture externe pour comprendre comment les asymétries du champ magnétique, considérablement façonnées par l'activité solaire, affectent notre manière de concilier théorie et observations. Nous explorons également l'importance de certains processus diffusifs nouveaux et cachés, qui émergent à cause de l'irrégularité naturelle du champ magnétique au plus proche voisinage de la Terre.

Title : Physical and numerical modeling of the dynamics of high-energy electrons trapped in the outer radiation belt of the Earth's magnetosphere

Keywords : Radiation belts, Fokker-Planck equation, Radial diffusion, Electron lifetime, Non dipole magnetic field, Adiabatic invariants

Abstract : Satellites are vulnerable to high-energy particles trapped in the Van Allen belts. To ensure their protection, it is necessary to predict properly the electron dynamics in the magnetosphere.
We first propose an original method to find the analytical solution of the reduced Fokker-Planck equation that models the transport and loss of electrons in the inner magnetosphere. The resolution relies on an eigenfunction expansion approach. If the analytical solution is proven to be useful at uncovering some of the physical properties of the radiation belts, it is also relevant to validate the numerical code that solves the reduced Fokker-Planck equation, which has been partly developed during the PhD. The latter code is used to generalize the previous study in illustrating the evolution of the electron fluxes for various energies and locations. We demonstrate that the structure of the radiation belts as well as their dynamical timescales only depend on a few well-chosen parameters. In the perspective of reproducing a specific storm-recovery event reported by the NASA Van Allen Probes, we are able to simulate the electron scattering in the Earth's atmosphere due to the interaction with magnetospheric electromagnetic waves. The consideration of data-driven and event-specific conditions enables us to corroborate the observed fluxes. Finally, various influences of the Earth's magnetic field on the dynamics of the radiation belts are investigated. We focus on the outer belt to find out how the magnetic field asymmetries, which are strongly shaped by solar activity, affect the way of conciliating theory and observations. We also explore the importance of new hidden diffusive processes that emerge due to the natural irregularity of the magnetic field in the closest vicinity of the Earth.

Université Paris-Saclay
Espace Technologique / Immeuble Discovery
Route de l'Orme aux Merisiers RD 128 / 91190 Saint-Aubin, France